D 3715

[07]

EurJIC

European Journal of Inorganic Chemistry

7/2012
1st March Issue

Eur. J. Inorg. Chem. 2012, 1009–1148

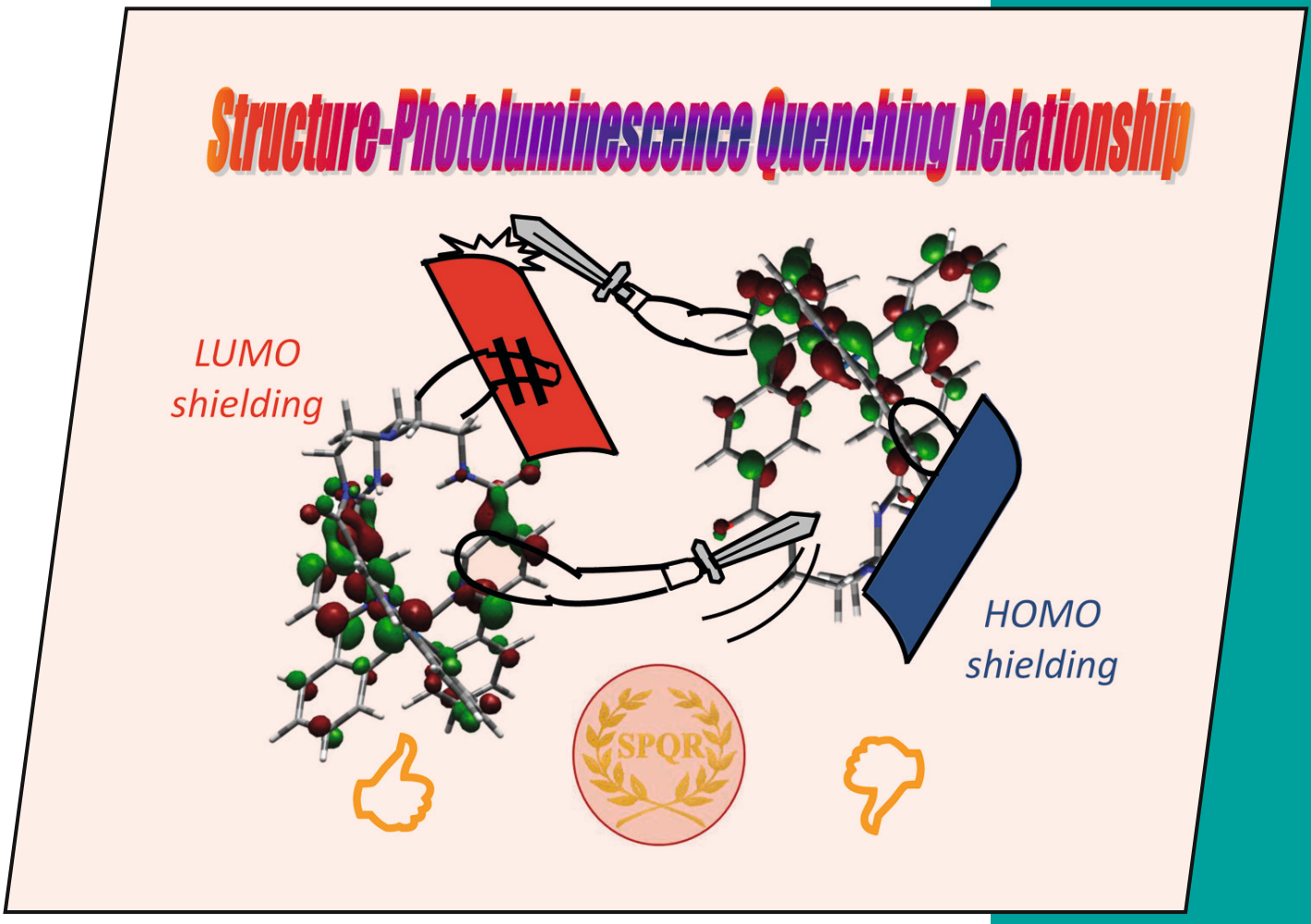

Cover Picture

Luisa De Cola, Aldrik H. Velders et al.

Iridium(III)–Tris(phenylpyridine) Complexes

A Journal of

ChemPubSoc Europe

WILEY-VCH

www.eurjic.org

EJICFK (7) 1009–1148 (2012) · ISSN 1434-1948 · No. 7/2012

EurJIC
European Journal of Inorganic Chemistry

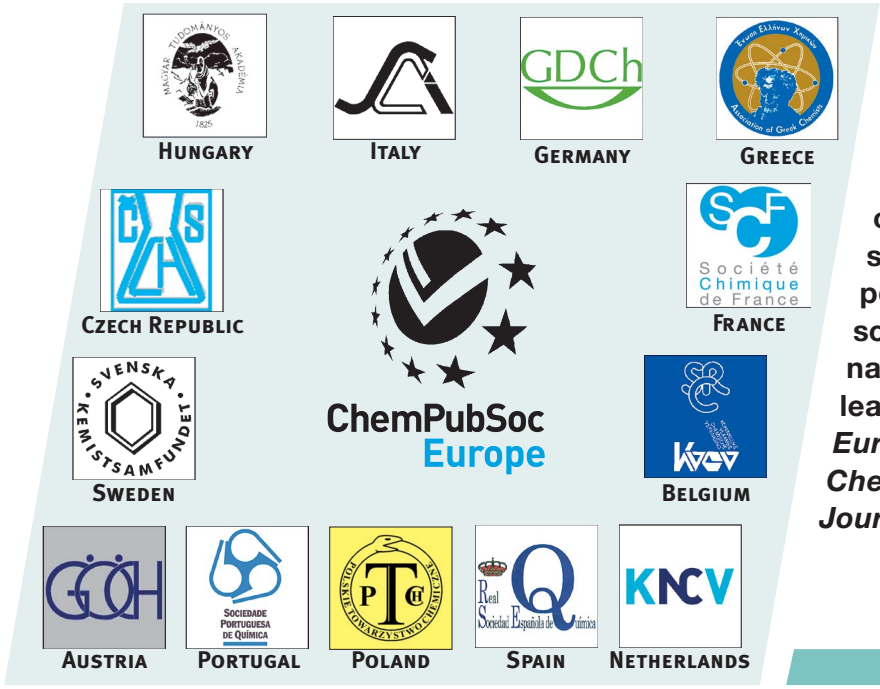

EurJIC is a journal of ChemPubSoc Europe, a union of 16 European chemical societies formed for the purpose of publishing high-quality science. All owners merged their national journals to form two leading chemistry journals, the *European Journal of Inorganic Chemistry* and the *European Journal of Organic Chemistry*.

Other ChemPubSoc Europe journals are *Chemistry – A European Journal*, *ChemBioChem*, *ChemPhysChem*, *ChemMedChem*, *ChemSusChem*, *ChemCatChem*, *ChemPlusChem* and *ChemistryOpen*.

COVER PICTURE

The cover picture shows two "gladiator compounds" illustrating the Structure-Photoluminescence Quenching Relationship (SPQR) observed in hemicaged Ir(III)−tris(2-phenylpyridine) complexes bearing a capping unit ("shield"), either on the pyridine or on the phenyl side. The presence of a capping unit on the pyridine side induces a dramatic 40 % decrease in oxygen quenching of the luminescence with respect to the uncapped complex, as a consequence of the shielding of the LUMO; conversely, shielding of the phenyl rings, where the HOMO is partially localized, does not induce any change in the degree of oxygen quenching. The Roman Empire initialism SPQR and the „hemicaged" laurel further symbolize this study, with the emperor's thumps up and down indicating the winning and losing gladiator, respectively. Details of the synthesis and the structural, photophysical, theoretical, and electrochemical characterization are discussed in the article by L. De Cola, A. H. Velders et al. on p. 1025ff.

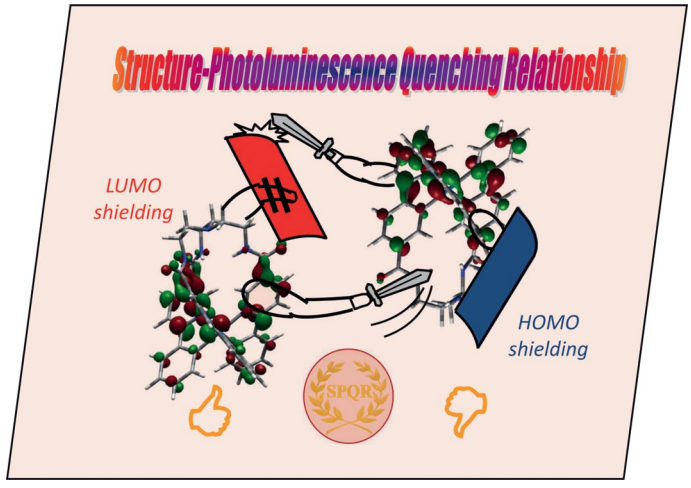

EurJIC
European Journal of Inorganic Chemistry

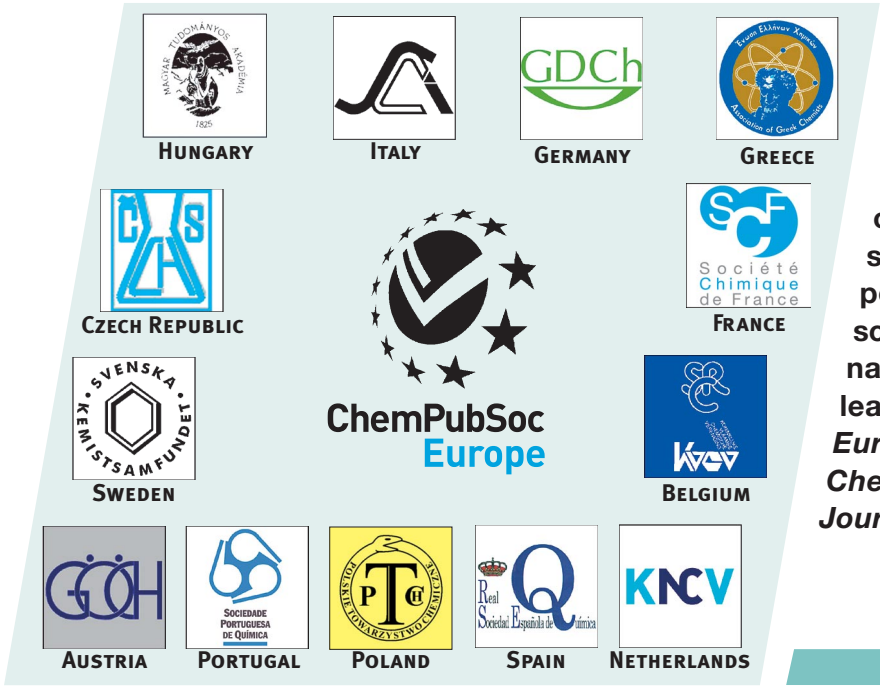

EurJIC is a journal of ChemPubSoc Europe, a union of 16 European chemical societies formed for the purpose of publishing high-quality science. All owners merged their national journals to form two leading chemistry journals, the *European Journal of Inorganic Chemistry* and the *European Journal of Organic Chemistry*.

Other ChemPubSoc Europe journals are *Chemistry – A European Journal*, *ChemBioChem*, *ChemPhysChem*, *ChemMedChem*, *ChemSusChem*, *ChemCatChem*, *ChemPlusChem* and *ChemistryOpen*.

COVER PICTURE

The cover picture shows two "gladiator compounds" illustrating the Structure-Photoluminescence Quenching Relationship (SPQR) observed in hemicaged Ir(III)−tris(2-phenylpyridine) complexes bearing a capping unit ("shield"), either on the pyridine or on the phenyl side. The presence of a capping unit on the pyridine side induces a dramatic 40 % decrease in oxygen quenching of the luminescence with respect to the uncapped complex, as a consequence of the shielding of the LUMO; conversely, shielding of the phenyl rings, where the HOMO is partially localized, does not induce any change in the degree of oxygen quenching. The Roman Empire initialism SPQR and the „hemicaged" laurel further symbolize this study, with the emperor's thumps up and down indicating the winning and losing gladiator, respectively. Details of the synthesis and the structural, photophysical, theoretical, and electrochemical characterization are discussed in the article by L. De Cola, A. H. Velders et al. on p. 1025ff.

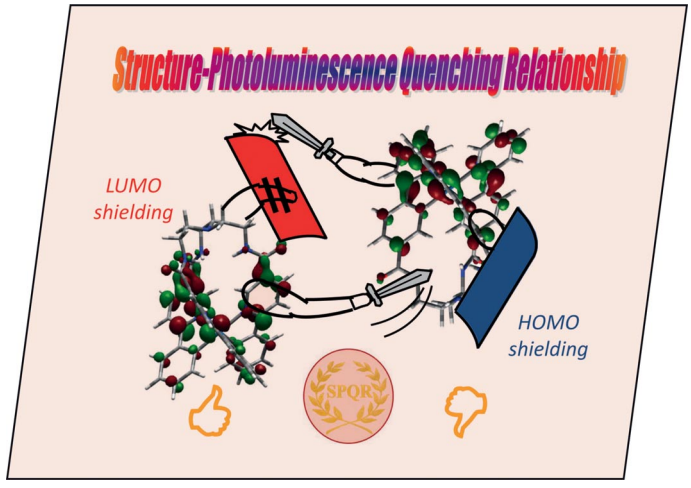

CONTENTS

SHORT COMMUNICATION

Manganese Difluoride Nanostructures

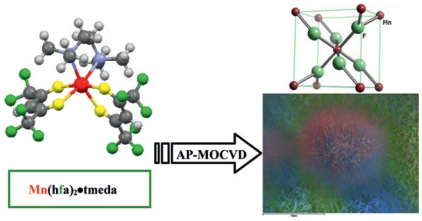

A mild approach, atmospheric pressure metalorganic chemical vapor deposition (AP-MOCVD), was applied for the fabrication of pompon-like assemblies of MnF_2 nanorods. $Mn(hfa)_2$·tmeda [(Hhfa = 1,1,1,5,5,5-hexafluoro-2,4-pentandione, tmeda = *N*,*N*,*N*′,*N*′-tetramethylethylenediamine)] was used as a single-source precursor.

Keywords: Nanostructures / Manganese / Fluorides / Single-source precursors / Chemical vapor deposition

FULL PAPERS

Structure–Photoluminescence Quenching

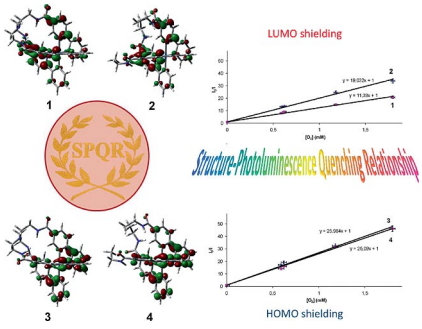

A family of four tris(2-phenylpyridine)-based Ir^{III} complexes with hemicaged or open (without capping unit but with similar functional groups on the ligand) structure are reported. Within the context of the parent tris(2-phenylpyridine) and the full-cage iridium(III) complexes, structure–photoluminescence quenching relationships (SPQR) of the four complexes have been investigated.

Keywords: Iridium / Luminescence / Photoluminescence / Electrochemistry / Oxygen sensitivity / Density functional calculation

Porphyrin Chemistry

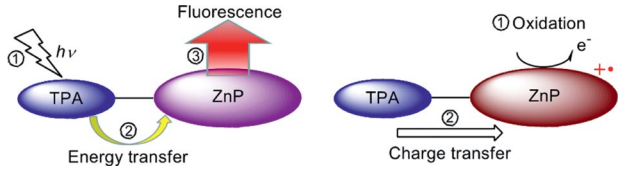

A series of porphyrin–triphenylamine (TPA) conjugates have been characterized by spectral and electrochemical methods. Due to the antenna effect of these conjugates, the fluorescence intensity was enhanced. The oscillator strength increases as the number of TPA substituents increases for the charge-transfer band in the near-IR region upon porphyrin-ring oxidation.

Keywords: Electrochemistry / Electron transfer / Charge transfer / Energy transfer / Luminescence / Zinc / Porphyrinoids / Antenna effect

Metal−Organic Macrocycles

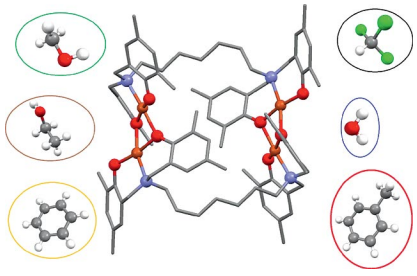

Keywords: Copper / Supramolecular chemistry / Magnetic properties / Density functional calculations

The geometrical parameters and magnetic properties of structurally interesting metal−organic macrocycles $\{[Cu_4(L)_2]\cdot xS$ and $[Cu_4(L)_2(H_2O)_2]\cdot xS\}$ can be varied drastically by changing the crystallization solvent. Six novel structures are reported along with their calculated magnetic coupling constants.

Gas-Phase Chemistry

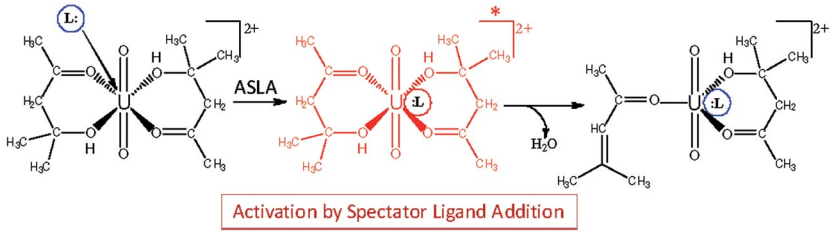

Keywords: Actinides / Uranium / Gas-phase chemistry

Gas-phase addition of a basic ligand to dipositive uranyl coordination complexes comprising diacetone alcohol results in dehydration to produce mesityl oxide. A novel attribute of this process is that a ligand exothermically associates to a coordination complex, providing excitation to induce chemistry in other ligands; the added "spectator ligand" remains intact.

Silver Sulfonate Complexes

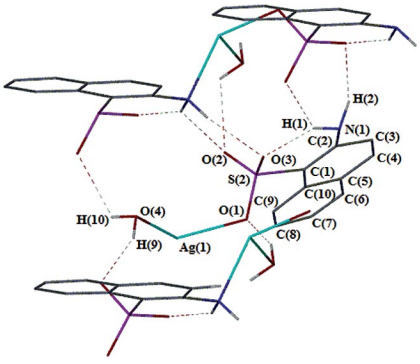

Keywords: Silver / Arenesulfonates / Zwitterions / Coordination polymers

Silver(I) amino-arenesulfonate complexes of the formula $[Ag(O_3SR)]_\infty$ were formed through treatment of a variety of amino-arenesulfonic acids with Ag_2O in water. Crystal structure analysis on four complexes indicate 1D chains and 2D and 3D networks depending on the nature and position of the amino (or N) substituent. FTIR and MS studies suggest all the complexes are polymeric in the solid state.

CO-Releasing Molecules

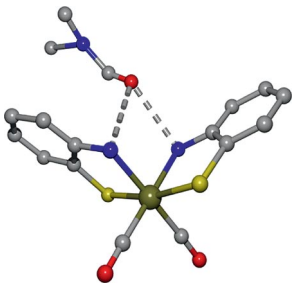

Keywords: Carbonyl ligands / Carbon monoxide / CO-releasing molecules / Iron / Ruthenium / Medicinal chemistry

CO-releasing molecules are important as therapeutic agents and pharmaceuticals. Light-triggered CO release can be achieved for iron-containing carbonyl complexes stabilized with aminoethylthiolate or related bases, whereas homologous ruthenium derivatives are stable when exposed to visible light. These complexes capture neutral Lewis bases through N−H···O hydrogen bridges.

CONTENTS

Vanadium Coordination Chemistry

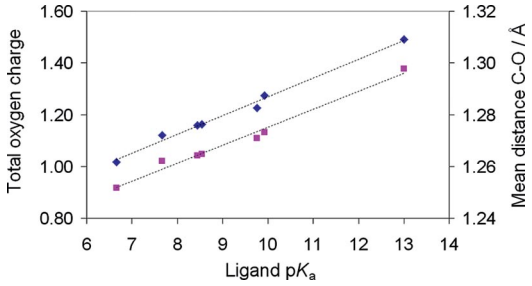

The chelating and spectroscopic properties of pyrone and pyridinone derivatives, tropolone and catechol (which form very effective antidiabetic compounds) towards the VO^{2+} ion are explained in terms of aromaticity of the fully deprotonated form of the ligands, and of total electric charge on the oxygen donors.

Multidentate Enaminone Ligands

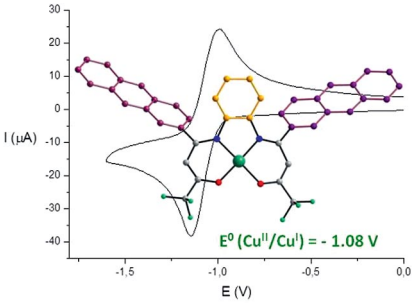

Structural variation of the trifluoromethylated enaminone building block gave rise to new bidentate and tetradentate ligands that bear redox-active units (anthracene, azobenzene and tetrathiafulvalene). Their coordination chemistry with copper(II), structural characterization, redox chemistry and UV/Vis properties of the ligands and complexes have been investigated.

Iron Carbonyl Thiocarbonyls

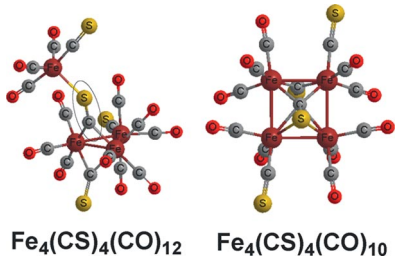

The lowest energy $Fe_4(CS)_4(CO)_{12}$ structures have a central Fe_3 triangle with an exotriangular iron atom joined to the Fe_3 triangle by a four-electron donor "end-on" CS bridge. An Fe_4 rhombus bridged by a six-electron donor η^2-μ_4-CS group is found in the lowest energy structures of $Fe_4(CS)_4(CO)_{10}$ and $Fe_4(CS)_4(CO)_9$ and makes $Fe_4(CS)_4(CO)_{10}$ viable enough to be a promising synthetic objective.

Metal–Metal Communication

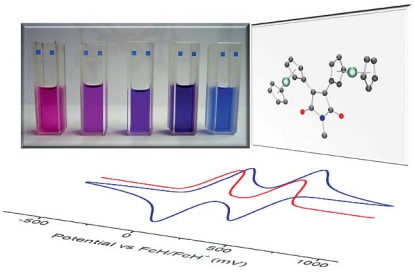

Ferrocenylmaleimides are accessible by bromine shift and oxidation with subsequent Negishi ferrocenylation of dibromo-*N*-methylpyrrole. Electrochemical and spectroelectrochemical studies highlight their redox and electron-transfer properties. Additionally, the ferrocenylmaleimides show a significant solvatochromic behavior.

Coordination Polymers

Keywords: Heterometallic complexes / Coordination polymers / Platinum / Silver / Ag–C interactions

Not (only) the available second-ring N atom of pyrazole and pyrazolate ligands in complexes of Pt^{II} appears to be the preferred Ag^+ binding site in moderately acidic aqueous solution, but rather the C4 atom and/or the C4,C5 double bond.

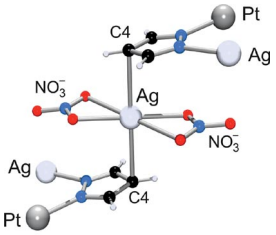

Ag-η¹-C4(pyrazole)!

Multinuclear Zinc Complexes

Keywords: Zinc / Halides / Multinuclear complexes / Schiff bases

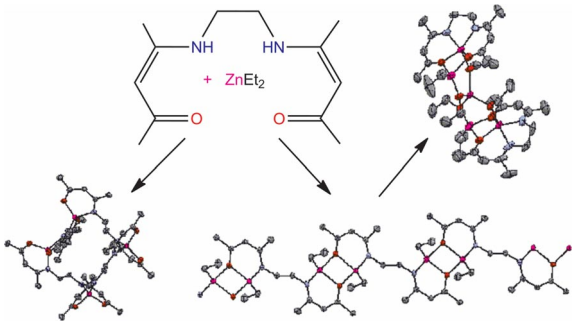

The coordination preferences of the tetradentate Schiff base *N*,*N*′-ethylenebis(4-iminopentan-2-one), H_2**L**, with Et_2Zn under various stoichiometries were investigated and the reactivity of the resultant products was explored. These reactions afforded a series of di-, tetra- and polynuclear zinc complexes.

Niobocene for ROP Catalysis

Keywords: Metallocenes / Ring-opening polymerization / Hydride ligands / Niobium / Lactones

The structure of $[Nb(\eta^5\text{-}C_5H_4SiMe_3)_2(H)_3]$ (**1**) justifies its classification as a "non-classical" transition metal hydride. Complex **1** is an initiator for the ROP of lactones. A mechanism consisting of an interaction between the lactone carbonyl group and the metal, insertion of the lactone into the Nb–H bond, and the generation of a metal alkoxide–aldehyde propagating species has been proposed.

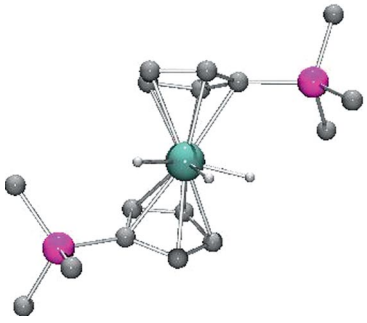

* Author to whom correspondence should be addressed.

Supporting information on the WWW (see article for access details).

This article is available online free of charge (Open Access).

If not otherwise indicated in the article, papers in issue 6 were published online on February 14, 2012

Donor–Acceptor Systems

D. Hablot, A. Sutter, P. Retailleau, R. Ziessel*

Unsymmetrical *p*-Carborane Backbone as a Linker for Donor–Acceptor Dyads

Fluorescent nanorods: Donor–acceptor dyads based on novel unsymmetrically disubstituted *closo*-1,12-dicarbadecaboranes have been prepared in a completely controlled manner by using a three-step procedure. Dyads with different donor–acceptor spacing were thereby obtained. Efficient energy transfer from the donor to the acceptor was determined in fluid solution at room temperature.

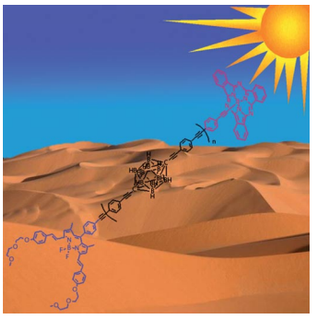

Chem. Eur. J.
DOI: **10.1002/chem.201103307**

Superhydrophobic Surfaces

J.-N. Wang, R.-Q. Shao, Y.-L. Zhang,* L. Guo, H.-B. Jiang, D.-X. Lu, H.-B. Sun*

Biomimetic Graphene Surfaces with Superhydrophobicity and Iridescence

The wonderful world of graphene! A simple one-step fabrication of biomimetic graphene surfaces that possess both superhydrophobicity and bright structural color is presented. By using two-beam laser interference, construction of periodic grating microstructures and removal of hydrophilic oxygen groups were realized at the same time.

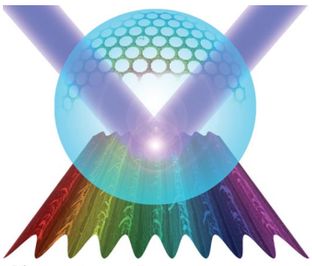

Chem. Asian J.
DOI: **10.1002/asia.201100882**

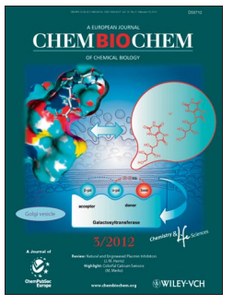

Biosynthesis

X. Yan, K. Probst, A. Linnenbrink, M. Arnold, T. Paululat, A. Zeeck, A. Bechthold*

Cloning and Heterologous Expression of Three Type II PKS Gene Clusters from *Streptomyces bottropensis*

Clusters of color: Three type II PKS gene clusters (*msn*, *mec*, and *rsl*) in *Streptomyces bottropensis* were screened. Heterologous expression of the *msn* and *rsl* clusters in *Streptomyces albus* led to the production of didesmethylmensacarcin (DDMM), and of rishirilide A and B, respectively. No product was isolated from *mec* (a putative spore pigment biosynthesis gene cluster).

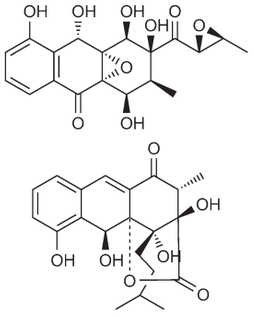

ChemBioChem
DOI: **10.1002/cbic.201100574**

Self-Assembly

D. Chen,* M.-S. Heberling, M. Nakata, L. E. Hough, J. E. Maclennan, M. A. Glaser, E. Korblova, D. M. Walba, J. Watanabe, N. A. Clark*

Structure of the B4 Liquid Crystal Phase near a Glass Surface

Nanofilaments: The B4 liquid crystal phase of bent-core molecules is one of the most complex hierarchical self-assemblies in soft materials. Near the glass substrate, the formation of twisted nanofilaments is suppressed and the chiral smectic layers self-assemble into parabolic focal conic arrays. Further from the substrate, homochiral helical nanofilaments nucleate smoothly on top of the underlying layers (see picture).

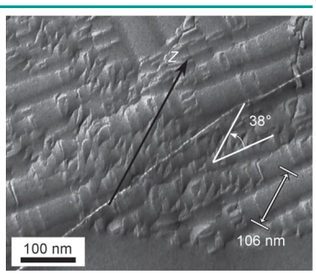

ChemPhysChem
DOI: **10.1002/cphc.201100589**

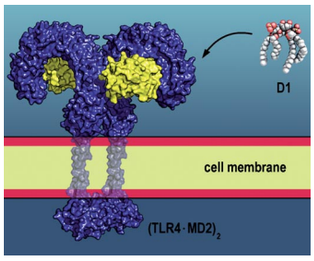

ChemMedChem
DOI: **10.1002/cmdc.201100494**

Immunochemistry

M. Piazza, V. Calabrese, G. Damore, R. Cighetti, T. Gioannini,* J. Weiss,* F. Peri*

A Synthetic Lipid A Mimetic Modulates Human TLR4 Activity

The sincerest form of flattery! A novel, symmetric lipid A mimetic (D1) formed by two glucose units linked through a 6-6' succinic diamide linker is active in modulating the activity of human TLR4. D1 inhibits endotoxin-stimulated TLR4 activation by inhibiting interaction of endotoxin with both receptors CD14 and MD-2 (associated to TLR4). D1 also has weak TLR4 agonist activity that makes it a promising lead compound for development as a vaccine adjuvant.

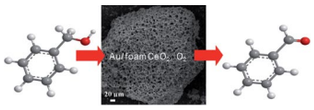

ChemSusChem
DOI: **10.1002/cssc.201100374**

Sustainable Chemistry

M. Alhumaimess, Z. Lin, W. Weng, N. Dimitratos, N. F. Dummer, S. H. Taylor, J. K. Bartley, C. J. Kiely, G. J. Hutchings*

Oxidation of Benzyl Alcohol by using Gold Nanoparticles Supported on Ceria Foam

Tailored foam bed: Cerium oxide with a foam morphology is used as a support for gold nanoparticles. The foams are synthesized using L-asparagine to produce a cerium coordination polymer foam, which is calcined to give the oxide foam. The activity of the Au/foamCeO_2 for solvent-free benzyl alcohol oxidation is superior to standard Au/CeO_2 catalysts.

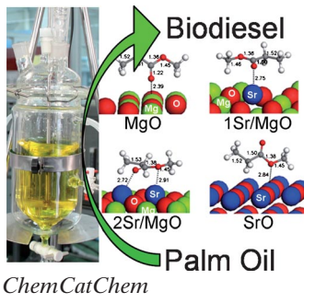

ChemCatChem
DOI: **10.1002/cctc.201100346**

Biodiesel

K. Faungnawakij,* B. Yoosuk, S. Namuangruk, P. Krasae, N. Viriya-empikul, B. Puttasawat

Sr–Mg Mixed Oxides as Biodiesel Production Catalysts

Build a base in your base: The synergistic effect of Sr and Mg species acting as heterogeneous catalysts is observed in biodiesel production as it enhances the activity, which is attributable to new strong basic sites as evidenced by using CO_2-TPD measurements and DFT calculations.

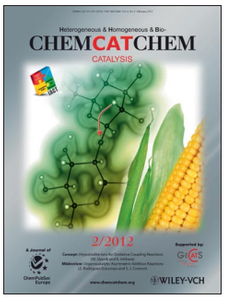

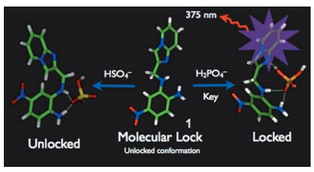

ChemPlusChem
DOI: **10.1002/cplu.201100036**

Molecular Locks

S. Dalapati, M. A. Alam,* S. Jana, R. Saha, S. Biswas, N. Guchhait*

A Molecular Lock and Key: "Unlocked–Locked" Conformational Switching of a Receptor by Anions

Lock up your valuables: Receptor **1** acts as a "molecular lock" and anions act as "keys"; $H_2PO_4^-$ can "lock" **1** by switching it from its "unlocked" conformation, however, the structurally similar HSO_4^- cannot "lock" receptor **1** as evidenced by single-crystal X-ray analysis (see scheme). The "unlocked–locked" conformational switching of **1** was investigated by monitoring changes in fluorescence intensity in the presence of different anions.

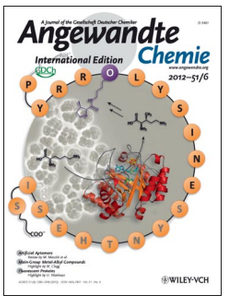

Sensing DNA Repair

T. Ono, S. Wang, C.-K. Koo, L. Engstrom, S. S. David, E. T. Kool*

Direct Fluorescence Monitoring of DNA Base Excision Repair

Uracil is a common form of DNA damage resulting from hydrolysis of cytosine, and cellular uracil DNA glycosylases (UDG) have evolved to remove it specifically. The use of an nonnatural pyrene deoxyriboside (Y) in short DNA oligomers is described that can directly report on UDG enzymatic activity. The mechanism relies on the use of uracil as a strong quencher of pyrene, and enzyme repair activity can be directly imaged with bacterial cells in real time.

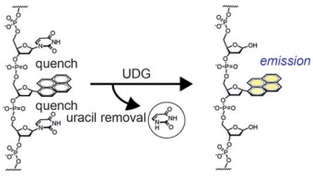

Angew. Chem. Int. Ed.
DOI: **10.1002/anie.201108135**

Enzyme Catalytic Promiscuity

L. N. Monsalve, F. Gillanders, A. Baldessari*

Promiscuous Behavior of *Rhizomucor miehei* Lipase in the Synthesis of *N*-Substituted β-Amino Esters

A mild and efficient enzymatic method for the aza-Michael addition of mono- and bifunctional amines to acrylates was developed. The high substrate specificity showed by *Rhizomucor miehei* lipase as the catalyst for this reaction was a key feature for obtaining various *N*-substituted β-amino esters in high yield and purity.

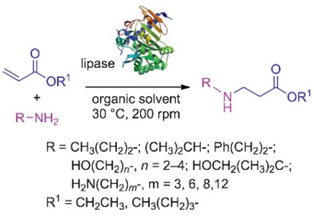

Eur. J. Org. Chem.
DOI: **10.1002/ejoc.201101624**

Wonderlab Comic – Fashion Chemistry

Sophie Lin

Wonderlab Comic – Fashion Chemistry

The IUPAC recommended new proposed names for the latest heavy elements to be added to the periodic table. The naming of the elements 114 and 116 cause a stir in the Wonderlab. In the this month's comic K Face, Sophie and Richpunzel meet.

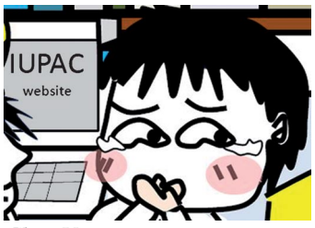

ChemViews magazine
DOI: **10.1002/chemv.201200003**

Enzyme–Inhibitor Interactions

A. Hernández Daranas,* S. Koteich Khatib, R. Lysek, P. Vogel, J. A. Gavín*

Determining the Role of the Aromatic Ring of *N*-Arylmethyl *ent*-conduramine F-1 in their Interactions with α-Glucosidases by Saturation Transfer Difference NMR Spectroscopy Experiments

Saturation transfer difference (STD) NMR spectroscopy was used to study the role of aromatic moieties in the inhibition of α-glucosidases by *N*-arylmethyl *ent*-conduramine F-1. STD epitope mapping and molecular docking simulations provide new insights into the structure-based design of drugs targeting this enzyme (see figure).

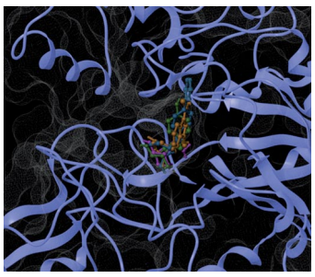

ChemistryOPEN
DOI: **10.1002/open.201100004**

DOI: 10.1002/ejic.201101121

Pompon-Like MnF_2 Nanostructures from a Single-Source Precursor through Atmospheric Pressure Chemical Vapor Deposition

Graziella Malandrino,*[a] Roberta G. Toro,[b] Maria R. Catalano,[a] Maria E. Fragalà,[a] Patrizia Rossi,[c] and Paola Paoli[c]

Keywords: Nanostructures / Manganese / Fluorides / Single-source precursors / Chemical vapor deposition

MnF_2 nanorod assemblies in a pompon-like fashion were synthesized by using a new complex, $Mn(hfa)_2$·tmeda [(Hhfa = 1,1,1,5,5,5-hexafluoro-2,4-pentandione, tmeda = *N*,*N*,*N*′,*N*′-tetramethylethylenediamine)]. The complex was synthesized in a single-step reaction, and single-crystal X-ray diffraction studies provide evidence of a mononuclear structure. The thermal analyses have shown that the complex is thermally stable and can be evaporated to leave less than 2 % residue at atmospheric pressure. On the basis of its thermal properties, it has been successfully applied to the atmospheric pressure metalorganic chemical vapor deposition (AP-MOCVD) of MnF_2 nanostructures.

Introduction

The past few years have witnessed an exponential growth of activities in the synthesis of nanostructures.[1] These nanoscale materials are interesting because new properties are acquired at this length scale and, equally important, these properties change with the size or shape of the materials. The development of new synthetic methods has made it possible to produce uniform nanostructures with sizes ranging from 1 to 100 nm and with various shapes (rods, wires, cubes, spheres). For the past few years, a great variety of quasi-one-dimensional (quasi-1D) nanostructures of various compositions (metals, oxides, and semiconductors) have been synthesized. Nevertheless, very few reports have appeared on the synthesis of fluoride nanostructures. CaF_2 nanostructures have been grown through molecular beam epitaxy (MBE) on Si, yielding ultrathin 2D wetting layers, quasi-1D wires at high growth temperatures, and well-organized dots at lower temperatures.[2] Nanostructured nickel fluoride thin films have been successfully prepared by pulsed laser deposition.[3] MBE has also been applied to the deposition of MnF_2 epitaxial layers.[4] MnF_2 thin films are interesting in device fabrication for their magnetic properties. In particular, various studies have been carried out, for example, on the magnetically nonlinear optical transmission of a Fabry–Perot resonator filled with the antiferromagnetic MnF_2 layer[4d] and on the focusing of bulk and surface spin waves in antiferromagnetic MnF_2 films.[4e]

Nevertheless, there are no reports, to the best of our knowledge, on the synthesis of MnF_2 nanostructures, which are interesting also in view of the intriguing relationship between nanoscale dimensions and luminescence properties.[5]

In addition, mixed fluoroperovskite nanostructures such as $NaMnF_3$ and $KMnF_3$ fluorides have attracted extensive attention as a result of their size-dependent properties, such as magnetism, piezoelectricity, and, when doped with rare-earth ions, photoluminescence.[6]

The metalorganic chemical vapor deposition (MOCVD) technique offers a softer approach with lower processing temperatures and greater throwing power (versatility and adaptability) than alternative techniques[7] for all these applications and has been extensively applied to the fabrication of nanostructures based on an accurate tuning of processing parameters.[8]

Herein, we report the synthesis through AP-MOCVD of pompon-like nanostructures formed by assemblies of MnF_2 nanorods from a single source, the complex $Mn(hfa)_2$·tmeda (Hhfa = hexafluoroacetylacetone, tmeda = *N*,*N*,*N*′,*N*′-tetramethylethylenediamine). Its single-crystal structure indicates that it is monomeric, and thermal studies have indicated an excellent behavior for application as precursor in AP-MOCVD processes.

Results and Discussion

The single-source Mn/F precursor was synthesized through a one-step reaction, from manganese(II) acetate

[a] Dipartimento di Scienze Chimiche, Università di Catania, ISTM-CNR and INSTM UdR Catania,
V.le Andrea Doria 6, 95125 Catania, Italy
Fax: +39-095-580138
E-mail: gmalandrino@dipchi.unict.it
[b] Istituto per lo Studio dei Materiali Nanostrutturati (ISMN)-CNR Area della Ricerca di Roma,
via Salaria Km 29.300, Monterotondo Stazione, Roma 00016, Italy
[c] Dipartimento di Energetica "S. Stecco", Università di Firenze, via Santa Marta 3, 50136 Firenze, Italy

Supporting information for this article is available on the WWW under http://dx.doi.org/10.1002/ejic.201101121.

tetrahydrate, hexafluoroacetylacetone, and *N*,*N*,*N*′,*N*′-tetramethylethylenediamine in dichloromethane [Equation (1)].

$$Mn(CH_3COO)_2{\cdot}4H_2O + 2Hhfa + tmeda \rightarrow Mn(hfa)_2{\cdot}tmeda + 2CH_3COOH + 4H_2O \quad (1)$$

The adduct is soluble in common organic solvents such as ethanol, chloroform, acetone, and slightly soluble in decane. The adduct is not hygroscopic, can be handled in air, and melts at 71–74 °C.

The single-crystal X-ray diffraction data show that the manganese cation is sixfold coordinated by four oxygen atoms of two hfa anions and by two nitrogen atoms of the tmeda molecule (Figure 1). The coordination geometry is a distorted octahedron (see Table S1). As expected, the two hfa anions show an extended conjugation. In fact, the two oxygen atoms and the three carbon atoms of each anion lie in one plane: the maximum deviation from these two mean planes (indicated as A and B in the following) are 0.05(1) and 0.04(1) Å for C(2) and C(7), respectively. Planes A and B form an angle of 79.7(2)°. While the mean plane containing the amine atoms C(11), C(12), N(1), and N(2) (C in the following) forms angles of 82.6(3) and 81.0(3)° with A and B, respectively.

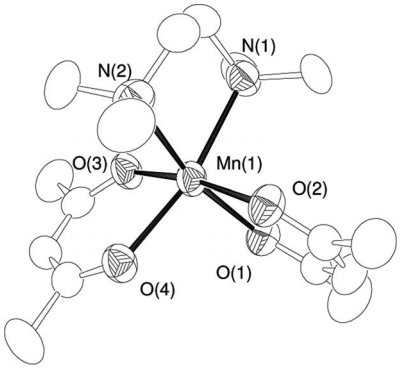

Figure 1. ORTEP3 view of $Mn(hfa)_2{\cdot}tmeda$. Fluorine and hydrogen atoms have been omitted for clarity.

The Mn–O and Mn–N bond lengths are in agreement with those retrieved for similar complexes (i.e. Mn^{II} complexes having polyamines and acetylacetonate derivatives as ligands) in the Cambridge Structural Database (CSD, v 5.31).

The mass transport properties and thermal behavior of the as-synthesized adduct, studied through atmospheric pressure thermal gravimetric analyses (TGA, 5 °C/min under N_2), have shown that the $Mn(hfa)_2{\cdot}tmeda$ adduct is thermally stable. The derivative thermal gravimetry curve (DTG) consists of a single peak (Figure S1), which indicates that the adduct evaporates quantitatively in the 100–230 °C temperature range, with a 1.5% residue at 300 °C. Its excellent behavior at atmospheric pressure renders this compound also appealing for applications in low-pressure MOCVD fabrication of $La_{1-x}(Sr)_xMnO_3$ films, which represents the most studied material as cathode in solid oxide fuel cells (SOFCs).[9]

The differential thermal analysis (DTA) indicates that the compound melts at 72.5 °C, which means that it can be used as a liquid precursor in the AP-MOCVD process of MnF_2 nanostructures.

The $Mn(hfa)_2{\cdot}tmeda$ adduct with its remarkable volatility and high thermal stability, as assessed by the thermogravimetric measurements carried out at atmospheric pressure, has been successfully applied to the AP-MOCVD deposition of MnF_2 nanostructures on Si (100) and quartz substrates. Depositions have been performed, under O_2 (150 sccm) as reaction gas and Ar (150 sccm) as carrier gas, in a horizontal quartz hot-wall reactor. The source temperature was maintained at 130 °C. The substrate temperature was varied in the range 400–600 °C. Note that the fluorinating agent is supplied by the source material itself. The XRD pattern of the nanostructure deposited at 600 °C, reported in Figure 2b, shows the formation of a polycrystalline MnF_2 phase; all the peaks can be associated with reflections of the polycrystalline powder (ICDD 24-0727). At this temperature the growth rate of MnF_2 in film form is about 1 μm/h (Figure S3).

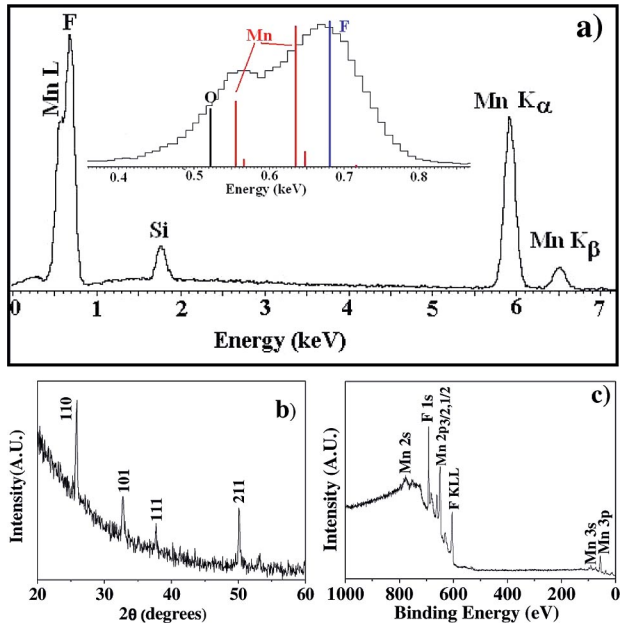

Figure 2. (a) EDX spectrum and enlarged version of the F peak (inset), (b) XRD pattern, and (c) XPS survey of the assemblies of MnF_2 nanorods grown by AP-MOCVD on quartz (XRD) or Si (EDX, XPS) from $Mn(hfa)_2{\cdot}tmeda$ as a single-source precursor.

The energy dispersive X-ray analysis (EDX) spectrum (Figure 2a) confirms the compositional purity of the MnF_2 films. It shows the presence of the Mn-K_α and -K_β peaks at 5.887 and 6.496 keV. The peak at 1.730 keV is due to the substrate Si-K_α peak, and the peak at 0.677 keV is due to F-K_α. In the inset in Figure 2a, the F peak zone is shown.

The shoulders on the left side of the peak are centered at the most intense *L* lines of Mn; the peak positions of Mn *L* lines and O *K* peaks are indicated in the inset. Thus, EDX

data confirm the purity of the sample, within the detection limit of the technique (< 1%), since no C, O, or N are present in the spectrum.

The survey XPS spectrum after 60 s sputtering is given in Figure 2c. It shows the presence of Mn and F. No peaks of O or C have been detected, thus confirming the compositional purity of the MnF_2 phase and excluding the presence of any Mn–O phase, even as an amorphous phase. The absence of C confirms the clean decomposition of the used precursor.

Figure 3 presents field-emission scanning electron microscopy (FE-SEM) images of a MnF_2 pompon-like structure. The secondary electron SEM image, recorded in a variable pressure (VP) mode to avoid any damage to the nanostructure, shows that over 80% of all individual pompon structures have diameters in the range 7–10 μm. From the high-magnification image (Figure 3 b), it is evident that each pompon-like nanostructure is covered with a high density of radially oriented nanorod structures. The nanorods are about 5 μm long and have diameters of about 200 nm. Depositions carried out at the same deposition temperature but at lower precursor temperature produce films with different morphologies. These findings may be explained by considering that the surface morphology of the as-deposited structures is determined by the complex interplay between mass transport and surface kinetics of the system. In the present case, the saturation degree of the precursor and the growth rate play a crucial role in determining the morphology of MnF_2 nanorods.

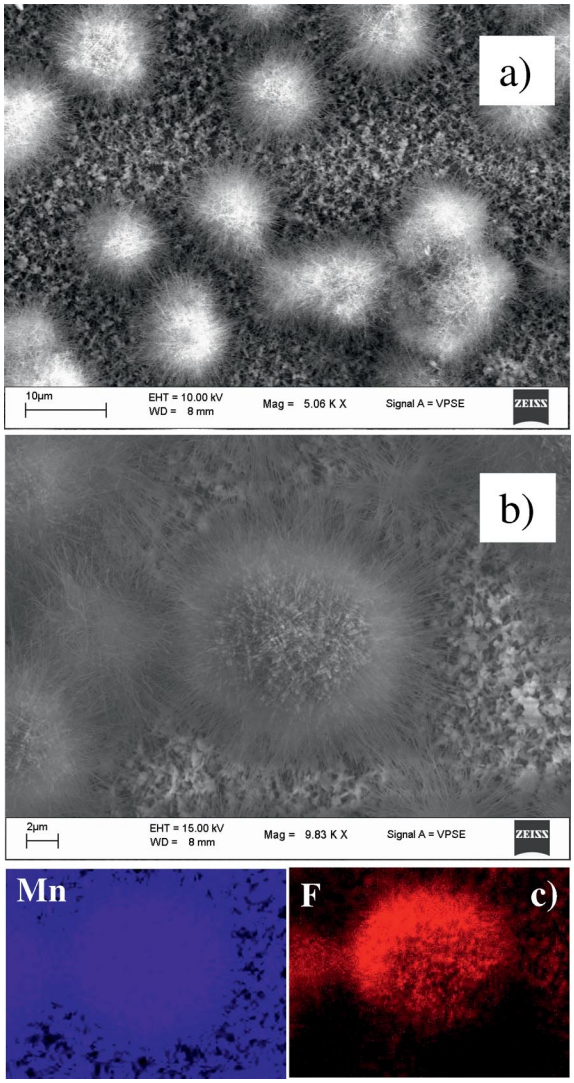

Figure 3. FE-SEM images of the assembly of MnF_2 nanorods at (a) low magnification, (b) higher magnification, (c) Mn and F distribution maps.

Conclusions

In summary, this contribution reports a bottom-up approach for the fabrication of MnF_2 nanorod assemblies in a pompon-like fashion by starting from the synthesis of the new adduct $Mn(hfa)_2$·tmeda, which behaves as a clean single source of manganese and fluorine. The complex shows a remarkable volatility even at atmospheric pressure, which allowed its use under very mild MOCVD conditions, that is, in AP-MOCVD processes. To the best of our knowledge, this represents the first case of fabrication of MnF_2 nanostructures. The simplicity and effectiveness of the reported AP-MOCVD process makes the approach very promising for low-cost manufacturing of manganese-containing systems.

Experimental Section

The reactions were conducted under normal laboratory conditions. The chemical reagents $Mn(CH_3COO)_2·4H_2O$, Hhfa and tmeda were purchased from STREM Chemicals Inc. and used without any further purification. Elemental microanalyses were performed in the Analytical Laboratories of the University of Catania. Infrared spectra were recorded with a Jasco FTIR 430 spectrometer by placing the samples as Nujol mulls between NaCl plates. Thermogravimetric analyses were performed with a Mettler Toledo TGA/SDTA 851^e instrument on samples whose weight was between 5 and 13 mg (TGA). Thermal measurements were made under prepurified nitrogen flow fed into the working chamber at 30 sccm, with a 5 °C/min heating rate. The melting point was measured in air with a Koffler instrument.

$Mn(hfa)_2$·tmeda: $Mn(CH_3COO)_2·4H_2O$ (1.586 g, 5.898 mmol) was first suspended in dichloromethane (30 mL), and then tmeda (0.555 g, 4.711 mmol) was added to the suspension. Hhfa (1.960 g, 9.420 mmol) was added to the flask after 10 min, and the mixture was kept at reflux, whilst stirring, at room temperature for 1 h. The solution was collected by filtration under vacuum, and the excess of $Mn(CH_3COO)_2·4H_2O$ was filtered off. Orange crystals were obtained upon evaporation of the solvent. They were washed two to three times in pentane. Upon the evaporation of pentane, orange crystals were decanted off, filtered with a Buchner funnel, and dried in air. The reaction yield was 80%. The melting point of the crude product was 71–74 °C/760 Torr. $C_{16}H_{18}F_{12}MnN_2O_4$ (585.26): calcd. C 32.72, H 3.43, N 4.77; found C 32.38, H 3.79, N 4.82.

Crystal Structure Determination

Crystallographic data were collected with an Oxford Xcalibur diffractometer with graphite-monochromated Mo-K_α radiation (λ =

0.71069 Å), T = 298 K. The cell parameters, the intensity data, and the reduction were performed by using the program package CRYSALIS v 1.17.[10] Intensity data were corrected for Lorentz and polarization effects.

The absorption correction was made by using an analytical method based on face indexing. The structure was solved by direct methods with the SIR97 program[11] and refined by full-matrix least-squares against F^2 using all data (SHELX97)[12]. Anisotropic thermal parameters were used for the non-hydrogen atoms. All the hydrogen atoms were introduced in calculated positions and refined according to the linked atoms. Geometrical calculations were performed with PARST97,[13] and molecular plots were produced with the program ORTEP3.[14]

CCDC-786868 contains the supplementary crystallographic data for this paper. These data can be obtained free of charge from The Cambridge Crystallographic Data Centre via www.ccdc.cam.ac.uk/data_request/cif.

Details of X-ray Diffraction Analysis: $C_{16}H_{18}F_{12}MnN_2O_4$, M = 585.26, monoclinic $P2_1/n$, a = 10.798(1) Å, b = 15.117(2) Å, c = 15.363(2) Å, β = 101.94(1)°, V = 2453.5(5) Å^3, T = 298 K, Z = 4, D_{calc} = 1.584 g/cm^3, μ = 0.653 mm^{-1}, 7158 reflections collected, 3502 reflections unique (R_{int} = 0.0308) 1867 reflections with $I > 2\sigma(I)$; R_1, wR_2 [$I > 2\sigma(I)$] = 0.0658, 0.1727; R_1, wR_2 (all data) = 0.1157, 0.2057. GoF = 0.971, largest difference peak, hole: 0.434/–0.287 e/Å^3.

Supporting Information (see footnote on the first page of this article): Tables on crystal data and selected bond lengths and angles; thermogravimetric data and details of film deposition and characterization.

Acknowledgments

The authors thank the Ministero dell'Università e della Ricerca (MIUR) for the financial support within the Fondo Integrativo Speciale Ricerca (FISR) thematic activities: Nanosystems of transition metal oxide for solid oxide fuel cells (SOFCs) (New systems for energy production and storage program). Centro di Cristallografia Strutturale (CRIST), University of Florence is gratefully acknowledged.

[1] Y. Mao, T.-J. Park, F. Zhang, H. Zhou, S. S. Wong, *Small* **2007**, *3*, 1122.
[2] a) N. S. Sokolov, S. M. Suturin, *Appl. Surf. Sci.* **2001**, *175–176*, 619; b) J. Viernow, D. Y. Petrovykh, F. K. Men, A. Kirakosian, J.-L. Lin, F. J. Himpsel, *Appl. Phys. Lett.* **1999**, *74*, 2125.
[3] H. Zhang, Y.-N. Zhou, Q. Sun, Z.-W. Fu, *Solid State Sci.* **2008**, *10*, 1166.
[4] a) R. N. Kyutt, A. G. Banshchikov, A. K. Kaveev, N. S. Sokolov, A. A. Lomov, Y. Ohtake, M. Tabuchi, Y. Takeda, *J. Phys. D: Appl. Phys.* **2007**, *40*, 4896; b) I. V. Golosovsky, N. S. Sokolov, A. Gukasov, A. Bataille, M. Boehm, J. Nogues, *J. Magn. Magn. Mater.* **2010**, *322*, 664; c) A. K. Kaveev, O. V. Anisimov, A. G. Banshchikov, N. F. Kartenko, V. P. Ulin, N. S. Sokolov, *J. Appl. Phys.* **2005**, *9*, 013519/1; d) Y. Zhao, S.-F. Fu, H. Li, X.-Z. Wang, *J. Appl. Phys.* **2011**, *110*, 023512/1; e) V. Veerakumar, R. E. Camley, *Phys. Rev. B* **2010**, *81*, 174432.
[5] I. Hernandez, F. Rodriguez, *J. Phys. Condens. Matter* **2007**, *19*, 356220.
[6] a) F. Zhang, Y. Mao, T.-J. Park, S. S. Wong, *Adv. Funct. Mater.* **2008**, *18*, 103; b) Y.-P. Du, Y.-W. Zhang, Z.-G. Yan, L.-D. Sun, S. Gao, C.-H. Yan, *Chem. Asian J.* **2007**, *2*, 965; c) Q. Tang, J. Shen, W. Zhou, J. Liu, Z. Liu, Y. Qian, *Inorg. Chem. Commun.* **2004**, *7*, 283.
[7] A. C. Jones, M. L. Hitchman *Chemical Vapour Deposition: Precursors, Processes and Applications*, RSC Publishing, Cambridge, **2009**.
[8] a) R. Lo Nigro, R. G. Toro, G. Malandrino, I. L. Fragalà, *J. Mater. Chem.* **2005**, *15*, 2328; b) R. Lo Nigro, G. Malandrino, I. L. Fragalà, *Chem. Mater.* **2001**, *13*, 4402; c) R. Lo Nigro, G. Malandrino, P. Fiorenza, I. L. Fragalà, *ACS Nano* **2007**, *1*, 183.
[9] R. G. Toro, G. Malandrino, L. M. S. Perdicaro, D. M. R. Fiorito, A. Andreone, G. Lamura, I. L. Fragalà, *Chem. Vap. Deposition* **2010**, *16*, 143.
[10] a) *CrysAlis CCD*, Oxford Diffraction Ltd., Version 1.171.pre23_10 beta (release 21.06.2004 CrysAlis171.NET) (compiled Jun 21 2004, 12:00:08); b) *CrysAlis RED*, Oxford Diffraction Ltd., Version 1.171.pre23_10 beta (release 21.06.2004 CrysAlis171.NET) (compiled Jun 21 2004, 12:00:08).
[11] A. Altomare, G. Cascarano, C. Giacovazzo, A. Guagliardi, M. C. Burla, G. Polidori, M. Camalli, *J. Appl. Crystallogr.* **1994**, *27*, 435.
[12] G. M. Sheldrick, *SHELXL-97*, **1997**, University of Göttingen, Germany.
[13] M. Nardelli, *Comput. Chem.* **1983**, *7*, 95.
[14] L. J. Farrugia, *J. Appl. Crystallogr.* **1997**, *30*, 565.

Received: October 14, 2011
Published Online: February 6, 2012

DOI: 10.1002/ejic.201101315

Structure–Photoluminescence Quenching Relationships of Iridium(III)–Tris(phenylpyridine) Complexes

Albert Ruggi,[a] Matteo Mauro,[b] Federico Polo,[b] David N. Reinhoudt,[a] Luisa De Cola,*[a,b] and Aldrik H. Velders*[a,c]

Keywords: Iridium / Luminescence / Photoluminescence / Electrochemistry / Oxygen sensitivity / Density functional calculations

The synthesis, structural, photophysical, theoretical, and electrochemical characterization of four tris(2-phenylpyridine)-based Ir^{III} complexes are reported. The complexes were functionalized on the pyridine or on the phenyl rings with amide moieties substituted with a tris(ethyl)amine or ethyl groups, thereby yielding a family of compounds with hemicaged or open (without a capping unit but with similar functional groups on the ligand) structure. Within the context of the parent tris(2-phenylpyridine) and the full-cage iridium(III) complexes, structure–photoluminescence quenching relationships (SPQR) of the four complexes have been investigated. Luminescence quenching by oxygen has been studied with Stern–Volmer plots and through evaluation of the thermodynamic parameters involved in the quenching process. Density functional theory (DFT) and time-dependent DFT (TD-DFT) calculations have been performed on the complexes to gain insights into structural and electronic features and the nature of the excited states involved in the electronic absorption processes. Interestingly, shielding by the capping unit of moieties in which the LUMO orbital is mostly localized (on the pyridines) results in a dramatic 40% decrease in oxygen quenching. Conversely, shielding of moieties in which the HOMO orbital is partially localized (on the phenyl rings) does not induce any change in the oxygen quenching degree. In both sets of compounds, the thermodynamic feasibility of oxygen quenching is the same for the hemicaged and open compounds, thus giving evidence of the structural origin of such quenching decrease. The SPQR opens up new routes to the design of tailored, more or less sensitive to oxygen, luminescent iridium complexes (e.g., for use as biolabels).

Introduction

Here we report the evidence for a structure-related shielding effect of the oxygen quenching of the luminescence of iridium(III)–tris(phenylpyridine) derivatives with hemicaged (i.e., with a capping unit) or open (i.e., without a capping unit) ligand structures. Iridium(III)-based luminophores have been the object of extensive studies in the last decades, especially due to their wide spectrum of possible applications.[1] The possibility of tuning the emission wavelength and the generally good emission properties make iridium(III) complexes ideal luminophores for the realization of organic light-emitting diodes (OLEDs),[2–4] and, more recently, also for several biomedical applications.[5–8] Moreover, the interaction of the excited states of transition-metal complexes with dioxygen (which results in the quenching of luminescence and the generation of highly reactive species like singlet oxygen and superoxide radical anion) has received increasing interest due to the possible realization of diagnostic and therapeutic agents.[9–14] Despite the studies directed towards understanding the theoretical relationship between structure and optical properties,[15,16] little is known about the structure–photoluminescence quenching relationship (SPQR) of these complexes. Transition-metal complexes with a cagelike ligand structure show a remarkable decrease in oxygen quenching. For instance, an Ru^{II} caged complex shows an 80% decrease in oxygen quenching with respect to $[Ru(bpy)_3]^{2+}$ (bpy = 2,2′-bipyridine),[17] and an Ir^{III} caged complex (**ii**, Scheme 1) that shows a similar decrease in oxygen quenching compared to the archetypical $[Ir(ppy)_3]$ (ppy = 2-phenylpyridine) (**i**, Scheme 1); this has been recently described by our group.[18] However, the origin of this quenching decrease is not yet clear. Moreover, many parameters (e.g., triplet energy, oxidation potential) are different from the caged to the respective reference complexes {i.e., $[Ru(bpy)_3]^{2+}$ and $[Ir(ppy)_3]$}, thus an univocal interpretation of the observed quenching decrease is not trivial.[13]

[a] Laboratory of Supramolecular Chemistry and Technology, MESA+ Institute for Nanotechnology, University of Twente, P. O. Box 217, Enschede, The Netherlands
E-mail: decola@uni-muenster.de
a.h.velders@utwente.nl
[b] Westfälische Wilhelms-Universität Münster, Physikalisches Institut and Center for Nanotechnology (CeNTech), Heisenbergstrasse 11, 48149 Münster, Germany
[c] BioMedical Chemistry, MIRA Institute of Biomedical Technology and Technical Medicine, University of Twente P. O. Box 217, Enschede, The Netherlands
Supporting information for this article is available on the WWW under http://dx.doi.org/10.1002/ejic.201101315.

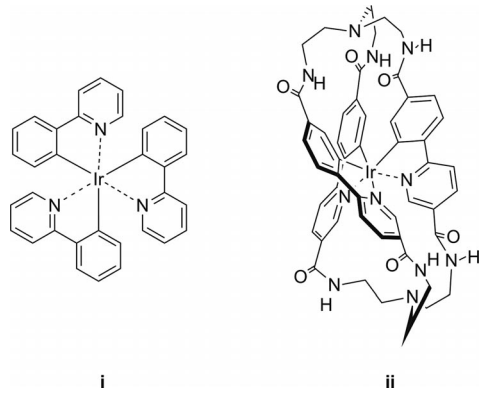

Scheme 1. Structure of the archetypical $[Ir(ppy)_3]$ (**i**) and Ir caged complex (**ii**).

The remarkably low oxygen quenching of the luminescence observed for caged Ru^{II}[17] and Ir^{III}[18] complexes suggests a possible structural contribution to the shielding mechanism of the excited state (i.e., of the atoms on which the LUMO is mostly localized). A selective modification of the HOMO or of the LUMO properties in homoleptic $[Ru(bpy)_3]^{2+}$-like complexes is challenging, since the HOMO is mostly localized on the metal center and the LUMO is localized on the (symmetric) bipyridine ligands. On the other hand, for iridium complexes, and in particular for the $[Ir(ppy)_3]$ derivatives, the 2-phenylpyridines are not symmetric and therefore are ideal candidates for a systematic study of the SPQR. In homoleptic $[Ir(ppy)_3]$-like complexes, the HOMO is usually localized on the metal ion and on the phenyl rings, whereas the LUMO (which can be considered a first approximation of the electronic distribution of the molecule in the excited state) is mostly localized on the pyridine rings.[1,15] The synthesis of caged complexes remains a great challenge and the versatility in tuning the ligands (and therefore properties) for these systems is complicated. Hemicaged systems are, on the other hand, much more accessible, and they might show similar shielding behavior but with a more accessible synthesis. In fact, upon introduction of suitable groups, either on the pyridine or phenyl side of the [Ir(ppy)] core, it is possible to selectively modify the electronic and/or shielding properties of the LUMO or HOMO, respectively, with a consequent change of the redox and optical properties like the emission energies.[1,16] In this paper we describe a series of Ir^{III}–tris(phenylpyridine) derivatives with a hemicaged or open structure in which we have selectively modified the HOMO and the LUMO orbitals.[11,19] Such a strategy allows us to understand the SPQR and to rationalize the behavior towards dioxygen quenching upon the shielding of the HOMO or of the LUMO.

More precisely, we present here the synthesis, characterization, and photophysical properties of a series of phenylpyridine-based Ir^{III} complexes functionalized with a tris(2-amidoethyl)amine capping unit or with an ethylamide moiety (i.e., with a hemicaged and open structure) (Scheme 2). The complexes possess a hemicaged (**1**, **3**) or an open (**2**, **4**) structure in which the substituents are on the pyridine (**1**, **2**) or on the phenyl (**3**, **4**) rings, respectively. These complexes are synthetically more accessible than the related fully caged system (**ii**),[18] and they show interesting structural shielding behavior. The introduction of a capping unit on the pyridine side (**1**) of the $[Ir(ppy)_3]$ core, on which the LUMO orbital is mostly localized, induces a different shielding towards oxygen quenching than the open (unshielded) complex **2**. We in fact find that for **1** the quenching from dioxygen is lower than for complex **2**. On the contrary, the presence of a capping unit on the phenyl side (**3**), on which the HOMO is mostly localized, does not influence the degree of oxygen quenching and, therefore, the behavior of the hemicaged (**3**) and open (**4**) complexes towards oxygen quenching is the same. It is interesting to note that the molecules of each pair are in principle electronically and energetically equivalent in terms of excited state, and therefore the differences in their oxygen quenching can derive only from a structural effect. The oxygen quenching efficiency has been evaluated by Stern–Volmer analysis and compared with the thermodynamic parameters involved in the possible quenching pathways (i.e., energy transfer and electron transfer) to obtain clear evidence of the structure-related shielding against oxygen quenching. From this systematic study it was found that the introduction of a capping unit on the pyridine side of Ir^{III}–tris(phenylpyridine) derivatives induces a remarkable decrease in oxygen quenching with respect to the open (uncapped) structure, whereas only a minor decrease in oxygen quenching is observed upon introduction of the same capping unit on the phenyl side of Ir^{III}–tris(phenylpyridine) derivatives with respect to the corresponding open structure.

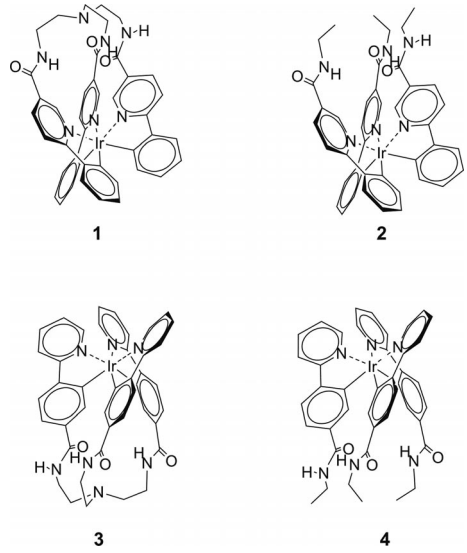

Scheme 2. Structures of the hemicaged (**1**, **3**) and open (**2**, **4**) Ir^{III} complexes.

Results and Discussion

Iridium(III) complexes **1**–**4** were synthesized according to the synthetic pathway shown in Scheme 3. The phenyl-

pyridine-based building blocks were obtained upon Suzuki coupling[20] of bromonicotinic acid with phenylboronic acid (to give the phenylpyridine derivative **5**) or upon Suzuki coupling of 4-carboxymethylboronic acid with 2-bromopyridine (to give the phenylpyridine derivative **8**) with subsequent amide formation through amide coupling with, respectively, tris(2-aminoethyl)amine (Tren) (**6**, **9**) or ethylamine (**7**, **10**). The so-obtained ligands were treated with Ir^{III} to obtain the desired target complexes. The hemicaged complexes were synthesized by direct reaction of the suitable tripodal ligand (**6**, **9**) with $IrCl_3$ in the presence of CF_3CO_2Ag in ethylene glycol heated at reflux to give the hemicaged complexes **1** and **3**.[18] This strategy was not successful in the case of the open complexes; they were synthesized in two steps.[21] First the dichlorido-bridged dimer was obtained by reaction of the desired ligand (**7**, **10**) with $IrCl_3$ in 2-ethoxyethanol, and the so-obtained intermediate was treated with an excess amount of ligand in the presence of CF_3SO_3Ag in toluene heated at reflux (see Scheme 3) to give the open complexes **2** and **4**.

All the intermediates and the target complexes were characterized by IR and NMR (^1H and ^{13}C) spectroscopy and mass spectrometry, and the characteristic data are reported in the Experimental Section and in the Supporting Information. Complexes **1**–**4** show only one set of NMR spectroscopic signals for the three phenylpyridine ligands, which proves that the threefold symmetry expected for *fac* complexes is maintained. The ^1H NMR spectra of the hemicaged complexes **1** and **3** (see the Supporting Information) show, in addition, that upon formation of the iridium(III) complexes, the hemicage ligands become quite rigid: due to the hampered rotation around the C–C bond of the ethyl linkers, the four protons on each linker unit become magnetically nonequivalent, thereby resulting in four different multiplet signals in the ^1H NMR spectrum. A similar behavior has been observed for the hemicaged and caged Ir^{III} complexes previously described by our group.[18] Conversely, the ^1H NMR spectra of the open complexes **2** and **4** do not show any nonequivalent CH_2 or CH_3 protons, as expected for ethyl moieties with rotational freedom. The

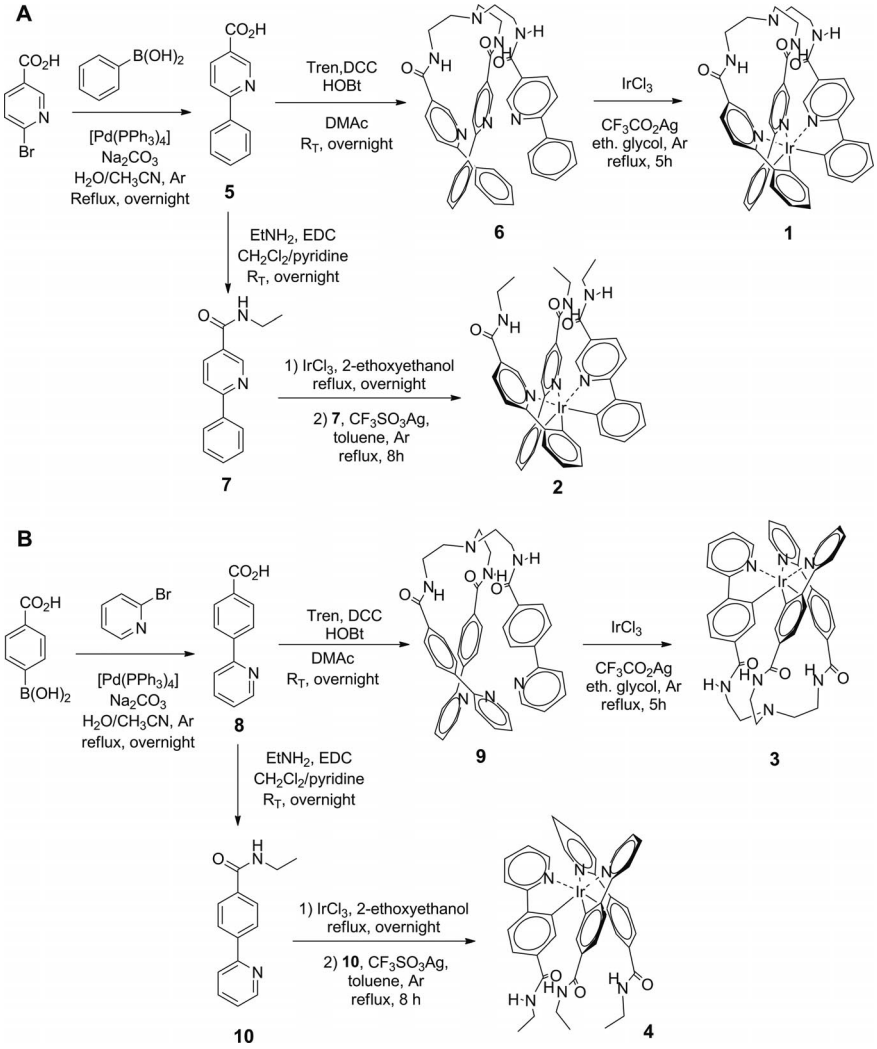

Scheme 3. Synthetic pathways for the synthesis of the hemicaged (**1**, **3**) and open (**2**, **4**) Ir^{III} complexes. The phenylpyridine derivatives **5** and **8** (obtained by Suzuki coupling) are coupled with Tren or ethylamine, thus giving the tripodal (**6**, **9**) or simple ligands (**7**, **10**), which are consecutively bound to Ir^{III}, thus giving the target molecules **1**–**4**.

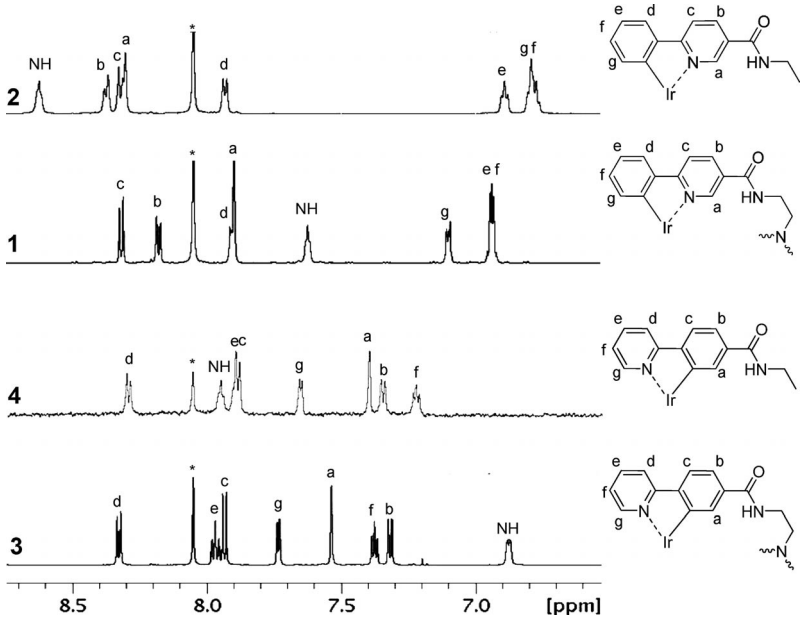

Figure 1. Aromatic region of the ^{1}H NMR spectra and peak assignment of hemicaged (**1**, **3**) and open (**2**, **4**) iridium(III) complexes; [D_7]DMF (* = residual solvent).

introduction of the capping unit induces a remarkable change in the signal of the amide proton (NH). Compared to the open complex **2**, the NH proton of the hemicaged complex **1** shows an upfield shift of 1 ppm (Figure 1). A similar upfield shift is also shown for the amide proton when comparing **4** to **3**. The observed change in the chemical shift of the amide proton (NH) is probably due to the change of the local polarity induced by the presence of the capping unit (vide infra). Interestingly, the proton Ha shows an upfield shift of 0.40 ppm from **2** to **1**, whereas only a modest (δ = 0.13 ppm) downfield shift is observed for Ha from **4** to **3**. The upfield shift of the Ha proton observed from **2** to **1** is possibly attributable to a magnetic shielding exerted by the aromatic rings located on the other branches of the molecule as a result of a higher degree of twisting of the helical structure of the [Ir(ppy)$_3$] core in the hemicage **1**: because of this higher twisting, the proton Ha in the hemicaged complex **1** faces the pyridine ring, thereby resulting in a downfield shift. On the other hand, the modest downfield shift observed for the proton Ha between **3** and **4** indicates that the structure of the [Ir(ppy)$_3$] core in the hemicaged complex **3** is only slightly distorted with respect to the open complex **4**.

To further investigate the geometry of the hemicaged complexes (**1**, **3**), a series of 2D NMR spectroscopic experiments (H,H-COSY, H,H-ROESY, H,C-HMBC and H,C-HMQC) was performed. The aromatic–aliphatic region of the ROESY spectrum of the hemicaged complex **1** (Figure 3) shows the coupling between the amide proton (NH) and three nonequivalent aliphatic protons on the ethyl linker (Hh, Hh′, Hi), analogously to what was found for the hemicaged complex previously described by our group.[18] The fourth proton (Hi′) is too far from the amide proton and does not give any through-space coupling. A similar coupling of the amide proton with three aliphatic protons on the ethyl linker was also observed for the hemicaged complex **3** (Figure 2), thus giving proof of the hemicaged structure of the two complexes **1** and **3**. In the aromatic region of the ROESY spectrum of the hemicaged complexes (Figure 2), the cross-peak between the protons Hc and Hd, which are located on the pyridine and phenyl ring, respectively, allows for a straightforward assignment of the remaining peaks from COSY data and the heteronuclear HMBC and HMQC experiments.

Careful analysis of the aromatic region of the ROESY spectrum of the hemicaged complex **1** (Figure 2) reveals the remarkable orientation of the amide moiety: the cross-peaks between the amide proton (NH) with both the internal (Ha) and the external (Hb) protons, *ortho* to the amide group, indicate that the NH group is not coplanar with the pyridine ring. To investigate the possibility of a certain degree of fluxionality in the capping unit of the hemicage system **1** to cause the characteristic two cross-peaks of the amide protons, variable-temperature (VT) NMR spectroscopy was performed. Neither the 1D VT measurements nor the ROESY performed at 250 K (see the Supporting Information) indicate the presence of more conformers of hemicage **1** to be present in solution on the NMR spectroscopic timescale.

A different behavior was observed for hemicage **3** (Figure 2), the amide proton of which gives a coupling only with the internal proton (Ha) on the phenyl ring; therefore, the NH group in **3** is likely coplanar with the phenyl ring and oriented towards the inner side of the molecule.

Two possible structures can be drawn for the hemicage **1** on the basis of the observed NOE cross-peaks. Either the entire amide moiety is not coplanar with the pyridine ring, or only the NH moiety of the amide group is bent out of

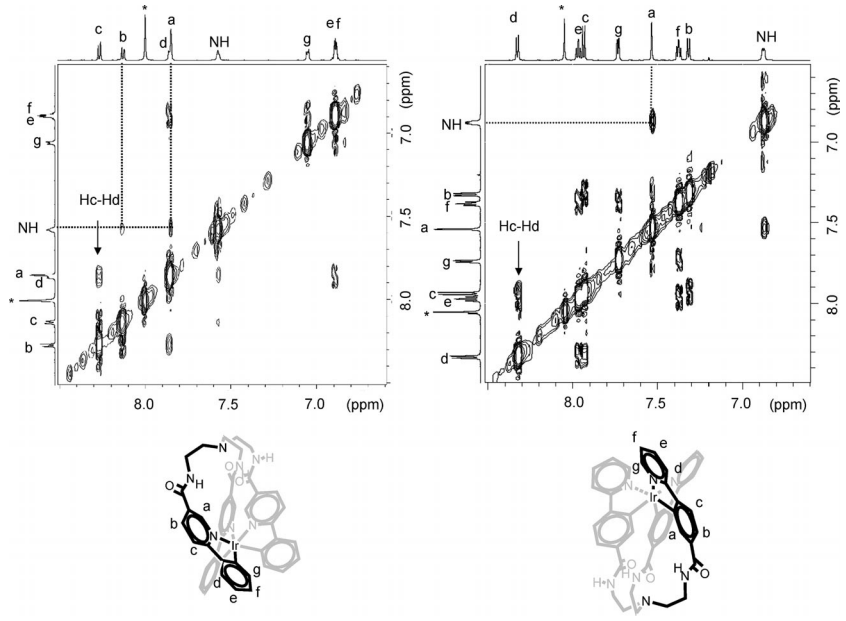

Figure 2. Downfield region of the H,H-ROESY spectra of the hemicaged complexes **1** (left) and **3** (right), recorded in [D_7]DMF. The residual solvent peaks are indicated with an asterisk.

the pyridine plane, with the carbonyl still coplanar with the pyridine. The first structure, with a lower conjugation of the pyridine ring and the carbonyl moiety, should influence the LUMO level less than the second structure in which the planarization of the system allows a stronger perturbation, and in particular a stabilization of the LUMO. Therefore, in the case of a lower conjugation of the pyridine ring and the carbonyl moiety, the emission of the hemicaged complex **1** is expected to be blueshifted compared to the open complex **2** (analogously to what has been observed in the case of the Ru^{II} caged complex).[17] Since complex **1** shows a small but clear bathochromic shift with respect to complex **2** (vide infra), it can be concluded that the carbonyl moiety of the amide group is conjugated with the pyridine ring. Therefore, most likely, the NH group is bent out of the pyridine plane.

Molecular structures of **1**–**4** were optimized at their electronic ground state (S_0) by means of DFT at the B3LYP/(6-31G(d,p) + SDD) level. The most meaningful computed geometrical parameters are reported in the Supporting Information (Table S7). The calculated S_0 structures are in good agreement when compared with experimental values of the closely related archetypical complex *fac*-[Ir(ppy)$_3$][22] within the known limitation of the density functional calculations used.[23] All the computed geometries investigated here possess a distorted octahedral arrangement around the heavy metal center, with C_3 point-group symmetry, and excellently reproduce the Ir–C bond length, with 2.036 Å being the value for **1** and 2.032–2.060 Å the theoretical and experimental values, respectively, whereas the Ir–N bond lengths are 2.192 (computed) and 2.071–2.095 Å (experimental).[24] It is also worth noting that the presence of the capping unit in the hemicaged complexes (**1** and **3**), seems not to affect the metal–ligand bond lengths with respect to the corresponding open derivatives (**2** and **4**), the computed bond displacements being ≤0.005 Å. As already reported by Nozaki et al.[23] and by Hay et al.,[15] Becke′s three-parameter together with the Lee–Yang–Parr exchange correlation hybrid functional (namely, B3LYP) tends to slightly overestimate the Ir–N bond lengths. Also, a similar agreement between theoretical and experimental geometrical values can be envisaged for the complexes **2**–**4**. This finding nicely highlights the suitability of the employed theoretical model for describing the geometrical parameters of the complexes investigated here. Also, the B3LYP functional has been already widely proven to properly describe the electronic and optical properties of phosphorescent cyclometalated iridium complexes.[25,26] In Figure 3, the schematic representation of the energy levels of the orbitals

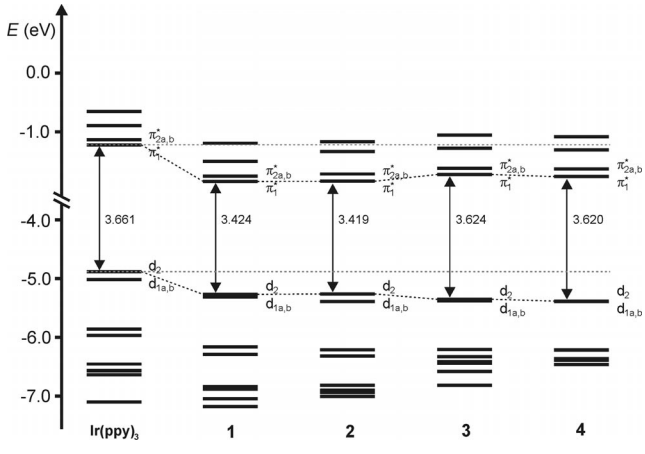

Figure 3. Partial molecular orbital diagram for complexes **1**–**4** and *fac*-[Ir(ppy)$_3$]. The arrows are intended to highlight the HOMO–LUMO energy gaps. All the DFT energy values are given in eV.

closer to the frontier region for the complexes **1**–**4** is reported, together with *fac*-[Ir(ppy)$_3$], which is used as reference. To provide deeper insight into the electronic structure of the complexes **1**–**4**, the isodensity surface plots of the most relevant Kohn–Sham molecular orbitals are shown in Figure 4 (for a more extended view, see Figures S5 and S6 in the Supporting Information). A list of the energies HOMO – 4 to LUMO + 4, along with the corresponding HOMO–LUMO energy gap, is reported in Table 1 (an extended version is available as Table S8 in the Supporting Information).

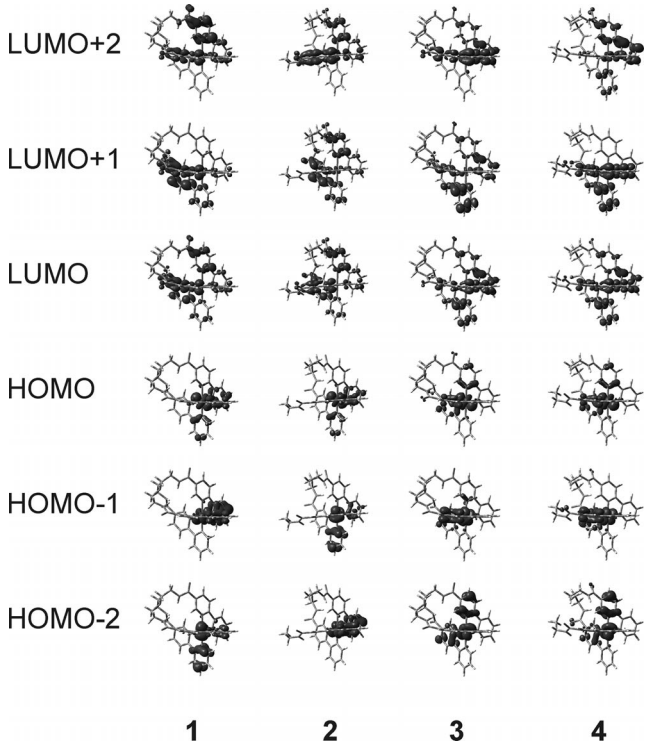

Figure 4. Isodensity surface plots of some selected frontier molecular orbitals for complexes **1**–**4** at their optimized S_0 geometry in the gas phase. Isodensity value: 0.035 e Bohr^{-3}. A larger version is given in Figures S4–S6 of the Supporting Information).

Table 1. List of selected molecular orbital energies [eV] for complexes **1**–**4** and *fac*-[Ir(ppy)$_3$] at their S_0-optimized geometry in vacuo, and HOMO–LUMO energy gap.

Orbital	*fac*-[Ir(ppy)$_3$]	**1**	**2**	**3**	**4**
LUMO + 4 (e)	–0.653	–1.192	–1.169	–1.054	–1.082
LUMO + 3 (a)	–0.894	–1.501	–1.337	–1.277	–1.306
LUMO + 2 (e)	–1.131	–1.758	–1.719	–1.620	–1.630
LUMO + 1 (e)	–1.131	–1.758	–1.719	–1.620	–1.630
LUMO (a)	–1.221	–1.844	–1.842	–1.728	–1.763
HOMO (a)	–4.881	–5.268	–5.261	–5.352	–5.384
HOMO – 1 (e)	–5.018	–5.314	–5.389	–5.382	–5.394
HOMO – 2 (e)	–5.018	–5.314	–5.389	–5.382	–5.394
HOMO – 3 (e)	–5.862	–6.165	–6.215	–6.207	–6.213[a]
HOMO – 4 (e)	–5.862	–6.165	–6.215	–6.207	–6.221
HOMO–LUMO gap	3.661	3.424	3.419	3.624	3.620

[a] "a" symmetry.

The three HOMOs mainly correspond to the 5d orbitals of the d^6 Ir^{III} center in a (distorted) octahedral environment, and are denoted d_{1a}, d_{1b}, and d_2, for which d_{1a} and d_{1b} are the twofold degenerated orbitals with "e" symmetry, and d_2 is the highest energy orbital with "a" symmetry. Nonetheless, a sizeable admixing between the three filled d orbitals of the iridium and the π-orbitals of the ligand can be clearly envisaged, as is typical of cyclometalated iridium(III) complexes. In particular, the HOMO (namely, d_2) is an antibonding combination of Ir(t_{2g}) and π orbitals of two of the cyclometalating phenyl rings of A symmetry. The corresponding energy was calculated to be –5.268, –5.261, –5.352, and –5.384 eV for complex **1**, **2**, **3**, and **4**, respectively. It is worth noting that in both couples of complexes the presence of the capping unit causes a negligible difference in the HOMO energy level. On the other hand, due to the nature of the HOMO, the position of the amido substituent (phenyl versus pyridyl ring) has a larger influence on the stabilization of the orbital. Complex **4** is stabilized by as much as 0.123 eV with respect to complex **2**. At slightly more negative energies, two degenerate d_{1a} and d_{1b}, namely, HOMO – 1 and HOMO – 2, are encountered. Their nature can be mainly described as the two antibonding combinations of the Ir(t_{2g}) and the π orbitals of two of the cyclometalating phenyl rings of E symmetry. These orbitals are stabilized with respect to the corresponding HOMO level by 0.046, 0.128, 0.029, and 0.01 eV, and lie at –5.314, –5.389, –5.382, and –5.394 eV, for **1**, **2**, **3**, and **4**, respectively. Going from the occupied to the virtual molecular orbitals, the three lowest-lying unoccupied molecular orbitals can be denoted, in order of increasing energy, as π^*_1, π^*_{2a}, and π^*_{2b}. The LUMO, namely, π^*_1, can be described as the combination π* orbitals of the ligands of "a" symmetry, mainly localized on the pyridyl rings, and extends over the carbonyl group of the amido substituents in complexes **1** and **2**. Such an orbital is calculated to lie at –1.844, –1.842, –1.728, and –1.763 eV for **1**, **2**, **3**, and **4**, respectively. As far as complexes **1** and **2** are concerned, the presence of the electron-withdrawing amido groups, which are strongly involved in the LUMO, induces a stabilization of the corresponding energy level with respect to the *fac*-[Ir(ppy)$_3$] as high as 0.623 and 0.621 eV, for **1** and **2**, respectively. On the other hand, such a stabilization effect is lower for complexes **3** and **4**, with values of 0.507 and 0.542 eV, respectively. Finally, a set of twofold degenerate orbitals of "e" symmetry lies at –1.758 (**1**), –1.719 (**2**), –1.620 (**3**), and –1.630 eV (**4**), which can be described as the combination of π* of the pyridyl moieties, and extends over the carbonyl group of the amido substituents in complexes **1** and **2**.

The UV/Vis absorption spectra of both pairs of hemicage and open complexes are reported in Figure 5, and the typical absorption maxima and shoulder are reported in Table 2 together with their molar extinction coefficients. Also, to gain deeper insight into the nature of the electronic transition involved in the absorption spectra, complexes **1**–**4** were investigated by means of time-dependent density functional theory (TD-DFT) calculations, and the computed vertical transitions described in terms of molecular orbitals of the

corresponding ground-state geometry. The most relevant lowest-lying singlet-to-singlet ($S_0 \rightarrow S_n$, n = 1–30) and the three lowest-lying singlet-to-triplet ($S_0 \rightarrow T_n$, n = 1–3) calculated transitions are respectively listed in the Supporting Information together with the nature of the involved orbitals and their expansion coefficients (see Tables S7 and S8). In the experimental spectra, all the complexes show a strong absorption band ($\varepsilon \geq 10^4$ M^{-1} cm^{-1}) between 280 and 320 nm and weaker absorption bands ($\varepsilon \leq 10^3$ M^{-1} cm^{-1}) between 350 and 450 nm. By comparison with the typical absorption shown by *fac*-[Ir(ppy)$_3$] derivatives,[27,28] the absorption bands centered around 300 nm can be assigned to ligand-centered $\pi \rightarrow \pi^*$ transitions, whereas the weaker bands centered around 400 nm can be assigned to the convolution of the lowest-lying spin-allowed singlet-to-singlet metal-to-ligand charge transfers (^{1}MLCTs). It is worth noting that the hemicaged complex **1** showed a slight bathochromic shift of its MLCT absorption bands compared to the open complex **2**, whereas no similar shift was observed for derivatives **3** and **4**. These findings nicely agree with the TD-DFT calculations. In particular, the lowest-energy transitions are the $S_0 \rightarrow S_1$ and mainly involve the iridium d orbitals (partially mixed with the π orbitals of the cyclometalating phenyl rings) and π* orbitals of the pyridyl moieties (HOMO → LUMO, ^{1}MLCT$_1$), and are computed to lie at 450, 453, 427, and 429 nm for complex **1**, **2**, **3**, and **4**, respectively. At slightly higher energies, two doubly generated ^{1}MLCT transitions with moderate oscillator strengths (f = 0.018–0.047) were computed, which can be ascribed to linear combinations of HOMO – 1/HOMO – 2 → LUMO (^{1}MLCT$_2$, with E symmetry) and HOMO – 1/HOMO – 2 → LUMO + 1/LUMO + 2 (^{1}MLCT$_3$, with A symmetry). Such transitions are calculated to occur at 435 and 423 nm (**1**); 425 and 410 nm (**2**); 414 and 399 nm (**3**); and 418 and 398 nm (**4**), respectively. At higher energies, such transitions are followed by A-symmetry excitation with intensities similar to the above-described processes and involve HOMO → LUMO + 3 (computed at 399 and 379 nm, for **1** and **2**, respectively) and linear combination of HOMO – 1/HOMO – 2 → LUMO + 1/LUMO + 2 (computed at 389 and 388 nm, for **3** and **4**, respectively). Moreover, the weak shoulder at lower energies (centered around 470 nm) can be assigned to spin-forbidden singlet-to-triplet ^{3}MLCT. The latter transitions are usually observed in complexes that contain heavy atoms (like iridium), which show a remarkable spin–orbit coupling that makes the singlet-to-triplet transitions partially allowed. Such transitions are in very good agreement with the theoretical ($S_0 \rightarrow T_1$) excitation energies, which are computed to be 502, 498, 485, and 486 nm, for **1**, **2**, **3**, and **4**, respectively.

All the reported complexes **1**–**4** showed intense luminescence at room temperature (Figure 6). As expected, the presence of electron-withdrawing groups on the pyridine ring induced a bathochromic shift in the emission of complexes **1** and **2** compared to the archetypical *fac*-[Ir(ppy)$_3$] as a consequence of the stabilization of the LUMO orbital. Conversely, the same groups on the phenyl ring minimally stabilize the HOMO orbital to result in a slight redshift of

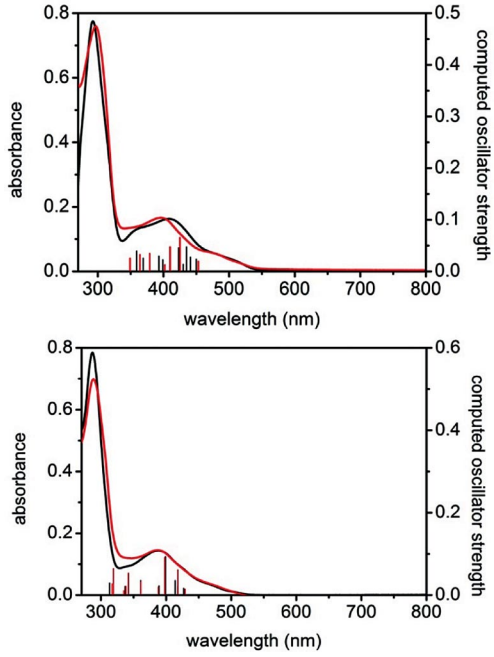

Figure 5. UV/Vis absorption of **1** (black), **2** (red) (top), and **3** (black), and **4** (red) (bottom) in DMF at room temp., and corresponding lower-lying computed excitation energies and oscillator strengths (vertical lines).

Table 2. UV/Vis absorption data of **1**–**4** and their molar extinction coefficient in DMF at room temp.

	Absorption[a] λ [nm], (ε [10^3 M^{-1} cm^{-1}])
1	292 (45), 302 (sh. 15), 361 (sh. 5.3),420 (6.5), 487 (sh. 2.1)
2	297 (32), 400 (6.9), 487 (sh. 2.1)
3	287 (52), 387 (9.4), 474 (sh. 2.1)
4*	288 (45), 387 (6.3), 474 (sh. 2.6)

[a] sh. = shoulder; * = estimated value because of the poor solubility of **4** in DMF.

the emission of the complexes **3** and **4** compared to [Ir(ppy)$_3$].[1] This different effect between **1** and **2** on the one hand and **3** and **4** on the other is due to the low atomic contribution given to the HOMO orbital by the atom on which the amide moiety is located.[29] The hemicaged complex **1** showed an evident redshift of the emission compared to the open complex **2**. Conversely, the hemicaged complex **3** showed a slight ipsochromic shift of the emission compared to the open complex **4**. As already mentioned, the rigidity and lack of flexibility induced by the capping unit blocks the rotation of the amido group, which is almost coplanar with the pyridine ring (see Table S7 in the Supporting Information).[17] Furthermore, the locally different polarity induced by the presence of the N atom of the capping unit can influence the degree of shift (e.g., a kind of local solvatochromism).[30] The situation is different when the phenyl is substituted with the amido group, since a destabilization of the HOMO orbital is expected. The slight blueshift observed for the hemicage **3** with respect to **4** can again be explained by the structural rigidity induced by the capping and by the locally different polarity induced by the

presence of the N atom of the capping unit.[30] The increase in energy for the HOMO–LUMO gap in the phenyl-substituted complexes **3** and **4** implies that the lowest excited state, ^{3}MLCT, is more mixed with the ^{3}LC energetically accessible, as can be seen by the structured emission and longer excited-state lifetimes. On the other hand, the structureless emission bands shown by complexes **1** and **2** indicate that the excited state of those complexes has mainly an ^{3}MLCT character.[27]

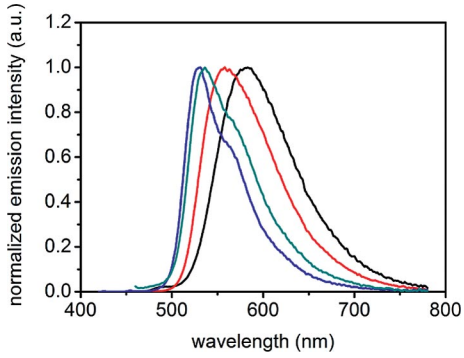

Figure 6. Normalized emission profile of **1** (black), **2** (red), **3** (blue), and **4** (green) in DMF at room temperature and upon excitation at λ = 400 nm.

The photophysical properties of **1**–**4** are summarized in Table 3; all complexes were highly luminescent in oxygen-free solvents, with quantum yields Φ_0 of 0.54 up to 0.81. Long excited-state lifetimes (τ_0 = 1.0–1.7 μs) were observed for all the complexes, thereby confirming the triplet nature of the emission. In air-equilibrated solutions, a general decrease of quantum yields and lifetimes was observed as a consequence of the oxygen quenching. Under these conditions, the hemicaged **1** showed a higher quantum yield (Φ = 0.048) than the open form **2** (Φ = 0.040), whereas complexes **3** and **4** show basically the same quantum yield (Φ = 0.035 and 0.034, respectively). The same trend was observed for the emission lifetimes in deaerated solution. The hemicage **1** showed a longer lifetime (τ = 100 ns) than the open complex **2** (τ = 78 ns), whereas the two complexes substituted on the phenyl ring showed practically the same lifetime (τ = 78 and 77 ns for **3** and **4**, respectively). The different trend observed for the quantum yields and excited-state lifetimes of the hemicaged **1** and the open form **2** in the absence and presence of oxygen provides a first indication of the different behavior towards oxygen quenching. In contrast, a quite similar decrease is observed for the two complexes **3** and **4**, which suggests a comparable behavior of these two compounds towards oxygen quenching. Therefore, comparison of the two pairs of complexes shielded on the pyridine (**1**, **2**) or on the phenyl (**3**, **4**) ring provides an explanation for the different oxygen sensitivity, which is induced by the shielding of the atoms on which the LUMO (**1**, **2**) or the HOMO (**3**, **4**) orbitals are localized. According to these qualitative data, the shielding of the LUMO exerts an important effect on the oxygen sensitivity, whereas the shielding of the HOMO does not have any relevant effect. A more quantitative evaluation of the difference in oxygen quenching was obtained by a Stern–Volmer analysis of the luminescence quenching (vide infra).

Table 3. Photophysical properties of hemicaged and open complexes in DMF at 25 °C (unless stated).[a]

	λ_{em} [nm]	ϕ_0		τ_0 [ns]	τ [ns]	λ_{em} [nm] (77 K)[a]	τ [μs] (77 K)[a]
1	580	0.54	0.048	1013	100	540	5.56
2	556	0.62	0.040	1110	78	532	5.06
3	532	0.81	0.035	1775	78	521	5.03
4	537	0.63	0.034	1620	77	519	4.68

[a] Measured in CH_2Cl_2/MeOH (1:1) glass. Values of ϕ_0 and ϕ are quantum yields in degassed and aerated solutions, respectively; τ_0 and τ are lifetimes in degassed and aerated solutions, respectively.

The emission spectra obtained in rigid matrices at 77 K (Figure 7) show that all the compounds **1**–**4** undergo a blue-shift of the emission maximum with respect to the room-temperature emission. This observation confirms that there is a ^{3}MLCT character of the emitting state.[31] The long lifetime recorded at 77 K for all the complexes and the structure of the emission again indicate the mixing with the ^{3}LC states and the triplet character of the emitting state.

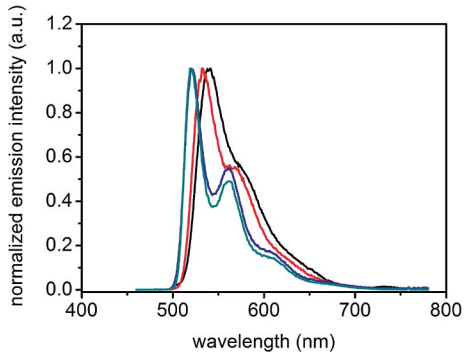

Figure 7. Normalized emission profile of **1** (black), **2** (red), **3** (blue), and **4** (green) in CH_2Cl_2/MeOH (1:1) glass at 77 K upon excitation at λ = 400 nm.

All the relevant electrochemical data are summarized in Table 4. For complex **1**, the main aspect that emerges from the electrochemical analysis is the effect played by the hemicage formation on lowering the LUMO level of **1** by about 0.1 eV compared to **2**. The presence of the hemicage seems to induce a more effective conjugation (coplanarity) of the amide bond in the *meta* position in the pyridyl moiety of **1** compared to that in **2**, thus stabilizing the LUMO. In fact, **1** is more easily reduced than its related open-form **2** ($E^{o}_{red,1} > E^{o}_{red,2}$). This finding could also be ascribed to a sizeable difference in solvation between **1** and **2**, but such stabilization is not evidenced by DFT calculations even if the solvation effect is taken into account by means of a conductor-like polarizable continuum model (PCM) as single-point calculation at the S_0-optimized geometry (see Table S11 in the Supporting Information). However, while comparing theoretical and electrochemical HOMO and LUMO energy levels, one should keep in mind that calculated values are approximations of the ionization

potential (HOMO) and electron affinity (LUMO) (i.e., vertical oxidation and reduction potentials), whereas the electrochemical values are the result of adiabatic (equilibrium) processes, which lead to the formation of radical cation and anion, respectively. The HOMO level is not affected by the hemicage structure ($E^{o}_{ox,1} \approx E^{o}_{ox,2}$), which confirms that it is mainly centered on the Ir metal core, as also supported by DFT calculations (vide supra).

Table 4. Electrochemical potential values (versus SCE) for samples **1**–**4** in DMF/0.1 M tetrabutylammonium hydroxide (TBAH).[a][b][c]

	E^{o}_{red} [LUMO]	E^{o}_{ox} [HOMO]	ΔE_{H-L}
1	–1.74 V, r	+0.92 V, r	2.66 eV
	[–2.60 eV]	[–5.26 eV]	
2	–1.87 V, r	+0.91 V, r	2.78 eV
	[–2.46 eV]	[–5.25 eV]	
3	–1.78 V, r	+1.06 V	2.84 eV
	[–2.56 eV]	[–5.40 eV]	
4	n/a[d]	n/a[d]	n/a[d]

[a] The sample solutions under investigation were 1 mM in DMF/0.1 M TBAH. A glassy carbon was employed as the working electrode, a platinum ring as the counter, and a silver wire as the reference. The scan rate was varied in the range of 0.2–5 V s^{-1}. $E = E^{o}$ calculated as the mean value between the cathodic and the anodic peak averaged in the scan rate range 0.2–0.5 V s^{-1}. [b] The peak-to-peak separation was ranging between 70 and 80 mV at 0.2 V s^{-1}, which is larger than expected for an ideal Nernstian behavior (59 mV). However, the behavior of the redox couple ferrocene/ferricenium ($Fc^{+}|Fc^{0}$), used as internal standard, showed the same trend. Therefore, we can attribute the observed effect to the ohmic drop of the system, as previously reported for aprotic media by Bard and co-workers.[47] The peak currents instead were found to be linearly dependent on the square root of the scan rate as expected for a diffusion-controlled redox process. [c] Reversible peak. [d] The solubility of **4** was poor under these experimental conditions, and it was not possible to estimate the potential values.

Furthermore, by comparison of **1** and **3**, the reduction potentials (E^{o}_{red}) of these two hemicaged systems differ by about 40 mV. The presence of the amide bond in the *meta* position in the pyridyl moiety is more effective in stabilizing the LUMO than in the phenyl moiety of **3**, thus corroborating the evidence of the redshift observed in the emission spectra (vide supra). Compound **4** is poorly soluble under the conditions used for the electrochemical measurements, and it was not possible to estimate the HOMO and LUMO values from electrochemical measurements. Nevertheless, because of the similar photophysical characteristics of **3** and **4**, it is possible to make an educated guess also for **4** (vide infra).

The luminescence oxygen quenching processes of complexes **1**–**4** were studied by monitoring the luminescence intensity of solutions with different concentrations of oxygen and by plotting the obtained results according to the Stern–Volmer equation [Equation (1)].

$$\frac{I_0}{I} = 1 + k_q \tau_0 [O_2] \quad (1)$$

for which I_0 and I are the emission intensities in the absence or presence of quencher, respectively, k_q is the quenching constant, τ_0 is the lifetime in the absence of quencher, and $[O_2]$ the concentration of oxygen in solution.[32] The Stern–Volmer plots for the four complexes are reported in Figure 8.

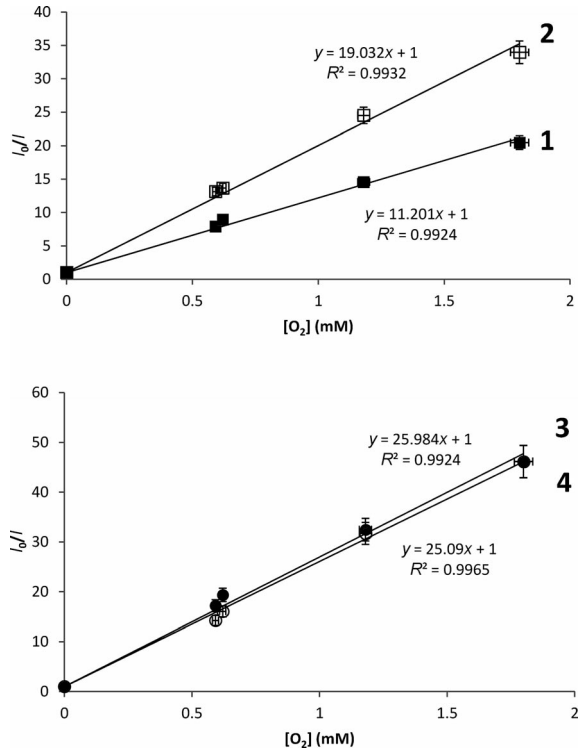

Figure 8. Stern–Volmer plot of complexes **1**–**4** in DMF at room temperature. Comparison of the oxygen quenching of the two couples of complexes shows that introduction of a capping unit on the pyridine side (hemicaged **1**) induces a decrease in oxygen quenching with respect to the open form **2**. Conversely, only a minor difference is observed between **3** and **4**, functionalized on the phenyl side.

The quenching constant k_q was calculated according to Equation (1) from the value of the slope obtained by fitting the Stern–Volmer plot. By consecutive comparison of the quenching constants (Table 5), it was possible to determine the efficiency of oxygen quenching. The pyridine-substituted complexes showed a remarkable decrease in oxygen quenching (40%) going from the open (**2**) to the hemicaged (**1**) complex, whereas no noticeable changes were observed in the case of the phenyl-substituted complexes (**3**, **4**). To exclude any difference in terms of energy or electron trans-

Table 5. Oxygen quenching constant (k_q) and thermodynamic parameters involved in the oxygen quenching mechanisms.

	E_{00} [eV]	ΔG_{et} [kJ mol^{-1}] [a]	ΔG_{el} [kJ mol^{-1}]	k_q [M^{-1} s^{-1}])
1	2.42	–139	–69	1.0×10^{10}
2	2.43	–140	–71	1.7×10^{10}
3	2.47	–144	–60	1.5×10^{10}
4	2.47	–144	–	1.6×10^{10}
IrCage[b]	–	–	–	0.5×10^{10}
$[Ir(ppy)_3]$[c]	2.52	–149	–95	2.4×10^{10}[b]

[a] Calculated assuming $E_{O_2*(^1\Delta_g)} = 0.98$ eV. [b] From the literature.[18] [c] Calculated on the basis of the photophysical data from the literature[21] unless otherwise stated.

fer, the free energies of energy transfer (ΔG_{et}) and of electron transfer (ΔG_{el}) were calculated according to Equations (2) and (3).

$$\Delta G_{et} = -(E_{00} - E_{O_2*}) \quad (2)$$

$$\Delta G_{el} = F(E_F^{ox} - E_{O_2}^{red}) - E_{00} + C \quad (3)$$

E_{00} is the energy of the 0–0 transition and E_{O_2*} the energy of the excited state of singlet oxygen: $E_{O_2*}(^1\Sigma_g)$ = 1.63 eV and $E_{O_2*}(^1\Delta_g)$ = 0.98 eV depending on which excited state of oxygen is initially produced during quenching, F is Faraday's constant, E_F^{ox} is the oxidation potential of the fluorophore, $E_{O_2}^{red}$ is the reduction potential of oxygen (–0.78 V), and C is a Coulomb term (usually neglected in polar solvents).[33–35] The calculated values of ΔG_{et} and ΔG_{el} are reported in Table 5. The evaluation of the ΔG_{el} of the open complex **4** was not possible because of its low solubility in DMF, which precludes the possibility of recording the potentiometric data. However, since both k_q and ΔG_{et} appeared to be identical for **3** and **4** within the experimental error, it is reasonable to assume that also ΔG_{el} will have the same value for both compounds. From the analysis of these data, it is possible to conclude that both the hemicaged and open molecule of each pair show only a modest difference in terms of thermodynamic feasibility of energy or electron transfer. The basically equal thermodynamic feasibility of energy and electron transfer between the pair of complexes **1**, **2** and **3**, **4** suggests that the remarkable difference observed in the quenching constant k_q between the hemicaged (**1**) and the open (**2**) complex functionalized on the pyridine side of the [Ir(ppy)$_3$] is due to a structural effect.

The caged complex (**ii**, Scheme 1) previously reported by our group shows a further 50% decrease in the oxygen quenching ($k_q = 0.5 \times 10^{10}$ M^{-1} s^{-1}) with respect to **1**.[18] On the basis of the emission maximum (λ_{em} = 570 nm), it is reasonable to hypothesize that the energy of the triplet state (E_{00}) of the cage has likely an intermediate value between the E_{00} of **1** (λ_{em} = 580 nm) and **2** (λ_{em} = 556 nm), therefore the value of the free energy of the energy transfer ΔG_{et} can be estimated to be similar to the ΔG_{et} of **1** and **2**. On the other hand, because of the presence of two amide moieties on the phenylpyridine ligands, the oxidation potential of the cage is probably higher than the oxidation potential of **1**.[1] Consequently, the value of the free energy of the electron transfer ΔG_{el} is probably higher than the value found for **1**, thereby resulting in a less favorable thermodynamic feasibility of electron transfer. In conclusion, on the basis of the estimated thermodynamic parameters, it is possible to hypothesize that the low degree of oxygen quenching observed for the caged complex **ii** probably derives from a decreased thermodynamic feasibility of the electron transfer with respect to **1**. We believe, however, that structural factors also play an important role in the low degree of oxygen quenching of the caged Ir^{III} complex **ii**: it has been observed that in the caged complex the amide moiety located on the pyridine side shows the carbonyl oriented towards the inner side of the molecule. According to computational models, in the hemicaged complexes **1** and **2** the LUMO orbital is partly localized on the carbonyl moiety (vide supra). Therefore, the orientation of the pyridine carbonyl towards the inner side of the cage would likely result in a higher degree of LUMO shielding and a consequent decrease in the oxygen quenching degree, since the lowest excited state is an MLCT in which the ligand involved is indeed the pyridine unit.

Conclusion

We have reported the synthesis, characterization, and photochemical properties of two pairs of iridium(III)–tris-(phenylpyridine) derivatives with a hemicaged (**1**, **3**) or open (**2**, **4**) structure. The results obtained from this systematic study of the oxygen quenching of hemicages and open complexes shielded on the pyridine (**1**, **2**) or on the phenyl (**3**, **4**) ring show the hemicaged complex that bears a capping unit on the pyridine ring (**1**) to have a much lower oxygen quenching constant ($k_q = 1.0 \times 10^{10}$ M^{-1} s^{-1}) than its parent open complex **2** with ethylamide on the pyridine rings ($k_q = 1.7 \times 10^{10}$ M^{-1} s^{-1}). Moreover, the hemicaged complex **3**, in which the capping unit is connected to the phenyl rings, shows basically the same degree of oxygen quenching as the open complex **4** functionalized with ethylamides on the phenyl rings ($k_q = 1.5 \times 10^{10}$ and 1.6×10^{10} M^{-1} s^{-1}, respectively). The ΔG_{et} and ΔG_{el} parameters show that in terms of thermodynamic feasibility only a modest difference exists between the members of each pair of compounds (**1**, **2** and **3**, **4**) and, therefore, the lower quenching shown by **1** with respect to **2** can be ascribed to a structural effect. The structural (shielding) effect induced by the presence of the capping unit is due to the shielding of the LUMO orbital exerted by the capping unit, which is possibly enforced by the high degree of twisting of the hemicaged complex **1**. It is reasonable to hypothesize that both these parameters give a contribution that results in a lower degree of oxygen quenching of **1** with respect to **2**, but on the basis of the structural and photophysical data available it was not possible to quantify the respective contributions of the two effects. The introduction of a capping unit on the phenyl ring induced only a minor change in the oxygen sensitivity of the hemicaged complex **3** with respect to the open complex **4**, which is explained by the fact that the LUMO of the hemicage **3** is mostly localized on the pyridine ring, and the luminescent state is an MLCT that involves the pyridine. The structure–photoluminescence quenching relationship obtained from this study together with thermodynamic considerations for the substituents on the phenylpyridine ring nicely explain the observed shielding mechanism in the hitherto only reported iridium(III) caged complex.

Experimental Section

General: The NMR spectroscopic experiments were performed with a Bruker Avance II NMR spectrometer operating at 600.35 MHz for ^{1}H and 150.09 MHz for ^{13}C. Chemical shifts are

given in ppm using the residual solvent signal as reference. The multiplicity of the peaks is reported by using the following abbreviations: s = singlet, d = doublet, t = triplet, quint = quintuplet, m = multiplet. The chemical shifts and assignments of ^{13}C signals are reported in the Supporting Information. Mass spectra were measured with a Micromass LCT (ESI-HRMS) spectrometer. IR spectra were measured with a Thermo Scientific Nicolet 6700 FTIR spectrometer equipped with a Smart Orbit diamond ATR accessory. Main bands are reported and assigned to functional groups by using the following abbreviations: br. = broad band, str. = stretching band, def. = deformation band. UV/Vis spectra were measured with a Perkin–Elmer Lambda 850 UV/Vis spectrophotometer by using a quartz cuvette with 1 cm path length. Steady-state luminescence spectra were measured with an Edinburgh FS900 fluorospectrometer. A 450 W xenon arc lamp was used as excitation source. Luminescence quantum yields at room temperature (Φ and Φ_{air}) were evaluated by comparing wavelength-integrated intensities (I) of isoabsorptive optically diluted solutions (abs. < 0.1) with reference to $[Ru(bpy)_3]Cl_2$ ($\Phi_R = 0.028$ in air-equilibrated water) or fluorescein ($\Phi_R = 0.95$ in 0.1 M NaOH) standard for the complexes **1**, **2** and **3**, **4**, respectively, and by using the Equation (4), in which n and n_R are the refractive index of the sample and reference solvent, respectively.[36]

$$\Phi = \Phi_R \frac{n^2 I}{n_R^2 I_R} \quad (4)$$

Luminescence lifetimes of the compounds were determined by recording the decay curves of the luminescence intensity at the emission maximum using the TCSPC option on a HORIBA Jobin Yvon Fluoromax 4 instrument and a pulsed solid-state LED as excitation source at 462 nm wavelength. The recorded data were analyzed using the DAS6 software package of HORIBA Jobin Yvon. Degassed solutions were prepared by four freeze–pump–thaw cycles. Electrochemical measurements were done in *N*,*N*-dimethylformamide (Acros, extra dry over molecular sieves, 99.8%), which was used as received without any further purification. Tetrabutylammonium hexafluorophosphate (electrochemical grade, ≥99%, Fluka) was used as supporting electrolyte, which was recrystallized from a 1:1 ethanol/water solution and dried at 60 °C under vacuum. For the electrochemical experiments, a CHI750C Electrochemical Workstation (CH Instruments, Inc., Astin, TX, USA) was used. The electrochemical experiments were performed in a glass cell under an Ar atmosphere. To minimize the ohmic drop between the working and the reference electrodes, feedback correction was employed. The electrochemical experiments were performed by using a 3 mm diameter glassy carbon disk electrode (homemade from Tokai glassy carbon rod). Before the experiments, the working electrode was polished with a 0.05 μm diamond suspension (Metadi Supreme Diamond Suspension, Buehler) and ultrasonically rinsed with ethanol for 5 min. The electrode was electrochemically activated in the background solution by means of several voltammetric cycles at 0.5 V s^{-1} between the anodic and cathodic solvent/electrolyte discharges until the same quality features were obtained. The reference electrode was a silver quasi-reference electrode (Ag-QRE), which was separated from the catholyte by a glass frit (Vycor). The reference electrode was calibrated at the end of each experiment against the ferrocene/ferricenium couple, the formal potential of which in *N*,*N*-dimethylformamide is 0.464 V against the standard calomel electrode (SCE) with satd. aqueous KCl; all potential values are reported against SCE. A platinum ring or coil served as the counter electrode.

Solutions with different oxygen concentration, suitable for the Stern–Volmer quenching studies, were prepared by using N_2/O_2 mixtures prepared with a Brooks 5850S Mass Flow control and by purging the fluorophore solutions for 40 min.

Computational Details: Geometries were optimized by means of DFT and employing the exchange correlation hybrid functional B3LYP.[15,37,38] The standard valence double-ζ polarized basis set 6-31G(d,p)[39] was used for C, H, N, and O. For Ir, the Stuttgart–Dresden (SDD) effective core potentials were employed along with the corresponding valence triple-ζ basis set. All the calculations were done assuming C_3 symmetry. The nature of all the stationary points was checked by computing vibrational frequencies, and all the species were found to be true potential energy minima, as no imaginary frequency was obtained ($N_{Imag} = 0$). Single-point calculations at the S_0-optimized geometry were done also in the solvent used for the electrochemical characterization (*N*,*N*-dimethylformamide), described by means of a conductor-like polarizable continuum model (PCM).[40–42]

To simulate the absorption electronic spectrum down to 300 nm, for each complex the lowest 30 singlet ($S_0 \rightarrow S_n$) as well as the four lowest triplet excitation energies ($S_0 \rightarrow T_n$) were computed on the optimized geometry at the S_0 by means of TD-DFT calculations.[43,44] Oscillator strengths were deduced from the dipole transition-matrix elements (for single states only). Isodensity surfaces plots of selected orbitals for the investigated structures in the gas phase at their optimized ground-state geometry were plotted at isodensity value of 0.035 *e* Bohr^{-3}. All the calculations were performed with Gaussian 09 program package.[45]

Materials: Oxygen-sensitive reactions were carried out by using standard Schlenk techniques. Commercial-grade reagents were purchased from Sigma–Aldrich and used without further purification. 4-(Pyridin-2-yl)benzoic acid (**8**) was prepared according to the literature procedure.[46]

6-Phenylnicotinic Acid (5): Phenylboronic acid (3 g, 24.6 mmol), 6-bromonicotinic acid (3.66 g, 18.2 mmol), and tetrakis(triphenylphosphane)palladium(0) (900 mg, 0.78 mmol) were dissolved in a mixture (180 mL) of Na_2CO_3 (0.2 M) and acetonitrile (1:1). After several argon/vacuum cycles, the reaction was heated at reflux for 48 h. The hot reaction mixture was filtered through Celite, the acetonitrile removed, and the resulting aqueous solution was extracted several times with CH_2Cl_2. The aqueous solution was then acidified with acetic acid and the white precipitate was filtered and dried with P_2O_5; yield 3.1 g (15.6 mmol; 85%) of pure compound. ^1H NMR ([D$_6$]DMSO): δ = 9.15 (s, 1 H), 8.33 (d, J = 12 Hz, 1 H), 8.15 (d, J = 6 Hz, 2 H), 8.10 (d, J = 12 Hz, 1 H), 7.54–7.49 (m, 3 H) ppm. ^{13}C NMR ([D$_6$]DMSO): see the Supporting Information. IR (neat): $\tilde{\nu}$ = 1673 (C=O str.), 1417 (OH def. acid), 935 (OH def. acid) cm^{-1}. ESI-HRMS: calcd. for $C_{12}H_9NO_2$ 199.063 [M$^+$]; found 199.065.

General Synthesis of Hemicaged Ligands: Acid (600 mg, 3 mmol), *N*,*N*′-dicyclohexylcarbodiimide (620 mg, 3 mmol), and *N*-hydroxybenzotriazole (400 mg, 3 mmol) were dissolved in dry *N*,*N*′-dimethylacetamide (50 mL). Tris(2-aminoethyl)amine (120 μL, 0.8 mmol) was added dropwise and the resulting mixture was stirred overnight at 60 °C. The reaction mixture was then filtered and added to ethyl ether (ca. 400 mL) under vigorous stirring. The white precipitate was then collected by filtration and washed with hot acetonitrile. In a typical experiment, 212 mg (0.3 mmol, 40%) of pure tripodal ligand was obtained.

Hemicaged Ligand (6): ^1H NMR ([D$_4$]MeOH): δ = 8.90 (s, 1 H), 7.93 (dd, J = 12 Hz, 1 H), 7.73 (d, J = 6 Hz, 2 H), 7.43 (d, J = 6 Hz, 1 H), 7.37 (t, J = 6 Hz, 1 H), 7.29 (t, J = 6 Hz, 2 H), 3.60 (t, J = 6 Hz, 2 H), 2.82 (t, J = 6 Hz, 2 H) ppm. ^{13}C NMR ([D$_4$]-

MeOH): see the Supporting Information. IR (neat): $\tilde{\nu}$ = 3396 (NH str.), 2948 (CH_2 str.), 2815 (N–CH_2/CH_2 str.), 1630 (C=O str.), 1587 (NH bend.), 1465 (CH_2–N str.), 743 (N–C–O str.) cm^{-1}. ESI-HRMS: calcd. 690.319 [M + H^+]; found 690.320.

Hemicaged Ligand (9): ^1H NMR ([D_4]MeOH): δ = 8.46 (s, 1 H), 7.69 (d, J = 6 Hz, 2 H), 7.66 (d, J = 6 Hz, 2 H), 7.59 (t, J = 12 Hz, 1 H), 7.49 (d, J = 6 Hz, 1 H), 7.24 (t, J = 6 Hz, 1 H), 3.59 (t, J = 6 Hz, 2 H), 2.82 (t, J = 6 Hz, 2 H) ppm. ^{13}C NMR ([D_4]MeOH): see the Supporting Information. IR (neat): $\tilde{\nu}$ = 3293 (NH str.), 3055 (CH_2 str.), 2925 (CH_2 str.), 2790 (N–CH_2/CH_2 str.), 1631 (C=O str.), 1537 (NH bend.), 1463 (CH_2–N str.), 752 (N–C–O str.) cm^{-1}. HRMS: calcd. 690.319 [M + H^+]; found 690.317.

General Synthesis of Ethylamide Ligands: Acid (1 g, 5 mmol) and 1-ethyl-3-[3-(dimethylamino)propyl]carbodiimide (1.9 g, 12.5 mmol) were dissolved in a mixture (60 mL) of CH_2Cl_2/pyridine (7:3). Ethylamine (3 mL, 2.0 M in THF) was added dropwise, and the mixture was stirred dropwise at room temperature. The solvent was removed under vacuum, and the crude was then suspended in water and extracted with ethyl acetate. The organic phase was washed with a satd. solution of $CuSO_4$, then with satd. NH_4Cl, and eventually with brine. The organic phase was then dried with Na_2SO_4 and the solvent removed by rotavapor. Typically, 1 g (4.25 mmol; 85%) of pure compound was obtained.

***N*-Ethyl-6-phenylnicotinamide (7):** ^1H NMR ([D_6]DMSO): δ = 9.21 (s, 1 H), 8.38 (d, J = 6 Hz, 1 H), 8.21 (d, J = 6 Hz, 2 H), 8.13 (d, J = 6 Hz, 1 H), 7.57–7.50 (m, 3 H), 3.43 (q, J = 6 Hz, 2 H), 1.21 (t, J = 6 Hz, 3 H) ppm. ^{13}C NMR ([D_4]MeOH): see the Supporting Information. IR (neat): $\tilde{\nu}$ = 3322 (N–H str.), 2975 (CH_3 str.), 2931 (CH_2 str.), 2877 (CH_3 str.), 1627 (C=O str.), 1522 (N–H str.), 1469 (CH_2–N str.), 1267 (CH_3 str.), 746 (N–C–O str.) cm^{-1}. ESI-HRMS: calcd. 226.111 [M^+]; found 226.113.

***N*-Ethyl-4-(pyridin-2-yl)benzamide (10):** ^1H NMR ([D_6]DMSO): δ = 8.71 (d, J = 6 Hz, 1 H), 8.57 (t, J = 6 Hz, 1 H), 8.18 (d, J = 6 Hz, 2 H), 8.05 (d, J = 6 Hz, 1 H), 7.96 (d, J = 6 Hz, 2 H), 7.94 (t, J = 12 Hz, 1 H), 7.41 (t, J = 6 Hz, 1 H), 3.31 (m), 1.15 (t, J = 6 Hz, 3 H) ppm. ^{13}C NMR ([D_4]MeOH): see the Supporting Information. IR (neat): $\tilde{\nu}$ = 3297 (N–H str.), 2973 (CH_3 str.), 2931 (CH_2 str.), 2870 (CH_3 str.), 1627 (C=O str.), 1548 (N–H bend.), 1463 (CH_2–N str.), 1288 (CH_3 str.), 746 (N–C–O str.) cm^{-1}. ESI-HRMS: calcd. 226.111 [M^+]; found 226.115.

General Synthesis of Ir^{III} Hemicages: Tripodal ligand (100 mg, 0.14 mmol), $IrCl_3$ (41 mg, 0.14 mmol), and CF_3CO_2Ag (89 mg, 0.4 mmol) were stirred in ethylene glycol (10 mL) previously purged with nitrogen. After several cycles of argon/vacuum, the resulting mixture was heated to reflux overnight. The reaction mixture was cooled to room temperature, diluted with water, and extracted several times with ethyl acetate. The organic phases were collected, washed with brine, and dried with Na_2SO_4. The products were then purified by column chromatography (SiO_2, CH_2Cl_2/MeOH, 95:5).

Ir-6 (1): ^1H NMR ([D_2]CH_2Cl_2): δ = 7.99 (d, J = 12 Hz, 1 H), 7.96 (d, J = 6 Hz, 1 H), 7.76 (s, 1 H), 7.71 (m, 1 H), 7.02 (d, J = 6 Hz, 1 H), 6.95–6.96 (m, 2 H), 6.34 (t, J = 6 Hz, 1 H), 3.62 (d, J = 18 Hz, 1 H), 3.41 (t, J = 12 Hz, 1 H), 2.91 (t, J = 6 Hz, 1 H), 2.30 (d, J = 12 Hz, 1 H) ppm. ^{13}C NMR ([D_2]CH_2Cl_2): see the Supporting Information. $\tilde{\nu}$ = IR (neat): 3274 (br., NH str.), 3041 (CH_2 str.), 2925 (CH_2 str.), 2815 (N–CH_2/CH_2 str.), 1633 (C=O str.), 1539 (NH bend.), 1471 (CH_2–N str.), 748 (N–C–O str.) cm^{-1}. ESI-HRMS: calcd. 880.259 [M + H^+]; found 880.260.

Ir-9 (3): ^1H NMR ([D_2]CH_2Cl_2): δ = 7.98 (d, J = 6 Hz, 1 H), 7.75 (d, J = 12 Hz, 1 H), 7.72 (d, J = 12 Hz, 1 H), 7.59 (d, J = 6 Hz, 1 H), 7.40 (d, J = 6 Hz, 1 H), 7.33 (s, 1 H), 7.09 (t, J = 6 Hz, 1 H), 6.25 (d, J = 6 Hz, 1 H), 3.90 (t, J = 6 Hz, 1 H), 3.05 (t, J = 12 Hz, 1 H), 2.79 (t, J = 12 Hz, 1 H), 2.37 (d, J = 12 Hz, 1 H) ppm. ^{13}C NMR ([D_2]CH_2Cl_2): see the Supporting Information. IR (neat): $\tilde{\nu}$ = 3290 (br., NH str.), 3066 (CH_2 str.), 2921 (CH_2 str.), 2850 (N–CH_2/CH_2 str.), 1643 (C=O str.), 1540 (NH bend.), 1470 (CH_2–N str.), 756 (N–C–O str.) cm^{-1}. ESI-HRMS: calcd. 880.259 [M + H^+]; found 880.262.

General Synthesis of Open Ir^{III} Complexes: Ligand (100 mg, 0.42 mmol) and $IrCl_3$ (66 mg, 0.22 mmol) were dissolved in a mixture of 2-ethoxyethanol and water (3:1). After several cycles of argon/vacuum, the mixture was heated to reflux overnight. The reaction mixture was cooled to room temperature, half of the solvent was evaporated, and the resulting solution was poured on ice. The resulting precipitate was filtered, washed with water and diethyl ether, and dried under vacuum. The solid (≈70 mg) was then suspended in toluene, ligand (36 mg, 0.15 mmol) and CF_3SO_3Ag (80 mg, 0.30 mmol) were added, several cycles argon/vacuum were performed to remove oxygen, and the mixture was heated to reflux overnight under inert atmosphere. The crude was then washed with methanol and then dissolved in CH_2Cl_2 (10% MeOH), filtered through Celite, and eventually purified by preparative TLC (CH_2Cl_2/MeOH, 95:5).

Ir-7_3 (2): ^1H NMR ([D_7]DMF): δ = 8.60 (t, J = 6 Hz, 1 H), 8.35 (d, J = 6 Hz, 1 H), 8.31–8.28 (m, 2 H), 7.90 (d, J = 12 Hz, 1 H), 6.87 (t, J = 6 Hz, 1 H), 6.79–6.74 (m, 2 H), 3.27 (quint., J = 6 Hz, 2 H), 1.08 (t, J = 6 Hz, 3 H) ppm. ^{13}C NMR ([D_7]DMF): see the Supporting Information. IR (neat): $\tilde{\nu}$ = 3290 (N–H str.), 3035 (CH_2 str.), 2970 (CH_3 str.), 2930 (CH_2 str.), 2873 (CH_3 str.), 1635 (C=O str.), 1540 (N–H bend.), 1473 (CH_2–N str.), 1257 (CH_3 str.), 748 (N–C–O str.) cm^{-1}. ESI-HRMS: calcd. 891.261 [M + Na^+]; found 891.262.

Ir-10_3 (4): ^1H NMR ([D_7]DMF): δ = 8.26 (d, J = 12 Hz, 1 H), 7.92 (t, J = 6 Hz, 1 H), 7.86–7.88 (m, 2 H), 7.63 (d, J = 6 Hz, 1 H), 7.37 (s, 1 H), 7.31 (d, J = 12 Hz, 1 H), 7.20 (t, J = 6 Hz, 1 H), 3.22 (quint., J = 6 Hz, 2 H), 1.05 (t, J = 6 Hz, 3 H) ppm. ^{13}C NMR ([D_7]DMF): see the Supporting Information. IR (neat): $\tilde{\nu}$ = 3297 (N–H str.), 3060 (CH_2 str.), 2966 (CH_3 str.), 2927 (CH_2 str.), 2852 (CH_3 str.), 1633 (C=O str.), 1540 (N–H bend.), 1467 (CH_2–N str.), 1257 (CH_3 str.), 754 (N–C–O str.) cm^{-1}. ESI-HRMS: calcd. 869.279 [M + H^+]; found 869.278.

Supporting Information (see footnote on the first page of this article): HH-COSY, HH-ROESY and ^{13}C NMR data, isodensity plots and energies of selected molecular orbitals, excitation energies and oscillator strength of the lowest transitions.

Acknowledgments

M. M. thanks the Alexander Humboldt Fundation for financial support.

[1] L. Flamigni, A. Barbieri, C. Sabatini, B. Ventura, F. Barigelletti, *Photochemistry and Photophysics of Coordination Compounds II*, vol. 281, **2007**, pp. 143–203.
[2] A. Tsuboyama, H. Iwawaki, M. Furugori, T. Mukaide, J. Kamatani, S. Igawa, T. Moriyama, S. Miura, T. Takiguchi, S. Okada, M. Hoshino, K. Ueno, *J. Am. Chem. Soc.* **2003**, *125*, 12971–12979.
[3] J. I. Kim, I. S. Shin, H. Kim, J. K. Lee, *J. Am. Chem. Soc.* **2005**, *127*, 1614–1615.
[4] M. A. Baldo, D. F. O'Brien, Y. You, A. Shoustikov, S. Sibley, M. E. Thompson, S. R. Forrest, *Nature* **1998**, *395*, 151–154.
[5] V. Fernandez-Moreira, F. L. Thorp-Greenwood, M. P. Coogan, *Chem. Commun.* **2010**, *46*, 186–202.

[6] A. Ruggi, D. N. Reinhoudt, A. H. Velders, in: *Bioinorganic Medicinal Chemistry* (Ed.: E. Alessio), Wiley-VCH, Weinheim, Germany, **2011**.
[7] D. Crespy, K. Landfester, U. S. Schubert, A. Schiller, *Chem. Commun.* **2010**, *46*, 6651–6662.
[8] J. Kuil, P. Steunenberg, P. T. K. Chin, J. Oldenburg, K. Jalink, A. H. Velders, F. W. B. van Leeuwen, *ChemBioChem* **2011**, *12*, 1897–1903.
[9] J. N. Demas, E. W. Harris, R. P. McBride, *J. Am. Chem. Soc.* **1977**, *99*, 3547–3551.
[10] M. P. Coogan, J. B. Court, V. L. Gray, A. J. Hayes, S. H. Lloyd, C. O. Millet, S. J. A. Pope, D. Lloyd, *Photochem. Photobiol. Sci.* **2010**, *9*, 103–109.
[11] J. N. Demas, D. Diemente, E. W. Harris, *J. Am. Chem. Soc.* **1973**, *95*, 6864–6865.
[12] S. J. Zhang, M. Hosaka, T. Yoshihara, K. Negishi, Y. Iida, S. Tobita, T. Takeuchi, *Cancer Res.* **2010**, *70*, 4490–4498.
[13] A. Ruggi, F. W. B. van Leeuwen, A. H. Velders, *Coord. Chem. Rev.* **2011**, *255*, 2542–2554.
[14] C. Li, M. Yu, Y. Sun, Y. Wu, C. Huang, F. Li, *J. Am. Chem. Soc.* **2011**, *133*, 11231–11239.
[15] P. J. Hay, *J. Phys. Chem. A* **2002**, *106*, 1634–1641.
[16] M. S. Lowry, S. Bernhard, *Chem. Eur. J.* **2006**, *12*, 7970–7977.
[17] F. Barigelletti, L. De Cola, V. Balzani, P. Belser, A. Von Zelewsky, F. Voegtle, F. Ebmeyer, S. Grammenudi, *J. Am. Chem. Soc.* **1989**, *111*, 4662–4668.
[18] A. Ruggi, M. B. Alonso, D. N. Reinhoudt, A. H. Velders, *Chem. Commun.* **2010**, *46*, 6726–6728.
[19] R. F. Beeston, S. L. Larson, M. C. Fitzgerald, *Inorg. Chem.* **1989**, *28*, 4187–4189.
[20] N. Miyaura, A. Suzuki, *Chem. Rev.* **2002**, *95*, 2457–2483.
[21] A. B. Tamayo, B. D. Alleyne, P. I. Djurovich, S. Lamansky, I. Tsyba, N. N. Ho, R. Bau, M. E. Thompson, *J. Am. Chem. Soc.* **2003**, *125*, 7377–7387.
[22] J. Breu, P. Stossel, S. Schrader, A. Starukhin, W. J. Finkenzeller, H. Yersin, *Chem. Mater.* **2005**, *17*, 1745–1752.
[23] K. Nozaki, K. Takamori, Y. Nakatsugawa, T. Ohno, *Inorg. Chem.* **2006**, *45*, 6161–6178.
[24] Experimental values are referred to *fac*-[Ir(ppy)$_3$], see: J. Breu, P. Stossel, S. Schrader, A. Starukhin, W. J. Finkenzeller, H. Yersin, *Chem. Mater.* **2005**, *17*, 1745–1752.
[25] S. Fantacci, F. De Angelis, *Coord. Chem. Rev.*, DOI: 10.1016/j.ccr.2011.1003.1008.
[26] A. Vlcek, S. Zalis, *Coord. Chem. Rev.* **2007**, *251*, 258–287.
[27] S. Lamansky, P. Djurovich, D. Murphy, F. Abdel-Razzaq, H. E. Lee, C. Adachi, P. E. Burrows, S. R. Forrest, M. E. Thompson, *J. Am. Chem. Soc.* **2001**, *123*, 4304–4312.
[28] W. Holzer, A. Penzkofer, T. Tsuboi, *Chem. Phys.* **2005**, *308*, 93–102.
[29] I. Avilov, P. Minoofar, J. Cornil, L. De Cola, *J. Am. Chem. Soc.* **2007**, *129*, 8247–8258.
[30] K. D. Oyler, F. J. Coughlin, S. Bernhard, *J. Am. Chem. Soc.* **2007**, *129*, 210–217.
[31] A. Juris, V. Balzani, F. Barigelletti, S. Campagna, P. Belser, A. Vonzelewsky, *Coord. Chem. Rev.* **1988**, *84*, 85–277.
[32] J. R. Lakowicz, *Principles of Fluorescence Spectroscopy*, Springer, Singapore, **2006**.
[33] Q. G. Mulazzani, H. Sun, M. Z. Hoffman, W. E. Ford, M. A. J. Rodgers, *J. Phys. Chem.* **1994**, *98*, 1145–1150.
[34] A. A. Abdel-Shafi, P. D. Beer, R. J. Mortimer, F. Wilkinson, *Helv. Chim. Acta* **2001**, *84*, 2784–2795.
[35] M. Bodesheim, M. Schutz, R. Schmidt, *Chem. Phys. Lett.* **1994**, *221*, 7–14.
[36] M. Montalti, A. Credi, L. Prodi, M. T. Gandolfi, *Handbook of Photochemistry*, CRC press, Boca Raton, **2006**.
[37] C. T. Lee, W. T. Yang, R. G. Parr, *Phys. Rev. B* **1988**, *37*, 785–789.
[38] A. D. Becke, *J. Chem. Phys.* **1993**, *98*, 5648–5652.
[39] M. M. Francl, W. J. Pietro, W. J. Hehre, J. S. Binkley, M. S. Gordon, D. J. Defrees, J. A. Pople, *J. Chem. Phys.* **1982**, *77*, 3654–3665.
[40] M. Cossi, N. Rega, G. Scalmani, V. Barone, *J. Comput. Chem.* **2003**, *24*, 669–681.
[41] M. Cossi, V. Barone, *J. Chem. Phys.* **2001**, *115*, 4708–4717.
[42] V. Barone, M. Cossi, *J. Phys. Chem. A* **1998**, *102*, 1995–2001.
[43] R. E. Stratmann, G. E. Scuseria, M. J. Frisch, *J. Chem. Phys.* **1998**, *109*, 8218–8224.
[44] M. E. Casida, C. Jamorski, K. C. Casida, D. R. Salahub, *J. Chem. Phys.* **1998**, *108*, 4439–4449.
[45] M. J. Frisch, G. W. Trucks, H. B. Schlegel, G. E. Scuseria, M. A. Robb, J. R. Cheeseman, G. Scalmani, V. Barone, B. Mennucci, G. A. Petersson, H. Nakatsuji, M. Caricato, X. Li, H. P. Hratchian, A. F. Izmaylov, J. Bloino, G. Zheng, J. L. Sonnenberg, M. Hada, M. Ehara, K. Toyota, R. Fukuda, J. Hasegawa, M. Ishida, T. Nakajima, Y. Honda, O. Kitao, H. Nakai, T. Vreven, J. A. Montgomery Jr, J. E. Peralta, F. Ogliaro, M. Bearpark, J. J. Heyd, E. Brothers, K. N. Kudin, V. N. Staroverov, R. Kobayashi, J. Normand, K. Raghavachari, A. Rendell, J. C. Burant, S. S. Iyengar, J. Tomasi, M. Cossi, N. Rega, J. M. Millam, M. Klene, J. E. Knox, J. B. Cross, V. Bakken, C. Adamo, J. Jaramillo, R. Gomperts, R. E. Stratmann, O. Yazyev, A. J. Austin, R. Cammi, C. Pomelli, J. W. Ochterski, R. L. Martin, K. Morokuma, V. G. Zakrzewski, G. A. Voth, P. Salvador, J. J. Dannenberg, S. Dapprich, A. D. Daniels, Ö. Farkas, J. B. Foresman, J. V. Ortiz, J. Cioslowski, D. J. Fox, *Gaussian 09*, revision B.1, Gaussian, Inc., Wallingford CT, **2009**.
[46] Y. Gong, H. W. Pauls, *Synlett* **2000**, 829–831.
[47] A. J. Bard, L. R. Faulkner, *Electrochemical Methods, Fundamentals and Applications*, Wiley, New York, **2001**.

Received: November 24, 2011
Published Online: January 11, 2012

DOI: 10.1002/ejic.201101033

A Systematic Study of Electrochemical and Spectral Properties for the Electronic Interactions in Porphyrin–Triphenylamine Conjugates

Chih-Yen Huang,[a] Chao-Yen Hsu,[a] Luo-Yi Yang,[a] Chia-Jung Lee,[a] Te-Fang Yang,[a] Chia-Chan Hsu,[a] Chung-Hsiu Ke,[a] and Yuhlong Oliver Su*[a,b]

Keywords: Electrochemistry / Electron transfer / Charge transfer / Energy transfer / Luminescence / Zinc / Porphyrinoids / Antenna effect

A series of mono-, di-, tri-, and tetra-triphenylamine (TPA)-substituted porphyrinatozinc complexes have been synthesized to investigate their spectral and electrochemical properties. The varied shapes of absorption spectra of porphyrin–triphenylamine (Por–TPA) conjugates in comparison with tetramesitylporphyrinatozinc (**ZnTMP**) indicate that there are strong interactions between porphyrin and TPA moieties. In general, the electron-donating capability of a substituent on TPA and the number of TPA derivatives that bond with porphyrin would cause Soret band broadening and intensification of the Q(0,0) band. Due to the antenna effect of these conjugates, the fluorescence quantum yields were enhanced when more TPA moieties were linked. Cyclic voltammetry and spectroelectrochemical methods revealed the redox properties of Por–TPA conjugates. Axial ligation of porphyrinatozinc with *N*-methylimidazole was useful in differentiating the oxidation site of Por–TPA conjugates. The first one-electron oxidations of these conjugates are at the porphyrin ring. The charge-transfer bands present in the near-IR region in the absorption spectra of Por–TPA radical cations are evidence of an electronic interaction between porphyrin and TPA. The electron-donating strength of the TPA group and the symmetry of the Por–TPA conjugate affect the intensity of the charge-transfer band.

Introduction

Porphyrin molecules have unique electrochemical and photophysical properties, which can be easily controlled by functionalization with specific groups at the *meso* and β positions.[1] Recently, the hybridization of porphyrins and photoelectronic molecules such as triphenylamine (TPA) has attracted much attention.[2–6] TPA-based derivatives are widely investigated for the application of dye-sensitized solar cells,[7] organic light-emitting diodes,[8] and electrochromic polymers.[9] Cheng's and Yeh's groups reported the spectral and electrochemical properties of porphyrin–triphenylamine hybrid conjugates.[2–4] Both of their studies showed an obvious bathochromic shift in the Soret and Q bands; the potential shift of porphyrin-ring oxidation and the charge-transfer band appeared in the near-IR region of the absorption spectrum as the porphyrin ring was oxidized. These phenomena indicated that there were strong electronic interactions between the porphyrin core and TPA moieties.

Recently, we published a spectral and electrochemical investigation of porphyrin–triphenylamine dendrimers[6] because of their interesting behavior in spectroscopy and electrochemistry. It is worth studying how each TPA group interacts with porphyrinatozinc and to establish the knowledge of the electronic properties of the Por–TPA conjugate. Thus the mono-, di-, tri-, and tetra-TPA-substituted Por–TPA conjugates were synthesized. Early work on the electronic effects of unsymmetrical phenyl substitution on the π-electron system of a porphyrin ring has been carried out by Walker and co-workers.[10] As shown in Figure 1, we report here a series of Por–TPA conjugates bound to one to four TPA derivatives and with different substituents at the *para* position of TPA in an investigation of the electronic interactions between a porphyrin core and the TPA moiety. Due to the solubility problem of a tetrakis(TPA-NO_2)-substituted porphyrin, conjugate **4** with four TPA-Cl was used instead. In this work, we have studied two kinds of effects on the spectral and electrochemical properties of Por–TPA conjugates. The first is the number of TPA derivatives bound with porphyrinatozinc, and the second is the functional group substituted at the *para* position of TPA.

[a] Department of Applied Chemistry, National Chi Nan University,
1, University Rd., Puli, Nantou County 545, Taiwan
Fax: +886-49-2917956
E-mail: yosu@ncnu.edu.tw
[b] Department of Materials Science and Engineering, National Chung Hsing University,
250 Kuo Kuang Rd., Taichung 402, Taiwan
Supporting information for this article is available on the WWW under http://dx.doi.org/10.1002/ejic.201101033.

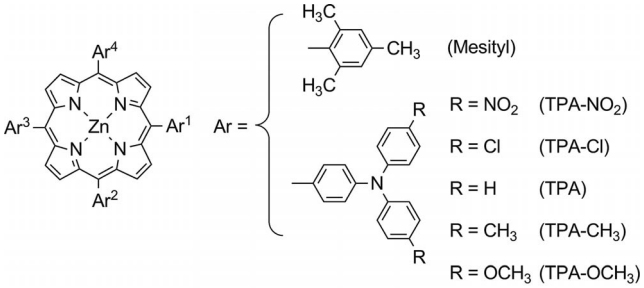

Porphyrins	Ar^1	Ar^2	Ar^3	Ar^4
ZnTMP	Mesityl	Mesityl	Mesityl	Mesityl
1	TPA-NO_2	Mesityl	Mesityl	Mesityl
2	TPA-NO_2	Mesityl	TPA-NO_2	Mesityl
3	TPA-NO_2	TPA-NO_2	TPA-NO_2	Mesityl
4	TPA-Cl	TPA-Cl	TPA-Cl	TPA-Cl
5	TPA	Mesityl	Mesityl	Mesityl
6	TPA	Mesityl	TPA	Mesityl
7	TPA	TPA	TPA	Mesityl
8	TPA	TPA	TPA	TPA
9	TPA-CH_3	Mesityl	Mesityl	Mesityl
10	TPA-CH_3	Mesityl	TPA-CH_3	Mesityl
11	TPA-CH_3	TPA-CH_3	TPA-CH_3	Mesityl
12	TPA-CH_3	TPA-CH_3	TPA-CH_3	TPA-CH_3
13	TPA-OCH_3	Mesityl	Mesityl	Mesityl
14	TPA-OCH_3	Mesityl	TPA-OCH_3	Mesityl
15	TPA-OCH_3	TPA-OCH_3	TPA-OCH_3	Mesityl
16	TPA-OCH_3	TPA-OCH_3	TPA-OCH_3	TPA-OCH_3

Figure 1. Structures of **ZnTMP** and Por–TPA conjugates.

Results and Discussion

Figure 2 shows the absorption spectra of **ZnTMP** and Por–TPA conjugates with different numbers of bound TPA-OCH_3 groups. The mono- to tetra(TPA-OCH_3)-substituted porphyrinatozinc complexes **13**–**16** exhibit very different

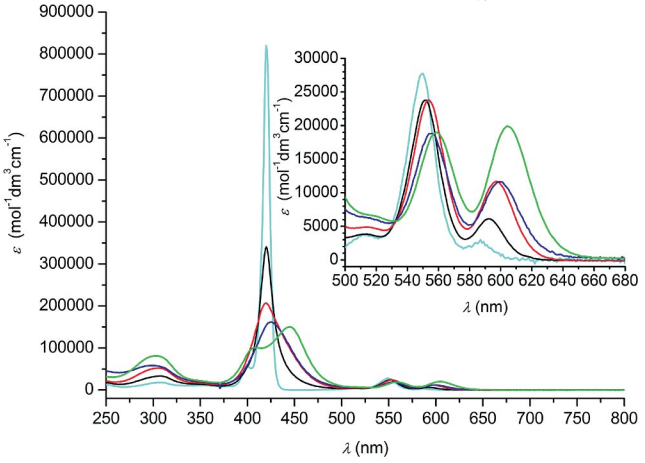

Figure 2. Absorption spectra of **ZnTMP** and **13**–**16** in CH_2Cl_2. Cyan: **ZnTMP**, black: **13**, red: **14**, blue: **15**, green: **16**.

shapes of spectra relative to **ZnTMP**. As the number of bound TPA-OCH_3 groups increased from one to four, the absorption spectra exhibited an intense specific absorption of TPA at around 300 nm. On the other hand, the Soret band absorption decreased in its molar extinction coefficient (ε) and broadened. Both Q bands exhibited bathochromic shifts and a significant increase in the ε of Q(0,0) band. These observations indicate that there are strong electronic interactions between TPA-OCH_3 and porphyrinatozinc. The absorption maxima (λ_{abs}) and molar extinction coefficients of **ZnTMP** and Por–TPA conjugates are summarized in Table 1. In general, more TPA bound with por-

Table 1. Absorption maximum (λ_{abs}) [nm] with molar extinction coefficient (ε) [10^4 mol^{-1} dm cm^{-1}] in parenthesis, emission maximum (λ_{em}) [nm], and quantum yields of **ZnTMP** and Por–TPA conjugates in CH_2Cl_2.

Porphyrins	Absorption					Emission		Antenna effect	
	TPA band	Soret band	Q(0,1)	Q(0,0)	$\varepsilon_{Q(0,0)}/\varepsilon_{Q(0,1)}$	λ_{em}[a]	Quantum yield[b]	λ_{em}[c]	Emission peak area[c,d]
ZnTMP	–	421 (74.82)	550 (2.63)	587 (0.25)	0.10	592, 644	0.044	–	–
1	–[e]	422 (45.03)	550 (1.86)	589 (0.25)	0.13	597, 646	0.021	598, 648	0.07×10^5
2	–[e]	423 (25.93)	551 (1.60)	593 (0.49)	0.31	599, 647	0.021	601, 650	0.05×10^5
3	–[e]	426 (43.63)	551 (2.19)	593 (0.65)	0.30	601, 650	0.028	601, 650	0.24×10^5
4	311 (7.79)	436 (18.80)	555 (1.65)	597 (1.03)	0.62	614	0.093	621	1.62×10^5
5	305 (3.68)	422 (33.79)	551 (2.34)	588 (0.44)	0.19	600, 648	0.060	601, 649	0.61×10^5
6	307 (5.76)	424 (29.07)	552 (2.56)	595 (0.87)	0.34	606, 651	0.077	602, 653	0.98×10^5
7	306 (7.77)	432 (23.30)	554 (2.47)	596 (1.31)	0.53	613, 653	0.081	606, 655	1.20×10^5
8	305 (8.71)[f]	438 (18.60)[f]	555 (2.24)[f]	599 (1.76)[f]	0.79	618	0.100	616	1.60×10^5
9	308 (3.90)	422 (37.64)	552 (2.51)	592 (0.51)	0.20	602, 648	0.070	601, 649	0.57×10^5
10	307 (4.86)	423 (19.05)	553 (2.10)	595 (0.89)	0.42	609, 652	0.088	603, 652	0.96×10^5
11	305 (6.67)	429 (13.50)	555 (1.85)	599 (1.19)	0.64	617	0.091	619	1.70×10^5
12	305 (9.45)[f]	442 (16.60)[f]	557 (2.15)[f]	602 (1.99)[f]	0.93	625	0.100	624	1.99×10^5
13	307 (3.93)	421 (37.16)	553 (2.64)	593 (0.59)	0.22	605, 650	0.059	601, 649	0.66×10^5
14	305 (5.90)	420 (23.04)	554 (2.71)	597 (1.34)	0.49	613	0.078	614	0.61×10^5
15	302 (5.02)	425 (14.20)	556 (1.67)	600 (1.06)	0.63	621	0.088	622	1.22×10^5
16	301 (6.98)[g]	445 (12.30)[g]	558 (1.59)[g]	604 (1.70)[g]	1.07	636[g]	0.130[g]	637	3.04×10^5

[a] **ZnTMP** and all the Por–TPA conjugates were excited at the Soret band. [b] Using H_2TPP as standard. The quantum yield of H_2TPP was set to 0.11[13]. [c] The Por–TPA conjugates were excited at the TPA moiety. In the spectra of conjugates **4**–**16**, the emission peak was overlapped with excitation overtone. [d] Plotting fluorescence spectra in the form of intensity versus wavenumber. The emission peak area was obtained by integration from 17857 to 12500 cm^{-1} (560 to 800 nm). For conjugates **1**–**3**, the areas were integrated from 17857 to 13888 cm^{-1} (560 to 720 nm). [e] The absorption maximum of TPA-NO_2 is at 417 nm in CH_2Cl_2. [f] Data from the literature[2]. [g] Data from the literature[6].

phyrinatozinc further causes a redshift of both Soret and Q bands, an increase in ε value of the TPA and Q(0,0) bands, and a decrease in the ε value of the Soret band. For example, the Q(0,0) band of tetrakis(TPA-OCH_3) porphyrinatozinc **16** is redshifted by 11 and 17 nm relative to porphyrinatozinc **13** and **ZnTMP**, respectively. The enhancement in the ($\varepsilon_{Q(0,0)}/\varepsilon_{Q(0,1)}$) ratio of **16** is about 5 and 11 times more than that of **13** and **ZnTMP**, respectively. We also found that the substituent effect at the TPA moieties is relatively small. The Q(0,0) band of the tetrakis(TPA-OCH_3) porphyrinatozinc **16** is redshifted only by 5 nm relative to the tetrakis(TPA)-substituted zinc complex **8**. Although the nitro group is strongly electron-withdrawing, zinc complexes **1**–**3** bound with TPA-NO_2 group still exhibit redshifts of Q bands relative to **ZnTMP**. Apparently, these phenomena suggest that the number of TPA derivatives bound with porphyrinatozinc is the major effect on the ground-state electronic configuration of the porphyrin as the result of π-conjugation expansion. The strongly enhanced Q(0,0) band should be due to the enlarged energy difference between a_{2u} and a_{1u} orbitals of porphyrin. From the four-orbital-model theory,[11] TPA derivatives bound at the *meso* position of the porphyrin ring can interact with the a_{2u} orbital of porphyrinatozinc and the strong electron-donating group, then raise the energy of the a_{2u} orbital.[12]

The fluorescence spectra and emission maximum (λ_{em}) of Por–TPA conjugates are shown and listed in Figure 3 and Table 1. In comparison with **ZnTMP**, the emission maximum of tetra-TPA-bonded Por–TPA conjugates **4**, **8**, **12**, and **16** were largely redshifted by 22, 26, 33, and 44 nm, respectively.

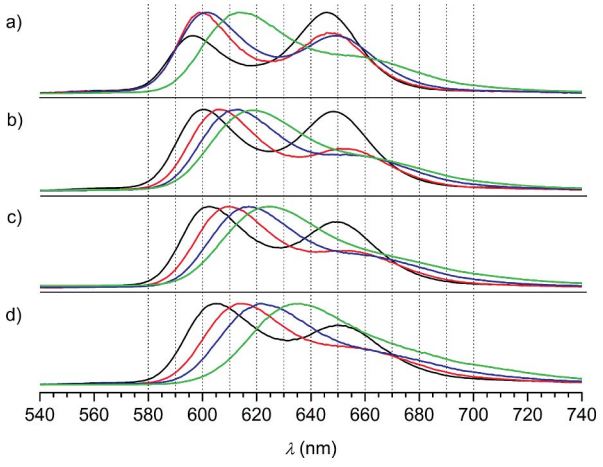

Figure 3. Normalized fluorescence spectra of Por–TPA conjugates in CH_2Cl_2. All of the conjugates were excited at the Soret band. The black, red, blue, and green lines indicate mono-, di-, tri-, and tetra(TPA-X)-substituted conjugates, respectively. (a) TPA-NO_2 (green line: TPA-Cl); (b) TPA; (c) TPA-CH_3; (d) TPA-OCH_3-substituted Por–TPA conjugates.

However, for mono-TPA-bonded conjugates **1**, **5**, **9**, and **13**, the redshifts in λ_{em} were less than 13 nm. It again demonstrated that the number of bound TPA has a major effect on the electronic configuration of porphyrinatozinc as the result of π-conjugation expansion. This is consistent with what we inferred from the absorption spectra. On the other hand, the quantum efficiency of conjugates was measured by using H_2TPP as standard in which the quantum yield of H_2TPP was set to 0.11.[13] Values obtained for Por–TPA conjugates are listed in Table 1. An enhancement in quantum efficiency was observed when TPA derivatives were bound to the zinc complex except for conjugates with strong electron-withdrawing nitro groups. Cheng's group and ours have reported the antenna effect of triphenylamine-bound porphyrinatozinc before.[2,6] In this study, we also examine the antenna effect of the Por–TPA conjugates by exciting at their corresponding TPA moieties (Figure S15 in the Supporting Information). All the fluorescence spectra of these conjugates are similar to those emitted by porphyrin with Soret-band excitation, thereby indicating an intramolecular energy transfer from TPA to porphyrinatozinc. The relaxation from the S_1 of porphyrin to S_0 was then observed. The λ_{em} obtained from TPA excitation are listed in Table 1. In the molecular structures of Por–TPA conjugates, the TPA moieties act as antennas to absorb radiation. Consequently, the fluorescence intensity was increased as more TPA bonded with porphyrinatozinc. This phenomenon is reflected in the increased emission peak area (Table 1). The typical emission peak of TPA can be observed slightly in the spectra of tri-TPA-bound conjugates only. At its simplest, it may due to the low symmetry of tri-TPA-bound conjugates. Further confirmation of the antenna effect was performed by recording the excitation profiles of Por–TPA conjugates (Figures S16 and S17 in the Supporting Information).

Electrochemical Properties

Cyclic voltammetry (CV) and spectroelectrochemistry were used to investigate the electrochemical behavior of Por–TPA conjugates. It can be expected that there would be multiple oxidations, including two steps of one-electron ring oxidation of porphyrinatozinc and the oxidation of the nitrogen atom of TPA in the cyclic voltammograms of Por–TPA conjugates in which several TPA groups were bound with porphyrinatozinc. Figure 4 shows the CVs of **ZnTMP** and zinc complexes **13**–**16** with different numbers of TPA-OCH_3. As only one TPA-OCH_3 group is bound to porphyrinatozinc, the CV of **13** exhibits three redox couples in oxidation. Subsequently, as more TPA-OCH_3 groups are bonded, **14**–**16** exhibit multiple and overlapping oxidation waves in their CVs. It is interesting to study the electrochemical behavior of each redox in the CVs of Por–TPA conjugates even though the CVs become more complex as the number of TPA increases. Hence, in the following discussion, we focus on the effect of the first-electron oxidation (Ox1) of conjugates after TPA derivatives were bound. The electrochemical data obtained from CV are summarized in Table 2. As more TPA groups bonded with porphyrinatozinc, the conjugates were easier to oxidize, as reflected in the cathodic shift in their onset potentials (E_{onset}). Basically,

TPA is an electron-donating group. Conjugate **1** and **2** show almost no difference in E_{onset} relative to **ZnTMP**. The results indicate a diminished electronic interaction by the nitro groups bound at TPA, whereas conjugate **16** with four TPA-OCH_3 exhibits a large cathodic shift of 0.19 V. Obviously, the E_{onset} values of these conjugates are dominated by electron-donating capability.

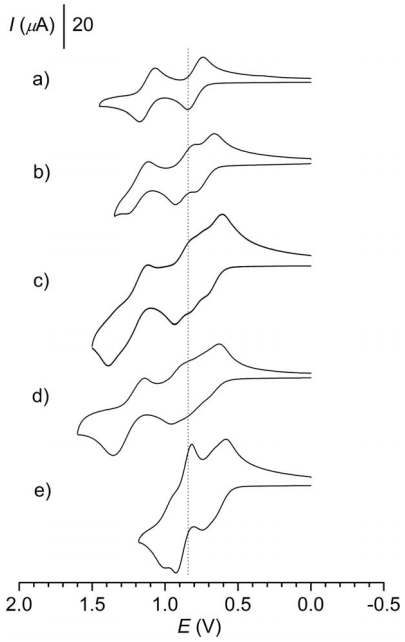

Figure 4. Cyclic voltammograms of (a) **ZnTMP**, (b) **13**, (c) **14**, (d) **15**, and (e) **16** in CH_2Cl_2 containing 0.1 M tetra-*n*-butylammonium perchlorate (TBAP). Scan rate: 0.1 $V s^{-1}$. Molar concentrations of compounds: 1.0×10^{-3} M.

Table 2. Half-wave potentials [$E_{1/2}$ versus Ag/AgCl (saturated)][a] and peak potentials (E_p) of **ZnTMP** and **1**–**16**.

	Ox5	Ox4	Ox3	Ox2	Ox1	E_{onset}	Ox1′[b]
ZnTMP	–	–	–	+1.12	+0.80	+0.71	+0.63
1	–	–	+1.66	+1.14	+0.82	+0.72	+0.72
2	–	–	+1.46[e]	+1.13	+0.83	+0.72	+0.76
3	–	–	–	+1.61[e]	+0.84	+0.67	+0.80[e]
4	–	+1.51[e]	+1.32[d]	+0.94	+0.74	+0.65	+0.66
5	–	–	+1.36[e]	+1.07	+0.79	+0.68	+0.65
6	–	–	+1.29[e]	+0.91	+0.73	+0.66	+0.60
7	–	–	+1.38[d,e]	+0.92	+0.73	+0.65	+0.59
8	–	–	+1.30[d,e]	+0.84	+0.71	+0.63	+0.59
9	–	+1.79[e]	+1.25	+1.00	+0.75	+0.66	+0.64
10	+1.70[e]	+1.26	+1.09	+0.95	+0.70	+0.63	+0.60
11	–	+1.33	+1.09[d]	+0.87	+0.71	+0.61	+0.58
12	+1.68[e]	+1.33	+1.08[d]	+0.76	+0.65	+0.60	+0.57
13	–	+1.44[e]	+1.20	+0.88	+0.74	+0.64	+0.60
14	+1.47[e]	+1.23	+0.93	+0.82	+0.68	+0.63	+0.58
15	–	+1.43[e]	+0.92[c]	+0.83[c]	+0.70[c]	+0.59	+0.57
16	+1.35[e]	+0.96	+0.87[d]	+0.69[c]	+0.62[c]	+0.52	+0.50

[a] $E_{1/2}$ of Fc^+/Fc is +0.54 V versus Ag/AgCl (saturated). [b] The $E_{1/2}$ of Ox1 of five-coordinate porphyrinatozinc. [c] Estimated half-wave potential by deconvoluting the overlapped CV. [d] Multiple electron transfer involved. [e] Peak potential of an irreversible wave.

In our previous study of the porphyrinatozinc core dendrimers, we were able to deconvolute the overlapping CV by introducing *N*-methylimidazole (*N*-MeIm) as an axial ligand.[6] Imidazole is a strong nitrogenous base that, ligated with porphyrinatozinc, would cause a cathodic shift in the potential for first porphyrinatozinc oxidation.[14] Thus, *N*-MeIm is useful to differentiate the oxidation site of Por–TPA conjugates. After ligating with electron-rich *N*-MeIm, the CVs of Por–TPA conjugates all exhibit a cathodic shift in the first oxidation potential (Ox1′ in Table 2; Figures S22 and S23 in the Supporting Information). The observation indicates that the Ox1 of four-coordinate Por–TPA conjugates belongs to the first ring oxidation of porphyrins. For example, Figure 5 is the CV of **13** in the presence of *N*-MeIm. As *N*-MeIm is added to the solution, the half-wave potentials exhibit a cathodic shift for Ox1 and an anodic shift for Ox3. Ox2, however, remains unchanged in potential. These observations indicate that Ox1 and Ox3 are due to the porphyrin-ring oxidations and that Ox2 is the oxidation at TPA. The first half-wave potentials of *N*-MeIm-ligated TPA–Por conjugates (Ox1′) are summarized in Table 2.

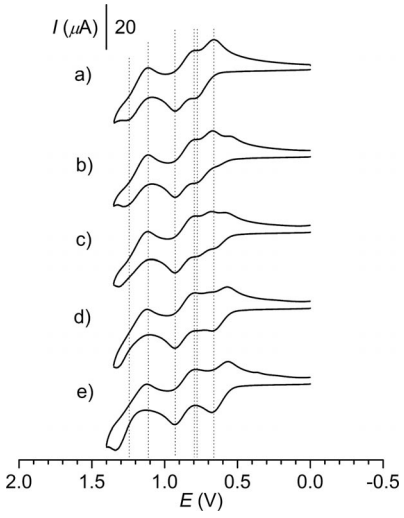

Figure 5. Cyclic voltammograms of Por–TPA conjugate **13** in CH_2Cl_2 containing 0.1 M TBAP. Scan rate: 0.1 $V s^{-1}$. Molar concentration of **13** is 1.0×10^{-3} M; [*N*-MeIm]: (a) 0, (b) 2.5×10^{-4}, (c) 5.0×10^{-4}; (d) 7.5×10^{-4}, and (e) 1.0×10^{-3} M.

The effects of the substituent at TPA on the oxidation potential of Por–TPA conjugates were also examined by CV. In Figure 6, the CVs of mono-TPA-bound conjugates **1**, **5**, **9**, and **13** clearly show three redox couples in their oxidations, including two electrons removed from the porphyrin ring and one electron removed from the nitrogen atom of TPA derivatives. For the above compounds, the first oxidation potentials are at +0.82, +0.79, +0.75, and +0.74 V, respectively. Addition of *N*-MeIm causes the potential shifts to +0.72, +0.65, +0.64, and +0.60 V, respectively. It is thus inferred that the first oxidation sites of Por–TPA conjugates **1**, **5**, **9**, and **13** are all at the porphyrin ring.

The second oxidation potentials of compounds **5**, **9**, and **13** remain unchanged upon *N*-MeIm addition and are thus assigned as their respective TPA oxidation. However, the second oxidation of compound **1** shifts concurrently to a more anodic potential, the third oxidation of which remains unchanged. Thus, the Ox1 and Ox2 of conjugate **1** are attributed to the first and second porphyrin-ring oxidations. Namely, the strong electron-withdrawing nitro groups attached to the *para* positions of TPA cause the TPA group to be more difficult to oxidize than porphyrin ring. Clearly, the nature of substituent at the *para* positions of TPA directly affects the oxidation potential of TPA more than that of porphyrinatozinc. Electron-donating methyl and methoxy groups of conjugates **9** and **13** cause both the first ring oxidation of porphyrin and nitrogen atom to be easier to oxidize than conjugate **5**, whereas the strong electron-withdrawing nitro group of conjugate **1** has the opposite effect.

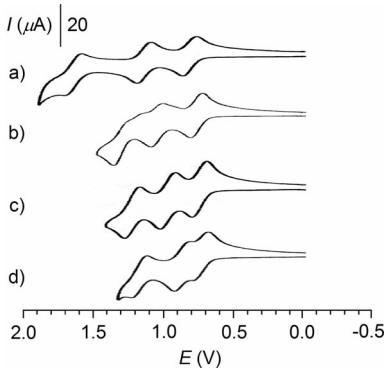

Figure 6. Cyclic voltammograms of mono-substituted Por–TPA conjugates (a) **1**, (b) **5**, (c) **9**, and (d) **13** in CH_2Cl_2 containing 0.1 M TBAP. Scan rate: 0.1 Vs^{-1}. Molar concentrations of conjugates: 1.0×10^{-3} M.

In the studies of Por–TPA conjugates, we found that both substituent effect and the number of bound TPA derivatives significantly affect the oxidation potentials of TPA and the porphyrin ring. Generally, the porphyrinatozinc ring is oxidized first, and the electron-donating substituents at the *para* position of TPA cause a cathodic shift in potential of Ox1, whereas electron-withdrawing groups cause the opposite effect. Furthermore, since triphenylamine itself is an electron-donating group, the presence of methoxy groups will enhance the effect on oxidation potential in the same direction. However, the presence of electron-withdrawing groups such as Cl and NO_2 will decrease the electron-donating capability of triphenylamine. For example, conjugate **4** is harder to oxidize by 0.06 V than conjugate **8**, but it is easier to oxidize than **ZnTMP** (Table 2).

Based on the results of cyclic voltammetry and absorption spectra discussed above, the Por–TPA conjugate **16**, which has four TPA-OCH_3 groups bound to porphyrinatozinc, would have the strongest electrochemical interaction between the porphyrinatozinc core and the TPA groups.

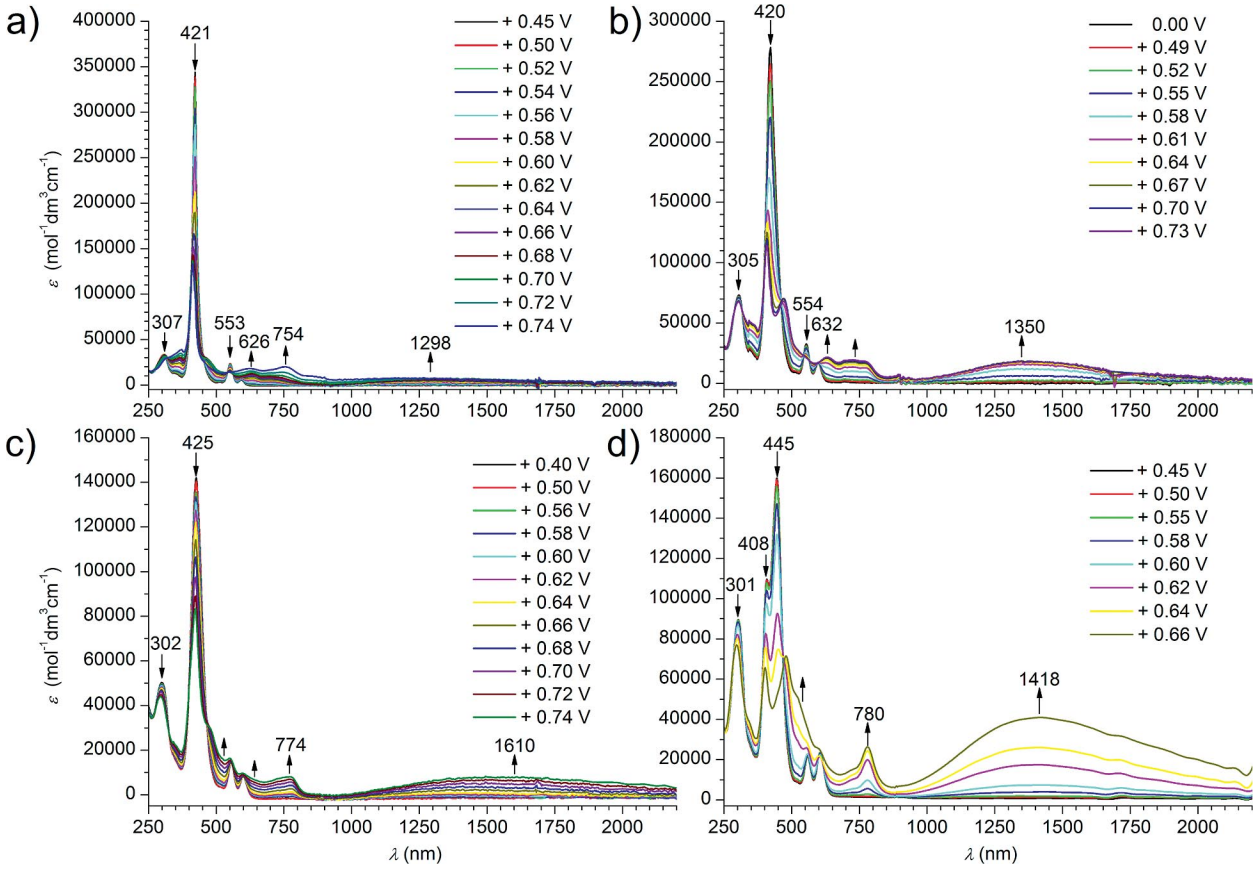

Figure 7. Spectral changes of (a) **13**, (b) **14**, (c) **15**, and (d) **16** in CH_2Cl_2 containing 0.1 M TBAP at various applied potentials.

Spectroelectrochemistry

The studies of electron interaction between TPA derivatives and porphyrinatozinc were carried out by UV/Vis/NIR spectroelectrochemistry. The spectral changes of **13**–**16** upon applied potentials to form their corresponding radical cation are shown in Figure 7. In Figure 7A, the diminishing Soret band at 421 nm and the formation of a specific absorption band of the porphyrin radical cation at 500–700 nm indicate that the porphyrin ring is oxidized. This result is consistent with that inferred from cyclic voltammetry. During the process of **13** oxidation to **13**$^{+\cdot}$, the absorbance of TPA-OCH_3 at 307 nm decreased slightly. New bands at 754 and 1298 nm were formed and are assigned as the specific absorption of triarylamine radical cation and the intramolecular charge transfer from TPA-OCH_3 moiety to porphyrinatozinc, respectively.[3,6] The porphyrin ring was oxidized first and the Por–TPA conjugate thus became an electron donor–acceptor complex in which the electron-rich TPA-OCH_3 moiety would transfer its electron cloud to the porphyrin ring, which lacks an electron after oxidation. The new charge-transfer band at the NIR region is evidence of the electronic interaction between the porphyrinatozinc radical cation and the TPA-OCH_3 moiety. Similar phenomena were also observed in the absorption spectra of conjugates **14**–**16** upon oxidation (Figure 7, B–D). The spectroscopic data of charge-transfer bands of the radical cation spectra of Por–TPA conjugates are summarized in Table 3. In the radical cation spectra of mono- and bis(TPA-NO_2)-bound zinc complexes **1** and **2**, there are no charge-transfer bands in the region of 900–2200 nm. Apparently, the presence of strong electron-donating methoxy groups can promote the charge-transfer process, and methyl groups or hydrogen atoms have less effect on it. On the other hand, the strong electron-withdrawing nitro groups would pull the electron cloud of the nitrogen atom of TPA away from the porphyrin ring and make it more difficult for charge transfer to proceed.

Table 3. Absorption maximum (λ_{abs}) [nm] with molar extinction coefficients (ε) [mol^{-1} dm^{3}cm^{-1}], full width at half-maximum height (fwhm) [cm^{-1}], and oscillator strength (f)[a] of the radical cation spectra of Por–TPA conjugates in CH_2Cl_2.

	meso-Substituents	λ_{abs}	ε	fwhm	f[a]
1	(TPA-NO_2)$_1$	–[b]	–[b]	–[b]	–[b]
2	(TPA-NO_2)$_2$	–[b]	–[b]	–[b]	–[b]
3	(TPA-NO_2)$_3$	994	6196	3818	0.077
4	(TPA-Cl)$_4$	1226	23435	3131	0.243
5	(TPA)$_1$	1254	5086	3680	0.045
6	(TPA)$_2$	1262	10530	3537	0.102
7	(TPA)$_3$	1190	11044	2398	0.077
8	(TPA)$_4$	1243	24063	3137	0.240
9	(TPA-CH_3)$_1$	1338	6757	2910	0.057
10	(TPA-CH_3)$_2$	1290	15534	2753	0.145
11	(TPA-CH_3)$_3$	1264	8459	2984	0.076
12	(TPA-CH_3)$_4$	1296	30093	3673	0.340
13	(TPA-OCH_3)$_1$	1298	7766	5681	0.106
14	(TPA-OCH_3)$_2$	1350	18252	2877	0.173
15	(TPA-OCH_3)$_3$	1610	9524	4116	0.116
16	(TPA-OCH_3)$_4$	1418	40107	4715	0.530

[a] Taken from the literature[15]. Oscillator strength (f) = 4.319×10^{-9} A/n, for which A = integrated area of peak and n = refractive index of CH_2Cl_2. Using the plot of ε versus cm^{-1} to obtain the integrated area (A) of each absorption peak in the spectrum. [b] No absorption band present in the region of 900–2200 nm.

The oscillator strengths[15] (f) of charge-transfer bands of that tri-TPA-substituted conjugates are much less than those of di- and tetra-TPA-substituted conjugates in their respective radical cation forms. These results may be attributed to their low symmetry. Conjugate **4** has a high f value of 0.243 even though chlorine possesses electron-withdrawing property. This could interpret that the number of bonded TPA groups is the major effect on the electronic properties of porphyrinatozinc again.

Conclusion

A series of Por–TPA conjugates have been synthesized and characterized by spectral and electrochemical methods. The absorption spectra of Por–TPA conjugates exhibit broadening of Soret band, intensifying of the Q(0,0) band, and redshifting of both Soret and Q bands as more TPA derivatives bond to porphyrinatozinc. These phenomena indicate the strong electronic interaction between porphyrin and triphenylamine moieties. In the emission spectroscopy study, the intramolecular energy transfer was found in all Por–TPA conjugates. When TPA moieties were excited, they would transfer energy to the porphyrinatozinc core from which fluorescence occurred. Due to the antenna effect found in these conjugates, an enhancement in quantum efficiency can be observed as the number of TPA derivatives increases. In cyclic voltammetry, more TPA groups in the Por–TPA conjugate cause more oxidation centers to be present in the molecular structure. We have characterized the Ox1 of each Por–TPA conjugate as the oxidation site. The porphyrin-ring oxidation has been identified by utilizing the *N*-MeIm ligation effect and spectroelectrochemical methods. In the radical cation absorption spectra of Por–TPA conjugates, the oscillator strength describes the intensity of charge-transfer bands in the NIR region. The Por–TPA conjugate that has a higher symmetry, more bound TPA groups, and stronger electron-donating at the *para* position of TPA would have a more intense charge-transfer band, which accounts for a stronger interaction.

Experimental Section

General: ^{1}H and ^{13}C NMR spectra were obtained with a Bruker Avance-III 300 spectrometer. A Varian Cary-50 scanning UV/Vis spectrometer was used to determine extinction coefficients of Por–TPA conjugates and to obtain absorption spectra with a 1 cm cuvette. Mass spectra were obtained with Applied Biosystem Voyager-DETM Pro spectrometer. Emission spectra, excitation profiles, and fluorescence quantum yield measurements were completed with a Varian Cary Eclipse spectrometer. For electrochemical studies, a CHI 700A electroanalytical workstation was used for cyclic voltammetry and conducted with a three-electrode cell. Glassy carbon

electrode (area: 0.07 cm^2) was used as working electrode. The auxiliary and reference electrodes were platinum wire and Ag/AgCl (aqueous satd. KCl), respectively. Spectroelectrochemistry was performed with JASCO V-570 UV/Vis/NIR spectrometer and Bioanalytical System Model SP-2 potentiostat. Platinum gauze, platinum wire, and Ag/AgCl (aqueous satd. KCl) were used as working, auxiliary, and reference electrodes, respectively, in a spectroelectrochemical cell with an 1 mm optical path length.

Materials: Tetramesitylporphyrinatozinc (**ZnTMP**),[16] 5-(4-aminophenyl)-10,15,20-trimesitylporphyrinatozinc [Zn(AP)(mesityl)$_3$P],[17] 5,15-bis(4-aminophenyl)-10,20-dimesitylporphyrinatozinc [Zn(AP)$_2$(mesityl)$_2$P],[18] and tetrakis(4-aminophenyl)porphyrinatozinc (ZnTAPP)[19] were synthesized according to literature methods, the metalation was performed with zinc acetate dihydrate in CH_2Cl_2/CH_3OH. *N*,*N*-Bis(4-methoxyphenyl)phenylamine (TPA-OCH_3) was obtained from the literature method.[20] *N*,*N*-Bis(4-nitrophenyl)phenylamine (TPA-NO_2) was synthesized by modifying the literature method,[21] in which 3,4-dimethylaniline was replaced by aniline. Except for nitro-containing compounds, *N*,*N*-bis(4-methylphenyl)phenylamine (TPA-CH_3),[22] *N*,*N*-bis(4-chlorophenyl)phenylamine (TPA-Cl),[23] and Por–TPA derivatives were obtained by means of the Ullmann reaction.[24] Other chemicals were all commercially available. Organic solvents used in electrochemical studies were dried and distilled before use. TBAP was recrystallized twice from ethyl acetate (EA) and dried before use.

General Procedures in Synthesis of Por–TPA Conjugates: The synthetic routes of Por–TPA are shown in Scheme 1. Generally, the amino compound and the corresponding iodo compound were added into a reaction vessel that contained copper powder, potassium carbonate, 18-crown-6, and *o*-dichlorobenzene (2–3 mL). The reaction mixture was heated to reflux with stirring for 24 h under N_2 atmosphere. After the reaction was complete, the mixture was cooled to room temperature, then filtered and washed with CH_2Cl_2. The filtrate was passed through a silica gel column. In general, hexane was used as the first eluent to elute *o*-dichlorobenzene. Next, hexane/CH_2Cl_2 mixed solvent was used to obtain each target compound. For tri-TPA-substituted Por–TPA conjugates, CH_2Cl_2/EA was necessary to use as final eluent. Nitro-containing Por–TPA conjugates were synthesized by treating 4-fluoronitrobenzene with the corresponding amino compound in the presence of cesium fluoride (CsF) in DMSO (5 mL). The reaction was performed at 140 °C for 24 h under N_2. The reaction mixture was cooled, poured into chilled water, and stirred for 2 h with an ice bath. The crude product was then collected by filtration and dried in vacuo. Further purifications are described individually in the following sections.

5,10,15-Tris(4-aminophenyl)-20-mesitylporphyrinatozinc [Zn(AP)$_3$(mesityl)P]: The precursor 5-mesityl-10,15,20-tris(4-nitrophenyl)-porphyrin free base was obtained from the condensation of mesitylaldehyde (0.37 g, 2.50 mmol) and 4-nitrobenzaldehyde (1.14 g, 7.50 mmol) with pyrrole (0.70 mL, 10.00 mmol) by using the same

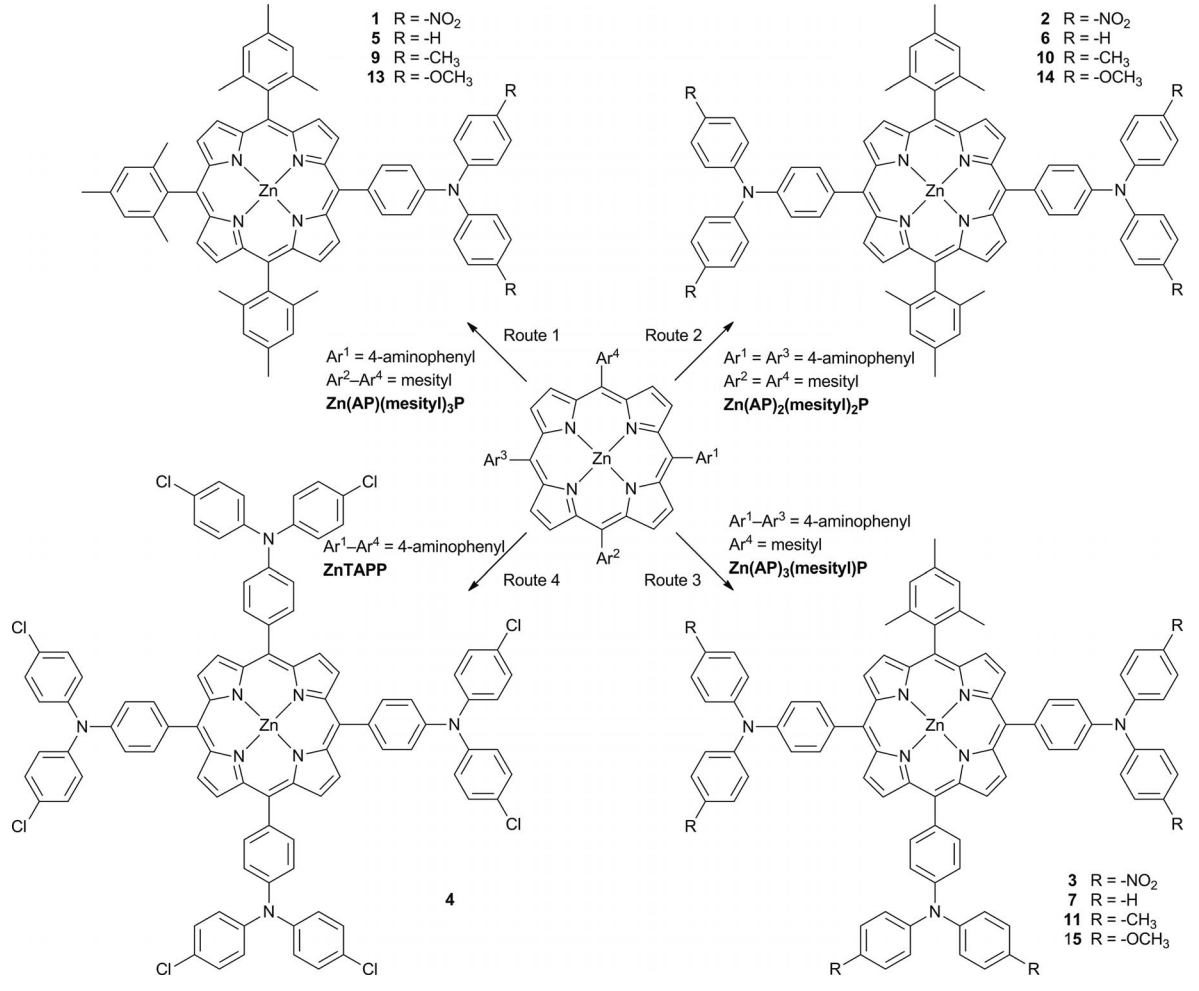

Scheme 1. Synthetic routes for Por–TPA conjugates.

reaction conditions of H_2TMP.[16] The crude solid first underwent soxhlet extraction with MeOH to wash the black substance away. Then acetone was used to wash H_2TMP, mono- and di-nitrophenyl-substituted porphyrin free base out of the crude solid. The tri- and tetra-nitrophenylporphyrin free bases remained in the thimble. These nitrophenylporphyrin mixtures were then reduced directly by using stannous chloride.[19] The resulting mixtures of aminophenylporphyrins were dissolved in CH_2Cl_2 and chromatographed by silica gel column with CH_2Cl_2/EA mixed solvent as eluent. 5,10,15-Tris(4-aminophenyl)-20-mesitylporphyrin free base [$H_2(AP)_3$(mesityl)P] was obtained; yield 0.23 g, 13%. Zn(AP)$_3$(mesityl)P was obtained by metalating $H_2(AP)_3$(mesityl)P with zinc acetate dihydrate in CH_2Cl_2/MeOH; yield 0.20 g, 78%. ^{1}H NMR (300 MHz, [D$_6$]DMSO): δ = 8.82–8.80 (a singlet overlapping with a doublet, 6 H, pyrrolic H), 8.50 [d, J(H,H) = 4.5 Hz, 2 H, pyrrolic H], 7.79 [d, J(H,H) = 7.8 Hz, 6 H, Ar–H], 7.29 (s, 2 H, Ar–H), 6.94 [d, J(H,H) = 8.0 Hz, 6 H, Ar–H], 5.46 (s, 6 H, NH_2), 2.57 (s, 3 H, CH_3), 1.76 (s, 6 H, CH_3) ppm. ^{13}C NMR (75 MHz, [D$_6$]-DMSO): δ = 149.87, 149.73, 148.69, 147.99, 139.49, 138.47, 136.71, 135.18, 132.13, 131.37, 130.34, 130.21, 129.47, 127.57, 121.37, 120.72, 116.94, 112.98, 112.27, 109.59, 21.54, 21.10 ppm. MS (FAB$^+$): m/z calcd. for $C_{47}H_{37}N_7Zn$: 763.24; found 763.3.

5-[4-{Bis(4-nitrophenyl)amino}phenyl]-10,15,20-trimesitylporphyrinatozinc (1): Zn(AP)(mesityl)$_3$P (50.0 mg, 0.061 mmol), 4-fluoronitrobenzene (34.6 mg, 0.245 mmol), CsF (185.5 mg, 1.221 mmol). The crude product was dissolved and passed through a silica gel column. The final product can be obtained by using hexane and CH_2Cl_2 mixed solvent as eluent; yield 0.04 g, 64%. ^{1}H NMR (300 MHz, CD_2Cl_2): δ = 8.99 [d, J(H,H) = 4.6 Hz, 2 H, pyrrolic H], 8.81 [d, J(H,H) = 4.6 Hz, 2 H, pyrrolic H], 8.72 (s, 4 H, pyrrolic H), 8.33–8.29 [dd, J(H,H) = 8.4 and 9.2 Hz, 6 H, Ar–H], 7.59 [d, J(H,H) = 8.3 Hz, 2 H, Ar–H], 7.51 [d, J(H,H) = 9.2 Hz, 4 H, Ar–H], 7.31 and 7.30 (two overlapping singlets, 6 H, Ar–H), 2.63 and 2.62 (two overlapping singlets, 9 H, CH_3), 1.85 (s, 18 H, CH_3) ppm. ^{13}C NMR (75 MHz, CD_2Cl_2): δ = 152.54, 150.41, 150.18, 150.06, 144.69, 143.44, 142.03, 139.54, 139.31, 139.23, 138.00, 136.65, 132.11, 131.57, 131.47, 131.03, 128.02, 125.99, 125.42, 123.30, 119.40, 119.00, 21.78, 21.74, 21.55 ppm. MS (FAB$^+$): m/z calcd. for $C_{65}H_{53}N_7O_4Zn$: 1059.35; found 1060.6.

5,15-Bis[4-{bis(4-nitrophenyl)amino}phenyl]-10,20-dimesitylporphyrinatozinc (2): Zn(AP)$_2$(mesityl)$_2$P (70.0 mg, 0.088 mmol), 4-fluoronitrobenzene (500.0 mg, 3.544 mmol), CsF (810.0 mg, 5.332 mmol). The crude was washed by acetone and CH_2Cl_2 until yellow filtrate became reddish brown. The solid maintain on filter paper is the final product; yield 0.02 g, 18%. ^{1}H NMR (300 MHz, [D$_7$]DMF): δ = 8.99 [d, J(H,H) = 4.7 Hz, 4 H, pyrrolic H], 8.71 [d, J(H,H) = 4.4 Hz, 4 H, pyrrolic H], 8.43–8.36 [dd, J(H,H) = 9.1 and 8.1 Hz, 12 H, Ar–H], 7.79 [d, J(H,H) = 7.8 Hz, 4 H, Ar–H], 7.72 [d, J(H,H) = 9.3 Hz, 8 H, Ar–H], 7.40 (s, 4 H, Ar–H), 2.65 (s, 6 H, CH_3), 1.88 (s, 12 H, CH_3) ppm. MS (FAB$^+$): m/z calcd. for $C_{74}H_{54}N_{10}O_8Zn$: 1274.34; found 1276.3. Due to the solubility problem, we could not obtain a ^{13}C spectrum.

5,10,15-Tris[4-{bis(4-nitrophenyl)amino}phenyl]-20-mesitylporphyrinatozinc (3): Zn(AP)$_3$(mesityl)P (75.0 mg, 0.098 mmol), 4-fluoronitrobenzene (186.0 mg, 1.318 mmol), CsF (980.0 mg, 6.451 mmol). The crude product was dissolved and passed through a silica gel column. The final product can be obtained by using CH_2Cl_2 as eluent; yield 0.04 g, 24%. ^{1}H NMR (300 MHz, CD_2Cl_2): δ = 9.12 (s, 4 H, pyrrolic H), 9.04 [d, J(H,H) = 4.7 Hz, 2 H, pyrrolic H], 8.87 [d, J(H,H) = 4.7 Hz, 2 H, pyrrolic H], 8.34–8.29 (m, 18 H, Ar–H), 7.64–7.59 (m, 6 H, Ar–H), 7.54–7.49 (m, 12 H, Ar–H), 7.34 (s, 2 H, Ar–H), 2.66 (s, 3 H, CH_3), 1.84 (s, 6 H, CH_3) ppm. MS (FAB$^+$): m/z calcd. for $C_{83}H_{55}N_{13}O_{12}Zn$: 1489.34; found 1490.2. Due to the solubility problem, we could not obtain a ^{13}C spectrum.

5,10,15,20-Tetrakis[4-{bis(4-chlorophenyl)amino}phenyl]-porphyrinatozinc (4): Zn(AP)$_4$P (0.10 g, 0.135 mmol), 1-chloro-4-iodobenzene (2.58 g, 10.837 mmol), Cu (0.69 g, 10.837 mmol), K_2CO_3 (1.31 g, 9.450 mmol), [18]crown-6 (0.11 g, 0.410 mmol); yield 0.12 g, 53%. ^{1}H NMR (300 MHz, $CDCl_3$): δ = 9.08 (s, 8 H, pyrrolic H), 8.11 [d, J(H,H) = 8.4 Hz, 8 H, Ar–H], 7.45–7.31 (m, 40 H, Ar–H) ppm. ^{13}C NMR (75 MHz, [D$_7$]DMF): δ = 150.67, 147.23, 147.10, 139.09, 136.56, 132.25, 130.47, 128.30, 126.52, 122.84, 120.87 ppm. MS(MALDI-TOF): m/z calcd. for $C_{92}H_{56}N_8O_8Zn$: 1621.14; found 1621.59.

5-[4-(Diphenylamino)phenyl]-10,15,20-trimesityporphyrinatozinc (5): Zn(AP)-(mesityl)$_3$P (20.0 mg, 0.024 mmol), iodobenzene (15.3 mg, 0.075 mmol), Cu (4.8 mg, 0.075 mmol), K_2CO_3 (6.9 mg, 0.050 mmol), [18]crown-6 (6.6 mg, 0.025 mmol); yield 0.02 g, 70%. ^{1}H NMR (300 MHz, CD_2Cl_2): δ = 9.02 [d, J(H,H) = 4.7 Hz, 2 H, pyrrolic H], 8.76 [d, J(H,H) = 4.6 Hz, 2 H, pyrrolic H], 8.68 (s, 4 H, pyrrolic H), 8.08 [d, J(H,H) = 8.3 Hz, 2 H, Ar–H], 7.44–7.39 (m, 10 H, Ar–H), 7.30 (s, 6 H, Ar–H), 7.12 [t, J(H,H) = 4.3 Hz, 2 H, Ar–H], 2.62 (s, 9 H, CH_3), 1.83 (s, 18 H, CH_3) ppm. ^{13}C NMR (75 MHz, $CDCl_3$): δ = 150.06, 149.80, 149.75, 149.68, 147.98, 147.08, 143.34, 139.30, 137.25, 137.14, 135.70, 135.30, 132.04, 131.19, 130.94, 130.41, 129.71, 129.41, 128.73, 127.57, 127.16, 124.67, 123.04, 121.78, 121.48, 119.84, 118.88, 118.57, 118.22, 21.67, 21.45 ppm. MS (FAB$^+$): m/z calcd. for $C_{65}H_{55}N_5Zn$: 969.37; found 970.4.

5,15-Bis[4-(diphenylamino)phenyl]-10,20-dimesitylporphyrinatozinc (6): Zn-(AP)$_2$(mesityl)$_2$P (150.0 mg, 0.189 mmol), 4-iodobenzene (385.0 mg, 1.887 mmol), Cu (150.0 mg, 2.360 mmol), K_2CO_3 (260.0 mg, 1.881 mmol), [18]crown-6 (16.0 mg, 0.061 mmol); yield 0.09 g, 42%. ^{1}H NMR (300 MHz, CD_2Cl_2): δ = 9.04 [d, J(H,H) = 3.9 Hz, 4 H, pyrrolic H], 8.78 [d, J(H,H) = 3.7 Hz, 4 H, pyrrolic H], 8.08 [d, J(H,H) = 7.9 Hz, 4 H, Ar–H], 7.44–7.40 (m, 20 H, Ar–H), 7.31 (s, 4 H, Ar–H), 7.13 (t, 4 H, Ar–H), 2.64 (s, 6 H, CH_3), 1.83 (s, 12 H, CH_3) ppm. ^{13}C NMR (75 MHz, $CDCl_3$): δ = 150.29, 149.85, 147.94, 147.22, 139.29, 139.10, 137.42, 136.70, 135.30, 132.33, 130.67, 129.45, 127.63, 124.77, 123.14, 121.39, 120.09, 119.19, 21.61, 21.48 ppm. MS (FAB$^+$): m/z calcd. for $C_{74}H_{58}N_6Zn$: 1094.4; found 1096.3.

5,10,15-Tris[4-(diphenylamino)phenyl]-20-mesitylporphyrinatozinc (7): Zn-(AP)$_3$(mesityl)P (140.0 mg, 0.183 mmol), iodobenzene (12.0 g, 0.059 mol), Cu (0.8 g, 0.013 mol), K_2CO_3 (1.54 g, 0.011 mol), [18]crown-6 (44.4 mg, 0.168 mmol); yield 0.09 g, 41%. ^{1}H NMR (300 MHz, [D$_6$]DMSO): δ = 8.91–8.87 (a singlet overlapping with a doublet, 6 H, pyrrolic H), 8.59 [d, J(H,H) = 4.6 Hz, 2 H, pyrrolic H], 8.06 [d, J(H,H) = 8.2 Hz, 6 H, Ar–H], 7.47–7.31 (m, 32 H, Ar–H), 7.15 [t, J(H,H) = 7.1 Hz, 6 H, Ar–H], 2.58 (s, 3 H, CH_3), 1.77 (s, 6 H, CH_3) ppm. ^{13}C NMR (75 MHz, $CDCl_3$): δ = 150.26, 149.89, 147.87, 147.18, 139.27, 139.04, 137.41, 136.85, 136.70, 135.43, 135.37, 132.43, 131.85, 130.76, 129.45, 127.64, 124.73, 123.11, 121.44, 121.36, 120.93, 120.47, 119.11, 21.73, 21.50 ppm. MS (FAB$^+$): m/z calcd. for $C_{83}H_{61}N_7Zn$: 1219.43; found 1221.3.

5-[4-(Ditolylamino)phenyl]-10,15,20-trimesitylporphyrinatozinc (9): Zn-(AP)(mesityl)$_3$P (50.0 mg, 0.061 mmol), 4-iodotoluene (106.4 mg, 0.488 mmol), Cu (31 mg, 0.488 mmol), K_2CO_3 (56.2 mg, 0.407 mmol), [18]crown-6 (16.1 mg, 0.061 mmol); yield 0.05 g, 78%. ^{1}H NMR (300 MHz, CD_2Cl_2): δ = 9.03 [d, J(H,H) = 4.6 Hz, 2 H, pyrrolic H], 8.75 [d, J(H,H) = 4.6 Hz, 2 H, pyrrolic H], 8.68 (s, 4 H, pyrrolic H), 8.04 [d, J(H,H) = 8.5 Hz, 2 H, Ar–H], 7.37–

7.20 (m, 16 H, Ar–H), 2.63 and 2.61 (two singlet overlapped, 9 H, CH_3), 2.38 (s, 6 H, CH_3), 1.84 and 1.83 (two singlet overlapped, 18 H, CH_3) ppm. ^{13}C NMR (75 MHz, $CDCl_3$): δ = 150.19, 149.85, 149.75, 149.69, 147.53, 145.48, 139.30, 139.13, 139.01, 137.33, 135.80, 135.14, 132.77, 132.24, 131.02, 130.45, 130.06, 127.60, 125.01, 120.28, 120.16, 118.70, 118.30, 21.73, 21.66, 21.47, 20.90 ppm. MS (FAB^+): *m*/*z* calcd. for $C_{67}H_{59}N_5Zn$: 997.41; found 998.6.

5,15-Bis[4-(ditolylamino)phenyl]-10,20-dimesitylporphyrinatozinc (10): $Zn(AP)_2(mesityl)_2P$ (150.0 mg, 0.189 mmol), 4-iodotoluene (410.0 mg, 1.880 mmol), Cu (150.0 mg, 2.360 mmol), K_2CO_3 (260.0 mg, 1.881 mmol), [18]crown-6 (16.0 mg, 0.061 mmol); yield 0.09 g, 41%. ^1H NMR (300 MHz, $CDCl_3$): δ = 9.03 [d, *J*(H,H) = 4.7 Hz, 4 H, pyrrolic H], 8.78 [d, *J*(H,H) = 4.6 Hz, 4 H, pyrrolic H], 8.04 [d, *J*(H,H) = 8.5 Hz, 4 H, Ar–H], 7.38 [d, *J*(H,H) = 8.5 Hz, 4 H, Ar–H], 7.31–7.29 (a doublet overlap-ping with a singlet, 12 H, Ar–H), 7.20 [d, *J*(H,H) = 8.3 Hz, 8 H, Ar–H], 2.65 (s, 6 H, CH_3), 2.39 (s, 12 H, CH_3), 1.84 (s, 12 H, CH_3) ppm. ^{13}C NMR (75 MHz, $CDCl_3$): δ = 150.36, 149.79, 147.58, 145.48, 139.30, 139.15, 137.37, 135.68, 135.18, 132.80, 132.36, 130.57, 130.07, 127.61, 125.05, 120.26, 120.12, 119.09, 21.61, 21.48, 20.90 ppm. MS (FAB^+): *m*/*z* calcd. for $C_{78}H_{66}N_6Zn$: 1150.46; found 1151.4.

5,10,15-Tris[4-(ditolylamino)phenyl]-20-mesitylporphyrinatozinc (11): Zn-$(AP)_3$(mesityl)P (0.12 g, 0.157 mmol), 4-iodotoluene (2.70 g, 0.013 mol), Cu (0.69 g, 0.011 mol), K_2CO_3 (1.32 g, 9.551 mmol), [18]crown-6 (0.04 g, 0.144 mmol); yield 0.10 g, 48%. ^1H NMR (300 MHz, CD_2Cl_2): δ = 9.12 (s, 4 H, pyrrolic H), 9.06 [d, *J*(H,H) = 4.7 Hz, 2 H, pyrrolic H], 8.78 [d, *J*(H,H) = 4.7 Hz, 2 H, pyrrolic H], 8.07–8.03 [dd, *J*(H,H) = 8.4 and 8.5 Hz, 6 H, Ar–H], 7.40–7.21 (m, 32 H, Ar–H), 2.64 (s, 3 H, CH_3), 2.38 (s, 18 H, CH_3), 1.84 (s, 6 H, CH_3) ppm. ^{13}C NMR (75 MHz, CD_2Cl_2): δ = 150.70, 150.16, 148.03, 145.77, 139.52, 137.89, 136.07, 135.95, 135.65, 135.58, 133.38, 132.73, 132.10, 130.83, 130.40, 127.96, 125.44, 121.46, 121.03, 120.30, 119.31, 21.76, 21.54, 20.96 ppm. MS (FAB^+): *m*/*z* calcd. for $C_{89}H_{73}N_7Zn$: 1303.52; found 1304.4.

5-[4-{Bis(4-methoxyphenyl)amino}phenyl]-10,15,20-trimesitylporphyrinatozinc (13): $Zn(AP)(mesityl)_3P$ (50.0 mg, 0.061 mmol), 4-iodoanisole (114.2 mg, 0.488 mmol), Cu (31.0 mg, 0.488 mmol), K_2CO_3 (56.2 mg, 0.407 mmol), [18]crown-6 (16.1 mg, 0.061 mmol); yield 0.05 g, 74%. ^1H NMR (300 MHz, $CDCl_3$): δ = 9.01 [d, *J*(H,H) = 4.6 Hz, 2 H, pyrrolic H], 8.77 [d, *J*(H,H) = 4.6 Hz, 2 H, pyrrolic H], 8.69 (s, 4 H, pyrrolic H), 8.00 [d, *J*(H,H) = 8.4 Hz, 2 H, Ar–H], 7.35 [d, *J*(H,H) = 8.9 Hz, 4 H, Ar–H], 7.30–7.26 (a doublet and a singlet overlapping with solvent peak, 8 H, Ar–H), 6.95 [d, *J*(H,H) = 8.9 Hz, 4 H, Ar–H], 3.84 (s, 6 H, OCH_3), 2.64 and 2.62 (two singlets overlapped, 9 H, CH_3), 1.85 (s, 18 H, CH_3) ppm. ^{13}C NMR (75 MHz, $CDCl_3$): δ = 156.02, 150.30, 149.87, 149.76, 148.09, 141.19, 139.33, 139.19, 139.05, 137.32, 135.11, 134.81, 132.28, 130.99, 130.40, 127.61, 126.90, 120.47, 118.68, 118.32, 114.89, 114.20, 55.55, 21.72, 21.65, 21.46 ppm. MS (FAB^+): *m*/*z* calcd. for $C_{67}H_{59}N_5O_2Zn$: 1029.4; found 1029.6.

5,15-Bis[4-{bis(4-methoxyphenyl)amino}phenyl]-10,20-dimesitylporphyrinatozinc (14): $Zn(AP)_2(mesityl)_2P$ (100.0 mg, 0.126 mmol), 4-iodoanisole (275.0 mg, 1.175 mmol), Cu (96.0 mg, 1.511 mmol), K_2CO_3 (139.5 mg, 1.009 mmol), [18]crown-6 (16.0 mg, 0.061 mmol); yield 0.05 g, 31%. ^1H NMR (300 MHz, $CDCl_3$): δ = 9.02 [d, *J*(H,H) = 4.6 Hz, 4 H, pyrrolic H], 8.77 [d, *J*(H,H) = 4.7 Hz, 4 H, pyrrolic H], 8.01 [d, *J*(H,H) = 8.5 Hz, 4 H, Ar–H], 7.35 [d, *J*(H,H) = 8.9 Hz, 8 H, Ar–H], 7.30–7.27 (a doublet overlapping with a singlet, 8 H, Ar–H), 6.95 [d, *J*(H,H) = 8.9 Hz, 8 H, Ar–H], 3.84 (s, 12 H, OCH_3), 2.65 (s, 6 H, CH_3), 1.83 (s, 12 H, CH_3) ppm. ^{13}C NMR (75 MHz, $CDCl_3$): δ = 156.02, 150.44, 149.74, 148.08, 141.14, 139.31, 139.20, 137.35, 135.15, 134.63, 132.38, 130.50, 127.60, 126.94, 120.37, 119.01, 118.22, 114.87, 55.54, 21.61, 21.48 ppm. MS (FAB^+): *m*/*z* calcd. for $C_{78}H_{66}N_6O_4Zn$: 1214.44; found 1214.4.

5,10,15-Tris[4-{bis(4-methoxyphenyl)amino}phenyl]-20-mesitylporphyrinatozinc (15): $Zn(AP)_3(mesityl)P$ (0.12 g, 0.157 mmol), 4-iodoanisole (2.97 g, 0.013 mol), Cu (0.69 g, 0.011 mol), K_2CO_3 (1.32 g, 9.551 mmol), [18]crown-6 (0.04 g, 0.144 mmol); yield 0.07 g, 33%. ^1H NMR (300 MHz, $CDCl_3$): δ = 9.09 (s, 4 H, pyrrolic H), 9.04 [d, *J*(H,H) = 4.6 Hz, 2 H, pyrrolic H], 8.78 [d, *J*(H,H) = 4.7 Hz, 2 H, pyrrolic H], 8.01 [d, *J*(H,H) = 8.4 Hz, 6 H, Ar–H], 7.37–7.28 (m, 20 H, Ar–H), 6.95 [d, *J*(H,H) = 8.9 Hz, 12 H, Ar–H], 3.83 (s, 18 H, OCH_3), 2.65 (s, 3 H, CH_3), 1.84 (s, 6 H, CH_3) ppm. ^{13}C NMR (75 MHz, $CDCl_3$): δ = 155.95, 150.39, 150.35, 150.29, 149.78, 148.05, 141.10, 139.31, 139.16, 137.33, 135.27, 135.22, 134.85, 134.68, 132.41, 131.78, 130.53, 127.59, 126.93, 121.23, 120.69, 118.78, 118.22, 118.17, 114.84, 55.52, 21.69, 21.48 ppm. MS (FAB^+): *m*/*z* calcd. for $C_{89}H_{73}N_7O_6Zn$: 1399.49; found 1400.7.

Supporting Information (see footnote on the first page of this article): ^1H NMR spectra, absorption spectra, excitation profiles, and cyclic voltammograms of Por–TPA conjugates are shown in the Supporting Information. The emission spectra obtained from the study of antenna effect and the absorption spectra of the radical cation of Por–TPA conjugates are also shown.

Acknowledgments

This work was supported by the National Science Council of the Republic of China (97-2113-M-260-005-MY3). We also thank Prof. Cheng for providing conjugates **8** and **12**.

[1] a) K. M. Kadish, in: *The Porphyrin Handbook* (Eds.: K. M. Kadish, K. M. Smith, R. Guilard), Academic Press, London, **2000**, vol. 1, pp. 1–44; b) J. S. Lindsey, in: *The Porphyrin Handbook* (Eds.: K. M. Kadish, K. M. Smith, R. Guilard), Academic Press, London, **2000**, vol. 1, pp. 45–118; c) K. M. Kadish, E. V. Caemelbecke, G. Royal, in: *The Porphyrin Handbook* (Eds.: K. M. Kadish, K. M. Smith, R. Guilard), Academic Press, London, **2000**, vol. 8, pp. 3–114; d) K. M. Kadish, G. Royal, E. V. Caemelbecke, L. Gueletti, in: *The Porphyrin Handbook* (Eds.: K. M. Kadish, K. M. Smith, R. Guilard), Academic Press, London, **2000**, vol. 9, pp. 1–219; e) M. Gouterman, in: *The Porphyrins* (Ed.: D. Dolphin), Academic Press, New York, **1978**, vol. 3, pp. 1–165.

[2] C. W. Huang, K. Y. Chiu, S. H. Cheng, *Dalton Trans.* **2005**, 2417–2422.

[3] a) J. C. Chang, C. J. Ma, G. H. Lee, S. M. Peng, C. Y. Yeh, *Dalton Trans.* **2005**, 1504–1508; b) W. N. Yen, S. S. Lo, M. C. Kuo, C. L. Mai, G. H. Lee, S. M. Peng, C. Y. Yeh, *Org. Lett.* **2006**, *8*, 4239–4242.

[4] a) M. C. Kuo, L. A. Li, W. N. Yen, S. S. Lo, C. W. Lee, C. Y. Yeh, *Dalton Trans.* **2007**, 1433–1439; b) C. W. Lee, H. P. Lu, C. M. Lan, Y. L. Huang, Y. R. Liang, W. N. Yen, Y. C. Liu, Y. S. Lin, E. W.-G. Diau, C. Y. Yeh, *Chem. Eur. J.* **2009**, *15*, 1403–1412.

[5] a) B. Li, X. Xu, M. Sun, Y. Fu, G. Yu, Y. Lin, Z. Bo, *Macromolecules* **2006**, *39*, 456–461; b) F. D'Souza, S. Gadde, D.-M. S. Islam, C. A. Wijesinghe, A. L. Schumacher, M. E. Zandler, Y. Araki, O. Ito, *J. Phys. Chem. A* **2007**, *111*, 8552–8560; c) N. K. Subbaiyan, I. Obraztsov, C. A. Wijesinghe, K. Tran, W. Kutner, F. D'Souza, *J. Phys. Chem. C* **2009**, *113*, 8982–8989; d) M. E. El-Khouly, J. B. Ryu, K. Y. Kay, O. Ito, S. Fukuzumi, *J. Phys. Chem. C* **2009**, *113*, 15444–15453; e) M. J. Frampton, R. Beavington, J. M. Lupton, I. D. W. Samuel, P. L. Burn, *Synth. Met.*

2001, *121*, 1671–1672; f) J. N. Clifford, G. Yahioglu, L. R. Milgrom, J. R. Durrant, *Chem. Commun.* **2002**, 1260–1261.
[6] C. Y. Huang, Y. O. Su, *Dalton Trans.* **2010**, *39*, 8306–8312.
[7] a) J. Preat, C. Michaux, D. Jacquemin, E. A. Perpete, *J. Phys. Chem. C* **2009**, *113*, 16821–16833; b) J. Shi, S. Peng, J. Pei, Y. Liang, F. Cheng, J. Chen, *ACS Appl. Mater. Interfaces* **2009**, *1*, 944–950; c) G. Li, K. J. Jiang, Y. F. Li, S. L. Li, L. M. Yang, *J. Phys. Chem. C* **2008**, *112*, 11591–11599; d) H. Tian, X. Yang, R. Chen, R. Zhang, A. Hagfeldt, L. Sun, *J. Phys. Chem. C* **2008**, *112*, 11023–11033; e) W. Xu, B. Peng, J. Chen, M. Liang, F. Cai, *J. Phys. Chem. C* **2008**, *112*, 874–880; f) M. Liang, W. Xu, F. Cai, P. Chen, B. Peng, J. Chen, Z. Li, *J. Phys. Chem. C* **2007**, *111*, 4465–4472.
[8] a) Y. Tao, Q. Wang, L. Ao, C. Zhong, C. Yang, J. Qin, D. Ma, *J. Phys. Chem. C* **2010**, *114*, 601–609; b) Y. Yang, Y. Zhou, Q. He, C. He, C. Yang, F. Bai, Y. Li, *J. Phys. Chem. B* **2009**, *113*, 7745–7752; c) D. Sek, A. Iwan, B. Jarzabek, B. Kaczmarczyk, J. Kasperczyk, Z. Mazurak, M. Domanski, K. Karon, M. Lapkowski, *Macromolecules* **2008**, *41*, 6653–6663; d) S. Tao, Y. Zhou, C. S. Lee, S. T. Lee, D. Huang, X. Zhang, *J. Phys. Chem. C* **2008**, *112*, 14603–14606; e) Z. Ge, T. Hayakawa, S. Ando, M. Ueda, T. Akiike, H. Miyamoto, T. Kajita, M. Kakimoto, *Chem. Mater.* **2008**, *20*, 2532–2537; f) J. M. Hancock, A. P. Gifford, Y. Zhu, Y. Lou, S. A. Jenekhe, *Chem. Mater.* **2006**, *18*, 4924–4932; g) N. Tamoto, C. Adachi, K. Nagai, *Chem. Mater.* **1997**, *9*, 1077–1085; h) S. J. Yeh, C. Y. Tsai, C. Y. Huang, G. S. Liou, S. H. Cheng, *Electrochem. Commun.* **2003**, *5*, 373–377.
[9] a) S. H. Hsiao, G. S. Liou, Y. C. Kung, H. J. Yen, *Macromolecules* **2008**, *41*, 2800–2808; b) S. Beaupre, J. Dumas, M. Leclerc, *Chem. Mater.* **2006**, *18*, 4011–4018; c) S. H. Cheng, S. H. Hsiao, T. H. Su, G. S. Liou, *Macromolecules* **2005**, *38*, 307–316.
[10] a) F. A. Walker, V. L. Balke, G. A. McDermott, *Inorg. Chem.* **1982**, *21*, 3342–3348; b) F. A. Walker, V. L. Balke, G. A. McDermott, *J. Am. Chem. Soc.* **1982**, *104*, 1569–1574; c) F. A. Walker, J. A. Barry, V. L. Balke, G. A. McDermott, M. Z. Wu, P. F. Linde, *Adv. Chem.* **1982**, *201*, 377–416.
[11] M. Gouterman, *J. Mol. Spectrosc.* **1961**, *6*, 138–163.
[12] M. Meot-Ner, A. D. Adler, *J. Am. Chem. Soc.* **1975**, *97*, 5107–5111.
[13] P. G. Seybold, M. Gouterman, *J. Mol. Spectrosc.* **1969**, *31*, 1–13.
[14] a) K. M. Kadish, L. R. Shiue, R. K. Rhodes, L. A. Bottomley, *Inorg. Chem.* **1981**, *20*, 1274–1277; b) C. L. Lin, M. Y. Fang, S. H. Cheng, *J. Electroanal. Chem.* **2002**, *531*, 155–162.
[15] D. J. Quimby, F. R. Longo, *J. Am. Chem. Soc.* **1975**, *97*, 5111–5117.
[16] J. S. Lindsey, R. W. Wagner, *J. Org. Chem.* **1989**, *54*, 828–836.
[17] K. Y. Chiu, Y. O. Su, *Chem. Commun.* **2009**, 2884–2886.
[18] I. Schmidt, J. Jiao, P. Thamyongkit, D. S. Sharada, D. F. Bocian, J. S. Lindsey, *J. Org. Chem.* **2006**, *71*, 3033–3050.
[19] A. Bettelheim, B. A. White, S. A. Raybuck, R. W. Murray, *Inorg. Chem.* **1987**, *26*, 1009–1017.
[20] A. A. Kelkar, N. M. Patil, R. V. Chaudhari, *Tetrahedron Lett.* **2002**, *43*, 7143–7146.
[21] D. J. Liaw, P. N. Hsu, W. H. Chen, S. L. Lin, *Macromolecules* **2002**, *35*, 4669–4676.
[22] Y. H. Liu, C. Chen, L. M. Yang, *Tetrahedron Lett.* **2006**, *47*, 9275–9278.
[23] R. R. Nelson, R. N. Adams, *J. Am. Chem. Soc.* **1968**, *90*, 3925–3930.
[24] a) S. Gauthier, J. M. J. Frechet, *Synthesis* **1987**, 383–385; b) C. T. Chen, I. Cha, S. J. Hsieh, *J. Chin. Chem. Soc.* **1998**, *45*, 741–748.

Received: September 30, 2011
Published Online: January 30, 2012

DOI: 10.1002/ejic.201101103

Syntheses and Structural Study of Novel Tetranuclear Bis(phenoxido)-Bridged Cu^{II} Metal–Organic Macrocycles

Antti Riisiö,[a] Mikko M. Hänninen,[a] and Reijo Sillanpää*[a]

Keywords: Copper / Supramolecular chemistry / Magnetic properties / Density functional calculations

Six new tetranuclear copper(II) complexes were prepared exploiting novel ditopic alkylenediamine-*N*,*N*,*N*′,*N*′-tetraphenolate ligands. The geometrical parameters of the compounds can be varied by introducing different solvents of crystallization into the lattice. The structures of all six complexes were determined from single-crystal X-ray diffraction analyses and the magnetic properties of the complexes were estimated by computational DFT calculations. The relationship between the magnetic exchange coupling constant (*J*) and the Cu–O–Cu angle (θ) in these bis(phenoxido)-bridged complexes was investigated and a magnetostructural correlation was established between *J* and the θ angle. All studied complexes showed strong antiferromagnetic behaviour.

Introduction

The amine-bis(phenol) ligands are versatile and important ligands that can be prepared relatively straightforwardly from common benchtop synthetic methods. The coordination chemistry of these ligands is eminently rich and the compounds have been exploited in numerous applications in applied coordination chemistry including mimicking the activity of biological compounds, catalysis and in molecular magnetism.[1,2] Progress has also been achieved in manipulating DNA[2c] using mono- and dinuclear aminophenol copper(II) complexes. Furthermore, the dinuclear bis(phenoxido)-bridged copper(II) complexes represent a class of important and well-studied compounds in the field of molecular magnetism.[3]

Recently, we have used amine-bis(phenol)s to prepare a series of bis(μ-phenoxido)dicopper(II) complexes with ω-[bis(2-hydroxy-3,5-dimethylbenzyl)amino]alkan-1-ol ligands[4] and established a linear relationship between the Cu–O–Cu angle (θ) and the magnetic exchange coupling constants (*J*). Our findings supported the experimental and theoretical magnetostructural studies performed during the past decades,[3] which have revealed several important correlations between the structural parameters and the magnetic properties of the compounds; the θ angle is probably the most important of these.

Earlier we reported on a novel and simple synthetic route for highly flexible and tunable ditopic alkylenediamine-*N*,*N*,*N*′,*N*′-tetraphenolate ligands,[5] which can be used in traditional coordination chemistry but also have potential as building blocks for molecular manufacturing used to produce molecular rings and metal–organic frameworks. This area of chemistry provides limitless possibilities in the design of molecular materials possessing extraordinary sensing, magnetic, catalytic and optical properties.[6] Until now, the ditopic alkylenediamine-*N*,*N*,*N*′,*N*′-tetraphenolate ligands and their complexes have not been extensively studied for these supramolecular applications.

In this contribution we have studied the reactions of these novel ligands (H_4L1, n = 7 and H_4L2, n = 8 in Scheme 1) with copper(II) salts and obtained a series of tetranuclear phenoxido-bridged copper(II) complexes. We were able to crystallize the complexes, with or without water bridges, as several different solvent adducts that alter the structural parameters around the Cu^{II} cations in the compounds. In addition, we have performed computational studies at the DFT level to estimate the magnetic exchange coupling constants of the complexes.

Results and Discussion

The syntheses of six new tetranuclear copper(II) diamine-bis(phenolate)s were performed according to Scheme 1. In the isolated complexes the copper(II) cations form two separate dinuclear units, which are connected by the alkyl chains to form molecular rings. Three of the complexes are tetranuclear $[Cu_4(L1)_2]\cdot x$S {x = 2 and S = methanol (**1**), x = 2 and S = chloroform (**2**), and x = 1 and S = H_2O (**3**)}. The other three are similar tetranuclear complexes with a water bridge on the coordination sphere of

[a] Department of Chemistry, University of Jyväskylä,
P. O. Box 35, 40014 Jyväskylä, Finland
E-mail: resillan@jyu.fi

Supporting information for this article is available on the WWW under http://dx.doi.org/10.1002/ejic.201101103.

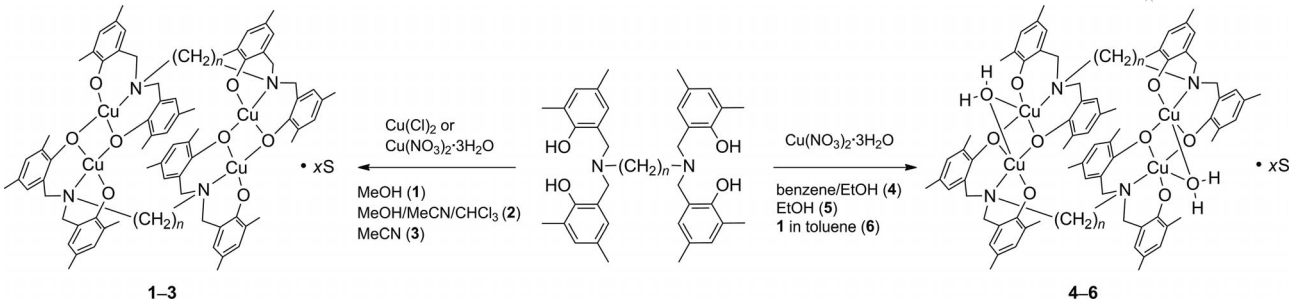

Scheme 1. Schematic synthetic route for the preparation of compounds **1**–**6**.

the Cu^{II} cations and solvates in the lattice: $[Cu_4(L1)_2(H_2O)_2]$·2EtOH·4benzene (**4**), $[Cu_4(L2)_2(H_2O)_2]$·2EtOH (**5**) and $[Cu_4(L1)_2(H_2O)_2]$·2EtOH·3toluene (**6**).

The complexes were characterized by elemental analyses, IR spectra, thermogravimetric measurements and X-ray diffraction. Furthermore, the magnetic properties of the complexes were estimated by DFT calculations. A thermogravimetric analysis revealed that in compounds **1**–**6** the solvent molecules can be removed quite easily. This is most likely because of the weak intermolecular interactions without strong hydrogen bonds. However, the removal of the solvents is a slow process, which begins at room temperature and lasts to about 160 °C. The solvent-free complexes start to decompose after 230 °C.

All solvents can be removed by 2 h of heating in a conventional thermal oven at 160 °C. The recrystallization attempts from the acquired solvent-free material did not improve the quality of the crystals or produce any additional solvates compared with the syntheses carried out from free ligand and copper(II) nitrate or chloride. However, we are confident that other packing structures, originating from the high flexibility of the ligand framework, are possible.

Complexes **1** and **2** crystallize in orthorhombic (*Pcab*) and complex **3** in monoclinic (*C*2/*c*) space groups, whereas complexes **4**–**6** crystallize in a triclinic ($P\bar{1}$) space group. All complexes **1**–**6** are similarly built from two tetra-anionic $L1^{4-}$ or $L2^{4-}$ (all phenol groups are deprotonated) alkylenediamine-*N*,*N*,*N*′,*N*′-tetraphenolate ligands coordinated to four copper(II) cations in a tridentate bridging manner, thus forming a neutral molecular metal–organic macrocycle (Figure 1, Figure 2 and Figures S1–S4). The selected geometrical parameters are presented in Table 1. The macrocycles **1**–**3** consist of two distinct Cu_2-(μ-OPh)$_2$ dinuclear units that are connected by alkyl bridges of the amino groups in amine-bis(phenol) ends of the alkylenediamine-*N*,*N*,*N*′,*N*′-tetraphenolate ligand. In complexes **1**–**3** the copper(II) cations have a slightly distorted square-planar coordination sphere around the copper(II) centres with the same donor atom sets, and the complexes **1** and **2** are isostructural. In complexes **4**–**6** each of the dinuclear copper units is also bridged by a weakly bonded water molecule, thus producing a strongly distorted square-based pyramidal fivefold coordination for the copper(II) cations with two μ_2-phenoxido, phenoxido and water oxygen atoms and an amine nitrogen atom.

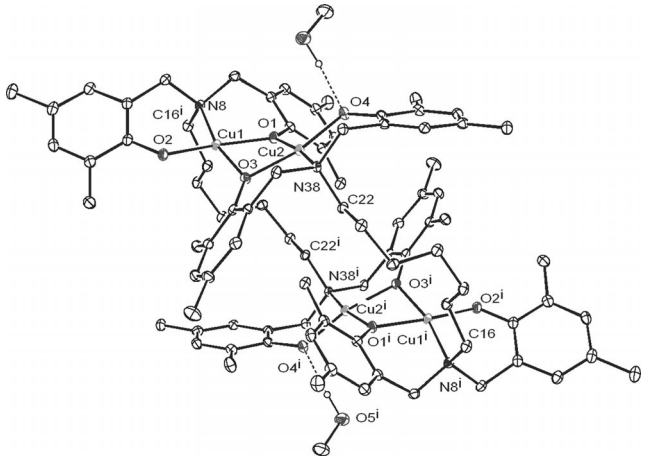

Figure 1. The tetranuclear unit of **1** showing the atomic labelling scheme with thermal ellipsoids drawn at the 20% probability level. CH hydrogen atoms have been omitted for clarity.

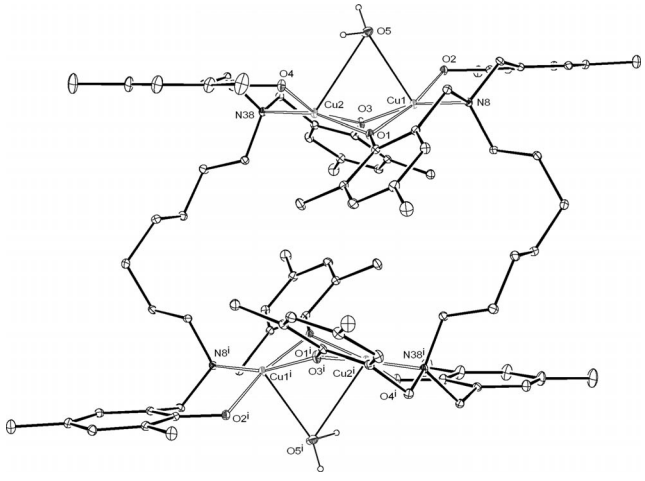

Figure 2. The tetranuclear unit of **6** showing the atomic labelling scheme with thermal ellipsoids drawn at the 20% probability level. CH hydrogen atoms and toluene molecules have been omitted for clarity.

All complexes **1**–**6** have additional noncoordinating solvents of crystallization, which notably alter the packing of the complexes, hence, changing the geometrical parameters and magnetic behaviour of the complexes. The unit cells of **1**–**3** contain noncoordinating methanol, chloroform and water molecules, respectively. The data for complex **3** is of

Table 1. Selected bond lengths [Å] and angles [°] for complexes **1**–**6**.

	1	**2**	**3**	**4**	**5**	**6**
Cu1–O1	1.918(2)	1.921(3)	1.920(9)	1.932(2)	1.942(2)	1.953(2)
Cu1–O2	1.857(2)	1.847(3)	1.847(9)	1.884(2)	1.890(2)	1.895(2)
Cu1–O3	1.995(2)	1.989(3)	1.995(9)	1.963(2)	1.937(2)	1.981(2)
Cu1–O5	–	–	–	2.776(3)	2.807(3)	2.496(3)
Cu1–N8	2.026(3)	2.029(3)	2.021(11)	2.009(2)	2.010(2)	2.025(3)
Cu2–O1	1.940(2)	1.960(3)	1.926(9)	1.981(2)	1.980(2)	1.956(2)
Cu2–O3	1.936(2)	1.926(3)	1.937(9)	1.937(2)	1.972(2)	1.940(2)
Cu2–O4	1.885(2)	1.878(3)	1.876(9)	1.881(2)	1.914(2)	1.881(2)
Cu2–O5	–	–	–	2.660(3)	2.330(3)	2.743(3)
Cu2–N38	1.996(2)	2.009(3)	1.996(10)	2.026(2)	2.010(2)	1.991(3)
Cu1–O1–Cu2 (θ)	101.76(9)	101.85(12)	102.6(5)	95.84(8)	95.59(9)	93.56(9)
Cu1–O3–Cu2	99.15(9)	100.60(12)	99.5(5)	96.24(8)	96.01(8)	93.20(8)
O1···O3–C31 (τ)[a]	12.5(2)	10.1(2)	16.1(9)	15.6(2)	19.5(2)	23.1(2)
O3···O1–C1 (τ)	18.6(2)	25.6(2)	19.6(9)	16.2(2)	16.7(2)	9.9(2)
Cu1–O5–Cu2	–	–	–	64.53(6)	68.17(8)	65.69(7)
Cu1–O1···O3–Cu2 (γ)[b]	–27.6(1)	–25.3(1)	–26.6(5)	–39.1(1)	–39.7(1)	–43.9(1)

[a] τ is the substituent angle from the bridging O···O line. [b] γ is the dihedral angle of the bridging O–Cu–O planes.

poor quality (i.e. large uncertainties in bond lengths and angles). Unfortunately, originating from the complexes tendency to crystallize with additional solvents in the lattice, we were not able to duplicate the synthesis of **3**, hence, the crystal structure is the only experimental data we can report.

Although the shapes of all the complexes are quite similar, the coordination environments around the copper centres can be clearly divided into two groups (**1**–**3** and **4**–**6**). Inside of these two groups the coordination spheres are comparable, but not identical. In the first group (**1**–**3**) the geometrical parameters around the central metal are uniform (see Table 1). Also the complexes **4** and **5** of the second group have similar main structural parameters regardless of the carbon chain being one carbon longer in **5** than in **4** and the quite unsymmetrical water bridge [Cu–O distances are 2.330(3) and 2.807(3) Å] in complex **5**. The structure of **6** shows several differences from that of **4** and **5** since the polar ethanol is missing from the structure of **6** (Table 1).

The solvents of crystallization affect the structural parameters of the coordination spheres in **1**–**6** by changing the packing system of the complexes. This is clearly seen from the packing diagrams of **1**–**2** where the water molecule is absent. The complexes form separate neutral units in the lattice without any major interaction between each other and the solvents of crystallization only fill the lattice with hydrogen bonds to the molecular rings (Figure 3). The bridging water molecule in complexes **4**–**6** causes new demands on the packing system since the OH hydrogen needs H acceptors. Complex **5** (Figure 4) is shown as an example of the packing diagrams of complexes **4**–**6**. It is evident that the bridging water molecule induces a hydrogen-bonding network connecting the complexes to 1D chains (see also Figures S7 and S8). In addition, there are no interactions or transmission pathways for magnetic effects in the other two directions, hence, these complexes could possess single-chain magnet behaviour (Figure S9). In addition, in complex **3**, weakly H-bonded water molecules connect the individual complexes forming a similar chain arrangement of

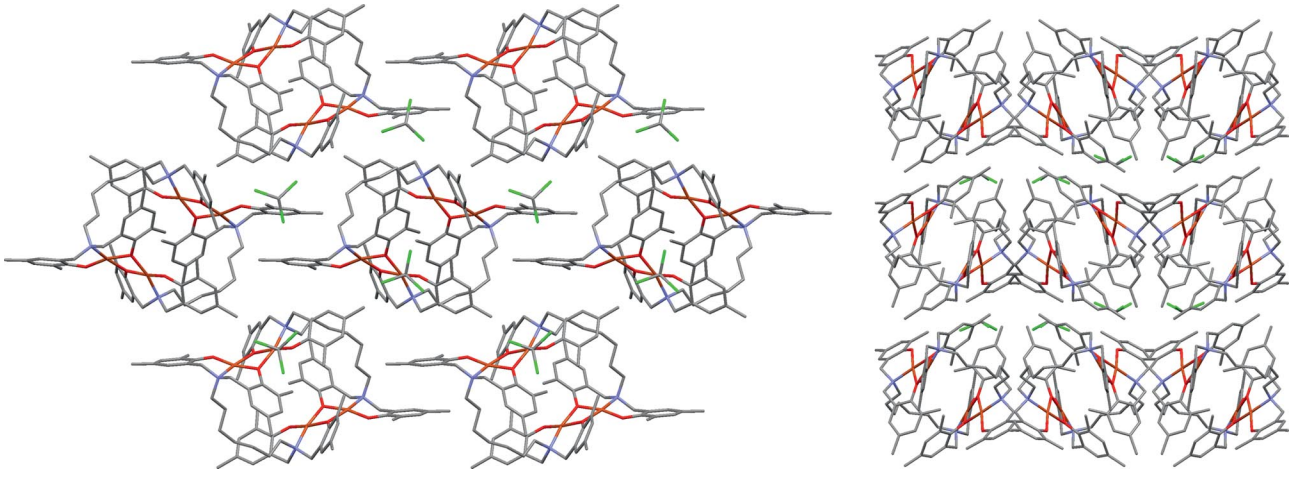

Figure 3. Packing diagram of complex **2** shown down the crystallographic c axis (left) and a axis (right).

the complexes (Figure S6). The solvate dependent structural changes have also been found in dinuclear [Cu_2(*o*-pba)$_2$] complexes [*o*-pba = *o*-phenylenebis(acetylacetonate)].[7]

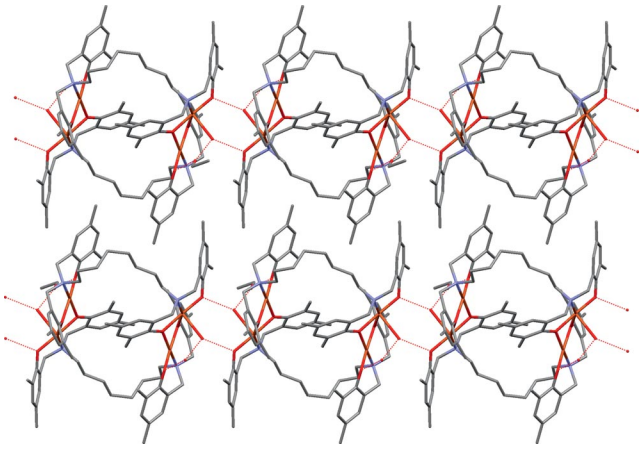

Figure 4. Packing diagram of complex **5** shown down the reciprocal cell a* axis.

In general, complexes **1**–**6** are interesting from the sense of molecular magnetism but also from a structural point of view. All complexes form metal–organic macrocycles, which by themselves could be used to trap small molecules in the cavities of the lattice or more likely as building blocks to large metal–organic frameworks. As shown by the coordinated water molecules, the individual complexes could be linked together with proper donor molecules with bridging abilities (for example some dinitroderivatives or dicarboxylic acids).

Furthermore, we are able to modify the length of the alkyl chain between the amine nitrogens connecting two amine-bis(phenol) ends of the ligand (eight methylene groups in complex **5** compared to seven methylenes in the other complexes), hence, the size of the macrocycle can be varied. We have prepared ligands with up to 12 carbon atoms between amine-bis(phenol) ends but unfortunately we were not able to crystallize any copper(II) complexes of these ligands (we also prepared similar ligands with five or six methylene groups, but no molecular rings were obtained). It is also possible to introduce heteroatoms to the alkyl chain (providing more donor atoms for metal cation bonding) and modify the substituents in the aromatic rings. The potential of these ligands and complexes is immense and the capability of these compounds to produce metal–organic frameworks and related materials is under study by our group.

Theoretical Studies

Because of the unstable nature of the solvent molecules in the lattice of the complexes **1**–**6**, the experimental measurement of the magnetic properties of the complexes would be at least ambiguous. Hence, we performed a thorough DFT computational analysis to evaluate the strength of the magnetic coupling in these novel tetranuclear complexes. The analysis was performed at the B3LYP/TZV[8] level using the Turbomole 6.3 program package.[9] In all calculations, the coupling between separate dinuclear units was neglected since there is no transmission pathway for magnetic effects between the copper centres, and the calculations showed that the coupling is virtually nonexistent compared to the coupling constant values within the dinuclear units. Hence, the final coupling constants (*J*) were obtained as the energy difference between the broken symmetry singlet state and the corresponding quintet state by single-point calculations to the crystallographic geometries without noncoordinating solvent molecules. The energy difference between the preceding states in this system of two separate dinuclear copper units is –2*J*. The calculated magnetic coupling constants (Table 2) are in good agreement with the experimental and computational values obtained earlier.[3,4]

Table 2. Calculated magnetic coupling constant values *J* [cm^{-1}] for complexes **1**–**8**.

	$J_{calcd.}$	J_{exp}	θ[a]	d[b]	Ref.
1	–488.3	–	100.48	2.994	this work
2	–473.8	–	101.23	3.013	this work
3	–437.1	–	100.97	3.001	this work
4	–297.0	–	96.04	2.904	this work
5	–288.4	–	95.80	2.906	this work
6	–205.2	–	93.38	2.849	this work
7	9.6	26.62	84.69	2.671	[10]
8	30.2	38.66	85.13	2.680	[10]

[a] Mean value of both Cu–O–Cu angles in °. [b] Cu···Cu distance in Å.

To estimate the effects of different noncoordinated solvent molecules in the lattice we tried to create a magnetostructural correlation between certain structural parameters and the magnetic behaviour. Previously these correlations have been found for example between the Cu–O–Cu (θ) angle and the coupling constant *J*.[3,4] For the complexes **1**–**6** the magnetostructural correlation of the *J* value to the Cu–O–Cu angle is evident, since there is an almost linear relationship (R = 0.993) between the *J* values and the θ angle (Figure 5). In addition, we were able to find a similar

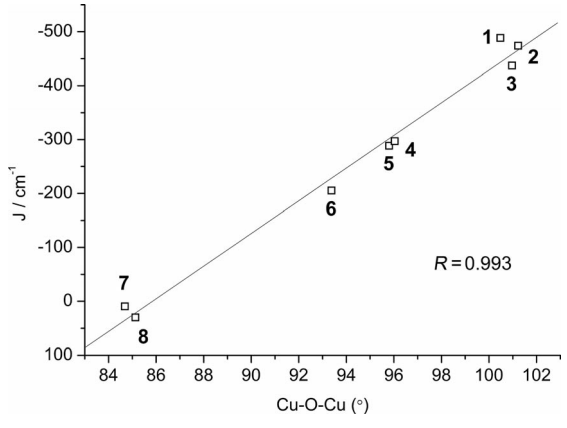

Figure 5. Plot of the calculated *J* value versus the average Cu–O–Cu angle of complexes **1**–**8**.

correlation between the Cu–Cu bond length and the coupling constant *J*. The correlation of the Cu–Cu bond length is clearly due to double bridges in the complexes, which bind the Cu–Cu bond firmly to the Cu–O–Cu angle and vice versa.

The effect of the weakly coordinating water molecule is obvious from the calculated *J* values. The water molecule bends the Cu–O–Cu angle thus weakening the magnetic transmission pathway between the copper centres. Hence, the values of coupling constants for **4**–**6** are more than 100 cm^{-1} smaller than complexes without the water bridge (**1**–**3**).

The reliability of the computed values was also estimated by calculating the coupling constants of recently published similar dinuclear copper(II) complexes **7** and **8**.[10] The calculated *J* values (Table 2, Entries 7 and 8) are in good agreement with experimental ones and they fit nicely in to the data from complexes **1**–**6** (Figure 5), thus confirming the observed magnetostructural correlation.

Conclusions

In this study we have shown that novel ditopic alkylenediamine-*N*,*N*,*N*′,*N*′-tetraphenolate ligands form tetranuclear complexes with copper(II) cations producing flexible metal–organic macrocycles. The geometries and structural parameters around the copper centres can be varied by introducing a weakly coordinated water molecule and different solvents of crystallization into the lattice. According to theoretical studies all these complexes show antiferromagnetic behaviour. Furthermore, we were able to constitute a magnetostructural correlation between the calculated coupling constant values (*J*) and Cu–O–Cu angle (θ). Future studies are aimed at investigating the performance of the prepared ligands and complexes as metal organic frameworks and/or molecular rings.

Experimental Section

Materials: $Cu(NO_3)_2{\cdot}3H_2O$, $CuCl_2$ and solvents were purchased from commercial sources and used as received. H_4L1 and H_4L2 were prepared using a known procedure.[5] X-ray crystallography, elemental and IR analyses were performed in situ after the removal of the liquid reaction medium because of the rapid decomposition of the crystalline complexes.

$[Cu_4(L1)_2]{\cdot}2MeOH$ (1): $Cu(NO_3)_2{\cdot}3H_2O$ (0.2 mmol, 48 mg) was dissolved in MeOH (1.0 mL) and H_4L1 (0.1 mmol, 66 mg) in MeOH (9.0 mL). The solutions were layered and after 18 h a few crystals of $[Cu_4(L1)_2]{\cdot}2MeOH$ were formed (confirmed by X-ray diffraction). NEt_3 (0.4 mmol, 56 μL) was dissolved in MeOH (5 mL) and was added to the mixture. After 24 h six-cornered, dark-green plates of $[Cu_4(L1)_2]{\cdot}2MeOH$ were collected by decantation, washed with methanol (10 mL) and air dried; yield 58 mg (88%). $C_{88}H_{116}Cu_4N_4O_{10}$ (1644.09): calcd. C 64.3, H 7.11, N 3.41; found C 64.3, H 7.03, N 3.10. IR: $\tilde{\nu}$ = 1474 (vs), 1305 (s), 1235 (s), 1159, 979, 803, 641, 506 cm^{-1}.

$[Cu_4(L1)_2]{\cdot}2CHCl_3$ (2): $CuCl_2$ (0.1 mmol, 14 mg) was dissolved in MeOH (1.0 mL) and H_4L1 (0.05 mmol, 33 mg) in $CHCl_3$ (1.0 mL). The solutions were mixed and MeCN (3.0 mL) was added. After the addition of NEt_3 (0.22 mmol, 30 μL) into the solution it was kept at room temp. for 24 h. Six-cornered, light-green plates of **2** were separated by decantation and washed with ether (3 mL); yield 29 mg (64%). $C_{88}H_{110}Cl_6Cu_4N_4O_8$ (1818.76): calcd. C 58.1, H 6.10, N 3.08; found C 58.7, H 6.29, N 3.25. IR: $\tilde{\nu}$ = 1473 (vs), 1307 (s), 1248 (vs), 1161 (m), 804 (s), 753 (s), 614 (m), 504 (m) cm^{-1}.

$[Cu_4(L1)_2]{\cdot}H_2O$ (3): The compound was obtained from a dilute acetonitrile mixture using stoichiometric amounts of $Cu(NO_3)_2{\cdot}3H_2O$ (0.1 mmol, 24 mg), H_4L1 (0.05 mmol, 33 mg) and NEt_3 (0.2 mmol, 30 μL). Starting materials were mixed in acetonitrile and immediately a precipitate formed, which was separated by decantation. The solution was kept at room temperature for several weeks. Only a few crystals were formed and they were characterized by X-ray diffraction. However, despite several attempts, we have not been able to crystallize this compound since then. Difficulties in preparation of **3** as a crystalline product revealed that the solvent-free tetranuclear complex is not thermodynamically stable. The high values of the thermal ellipsoids of **3** also support this.

$[Cu_4(L1)_2(H_2O)_2]{\cdot}2EtOH{\cdot}4benzene$ (4): $Cu(NO_3)_2{\cdot}3H_2O$ (1.0 mmol, 24 mg) and H_4L1 (0.05 mmol, 33 mg) were dissolved in a mixture of benzene (5.0 mL) and EtOH (3.0 mL). NEt_3 (0.22 mmol, 30 μL) was added and the solution was concentrated to 2.0 mL over 24 h. Compound **4** was separated by decantation and air dried; yield 35 mg (69%). $C_{114}H_{148}Cu_4N_4O_{12}$ (2020.63): calcd. C 67.8, H 7.38, N 2.77; found C 67.5, H 7.41, N 2.83. IR: $\tilde{\nu}$ = 1476 (s), 1309 (s), 1253 (s), 806 (s), 672 (vs), 614 (m), 504 (m) cm^{-1}.

$[Cu_4(L2)_2(H_2O)_2]{\cdot}2EtOH$ (5): $Cu(NO_3)_2{\cdot}3H_2O$ (0.2 mmol, 48 mg) was dissolved in EtOH (3.0 mL) and H_4L2 (0.1 mmol, 68 mg) was dissolved in boiling EtOH (3.0 mL) and the solutions were mixed. NEt_3 (0.44 mmol, 60 μL) was dissolved in EtOH (3 mL) and added as a layer on top of the previous mixture. After 4 d **5** was separated by decantation; yield 62 mg (71%). $C_{92}H_{128}Cu_4N_4O_{12}$ (1736.23): calcd. C 63.64, H 7.43, N 3.23; found C 63.16, H 7.47, N 3.13. IR: $\tilde{\nu}$ = 1473 (vs), 1309 (s), 1254 (vs), 1048 (s), 880 (s), 805 (s), 612 (s), 502 (s), 457 (m) cm^{-1}.

$[Cu_4(L1)_2(H_2O)_2]{\cdot}3toluene$ (6): Compound **1** (20 mg, 0.012 mmol) was dissolved in hot toluene (5.0 mL). The solution was concentrated to a final volume of 1.0 mL and allowed to obtain moisture from the air for 24 h. Crystals of **6** were separated by decantation and air dried; yield 23 mg (98%). $C_{107}H_{136}Cu_4N_4O_{10}$ (1892.46): calcd. C 67.9, H 7.24, N 2.96; found C 67.8, H 7.15, N 2.89. IR: $\tilde{\nu}$ = 1472 (s), 1305 (m), 1252 (s), 804 (s), 727 (vs), 693 (s), 463 (s) cm^{-1}.

IR Spectra: The infrared spectra were measured using a Bruker Tensor 27 IR device with an ATR. The spectra were recorded in situ directly from the surface of the sample after removal from the reaction mixture. The IR spectra of complexes **1**, **2**, **4**–**6**, H_4L1 and H_4L2 over the wavenumber region 2000–300 cm^{-1} are provided in the Supplementary Information.

X-ray Measurements: Suitable single crystals of **1**–**6** for X-ray measurements were obtained directly from the batches of isolated complexes. Crystallographic data were collected at 123 or 173 K with a Nonius-Kappa CCD area-detector diffractometer using graphite-monochromatized Mo-K_α radiation (α = 0.71073 Å) (Table 3). The structures were solved by direct methods using the SIR97 or SHELXS-97 programs[11,12] and full-matrix, least-squares refinements on F^2 were performed using the SHELXL-97 program.[12] The CH hydrogen atoms were included at the fixed distances with the fixed displacement parameters from their host atoms (1.2 or 1.5 times that of the host atom). The OH hydrogen atoms were

Table 3. Summary of crystallographic data for complexes **1**–**6**.

	1	**2**	**3**	**4**	**5**	**6**
Empirical formula	$C_{88}H_{108}Cu_4N_4O_{10}$	$C_{88}H_{110}Cl_6Cu_4N_4O_8$	$C_{86}H_{108}Cu_4N_4O_9$	$C_{114}H_{148}Cu_4N_4O_{12}$	$C_{92}H_{128}Cu_4N_4O_{12}$	$C_{107}H_{136}Cu_4N_4O_{10}$
M_r [g mol^{-1}]	1644.01	1818.66	1579.92	2020.52	1736.14	946.18
Crystal system	orthorhombic	orthorhombic	monoclinic	triclinic	triclinic	triclinic
Space group (no.)	*Pcab* (61)	*Pcab* (61)	*C2/c* (15)	$P\bar{1}$ (2)	$P\bar{1}$ (2)	$P\bar{1}$ (2)
a [Å]	17.6471(2)	17.5688(2)	21.6901(19)	13.4103(3)	13.5339(3)	13.5582(3)
b [Å]	20.5513(2)	20.8245(3)	13.3687(11)	14.8022(3)	14.0812(3)	14.1141(3)
c [Å]	22.2862(3)	22.7194(3)	27.680(2)	16.0649(4)	14.2794(4)	14.2786(3)
α [°]	90	90	90	104.3620(10)	92.913(2)	103.478(2)
β [°]	90	90	93.887(4)	102.2830(10)	117.3250(10)	108.7970(10)
γ [°]	90	90	90	115.2330(10)	110.0820(10)	101.3790(10)
V [Å]	8082.56(16)	8312.15(19)	8007.9(11)	2603.39(10)	2198.65(9)	2402.77(9)
Z	4	4	4	1	1	1
$D_{calcd.}$ [g cm^{-1}]	1.351	1.453	1.324	1.289	1.311	1.308
μ (Mo-K_α) [mm^{-1}]	1.099	1.261	1.106	0.868	1.015	0.934
T [K]	123(2)	123(2)	173(2)	123(2)	173(2)	123(2)
Observed reflections	7945	9040	6888	10179	8475	9184
R_{int}	0.0813	0.0615	0.1029	0.0582	0.0505	0.0447
Parameters	490	504	447	652	523	587
R_1[a]	0.0750 (0.0423)[b]	0.0782 (0.0539)	0.2512 (0.1341)	0.0717 (0.453)	0.0780 (0.0486)	0.0707 (0.0464)
wR_2[c]	0.0984 (0.0855)	0.1664 (0.1452)	0.3256 (0.2680)	0.0945 (0.0853)	0.1084 (0.0986)	0.1135 (0.1034)
$\Delta\rho_{max./min.}$ [e Å^{-3}]	0.470/–0.492	0.679/–1.16	0.657/–0.444	0.402/–0.342	0.386/–0.327	0.924/–0.484

[a] $R_1 = \Sigma||F_o| - |F_c||/\Sigma|F_o|$. [b] Values in parentheses are for reflections with $I > 2\sigma(I)$. [c] $wR_2 = \{\Sigma[w(F_o^2 - F_c^2)^2]/\Sigma[w(F_o^2)^2]\}^{1/2}$ and $w = 1/[\sigma^2(F_o^2) + (aP)^2 + (bP)]$, where $P = (2F_c^2 + F_o^2)/3$.

refined isotropically with a thermal displacement of 1.2 times that of the host atom. The figures were drawn with the programs Ortep-III for Microsoft Windows®[13] and Mercury.[14]

CCDC-848123 (for **1**), -848124 (for **2**), -848125 (for **3**), -848126 (for **4**), -848127 (for **5**) and -848128 (for **6**) contain the supplementary crystallographic data for this paper. These data can be obtained free of charge from The Cambridge Crystallographic Data Centre via www.ccdc.cam.ac.uk/data_request/cif.

Computational Details: All the calculations were performed for crystallographic geometries using the Turbomole 6.3[9] program package. B3LYP[8] hybrid functional and Ahlrichs TZV[8] basis sets were used throughout the entire analysis. A Mulliken population analysis[15] was used to confirm that the SCF procedure converged to a proper electronic state.

Supporting Information (see footnote on the first page of this article): Molecular structures of complexes **2**–**6** (Figures S1–S4), packing diagrams of **1**, **3**, **4** and **6** (Figures S5–S9) and IR spectra of all complexes as well as H_4L1 and H_4L2 are reported.

Acknowledgments

We are grateful to the Inorganic Materials Chemistry Graduate Program (EMTKO) for financing the project and to Elina Hautakangas for performing the elemental analysis.

[1] O. Wichmann, R. Sillanpää, A. Lehtonen, *Coord. Chem. Rev.* **2012**, *256*, 371–392.
[2] a) C. A. Reed, R. D. Orosz, *Spin Coupling Concepts in Bioinorganic Chemistry*, in: *Research Frontiers in Magnetochemistry* (Ed.: C. J. O'Connor), World Scientific, Singapore, **1993**, p. 351; b) O. Kahn, *Molecular Magnetism*, Wiley-VCH, Weinheim, Germany, **1993**; c) S. Anbu, M. Kandaswamy, *Polyhedron* **2011**, *30*, 123–131.
[3] D. Venegas-Yazigi, D. Aravena, E. Spodine, E. Ruiz, S. Alvarez, *Coord. Chem. Rev.* **2010**, *254*, 2086–2095.
[4] O. Wichmann, H. Sopo, E. Colacio, A. J. Mota, R. Sillanpää, *Eur. J. Inorg. Chem.* **2009**, 4877–4886.
[5] A. Riisiö, O. Wichmann, R. Sillanpää, *Lett. Org. Chem.* **2010**, *7*, 298–305.
[6] a) R. Chakrabarty, P. S. Mukherjee, P. J. Stang, *Chem. Rev.* **2011**, *111*, 6810–6918; b) P. Thanasekarana, R.-T. Liaoa, Y.-H. Liua, T. Rajendrana, S. Rajagopalb, K.-L. Lua, *Coord. Chem. Rev.* **2005**, *249*, 1085–1110; c) C. R. Kim, J. Ahn, T. H. Noh, O.-S. Jung, *Polyhedron* **2010**, *29*, 823–826.
[7] C. Pariya, F. R. Froczek, A. W. Maverick, *Inorg. Chem.* **2011**, *50*, 2748–2753.
[8] a) A. D. Becke, *Phys. Rev. A* **1988**, *38*, 3098–3100; b) C. Lee, W. Yang, R. G. Parr, *Phys. Rev. B* **1988**, *37*, 785–789; c) A. D. Becke, *J. Chem. Phys.* **1993**, *98*, 5648–5652; d) A. Schäfer, C. Huber, R. Ahlrichs, *J. Chem. Phys.* **1994**, *100*, 5829–5835.
[9] *TURBOMOLE*, v. 6.3 (2011), a development of the University of Karlsruhe and Forschungszentrum Karlsruhe GmbH, **1989–2007**, TURBOMOLE GmbH (since **2007**); available from http://www.turbomole.com.
[10] E. Safaei, M. Rasouli, T. Weyhermüller, E. Bill, *Inorg. Chim. Acta* **2011**, *375*, 158–165.
[11] A. Altomare, M. C. Burla, M. Camalli, G. L. Cascarano, C. Giacovazzo, A. Guagliardi, A. G. G. Moliterni, G. Polidori, R. Spagna, *J. Appl. Crystallogr.* **1999**, *32*, 115–119.
[12] G. M. Sheldrick, *Acta Crystallogr., Sect. A* **2008**, *64*, 112–122.
[13] L. J. Farrugia, *J. Appl. Crystallogr.* **1999**, *32*, 837–838.
[14] Mercury: for visualization and analysis of crystal structures, see: C. F. Macrae, P. R. Edgington, P. McCabe, E. Pidcock, G. P. Shields, R. Taylor, M. Towler, J. van de Streek, *J. Appl. Crystallogr.* **2006**, *39*, 453–457.
[15] R. S. Mulliken, *J. Chem. Phys.* **1955**, *23*, 1831–1840.

Received: October 12, 2011
Published Online: January 27, 2012

DOI: 10.1002/ejic.201200024

Activation of Gas-Phase Uranyl Diacetone Alcohol Coordination Complexes by Spectator Ligand Addition

Daniel Rios[a] and John K. Gibson*[a]

Keywords: Actinides / Uranium / Gas-phase chemistry

Gas-phase addition of a basic ligand to dipositive uranyl coordination complexes comprising diacetone alcohol (DAA) results in water-elimination, which indicates aldol dehydration of DAA to produce mesityl oxide. A novel attribute of the observed gas-phase chemistry is that a ligand exothermically associates to a coordination complex to provide the excitation required to induce chemistry in other ligands, with the added "spectator ligand" remaining intact in the product. Dehydration of DAA was observed for addition of tetrahydrofuran, acetone, and 2-propanol to uranyl complexes $[UO_2(DAA)_2]^{2+}$ and $[UO_2(DAA)(acetone)_2]^{2+}$. In contrast, $[UO_2(DAA)_2(acetone)]^{2+}$ did not exhibit ligand-addition chemistry, which is attributed to a high degree of coordinative saturation at the uranium metal center.

Introduction

Gas-phase complexes comprising a neutral or cationic metal center M coordinated by Lewis base ligands L, i.e., $ML_n^{0/x+}$, can serve as molecular scale chemical reactors in which stimulation to produce an $\{ML_n^{0/x+}\}^*$ excited intermediate can lead to ligand decomposition. We report a new means for inducing such gas-phase coordination chemistry at room temperature: exothermic addition of a Lewis base ligand to cationic coordination complexes, a process which may be referred to as "activation by *spectator* ligand addition," abbreviated here as ASLA, which contrasts with conventional metal-ion-mediated ligand chemistry, or "activation by ligand addition" (ALA), as discussed below.

There is an extensive body of previous studies of ligand chemistry induced by excitation of coordination complexes. Examples of ligand chemistry induced by photo-excitation of gas-phase metal coordination complexes include decomposition of acetone in $\{Ag[CH_3C(O)CH_3]\}^+$,[1] dehydration of ethanol in $\{Fe[CH_3CH_2(OH)]\}^+$,[2] C–H bond cleavage in $[Mg(NH_2CH_3)]^+$,[3] and O-atom loss from β-diketonate complexed to Gd.[4]

The archetypal aldol dehydration of diacetone alcohol [DAA = $CH_3C(O)CH_2C(OH)(CH_3)_2$] to mesityl oxide [MOX = $CH_3C(O)CH{=}C(CH_3)_2$] proceeds according to Equation (1) in acidic or basic solutions,[5] as well as at catalytic surfaces.[6]

DAA dehydration according to Equation (1) has also been induced by collisional excitation of isolated gas-phase complexes in which DAA ligands are coordinated to dipositive metal ions, M^{2+} = Ba^{2+}, Fe^{2+}, Cu^{2+}, etc., as shown in Equation (2).[7]

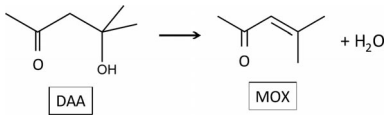

(1)

$$[M(DAA)_2]^{2+} \xrightarrow{\text{collisional excitation}} \{[M(DAA)_2]^{2+}\}^* \longrightarrow [M(MOX)(DAA)]^{2+} + H_2O \quad (2)$$

In Equation (2), thermal excitation of the reactant complex is achieved by kinetic excitation in an ion trap and resulting energetic collisions with the inert helium bath gas, which process is generally referred to as collision induced dissociation (CID). An alternative approach identified here for inducing this particular ligand chemistry in low-energy gas-phase complexes, which have been thermalized to ca. 300 K by collisional cooling in an ion trap, is by thermal excitation resulting from exothermic addition of another Lewis base ligand to the complex, which we refer to as "activation by *spectator* ligand addition," abbreviated as ASLA.

The novel attribute of ASLA is that the incoming base ligand is not directly involved in the induced ligand chemistry but rather acts as a spectator ligand. This is in contrast to the plethora of reported reactions of bare and ligated metal ions with neutral ligands,[8–14] such as the particularly significant and classic early ion-molecule reaction given by Equation (3).[15]

$$Fe^+ + C_4H_{10} \rightarrow FeC_3H_6^+ + CH_4 \quad (3)$$

Examples of reactions of ligated metal ions include those shown in Equations (4) and (5).[16]

$$FeC_5H_6^+ + C_2H_2 \rightarrow FeC_7H_7^+ + H \quad (4)$$

$$FeC_5H_6^+ + C_2H_2 \rightarrow FeC_7H_8^+ \quad (5)$$

[a] Chemical Sciences Division, Lawrence Berkeley National Laboratory,
Berkeley, CA 94720, U.S.A
E-mail: jkgibson@lbl.gov

In Equation (4) the ionic product has a Fe(tropylium)$^+$ structure; in Equation 5 the addition product has a Fe(norbornadiene)$^+$ structure.

As in the present work H_2O is eliminated from an alcohol by ASLA, ion-molecule reactions such as that given by Equation (6) are especially pertinent; in this early example of this type of chemistry, the Li^+ ion activates *tert*-butyl alcohol to produce H_2O and a Li^+-alkene complex.[17,18]

$$Li^+ + (CH_3)_3COH \rightarrow Li(C_4H_8)^+ + H_2O \quad (6)$$

There are many other reports of such activation of alcohols by metal ions, with elimination of water.[9] Classic ion-molecule reactions such as given by Equation (3), Equation (4), Equation (5), and Equation (6) correspond to "activation by ligand addition" (ALA), in which chemical modification of a ligand is induced by its association with a bare or ligated metal ion; in the case of Equation (6), the ligand $(CH_3)_3COH$ is activated by its addition to the Li^+ ion. For each of these reactions, the reactant ligand molecule is chemically modified in the course of the reaction. The distinguishing feature of "activation by *spectator* ligand addition" (ASLA) reported here is that the added ligand is indeed a "spectator"; it is not involved in the observed chemistry, and it remains intact and coordinated to the metal center in the product complex.

There are also many examples of ligand addition to metal complexes to produce condensation products, without modification to any of the ligands, such as in Equations (7) (Ln = lanthanide; n = 1–6)[19] and (8).[20]

$$Ln^+ + nNH_3 \rightarrow Ln(NH_3)_n^+ \quad (7)$$

$$Fe(tropylium)^+ + acetone \rightarrow Fe(tropylium)(acetone)^+ \quad (8)$$

The concept of "activation by *spectator* ligand addition" (ASLA) is generically represented by Equation (9), where $M(L)_n^{x+}$ is a coordination complex with one or more ligands L, ligand L′ is added to the complex in the gas phase, and (L–R) in the product ion is a ligand L from which neutral R has been eliminated.

$$M(L)_n^{x+} + L' \rightarrow M(L)_{n-1}(L\text{–}R)(L') + R \quad (9)$$

In Equation (9) the added ligand L′ is a "spectator" ligand in that it is not involved in the observed chemistry, but rather remains intact and coordinated to the metal center in the product complex. The chemistry exhibited in ASLA is distinct from both classic ion-molecule reactions such as in Equations 3–6, and also from simple adduct formation such as in Equations 7 and 8. We here report ASLA for the particular case of addition of Lewis base ligands to dipositive uranyl diacetone alcohol complexes.

Results

Dehydration of DAA ligands coordinated to the dipositive uranyl ion, UO_2^{2+}, is stimulated by addition of another base ligand, as represented by Equation (10) and Equation (11), where d^{11}DAA is $CD_3C(O)CD_2C(OH)C(CD_3)_2$, d^{10}MOX is $CD_3C(O)CD{=}C(CD_3)_2$, and L = tetrahydrofuran (THF), acetone (ACO), or 2-propanol (*i*PrOH).

The UO_2^{2+} ion is well suited to such chemistry as it can be conveniently prepared and isolated in the gas phase, and presents a highly acidic metal center to which Lewis base ligands can be anchored.[21] Using techniques described elsewhere,[22] the following gas-phase complex ions were produced by ESI of uranyl perchlorate in solutions of 0.2%DAA/d^6ACO or 0.2%d^{12}DAA/ACO: $[UO_2(DAA)_2]^{2+}$, $[UO_2(d^{11}DAA)(ACO)_2]^{2+}$, $[UO_2(DAA)_2(d^6ACO)]^{2+}$, and $[UO_2(d^{11}DAA)_3]^{2+}$. Normal DAA is isobaric with two ACO molecules; the use of d^6ACO and d^{11}DAA enabled identification of ligands and their reaction pathways. Facile exchange of the alcoholic D-atom in d^{12}DAA with gaseous H_2O during ion transport from the ESI source to the ion

$$[UO_2(DAA)_2]^{2+} + L \xrightarrow{ASLA} \{[UO_2(DAA)_2(L)]^{2+}\}^* \longrightarrow [UO_2(MOX)(DAA)(L)]^{2+} + H_2O \quad (10)$$

$$[UO_2(d^{11}DAA)(ACO)_2]^{2+} + L \xrightarrow{ASLA} \{[UO_2(d^{11}DAA)(ACO)_2(L)]^{2+}\}^* \rightarrow [UO_2(d^{10}MOX)(ACO)_2(L)]^{2+} + HDO \quad (11)$$

Table 1. Results for addition of gaseous bases L to uranyl coordination complexes at ca. 300 K.

Ligands coordinated to UO_2^{2+} in the reactant ion	Maximum oxo-coordination[a]	Observed reactions and ligands coordinated to UO_2^{2+} after addition of base gas ligand L[b]
{2 DAA}	4	ASLA H_2O elimination: {MOX + DAA + L} (> 90%) ligand addition: {2DAA + L} (< 10%)
{d^{11}DAA + 2 ACO}	4	ASLA HDO elimination: {d^{10}MOX + 2ACO + L} (10–20%) ligand addition: {d^{11}DAA + 2ACO + L} (80–90%)
{2 DAA + d^6ACO}	5	ligand exchange: {2 DAA + L}[c]
{3 d^{11}DAA}	6	no reaction[d]

[a] Total number of potential coordinating oxygen sites on the ligands: one ketone oxygen for each ACO; one ketone oxygen and one alcohol oxygen for each DAA. [b] L = THF, ACO or *i*PrOH. Approximate branching ratios for ASLA dehydration and unreactive ligand addition are given in parentheses. [c] No reaction observed to less than about 1% product abundance for *i*PrOH, the weakest base. [d] Studied for L = THF, the strongest base; no reaction observed to less than about 1% product abundance.

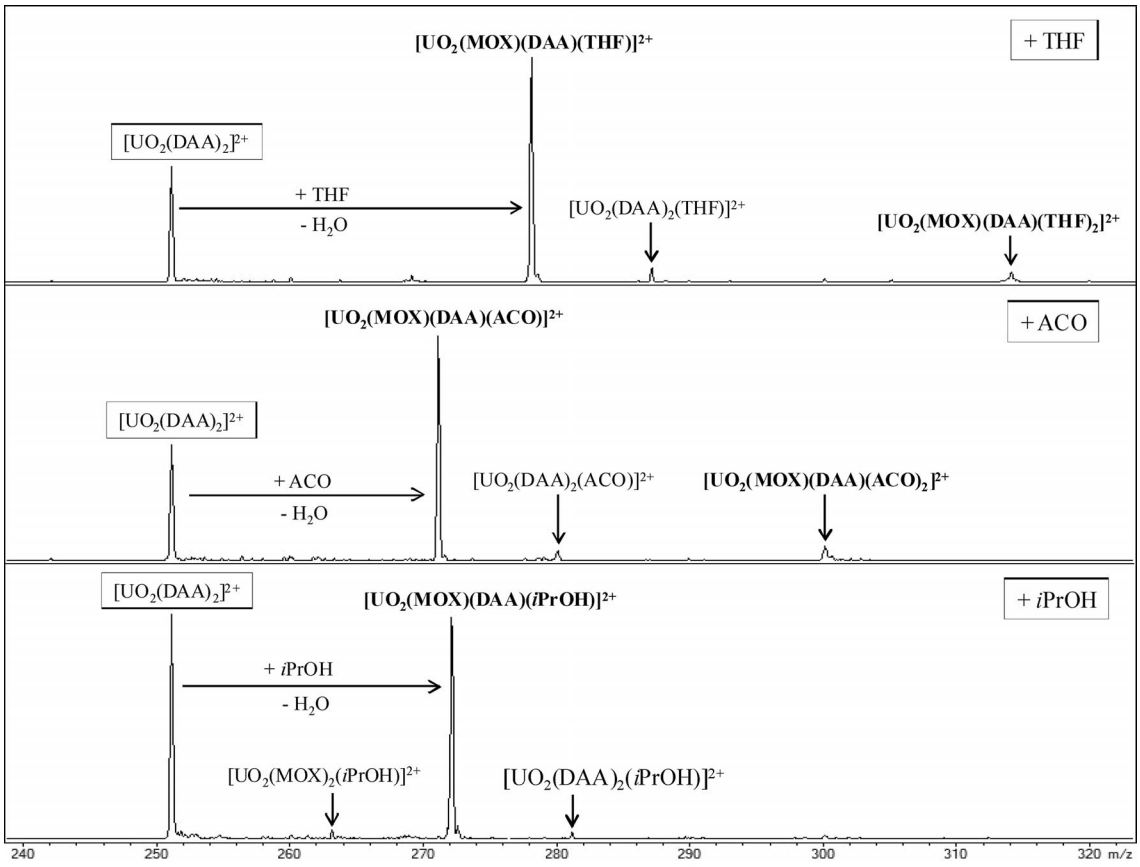

Figure 1. Mass spectra of isolated gas-phase complex $[UO_2(DAA)_2]^{2+}$ acquired after reaction with THF(g), ACO(g) and *i*PrOH(g) for 300 ms. To ensure its composition, the $[UO_2(DAA)_2]^{2+}$ reactant complex was prepared by elimination of d^6ACO from $[UO_2(DAA)_2(d^6ACO)]^{2+}$ by CID in the ion trap. The dominant reaction is addition of the gas base ligand concomitant with elimination of H_2O to produce MOX (products indicated in bold).

trap accounts for conversion to d^{11}DAA, which predictably dehydrates via HDO loss to give d^{10}MOX (Equation 11). After isolation in the ion trap at ca. 300 K[23] with a He buffer gas pressure of ca. 10^{-4} Torr, a selected complex ion composition was allowed to react with gaseous THF, ACO, or *i*PrOH (reagent pressure estimated as ca. 10^{-6} Torr) for a controlled time in the range of 300 ms to 1000 ms under thermal conditions; after the reaction period, a product mass spectrum was acquired. Identified products correspond to ligand-addition; ligand-exchange; and elimination of H_2O or HDO, indicating aldol dehydration of DAA to MOX, or d^{11}DAA to d^{10}MOX; see Equation (1).

The results are summarized in Table 1. Mass spectra shown in Figure 1 and Figure 2 reveal that the reactions given by Equations (10) and (12) proceed for L = THF, ACO and *i*PrOH. In Figure 3 are shown the mass spectra for exposure of $[UO_2(DAA)_2(d^6ACO)]^{2+}$ to the three gas-phase ligands: ligand-exchange occurs for L = THF and ACO according to Equation (12), whereas no exchange occurs with *i*PrOH.

$$[UO_2(DAA)_2(ACO)]^{2+} + L \xrightarrow{\text{ligand exchange}} [UO_2(DAA)_2(L)]^{2+} + ACO \quad (12)$$

The $[UO_2(d^{11}DAA)_3]^{2+}$ complex was exposed to THF and no reaction or ligand-exchange was observed. To confirm that reactions with background gases in the ion trap were insignificant, $[UO_2(DAA)_2]^{2+}$ and $[UO_2(DAA)(d^6ACO)_2]^{2+}$ were isolated for 1 s, the longest reaction time employed; only minuscule (less than about 2%) H_2O elimination from $[UO_2(DAA)_2]^{2+}$ was observed.

Discussion

As is apparent in Table 1, the tendency for ASLA dehydration of DAA to MOX decreases as the coordination by ligand oxo-groups in the parent reactant ion increases. This suggests that the propensity for DAA dehydration diminishes as the coordination of the metal center increases and the binding energy of the incoming ligand decreases. Decreasing ligand binding energy with increasing coordination has been reported for ACO ligands with UO_2^{2+}; the binding energy of ACO to UO_2^{2+} – i.e., ΔE for $[UO_2(ACO)_n]^{2+} \rightarrow [UO_2(ACO)_{n-1}]^{2+} + ACO$ – progressively decreases as n increases, from $\Delta E \approx 500$ kJ mol^{-1} for $n = 1$, to $\Delta E < 100$ kJ mol^{-1} for $n = 5$.[24,25]

The ligand-exchange results suggest that it is the proton affinity (PA), an indicator of basicity, which determines the

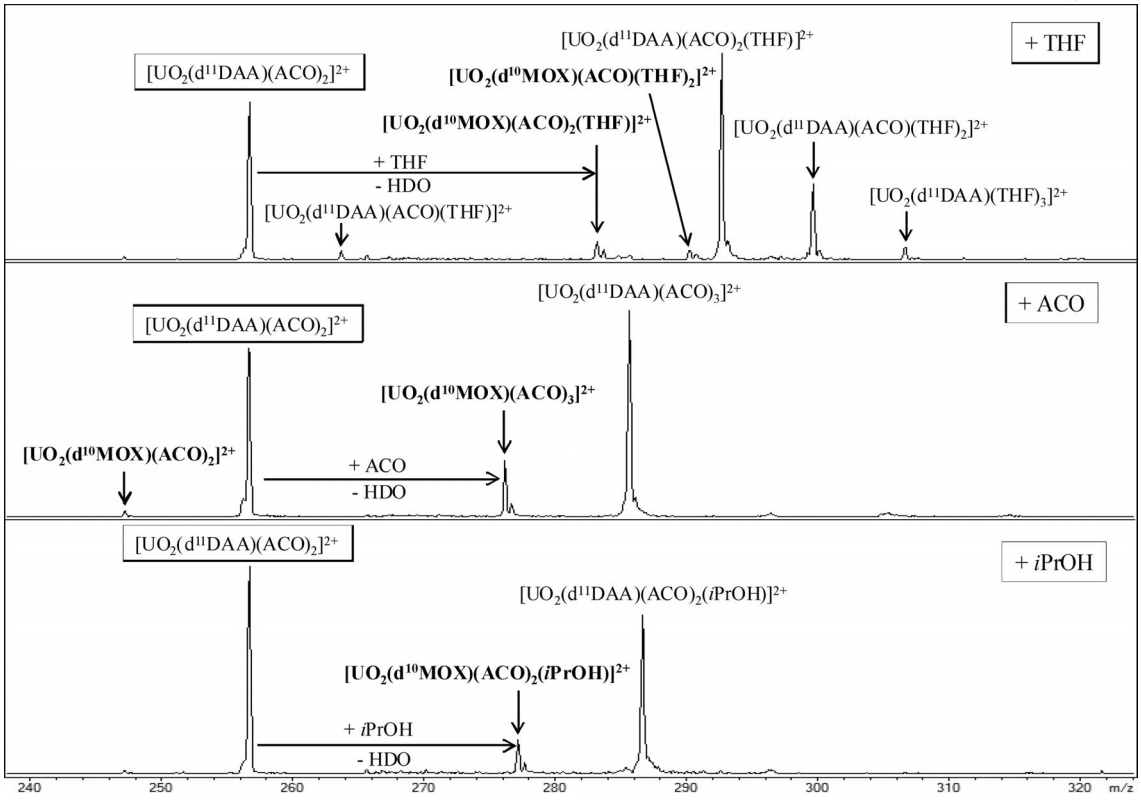

Figure 2. Mass spectra of isolated gas-phase complex $[UO_2(d^{11}DAA)(ACO)_2]^{2+}$ acquired after reaction with THF(g), ACO(g) and *i*PrOH(g) for 500–1000 ms. The dominant reactions are addition of a ligand; minor reactions are addition of a ligand concomitant with elimination of HDO to produce d^{10}MOX (products indicated in bold). The d^{11}DAA ligands were produced by ESI of a 0.2% d^{12}DAA/ACO solution; gas-phase exchange of the alcoholic deuteron (OD) with H_2O in the ion transport section of the instrument results in exclusively d^{11}DAA. The water eliminated from DAA derives from the association of the OH group with a methylene hydrogen; the composition of d^{11}DAA as $CD_3C(O)CD_2C(OH)C(CD_3)_3$ is indicated by the appearance of exclusively HDO loss to give d^{10}MOX, $CD_3C(O)CD = C(CD_3)_2$. In the top spectrum, replacement of ACO by THF is apparent.

efficacy of binding of an electron-donor ligand to a cation. The requirement for ligand-exchange (or any reaction) under low-energy conditions such as those employed in these experiments is that it be exothermic or thermoneutral: i.e., $\Delta H_r \leq 0$. The PAs (in kJ mol^{-1}) of ligands used in this study are as follows: MOX (879) > DAA (823) ≈ THF (822) > ACO (812) > *i*PrOH (793) >> H_2O (691),[26] where the uncertainties in some of these values may be up to 8 kJ mol^{-1}.[27] Both THF and ACO replace d^6ACO, while the weaker base *i*PrOH does not (Figure 3). The replacement of d^6ACO by ACO demonstrates essentially thermoneutral exchange. These ligand-exchange results – i.e., that a ligand with a higher PA replaces one with a lower PA – substantiate that it is the PA (i.e., basicity) which determines binding energies of the ligands to uranyl. Among other molecular properties which may affect binding of a neutral to a cation are polarizability and dipole moment. However, the ligand exchange results suggest that these parameters are not directly pertinent in binding of ligands to dipositive uranyl. In particular, the polarizability of *i*PrOH (7.6 Å^3) is greater than that of ACO (6.4 Å^3)[28] yet *i*PrOH does not displace ACO; also, the dipole moment of ACO (2.88 D) is greater than that of THF (1.63 D)[28] yet THF does displace ACO. There was no evidence for replacement of either DAA or MOX by the gas bases; as the PAs of DAA and THF are similar, the inability of THF to displace DAA may reflect bidentate coordination of DAA.

Among the six complexes studied, only those with a total of four potential coordinating oxygen atoms on the ligands undergo dehydration of DAA; the complex with five ligand oxygens undergoes only ligand exchange, while that with six is inert (Table 1). Although the actual coordination in the complexes is not known, this correlation suggests that ASLA occurs only for addition of a Lewis base ligand to coordinatively unsaturated complexes; as remarked above, it is such ligand addition which is substantially exothermic, and could thus result in significant excitation and activation of a coordination complex, as represented in Scheme 1 for the case of Equation (10). As the water product is eliminated and the MOX product remains ligated [Equations (10) and (11)], the net change in coordination from the reactant complex to the product complex is replacement of an alcohol ligand in DAA by the added base ligand. The coordinating alcohol ligand in DAA is swapped for an ether oxygen in THF, a ketone oxygen in ACO, or another alcohol oxygen in *i*PrOH.

The striking result of this work is the appearance of ASLA under thermal conditions, as given by Equation (10)

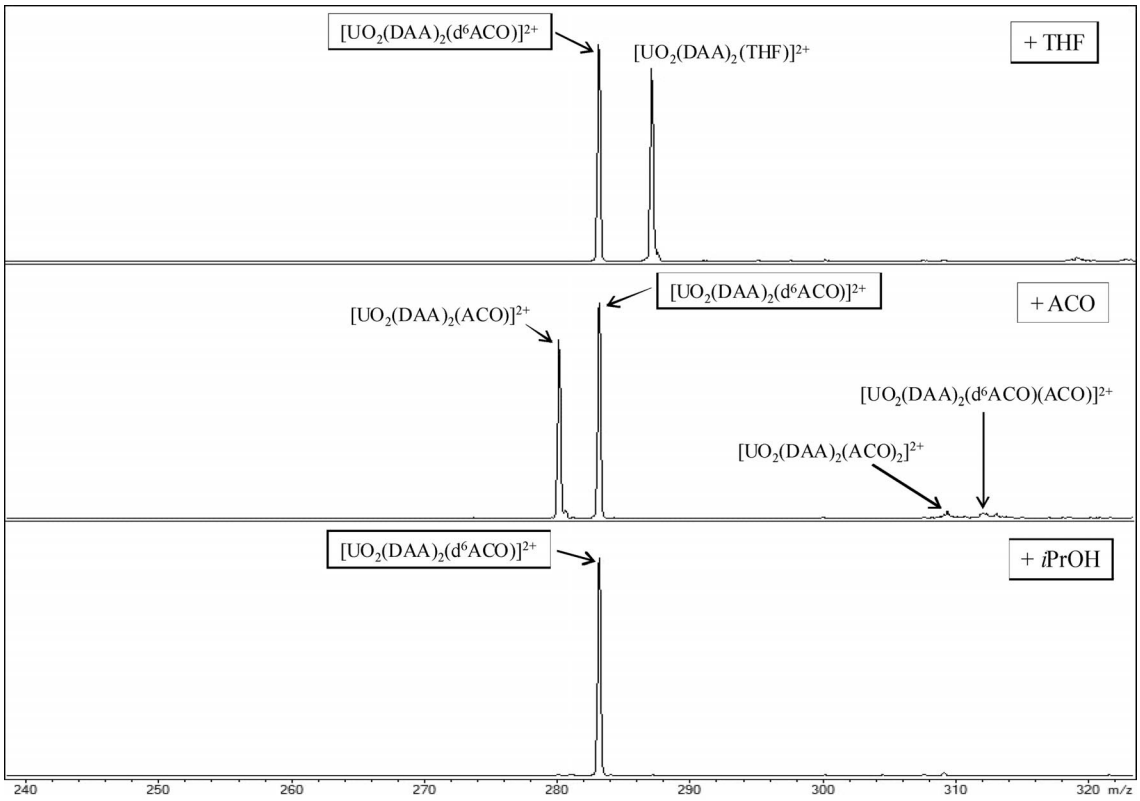

Figure 3. Mass spectra of isolated gas-phase complex $[UO_2(DAA)_2(d^6ACO)]^{2+}$ acquired after reaction with THF, ACO and *i*PrOH for 500 ms. Both THF and ACO displace d^6ACO; *i*PrOH does not.

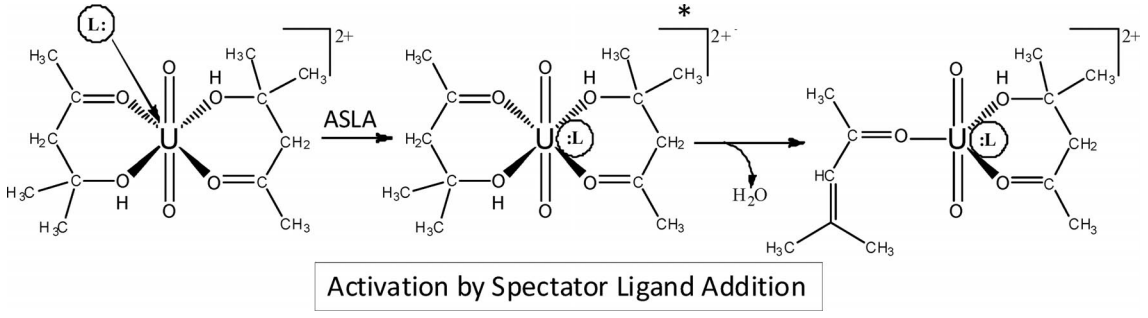

Scheme 1. Representation of gas-phase dehydration of $[UO_2(DAA)_2]^{2+}$ induced by addition of a base ligand L. A DAA ligand in ASLA intermediate $\{[UO_2(DAA)_2(L)]^{2+}\}^*$ undergoes aldol dehydration to produce $[UO_2(MOX)(DAA)(L)]^{2+} + H_2O$.

and Equation (11). As it has been previously shown that collisional excitation of DAA complexed to dipositive metal ions, M^{2+}, induces aldol dehydration,[7] it is not necessarily remarkable that DAA complexed to UO_2^{2+} should behave similarly. However, it is remarkable that aldol dehydration is induced by ASLA as an alternative to conventional gas-phase ion activation by ion/neutral, ion/electron, ion/photon or ion/ion interactions,[29] including the many reported examples of ALA as mentioned above in which the reactant ligand does not merely serve as a source of excitation but is modified in the course of the reaction. In contrast to activation by high-energy ion/neutral collisions, the ion/neutral interactions in ASLA occur under thermal conditions; in ASLA it is the ion-ligand binding energy, not collisional energy, which induces ion excitation. There is a correspondence between ASLA and chemi-ionization, in which exothermic reaction between two low-energy neutrals induces ionization, as in $U + O_2 \rightarrow UO_2^+ + e^-$.[30] The distinctive nature of ASLA is that an exothermic reaction between an ionic coordination complex and a neutral induces chemistry within a coordinating ligand, with the intact added ligand and the decomposed ligand remaining associated to the metal center in the product complex, and with no change in the complex charge state.

We propose that the observed aldol dehydration of DAA complexed to uranyl – Equation (10) and Equation (11) – can be represented by ASLA as shown in Scheme 1 for the case of Equation (10). Addition of a base ligand to dipositive uranyl is exothermic, for example computed as ca. 130 kJ mol^{-1} for addition of ACO to $[UO_2(ACO)_3]^{2+}$, and

as ca. 50 kJ mol^{-1} for addition of ACO to $[UO_2(ACO)_4]^{2+}$.[31] As postulated in Scheme 1, deposition of the ligand association energy to produce an excited $\{[UO_2(DAA)_2(L)]^{2+}\}^*$ intermediate induces aldol dehydration with elimination of a water molecule from the product ion. The base ligand L remains associated with the product complex; as it is not regenerated, it is not behaving as a catalyst but rather as the source of excitation in ASLA. The uranyl ion is crucial as presenting an electrophilic metal center which anchors the reactant and product ligands, and also serves as the binding site for exothermic attachment of the excitation ligand. Whereas aldol dehydration is dominant for $[UO_2(DAA)_2]^{2+}$, it is minor for $[UO_2(DAA)(d^6ACO)_2]^{2+}$. This disparity may reflect lesser electron donation from the ketone and alcohol oxygens of a DAA ligand as compared with the ketone oxygens of two d^6ACO ligands; a result of lesser electron donation to the uranium metal center in $[UO_2(DAA)_2]^{2+}$ would be greater exothermicity for association of the incoming base ligand, and greater excitation of the complex to induce ASLA.

Conclusions

The observation of Lewis base-induced ligand decomposition by ASLA in uranyl/DAA cation complexes represents a new type of activation of coordination complexes, by ion/neutral interactions under thermal conditions with the neutral reactant as a spectator ligand which remains unaltered. As ASLA essentially proceeds by transfer of charge from a Lewis base ligand to a cation metal center, it can be envisioned as a "mild" type of electron capture dissociation.[32] The uranyl/DAA results suggest that ASLA might similarly occur for other special cases of cationic coordination complexes which can strongly bind an incoming base ligand, like THF, and comprise a ligand, like DAA, which easily degrades to a strongly bound product, like MOX.

Experimental Section

General: All organic reagents were commercial products with a purity of 99.9%, except for 99% diacetone alcohol. The isotopic purity of the d^6ACO was reported as 99.97 atom-% D; that of the d^{12}DAA was 98 atom-% D. The organic bases introduced into the ion trap as gases were subjected to freeze–pump–thaw cycles of the source liquid prior to use.

List of Abbreviations

ACO = acetone, $CH_3C(O)CH_3$

d^6ACO = perdeuterated acetone, $CD_3C(O)CD_3$

ALA = activation by ligand addition

ASLA = activation by spectator ligand addition

CID = collision-induced dissociation

DAA = diacetone alcohol, $CH_3C(O)CH_2C(OH)C(CH_3)_3$

d^{12}DAA = perdeuterated diacetone alcohol, $CD_3C(O)CD_2C(OD)C(CD_3)_3$

d^{11}DAA = partially deuterated diacetone alcohol, $CD_3C(O)CD_2C(OH)C(CD_3)_3$

ESI = electrospray ionization

*i*PrOH = 2-propanol, $(CH_3)_2CH(OH)$

MOX = mesityl oxide, $CH_3C(O)CH=C(CH_3)_2$

d^{10}MOX = perdeuterated mesityl oxide, $CD_3C(O)CD=C(CD_3)_2$

PA = proton affinity

THF = tetrahydrofuran

QIT/MS = quadrupole ion trap mass spectrometry.

The uranyl(VI) solutions for electrospray ionization (ESI) were prepared using a stock aqueous acidic solution of $^{238}U^{VI}O_2(ClO_4)_2$. The compositions of the ESI solutions were as follows: 180 μM UO_2^{2+}/0.1% H_2O/0.2% DAA/99.7 d^6ACO; and 180 μM UO_2^{2+}/0.1% H_2O/0.2% d^{12}DAA/99.7% ACO (acetone). All handling of the uranium solutions (> 99%U-238) was performed in a radiological laboratory. ESI and ion-molecule reactions were studied using an Agilent 6340 Quadrupole Ion Trap Mass Spectrometer (QIT/MS) with the ion source located inside of a radiological containment glove box, as described in detail elsewhere.[22,33] The MS^n CID capabilities of the QIT/MS allow isolation of ions with a particular mass-to-charge ratio, *m*/*z*, and subsequent insertion of an ion-molecule reaction time without applying ion excitation. Reactions times of between 300 ms and 1000 ms were employed to obtain suitable product ion abundances; product ions were identified by acquiring a mass spectrum using mass-selective ion ejection from the trap. The effective ion temperature in the trap is estimated as ca. 300 K.[23]

In high resolution mode the QIT/MS has a detection range of 50–2200 *m*/*z* and a resolution of ≈ 0.25 *m*/*z* (full width half maximum). Mass spectra were acquired in the positive ion accumulation and detection mode using the following typical ESI, desolvation, ion transport/focusing, and ion trapping parameters: nebulizer gas pressure, 12 psi; capillary voltage and current, –4500 V, 1.221 nA; end plate voltage offset and current, –500 V, 22.5 nA; dry gas flow rate, 5 l/min; dry gas temperature, 100 °C; capillary exit, 75 V; skimmer, 29.2 V; octopole 1 and 2 DC, 11.46 V and 7.40 V; octopole RF amplitude, 50.0 Vpp; lens 1 and 2, –2.3 V and –77.5 V; trap drive, 49.9. The parameters were somewhat different when conditions were optimized to enhance the abundance of a particular species. The 180 μM uranyl(VI) solution was injected into the ESI capillary at a rate of 60 μL h^{-1} using a syringe pump. Nitrogen gas for nebulization and drying in the ion transfer capillary was supplied from the boil-off of a liquid-nitrogen Dewar flask.

Pressures in the trap were ca. 10^{-4} Torr helium buffer gas and ca. 10^{-6} Torr background water.[34] Gas-phase reagent bases were introduced from a liquid reservoir into the same gas inlet through which the buffer gas was injected into the ion trap; the reagent gas pressure was controlled by a variable leak valve. The reagent gas pressure in the trap was not directly measured and could only be roughly estimated as ca. 10^{-6} Torr, based on the ion gauge response in comparison with that for addition of water vapor to the trap. Knowledge of the reagent pressure is not needed for interpretation of the observed ligand-addition reactions; pressure variations are estimated as up to a factor of two between experiments. As the absolute reagent pressures were not known, it was not feasible to obtain rate constants.

Acknowledgments

This work was supported by the Director, Office of Science, Office of Basic Energy Sciences, Division of Chemical Sciences, Geosci-

ences and Biosciences of the U.S. Department of Energy at LBNL, under contract number DE-AC02-05CH11231.

[1] K. F. Willey, P. Y. Cheng, M. B. Bishop, M. A. Duncan, *J. Am. Chem. Soc.* **1991**, *113*, 4721.
[2] D. A. Kirkwood, A. J. Stace, *J. Am. Chem. Soc.* **1998**, *120*, 12316.
[3] W. Y. Guo, H. C. Liu, S. H. Yang, *J. Chem. Phys.* **2002**, *117*, 6061.
[4] M. T. Berry, F. P. Ow, P. S. May, J. I. Zink, *J. Phys. Chem. A* **2007**, *111*, 4144.
[5] Y. K. Kim, J. D. Hatfield, *J. Chem. Eng. Data* **1985**, *30*, 149.
[6] J. I. DiCosimo, V. K. Diez, C. R. Apesteguia, *Appl. Catal. A* **1996**, *137*, 149.
[7] A. A. Shvartsburg, J. G. Wilkes, *Int. J. Mass Spectrom.* **2003**, *225*, 155.
[8] P. B. Armentrout, *Int. J. Mass Spectrom.* **2000**, *200*, 219.
[9] K. Eller, H. Schwarz, *Chem. Rev.* **1991**, *91*, 1121.
[10] J. Allison, D. P. Ridge, *J. Organomet. Chem.* **1975**, *99*, C11.
[11] A. Bjarnason, D. P. Ridge, *Organometallics* **1998**, *17*, 1889.
[12] M. T. Bowers, A. G. Marshall, F. W. McLafferty, *J. Phys. Chem.* **1996**, *100*, 12897.
[13] A. Shayesteh, V. V. Lavrov, G. K. Koyanagi, D. K. Bohme, *J. Phys. Chem. A* **2009**, *113*, 5602.
[14] D. K. Bohme, H. Schwarz, *Angew. Chem.* **2005**, *117*, 2388; *Angew. Chem. Int. Ed.* **2005**, *44*, 2336.
[15] J. Allison, R. B. Freas, D. P. Ridge, *J. Am. Chem. Soc.* **1979**, *101*, 1332.
[16] Q. Chen, C. Sioma, S. Z. Kan, B. S. Freiser, *Int. J. Mass Spectrom.* **1998**, *180*, 231.
[17] R. D. Wieting, R. H. Staley, J. L. Beauchamp, *J. Am. Chem. Soc.* **1975**, *97*, 924.
[18] W. R. Creasy, J. M. Farrar, *J. Phys. Chem.* **1985**, *89*, 3952.
[19] G. K. Koyanagi, P. Cheng, D. K. Bohme, *J. Phys. Chem. A* **2010**, *114*, 241.
[20] Y. C. Xu, E. Garcia, B. S. Freiser, C. W. Bauschlicher, *Int. J. Mass Spectrometry Ion Processes* **1996**, *157*, 249.
[21] G. R. Choppin, L. F. Rao, *Radiochim. Acta* **1984**, *37*, 143.
[22] D. Rios, P. X. Rutkowski, M. J. Van Stipdonk, J. K. Gibson, *Inorg. Chem.* **2011**, *50*, 4781.
[23] S. Gronert, *J. Am. Soc. Mass Spectrom.* **1998**, *9*, 845.
[24] G. Schoendorff, W. A. de Jong, M. J. Van Stipdonk, J. K. Gibson, D. Rios, M. S. Gordon, T. L. Windus, *Inorg. Chem.* **2011**, *50*, 8490.
[25] G. Schoendorff, W. A. de Jong, M. J. Van Stipdonk, J. K. Gibson, D. Rios, M. S. Gordon, T. L. Windus, *Inorg. Chem.* **2011**, *50*, 11846.
[26] E. P. Hunter, S. G. Lias, in: *NIST Chemistry WebBook, NIST Standard Reference Database Number 69*, vol. 2011 (Eds.: P. J. Linstrom, W. G. Mallard), NIST, Gaithersburg, MD, **2011**.
[27] E. P. L. Hunter, S. G. Lias, *J. Phys. Chem. Ref. Data* **1998**, *27*, 413.
[28] D. R. Lide, *Handbook of Chemistry and Physics*, 71 ed., CRC Press, Boca Raton, **1990**.
[29] S. A. McLuckey, M. Mentinova, *J. Am. Soc. Mass Spectrom.* **2011**, *22*, 3.
[30] W. L. Fite, P. Irving, *J. Chem. Phys.* **1972**, *56*, 4227.
[31] G. Schoendorff, T. L. Windus, W. A. de Jong, *J. Phys. Chem. A* **2009**, *113*, 12525.
[32] K. Breuker, F. W. McLafferty, *Angew. Chem.* **2003**, *115*, 5048; *Angew. Chem. Int. Ed.* **2003**, *42*, 4900.
[33] D. Rios, P. X. Rutkowski, D. K. Shuh, H. T. Bray, J. K. Gibson, M. J. V. Stipdonk, *J. Mass Spectrometry* **2011**, *46*, 1247.
[34] P. X. Rutkowski, M. C. Michelini, T. H. Bray, N. Russo, J. Marcalo, J. K. Gibson, *Theor. Chem. Acc.* **2011**, *129*, 575.

Received: January 9, 2012
Published Online: February 2, 2012

DOI: 10.1002/ejic.201101119

Synthesis and Structure of Silver Amino-Arenesulfonates

Madleen Busse,[a] Philip C. Andrews,*[a] and Peter C. Junk[a]

Keywords: Silver / Arenesulfonates / Zwitterions / Coordination polymers

Treatment of a variety of zwitterionic amino-arenesulfonic acids with silver oxide has resulted in the synthesis of seven new Ag^I amino-arenesulfonates $[Ag(O_3SR)]_\infty$ [R = *o*-aminobenzyl (*o*AB) (**1**), *m*-aminobenzyl (*m*AB) (**2**), 6-amino-3-methoxybenzyl (6A3MB) (**3**), *o*-aminonaphthyl (*o*AN) (**4**), 5-aminonaphthyl (5AN) (**5**), 4-amino-3-hydroxynaphthyl (4A3HN) (**6**) and 5-isoquinolinyl (I) (**7**)]. This has allowed an exploration of their coordination chemistry, whereby we examine the impact of structural diversity in the anions: the position of the amino functionality on the arene moiety, inclusion of the N within a heterocycle and an increase in ring size from phenyl to naphthyl. The solid-state structures of **1**, **2** and two forms of **4**, one with a coordinated water molecule, have been determined by X-ray diffraction and are all polymeric. Analytical data is provided for two of the structurally known complexes: known silver *p*-aminobenzenesulfonate **8** $[Ag(O_3SBA\textit{p})]_\infty$ and Ag^I 2-pyridinesulfonate $[Ag(O_3SP)]_\infty$ (**9**). The composition of all nine complexes has been confirmed through NMR spectroscopy, MS-ES$^+$, FTIR and elemental analysis.

Introduction

Interest in the medical and biological applications of silver metal and Ag^I complexes has grown substantially over the past decade.[1] Today they are present as antimicrobial agents in materials as diverse as topical creams for the treatment of burns (e.g., Ag^I sulfadiazine) and in immobilized polymer–silver membranes, which are now employed in a wide range of infection-resistant biomedical devices, coated medical instruments, wound dressings and in food-processing equipment.[1]

The incorporation of silver nanoparticles into polymeric membranes that contain sulfonated surfaces [e.g., sulfonated polyethersulfone (SPES)],[1c] polyvinyl sulfonate (PVS),[1h] styrene sulfonate polymers[1g] and even naturally available polysaccharides[1f] has proven to provide bactericidal properties against a range of different bacteria, including *Staphylococcus aureus*,[1c] *Staphylococcus albus*,[1c] *Staphylococcus epidermidis*,[1h] *Escherichia coli*[1c] and *Pseudomonas aeruginosa*.[1d]

Beyond polymers, Ag^I sulfonate complexes themselves have demonstrated potential application in selective and reversible guest inclusion,[2] especially when the metal–organic complexes incorporate neutral N-containing secondary ligands,[2g,2h,2k,3] whereas arenesulfonates have found commercial application in the cosmetics industry as hair dying agents[4] and in the laser and thermal printing industry.[5]

Surprising is the fact that the majority of these applications have been developed only recently. Until around the beginning of this century, the coordination chemistry of sulfonates was not well investigated or understood, the change being marked by a series of papers by Côté and Shimizu et al.,[2a,2b,2d–2f,6] Cai et al.[7] and others,[8] by investigating metal sulfonates as a family of layered solids. The former lack of activity most likely derives from our understanding that the monoanionic sulfonate group is generally a weaker coordinating ligand than other acidato anions such as carbonates or phosphonates,[6e–6g,9] often rendering the sulfonate ligand incapable of forming functional extended solids. However, ligands that allow flexibility in their binding modes to metal centres have become more sought after, and the number of coordination solids that incorporate them in a variety of bonding modes and motifs has continued to increase over the past few years.[7a,10]

Systematic studies of Ag^I arenesulfonates have previously been undertaken by Côté and Shimizu et al.,[2b] and more recently by Zhu and Gao et al.[11] The former study charts the influence of an increase in the size of the ring system on observed structural outcomes, whereas in the latter, *o*-hydroxy arenesulfonic acids, which contain one or more $-SO_3H$ groups positioned at various points on a single phenyl ring, are used to provide a diverse range of supramolecular frameworks.

Our current investigations represent the first systematic study of the coordination chemistry of Ag^I amino-arenesulfonates. In choosing the range of amino-arenesulfonic acids, four key structural factors were considered important: (i) the position of the amino group on the arene moiety would be varied from *ortho* to *meta* to *para*; (ii) heterocyclic amines would be studied to increase structural diver-

[a] School of Chemistry, Monash University,
Melbourne, 3800 VIC, Australia
Fax: +61-3-9905-4597
E-mail: phil.andrews@monash.edu

sity and to act as comparators with the exocyclic amines; (iii) the acids would be monoprotic zwitterions; and (iv) ring size would be varied from phenyl to naphthyl.

From this study we now report the synthesis and characterization of seven new Ag^I amino-arenesulfonates $[Ag(O_3SR)]_\infty$ [R = *o*-aminobenzyl (*o*AB) (**1**), *m*-aminobenzyl (*m*AB) (**2**), 6-amino-3-methoxybenzyl (6A3MB) (**3**), *o*-aminonaphthyl (*o*AN) (**4**), 5-aminonaphthyl (5AN) (**5**), 4-amino-3-hydroxynaphthyl (4A3HN) (**6**) and 5-isoquinolinyl (I) (**7**)]. The acids are shown in Scheme 1.

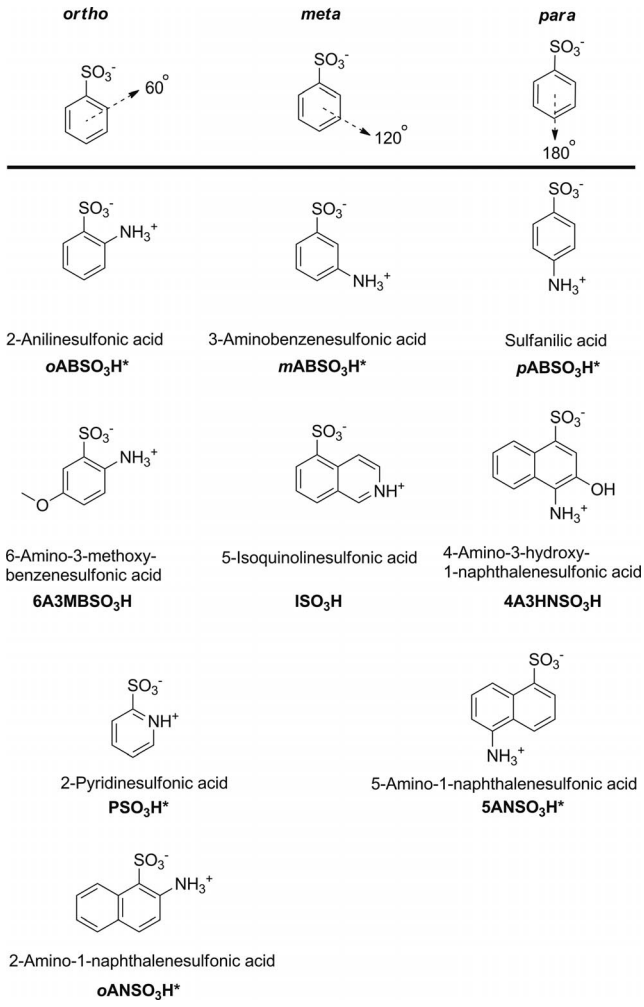

Scheme 1. Structures of the aminosulfonic acid ligands applied in the synthesis of the Ag^I amino-arenesulfonates. X-ray structures were obtained for those structures labelled with asterisks (*).

Possible coordination modes of the *o*-aminobenzenesulfonate ligand involving the amino functionality are shown in Scheme 2 (only one type or a combination of these displayed). The solid-state structures of complexes **1**, **2**, **4a** and **4b** have been determined by single-crystal X-ray diffraction, and we provide further analytical data for the known silver *p*-aminobenzenesulfonate[12] $[Ag(O_3SBA\textit{p})]_\infty$ **8** and Ag^I 2-pyridinesulfonate[2i] $[Ag(O_3SP)]_\infty$ **9**, since only structural information has been reported thus far.

Results and Discussion

Synthesis

Target compounds **1**–**9** were all synthesized from the appropriate sulfonic acid and freshly prepared Ag_2O[13] in water at 90 °C by using the stoichiometric ratio of 2:1 (Scheme 3). Crystalline material suitable for single-crystal X-ray diffraction studies was obtained through very slow cooling of the homogeneous solution in a water bath to room temperature for complexes **1**, **2** and **4a**, and for **4b** through recrystallization in a small amount of ethanol. All the Ag^I complexes **1**–**9** were characterized through ^1H and ^{13}C NMR spectroscopy, FTIR and MS-ES$^+$. Elemental analysis and melting-point determination were also performed.

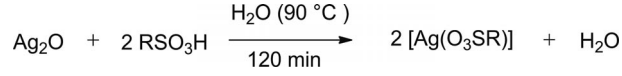

Scheme 3. General reaction scheme of the synthesis of $[Ag(O_3SR)]_\infty$ [R = *o*-aminobenzyl (*o*AB) (**1**), *m*-aminobenzyl (*m*AB) (**2**), 6-amino-3-methoxybenzyl (6A3MB) (**3**), *o*-aminonaphthyl (*o*AN) (**4**), 5-aminonaphthyl (5AN) (**5**), 4-amino-3-hydroxynaphthyl (4A3HN) (**6**), 5-isoquinolinyl (I) (**7**), *p*-aminobenzyl (*p*AB) (**8**) and 2-pyridyl (P) (**9**)].

X-ray Crystallographic Studies

$[Ag(O_3SBA_o)]_\infty$ (1)

Compound **1** is represented by a 1D chain growing along the crystallographic *c* axis (Figure 1). A summary of bond lengths and angles is given in Table 1. In each chain only one type of Ag^I centre is present and has a pseudo-tetrahedral coordination geometry composed of two sulfonate oxygen atoms, the nitrogen atom and two aromatic carbon

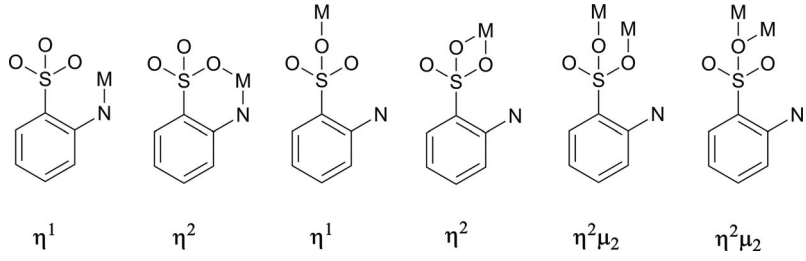

Scheme 2. Possible coordination modes shown for the *o*-aminobenzenesulfonate ligand in the solid-state involving the amino group in bonding to the metal ion.

atoms. This differs from the previously described 2-pyridinesulfonate analogue **9**,[2i] in which the polymeric structure forms a 2D network with one type of silver centre in an asymmetrical trigonal-bipyramidal coordination geometry. The trigonal basis of the trigonal bipyramid is composed of two sulfonate oxygen atoms in a μ_4 [μ_2O(1) and μ_2O(3)] bridging mode; the apices are occupied by one sulfonate oxygen atom and the pyridyl nitrogen atom. Therefore, the 2-pyridinesulfonate ligand stabilizes the molecular scaffold by linking four metal centres.[2i] Another key difference is the η^2 interaction of the Ph ring with the Ag centre, which is apparent in **1** but not in **9**.

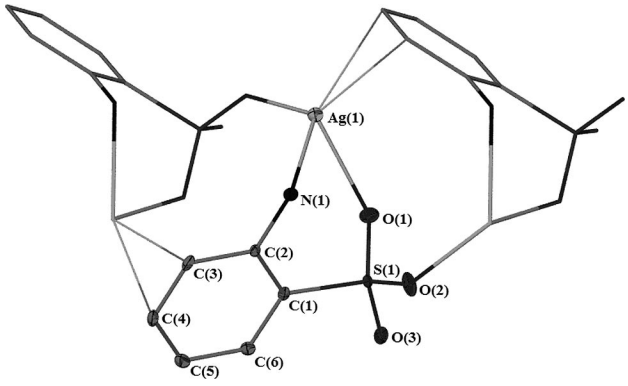

Figure 1. Structure of $[Ag(O_3SBA\textit{o})]_\infty$ (**1**). View of an individual 1D polymeric chain growing along the crystallographic *c* axis showing the connectivity modes observed of the amino-arenesulfonate ligand to the Ag^I centre. Hydrogen atoms are omitted for clarity. Ellipsoids are shown at 50% probability.

In contrast to **9**, compound **1** possesses a μ_2 [κ^2-*O*(1),*O*(2)] coordination mode for the sulfonate group [Ag(1)–O(1), 2.496(3) Å; Ag(1)–O(2′), 2.335(3) Å (′ = *x*, –1/2 – *y*, *z* – 1/2)] and a κ*N* bridge for the NH_2 group [Ag(1)–N(1), 2.321(4) Å]. Thus, one *o*-aminobenzenesulfonate ligand is capable of connecting to three Ag^I centres in an overall μ_2:η^3 coordination mode. No bridging sulfonate oxygen atoms are observed in **1** and therefore no extended network is formed. As might be expected with the amino group in the *ortho* position, the Ag^I centre is chelated by one sulfonate oxygen atom and the nitrogen atom to form a boat-shaped six-membered ring. The arene moiety forms a weak electrostatic interaction with the silver centre, thereby establishing an η^2 coordination mode from the 3,4-positions of the ring [Ag(1)–C(3′), 2.521(4) Å; Ag(1)–C(4′), 2.502(4) Å (′ = *x*, –1/2 – *y*, 1/2 – *z*)]. The interaction places the phenyl ring perpendicular to the Ag^I centre [Ag(1)–C(1)–C(4), 90.0(7)°] as the sulfur atom of the sulfonate group holds on to its almost perfect tetrahedral geometry. The packing of the 1D chains results in a 3D network in which the individual 1D chains are connected through hydrogen-bonding interactions along the crystallographic *a* axis (Figure 2), whereas π-stacking (face-to-face) interactions are observed along the crystallographic *b* axis. The 2-pyridinesulfonate analogue **9** shows a perpendicular arrangement of the phenyl rings along the crystallographic *c*

Table 1. Selected bond lengths [Å] and angles [°] of compounds **1**, **2**, **4a** and **4b**. Symmetry operators: **1** (′ = *x*, –*y* – 1/2, *z* – 1/2); **2** (′ = –*x* + 1/2 – *y*, *z* + 1/2, ′′ = *x* + 1/2, –*y* + 1/2, –*z*); **3** (′ = –*x*, *y* + 1/2, –*z*); **4** (′ = –*x*, –*y*, –*z*, ′′ = *x* + 1/2, –*y* + 1/2, *z* – 1/2).

1							
Ag(1)–N(1)	2.324(3)	S(1)–O(3)	1.456(2)	N(1)–Ag(1)–O(2′)	122.65(10)	O(3)–S(1)–O(2)	113.22(15)
Ag(1)–O(2′)	2.336(2)	S(1)–O(2)	1.457(2)	N(1)–Ag(1)–O(1)	80.54(9)	O(3)–S(1)–O(1)	112.27(14)
Ag(1)–O(1)	2.497(3)	S(1)–O(1)	1.459(2)	O(2′)–Ag(1)–O(1)	93.54(9)	O(2)–S(1)–O(1)	112.70(16)
Ag(1)–C(4′)	2.501(3)	N(1)–C(2)	1.416(4)	S(1)–O(2′)–Ag(1)	142.12(17)		
Ag(1)–C(3′)	2.522(3)			S(1)–O(1)–Ag(1)	121.71(13)		
2							
Ag(1)–N(1′)	2.2402(18)	S(1)–O(3)	1.4504(14)	N(1′)–Ag(1)–O(2)	142.19(6)	O(3)–S(1)–O(2)	113.84(9)
Ag(1)–O(2)	2.2957(13)	S(1)–O(2)	1.4557(16)	N(1′)–Ag(1)–O(1′′)	126.21(6)	O(3)–S(1)–O(1)	111.92(8)
Ag(1)–O(1′′)	2.3719(15)	S(1)–O(1)	1.4678(15)	O(2)–Ag(1)–O(1′′)	88.46(5)	O(2)–S(1)–O(1)	111.64(9)
Ag(1)–O(1)	2.5168(14)	N(1)–C(3)	1.417(2)	N(1′)–Ag(1)–O(1)	93.31(6)		
				O(2)–Ag(1)–O(1)	94.42(5)		
				Ag(1′′)–O(1)–Ag(1)	111.34(5)		
4a							
Ag(1)–N(1)	2.320(6)	S(1)–O(3)	1.461(5)	N(1)–Ag(1)–O(1)	125.3(2)	O(3)–S(1)–O(2)	114.4(3)
Ag(1)–O(1)	2.385(6)	S(1)–O(2)	1.472(5)	N(1)–Ag(1)–O(4)	86.9(2)	O(3)–S(1)–O(1)	111.8(3)
Ag(1)–O(4)	2.397(5)	S(1)–O(1)	1.478(6)	O(1)–Ag(1)–O(4)	106.7(2)	O(2)–S(1)–O(1)	110.4(4)
Ag(1)–C(6′)	2.485(6)	S(2)–O(1)	1.462(5)	N(1)–Ag(1)-C(7′)	108.6(2)		
Ag(1)–C(7′)	2.464(7)	S(2)–O(3)	1.480(6)	S(1)–O(1)–Ag(1)	116.0(3)		
		C(2)–N(1)	1.397(8)				
4b							
Ag(1)–N(1′)	2.2829(16)	S(1)–O(3)	1.4447(14)	N(1′)–Ag(1)–O(2′)	127.95(5)	O(3)–S(1)–O(1)	113.35(9)
Ag(1)–O(2′)	2.422(14)	S(1)–O(1)	1.4540(14)	N(1′)–Ag(1)–O(1)	113.15(5)	O(3)–S(1)–O(2)	111.09(8)
Ag(1)–O(1)	2.4493(18)	S(1)–O(2)	1.4658(13)	O(2′)–Ag(1)–O(1)	101.31(4)	O(1)–S(1)–O(2)	110.97(8)
Ag(1)–C(6′′)	2.5427(19)			S(1)–O(1)–Ag(1)	125.61(8)		
Ag(1)–C(7′′)	2.5615(17)			S(1)–O(2′)–Ag(1)	109.90(7)		

axis to result in T-shaped C–H/π interactions between the sheets (distance 3.698 Å). As the amino functionality is part of the pyridyl ring, no hydrogen bonding is observed in **9**.

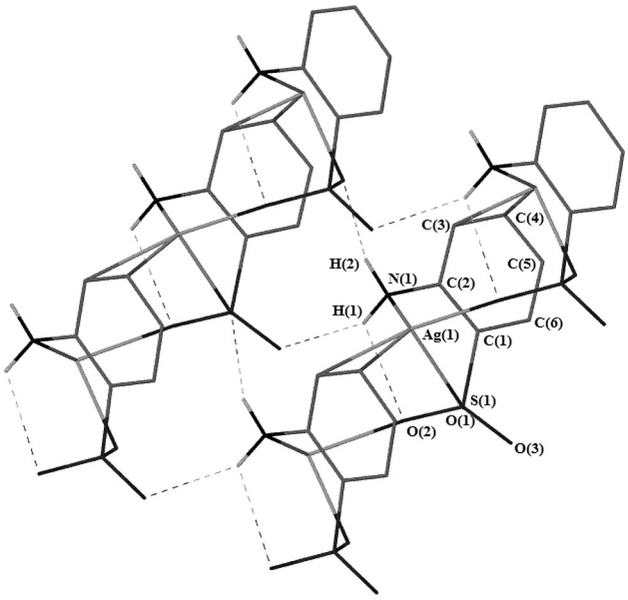

Figure 2. Hydrogen-bonding network of **1**. Only hydrogen atoms involved in hydrogen-bonding interactions are shown.

[Ag(O$_3$SBA$_m$)]$_\infty$ (2)

Shifting the amino group to the *meta* position results in complex **2**, which forms a 3D network in the solid state. The amino group and one oxygen atom of the sulfonate group allow the network to grow along the crystallographic *c* axis, whereas bridging through the second and third sulfonate oxygen atoms allows growth along the divergent crystallographic *a* and *b* axes. Only one type of Ag^I centre is present and again shows pseudo-tetrahedral geometry. However, one Ag^I centre is connected to four individual *m*-aminobenzenesulfonate ligands to exhibit an overall μ_4:η^4 coordination mode (Figure 3). The pyridyl complex [Ag(3-pySO$_3$)]$_\infty$, previously described by Mäkinen and Shimizu et al.,[2d] also forms a 3D network that consists of Ag^I ribbons growing along the crystallographic *c* axis. However, this compound accommodates two types of Ag^I ions, analogous to those previously observed in the Ag^I 2-pyridinesulfonate analogue **9**.[2i] In [Ag(3-pySO$_3$)]$_\infty$ only one metal centre is bound to sulfonate oxygen atoms, whereas the other binds through the third sulfonate oxygen atom and the pyridyl nitrogen atom.

As might be expected for this family of compounds, the amino group of **2** engages in a κ*N* bridge to the Ag^I centre [Ag(1)–N(1′), 2.241(2) Å (′ = 1/2 – *x*, –*y*, 1/2 + *z*)] and forms the shortest Ag–N bond of all the complexes **1**, **4a** and **4b** (see below). A summary of bond lengths and angles is given in Table 1. The sulfonate group adopts a μ_3:η^3 coordination mode [κ^2*O(1)* and κ*O(2)*]. The oxygen atom O(1) bridges two Ag^I centres thereby showing two different Ag–O bonds [O(1′′)–Ag(1), 2.3719(15) Å (′′ = *x* + 1/2, 1/2 – *y*, –*z*), O(1′′′)–Ag(1), 2.5168(14) Å (′′′ = *x*,*y*,*z*)], whereas

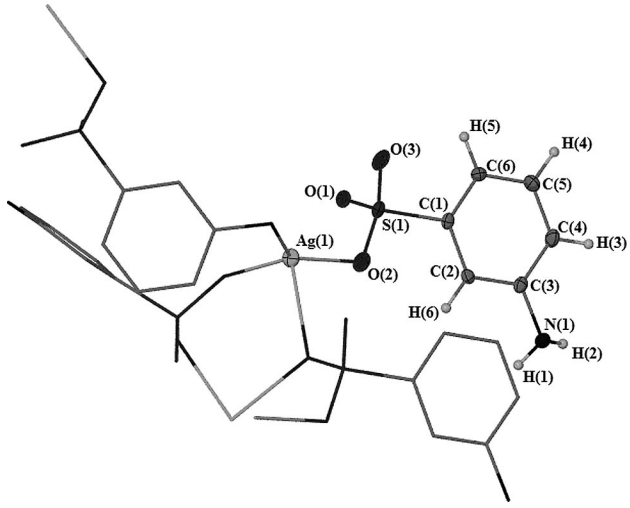

Figure 3. Structure of [Ag(O$_3$SBA*m*)]$_\infty$ (**2**). A 3D network is obtained for compound **2** as the amino group in the *meta* position on the ring and one oxygen atom of the sulfonate group allow growth of the network along the crystallographic *c* axis, whereas bridging through sulfonate oxygen atoms allows growth along the crystallographic *a* and *b* axes. Hydrogen atoms of the asymmetric unit are displayed. Ellipsoids are shown at 50% probability.

the bond to O(2) is the shortest at 2.2957(13) Å. The bridge angle for O(1) is 111.35(6)°. As in **1** (and in **4b**), the O(3) atom is not involved in any bonding with the Ag^I centres. Instead it bridges two hydrogen bonds [O(3′′′′)···H1–N(1), 2.34(3) Å (′′′′ = –*x*, *y* + 1/2 –*z* + 1/2), O(3′)···H(2)–N(1), 2.08(3) Å (′ = –*x* + 1/2, –*y*, *z* + 1/2)], which further enhances the stability of the network along the crystallographic *a*

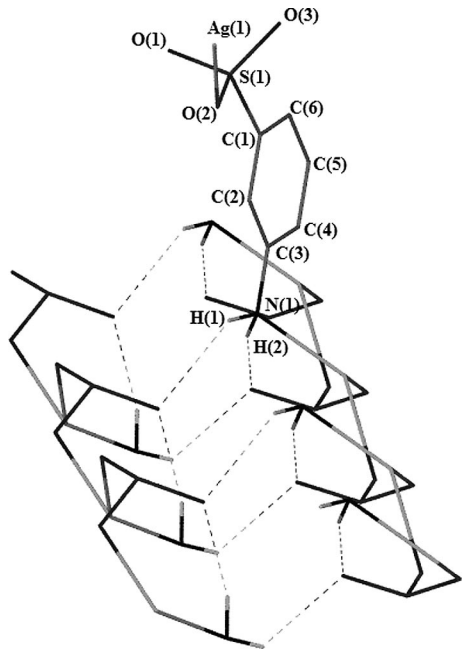

Figure 4. Display of the hydrogen bonds bridged by O(3) of the sulfonate group, which further enhances the stability of the network of **2** along the crystallographic *a* axis; the hydrogen bonds of one repeating unit show the motif of an *R*-helix winding down the crystallographic *a* axis.

axis; the hydrogen bonds of one repeating unit show the motif of an *R* helix winding down the crystallographic *a* axis (Figure 4). The phenyl group in **2** packs in a classical herringbone motif (also seen in **4b** below) that shows an array of nonclassical C–H/π-stacking interactions along the two crystallographic axes defined by the face-to-edge contacts of the phenyl ring.

[Ag(O$_3$SNA$_o$)(H$_2$O)]$_\infty$ (4a)

It is known that Ag^I *mono*-sulfonates will generally form anhydrous solids even when synthesized and isolated from aqueous solutions.[2b] There are rare exceptions to this and compound **4a** is one. The crystal structure shows one water molecule binding directly to the metal centre. This phenomenon was first observed in [Ag(H$_2$O)$_{0.5}$(1-naphthylenesulfonate)]$_\infty$[2b] and was ascribed to the increased length of the naphthyl moiety. The increased intramolecular space created by the naphthyl group also allows **4a** to retain the structural motif of the 1D chain, as adopted by the Ph analogue **1**. Bridging water molecules are thus incorporated into the polymeric chain (Figure 5), thus saturating the coordination environment of the Ag^I centre.

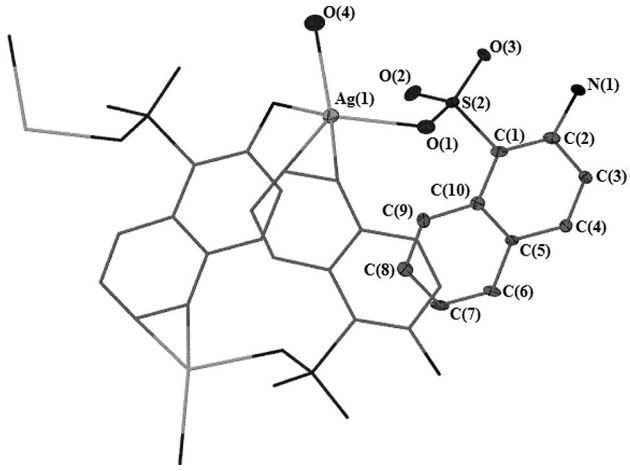

Figure 5. Structure of [Ag(O$_3$SNA*o*)(H$_2$O)]$_\infty$ (**4a**). View of an individual 1D polymeric chain growing along the crystallographic *b* axis showing the connectivity modes observed of the amino-arenesulfonate ligand to the unique Ag^I centre. Hydrogen atoms are omitted for clarity. Ellipsoids are shown at 50% probability.

As in **1**, the 1D chain in **4a** grows along the crystallographic *b* axis. In turn, only one unique Ag^I centre is again present and once more displays pseudo-tetrahedral coordination geometry. However, significant differences in the connectivity are seen due to the much more expanded structure (Figure 3). A summary of the bond lengths and angles is given in Table 1. Here only O(1) of the sulfonate group [Ag(1)–O(1), 2.383(6) Å] is involved in bonding to the metal centre. The sulfonate and amino groups show no chelation to any Ag^I centre. Instead the nitrogen atom bridges to a second Ag^I centre [Ag(1)–N(1′), 2.320(6) (′ = *x*, *y*, *z*)]. The Ag^I centre is again involved in π bonding to the arene moiety (Figure 6), but here the interaction is established with the more distant phenyl ring rather than that which contains the sulfonate moiety [Ag(1)–C(6′′), 2.464(7) Å; Ag(1)–C(7′′), 2.467(7) Å (′′ = –*x*, 1/2 + *y*, –*z*)]. On account of this coordination environment, the ligand is locked into place as the naphthyl moiety is perpendicular to the sulfonate group [S(1)–C(1)–C(9), 89.5(2)°] and the η^2 coordination mode from the 6,7-positions of the ring to the silver centre is fixed by a mean angle of 109.2(8)°. The coordination sphere of the silver centre is completed by an auxiliary ligation to one water molecule [Ag(1)–O(4), 2.397(5) Å] that points to the left and right of the chain.

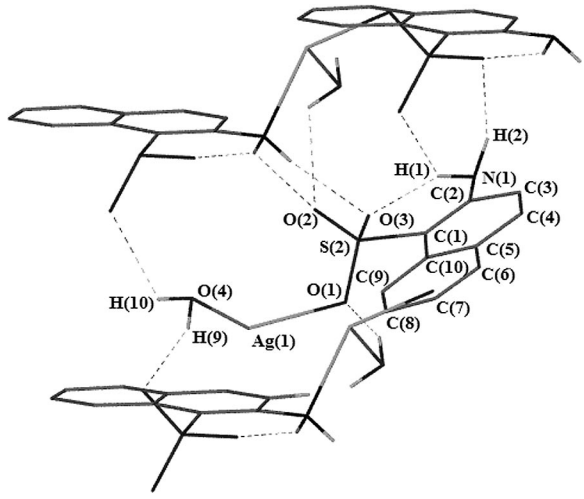

Figure 6. Hydrogen-bonding network of **4a**. The two sulfonate oxygen atoms that are not involved in the direct bonding to the metal centre play a significant role in intermolecular hydrogen bonding between the 1D chains; they are connected along the crystallographic *a* axis. An intramolecular hydrogen bond is observed for O(3) as a secondary interaction seen within one chain.

Looking down the crystallographic *a* axis, a zigzag pattern occurs similar to that observed in **1**. The two individual silver(I) chains are orientated exactly opposite to each other with respect to the arene moiety and its functional groups. The zigzag angle at the silver centre is 62.1(3)°. This facilitates a perfect alignment of the naphthyl rings to allow T-shaped C–H/π interactions (face-to-edge) with a distance of 3.581 Å. These interactions are also present between individual chains, which results in an overall classical herringbone motif along the crystallographic *c* axis, as reported for simple aromatic hydrocarbons,[14] naphthalene itself[12e] and its Ag^I arenesulfonate analogue.[2b] The two sulfonate oxygen atoms that are not involved in bonding to the metal centre play a significant role in intermolecular hydrogen bonding between the 1D chains; two originate from the water molecule [O(1′′)···H(9)–O(4), 2.040(8) Å, O(2′′)···H(10)–O(4), 2.390(15) Å (′′ = –*x*, 1/2 + *y*, –*z*)] and two from the amino functionality [O(2′′)···H(1)–N(1), 2.55 Å, O(3′′)···H(2)–N(1), 2.36 Å (′′ = –*x*, 1/2 + *y*, –*z*)]; and connect them along the crystallographic *a* axis (Figure 6). Another intramolecular hydrogen bond is observed for O(3) [O(3)···H(1)–N(1), 1.88 Å] as a secondary interaction within one chain (Figure 6).

{[Ag(O$_3$SNA$_o$)]·H$_2$O}$_\infty$ (4b)

In attempting to generate the anhydrous analogue of **4a**, crystals of **4a** were dissolved in ethanol and recrystallized. The result was complex **4b**, which retains a water molecule in the crystal lattice but not directly bound to the Ag^I centre. The absence of water bridging to the silver centre allows the formation of a 2D network that grows along the crystallographic *b* axis. The overall pseudo-tetrahedral geometry of the unique metal centre similar to that seen in **4a** (and in **1**) is maintained. As in compound **1**, two sulfonate oxygen atoms coordinate to the Ag^I centre along with the nitrogen atom and two aromatic carbon atoms. In contrast to **1**, however, the formation of a 2D network and the accommodation of the naphthyl moiety do not allow the chelation of the ligand to the metal centre. Therefore, in **4b** an overall coordination mode of μ_3:η^3 to three independent Ag^I centres is present [Ag(1)–N(1′), 2.2830(2) Å; Ag(1)–O(1), 2.450(2) Å; and Ag(1)–O(2′), 2.4230(2) Å (′ = –*x*, –*y*, –*z*)]. To maintain the pseudo-tetrahedral geometry around the Ag^I centre, the arene moiety coordinates in an η^2 mode from the 6,7-positions of the ring [Ag(1)–C6′′, 2.5620(2) Å; Ag(1)–C7′′, 2.5620(2) Å (′′ = 1/2 + *x*, 1/2 – *y*, 1/2 + *z*)]. Again O(3) of the sulfonate group is not involved in bonding to the Ag^I centre (Figure 7).

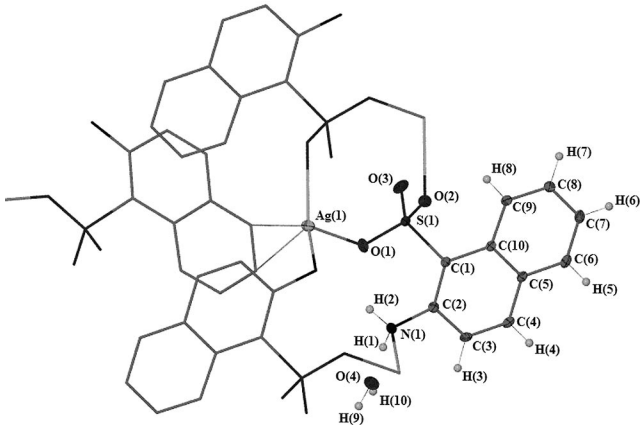

Figure 7. Structure of {[Ag(O$_3$SNA*o*)]·(H$_2$O)}$_\infty$ (**4b**). Connectivity of compound **4b** is shown with μ_3:η^3 coordination mode to three independent Ag^I centres. Hydrogen atoms of the asymmetric unit are shown. Ellipsoids are shown at 50% probability.

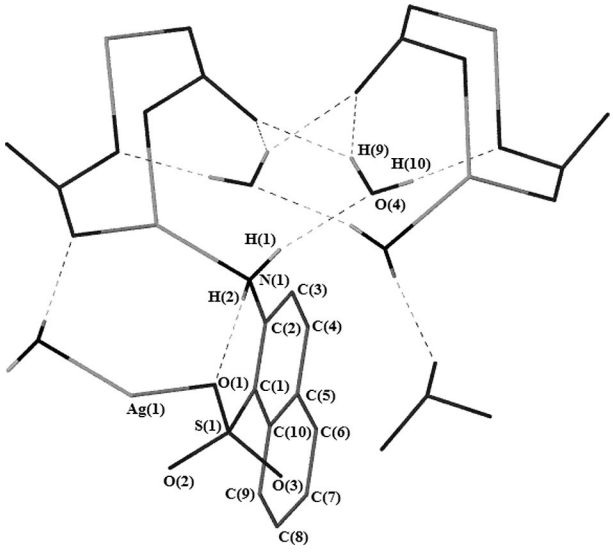

Figure 8. Hydrogen-bonding network of **4b**. Only hydrogen atoms involved in hydrogen-bonding interactions are shown.

A summary of bond lengths and angles for **4b** is given in Table 1. Five hydrogen bonds are observed within the structure (Figure 8): two derived from the amino group [O(1)···H2–N(1), 1.990(2) Å, O4···H1–N(1), 2.250(2) Å] and three from the water molecule that are present in the lattice [O(3)···H9–O4, 2.2400(2) Å, O(3′)···H9–O4, 2.4500(2) Å (′ = –*x*, *y*, –*z* + 1/2) and O(2′)′···H10–O4, 1.9900(2) Å (′′ = *x*, –*y*, *z* – 1/2)]. Compound **4b** is assigned as an anhydrous Ag^I amino-arenesulfonate as the coordination geometry around the Ag^I centre is exclusively made up of the ligand and does not include the water molecule.

Characterization

Complexes **1**–**9** and the starting acids were all studied by NMR spectroscopy in D_2O and/or [D_6]DMSO. In the ^{1}H NMR spectra the acids show the acidic proton as a broad singlet with chemical shift values in the range δ = 7–9 ppm. Upon deprotonation and complexation with Ag^I, this signal disappears thereby confirming formation of the ligand and the corresponding silver compounds. In comparison with the free acids, upon complexation the ^{13}C NMR spectra show low-frequency shifts for the resonance that corresponds to the quaternary carbon *C*-(SO$_3$Ag) by between

Table 2. Observed coordination modes for Ag^I to the sulfonate group and the assignment of the corresponding absorption bands.

	$\tilde{\nu}$(NH$_2$)[a]	$\tilde{\nu}$(SO$_3$)[a]	CM[b]	CS[c]
*o*ABSO$_3$H	3418	1228, 1204, 1027		
1	3320, 3257	1204, 1174, 1013	μ_2:η^3	x
*m*ABSO$_3$H	3437	1208, 1101, 1026		
2	3362, 3246	1210, 1147, 1108, 1027	μ_4:η^4	x
6A3MBSO$_3$H	3391	1260, 1187, 1024		
3	3336, 3070	1253, 1186, 1134, 1023		
*o*ANBSO$_3$H	3470	1242, 1182, 1045		
4a	3433, 3342	1193, 1050	μ_2:η^2	x
4b	3412, 3341	1158, 1029	μ_3:η^3	x
5ANSO$_3$H	3421	1226, 1170, 1057		
5	3401, 3348	1167, 1027		
3H4ASO$_3$H	3239	1218, 1169, 1048		
6	3159, 3078	1197, 1157, 1042		
ISO$_3$H	3429	1215, 1198, 1052		
7	3437, 3351	1210, 1175, 1056		
*p*ABSO$_3$H	3418	1245, 1156, 1033		
8	3319, 3266	1249, 1186, 1153, 1123	μ_4:η^4	x[d]
PSO$_3$H	–	1269, 1148, 1039		
9	–	1207, 1165, 1146, 1019	μ_5:η^5	x[e]

[a] FTIR absorption bands are taken from the Nujol spectra [cm^{-1}]. [b] CM = coordination mode. CM assigned in red were confirmed through X-ray crystallography. [c] CS = crystal structure. Overall CM was confirmed through X-ray crystallography. [d] Crystal structure is known in the literature of compound [Ag(2-pySO$_3$)]$_\infty$.[2i] [e] Crystal structure is known in the literature of compound [Ag(O$_3$SBA*p*)]$_\infty$.[12a–12d]

3 and 5 ppm. Full details of the chemical shifts and their assignments for **1**–**9** are given in the Experimental Section.

FTIR spectra visualize the different coordination modes of the silver metal to the sulfonic acid group by showing the appropriate number of absorption bands. A bathochromic shift for the amino absorption band is ascribed to the coordination of the amino functionality to the Ag^I centre. The sulfonate group shows a range of absorption bands in the region 1200–1000 cm^{-1} according to the coordination mode this functional group displays within the solid-state structure. The coordination modes for **1**, **2**, **4a**, **4b**, **8** and **9** have been established through crystallography and as such their coordination mode is known. Table 2 summarizes the main features observed in FTIR spectroscopy and the observed bonding modes of the sulfonato ligands. However, too little data currently exists to allow the binding and coordination of the other complexes to be predicted based on the IR spectroscopic data alone.

Mass spectrometry provided unambiguous evidence for silver complexes **1**–**9** to be arranged as polymeric structures. In the case of the *p*-aminobenzenesulfonate, two quartets (1/3/3/1) at 665/667/669/671 $[Ag_3\mathbf{L}_2]^+$ and 743/745/747/749 $[Ag_3\mathbf{L}_2(DMSO)]^+$ and a quintet (1/4/6/4/1) at 944/946/948/950/952 $[Ag_4\mathbf{L}_3]^+$ were observed underlining the polymeric nature of the silver compound **8**. A summary of the common ions detected for all the structures can be found in Table 3.

Table 3. Summary of common ions detected in mass spectra for compounds **1**–**9**.

	$\mathbf{L}^-$	$[Ag\mathbf{L} + Na]^+$	$[Ag\mathbf{L}(s) + Na]^+$	$[Ag_2\mathbf{L}]^+$	$[Ag_2\mathbf{L}(s)]^+$
1	*o*$ABSO_3$			386/388/390	464/466/468[b]
2	*m*$ABSO_3$	302/304		386/388/390	464/466/468[b]
3	6A3MBSO$_3$	332/334			
4a	*o*$ANSO_3$			436/438/440	520/522/524[c]
5	5$ANSO_3$			436/438/440	
6	3H4ANSO$_3$	368/370			470/472/474[a]
7	ISO_3		356/358[a]		
8	*p*$ABSO_3$				464/466/468[b]
					542/544/546[b]*
9	PSO_3			372/374/376	456/458/460[c]

[a] Solvent H_2O. [b] Solvent DMSO or * $(DMSO)_2$. [c] Solvent dichloromethane.

Conclusion

We have described the synthesis and characterization of seven new Ag^I amino-arenesulfonates and a systematic study on their coordination chemistry. Mass spectroscopic data indicate the compounds to be polymeric in nature and are supported by those complexes **1**, **2**, **4a** and **4b** that have been confirmed by single-crystal X-ray diffraction. Structural changes in the position of the amino functionality on the arene moiety from *ortho* to *meta* to *para*, the increase in ring size from a phenyl to a naphthyl moiety and inclusion of the N atom in a heterocycle all impact directly on the adopted structures. All presented structures have a unique silver ion incorporated that displays pseudo-tetrahedral geometry. This phenomenon of having a unique Ag^I centre is in contrast to the reported pyridyl analogues, which consist of two geometrically different Ag^I centres. Despite being synthesized in water, anhydrous compounds were obtained for all compounds **1**–**9**. An exception is the *o*-aminonaphthalenesulfonate ligand **4a**, which results in a hydrated solid structure with one water molecule bound directly to the Ag centre. Recrystallization from ethanol yielded the anhydrous compound.

We are currently exploring the antimicrobial properties of these compounds for use in medical applications (see Introduction) and assessing their potential as precursors to new metal sulfonates through metathesis, especially when the zwitterionic nature of the aminosulfonate inhibits direct complex formation.

Experimental Section

General Considerations: All sulfonic acids were purchased from Aldrich Chemical Co. Ag_2O was freshly synthesized according to Tanabe and Peters.[13] Infrared spectra were obtained with a Perkin–Elmer 1600 FTIR spectrometer. NMR spectra were obtained with Bruker AV300 or AV400 spectrometers with chemical shifts referenced to $[D_6]$DMSO or D_2O. Electrospray ionization mass spectrometry (ESI-MS) was performed with a Micromass Platform electrospray mass spectrometer. Elemental analysis (EA) was performed by The Campbell Microanalytical Laboratory, Department of Chemistry, University of Otago, New Zealand. Melting points are uncalibrated and were determined with a Bibby Stuart Scientific melting-point apparatus SMP3.

Synthesis, General Procedure: The individual sulfonic acid (2 mmol, 2 equiv.) was dissolved in water (50 mL) and the temperature was set to 90 °C. Fresh Ag_2O (1 mmol, 1 equiv.) was added to this solution, and the reaction mixture was stirred for 2 h. The solution was filtered hot and the filtrate was kept in a water bath at 50 °C overnight. The filtrate was allowed to cool to room temperature very slowly to yield the desired product either as crystalline material (**1**, **2**, **4a**, **4b**, **8** and **9**) or as an amorphous powder (**3**, **5**–**7**).

$[Ag(O_3SBAo)]_\infty$ (1): The general procedure was followed using *o*-aminobenzenesulfonic acid to yield pink crystalline needles (269 mg, 96%) suitable for X-ray crystallography; m.p. > 250 °C (decomp.). ^1H NMR (300 MHz, $[D_6]$DMSO, 30 °C): δ = 7.43 (dd, ^3J = 1.6, 7.7 Hz, 1 H, H^6), 7.02 (ddd, ^3J = 3.0, 3.0, 6.0 Hz, 1 H, H^4), 6.66 (dd, ^3J = 1.6, 7.7 Hz, 1 H, H^3), 6.51 (ddd, ^3J = 3.0, 3.0, 6.0 Hz, 1 H, H^5) ppm. ^{13}C NMR (75 MHz, $[D_6]$DMSO, 30 °C): δ = 144.69 (C^1), 130.88 (C^2), 129.72 (C^6), 127.21 (C^4), 116.04 (C^3), 115.43 (C^5) ppm. FTIR (KBr): $\tilde{\nu}$ = 3424 (m), 3370 (m), 1619 (s), 1560 (s), 1482 (s), 1317 (m), 1231 (s), 1187 (s), 1117 (m), 1065 (w), 1023 (m), 1035 (m), 826 (w), 750 (s), 709 (s), 619 (s), 576 (m), 528 (m) cm^{-1}. FTIR (Nujol): $\tilde{\nu}$ = 3320 (m), 3257 (m), 1599 (w), 1565 (w), 1296 (w), 1204 (s), 1174 (s) 1160 (m), 1131 (m), 1074 (m), 1033 (m), 1013 (s), 947 (w), 827 (m), 778 (s), 703 (s) cm^{-1}. ESI-MS^+ (solvent: DMSO/MeOH): *m*/*z* (%) = 464/466/468 (5) {triplet (1/2/1 $^{107}Ag/^{107/109}Ag/^{109}Ag$), $[Ag_2\mathbf{L}(DMSO)]^+$}; 386/388/390 (5) {triplet (1/2/1 $^{107}Ag/^{107/109}Ag/^{109}Ag$), $[Ag_2\mathbf{L}]^+$}; 263/265 (95) {doublet (1/1 $^{107}Ag/^{109}Ag$), $[Ag(\mathbf{L}–NH_2)]^+$}; 185/187 (100) {doublet (1/1 $^{107}Ag/^{109}Ag$), $[Ag(DMSO)]^+$}. $C_6H_6AgNO_3S$ (280.046): calcd. C 25.73, H 2.16, N 5.00; found C 25.57, H 2.06, N 4.87.

$[Ag(O_3SBAm)]_\infty$ (2): *m*-Aminobenzenesulfonic acid was applied to the general procedure to yield a dark purple amorphous powder

(258 mg, 92%). Recrystallization of 50 mg in water resulted in crystalline plates (55%) suitable for X-ray crystallography; m.p. > 270 °C (decomp.). ^{1}H NMR (300 MHz, [D$_6$]DMSO, 30 °C): δ = 7.03 (m, 1 H, H^5), 6.99 (s, 1 H, H^2), 6.91 (d, ^3J = 9.0 Hz, 1 H, H^6), 6.62 (m, 1 H, H^4) ppm. ^{13}C NMR (100 MHz, [D$_6$]DMSO, 30 °C): δ = 148.49 (C^1), 146.47 (C^3), 128.15 (C^5), 115.47 (C^4), 114.89 (C^6), 112.82 (C^2) ppm. FTIR (KBr): $\tilde{\nu}$ = 3432 (s), 1629 (m), 1600 (m), 1482 (m), 1452 (m), 1384 (m), 1313 (w), 1270 (w), 1188 (s), 1110 (s), 1037 (s), 992 (m), 875 (w), 791 (m), 710 (s), 691 (m), 623 (s), 562 (m), 526 (m) cm^{-1}. FTIR (Nujol): $\tilde{\nu}$ = 3362 (m), 3246 (w), 1599 (m), 1314 (w), 1254 (m), 1210 (s), 1169 (m), 1147 (s), 1108 (s), 1027 (s), 982 (m), 881 (m), 785 (m), 709 (m), 685 (m), 613 (m) cm^{-1}. ESI-MS$^+$ (solvent: DMSO/MeOH): *m*/*z* (%) = 464/466/468 (5) {triplet (1/2/1 ^{107}Ag/$^{107/109}$Ag/^{109}Ag), [Ag$_2$**L**(DMSO)]$^+$}; 386/388/390 (5) {triplet (1/2/1 ^{107}Ag/$^{107/109}$Ag/^{109}Ag), [Ag$_2$**L**]$^+$}; 313/315 (10) {doublet (1/1 ^{107}Ag/^{109}Ag), [Ag(**L**–NH$_2$)(MeOH)(H$_2$O)]$^+$}; 302/304 (5) {doublet (1/1 ^{107}Ag/^{109}Ag), [Ag**L** + Na]$^+$}; 263/265 (95) {doublet (1/1 ^{107}Ag/^{109}Ag), [Ag(**L**–NH$_2$)]$^+$}; 185/187 (100) {doublet (1/1 ^{107}Ag/^{109}Ag), [Ag(DMSO)]$^+$}; 107/109 (30){doublet (1/1), [Ag]$^+$}. $C_6H_6AgNO_3S$ (280.046): calcd. C 25.73, H 2.16, N 5.00; found C 25.80, H 2.14, N 5.22.

[Ag(O$_3$SBM3A6)]$_\infty$ (3): The general procedure was followed by using 6-amino-3-methoxybenzenesulfonic acid to yield a dark purple amorphous powder (289 mg, 93%); m.p. > 150 °C (decomp.). ^{1}H NMR (300 MHz, [D$_6$]DMSO, 30 °C): δ = 7.28 (d, ^3J = 6.0 Hz, 1 H, H^3), 7.26 (s, 1 H, H^6), 7.04 (dd, ^3J = 3.0, 9.0 Hz, 1 H, H^4), 3.79 (s, 3 H, –OCH$_3$) ppm. ^{13}C NMR (100 MHz, [D$_6$]DMSO, 30 °C): δ = 158.39 (C^2), 141.78 (C^5), 125.41 (C^3), 120.08 (C^1), 115.96 (C^4), 112.21 (C^6), 55.66 (C^7) ppm. FTIR (KBr): $\tilde{\nu}$ = 3448 (s), 3079 (s), 1608 (m), 1560 (m), 1508 (m), 1492 (s), 1411 (w), 1384 (w), 1330 (m), 1252 (s), 1236 (s), 1210 (s), 1197 (s), 1132 (s), 1093 (m), 1060 (s), 1022 (s), 886 (m), 829 (m), 696 (s), 670 (w), 638 (s), 627 (s), 560 (w), 527 (m) cm^{-1}. FTIR (Nujol): $\tilde{\nu}$ = 3077 (m), 1634 (w), 1608 (w), 1494 (s), 1413 (w), 1331 (w), 1253 (s), 1237 (s), 1211 (s), 1186 (s), 1134 (m), 1095 (w), 1061 (m), 1023 (s), 888 (m), 830 (m), 697 (s), 639 (m), 629 (m) cm^{-1}. ESI-MS$^+$: (solvent: DMSO/MeOH): *m*/*z* (%) = 332/334 (10) {doublet (1/1 ^{107}Ag/^{109}Ag), [Ag**L** + Na]$^+$}; 310/312 (10) {doublet (1/1 ^{107}Ag/^{109}Ag), [Ag**L** + H]$^+$}; 122/124 (25) {doublet (1/1 ^{107}Ag/^{109}Ag), [Ag$_2$O + H]$^+$}; 107/109 (100) {doublet (1/1), [Ag]$^+$}. $C_7H_8AgNO_4S$ (310.071): calcd. C 27.11, H 2.60, N 4.52; found C 27.27, H 2.81, N 5.21.

[Ag(O$_3$SNA*o*)(H$_2$O)$_{0.5}$]$_\infty$ (4a): The general procedure was carried out with *o*-amino-1-naphthalenesulfonic acid to yield pale pink crystalline needles (304 mg, 92%) suitable for X-ray crystallography; m.p. > 140 °C (decomp.). ^{1}H NMR (300 MHz, [D$_6$]DMSO, 30 °C): δ = 8.95 (d, ^3J = 6.0 Hz, 1 H, H^9), 7.96 (d, ^3J = 9.0 Hz, 1 H, H^4), 7.88 (d, ^3J = 9.0 Hz, 1 H, H^6), 7.59–7.46 (m, 2 H, H^7 and H^8), 7.29 (d, ^3J = 9.0 Hz, 1 H, H^3) ppm. ^{13}C NMR (100 MHz, [D$_6$]-DMSO, 30 °C): δ = 143.16 (C^1), 131.98 (C^2), 129.83 (C^4), 127.35 (C^{10}), 126.77 (C^6), 126.08 (C^9), 125.41 (C^5), 120.61 (C^8), 120.31 (C^7), 118.97 (C^3) ppm. FTIR (KBr): $\tilde{\nu}$ = 3430 (s), 2959 (w), 2625 (w) 1624 (s), 1559 (s), 1552 (s), 1518 (s), 1473 (m), 1427 (m), 1384 (s), 1360 (w), 1332 (w), 1233 (m), 1200 (s), 1145 (m), 1050 (s), 990 (m), 913 (w), 881 (w), 827 (w), 809 (s), 779 (m), 763 (w), 749 (w), 676 (m), 655 (m), 623 (m), 559 (m), 513 (m) cm^{-1}. FTIR (Nujol): $\tilde{\nu}$ = 3433 (w), 3342 (w), 1611 (m), 1597 (w), 1553 (m), 1503 (m), 1351 (w), 1234 (w), 1193 (s), 1146 (m), 1050 (s), 991 (m), 905 (w), 828 (w), 810 (m), 782 (m), 764 (w), 676 (m), 657 (w), 623 (m) cm^{-1}. ESI-MS$^+$ (solvent: CH_2Cl_2): *m*/*z* (%) = 520/522/524 (5) {triplet (1/2/1 ^{107}Ag/$^{107/109}$Ag/^{109}Ag), [Ag$_2$**L**(CH_2Cl_2)]$^+$}; 436/438/440 (5) {triplet (1/2/1 ^{107}Ag/$^{107/109}$Ag/^{109}Ag), [Ag$_2$**L**]$^+$}; 275/277 (5) {doublet (1/1), [Ag(CH_2Cl_2)$_2$]$^+$}; 191/193 (100) {doublet (1/1), [Ag(CH_2Cl_2)]$^+$}; 107/109 (70) {doublet (1/1), [Ag]$^+$}. $C_{10}H_9AgNO_{3.5}S$ (339.112): calcd. C 35.42, H 2.68, N 4.13; found C 32.36, H 2.60, N 3.99.

{[Ag(O$_3$SNA*o*)]·(H$_2$O)$_{0.5}$}$_\infty$ (4b): Crystalline material of **4a** (50 mg) was dissolved in EtOH and left for crystallization. After one week, pink needles were obtained [yield: 28 mg (56%)] that were suitable for X-ray crystallography. The crystals were isolated and dried in vacuo. Further analysis indicates the loss of the water molecule present in the lattice; m.p. > 160 °C (decomp.). $C_{10}H_8AgNO_3S$ (330.104): calcd. C 36.38, H 2.44, N 4.24; found C 37.57, H 2.98, N 4.53.

[Ag(O$_3$SN5A)]$_\infty$ (5): The general procedure was followed by using 5-amino-1-naphthalenesulfonic acid to yield a dark red amorphous powder (293 mg, 89%); m.p. > 220 °C (decomp.). ^{1}H NMR (300 MHz, [D$_6$]DMSO, 30 °C): δ = 8.86 (d, ^3J = 6.0 Hz, 1 H, H^9), 8.05 (d, ^3J = 9.0 Hz, 1 H, H^4), 7.95 (d, ^3J = 9.0 Hz, 1 H, H^2), 7.59 (d, ^3J = 9.0 Hz, 1 H, H^3), 7.55–7.52 (m, 2 H, H^7 and H^8) ppm. ^{13}C NMR (100 MHz, [D$_6$]DMSO, 30 °C): δ = 144.39 (C^1), 129.73 (C^6), 128.58 (C^{10}), 127.46 (C^9), 126.71 (C^5), 125.66 (C^3), 125.41 (C^4), 125.25 (C^8), 122.93 (C^2), 119.71 (C^7) ppm. FTIR (KBr): $\tilde{\nu}$ = 3469 (s), 1654 (s), 1399 (m), 1384 (m), 1350 (w), 1322 (w), 1199 (s), 1035 (s), 785 (m), 755 (w), 646 (m), 581 (m) cm^{-1}. FTIR (Nujol): $\tilde{\nu}$ = 3427 (w), 1654 (m), 1167 (s), 1027 (s), 783 (m), 645 (w), 629 (w), 582 (w) cm^{-1}. ESI-MS$^+$ (solvent: DMSO/MeOH): *m*/*z* (%) = 436/438/440 (5) {triplet (1/2/1 ^{107}Ag/$^{107/109}$Ag/^{109}Ag), [Ag$_2$L]$^+$}; 341/343 (60) {doublet (1/1 ^{107}Ag/^{109}Ag), [Ag(DMSO)$_3$]$^+$}; 263/265 (60) {doublet (1/1 ^{107}Ag/^{109}Ag), [Ag(DMSO)$_2$]$^+$}; 217/219 (10) {doublet (1/1 ^{107}Ag/^{109}Ag), [Ag(DMSO)(MeOH)]$^+$}; 185/187 (100) {doublet (1/1 ^{107}Ag/^{109}Ag), [Ag(DMSO)]$^+$}. $C_{10}H_{12}AgNO_5S$ (366.134): calcd. C 32.80, H 2.75, N 3.83; found C 32.36, H 2.72, N 3.83.

[Ag(O$_3$SN4A3H)]$_\infty$ (6): 4-Amino-3-hydroxy-1-naphthalenesulfonic acid was applied to the general procedure to yield a dark red amorphous powder (276 mg, 80%); m.p. 176–180 °C. ^{1}H NMR (300 MHz, D_2O, 30 °C): δ = 8.51–8.48 (m, 1 H, H^9), 8.12–8.09 (m, 1 H, H^6), 7.84 (s, 1 H, H^2), 7.56–7.52 (m, 2 H, H^7 and H^8) ppm. ^{13}C NMR [100 MHz, D_2O (TMS), 30 °C]: δ = 140.34 (C^3), 137.16 (C^1), 130.24 (C^4), 126.02 (C^9), 125.97 (C^{10}), 125.37 (C^7), 124.82 (C^8), 124.17 (C^5), 121.12 (C^6), 118.90 (C^2) ppm. FTIR (KBr): $\tilde{\nu}$ = 3169 (s), 1637 (s), 1607 (m), 1577 (m), 1514 (m), 1441 (s), 1400 (s), 1352 (s), 1290 (m), 1221 (s), 1196 (s), 1159 (m), 1145 (m), 1105 (m), 1081 (m), 1043 (s), 983 (w), 970 (m), 877 (m), 781 (w), 759 (m), 725 (w), 656 (m), 640 (m), 593 (s), 545 (m), 514 (m) cm^{-1}. FTIR (Nujol): $\tilde{\nu}$ = 3156 (m), 1635 (m), 1601 (m), 1576 (m), 1515 (m), 1351 (s), 1292 (m), 1197 (s), 1157 (s), 1145 (s), 1105 (m), 1042 (s), 969 (m), 946 (w), 878 (w), 760 (m), 676 (w), 657 (m), 640 (m), 594 (m) cm^{-1}. ESI-MS$^+$ (solvent: DMSO/MeOH): *m*/*z* (%) = 470/472/474 (5) {triplet (1/2/1 ^{107}Ag/$^{107/109}$Ag/^{109}Ag), [Ag$_2$**L** + H$_2$O]$^+$}; 368/370 (10) {doublet (1/1 ^{107}Ag/^{109}Ag), [Ag**L** + Na]$^+$}; 147/149 (100) {doublet (1/1 ^{107}Ag/^{109}Ag), [AgOH + Na]$^+$}. $AgC_{10}H_{12}O_6NS$ (382.131): calcd. C 31.43, H 3.17, N 3.67; found C 31.05, H 3.04, N 3.82.

[Ag(O$_3$SI)]$_\infty$ (7): The general procedure was carried out with 5-isoquinolinesulfonic acid to yield a pale yellow amorphous powder (308 mg, 98%); m.p. > 220 °C (decomp.). ^{1}H NMR (300 MHz, [D$_6$]DMSO, 30 °C): δ = 9.37 (s, 1 H, H^6), 8.71 (d, ^3J = 6.0 Hz, 1 H, H^4), 8.54 (d, ^3J = 6.0 Hz, 1 H, H^3), 8.21 (dd, ^3J = 3.0, 9.0 Hz, 1 H, H^{10}), 8.16 (d, ^3J = 9.0 Hz, 1 H, H^8), 7.69 (dd, ^3J = 3.0, 9.0 Hz, 1 H, H^9) ppm. ^{13}C NMR (100 MHz, [D$_6$]DMSO, 30 °C): δ = 153.92 (C^6), 143.17 (C^{10}), 143.10 (C^1), 131.88 (C^2), 129.46 (C^8), 129.18 (C^3), 128.68 (C^9), 126.97 (C^7), 120.90 (C^4) ppm. FTIR (KBr): $\tilde{\nu}$ = 3435 (s), 3093 (w), 3070 (w), 3026 (w), 3008 (w), 1622 (s), 1558 (s), 1569 (m), 1487 (s), 1424 (m), 1382 (w), 1369 (s), 1326 (m), 1267 (m), 1250 (s), 1218 (s), 1186 (m), 1068 (s), 1077 (m), 1055

(s), 984 (m), 934 (w), 918 (m), 842 (m), 814 (s), 802 (m), 751 (s), 709 (s), 629 (s), 575 (s), 537 (m), 515 (s), 466 (m), 426 (m), 410 (m) cm^{-1}. FTIR (Nujol): $\tilde{\nu}$ = 3437 (s), 3351 (s), 3094 (m), 1623 (s), 1591 (m), 1561 (w), 1487 (m), 1320 (w), 1274 (m), 1210 (s), 1175 (s), 1056 (s), 988 (m), 969 (w), 956 (w), 944 (w), 926 (w), 843 (m), 831 (m), 814 (m), 763 (s), 705 (m), 624 (m) cm^{-1}. ESI-MS^+ (DMSO/MeOH): *m*/*z* (%) = 373/375 (10) {doublet (1/1 $^{107}Ag/^{109}Ag$), $[AgL(LH)(DMSO)_2(MeOH)_2 + 2H]^{2+}$}; 368/370/372 (5) {triplet (1/2/1 $^{107}Ag/^{107/109}Ag/^{109}Ag$), $[Ag_2L(LH)(MeOH)_2(H_2O) + Na]^{2+}$}; 356/358 (5) {doublet (1/1 $^{107}Ag/^{109}Ag$), $[AgL(H_2O) + Na]^+$}; 341/343 (80) {doublet (1/1 $^{107}Ag/^{109}Ag$), $[AgL(LH)(DMSO)_2 + 2H]^{2+}$}; 317/319 (40) {doublet (1/1 $^{107}Ag/^{109}Ag$), $[AgL(LH)(H_2O)_6 + 2H]^{2+}$}; 295/297 (15) {doublet (1/1 $^{107}Ag/^{109}Ag$), $[AgL(LH)(MeOH)_2 + 2H]^{2+}$}; 290/2920 (50) {doublet (1/1 $^{107}Ag/^{109}Ag$), $[AgL(LH)(H_2O)_3 + 2H]^{2+}$}; 263/265 (100) {$[AgL(LH) + 2H]^{2+}$}. $C_9H_8AgNO_4S$ (334.093): calcd. C 32.35, H 2.41, N 4.19; found C 32.03, H 2.40, N 4.15.

$[Ag(O_3SBAp)]_\infty$ (8): The general procedure was carried out with *p*-aminobenzenesulfonic acid as ligand to yield amber crystalline blocks (278 mg, 99%) suitable for X-ray crystallography; m.p. > 250 °C (decomp.). ^1H NMR (300 MHz, [D$_6$]DMSO, 30 °C): δ = 7.33 (d, ^3J = 8.6 Hz, 2 H, H^2 and H^6), 6.58 (d, ^3J = 6.4 Hz, 2 H, H^3 and H^5) ppm. ^{13}C NMR (75 MHz, [D$_6$]DMSO, 30 °C): δ = 149.91 (C^1), 135.56 (C^4), 127.72 (C^2 and C^6), 114.66 (C^3 and C^5) ppm. FTIR (KBr): $\tilde{\nu}$ = 3469 (m), 3320 (s), 3268 (s), 3185 (s), 1905 (w), 1600 (s), 1498 (s), 1437 (s), 1332 (w), 1298 (w), 1248 (m), 1197 (s), 1183 (s), 1152 (s), 1124 (s), 1032 (s), 1000 (s), 945 (s), 841 (m), 826 (s), 692 (s), 568 (s) cm^{-1}. FTIR (Nujol): $\tilde{\nu}$ = 3319 (m), 3267 (m), 3184 (m), 1714 (w), 1599 (m) 1498(m), 1304 (w), 1249 (w), 1186 (s), 1153 (s), 1123 (s), 991 (s), 946 (m), 843 (w), 827 (m), 691 (m), 569 (s) cm^{-1}. ESI-MS^+ (solvent: DMSO/MeOH): *m*/*z* (%) = 944/946/948/950/952 (5) {quintet (1/4/6/4/1 $^{107}Ag/^{3\times107/109}Ag/^{3\times109/107}Ag/^{2\times107/2\times109}Ag/^{109}Ag$), $[Ag_4L_3]^+$}; 743/745/747/749 (5) {quartet (1/3/3/1 $^{107}Ag/^{2\times107/109}Ag/^{2\times109/107/109}Ag$), $[Ag_3L_2(DMSO)]^+$}; 665/667/669/671 (5) {quartet (1/3/3/1 $^{107}Ag/^{2\times107/109}Ag/^{2\times109/107/109}Ag$), $[Ag_3L_2]^+$}; 542/544/546 (5) {triplet (1/2/1 $^{107}Ag/^{107/109}Ag/^{109}Ag$), $[Ag_2L(DMSO)_2]^+$}; 464/466/468 (10) {triplet (1/2/1 $^{107}Ag/^{107/109}Ag/^{109}Ag$), $[Ag_2L(DMSO)]^+$}; 263/265 (15) {doublet (1/1 $^{107}Ag/^{109}Ag$), $[Ag(L–NH_2)]^+$}; 185/187 (100) {doublet (1/1 $^{107}Ag/^{109}Ag$), $[Ag(DMSO)]^+$}; 107/109 (30) {doublet (1/1), $[Ag]^+$}. $C_6H_6AgNO_3S$ (280.046): calcd. C 25.73, H 2.16, N 5.00; found C 25.86, H 2.20, N 4.78.

$[Ag(O_3SP)]_\infty$ (9): 2-Pyridinesulfonic acid was applied to the general procedure to yield colourless crystalline blocks (264 mg, 99%) suitable for X-ray crystallography; m.p. > 245 °C (decomp.). ^1H NMR (300 MHz, [D$_6$]DMSO, 30 °C): δ = 8.60 (d, ^3J = 3.0 Hz, 1 H, H^3), 8.05 (td, ^3J = 3.0, 9.0 Hz, 1 H, H^5), 7.95 (d, ^3J = 9.0 Hz, 1 H, H^6), 7.58 (m, 1 H, H^4) ppm. ^{13}C NMR (100 MHz, [D$_6$]DMSO, 30 °C): δ = 162.18 (C^1), 149.91 (C^5), 139.53 (C^3), 125.24 (C^4), 121.35 (C^6) ppm. FTIR (KBr): $\tilde{\nu}$ = 3422 (m), 1617 (w), 1579 (m), 1458 (m), 1425 (m), 1291 (w), 1208 (s), 1164 (m), 1093 (m), 1049 (m), 1040 (m), 994 (m), 777 (m), 747 (m), 645 (s), 618 (m), 566 (m), 556 (m) cm^{-1}. FTIR (Nujol): $\tilde{\nu}$ = 3394 (w), 1634 (w), 1584 (w), 1429 (m), 1294 (w), 1256 (m), 1232 (m), 1207 (s), 1165 (s), 1146 (s), 1094 (m), 1049 (s), 1019 (m), 1005 (m), 7778 (m), 736 (m), 628 (m) cm^{-1}. ESI-MS^+ (solvent: CH_2Cl_2): *m*/*z* (%) = 456/458/460 (5) {triplet (1/2/1 $^{107}Ag/^{107/109}Ag/^{109}Ag$), $[Ag_2L(CH_2Cl_2)]^+$}; 372/374/376 (10) {triplet (1/2/1 $^{107}Ag/^{107/109}Ag/^{109}Ag$), $[Ag_2L]^+$}; 191/193 (100) {doublet (1/1 $^{107}Ag/^{109}Ag$), $[Ag(CH_2Cl_2)]^+$}; 107/109 (60) {doublet (1/1), $[Ag]^+$}. $C_5H_4AgNO_3S$ (266.022): calcd. C 22.57, H 1.52, N 5.27; found C 22.77, H 1.40, N 5.22.

X-ray Crystallography: Crystalline samples of **1**, **2**, **4a** and **4b** were mounted onto a glass fibre in viscous hydrocarbon oil. Crystal data were collected with either an Enraf–Nonius Kappa CCD or a Bruker X8 APEX CCD instrument with monochromated Mo-K_α radiation, λ = 0.71073 Å. All data were collected at 123 K, maintained using an open flow of nitrogen from an Oxford Cryostreams cryostat. X-ray data were processed with the DENZO program.[15] Structural solution and refinement was carried out using SHELXL-97[16] with the graphical interface X-Seed.[17] Data were corrected for absorption using the SADABS[18] package. The refinements were carried out by using full-matrix least-squares techniques on F^2, minimizing the function $(F_o - F_c)^2$, for which the weight is defined as $4F_o^2/2F_{o(2)}$ and F_o and F_c are the observed and calculated structure factor amplitudes using the program SHELXL-97.[16] During the refinement of **2**, the Flack parameter

Table 4. Crystallographic data and structure refinement for compounds **1**, **2**, **4a** and **4b**.

	1	**2**	**4a**	**4b**
Formula	$C_6H_6AgNO_3S$	$C_6H_6AgNO_3S$	$C_{10}H_{10}AgNO_4S$	$C_{10}H_8AgNO_3S{\cdot}H_2O$
M_r	280.05	280.05	348.12	348.12
Crystal size [mm]	0.28 × 0.16 × 0.13	0.42 × 0.26 × 0.23	0.21 × 0.23 × 0.15	0.45 × 0.15 × 0.30
Crystal system	monoclinic	orthorhombic	monoclinic	monoclinic
Space group	$P2_1/c$ (no. 14)	$P2_12_12_1$ (no. 19)	$P2_1$ (no. 4)	$C2/c$ (no. 15)
a [Å]	5.5730(11)	5.7400(11)	7.2689(15)	22.4750(5)
b [Å]	17.435(4)	8.3240(17)	7.5693(15)	7.4410(15)
c [Å]	7.8510(16)	16.477(3)	9.6200(19)	14.5490(3)
α [°]	90	90	90	90
β [°]	108.43(3)	90	104.48(3)	123.05(3)
γ [°]	90	90	90	90
V [Å^3]	723.7(3)	787.3(3)	512.47(18)	2039.4(10)
Z	4	4	2	8
T [K]	123(2)	123(2)	123(2)	123(2)
$\rho_{calcd.}$ [g cm^{-1}]	2.570	2.363	2.256	2.268
μ [mm^{-1}]	3.030	2.785	2.171	2.182
Reflections collected/unique	7215/1713	22987/3402	2423/2037	28377/3861
Flack *x*	–	0.50(2)	0.18(6)	–
R_{int}	0.0593	0.0394	0.0528	0.0371
*R*1 [$I > 2\sigma(I)$]	0.0368	0.0315	0.0580	0.0335
*wR*2 (all data)	0.0909	0.0467	0.1417	0.0598
GoF	1.177	1.059	1.059	1.084

was 0.5, which was not due to missing symmetry. Therefore the data was refined as a racemic twin. The final values of refinement parameters are given in Table 4.

CCDC-848459 (for **1**), -848460 (for **2**), -848461 (for **4a**) and -848462 (for **4b**) contain the supplementary crystallographic data for this paper. These data can be obtained free of charge from The Cambridge Crystallographic Data Centre via www.ccdc.cam.ac.uk/data_request/cif.

Acknowledgments

We thank the Australian Research Council and Monash University for funding.

[1] a) U. S. Agarwal, S. Thampi, A. K. Jain, Reliance Industries Limited, India, **2009**, PCT Int. Appl. WO 2009072144; b) D. Baram-Pinto, S. Shukla, N. Perkas, A. Gedanken, R. Sarid, *Bioconjugate Chem.* **2009**, *20*, 1497–1502; c) X. Cao, M. Tang, F. Liu, Y. Nie, C. Zhao, *Colloids Surf. B: Biointerfaces* **2010**, *81*, 555–562; d) T. Kawakami, S. Teshima, Y. Asako, H. Tsuboi, Nippon Shokubai Kagaku Kogyo Co., Ltd., Japan, **1997**, Jpn. Kokai Tokkyo Koho JP 09301812; e) K. Shirai, Y. Ishii, S. Nomura, S. Shoji, O. Suzuki, T. Sato, Nippi Inc., Japan, **2002**, Jpn. Kokai Tokkyo Koho JP 2002220311; f) L. Stephen, Specialty Fibres and Materials Limited, UK, **2010**, PCT Int. Appl. WO 2010061225; g) D. Vachon, G. E. Wnek, Aegis Biosciences, LLC, USA, **2001**, US Pat. Appl. US 6306419; h) K. Vasilev, V. R. Sah, R. V. Goreham, C. Ndi, R. D. Short, H. J. Griesser, *Nanotechnology* **2010**, *21*, 215102/1–215102/6.

[2] a) A. P. Cote, M. J. Ferguson, K. A. Khan, G. D. Enright, A. D. Kulynych, S. A. Dalrymple, G. K. H. Shimizu, *Inorg. Chem.* **2002**, *41*, 287; b) A. P. Cote, G. K. H. Shimizu, *Inorg. Chem.* **2004**, *43*, 6663–6673; c) D. J. Hoffart, S. A. Dalrymple, G. K. H. Shimizu, *Inorg. Chem.* **2005**, *44*, 8868–8875; d) S. K. Makinen, N. J. Melcer, M. Parvez, G. K. H. Shimizu, *Chem. Eur. J.* **2001**, *7*, 5176; e) G. K. H. Shimizu, G. D. Enright, C. I. Ratcliffe, K. F. Preston, J. L. Reid, J. A. Ripmeester, *Chem. Commun.* **1999**, 1485–1486; f) G. K. H. Shimizu, G. D. Enright, C. I. Ratcliffe, G. S. Rego, J. L. Reid, J. A. Ripmeester, *Chem. Mater.* **1998**, *10*, 3282–3283; g) G. K. H. Shimizu, G. D. Enright, C. I. Ratcliffe, J. A. Ripmeester, *Chem. Commun.* **1999**, 461–462; h) G. Smith, B. A. Cloutt, D. E. Lynch, K. A. Byriel, C. H. L. Kennard, *Inorg. Chem.* **1998**, *37*, 3236–3242; i) F. Charbonnier, R. Faure, H. Loiseleur, *Cryst. Struct. Commun.* **1981**, *10*, 1129; j) C.-H. Chen, J.-W. Cai, X.-L. Feng, X.-M. Chen, *Polyhedron* **2002**, *21*, 689; k) G. Smith, J. H. Thomasson, J. M. White, *Aust. J. Chem.* **1999**, *52*, 317; l) N. J. Melcer, G. D. Enright, J. A. Ripmeester, G. K. H. Shimizu, *Inorg. Chem.* **2001**, *40*, 4641; m) G. K. H. Shimizu, G. D. Enright, G. S. Rego, J. A. Ripmeester, *Can. J. Chem.* **1999**, *77*, 313; n) J.-F. Ma, J. Yang, S.-L. Li, S.-Y. Song, H.-J. Zhang, H.-S. Wang, K.-Y. Yang, *Cryst. Growth Des.* **2005**, *5*, 807; o) A. D. Kulynych, G. K. H. Shimizu, *CrystEngComm* **2002**, *18*, 102; p) G. Wulfsberg, K. D. Parks, R. Rutherford, D. J. Jackson, F. E. Jones, D. Derrick, W. Ilsley, S. H. Strauss, S. M. Miller, O. P. Anderson, T. A. Babushkina, S. I. Gushchin, E. A. Kravchenko, V. G. Morgunov, *Inorg. Chem.* **2002**, *41*, 2032; q) D. Sun, R. Cao, Y. Liang, M. Hong, *Chem. Lett.* **2002**, 198; r) D. Sun, R. Cao, Y. Sun, W. Bi, X. Li, M. Hong, Y. Zhao, *Eur. J. Inorg. Chem.* **2003**, 38; s) D. Sun, R. Cao, W. Bi, X. Li, Y. Wang, M. Hong, *Eur. J. Inorg. Chem.* **2004**, 2144; t) L. J. May, G. K. H. Shimizu, *Chem. Mater.* **2005**, *17*, 217; u) P. F. Charbonnier, *Acta Crystallogr. Sect. B: Struct. Crystallogr. Cryst. Chem.* **1977**, *33*, 2824; v) P. F. Charbonnier, R. F. H. Loiseleur, *Acta Crystallogr. Sect. B: Struct. Crystallogr. Cryst. Chem.* **1978**, *34*, 3598; w) P. F. Charbonnier, R. F. H. Loiseleur, *Acta Crystallogr. Sect. B: Struct. Crystallogr. Cryst. Chem.* **1979**, *35*, 1773; x) M. Sebastian, H. K. Y. John, J. V. Jagadese, *J. Chem. Soc. Dalton Trans.* **2002**, 4561.

[3] a) X.-H. Bu, H. Liu, M. Du, K. M.-C. Wong, V. W.-W. Yam, M. Shionoya, *Inorg. Chem.* **2001**, *40*, 4143; b) Y.-B. Dong, J.-Y. Cheng, R.-Q. Huang, *Inorg. Chem.* **2003**, *42*, 5699; c) Y.-B. Dong, J.-P. Ma, R.-Q. Huang, *Inorg. Chem.* **2003**, *42*, 294; d) R. P. Feazell, C. E. Carson, K. Klausmeyer, *Inorg. Chem.* **2006**, *45*, 2635; e) K. A. Hirsch, S. R. Wilson, J. S. Moore, *Inorg. Chem.* **1997**, *36*, 2960; f) C. Kaes, M. W. Hosseini, C. E. F. Rickard, B. W. Skelton, A. H. White, *Angew. Chem.* **1998**, *110*, 970; *Angew. Chem. Int. Ed.* **1998**, *37*, 920; g) F.-F. Li, J.-F. Ma, S.-Y. Song, J. Yang, H.-Q. Jia, N.-H. Hu, *Cryst. Growth Des.* **2006**, *6*, 209; h) F.-F. Li, J.-F. Ma, S.-Y. Song, J. Yang, Y.-Y. Liu, Z.-M. Su, *Inorg. Chem.* **2005**, *44*, 9374–9383; i) F.-F. Li, J.-F. Ma, J. Yang, H.-Q. Jia, N.-H. Hu, *THEOCHEM* **2006**, *787*, 106; j) C.-S. Liu, P.-Q. Chen, E.-C. Yang, J.-L. Tian, X.-H. Bu, Z.-M. Li, H.-W. Sun, Z. Lin, *Inorg. Chem.* **2006**, *45*, 5812; k) H.-Y. Liu, H. Wu, J.-F. Ma, S.-Y. Song, J. Yang, Y.-Y. Liu, Z.-M. Su, *Inorg. Chem.* **2007**, *46*, 7299; l) H.-Y. Liu, H. Wu, J.-F. Ma, J. Yang, Y.-Y. Liu, *Dalton Trans.* **2009**, 7957–7968; m) K. Matsumoto, Y. Harada, N. Yamada, H. Kurata, T. Kawase, M. Oda, *Cryst. Growth Des.* **2006**, *6*, 1083; n) G. Smith, B. A. Cloutt, K. A. Byriel, C. H. L. Kennard, *Aust. J. Chem.* **1997**, *50*, 741; o) G. Smith, D. E. Lynch, C. H. L. Kennard, *Inorg. Chem.* **1996**, *35*, 2711; p) D. Sun, R. Cao, Y. Sun, W. Bi, X. Li, Y. Wang, Q. Shi, X. Li, *Inorg. Chem.* **2003**, *42*, 7512; q) H. Wu, X.-W. Dong, H.-Y. Liu, J.-F. Ma, S.-L. Li, J. Yang, Y.-Y. Liu, Z.-M. Su, *Dalton Trans.* **2008**, 5331–5341; r) S.-P. Yang, X.-M. Chen, L.-N. Ji, *J. Chem. Soc. Dalton Trans.* **2000**, 2337.

[4] Y. Jimbo, E. Takahashi, Y. Shimada, K. Sato, Fujifilm Corporation, Japan, **2008**, Eur. Pat. Appl. EP 1889601.

[5] a) J. Ibata, Y. Shimamura, Asahi Chemical Industry Co., Ltd., Japan, **1989**, Jpn. Kokai Tokkyo Koho JP 01274129; b) R. A. Lee, du Pont de Nemours, E. I., and Co., USA, **1985**, US Pat. Appl. US 4504575.

[6] a) B. D. Chandler, A. P. Cote, D. T. Cramb, J. M. Hill, G. K. H. Shimizu, *Chem. Commun.* **2002**, 1900; b) A. P. Cote, G. K. H. Shimizu, *Chem. Commun.* **2001**, 251; c) A. P. Cote, G. K. H. Shimizu, *Coord. Chem. Rev.* **2003**, *245*, 49–64; d) A. P. Cote, G. K. H. Shimizu, *Chem. Eur. J.* **2003**, *9*, 5361; e) S. A. Dalrymple, M. Parvez, G. K. H. Shimizu, *Chem. Commun.* **2001**, 2672; f) S. A. Dalrymple, M. Parvez, G. K. H. Shimizu, *Inorg. Chem.* **2002**, *41*, 6986; g) S. A. Dalrymple, G. K. H. Shimizu, *Chem. Commun.* **2002**, 2224; h) S. A. Dalrymple, G. K. H. Shimizu, *Chem. Eur. J.* **2002**, *8*, 3010; i) D. J. Hoffart, A. P. Cote, G. K. H. Shimizu, *Inorg. Chem.* **2003**, *42*, 8603; j) D. S. Reddy, S. Duncan, G. K. H. Shimizu, *Angew. Chem.* **2003**, *115*, 1398; *Angew. Chem. Int. Ed.* **2003**, *42*, 1360; k) J. O. Yu, A. P. Cote, G. D. Enright, G. K. H. Shimizu, *Inorg. Chem.* **2001**, *40*, 582; l) G. K. H. Shimizu, R. Vaidhyanathan, J. M. Taylor, *Chem. Soc. Rev.* **2009**, *38*, 1430–1449.

[7] a) J. Cai, *Coord. Chem. Rev.* **2004**, *248*, 1061–1083; b) J. Cai, C.-H. Chen, C.-Z. Liao, J.-H. Yao, X.-P. Hu, X.-M. Chen, *J. Chem. Soc. Dalton Trans.* **2001**, 1137; c) J. W. Cai, C. H. Chen, X. L. Feng, C. Z. Liao, X. M. Chen, *J. Chem. Soc. Dalton Trans.* **2001**, 2370; d) J. W. Cai, C. H. Chen, C. Z. Liao, X. L. Feng, X. M. Chen, *Acta Crystallogr. Sect. B* **2001**, *57*, 520; e) J. W. Cai, J. S. Zhou, M. L. Lin, *J. Mater. Chem.* **2003**, *13*, 1806; f) J.-W. Cai, C.-H. Chen, J.-S. Zhou, *Chin. J. Inorg. Chem.* **2003**, *19*, 81; g) J.-W. Cai, J.-S. Zhou, M.-L. Lin, *J. Mater. Chem.* **2003**, *13*, 1906; h) C. H. Chen, J. W. Cai, C. Z. Liao, X. L. Feng, X. M. Chen, S. W. Ng, *Inorg. Chem.* **2002**, *41*, 4967; i) J.-S. Zhou, J. Cai, L. Wang, *Dalton Trans.* **2004**, 1493.

[8] a) J. L. Atwood, L. J. Barbour, M. J. Hardie, C. L. Raston, *Coord. Chem. Rev.* **2001**, *222*, 3; b) R. Custelcean, M. D. Ward, *Angew. Chem.* **2002**, *114*, 1800; *Angew. Chem. Int. Ed.* **2002**, *41*, 1724; c) K. T. Holman, A. M. Pivovar, J. A. Swift, M. D. Ward, *Acc. Chem. Res.* **2001**, *34*, 107; d) M. J. Horner, K. T. Holman, M. D. Ward, *Angew. Chem.* **2001**, *113*, 4169; *Angew.*

Chem. Int. Ed. **2001**, *40*, 4045; e) A. R. Kennedy, M. P. Hughes, M. L. Monaghan, E. Staunton, S. J. Teat, W. E. Smith, *J. Chem. Soc. Dalton Trans.* **2001**, 2199; f) G. Mezei, R. G. Rapris, *New J. Chem.* **2003**, *27*, 1399; g) S. H. Park, C. E. Lee, *Chem. Commun.* **2003**, 1838; h) J. A. Swift, M. D. Ward, *Chem. Mater.* **2000**, *12*, 1501; i) X.-L. Zhang, B.-H. Ye, X.-M. Chen, *Cryst. Growth Des.* **2005**, *5*, 1609; j) A. Mietrach, T. W. T. Muesmann, J. Christoffers, M. S. Wickleder, *Eur. J. Inorg. Chem.* **2009**, 5328–5334; k) A. Mietrach, T. W. T. Muesmann, C. Zilinski, J. Christoffers, M. S. Wickleder, *Z. Anorg. Allg. Chem.* **2011**, *637*, 195–200; l) T. W. T. Muesmann, A. Mietrach, J. Christoffers, M. S. Wickleder, *Z. Anorg. Allg. Chem.* **2010**, *636*, 1307–1312; m) T. W. T. Muesmann, C. Zitzer, A. Mietrach, T. Kluener, J. Christoffers, M. S. Wickleder, *Dalton Trans.* **2011**, *40*, 3128–3141; n) T. W. T. Muesmann, C. Zitzer, M. S. Wickleder, J. Christoffers, *Inorg. Chim. Acta* **2011**, *369*, 45–48.

[9] a) G. Alberti, U. Constantino, in: *Inclusion Compounds*. (Eds.: J. L. Atwood, J. E. D. Davis, D. D. MacNicol), Oxford University Press, New York, **1991**, vol. 5, p. 136; b) G. Alberti, U. Constantino in *Comprehensive Supramolecular Chemistry* (Eds.: G. Alberti, T. Bein), Elsevier Science, New York, **1996**, vol. 7; c) A. Clearfield, *Prog. Inorg. Chem.* **1998**, *47*, 371; d) C. P. Johnson, J. L. Atwood, J. W. Steed, C. B. Bauer, R. D. Rogers, *Inorg. Chem.* **1996**, *35*, 2602; e) E. J. Kosnic, E. L. McClymont, R. A. Hodder, P. J. Squattrito, *Inorg. Chim. Acta* **1992**, *201*, 143.

[10] a) B. F. Abrahams, M. J. Hardie, B. F. Hoskins, R. Robson, G. A. Williams, *J. Am. Chem. Soc.* **1992**, *114*, 10641; b) K. Biradha, M. Fujita, *Angew. Chem.* **2002**, *114*, 3542; *Angew. Chem. Int. Ed.* **2002**, *41*, 3392; c) K. Biradha, Y. Hongo, M. Fujita, *Angew. Chem.* **2002**, *114*, 3545; *Angew. Chem. Int. Ed.* **2002**, *41*, 3395; d) C. J. Kepert, T. J. Prior, M. J. Rosseinsky, *J. Am. Chem. Soc.* **2000**, *122*, 5158; e) Z.-X. Lian, J. Cai, C.-H. Chen, *Polyhedron* **2007**, *26*, 2647–2654; f) D. V. Soldatov, J. A. Ripmeester, S. I. Shergina, I. E. Sokolov, A. S. Zanina, S. A. Gromilov, Y. A. Dyadin, *J. Am. Chem. Soc.* **1999**, *121*, 4179; g) D. V. Soldatov, P. Tinnemans, G. D. Enright, C. I. Ratcliffe, P. R. Diamente, J. A. Ripmeester, *Chem. Mater.* **2003**, *15*, 3826; h) L. C. Tabares, J. A. R. Navarro, J. M. Salas, *J. Am. Chem. Soc.* **2001**, *123*, 393; i) K. Uemura, S. Kitagawa, K. Fukui, K. Saito, *J. Am. Chem. Soc.* **2004**, *126*, 3817; j) K. Uemura, S. Kitagawa, M. Kondo, K. Fukui, R. Kitaura, H. C. Chang, T. Mizutani, *Chem. Eur. J.* **2002**, *8*, 3586; k) J. J. Vittal, X. Yang, *Cryst. Growth Des.* **2002**, *2*, 259.

[11] a) Z.-P. Deng, L.-H. Huo, M.-S. Li, L.-W. Zhang, Z.-B. Zhu, H. Zhao, S. Gao, *Cryst. Growth Des.* **2011**, *11*, 3090–3100; b) Z.-P. Deng, M.-S. Li, Z.-B. Zhu, L.-H. Huo, H. Zhao, S. Gao, *Organometallics* **2011**, *30*, 1961–1967; c) Z.-P. Deng, Z.-B. Zhu, S. Gao, L.-H. Huo, H. Zhao, *Dalton Trans.* **2009**, *38*, 1290–1292; d) Z.-P. Deng, Z.-B. Zhu, S. Gao, L.-H. Huo, H. Zhao, S. W. Ng, *Dalton Trans.* **2009**, *38*, 6552–6561.

[12] a) A. Leon, *Historia Natural das Doencas Mexico, Mexico* **1992**, *Centro de Documentacion Institucional*, p. 782; b) Y.-J. Pan, F.-J. Meng, X.-J. Wang, H.-L. Zhu, D.-Q. Wang, *Z. Kristallogr. New Cryst. Struct.* **2003**, *218*, 253–254; c) J. Schreuer, *Z. Kristallogr. New Cryst. Struct.* **1999**, *214*, 311–312; d) O. Sadeghi, M. M. Amini, S. W. Ng, *Acta Crystallogr. Sect. E Struct. Rep. Online* **2010**, *66*, m855–m856; e) F. R. Ahmed, D. W. J. Cruickshank, *Acta Crystallogr.* **1952**, *5*, 852.

[13] M. Tanabe, R. H. Peters, *Org. Synth. Coll. Vol.* **1990**, 7.

[14] J. W. Steed, J. L. Atwood, *Supramolecular Chemistry*, Wiley, Toronto, **2000**, p. 19.

[15] Z. Otwinowski, W. Minor, *Methods Enymol.* **1997**, *276*, 307.

[16] G. M. Sheldrick, *Acta Crystallogr. Sect. A* **2008**, *64*, 112.

[17] L. J. Barbour, *XSEED: A graphical interface for use with the SHELX97 program suite*, University of Missouri, USA, **1999**.

[18] G. M. Sheldrick, *SADABS, Program for area detector adsorption correction*, Institute for Inorganic Chemistry, University of Göttingen, Germany, **1996**.

Received: October 14, 2011
Published Online: January 31, 2012

DOI: 10.1002/ejic.201101230

Derivatives of Photosensitive CORM-S1 – CO Complexes of Iron and Ruthenium with the $(OC)_2M(S–C–C–NH_2)_2$ Fragment

Vaneza P. Lorett Velásquez,[a][‡] Taghreed M. A. Jazzazi,[a][‡] Astrid Malassa,[a] Helmar Görls,[a] Guido Gessner,[b] Stefan H. Heinemann,[b] and Matthias Westerhausen*[a]

Keywords: Carbonyl ligands / Carbon monoxide / CO-releasing molecules / Iron / Ruthenium / Medicinal chemistry

$[Fe(CO)_2(SCH_2CH_2NH_2)_2]$ (**1**, CORM-S1), $[Fe(CO)_2(SC_6H_4\text{-}2\text{-}NH_2)_2]$ (**2**, CORM-S2), $[Ru(CO)_2(SCH_2CH_2NH_2)_2]$ (**3**), and $[Ru(CO)_2(SC_6H_4\text{-}2\text{-}NH_2)_2]$ (**4**) were prepared from the corresponding metal carbonyl compounds and cysteamine (deprotonation of the thiol functionality) or cystamine (oxidative addition of the S–S bond). They crystallized from donor solvents, such as tetrahydrofuran and dimethylformamide, as adducts with the bases bound by hydrogen bridges to the amino functionalities. Although the iron derivatives proved to be valuable photosensitive CO-releasing molecules (CORMs), CO was not released from the ruthenium analogs with visible light.

Introduction

Carbon monoxide is a colorless toxic gas, which blocks oxygen transport in the blood. However, substantial amounts of CO are endogenously produced in animals and humans, mostly by the enzyme-driven degradation of heme to yield Fe^{2+}, CO, and biliverdin. CO, thus released, is an essential signaling molecule. Many physiological effects have been documented for the controlled application of CO[1–5] such as the regulation of blood pressure, modulation of vascular smooth muscle tone, and protection against ischemia, septic shock, and hypoxia. In addition, CO shows diverse beneficial properties, such as the suppression of organ graft rejection and arteriosclerotic lesions, and possesses anti-inflammatory, antiapoptotic, and antiproliferative functions.[6,7] Therefore, intense research efforts have been directed towards CO as a potentially valuable pharmaceutical.[8,9] However, owing to its toxicity, direct volumetric dosing of CO gas in therapeutic applications is challenging. Therefore, for scientific and clinical applications CO-releasing molecules (CORMs) are needed as carriers to supply a definite amount of CO to a predetermined location.[10–15] For that purpose, CORMs should fulfill specific requirements such as solubility in aqueous solutions, low toxicity of the CORMs and their degradation products, and a mode of CO release that can be triggered (e.g. by a change of pH, ligand substitution, or light irradiation). To date, the most important CORMs are water-insoluble $[Mn_2(CO)_{10}]$ (CORM-1, light-dependent CO release) and $[RuCl(\mu\text{-}Cl)(CO)_3]_2$ (CORM-2, CO release by ligand substitution) and water-soluble $[Ru(Cl)(CO)_3(H_2NCH_2COO)]$ (CORM-3, CO release by ligand substitution), $Na_2[H_3B–COO]$ (CORM-A1, pH-controlled CO release),[2,5] and $[Mn(CO)_3(tpm)]Br$ [light-dependent CO release, tpm = tris(pyrazolyl)methane].[14,15] Metal carbonyl complexes are appropriate carriers for CO and are a promising class of pharmaceuticals.[16]

Iron-based CORMs[17] represent a promising target because iron is a nontoxic 3d metal whose concentration is tightly regulated in biological systems. Therefore it is not surprising that these compounds have been investigated for many years. Photolabile iron carbonyl complexes are well known,[18–31] and quantum chemical investigations have been performed to shed light on the CO-releasing properties of CORMs.[32] Photolabile ruthenium carbonyl complexes, in analogy to iron, also represent an important target because these systems are often more air stable and less labile. In particular, bis(carbonyl)ruthenium–salen complexes have received considerable attention owing to their catalytic efficiency for C–O, C–C, C–N, and N–S bond formation reactions.[33] The catalysts were activated with light to remove at least one CO molecule. The early investigations of Cremer showed that iron complexes with biogenic ligands such as cysteine and isocysteine reversibly bind CO.[34,35] A systematic approach verified that iron(II) thiolates generally act as reversible CO carriers,[23] which make these compounds ideal CORMs for medical and physiological applications. $[Fe(CO)_2(SCH_2CH_2NH_2)_2]$ (**1**, CORM-S1) and $[Fe(CO)_2(SC_6H_4\text{-}2\text{-}NH_2)_2]$ (**2**, CORM-S2) were prepared from $FeSO_4$ and the appropriate thiol in methanol in the presence of NEt_3 in a CO atmosphere in

[a] Institute of Inorganic and Analytical Chemistry, Friedrich Schiller University Jena,
August-Bebel-Str. 2, 07743 Jena, Germany
Fax: +49-3641-948102
E-mail: m.we@uni-jena.de
[b] Center for Molecular Biomedicine, Department of Biophysics, Friedrich Schiller University Jena and Jena University Hospital, Hans-Knöll-Strasse 2, 07745 Jena, Germany
[‡] Equal contributors

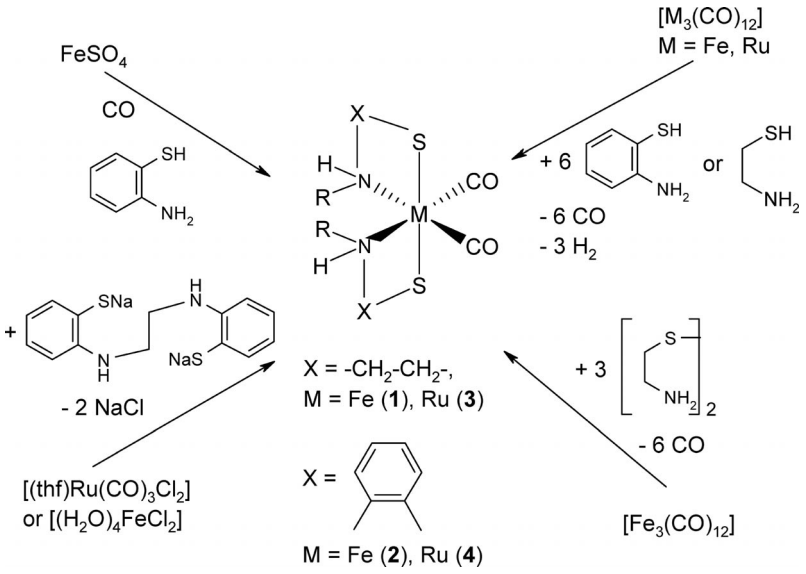

Scheme 1. Synthesis of **1**–**4**.

poor yields (Scheme 1).[25] A similar procedure using KOH as a base was published for the synthesis of **2** in 43% yield,[36] which crystallized as **2**·THF with the THF molecule bridging the amino functionalities through hydrogen bridges. However, the bridging THF clamp does not influence the coordination pattern of iron(II) because in complexes of the type $[Fe(CO)_2(SR)_2(en)]$ (en = ethylenediamine), the thiolate ligands also show a *trans* arrangement and the two carbonyl ligands a *cis* alignment. We have shown in physiological studies that THF-free **1** is an ideal CORM with a similar coordination sphere of the iron(II) center that releases CO upon irradiation with visible light.[29,30] This complex was prepared from carbonyliron complexes and cysteamine in good yields.

In addition, **2** was prepared from the reaction of bis(2-aminophenyl)disulfane with the $[HFe(CO)_4]^-$ anion.[37] Mechanistically, the first step was proposed as the addition of the Fe–H bond to the disulfane moiety to give intermediate $[(OC)_4Fe(SC_6H_4\text{-}2\text{-}NH_2)]^-$ with the liberation of 2-aminothiophenol. The oxidative addition of another equivalent of disulfane to this iron(0) anion yielded $[(OC)_3Fe(SR)_3]^-$. Subsequent loss of a 2-aminothiophenolate anion and one carbonyl molecule finally gave **2**.

Ruthenium-based CORMs (e.g. CORM-2 and CORM-3) release CO upon ligand substitution. The orange-brown diamagnetic complex $[Ru(CO)_2(SC_6H_4\text{-}2\text{-}NH_2)_2]$ (**4**) was prepared in 30% yield by the reduction of $RuCl_3$ with CO in ethanol and subsequent addition of 2-aminothiophenol.[38] The IR spectrum of **4** shows CO stretching vibrations at 2035 and 1970 cm^{-1}. Iron and ruthenium complexes with comparable metal environments have been studied by Sellmann and coworkers[39–43] who showed that these complexes are thermally stable but release one CO ligand upon UV irradiation, which leads to ligand substitution. These compounds were prepared from the reaction of $[(thf)Ru(CO)_3Cl_2]$ with the sodium salt of 1,2-bis(2-mercaptoanilino)ethane and 2,3-bis(2-mercaptoanilino)butane (Scheme 1)[39] and show coordination spheres similar to the related iron(II) compounds. The promising properties of **1** and the possibility to activate the Sellmann complexes with UV light led to an expansion of our investigations with respect to photosensitive CORMs.

Results and Discussion

Synthesis

The iron(II) complexes **1** and **2**, and the homologous Ru-based derivatives $[Ru(CO)_2(SCH_2CH_2NH_2)_2]$ (**3**) and **4** were prepared in good yields from the direct metalation of the appropriate thiol with carbonyliron or -ruthenium complexes or by the oxidative addition of cystamine to carbonyliron compounds (Scheme 1). These approaches ease the work up because gaseous byproducts are easily removed and no salt-like byproducts enforce purification by fractional crystallization.

Molecular Structures

The iron-based CORMs **1** and **2** form THF adducts through hydrogen bridges, and these adducts are displayed in Figure 1. Although the environments of the iron(II) centers are very similar in **1** and **2**, additional THF molecules show different coordination modes. In **2**, the THF molecule occupies a bridging position between the two amino functionalities,[25] whereas the THF molecule is only bound to one amino group in **1**.

The molecular structures of **3** and **4** are shown in Figures 2 and 3, respectively, together with representations of their adducts with solvent molecules. Complexes **1** and **3** precipitate from THF with isotypic crystal structures, which both show a THF molecule bound to one of the amino

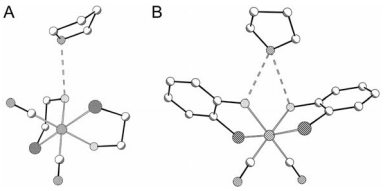

Figure 1. Structural models of **1**·THF (A) and **2**·THF (B). The heavy atoms are shown with arbitrary radii, and H atoms are omitted for clarity. The THF molecules are bound by N–H···O_{thf} hydrogen bridges.

functionalities. Complex **4** was recrystallized from *N*,*N*-dimethylformamide (DMF), and a DMF adduct formed during crystallization. Nevertheless, the adduct formation of **4** shows far-reaching similarities with that of **2**. The coordination spheres of the metal centers in all of these complexes are very similar with *cis*-arranged carbonyl ligands. Due to electrostatic repulsion, the thiolato anions show a *trans* arrangement. Selected physical parameters are summarized in Table 1 and data for **1**[29] are included for comparison. The structural parameters are very similar and the metal atoms have only a weak influence on the structural data. Due to the fact that the Ru–S and Ru–N bonds are longer than the corresponding Fe–S and Fe–N bonds in **1** and **2**, a small N···S distance (bite) of the chelate ligands leads to endocyclic S–Ru–N bond angles, which are smaller than the corresponding values for the iron compounds.

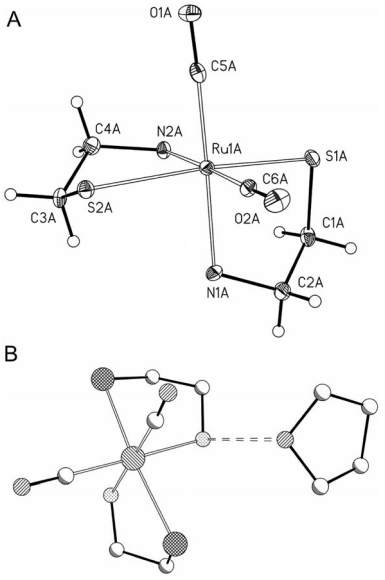

Figure 2. Molecular structure and numbering scheme of **3** (A). The asymmetric unit contains two molecules but only one is displayed. H atoms are drawn with arbitrary radii. (B) The structure of **3**·THF with the coordination of THF through a hydrogen bridge. Selected bond lengths [pm]: Ru1A–S1A 241.7(2), Ru1A–S2A 240.7(1), Ru1A–N1A 216.8(4), Ru1A–N2A 217.2(4), Ru1A–C5A 186.1(6), Ru1A–C6A 187.1(6), C5A–O1A 114.3(7), C6A–O2A 114.6(7); selected bond angles [°]: S1A–Ru1A–S2A 167.88(5), N1A–Ru1A–C5A 178.6(2), N2A–Ru1A–C6A 178.2(2), S1A–Ru1A–N1A 83.6(1), S2A–Ru1A–N2A 84.0(1), S1A–Ru1A–N2A 86.2(1), S2A–Ru1A–N1A 88.8(1), S1A–Ru1A–C5A 97.5(2), S2A–Ru1A–C5A 90.0(2), S1A–Ru1A–C6A 94.9(2), S2A–Ru1A–C6A 94.7(2), C5A–Ru1A–C6A 89.2(2).

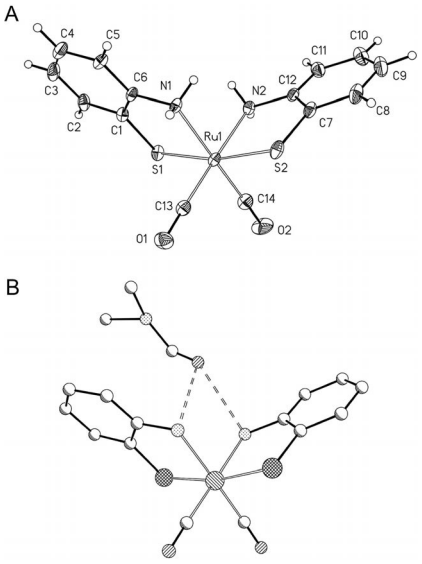

Figure 3. Molecular structure and numbering scheme of **4** (top; the ellipsoids represent a probability of 40%, and H atoms are shown with arbitrary radii) and the structure of **4**·DMF (bottom; atoms drawn with arbitrary radii, H atoms omitted for clarity). Selected bond lengths [pm]: Ru1–S1 239.4(1), Ru1–S2 239.3(1), Ru1–N1 214.9(4), Ru1–N2 215.5(4), Ru1–C13 186.7(5), Ru1–C14 187.6(5), C13–O1 114.2(6), C14–O2 114.3(6); selected bond angles [°]: S1–Ru1–S2 168.54(5), N1–Ru1–C14 177.5(2), N2–Ru1–C13 178.7(2), S1–Ru1–N1 83.8(1), S2–Ru1–N2 83.4(1), S1–Ru1–N2 89.0(1), S2–Ru1–N1 87.4(1), S1–Ru1–C13 92.2(2), S2–Ru1–C14 94.2(2), S1–Ru1–C14 94.3(2), S2–Ru1–C13 95.5(2), C13–Ru1–C14 89.2(2).

Table 1. Comparison of physical data of **1**–**4** (average values for bond lengths [pm] and angles [°]).

	1	**2**	**3**	**4**
M	Fe	Fe	Ru	Ru
ν_{as}(CO) [cm^{-1}]	2014	2035	2023	2044
ν_{s}(CO) [cm^{-1}]	1945	1976	1950	1989
$\delta(^{13}CO)$ [ppm]	215.0	213.6	201.3	189.3
$M–C_{CO}$	176.8	178.0	186.6	187.2
M–N	204.4	203.9	217.4	215.2
M–S	230.6	229.3	241.2	239.4
C–M–C	90.7	88.3	89.8	89.2
S–M–S	172.9	174.8	168.5	168.5
N–M–N	89.1	89.9	87.0	87.9
$S–M–N_{endo}$	86.0	85.8	83.8	83.6
$S–M–N_{exo}$	89.0	90.5	87.9	88.2
S–M–C	92.5	91.9	94.1	94.1
$N–M–C_{trans}$	178.0	178.9	178.3	178.1
$N–M–C_{cis}$	89.8	90.9	91.6	91.5

Larger differences with respect to the metal center and substitution pattern of the chelate base are evident for the CO stretching frequencies and the ^{13}C chemical shifts of the carbonyl ligands in the IR and NMR spectra, respectively. Takács et al.[25] reported identical stretching frequencies of 2020 and 1963 cm^{-1} for **1** and **2** in methanol solution. Nujol suspensions of pure compounds, however, gave another picture, which is in agreement with the trend of the parameters

of **3** and **4**. The aromatic backbone of the chelate base leads to higher wavenumbers by 20 cm^{-1} for the asymmetric and ca. 30 cm^{-1} for the symmetric stretching vibrations. In addition, substitution of iron(II) by ruthenium(II) causes a shift to higher wavenumbers. In agreement with the expectation that the anionic charge on the sulfur atom in **2** and **4** might be partially delocalized into the arene backbone, the π-backdonation from the metal center into the π*(CO) orbital is lower than in complexes with an aliphatic backbone. This situation leads to a shift of the ^{13}C NMR resonances to lower frequency for the complexes with bidentate 2-thiolatoaniline bases.

The IR spectrum of DMF-free **4** shows characteristic vibrations at 3243 and 3235 cm^{-1} for the NH_2 group and at 2044 and 1989 cm^{-1} in the carbonyl region. Upon formation of a DMF adduct, the NH_2 vibrations shifted to lower wavenumbers and two bands at 2044 and 1963 cm^{-1} were observed in the carbonyl region (Figure 4). Recrystallization of **4** from DMF yielded the DMF adduct, however, storage at room temperature led to partial loss of DMF and deterioration of the crystals. Due to the fixed geometry of the bidentate chelating ligands, the protons at the nitrogen atoms are chemically nonequivalent, which leads to significantly different chemical shifts in the ^1H NMR spectra of 3.85 and 5.00 ppm for **3** and of 5.75 and 6.83 ppm for **4**.

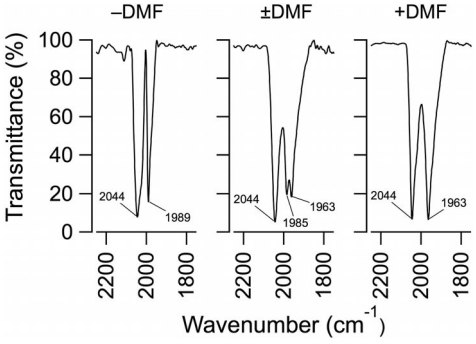

Figure 4. IR spectra of the carbonyl region of **4** (left), **4**·DMF (right), and **4**·DMF with partial loss of DMF (center).

CO Release Properties

Light-triggered CORMs are useful therapeutic agents.[1,4] Therefore, CO release during irradiation with visible light in a buffer solution was studied with a myoglobin assay. For neither **3** or **4**, even at a concentration of 200 μM, could we observe release of CO upon irradiation with visible light from a cold light source (Figure 5, A). Hence, **3** and **4** cannot be used as photo-CORMs in the visible light domain. Sellmann and coworkers[39] have shown that only one CO molecule was liberated during irradiation with a mercury lamp in the presence of triphenylphosphane, which led to the formation of complexes with one CO and one phosphane ligand bound to ruthenium. However, the use of UV light from a mercury source for the activation of metal complexes is limited because of its phototoxicity, which ultimately damages cells and tissues.

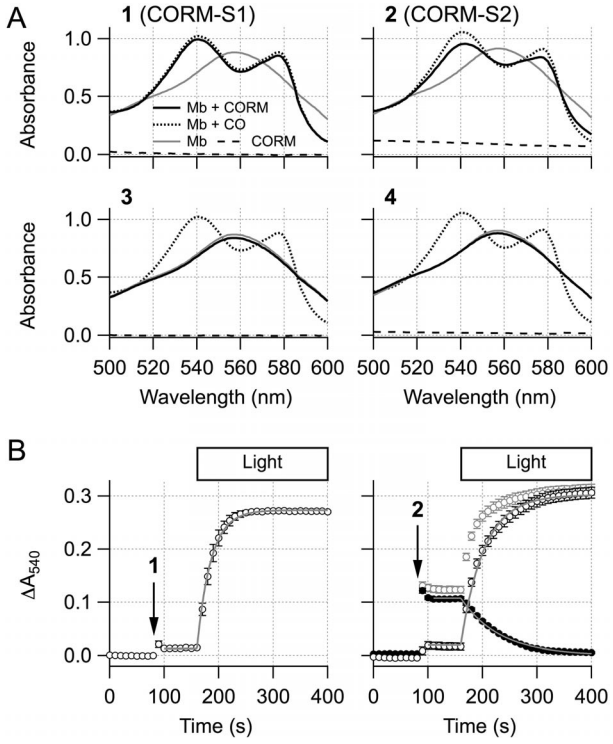

Figure 5. Light dependence of CO release. (A) Absorption spectra for **1**–**4**: compound without myoglobin (dashed line), myoglobin alone (gray), myoglobin saturated with CO (dotted line), and myoglobin with the compound after irradiation with visible light (black). Each trace is the mean of four or five measurements. (B) Absorbance of **1** and **2** at 540 nm. Compounds **1** and **2** were applied to myoglobin as indicated by the arrows, and the absorbance sharply increased upon irradiation of the samples with visible light. Continuous gray curves are single-exponential fits. On the right, filled data points show the absorbance of **2** alone, which was subtracted from the raw absorbance data (open symbols, gray) to yield the corrected increase in absorbance (open symbols, black), which indicates CO release. Data points are means ± SEM (n = 4–6).

In contrast, 50 μM of iron-based **1** upon irradiation with visible light was sufficient to almost fully convert 100 μM deoxymyoglobin (96.5 ± 2.8%, n = 3; see parts A and B of Figure 5). The same concentration of **2** only released 82.7 ± 6.3 μM CO (n = 4). The time constant (τ) was derived from a single-exponential fit to the data shown in Figure 5 (B). The time course of CO release by **1** was fitted reasonably well by a single exponential function with τ = 26 ± 4 s (n = 4), which suggests that two molecules CO were released practically simultaneously upon the light-induced breakdown of **1**. The CO release from **2**, τ = 43 ± 2 s (n = 6), was significantly ($P < 0.05$ based on a two-sided student's t-test) slower than for **1**, but faster ($P < 0.001$) than the light-induced breakdown of **2** in the absence of myoglobin (τ = 71 ± 2 s, n = 4), indicative of stepwise release of CO (Figure 5, B).

As such a stepwise release of CO should result in at least transient occurrence of CO-containing intermediates, IR spectroscopy was used to follow the light-triggered degradation of these complexes. The CO release properties of **1** have been reported,[29] and IR spectroscopic monitoring during

the light-triggered degradation of **1** showed no evidence of CO-containing intermediates. However, the degradation mechanism of **2** differs significantly, and CO-containing intermediates were observed during the irradiation of **2** at 470 nm (Figure 6). Complex **2** shows two bands at 2035 and 1976 cm^{-1}. Upon irradiation, another band at 1962 cm^{-1} appeared, indicative of a carbonyl-containing intermediate. This supports stepwise release of CO from **2** during irradiation. Extended exposure to light led to further degradation of the carbonyl complexes, and the bands of **2** and its immediate degradation product vanish to give numerous weak bands in the carbonyl region.

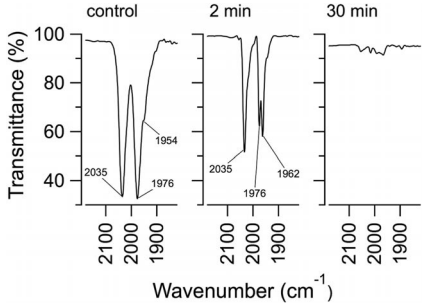

Figure 6. IR spectra of nujol suspensions of the carbonyl region of **2** (left), after 2 min of irradiation (center), and after 30 min of irradiation (right).

Conclusions

CO is a biologically important signaling molecule with several beneficial physiological effects but the enormous toxicity of this gas compromises its application in medicine and biology. Therefore, carriers of CO are needed that can be used as potentially valuable therapeutic agents and pharmaceuticals. In addition, triggered release is necessary to liberate CO at predetermined domains. One approach is to generate photosensitive CORMs based on water-soluble carbonyl complexes. The iron(II) compounds $[Fe(CO)_2(SCH_2CH_2NH_2)_2]$ (**1**) and $[Fe(CO)_2(SC_6H_4\text{-}2\text{-}NH_2)_2]$ (**2**) were prepared from carbonyliron complexes and cysteamine (deprotonation of the thiol functionality) or cystamine (oxidative addition of the S–S bond). These complexes act as CORMs that are stable in the dark and release CO upon irradiation with visible light. Although both compounds contain iron(II) ions in very similar coordination environments, the degradation mechanisms of **1** and **2** differ significantly. Complex **1** liberates both CO molecules at once, whereas stepwise liberation of CO is observed for **2**, which leads to carbonyl-containing intermediates.

The homologous ruthenium derivatives $[Ru(CO)_2(SCH_2CH_2NH_2)_2]$ (**3**) and $[Ru(CO)_2(SC_6H_4\text{-}2\text{-}NH_2)_2]$ (**4**) were also prepared from the deprotonation of cysteamine and 2-aminothiophenol, respectively, with $Ru_3(CO)_{12}$ and show similar molecular structures to the iron derivatives. However, CO release was not achieved with visible light because the metal-centered electronic transitions move to higher energies on going from Fe to Ru.

Complexes **1**–**4** reversibly form adducts with solvent molecules such as THF and DMF, which are bound by N–H···O hydrogen bridges to the amino functionalities.

Experimental Section

General: $Ru_3(CO)_{12}$, $Fe_3(CO)_{12}$, myoglobin from equine skeletal muscle, and sodium dithionite were purchased from Sigma–Aldrich; $HSCH_2CH_2NH_2$, $(H_2NCH_2CH_2S)_2$, and $HSC_6H_4\text{-}2\text{-}NH_2$ from Acros Organics. All compounds were prepared and handled in an inert gas atmosphere under anaerobic conditions using Schlenk techniques. THF and heptane were distilled from sodium benzophenone, and DMF was dried with molecular sieves. ^1H and ^{13}C NMR spectra were obtained with Bruker Avance 200, 400, and 600 MHz spectrometers. Assignment of NMR spectroscopic data was performed on the basis of ^1H, ^{13}C, HSQC, HMBC, and H,H COSY experiments. Mass spectra were obtained with a Finnigan MAT SSQ 710. IR spectra were recorded with a Perkin–Elmer FTIR Spectrometer System 2000 as nujol mulls between KBr windows. Elemental analysis (LECO CHNS-932) gave values for C, H, N, and S. UV/Vis spectra of the myoglobin assay were recorded with an Ultrospec 1100pro spectrophotometer (Amersham Biosciences).

$[Fe(CO)_2(SCH_2CH_2NH_2)_2]$ (1): A suspension of $Fe_3(CO)_{12}$ (510 mg, 1.01 mmol) and 2,2′-disulfanediyldiethanamine (463 mg, 3.04 mmol) in THF (20 mL) were stirred under reflux for 3 h, and an orange suspension was formed. All solids were collected, and the filter cake was dried in vacuo to give pure microcrystalline **1**. The filtrate was reduced to 5 mL and stored at –18 °C to yield red-brown single crystals of **1** suitable for X-ray diffraction. Total yield: 465 mg (1.76 mmol, 58%). The physical data are identical to those published.[29]

$[Fe(CO)_2(SC_6H_4\text{-}2\text{-}NH_2)_2]$ (2): A suspension of $Fe_3(CO)_{12}$ (510 mg, 1.01 mmol) and 2-aminothiophenol (760 mg, 6.07 mmol) in THF (15 mL) were stirred under reflux for 4 h, and a red suspension was formed. The solids were collected by filtration, and the filter cake was dried in vacuo to give pure microcrystalline **2**. The solvent was removed from the filtrate in vacuo and the residue dissolved in THF. Slow diffusion of pentane into this solution at –18 °C gave red-brown single crystals suitable for X-ray diffraction within one week. Total yield: 812 mg (1.88 mmol, 62%); m.p. 155 °C (dec.). ^1H NMR (600 MHz, [D$_6$]DMSO): δ = 1.77 (s, 2 H), 3.59 (s, 2 H), 5.77 (d, J = 14.1 Hz, 2 H), 6.79 (t, J = 7.0 Hz, 2 H), 6.84 (d, J = 14.1 Hz, 2 H), 6.88 (t, J = 7.1 Hz, 2 H), 7.11 (d, J = 7.0 Hz, 2 H), 7.21 (d, J = 7.1 Hz, 2 H) ppm. ^{13}C NMR (600 MHz, [D$_6$]DMSO): δ = 25.1, 67.0, 121.0, 125.7, 125.9, 128.1, 143.4, 147.3, 213.6 ppm. MS (FAB): m/z (%) = 361 $[M + H]^+$ (16), 333 $[M + H – CO]^+$ (10), 305 $[M + H – 2CO]^+$ (56), 304 $[M – 2CO]^+$ (88). IR: 3227 (w), 3153 (m), 3116 (m), 3055 (m), 2925 (vs), 2854 (vs), 2724(w), 2035 (vs), 1976 (vs), 1609 (w), 1589 (m), 1553 (w), 1465 (vs), 1377 (s), 1294 (w), 1261 (w), 1201 (w), 1162 (w), 1138 (w), 1120 (m), 1063 (w), 1041 (m), 934 (w), 889 (m), 803 (w), 779 (w), 753 (m), 740 (s), 722 (m), 682 (m), 640 (w), 608 (m), 545 (m), 527 (s), 504 (m), 487 (w) cm^{-1}. $C_{18}H_{20}FeN_2O_3S_2$ (**2**·THF, 432.34): calcd. C 50.01, H 4.66, N 6.48, S 14.83; found C 49.86, H 4.52, N 6.57, S 15.18.

$[Ru(CO)_2(SCH_2CH_2NH_2)_2]$ (3): Complex **3** was prepared in a manner similar to the preparation of homologous **1**[29] starting from $Ru_3(CO)_{12}$ (645 mg, 1.03 mmol) and cysteamine (463 mg, 7.4 mmol) in THF (20 mL). After 3 h, **3** was isolated as a yellow solid (678 mg, 2.19 mmol, 72%) and recrystallized from a saturated THF solution at 6 °C; dec. above 240 °C. ^1H NMR (200 MHz,

[D$_7$]DMF): δ = 2.53 (m, J = 4.8 Hz, 4 H), 2.89 (m, J = 3.9 Hz, 2 H), 3.21 (m, J = 5.3 Hz, 2 H), 3.85 (br, NH_2, 2 H), 5.00 (m, NH_2, 2 H) ppm. ^{13}C NMR (400 MHz, [D$_7$]DMF): δ = 30.3, 52.23, 201.3 ppm. MS (FAB): m/z (%) = 310 $[M + H]^+$ (83), 282 $[M + H - CO]^+$ (64), 254 $[M + H - 2CO]^+$ (76). IR: 3950 (w), 3852 (w), 3223 (m), 3179 (m), 3091 (m), 2684 (w), 2494 (vw), 2356 (mw), 2023 (s), 1950 (m), 1716 (mw), 1583 (w), 1313 (m), 1269 (m), 1224 (m), 1126 (s), 1054 (s), 971 (m), 917 (m), 846 (m), 668 (m), 632 (m), 593 (s), 546 (m), 525 (s), 492 (m), 473 (m) cm^{-1}. $C_6H_{12}N_2S_2O_2Ru$ (309.07): calcd. C 23.31, H 3.91, N 9.06, S 20.75; found C 23.00, H 3.81, N 8.68, S 20.79.

[Ru(CO)$_2$(SC$_6$H$_4$-2-NH$_2$)$_2$] (4): Complex **4** was prepared from $Ru_3(CO)_{12}$ (146 mg, 0.228 mmol) and 2-aminothiophenol (270 mg, 1.94 mmol) in heptane (20 mL). The suspension was heated to reflux for 3 h and then filtered. The filter cake was dried to yield an orange solid (260 mg, 0.64 mmol, 94%). Crystals of **4** suitable for X-ray diffraction experiments were obtained by layering a saturated DMF solution with diethyl ether at room temp; dec. above 145 °C. ^{1}H NMR (600 MHz, [D$_6$]DMSO): δ = 5.75 (d, J = 12.9 Hz, NH_2, 1 H), 6.78 (t, J = 7.44 Hz, 1 H), 6.83 (d, J = 13.0 Hz, NH_2, 1 H), 6.90 (t, J = 7.5 Hz, 1 H), 7.06 (d, J = 7.80 Hz, 1 H), 7.27 (d, J = 7.80 Hz, 1 H) ppm. ^{13}C NMR (600 MHz, [D$_6$]DMSO): δ = 120.46, 125.35, 125.73, 128.55, 142.12, 146.76, 189.26 ppm. MS (ESI): m/z = 404.9 $[M]^+$, 377 $[M - CO]^+$, 346 $[M - 2CO]^+$. IR: 3562 (w), 3271 (w), 3243 (m), 3225 (m), 3152 (w), 3082 (w), 2735 (w), 2670 (w), 2356 (vw), 2317 (vw), 2240 (w), 2111 (w), 2044 (vs), 1989 (s), 1791 (sw), 1714 (s), 1617 (w), 1586 (m), 1547 (m), 1493 (s), 1434 (m), 1378 (m), 1291 (w), 1265 (w), 1204 (w), 1191 (m), 1136 (m), 1116 (s), 1061 (m), 1035 (m), 967 (w), 939 (w), 865 (vw), 847 (vw), 816 (w), 756 (m), 745 (m), 729 (s), 678 (m), 655 (w), 618 (m), 605 (m), 542 (w), 518 (w), 505 (w), 490 (w) cm^{-1}. $C_{14}H_{12}N_2O_2S_2Ru$ (405): calcd. C 41.48, H 2.96, N 6.91, S 15.80; found C 40.69, H 2.88, N 6.72, S 15.69.

Myoglobin Assay: The amount of CO released from the complexes prepared in this study was evaluated in a spectrophotometric assay by measuring the conversion of deoxymyoglobin to the CO myoglobin complex. Reduced myoglobin solutions (100 μmol/L) were prepared immediately before the experiments by dissolving the protein in phosphate buffered saline (PBS, pH 7.4) with freshly added 0.1% sodium dithionite. Carbonyl complexes were added from 10 mmol/L dimethylsulfoxide stock solutions to a final concentration of 50–200 μmol/L. The light-dependent CO release from the CORMs was measured by recording IR spectra before the carbonyl complexes were added to the deoxymyoglobin solution and 15 min after exposing these solutions to light from a cold light source (20 W halogen lamp, Osram GZX4, with 2 W output power at the end of the light guide; the light guide was placed at the top of a 1 mL cuvette at a distance of 20 mm). The time course of CO release was monitored by measuring the changes in absorbance at 540 nm. For **2**, absorption of the compound itself was corrected for by performing equivalent experiments in the absence of myoglobin. Variations of this assay have been critically reviewed by Atkin et al.[44]

X-ray Structure Determinations: The intensity data for the compounds were collected with a Nonius KappaCCD diffractometer using graphite-monochromated Mo-K_α radiation. Data were corrected for Lorentz and polarization effects but not for absorption effects.[45,46] The molecular structures of **1**[29] and **2**[25] have been reported, but for **1** another modification was observed and for **2** the published structure is based on room temperature data. The structures of **1**–**4** were solved by direct methods (SHELXS)[47] and refined by full-matrix least-squares techniques against F_o^2 (SHELXL-97).[47] The hydrogen atoms bound to the amine groups N1 and N2 of **2** and **4** were located by difference Fourier synthesis and refined isotropically. All other hydrogen atoms were included at calculated positions with fixed thermal parameters. Disorder was observed for the coordinated DMF molecule of **4**. Three alternative sites were refined that resulted in equal occupancies of 33.33%. The uncoordinated DMF molecule was refined in two alternative sites with occupancies of 69(2) and 31(2)% for atoms C1DA–C3DA and C1DF–C3DF, respectively. All nondisordered non-hydrogen

Table 2. Crystal data and refinement details for **1**–**4**.

	1	**2**	**3**	**4**
Formula	$C_6H_{12}FeN_2O_2S_2{\cdot}C_4H_8O$	$C_{14}H_{12}FeN_2O_2S_2{\cdot}C_4H_8O$	$C_6H_8N_2O_2RuS_2{\cdot}C_4H_8O$	$C_{14}H_{12}N_2O_2RuS_2{\cdot}2\ C_3H_7NO$
fw [g mol^{-1}]	336.25	432.33	377.44	551.64
T [K]	–140(2)	–140(2)	–140(2)	–140(2)
Crystal system	monoclinic	triclinic	monoclinic	monoclinic
Space group	$P2_1/n$	$P\bar{1}$	$P2_1/n$	$P2_1/n$
a [Å]	16.3227(3)	5.6236(1)	16.5181(6)	5.6470(1)
b [Å]	9.7721(2)	8.8547(2)	9.7343(3)	20.4208(3)
c [Å]	20.0057(4)	10.5982(2)	20.1750(8)	22.3020(3)
α [°]	90	106.325(1)	90	90
β [°]	111.759(1)	103.221(1)	111.248(2)	90.743(2)
γ [°]	90	94.462(1)	90	90
V [Å^3]	2963.69(10)	487.304(17)	3023.46(19)	2571.57(7)
Z	8	1	8	4
ρ [g cm^{-3}]	1.507	1.473	1.658	1.519
μ [mm^{-1}]	13.01	10.08	13.14	8.09
Measured data	17902	12952	17299	13093
Data with $I > 2\sigma(I)$	5868	4148	5362	5004
Unique data (R_{int})	6762/0.0338	4232/0.0453	6854/0.0588	5584/0.0256
wR_2 (all data, on F^2)[a]	0.0888	0.0598	0.1172	0.1342
R_1 [$I > 2\sigma(I)$] [a]	0.0404	0.0238	0.0559	0.0615
s[b]	1.185	1.050	1.117	1.301
Residual el. density [e Å^{-3}]	0.466/–0.505	0.297/–0.333	0.956/–0.639	1.761/–0.629
Flack parameter		–0.025(9)		
Absorption correction	–	–	–	–

[a] Definition of the R indices: $R_1 = (\Sigma||F_o| - |F_c||)/\Sigma|F_o|$; $wR_2 = \{\Sigma[w(F_o^2 - F_c^2)^2]/\Sigma[w(F_o^2)^2]\}^{1/2}$ with $w^{-1} = s^2(F_o^2) + (aP)^2 + bP$; $P = [2F_c^2 + \max(F_o^2)]/3$. [b] $s = \{\Sigma[w(F_o^2 - F_c^2)^2]/(N_o - N_p)\}^{1/2}$.

atoms were refined anisotropically.[47] Crystallographic, structure solution, and refinement details are summarized in Table 2. XP (SIEMENS Analytical X-ray Instruments, Inc.) was used for structure representations.

CCDC-848989 (for **1**), -848990 (for **2**), -848991 (for **3**), and -848992 (for **4**) contain the supplementary crystallographic data for this paper. These data can be obtained free of charge from The Cambridge Crystallographic Data Centre via www.ccdc.cam.ac.uk/data_request/cif.

Acknowledgments

This work was supported by ProExcellence Thuringia PE-114 (to M. W., S. H. H.), the Carl Zeiss Foundation (to T. M. A. J.), and the German Academic Exchange Service (DAAD) (to V. P. L. V).

[1] B. E. Mann, T. R. Johnson, J. E. Clark, R. Foresti, C. Green, R. Motterlini, *Angew. Chem.* **2003**, *115*, 3850; *Angew. Chem. Int. Ed.* **2003**, *42*, 3722–3729.
[2] R. Motterlini, R. Foresti, in: L. E. Otterbein, B. S. Zuckerbraun (Eds.) *Heme Oxygenase*, Nova Science Publishers, Hauppauge, **2005**, pp. 191–210.
[3] R. Foresti, M. G. Bani-Hani, R. Motterlini, *Int. Care Med.* **2008**, *34*, 649–658.
[4] B. E. Mann, *Top. Organomet. Chem.* **2010**, *32*, 247–285.
[5] W. J. Wilkinson, P. J. Kemp, *J. Physiol.* **2011**, *589*, 3055–3062.
[6] R. Motterlini, *Biochem. Soc. Trans.* **2007**, *35*, 1142–1146.
[7] B. E. Mann, R. Motterlini, *Chem. Commun.* **2007**, 4197–4208 (*erratum*: *ibid.*, p. 4818).
[8] B. Mann, R. Motterlini, *Chem. Ind.* **2005**, *16*, 16–18.
[9] R. Motterlini, L. E. Otterbein, *Nature Rev. Drug Discovery* **2010**, *9*, 728–743.
[10] J. Boczkowski, J. J. Poderoso, R. Motterlini, *Trends Biochem. Sci.* **2006**, *31*, 614–621.
[11] R. Alberto, R. Motterlini, *Dalton Trans.* **2007**, 1651–1660.
[12] T. R. Johnson, B. E. Mann, I. P. Teasdale, H. Adams, R. Foresti, C. J. Green, R. Motterlini, *Dalton Trans.* **2007**, 1500–1508.
[13] M. J. Alcaraz, M. I. Guillen, M. L. Ferrandiz, J. Megias, R. Motterlini, *Curr. Pharm. Des.* **2008**, *14*, 465–472.
[14] U. Schatzschneider, *Eur. J. Inorg. Chem.* **2010**, 1451–1467.
[15] U. Schatzschneider, *Inorg. Chim. Acta* **2011**, *374*, 19–23.
[16] B. E. Mann, T. R. Johnson, J. E. Clark, R. Foresti, C. Green, R. Motterlini, *J. Inorg. Biochem.* **2003**, *96*, 40.
[17] M. Melník, J. Valentová, F. Devínsky, *Rev. Inorg. Chem.* **2011**, *31*, 57–82, and references cited therein.
[18] C. S. Jackson, S. Schmitt, Q. P. Dou, J. J. Kodanko, *Inorg. Chem.* **2011**, *50*, 5336–5338.
[19] M. A. Gonzalez, N. L. Fry, R. Burt, R. Davda, A. Hobbs, P. K. Mascharak, *Inorg. Chem.* **2011**, *50*, 3127–3134.
[20] L. Hewison, S. H. Crook, T. R. Johnson, B. E. Mann, H. Adams, S. E. Plant, P. Sawle, R. Motterlini, *Dalton Trans.* **2010**, *39*, 8967–8975.
[21] W.-Q. Zhang, A. J. Atkin, R. J. Thatcher, A. C. Whitwood, J. S. Fairlamb, J. M. Lynam, *Dalton Trans.* **2009**, 4351–4358.
[22] D. Scapens, H. Adams, T. R. Johnson, B. E. Mann, P. Sawle, R. Aqil, T. Perrior, R. Motterlini, *Dalton Trans.* **2007**, 4962–4973.
[23] F. Ferrier, G. Terzian, J. Mossoyan, D. Benlian, *J. Mol. Struct.* **1995**, *344*, 189–193.
[24] A. Szakács-Schmidt, J. Kreisz, L. Markó, Z. Nagy-Magos, J. Takács, *Inorg. Chim. Acta* **1992**, *198–200*, 401–405.
[25] J. Takács, E. Soós, Z. Nagy-Magos, L. Markó, G. Gervasio, T. Hoffmann, *Inorg. Chim. Acta* **1989**, *166*, 39–46.
[26] A. Tomita, H. Hirai, S. Makishima, *Inorg. Nucl. Chem. Lett.* **1968**, *4*, 715–718.
[27] A. Tomita, H. Hirai, S. Makishima, *Inorg. Chem.* **1967**, *6*, 1746–1749.
[28] M. P. Schubert, *J. Am. Chem. Soc.* **1933**, *55*, 4563–4570.
[29] R. Kretschmer, G. Gessner, H. Görls, S. H. Heinemann, M. Westerhausen, *J. Inorg. Biochem.* **2011**, *105*, 6–9.
[30] M. Westerhausen, R. Kretschmer, S. H. Heinemann, Patent DE 10 2010 014 411.8, **2011**.
[31] M. Westerhausen, R. Kretschmer, S. H. Heinemann, Patent DE 10 2010 014 412.6, **2011**.
[32] B. Pathak, D. Majumdar, J. Leszczynski, *Int. J. Quantum Chem.* **2009**, *109*, 2263–2272.
[33] Z.-J. Xu, R. Fang, C. Zhao, J.-S. Huang, G.-Y. Li, N. Zhu, C.-M. Che, *J. Am. Chem. Soc.* **2009**, *131*, 4405–4417, and references cited therein.
[34] W. Cremer, *Biochem. Z.* **1928**, *194*, 231–232.
[35] W. Cremer, *Biochem. Z.* **1929**, *206*, 228–239.
[36] L. Hewison, T. R. Johnson, B. E. Mann, A. J. H. M. Meijer, P. Sawle, R. Motterlini, *Dalton Trans.* **2011**, *40*, 8328–8334.
[37] W.-F. Liaw, J.-H. Lee, H.-B. Gau, C.-H. Chen, G.-H. Lee, *Inorg. Chim. Acta* **2001**, *322*, 99–105.
[38] J. V. Kingston, J. W. S. Jamieson, G. Wilkinson, *J. Inorg. Nucl. Chem.* **1967**, *29*, 133–138.
[39] D. Sellmann, U. Reineke, G. Huttner, L. Zsolnai, *J. Organomet. Chem.* **1986**, *310*, 83–93.
[40] D. Sellmann, O. Käppler, F. Knoch, *J. Organomet. Chem.* **1989**, *367*, 161–174.
[41] D. Sellmann, R. Ruf, F. Knoch, M. Moll, *Z. Naturforsch. B* **1995**, *50*, 791–801.
[42] D. Sellmann, R. Ruf, F. Knoch, M. Moll, *Inorg. Chem.* **1995**, *34*, 4745–4755.
[43] D. Sellmann, U. Reineke, *J. Organomet. Chem.* **1986**, *314*, 91–103.
[44] A. J. Atkin, J. M. Lynam, B. E. Moulton, P. Sawle, R. Motterlini, N. M. Boyle, M. T. Pryce, I. J. S. Fairlamb, *Dalton Trans.* **2011**, *40*, 5755–5761.
[45] *COLLECT*, Data Collection Software, Nonius B. V., The Netherlands, **1998**.
[46] *Processing of X-ray Diffraction Data Collected in Oscillation Mode*: Z. Otwinowski, W. Minor, in: *Methods in Enzymology* (Eds.: C. W. Carter, R. M. Sweet), vol. 276, *Macromolecular Crystallography*, part A, pp. 307–326, Academic Press, New York **1997**.
[47] G. M. Sheldrick, *Acta Crystallogr., Sect. A* **2008**, *64*, 112–122.
Received: November 4, 2011
Published Online: January 31, 2012

DOI: 10.1002/ejic.201101249

Coordinating Properties of Pyrone and Pyridinone Derivatives, Tropolone and Catechol toward the VO^{2+} Ion: An Experimental and Computational Approach

Daniele Sanna,[a] Péter Buglyó,[b] Linda Bíró,[b] Giovanni Micera,[c] and Eugenio Garribba*[c]

Keywords: Vanadium / Bioinorganic chemistry / Structure elucidation / EPR spectroscopy / UV/Vis spectroscopy / Density functional calculations

The interaction of the VO^{2+} ion with pyrone derivatives and tropolone, which form very effective antidiabetic compounds, is critically re-examined. The binary systems with ethylmaltol (Hema) and tropolone (Htrop) were studied in aqueous solution and in the solid state through the combined application of spectroscopic (EPR, UV/Vis and IR) and pH-potentiometric techniques. The results were compared with those of the systems with maltol (Hma) and kojic acid (Hkoj) and rationalized on the basis of DFT simulations. All the ligands $\mathbf{L}^-$ form $[VO\mathbf{L}]^+$, *cis*-$[VO\mathbf{L}_2(H_2O)]$ and *cis*-$[VO\mathbf{L}_2(OH)]^-$ species in aqueous solutions and a square-pyramidal $[VO\mathbf{L}_2]$ complex in the solid state, which transforms into *cis*-$[VO\mathbf{L}_2$(solvent)] when it is dissolved in water or in a coordinating solvent. The coordinating properties of the ligands studied were compared with those of pyridinone [3-hydroxy-1,2-dimethyl-4(1*H*)pyridinone (Hdhp), and 1,2-diethyl-3-hydroxy-4(1*H*)pyridinone (Hdepp)] derivatives and catechol (H_2cat), and were explained by postulating that from pyrones to pyridinones and to catechol the donor set changes progressively from (CO, O^-) to (O^-, O^-). DFT calculations allowed us to determine the relative stability of the four possible structures (square pyramidal, *trans*- and two *cis*-octahedral) of the bischelated species and the aromaticity of the protonated, neutral and deprotonated form of the ligands through the calculation of the HOMA (harmonic oscillator model of aromaticity) index. The relationship between the electric charge on the oxygen donors, the mean distances and the difference between the lengths of $C–O_{ket}$ and $C–O_{phen}$ bonds with (i) the pK_a of the ligands, (ii) the pK of deprotonation of the equatorially coordinated water molecule in *cis*-$[VO\mathbf{L}_2(H_2O)]$, and (iii) the ^{51}V hyperfine coupling constant (A_z) of $[VO\mathbf{L}_2]$, *cis*-$[VO\mathbf{L}_2(H_2O)]$ and *cis*-$[VO\mathbf{L}_2(OH)]^-$ was also found and discussed.

Introduction

Vanadium compounds exhibit a wide variety of pharmacological properties.[1] One of the most important applications is their potential use in the therapy of patients who suffer from type-II diabetes mellitus.[2] Since type-II diabetes goes along with an increasing lack of response to insulin, insulin injections can become ineffective and alternative methods of treatment are desirable. About 30 years ago, the insulin-enhancing action of vanadate was demonstrated and highlighted with respect to the possibility of oral administration. Vanadium species stimulate the uptake and degradation of glucose by adipocytes (fat cells), glycogenesis in the liver, and inhibition of hepatic gluconeogenesis.[3] After the initial use of vanadium(IV) and vanadium(V) inorganic salts, not easily applicable as antidiabetic drugs on account of their toxicity and low absorption rate, several peroxovanadium(V) complexes with (N,N), (N,O), and (O,O) ligands,[4] and vanadyl species with bidentate anionic ligands ($VO\mathbf{L}_2$, in which **L** is called the organic carrier) were tested.[2] It was found that neutral VO^{2+} complexes ($VO\mathbf{L}_2$) are more effective, better tolerated, and result in reliable glucose-lowering in all the animal models of diabetes than VO^{2+} and vanadium(V) inorganic salts.[1b]

Among insulin-enhancing compounds with $VO\mathbf{L}_2$ composition, bis(maltolato)oxidovanadium(IV) {$[VO(ma)_2]$, in which Hma is maltol (called BMOV)} became the most widely and extensively tested, and now is considered the benchmark for new oral antidiabetic vanadium compounds.[2a–2c,5,6] It was demonstrated that BMOV has high hypoglycemic activity,[7] approximately 1.5 and 3.0 times that of $VOSO_4$ in chronic experimental animal treatment and in acute treatment protocols, respectively.[8] A derivative, bis(ethylmaltolato)oxidovanadium(IV) {$[VO(ema)_2]$, in which Hema is ethylmaltol (called BEOV)}, arrived at phase IIa of the clinical trials.[9] Maltol and ethylmaltol

[a] Istituto CNR di Chimica Biomolecolare,
Trav. La Crucca 3, 07040 Sassari, Italy
[b] Department of Inorganic and Analytical Chemistry, University of Debrecen,
4010 Debrecen, Hungary
[c] Dipartimento di Chimica e Farmacia and Centro Interdisciplinare per lo Sviluppo della Ricerca Biotecnologica e per lo Studio della Biodiversità della Sardegna, Università di Sassari,
Via Vienna 2, 07100 Sassari, Italy
Fax: +39-079-229559
E-mail: garribba@uniss.it
Supporting information for this article is available on the WWW under http://dx.doi.org/10.1002/ejic.201101249.

have the advantage of being approved as food additives in the USA, UK and Canada.[10] It must, however, be noticed that the clinical trials have provisionally been abandoned due to renal problems observed in several of the tested individuals.[1c]

After the isolation of BMOV and BEOV, other VO^{2+} species formed by maltol derivatives have been synthesized.[11–13] These complexes have been examined for hypoglycemic activity in diabetic animals, and only one of them, bis(allixinato)oxidovanadium(IV), was found to show insulin-enhancing activity comparable to that of BMOV.[13a]

However, the biotransformation of these complexes in the blood, the mechanism with which vanadium is transported to the target organs and the in vivo form is not fully known and is the subject of much debate. In particular, the form with which a pharmacologically active compound is transported is connected to the transformation of the solid drug VOL_2 in an aqueous solution at physiological conditions.[14,15] Loss of the coordinated ligand molecules, changes in the coordination geometry and redox processes are possible. Therefore, the knowledge of the complexation scheme and stability of the species formed is fundamental to understand the active species in the organism. For example, for the complexes formed by maltol derivatives, the transformation of the square-pyramidal form $[VOL_2]$ to *cis*-octahedral, *cis*-$[VOL_2(H_2O)]$, with the two ligand molecules adopting an equatorial–equatorial and equatorial–axial arrangement, has been demonstrated,[16,17] even if it is not clear which of the two oxygen donors that belongs to the molecule in the equatorial–axial arrangement occupies the equatorial position. Such *cis*-octahedral species are of significant importance since they can interact with the blood serum proteins, and a side-chain donor of the amino acids that constitute the polypeptide can bind vanadium in the fourth equatorial position.

The transformation of the square-pyramidal to *cis*-octahedral geometry is strictly related to the electronic structure of the ligands and/or complexes: for example, strong ligands stabilize the square-pyramidal arrangement, whereas by decreasing their strength, the stability of the *cis*-octahedral form increases. The formation of *cis*-octahedral complexes is often accompanied by a detectable change in the spectroscopic parameters and a deprotonation process observable through pH-potentiometric titrations. Thus, computational and potentiometric methods, combined with the spectroscopic techniques, can be helpful in the characterization of these systems. In particular, computational approaches have been revealed to be useful in the prediction of structural details, electronic properties and spectroscopic features of many transition-metal complexes.[18]

In this work, the interaction of VO^{2+} ion with maltol (Hma), ethylmaltol (Hema), kojic acid (Hkoj) and tropolone (Htrop) has been examined and/or re-examined through the combined application of spectroscopic (EPR, UV/Vis and IR), pH-potentiometric and DFT methods. The ligands are shown in Scheme 1. The first goal of the paper is to relate the electronic structure of pyrones and of their VO^{2+} complexes with the spectroscopic parameters, chemical behaviour and geometry assumed in aqueous solution. The second goal is to compare the data obtained with those shown by the family of antidiabetic compounds formed by the structurally similar pyridinone ligands. The results might contribute to a deeper understanding of the possible transformation in the organism and of the mechanism of action of these antidiabetic compounds.

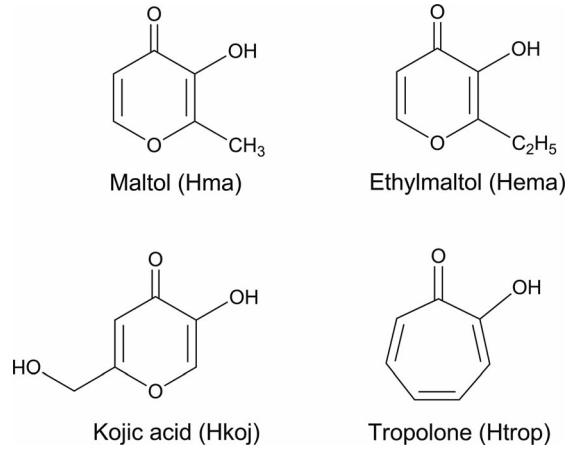

Scheme 1. Structure of the ligands studied.

Results

VO^{2+}/Hma System

In this work, the system VO^{2+}/Hma has been diffusely studied by DFT methods. The results obtained with Hma can be considered valid and used as comparison for all the other pyrone derivatives.

The structure of the solid complex formed by maltol with the VO^{2+} ion, $[VO(ma)_2]$, has been determined through X-ray diffractometric analysis.[5] The geometry is square pyramidal with the two ligand molecules in the equatorial position. Dissolution of $[VO(ma)_2]$ in coordinating organic solvents (DMSO, pyridine) is accompanied by the transformation of the square-pyramidal to a *cis*-octahedral structure.[16] In contrast, in noncoordinating solvents, $[VO(ma)_2]$ maintains its pentacoordinate structure with the sixth coordination site being empty. EPR parameters are $g_z = 1.948$, $A_z = 161 \times 10^{-4}$ cm^{-1} for the penta- and $g_z = 1.939$, $A_z = 169 \times 10^{-4}$ cm^{-1} for the hexacoordinate complex.[16]

The isolation of the square-pyramidal complex in the solid state does not imply that this is the preferred configuration in water. Indeed, it has been demonstrated that in aqueous solution the structure of the bis-chelated species is *cis*-octahedral with an equatorial–equatorial and equatorial–axial arrangement of the two ligand molecules and a water ligand completing the equatorial coordination of VO^{2+}. The value of A_z for *cis*-$[VO(ma)_2(H_2O)]$ is much larger than that of the pentacoordinate species ($A_z = 171 \times 10^{-4}$ cm^{-1} versus $A_z = 161 \times 10^{-4}$ cm^{-1}). The structures of $[VO(ma)_2]$ and of the bis-chelated complexes

formed in aqueous solution, *cis*-[VO(ma)$_2$(H$_2$O)] and *cis*-[VO(ma)$_2$(OH)]$^-$, have been optimized with Gaussian 03 software[19] and DFT methods, which, as demonstrated over the last few years, yield good results in the simulation of the geometries of transition-metal complexes.[20] The popular B3LYP functional was used:[21,22] its suitability to predict structures and energies of several metal compounds, including vanadium, is well documented.[23] We recently provided evidence that the basis set 6-311g allows calculations in good agreement with the experimental bond lengths and angles for 32 representative VO^{2+} complexes in a reasonable calculation time.[24] Furthermore, the level of theory applied is enough to obtain a good prediction of the EPR and UV/Vis spectra.[25,26]

The optimized structures are represented in Figure 1 and the comparison between experimental and calculated structural details is reported in Table S1 in the Supporting Information.

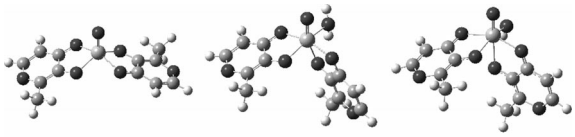

Figure 1. Structure of the complexes (a) [VO(ma)$_2$], (b) *cis*-[VO(ma)$_2$(H$_2$O)] and (c) *cis*-[VO(ma)$_2$(OH)]$^-$, optimized with DFT methods at the B3LYP/6-311g level of theory.

From an examination of Table S1, it is possible to observe that the agreement between the bond lengths is rather good, even if all the metal–donor distances are overestimated according to the general tendency of the all-electron calculations.[20d] For [VO(ma)$_2$] the simulation foresees a structure distorted toward the trigonal bipyramidal, with a trigonality index τ [$\tau = (\beta - \alpha)/60$, in which β and α are the angles between the axial and equatorial donors, respectively][27] larger than the experimental one (0.314 versus 0.102). An examination of the data reveals that, from *cis*-[VO(ma)$_2$(H$_2$O)] to *cis*-[VO(ma)$_2$(OH)]$^-$, the structure approaches a regular octahedron with an angle O=V–O$_{phen}$ that goes from 161.1 to 176.0°.

Over the past years, DFT methods have been widely applied to the calculation of EPR parameters of transition-metal complexes[28] and VO^{2+} species.[23b,25,29] Recently, the ^{51}V hyperfine coupling constant (A_z) has been calculated with Gaussian 03 software for 22 representative VO^{2+} complexes with different charges, geometries, and coordination modes at the BHandHLYP/6-311g(d,p) level of theory with a mean deviation below 3% from the experimental values.[25] The use of half-and-half hybrid functionals like BHandHLYP and BHandH, which allow for treating core–shell spin polarization, seems to be necessary to obtain a satisfactory agreement with the experimental results. Therefore, it is reasonable to suppose that DFT methods may be used to calculate A_z for any VO^{2+} complex. The components of the tensor $\boldsymbol{A}$ and the comparison with the experimental values ($A_z^{exp.}$) are listed in Table 1.

The possibility to calculate A_z can be useful to understand which of the two isomers with *cis*-octahedral geometry is present in aqueous solution (Scheme 2). In fact, in spite of the high number of studies published on the interaction between the VO^{2+} ion and maltol and its derivatives, this aspect has not been clarified.[5,11a,11d,12,14,16,17,30,31] Therefore, the structures of the possible isomers for the species *cis*-[VO(ma)$_2$(H$_2$O)] with coordination mode [(O$_{ket}$, O$_{phen}$; O$_{ket}$, O$_{phen}^{ax}$); H$_2$O] and [(O$_{ket}$, O$_{phen}$; O$_{ket}^{ax}$, O$_{phen}$); H$_2$O] have been optimized and the values of A_z calculated (Table 1).

Table 1. EPR parameters calculated at the BHandHLYP/6-311g(d,p) level of theory on the VO^{2+} complexes formed by pyrone derivatives and tropolone.[a]

Complex	$A_{iso}^{calcd.}$	$A^{D}{}_{x}^{calcd.}$	$A^{D}{}_{y}^{calcd.}$	$A^{D}{}_{z}^{calcd.}$	$A_x^{calcd.}$	$A_y^{calcd.}$	$A_z^{calcd.}$	$A_z^{exp.}$	%$\lvert A_z\rvert$[b]
[VO(ma)(H$_2$O)$_2$]$^+$	–113.0	33.4	35.5	–68.9	–79.5	–77.4	–181.9	–177.5	2.5
[VO(ma)(H$_2$O)$_3$]$^+$	–105.5	33.4	34.8	–68.2	–72.1	–70.7	–173.7	–177.5	–2.2
cis-[VO(ma)$_2$(H$_2$O)][c]	–103.1	32.9	35.3	–68.3	–70.2	–67.8	–171.4	–170.8	0.3
cis-[VO(ma)$_2$(H$_2$O)][d]	–99.0	31.6	36.7	–68.3	–68.0	–62.8	–167.3	–170.8	–2.0
cis-[VO(ma)$_2$(OH)]$^-$[e]	–96.0	33.9	34.9	–68.8	–62.1	–61.1	–164.9	–167.1	–1.3
cis-[VO(ma)$_2$(OH)]$^-$[f]	–89.5	31.6	37.8	–69.4	–57.9	–51.7	–158.9	–167.1	–4.9
[VO(ema)(H$_2$O)$_2$]$^+$	–112.8	33.4	35.5	–69.0	–79.4	–77.3	–181.7	–176.6	2.9
[VO(ema)(H$_2$O)$_3$]$^+$	–105.4	33.4	34.8	–68.2	–72.0	–70.5	–173.6	–176.6	–1.7
cis-[VO(ema)$_2$(H$_2$O)][c]	–103.0	32.9	35.3	–68.2	–70.1	–67.7	–171.3	–170.1	0.7
cis-[VO(ema)$_2$(OH)]$^-$[e]	–97.1	33.8	35.0	–68.8	–63.3	–62.2	–165.9	–167.3	–0.8
[VO(koj)(H$_2$O)$_2$]$^+$	–113.3	33.3	35.7	–69.0	–80.0	–77.7	–182.3	–178.5	2.1
[VO(koj)(H$_2$O)$_3$]$^+$	–105.8	33.5	34.8	–68.2	–72.3	–71.0	–174.0	–178.5	–2.5
cis-[VO(koj)$_2$(H$_2$O)][c]	–103.4	33.1	35.2	–68.2	–70.4	–68.2	–171.7	–171.1	0.3
cis-[VO(koj)$_2$(OH)]$^-$[e]	–97.8	33.4	35.4	–68.8	–64.4	–62.3	–166.6	–168.6	–1.2
[VO(trop)(H$_2$O)$_2$]$^+$	–113.0	33.5	35.5	–69.0	–79.5	–77.4	–182.0	–175.8	3.5
[VO(trop)(H$_2$O)$_3$]$^+$	–105.2	33.2	35.2	–68.3	–72.1	–70.1	–173.5	–175.8	–1.3
cis-[VO(trop)$_2$(H$_2$O)]	–101.4	32.8	35.7	–68.5	–68.6	–65.7	–169.9	–167.6	1.3
cis-[VO(trop)$_2$(OH)]$^-$	–95.1	33.9	35.0	–68.9	–61.2	–60.1	–164.0	–164.2	–0.1

[a] Values reported in 10^{-4} cm^{-1}. [b] Percent deviation from the experimental value calculated as $100 \times (|A_z|^{calcd.} - |A_z|^{exp.})/|A_z|^{exp.}$. [c] Coordination mode [(O$_{ket}$, O$_{phen}$; O$_{ket}$, O$_{phen}^{ax}$); H$_2$O]. [d] Coordination mode [(O$_{ket}$, O$_{phen}$; O$_{ket}^{ax}$, O$_{phen}$); H$_2$O]. [e] Coordination mode [(O$_{ket}$, O$_{phen}$; O$_{ket}$, O$_{phen}^{ax}$); OH$^-$]. [f] Coordination mode [(O$_{ket}$, O$_{phen}$; O$_{ket}^{ax}$, O$_{phen}$); OH$^-$].

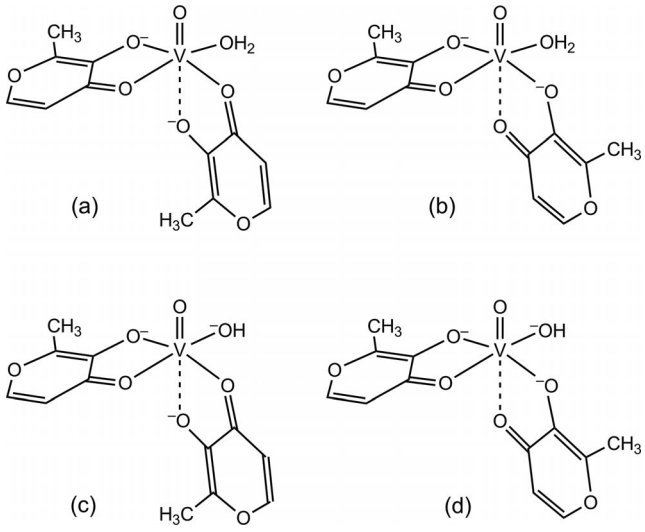

Scheme 2. Structure for the isomers of the species (a and b) *cis*-$[VO(ma)_2(H_2O)]$ and (c and d) *cis*-$[VO(ma)_2(OH)]^-$ with the two possible coordination modes.

It can be seen that the first hypothesis gives a better agreement than the second one, so it can be supposed that, for the ligand with the equatorial–axial arrangement, the carbonyl oxygen (O_{ket}) occupies the equatorial plane, whereas the deprotonated oxygen of the phenolic group (O_{phen}) is in the axial position *trans* to the V=O bond. The percent deviation with respect to the experimental value of $|A_z|$ ($|A_z|^{exp.}$) is +0.3 in the first and –2.0% in the second case. Moreover, the "additivity" rule[32] used with the contribution for O_{ket} proposed by Hamstra et al.[33] allowed us to calculate a value of A_z of 171.5×10^{-4} cm^{-1} for the coordination [(O_{ket}, O_{phen}; O_{ket}, O_{phen}^{ax}); H_2O] and 166.9×10^{-4} cm^{-1} for [(O_{ket}, O_{phen}; O_{ket}^{ax}, O_{phen}); H_2O], thereby confirming the results of the DFT simulations.

If the coordination mode of maltolate in *cis*-$[VO(ma)_2(H_2O)]$ is [(O_{ket}, O_{phen}; O_{ket}, O_{phen}^{ax}); H_2O], then it should be [(O_{ket}, O_{phen}; O_{ket}, O_{phen}^{ax}); OH^-] in *cis*-$[VO(ma)_2(OH)]^-$. The two possibilities for *cis*-$[VO(ma)_2(OH)]^-$ have been examined, and the values of $|A_z|^{calcd.}$ for the two structures are in agreement with what is expected, with deviations with respect to $|A_z|^{exp.}$ of –1.3 and –4.9%. In this case too, the value of A_z expected on the basis of the additivity rule for [(O_{ket}, O_{phen}; O_{ket}, O_{phen}^{ax}); OH^-] (164.6×10^{-4} cm^{-1}) is comparable with $|A_z|^{exp.}$ and with that calculated through DFT simulations.

Finally, the value of A_z for the mono-chelated species with or without a water molecule in the axial position was simulated; as has been demonstrated in the literature recently, the presence of a water ligand *trans* to the V=O group can significantly lower A_z.[34] In this case, however, the results of the simulation did not allow us to demonstrate unambiguously which of the two structures, $[VO(ma)(H_2O)_2]^+$ or $[VO(ma)(H_2O)_3]^+$, really exists in solution; indeed, the experimental constant is intermediate with respect to the data calculated, even if $|A_z|^{calcd.}$ is slightly closer to the experimental value for $[VO(ma)(H_2O)_3]^+$ than for $[VO(ma)(H_2O)_2]^+$. Analogous results have been obtained for Hema and Htrop (Table 1). It is possible that, when the equatorial donors are weak, a water molecule can interact with vanadium in the apical position. This is confirmed by the X-ray structure of the mono-chelated complex formed by another (O,O) ligand, oxalate (ox), that is $[VO(ox)(H_2O)_3]$.[35]

The electronic absorption spectra of *cis*-$[VO(ma)_2(H_2O)]$ and *cis*-$[VO(ma)_2(OH)]^-$ are characterized by three bands at 443, 627, 880 nm in the first case and 453, 588, 932 nm in the second one (Figure S1 in the Supporting Information); the values of the absorption molar coefficient ε are 81, 14, 30 M^{-1} cm^{-1} and 64, 11, 20 M^{-1} cm^{-1}, respectively. No electronic transitions were detected at wavelengths larger than 1000 nm. It can be observed that in the transformation of *cis*-$[VO(ma)_2(H_2O)]$ to *cis*-$[VO(ma)_2(OH)]^-$, the low-energy transition shifts to higher wavelength, whereas the second band shifts to lower wavelength.

The electronic structures of *cis*-$[VO(ma)_2(H_2O)]$ and *cis*-$[VO(ma)_2(OH)]^-$ have been calculated by DFT methods and the results are shown in Scheme S1 (see the Supporting Information). For better comparison of the two diagrams, the energy of the molecular orbitals (MO) is relative to the highest occupied molecular orbital (HOMO), which is considered to be a reference at 0.0 eV. Analysis of the electronic structure and MO composition has been performed by choosing a coordinate system in which the V=O bond occupies the *z* axis, the two keto oxygen atoms the *x* axis and the phenolate oxygen and the water/hydroxido the *y* axis. Examination of Scheme S1 suggests the following considerations: (i) the HOMO has mainly V d_{xy} character; (ii) among the five vanadium d orbitals, V d_{xy} is always at lower energy and V $d_{x^2-y^2}$ and V d_{z^2} are at higher energy; (iii) the order of the vanadium d levels is that calculated by Ballhausen and Gray for a distorted octahedral geometry $d_{xy} < d_{xz} \approx d_{yz} < d_{x^2-y^2} < d_{z^2}$;[36] (iv) a small energy separation between the MOs V d_{xz} and V d_{yz} exists; (v) the energy order of the MOs V d_{xz} and V d_{yz} is reversed in the two cases; (vi) the lowest unoccupied molecular orbital (LUMO) is always a π* orbital of the pseudo-aromatic system; and (vii) four MOs among the low-energy virtual orbitals are based on the π* system of the six-membered ring. It is worth noting that from *cis*-$[VO(ma)_2(H_2O)]$ to *cis*-$[VO(ma)_2(OH)]^-$ the energy separation between HOMO and LUMO (1.99 versus 3.40 eV) and between V d_{xy} and the other V-based molecular orbitals decreases significantly. A comparable electronic structure has been recently found for other VO^{2+} complexes.[37] The most representative MOs for *cis*-$[VO(ma)_2(H_2O)]$ are shown in Figure S2 (see the Supporting Information).

VO^{2+}/Hema System

The binary system formed by the VO^{2+} ion and ethylmaltol has been studied by the research group of Orvig,[30,38] and is re-examined by us here. In aqueous solution, ethylmaltol forms mononuclear complexes with com-

position VO**L**, VO**L**$_2$ and VO**L**$_2$(OH), and a dinuclear species (VO)$_2$**L**$_2$(OH)$_2$. This is suggested both by EPR spectroscopy and pH-potentiometry.

The values of the stability constant for such species can be found in Table 2, whereas the distribution curves as a function of pH in Figure 2. As expected, ethylmaltol is slightly more basic than maltol due to the presence of an ethyl instead of a methyl group in position 2 of the six-membered ring. Consequently, the complexes formed are more stable than those of maltol (logβ for the mono-chelated species 8.80 versus 8.69 and for the bis-chelated species 16.51 versus 16.29). However, the "basicity-adjusted" stability constants K*, which take into account the difference in basicity of the coordinating donors, defined as $\log K_n^* = \log K_n - pK_{HL}$ with n = 1,2 – for the reactions $VO^{2+} + HL \rightarrow VOL + H^+$ and $VOL + HL \rightarrow VOL_2 + H^+$ are 0.26 (Hema) versus 0.25 (Hma) and –0.83 (Hema) versus –0.84 (Hma), respectively, thereby indicating that the different substituent (ethyl versus methyl) far from the coordination sites does not influence the "intrinsic" stability of the complexes.

Table 2. Ligand protonation (pK_a) and stability constants of the VO^{2+} complexes (logβ_{pqr}) formed by Hma, Hema, Hkoj and Htrop at (25.0 ± 0.1) °C.[a]

Species	Hma[b]	Hema[b]	Hema[c]	Hkoj[b]	Htrop[b]
H**L**	8.44	8.54(1)	8.53	7.67	6.66(1)
VO**L**	8.69	8.80(1)	8.79	7.63	8.60(2)
VO**L**$_2$	16.29	16.51(1)	16.43	14.37	16.36(3)
VO**L**$_2$(OH)	7.5	7.60(2)	7.74	5.9	9.16(6)
(VO)$_2$**L**$_2$(OH)$_2$	9.88	9.98(3)	–	7.93	–
pK(VO**L**$_2$)	8.79	8.91	8.69	8.47	7.20
Ref.	[17]	this work	[30]	[17]	this work

[a] The uncertainties (3σ values) of the protonation and stability constants are given in parentheses. [b] I = 0.2 M (KCl). [c] I = 0.16 M (NaCl).

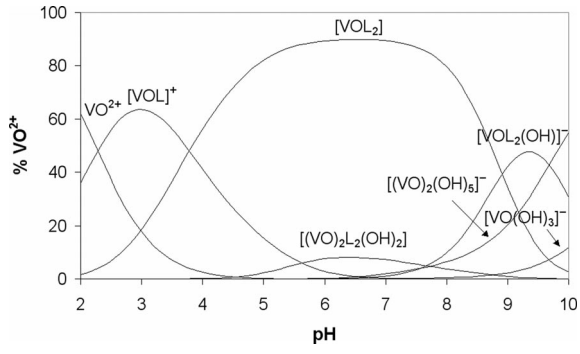

Figure 2. Distribution diagram as a function of pH of the species formed in the system VO^{2+}/Hema with VO^{2+} 2×10^{-3} M and **L**/M = 2.

Anisotropic EPR spectra recorded as a function of pH are shown in Figure 3. Analogously to what was observed in the system VO^{2+}/Hma,[17] with a metal-to-ligand molar ratio of 1:2, the complexation starts with the formation of mono-chelated species $[VO(ema)(H_2O)_x]^+$, x = 2 or 3, (VO**L**, **I** in Figure 3), which exists in the pH range 2–3 and has EPR parameters similar to those of aquaion $[VO(H_2O)_5]^{2+}$ (g_z = 1.934, $A_z = 177 \times 10^{-4}$ cm^{-1}). This species transforms completely at pH higher than 3 in the main complex *cis*-$[VO(ema)_2(H_2O)]$ (VO**L**$_2$, **II** in Figure 3), which can be easily detected and characterized by EPR spectroscopy. As in the case of maltol, the geometry is *cis*-octahedral with an equatorial–equatorial and equatorial–axial arrangement of the two ligand molecules. The ^{51}V hyperfine coupling constant along the z axis for *cis*-$[VO(ema)_2(H_2O)]$ is 170×10^{-4} cm^{-1} (Table 1), which is in good agreement with what is expected by the "additivity" rule for the coordination mode [(O_{ket}, O_{phen}; O_{ket}, O_{phen}^{ax}); H_2O]. Around pH 5–6, the weakening of the spectral signal strongly supports the formation of an EPR-silent dihydroxido-bridged dimer $[(VO)_2(ema)_2(OH)_2]$, not detected previously by Orvig and co-workers,[30] according to the reaction $2[VO(ema)(H_2O)_x]^+ \rightarrow [(VO)_2(ema)_2(OH)_2] + 2H_3O^+ + (2x - 4)H_2O$, x = 2 or 3. From an examination of EPR spectra it can be noted that *cis*-$[VO(ema)_2(H_2O)]$ transforms into *cis*-$[VO(ema)_2(OH)]^-$ {VO**L**$_2$(OH), **III** in Figure 3} above pH 8. The decrease of $4–5 \times 10^{-4}$ cm^{-1} in the value of A_z is in agreement with the "additivity" rule for the replacement of an H_2O with an OH^- ligand on the equatorial plane and the experimental A_z is that expected for a coordination [(O_{ket}, O_{phen}; O_{ket}, O_{phen}^{ax}); OH^-]. The species *cis*-$[VO(ema)_2(H_2O)]$ is characterized by a pK of deprotonation of the equatorial water much lower than that of the bulk water, and slightly larger than that of

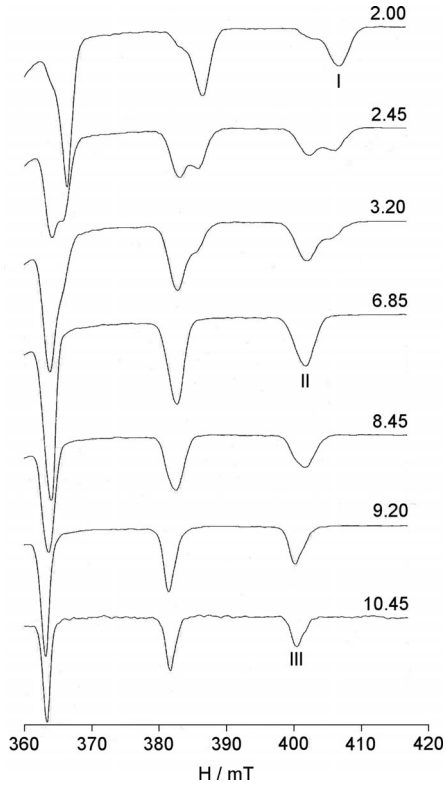

Figure 3. High-field region of the X-band anisotropic EPR spectra recorded as a function of pH in the system VO^{2+}/Hema with VO^{2+} 4×10^{-3} M and **L**/M = 2. With **I**, **II** and **III** are indicated the M_I = 7/2 resonances of $[VO(ema)(H_2O)_x]^{2+}$, x = 2 or 3, *cis*-$[VO(ema)_2(H_2O)]$ and *cis*-$[VO(ema)_2(OH)]^-$, respectively.

cis-[VO(ma)$_2$(H$_2$O)] (8.91 versus 8.79; Table 2). Interestingly, the p*K* value increases with the basicity of the ligand as observed for pyridinone derivatives.[39]

The results of DFT calculations of the ^{51}V A_z values for the complexes formed by ethylmaltol are very similar to those of maltol, an expected result since Hema is chemically analogous to Hma. The slight differences observed can be attributed to the different basicity of the two ligands.

VO^{2+}/Hkoj System

The chemistry of the complexes formed by VO^{2+} ion and kojic acid, a ligand structurally similar to maltol, is much less known. However, the spectroscopic and potentiometric evidence allowed us to prove that the coordination scheme is consistent with that of maltol and ethylmaltol. In particular, EPR parameters (Table 1) and stability constants (Table 2) are similar, even if kojic acid is a ligand slightly weaker than Hma and Hema. Indeed, the "basicity-adjusted" stability constants (K_1* and K_2*) for the mono- and bis-chelated complexes are –0.04 and –0.93, respectively; the difference in the thermodynamic stability can be ascribed to a less favourable electron release effect of –CH_2OH (Hkoj) with respect to –CH_3 (Hma) and –CH_2CH_3 (Hema). Analogous differences in the stability of the complexes formed by kojate and maltolate are reported for other bivalent or trivalent metal ions.[40]

EPR parameters for bis-chelated species are practically coincident with those observed for maltol (g_z = 1.939, A_z = 171 × 10^{-4} cm^{-1}; Table 1) and indicate irrefutably that, also in this case, the geometry around VO^{2+} ion is *cis*-octahedral with a water molecule in the equatorial position. In aqueous solution, *cis*-[VO(koj)$_2$(H$_2$O)] transforms into *cis*-[VO(koj)$_2$(OH)]$^-$ with a p*K* of 8.47: this value, lower by approximately 0.3 and 0.4 p*K* units than those of maltol and ethylmaltol, reflects the lower stability of the bis complex. In agreement with the lower basicity of Hkoj, in this system hydrolysis starts at lower pH values with respect to those with Hma and Hema.

For kojic acid, too, the results of the DFT simulations are comparable with those obtained in the systems with maltol and ethylmaltol.

VO^{2+}/Htrop System

The X-ray structure of the bis-chelated complexes of tropolone with Cu^{2+} and Zn^{2+} is known.[41] With vanadium, non-oxido complexes have been studied,[42] and recently a pentacoordinate species, [VO(trop)$_2$], has been characterized by Baran and co-workers.[43] Values of pK_a for the –OH group in the range of 6.7–7.0 have been reported in the literature, much smaller than those of Hma, Hema and Hkoj.[44] However, to the best of our knowledge, no study in aqueous solution has been published to date.

The protonation constant of the ligand has been determined to check the purity of Htrop. The obtained value (Table 2) is in excellent agreement with previous data if the different experimental conditions are taken into account. Since the neutral [VO(trop)$_2$] complex has poor aqueous solubility, pH-metric titrations have been carried out at low concentrations. Due to these experimental difficulties, the obtained stability constants have uncertainties slightly higher than usual (Table 2). The best model obtained for this system also consists of VO**L**, VO**L**$_2$ and VO**L**$_2$(OH), as with the previous ligands. The p*K* value of VO**L**$_2$ is smaller than other systems (7.20) and this should be in agreement with the lower basicity of tropolone.

EPR spectra as a function of pH are shown in Figure S3 (see the Supporting Information). It can be observed that, when a vanadium concentration of 4 × 10^{-3} M is used, they are strongly disturbed due to the presence of the solid complex [VO(trop)$_2$], which exists in the pH range 3–10. Nevertheless, the examination of the variation of the spectra allows us to describe the complexation scheme of Htrop in aqueous solution. At pH lower than 2, the resonances of the species [VO(trop)(H$_2$O)$_x$]$^+$, x = 2 or 3, and *cis*-[VO(trop)$_2$(H$_2$O)] (VO**L** and VO**L**$_2$, **I** and **II** in Figure S3) can be detected; they are characterized by A_z values of 176 and 168 × 10^{-4} cm^{-1}. The resonance M_I = 7/2 around 400 mT of the *cis*-octahedral species enlarges at pH higher than 6 and this indicates the appearance of another complex in solution, which becomes predominant above pH 9 [VO**L**$_2$(OH), **III** in Figure S3]. In this case too, variation of the spectra as a function of pH can be explained by the transformation of *cis*-[VO(trop)$_2$(H$_2$O)] into the mono-hydroxido species *cis*-[VO(trop)$_2$(OH)]$^-$; it can be observed that the deprotonation of the water molecule starts above pH 7, in agreement with the pH-metric measurements.

It is surprising that the $|A_z|$ value of *cis*-[VO(trop)$_2$(H$_2$O)] and *cis*-[VO(trop)$_2$(OH)]$^-$ is significantly smaller than that of the analogous species formed by Hma, Hema and Hkoj (Table 1); this should be in contradiction with the observation that the ^{51}V hyperfine coupling constant should increase with decreasing basicity of the donors.[39] As a matter of fact, this can be easily explained if, in agreement with DFT data, it is supposed that keto oxygen (the contribution of which to A_z is significantly smaller than that of a deprotonated phenolic oxygen) of the ligand molecule arranged in an equatorial–axial position occupies the equatorial position in *cis*-[VO**L**$_2$(H$_2$O)] and *cis*-[VO**L**$_2$(OH)]$^-$ (**L** = ma, ema and koj). Tropolone in the deprotonated form is instead a symmetric ligand and its two oxygen atoms are equivalent, stronger than a keto and weaker than a phenolate oxygen; therefore, the oxygen of the equatorial–axial ligand that equatorially binds vanadium is stronger than that of maltol, ethylmaltol and kojic acid, with the consequence that $|A_z|$ of *cis*-[VO(trop)$_2$(H$_2$O)] and *cis*-[VO(trop)$_2$(OH)]$^-$ is smaller than in the other cases.

The solid complex [VO(trop)$_2$] has been isolated and characterized through elemental analysis and EPR, UV/Vis and IR spectroscopy. The elemental analysis and IR spectrum suggest that there are no water molecules bound to the VO^{2+} ion; the structure, therefore, is pentacoordinate with a square-pyramidal geometry. The stretching frequency of V=O group falls at 986 cm^{-1}, which is in agree-

Table 3. EPR parameters calculated at the BHandHLYP/6-311g(d,p) level of theory on the VO^{2+} complexes formed by Hma and Htrop in the solid state and DMSO.[a]

Complex	$A_{iso}^{calcd.}$	$A^{D}{}_{x}^{calcd.}$	$A^{D}{}_{y}^{calcd.}$	$A^{D}{}_{z}^{calcd.}$	$A_{x}^{calcd.}$	$A_{y}^{calcd.}$	$A_{z}^{calcd.}$	$A_{z}^{exp.}$	%$\lvert A_z\rvert$[b]
$[VO(ma)_2]$	–92.7	30.2	38.8	–69.0	–62.5	–53.9	–161.6	–161.1	0.3
$[VO(trop)_2]$	–93.2	29.1	39.7	–68.8	–64.1	–53.5	–162.0	–161.6	0.3
cis-$[VO(ma)_2(dmso)]$	–98.1	30.9	36.1	–67.0	–67.1	–62.0	–165.1	–168.0	–1.7
cis-$[VO(trop)_2(dmso)]$	–96.6	31.4	36.2	–67.6	–65.2	–60.4	–164.2	–166.2	–1.2

[a] Values reported in 10^{-4} cm^{-1}. [b] Percent deviation from the experimental value calculated as $100 \times (|A_z|^{calcd.} - |A_z|^{exp.})/|A_z|^{exp.}$.

ment with what reported in the literature.[43] When the solid compound was dissolved in a coordinating solvent such as DMSO and DMF, only one species was formed, which can be revealed by EPR spectroscopy (Figure S4, traces a and b, in the Supporting Information); its parameters (g_z = 1.941, A_z = 166.4×10^{-4} cm^{-1} in DMF and g_z = 1.942, A_z = 166.2×10^{-4} cm^{-1} in DMSO) are comparable to those of *cis*-$[VO(trop)_2(H_2O)]$ and this induces us to think that the transformation of $[VO(trop)_2]$ in *cis*-$[VO(trop)_2(dmf)]$ or *cis*-$[VO(trop)_2(dmso)]$ occurs, analogously to what observed for maltol.[16] The values of A_z for the *cis*-octahedral complexes formed by Hma and Htrop in DMSO (and that for the square-pyramidal species) have been simulated with DFT methods and reported in Table 3; it can be seen that the agreement between experimental and calculated values is very good.

When the solid is dissolved in a solvent or in a mixture of noncoordinating solvents such as CH_2Cl_2/toluene 50:50 v/v (Figure S4, trace c, in the Supporting Information), the value of the hyperfine coupling constant is much smaller (A_z = 161.6×10^{-4} cm^{-1}), which is in agreement with the presence of four oxygen donors in the equatorial plane. Thus $[VO(trop)_2]$, like $[VO(ma)_2]$, maintains its structure in noncoordinating solvents. It is interesting to observe that, unlike *cis*-octahedral species, the A_z value for $[VO(trop)_2]$ is larger than that of $[VO(ma)_2]$ because the two ligand molecules equatorially bind the metal ion with their four oxygen atoms and, on the whole, those of maltolate are more basic than those of tropolonate.

Discussion

Relative Stability of the Bis-Chelated Complexes in Aqueous Solution

The four ligands studied show similar chemical behaviour: while in the solid state they form square-pyramidal complexes, in aqueous solution *cis*-octahedral species with a water molecule in the equatorial plane are formed. This prompts us to suppose that the energy of the four possible bis-chelated species formed by these ligands with two different oxygen donors (O_k and O_p in Scheme 3) is comparable.

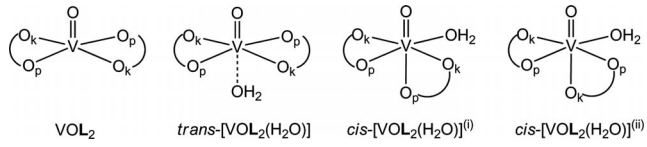

Scheme 3. Structures for the four possible bis-chelated complexes formed by a pyrone ligand. The subscripts k and p indicate the keto and phenolate oxygens.

An interesting application of the DFT methods is the calculation of the relative stability of the bis-chelated complexes formed by maltolate in aqueous solution. The stability can be evaluated by calculating the Gibbs free energy in aqueous solution (ΔG_{aq}^{tot}) for Reactions (1), (2) and (3) for the formation of *trans*- and two *cis*-octahedral species from the square-pyramidal complex.

$$[VO(ma)_2] + H_2O \rightarrow \textit{cis}\text{-}[VO(ma)_2(H_2O)]^{(i)} \quad (1)$$

$$[VO(ma)_2] + H_2O \rightarrow \textit{cis}\text{-}[VO(ma)_2(H_2O)]^{(ii)} \quad (2)$$

$$[VO(ma)_2] + H_2O \rightarrow \textit{trans}\text{-}[VO(ma)_2(H_2O)] \quad (3)$$

with the superscript (i) and (ii) indicating the coordination modes [(O_{ket}, O_{phen}; O_{ket}, $O_{phen}{}^{ax}$); H_2O] and [(O_{ket}, O_{phen}; $O_{ket}{}^{ax}$, O_{phen}); H_2O] of the two isomers of *cis*-octahedral species.

The value of ΔG_{aq}^{tot} can be separated into three parts: the electronic plus nuclear repulsion energy (ΔE^{ele}), the thermal contribution (ΔG^{therm}) and the solvation free energy [$\Delta(\Delta G^{solv})$], as given in Equation (4). The thermal contribution was estimated by using the ideal gas model and the calculated harmonic vibrational frequencies to determine the correction due to zero-point energy (ZPE) and to thermal population of the vibrational levels.

$$\Delta G_{aq}^{tot} = \Delta E^{ele} + \Delta G^{therm} + \Delta(\Delta G^{solv}) \quad (4)$$

The Gibbs free energy in the gas phase (ΔG_{gas}^{tot}) can instead be found by neglecting the term [$\Delta(\Delta G^{solv})$] [Equation (5)].

$$\Delta G_{gas}^{tot} = \Delta E^{ele} + \Delta G^{therm} \quad (5)$$

The results are reported in Table 4. It can be observed that the stability order in the gas phase and in an aqueous solution is *cis*-octahedral (O_{ket}, $O_{phen}{}^{ax}$) > *cis*-octahedral ($O_{ket}{}^{ax}$, O_{phen}) > square pyramidal >> *trans*-octahedral. Therefore, DFT methods confirm that the two *cis*-octahedral isomers are more stable than the square-pyramidal

Table 4. Values of ΔG in the gas phase and in aqueous solution for Hma for the reaction of formation of *trans*-and *cis*-octahedral species from the square-pyramidal complex.[a,b]

Reaction	ΔE^{ele}	ΔG^{therm}[c]	ΔG^{tot}_{gas}	$\Delta(\Delta G^{solv})$[d]	ΔG^{tot}_{aq}
$[VO(ma)_2] + H_2O \rightarrow$ *trans*-$[VO(ma)_2(H_2O)]$	–48.4	51.0	2.6	8.1	10.7
$[VO(ma)_2] + H_2O \rightarrow$ *cis*-$[VO(ma)_2(H_2O)]$[(i)][e]	–62.0	53.0	–9.1	7.7	–1.4
$[VO(ma)_2] + H_2O \rightarrow$ *cis*-$[VO(ma)_2(H_2O)]$[(ii)][f]	–50.1	48.6	–1.5	0.9	–0.6

[a] Energies reported in kJ mol^{-1}. [b] Calculations performed at the level of theory B3LYP/6-311g. [c] Thermal contribution at 298 K with the zero-point energy included in the calculations. [d] Polarizable continuum model (PCM) used with water as solvent. [e] Isomer with coordination mode [(O_{ket}, O_{phen}; O_{ket}, O_{phen}^{ax}); H_2O]. [f] Isomer with coordination mode [(O_{ket}, O_{phen}; O_{ket}^{ax}, O_{phen}); H_2O].

complex, even if in water the energy difference is rather small (0.6 and 1.4 kJ mol^{-1}). On the contrary, the energy of the *trans*-octahedral species is much higher both in the gas phase and in solution, and no experimental evidence of its existence has ever been reported. It can also be noted that the solvation favours the *cis*-octahedral isomer with two phenolate oxygens in the equatorial position; the consequence is that the energy separation of the two *cis*-octahedral species, rather large in the gas phase, significantly decreases in aqueous solution and the stability of the isomers becomes comparable. However, as EPR data suggest, the complex with two keto oxygen atoms in the equatorial plane should be slightly favoured.

Coordinating Properties of Pyrone and Pyridinones Derivatives, Tropolone and Catechol

The coordinating properties of the molecules studied can be put in relationship with the structure of the free ligands and with their protonation/deprotonation processes in water. The maltol derivatives can give the equilibria represented in Scheme 4. Such equilibria have been demonstrated also for pyridinone derivatives, formally derived from maltol by the replacement of the endocyclic oxygen with a group –NR–, which show high insulin-enhancing activity.[45] The behaviour of tropolone and three pyrones studied in this work has been compared with that of two pyridinones [3-hydroxy-1,2-dimethyl-4(1*H*)pyridinone (Hdhp)[45] and 1,2-diethyl-3-hydroxy-4(1*H*)pyridinone (Hdepp)[39]] and catechol (H_2cat), which has two phenolic –OH groups in the *ortho* position and a fully aromatic structure.

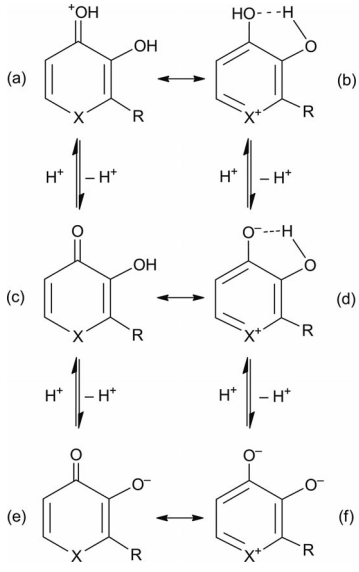

Scheme 4. Equilibria and resonance structures for a pyrone and pyridinone ligand in the protonated, neutral and deprotonated form.

All the ligands can be protonated at acidic pH, and are deprotonated at pH values higher than neutrality, depending on the pK_a of the specific compound. Pyrone (X = O in Scheme 4) and pyridinone (X = NR in Scheme 4) forms are in resonance with the aromatic structure, in which a positive charge is delocalized along the atoms of the six-membered ring. The aromaticity of the forms (b), (d) and (f) in Scheme 4 can be described by the HOMA (harmonic oscillator model of aromaticity) index,[46] which is based on the optimal interatomic distance for an aromatic molecule with full π-electron delocalization, calculated according to the Equation (6).

$$\mathrm{HOMA} = 1 - \frac{1}{n}\sum_{i=1}^{n}\alpha_i\left(R_{i,\mathrm{opt}} - R_i\right)^2 \quad (6)$$

in which n represents the total number of bonds in the molecule, and α_i is a normalization constant depending on the type of bond [α(CC) = 257.7, α(CO) = 157.38, α(CN) = 93.52], fixed to give HOMA = 0 for a model nonaromatic system (e.g., the Kekulé structure of benzene) and HOMA = 1 for the system with all the bonds equal to the optimal value $R_{i,\mathrm{opt}}$. The value of R_{opt} is 1.388 Å for C–C, 1.334 Å for C–N and 1.265 Å for C–O bonds. The higher the HOMA value, the more aromatic the ring in question, and hence more delocalized the π electrons of the system. The results are presented in Table 5 and show that the aromatic-

Table 5. Values of HOMA calculated by DFT methods on the protonated, neutral and deprotonated form of pyrone and pyridinone derivatives, tropolone and catechol.

	Free ligand			$[VOL_2]$	*cis*-$[VOL_2(H_2O)]$
	Prot.	Neutr.	Deprot.	Deprot.	Deprot.
H_2cat[a]	0.98	0.85	0.37	0.84[b]	[c]
Hdhp	0.94	0.72	0.36	0.86	0.86, 0.82
Hdepp	0.94	0.75	0.50	0.87	0.87, 0.82
Hma	0.77	0.50	0.17	0.75	0.74, 0.70
Hema	0.78	0.51	0.30	0.75	0.74, 0.70
Hkoj	0.75	0.46	0.13	0.70	0.70, 0.65
Htrop	0.92	0.57	0.08	0.76	0.75, 0.70

[a] For H_2cat the values refer to neutral, singly and doubly deprotonated form. [b] Cat(2–) in the doubly deprotonated form. [c] Species not formed.

ity of all the ligands increases in the order: anion < neutral ligand < cation. This confirms the data of Zborowski et al., who studied several hydroxypyrones,[46] and reflects the fact that the more stable cationic structure does not have a charge separation, whereas the anionic structure has a negative charge in addition to the charge separation and is for this reason less stable.

The simulations show that the stabilization of the aromatic form is a consequence of the delocalization of the positive charge on the heteroatom X of the ring; this is favoured when the heterogroup is NR (which bears a positive charge of +0.14 and +0.22; Table 6) rather than O (on which there is only negative charge; Table 6). Therefore, pyridinones have more aromatic character than pyrones. This insight has been already highlighted on the basis of only chemical considerations.[39] The aromaticity increases when there is an ethyl instead of a methyl group in the ring for an electron-releasing effect that stabilizes the positive charge; thus, Hdepp is more aromatic (in all the forms) than Hdhp, and Hema is more than Hma. Instead, the $–CH_2OH$ group suppresses the aromaticity of kojic acid. Tropolone shows an interesting behaviour: its aromaticity in the cationic form is comparable to that of catechol and pyridinones, in the neutral form is larger than pyrone derivatives, whereas in the deprotonated form the HOMA index becomes the smallest and close to 0. As already pointed out,[47] this is a consequence of the Hückel rule: a positively charged hydroxy group in the cationic form withdraws electrons from the ring, thus moving closer to the $(4n + 2)$ number of electrons, whereas a negatively charged phenolate oxygen acts in the opposite direction. It is worth noting that stabilization of the resonance form (d) in Scheme 4 for pyridinones also causes a decrease in the acidity of the neutral ligands due to the strong intramolecular hydrogen bond. This is confirmed by the comparison between the acidity of maltol and ethylmaltol (pK_a 8.44 and 8.54; Table 2), and that of Hdhp and Hdepp (pK_a 9.76 and 9.92[39,45b]).

In Table 5, the HOMA indexes for the ligands coordinated to the VO^{2+} ion in the fully deprotonated form are also listed. In both $[VOL_2]$ and *cis*-$[VOL_2(H_2O)]$, they are much larger (in the range 0.70–0.87) than in the deprotonated free ligands and approach the values calculated for the neutral and protonated forms of the uncomplexed ligands. It must be noted that the HOMA of the ligands is increased both in the protonated (in the free ligand) and in the deprotonated (coordinated ligand) form and this means that a metal ion, in addition to a proton, is able to stabilize the aromatic structure. This phenomenon can be described in terms of metalloaromaticity, the manifestation of aromatic properties in a chelate metallocycle.[48] Our results are in agreement with those of Zborowski et al. on the metalloaromaticity in the complexes formed by hydroxypyrones.[49] Interestingly, cat(2–) in $[VO(cat)_2]^{2–}$, although it has a double negative charge, reaches an aromaticity degree very similar to that of dhp(–) and depp(–) in $[VO(dhp)_2]$ and $[VO(depp)_2]$, in which the ligands have only one negative charge.

The results of DFT simulations, performed in water within the framework of the polarizable continuum model (PCM) on the fully deprotonated form of the ligands, are summarized in Table 6, in which the bond lengths and the atomic charges are reported.

The results can be summarized as follows: from pyrones to catechol, the donor set changes progressively from (CO, $O^–$) to ($O^–$, $O^–$) (Scheme 5), and it can be supposed that for kojic acid, maltol and ethylmaltol the form (a) is predominant, that pyridinones have an intermediate structure with a partial positive charge on the nitrogen in position 1 of the ring and a pseudo-aromatic electronic structure [form (b)], whereas catechol is present almost exclusively in the form (c).

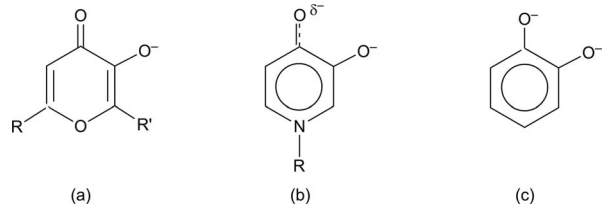

Scheme 5. Predominant structures for the fully deprotonated form of (a) pyrones, (b) pyridinones and (c) catechol.

On the basis of the results obtained, some interesting correlations can be obtained that allow us to put in relationship the pK_a of the ligands (pK_a refers to the deprotonation of H**L** form) with the bond lengths and the charge on specific atoms. In particular, it seems to be plausible to re-

Table 6. Values of the distance and electric charge calculated by DFT methods on the fully deprotonated form of pyrone and pyridinone derivatives, tropolone and catechol in water.

	Distance[a]				Charge				
	$C–O_{phen}$	$C–O_{ket}$	Δd[b]	d^{mean}[c]	O_{ket}	O_{phen}	N	Tot.[d]	pK_a[e]
cat(2–)	1.298	1.298	0.000	1.298	–0.745	–0.745	–	–1.490	13.0
dhp(–)	1.279	1.262	0.017	1.271	–0.586	–0.640	+0.135	–1.226	9.76
depp(–)	1.281	1.265	0.016	1.273	–0.603	–0.670	+0.216	–1.273	9.92
ma(–)	1.278	1.250	0.028	1.264	–0.510	–0.649	–0.088	–1.159	8.44
ema(–)	1.279	1.256	0.023	1.267	–0.525	–0.647	–0.073	–1.172	8.54
koj(–)	1.276	1.245	0.031	1.260	–0.444	–0.656	–0.101	–1.100	7.67
trop(–)	1.252	1.252	0.000	1.252	–0.478	–0.478	–	–0.956	6.66

[a] Values reported in Å. [b] $\Delta d = d_{CO_{ket}} – d_{CO_{phen}}$. [c] Mean distance between $C–O_{ket}$ and $C–O_{phen}$ bonds. [d] Sum of the charge on O_{ket} and O_{phen}. [e] pK_a refers to the deprotonation of H**L** form of the ligands.

late the strength of a ligand with the total electric charge present on both the coordinating atoms (keto and phenolate oxygens). Furthermore, by increasing the importance of the resonance form (c) in Scheme 5, the mean distance of the C–O bonds (d^{mean}) should increase, whereas the difference between the two length distances ($\Delta d = d_{CO_{ket}} - d_{CO_{phen}}$) should decrease; these parameters have been plotted as a function of pK_a in Figure 4 and Figure 5. It can be noted that a linear relationship exists between the absolute value of the charge on the two oxygen atoms in *ortho* position on one hand and the parameters d^{mean} and Δd on the other with the pK_a of the ligands.

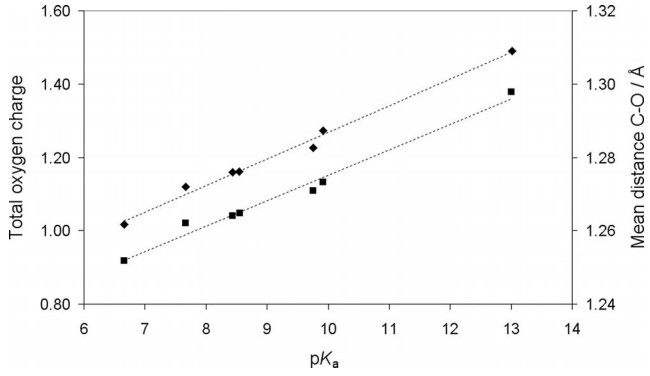

Figure 4. Total electric charge (as the absolute value) on the keto and phenolate oxygens (rhombi) and mean distances of the C=O_{ket} and C–O_{phen} bonds (squares) in the ligands in the fully deprotonated form in water as a function of pK_a (pK_a refers to the deprotonation of the H**L** form of the ligands).

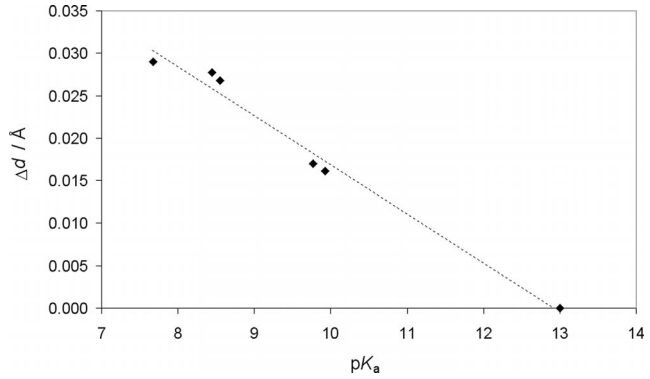

Figure 5. Difference between the bond lengths C=O_{ket} and C–O_{phen} as a function of ligand pK_a (pK_a refers to the deprotonation of the H**L** form of the ligands).

It has been noticed that, by increasing the importance of form (c) in Scheme 5 and consequently the ligand basicity, a greater tendency to stabilize the square-pyramidal geometry with an equatorial–equatorial arrangement of the two ligand molecules can be observed. As a proof of this, the bis-chelated complexes of Hma, Hema and Hkoj are present in an aqueous solution exclusively in the *cis*-octahedral geometry, with Hdhp and Hdepp the *cis*-octahedral species is less important with respect to the square-pyramidal complex and, finally, with catechol and its derivatives only the formation of pentacoordinate species is observed. This is confirmed by pH-potentiometric results, which suggest the presence in solution of a species with stoichiometry *cis*-[VO**L**$_2$(OH)]$^-$ {i.e., with a hydroxido ion in *cis* position to the V=O bond and formed after the deprotonation of the equatorial water in the *cis*-octahedral complex *cis*-[VO**L**$_2$(H_2O)]} in all the systems except that with catechol.

Our idea is to correlate the p*K* values of *cis*-[VO**L**$_2$(H_2O)] species with the absolute value of the coordinated oxygen charge. However, in this case the structural details and the charges of the complexed instead of the free ligands must be considered. The graph that represents the relationship between the p*K* values and the absolute value of the total oxygen charge (left axis) or the mean distance of the four C–O bonds (right axis) is shown in Figure 6. As expected, a linear plot is obtained.

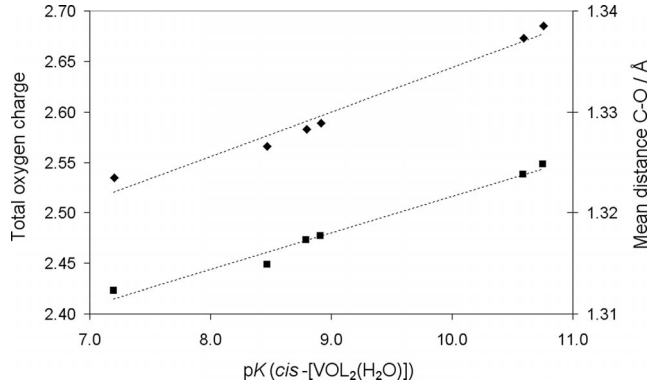

Figure 6. Total electric charge (as the absolute value) on the keto and phenolate oxygens (rhombi) and mean distances of the C=O_{ket} and C–O_{phen} bonds (squares) in *cis*-[VO**L**$_2$(H_2O)] as a function of deprotonation p*K* of the equatorial water molecule.

^{51}V A_z Value of the Bis-Chelated Complexes Formed by Pyrone, Pyridinone, Tropolone and Catechol Ligands

The additivity rule (see below) allows us to calculate the value of A_z for a given VO^{2+} complex from the contribution of the four equatorial donors, according to Equation (7).[32]

$$A_z = \sum_{i=1}^{4} A_z(\text{donor } i) = A_z(\text{donor 1}) + A_z(\text{donor 2}) + A_z(\text{donor 3}) + A_z(\text{donor 4}) \quad (7)$$

This rule is based on the fact that with an increase in the donor basicity (i.e., their strength as ligands) the covalence of the V-donor bonds increases, whereas the hyperfine coupling constant along the *z* axis between the unpaired electron and ^{51}V nucleus decreases. Therefore, it could be interesting to evaluate whether there is a correlation between the value of A_z measured for the solid species [VO**L**$_2$] formed by pyrone and pyridinone derivatives, tropolone and catechol, or for *cis*-[VO**L**$_2$(H_2O)] and *cis*-[VOL_2(OH)]$^-$ formed in aqueous solution by pyrones, pyridinones and tropolone, and the electric charge (as the absolute value) present on the equatorial oxygen atoms (two keto and two phenolate oxygens for square pyramidal, or two keto and one phenolate oxygen for *cis*-octahedral species). This has been made

in Figures 7, 8 and S5 (for the latter see the Supporting Information). In all the cases, a linear plot is obtained. The correlation explains why the *cis*-octahedral species formed by the weakest ligand, tropolonate, *cis*-[VO(trop)$_2$(H$_2$O)] and *cis*-[VO(trop)$_2$(OH)]$^-$, have A_z smaller than the analogous complexes formed by maltol, ethylmaltol, kojic acid and approaches the values of Hdhp and Hdepp (Table 1): for tropolonate the two oxygen atoms are equivalent and the oxygen donor of the ligand arranged equatorial–axial in the *cis*-octahedral species is intermediate between one keto and one phenolic and is, therefore, stronger than that of maltol, ethylmaltol and kojic acid (keto oxygen), thereby giving a smaller contribution to the A_z value (Figure 8 and Figure S5 in the Supporting Information). Thus, when the complex is *cis*-octahedral, the total charge (as the absolute value) present on the equatorial oxygen atoms is larger for tropolone than for other pyrone derivatives; instead, when the complex is square pyramidal and all of the four oxygen donors are on the equatorial plane and contribute to A_z, the total equatorial charge follows the trend of the basicity ethylmaltol > maltol > kojic acid > tropolone. Therefore, the order of A_z values should be that which is expected

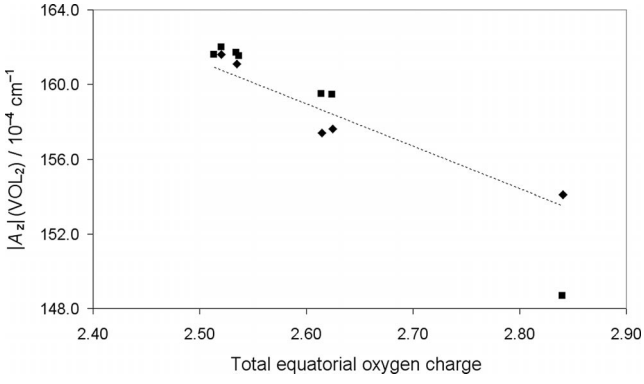

Figure 7. A_z values for [VO**L**$_2$] as a function of the total electric charge (as the absolute value) on the keto and phenolate oxygen atoms. The squares and rhombi indicate the calculated and experimental values, respectively.

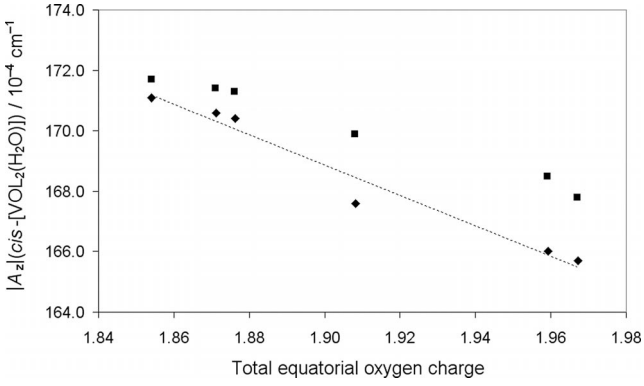

Figure 8. A_z values for *cis*-[VO**L**$_2$(H$_2$O)] as a function of the electric charge (as the absolute value) on the equatorial oxygen donors. The squares and rhombi indicate the calculated and experimental values, respectively.

{and this is confirmed by the experimental values for [VO(ma)$_2$] and [VO(trop)$_2$], and by the calculated values for [VO(ma)$_2$], [VO(ema)$_2$], [VO(koj)$_2$] and [VO(trop)$_2$]}.

Conclusions

VO^{2+} complexes formed by pyrone ligands have been extensively studied in the last few years for their insulin-like effect. In this work, experimental and computational studies have allowed us to clarify the chemical behaviour of these compounds. In particular, DFT methods suggest that in aqueous solution the *cis*-octahedral geometry with a water molecule in the equatorial position is strongly preferred with respect to the square pyramidal (favoured in the solid state) and *trans*-octahedral. This transformation is important with regard to the biotransformation at physiological conditions of the antidiabetic compounds, which may be bound by the blood serum proteins through the coordination of a side-chain donor of the amino acids present on the surface; this has been recently demonstrated for the bis-chelated complex of maltol.[15d]

The complexing properties of the pyrones can be put into relationship with the electronic structure of the free ligands and of the complexes: in particular, the structure assumed in water seems to be strongly influenced by the charge present on the donor atoms (related to their basicity) and by the aromaticity of the ligands (related to the relative importance of the resonance form in which a partial positive charge is present on the heteroatom and the two donors become similar to phenolate oxygen atoms). The results have been compared to those displayed by the family of the pyrdinones, for which the main form in water is the square pyramidal and *cis*-octahedral is a minor species, and by catechol, for which only the square-pyramidal complex exists in aqueous solution. By going from pyrones to pyridinones and catechol, the electron density on the donor oxygen atoms and the aromaticity of the ligands increases and simultaneously the donor set changes from (CO, O$^-$) to (O$^-$, O$^-$). The electronic structure of the ligands also influences the spectroscopic parameters, in particular ^{51}V hyperfine coupling constant A_z, which is the most used datum for the identification of the equatorial donors in a VO^{2+} species. It has been found that, by increasing the charge on the donors, a decrease in A_z (for square-pyramidal and *cis*-octahedral species with one water or hydroxido ligand in the fourth equatorial position) is expected.

Experimental Section

Chemicals: Water was deionized prior to use with the purification system Millipore MilliQ Academic. All the ligands were of the highest grade available and used as received. VO^{2+} solutions were prepared from $VOSO_4 \cdot 3H_2O$ following a literature method.[50]

Potentiometric Measurements: The stability constants of the proton and VO^{2+} complexes were determined by pH-potentiometric titrations on 25.00 mL samples. The ligand-to-metal molar ratio was between 1:1 and 4:1 and VO^{2+} concentration was 0.40–4.0 mM. For

the VO^{2+}/Htrop system, due to the very limited solubility of the neutral $[VO(trop)_2]$, titrations were carried out in large volume samples (50–80 mL) at low analytical concentrations (c_{VO} = 0.4–1.0 mM). Titrations were performed from pH 2.0 until precipitation or very extensive hydrolysis by adding carbonate-free KOH of known concentration (approx. 0.2 M KOH).[51] The pH was measured with a Mettler Toledo DL50 titrator equipped with a DG-114SC combined electrode, calibrated for hydrogen-ion concentration by the method of Irving et al.[52] The water-ionization constant, pK_w, is 13.76 ± 0.01 under the conditions employed. Measurements were carried out at (25.0 ± 0.1) °C and at a constant ionic strength of 0.20 M KCl. Purified argon was bubbled through the samples to ensure the complete absence of oxygen and carbon dioxide. The number of experimental points used in the calculations was 150–200 for each system and the reproducibility of the points included in the evaluation was within 0.005 pH unit in the whole pH range measured.

The stability constants, $\beta_{pqr} = [(VO)_p\mathbf{L}_qH_r]/[VO]^p[\mathbf{L}]^q[H]^r$, in which VO stands for VO^{2+} ion and **L** is the deprotonated form of the ligands, have been calculated with the aid of the PSEQUAD program.[53] Standard deviations were calculated by assuming random errors. Hydroxido complexes of VO^{2+} were taken into account and the following species were assumed: $[VO(OH)]^+$ ($\log\beta$ = –5.94), $[(VO)_2(OH)_2]^{2+}$ ($\log\beta$ = –6.95), with stability constants calculated from the data of Henry et al.[54] and corrected for the different ionic strengths by use of the Davies equation,[54] $[VO(OH)_3]^-$ ($\log\beta$ = –18.0) and $[(VO)_2(OH)_5]^-$ ($\log\beta$ = –22.0).[55]

Synthesis of $[VO(trop)_2]$: $[VO(trop)_2]$ was obtained by the reaction of an aqueous solution of $VOSO_4{\cdot}3H_2O$ (4×10^{-3} M) with tropolone (8×10^{-3} M) at room temperature. The reaction mixture was kept whilst stirring under argon and pH was increased with a dilute solution of NaOH to a value around 5. The polycrystalline samples were filtered off, washed with water and diethyl ether and dried at room temperature. $C_{14}H_{10}O_3V$ (277.17): calcd. C 54.38, H 3.26; found C 55.04, H 3.26.

Spectroscopic and Analytical Measurements: Anisotropic EPR spectra were recorded on aqueous solutions with an X-band (9.15 GHz) Varian E-9 spectrometer at 100 K. As usual for low-temperature measurements, a few drops of DMSO were added to the samples to ensure good glass formation. All operations were performed under a purified argon atmosphere to avoid oxidation of VO^{2+} ion. EPR spectra were simulated with the computer program Bruker WinEPR SimFonia.[57] The coordination mode of the species formed has been attributed with the comparison of the ^{51}V A_z experimental values with those obtained through DFT simulations and the application of the "additivity" rule [Equation (7)];[32] unfortunately, the additivity rule does not take into account the influence of an axial donor, recently demonstrated,[34] but usually the predicted values fall in the range of around 3×10^{-4} cm^{-1} with respect to the experimental ones. Electronic absorption spectra on the aqueous solution were recorded with a Jasco Uvidec 610 spectrophotometer in the same concentration range as used for potentiometry. No deconvolution of the absorption spectra was carried out and therefore the molar absorption coefficients ε have been calculated by measuring the absorbance at the wavelength maxima. Infrared spectra (4000–600 cm^{-1}) were obtained with a Jasco FT/IR-480Plus spectrometer using KBr disks. Elemental analysis (C, H, N) was carried out with a Perkin–Elmer 240 B elemental analyser.

DFT Calculations: All the calculations presented in this paper were performed with DFT methods,[58] and Gaussian 03 (revision C.02) software.[19] The hybrid exchange-correlation B3LYP,[21,22] and the half-and-half BHandHLYP functional, as incorporated in the Gaussian 03, were used. The performance of BHandHLYP functional in the calculation of ^{51}V hyperfine coupling constant along the z axis on several representative VO^{2+} complexes with different charges, geometries and coordination modes was recently tested, with a mean deviation from $|A_z|^{exp.}$ below 3%.[25]

The geometries of the ligands in the protonated, neutral and deprotonated form were optimized at the B3LYP/6-311++g(d,p) level of theory in water within the framework of the polarizable continuum model (PCM).[59] The geometries of the VO^{2+} complexes investigated were first preoptimized at the B3LYP/sto-3g level and further optimized at the B3LYP/6-311g level of theory in the gas phase. For all the structures, minima were verified through frequency calculations. The energy of the possible bis-chelated species formed in water by maltol (Table 4) was calculated at the B3LYP/6-311g level of theory within the framework of PCM.[59]

The optimized structures in the gas phase of the VO^{2+} complexes were used to predict the ^{51}V hyperfine coupling constants (A_{iso}, A_x, A_y and A_z). A_{iso}, A_x, A_y and A_z were simulated at the BHandHLYP/6-311g(d,p) level of theory; $A_{x,y,z}$ were calculated as sum of the isotropic Fermi contact (A_{iso}) and the anisotropic or dipolar hyperfine interaction ($A^D_{x,y,z}$): $A_{x,y,z} = A_{iso} + A^D_{x,y,z}$. The percent deviation from the absolute experimental value, $|A_z|^{exp.}$, was calculated as: $100 \times [(|A_z|^{calcd.} - |A_z|^{exp.})/|A_z|^{exp.}]$ (Table 1).

The analysis of the molecular orbital (MO) composition in terms of atomic orbitals or groups of atoms was performed using the AOMix program (revision 6.52).[60]

Supporting Information (see footnote on the first page of this article): Table with the experimental and calculated geometric parameters for maltol complexes (Table S1); figures with the electronic spectra of *cis*-$[VO(ma)_2(H_2O)]$ and *cis*-$[VO(ma)_2(OH)]^-$ (Figure S1), with representative molecular orbitals of *cis*-$[VO(ma)_2(H_2O)]$ (Figure S2), with X-band anisotropic EPR spectra of the system VO^{2+}/Htrop (Figure S3) and of $[VO(trop)_2]$ dissolved in organic solvents (Figure S4), with A_z values for *cis*-$[VOL_2(OH)]^-$ as a function of the absolute value of the electric charge on the equatorial oxygen donors (Figure S5); and scheme with the relative energy levels of the molecular orbitals of *cis*-$[VO(ma)_2(H_2O)]$ and *cis*-$[VO(ma)_2(OH)]^-$ (Scheme S1).

[1] a) D. Rehder, in: *Metal Ions in Biological Systems* (Eds.: A. Sigel, H. Sigel), Marcel Dekker, New York, **1995**, vol. 31, pp. 1–43; b) D. C. Crans, J. J. Smee, E. Gaidamauskas, L. Yang, *Chem. Rev.* **2004**, *104*, 849–902; c) J. Costa Pessoa, I. Tomaz, *Curr. Med. Chem.* **2010**, *17*, 3701–3738, and references cited therein.

[2] a) K. H. Thompson, J. H. McNeill, C. Orvig, *Chem. Rev.* **1999**, *99*, 2561–2571, and references cited therein; b) K. H. Thompson, C. Orvig, *J. Chem. Soc., Dalton Trans.* **2000**, 2885–2892; c) K. H. Thompson, C. Orvig, *Coord. Chem. Rev.* **2001**, *219–221*, 1033–1053 and references cited therein; d) Y. Shechter, I. Goldwaser, M. Mironchik, M. Fridkin, D. Gefel, *Coord. Chem. Rev.* **2003**, *237*, 3–11; e) H. Sakurai, Y. Yoshikawa, H. Yasui, *Chem. Soc. Rev.* **2008**, *37*, 2383–2392.

[3] a) E. L. Tolman, E. Barris, M. Burns, A. Pansini, R. Partridge, *Life Sci.* **1979**, *25*, 1159–1164; b) Y. Shechter, S. J. D. Karlish, *Nature* **1980**, *284*, 556–558.

[4] a) B. I. Posner, R. Faure, J. W. Burgess, A. P. Bevan, D. Lachance, G. Zhang-Sun, I. G. Fantus, J. B. Ng, D. A. Hall, B. Soo Lum, A. Shaver, *J. Biol. Chem.* **1994**, *269*, 4596–4606; b) B. I. Posner, C. R. Yang, A. Shaver, in: *Vanadium Compounds: Chemistry, Biochemistry and Therapeutic Applications* (Eds.: A. S. Tracey, D. C. Crans), ACS symposium series 711, Washington DC, **1998**, pp. 316–328.

[5] P. Caravan, L. Gelmini, N. Glover, F. G. Herring, J. H. McNeill, J. Rettig, I. A. Setyawati, E. Shutter, Y. Sun, A. S. Tracey, V. G. Yuen, C. Orvig, *J. Am. Chem. Soc.* **1995**, *117*, 12759–12770.

[6] K. H. Thompson, B. D. Liboiron, G. R. Hanson, C. Orvig, in: *Medicinal Inorganic Chemistry* (Eds.: J. L. Sessler, S. R. Doctrow, T. J. McMurry, S. J. Lippard), ACS Symposium Series 903, Washington DC, **2005**, pp. 384–399.

[7] J. H. McNeill, V. G. Yuen, H. R. Hoveyda, C. Orvig, *J. Med. Chem.* **1992**, *35*, 1489–1491.

[8] V. G. Yuen, C. Orvig, J. H. McNeill, *Can. J. Physiol. Pharmacol.* **1993**, *71*, 263–269.

[9] K. H. Thompson, J. Lichter, C. LeBel, M. C. Scaife, J. H. McNeill, C. Orvig, *J. Inorg. Biochem.* **2009**, *103*, 554–558.

[10] a) M. A. Barrand, B. A. Callingham, R. C. Hider, *J. Pharm. Pharmacol.* **1987**, *39*, 203–211; b) M. A. Barrand, B. A. Callingham, *Br. J. Pharmacol.* **1991**, *102*, 408–414; c) S. J. Lord, N. A. Epstein, R. L. Paddock, C. M. Vogels, T. L. Hennigar, M. J. Zaworotko, N. J. Taylor, W. R. Driedzic, T. L. Broderick, S. A. Westcott, *Can. J. Chem.* **1999**, *77*, 1249–1261.

[11] a) B. Song, K. Saatchi, G. H. Rawji, C. Orvig, *Inorg. Chim. Acta* **2002**, *339*, 393–399; b) K. H. Thompson, C. Orvig, in: *Metal Ions in Biological Systems* (Eds.: A. Sigel, H. Sigel), Marcel Dekker, New York, **2004**, vol. 41, pp. 221–252; c) V. Monga, K. H. Thompson, V. G. Yuen, V. Sharma, B. O. Patrick, J. H. McNeill, C. Orvig, *Inorg. Chem.* **2005**, *44*, 2678–2688; d) K. Saatchi, K. H. Thompson, B. O. Patrick, M. Pink, V. G. Yuen, J. H. McNeill, C. Orvig, *Inorg. Chem.* **2005**, *44*, 2689–2697.

[12] a) V. G. Yuen, P. Caravan, L. Gelmini, N. Glover, J. H. McNeill, I. A. Setyawati, Y. Zhou, C. Orvig, *J. Inorg. Biochem.* **1997**, *68*, 109–116.

[13] a) Y. Adachi, J. Yoshida, Y. Kodera, A. Katoh, J. Takada, H. Sakurai, *J. Med. Chem.* **2006**, *49*, 3251–3256; b) H. Yasui, Y. Adachi, A. Katoh, H. Sakurai, *J. Biol. Inorg. Chem.* **2007**, *12*, 843–853; c) H. Sakurai, A. Katoh, T. Kiss, T. Jakusch, M. Hattori, *Metallomics* **2010**, *2*, 670–682.

[14] B. D. Liboiron, K. H. Thompson, G. R. Hanson, E. Lam, N. Aebischer, C. Orvig, *J. Am. Chem. Soc.* **2005**, *127*, 5104–5115.

[15] a) D. Sanna, G. Micera, E. Garribba, *Inorg. Chem.* **2010**, *49*, 174–187; b) D. Sanna, P. Buglyó, G. Micera, E. Garribba, *J. Biol. Inorg. Chem.* **2010**, *15*, 825–839; c) D. Sanna, G. Micera, E. Garribba, *Inorg. Chem.* **2011**, *50*, 3717–3728; d) D. Sanna, L. Bíró, P. Buglyó, G. Micera, E. Garribba, *Metallomics* **2012**, *4*, 33–36.

[16] G. R. Hanson, Y. Sun, C. Orvig, *Inorg. Chem.* **1996**, *35*, 6507–6512.

[17] P. Buglyó, E. Kiss, I. Fábián, T. Kiss, D. Sanna, E. Garribba, G. Micera, *Inorg. Chim. Acta* **2000**, *306*, 174–183.

[18] F. Neese, *Coord. Chem. Rev.* **2009**, *253*, 526–563 and references cited therein.

[19] M. J. Frisch, G. W. Trucks, H. B. Schlegel, G. E. Scuseria, M. A. Robb, J. R. Cheeseman, J. A. Montgomery Jr., T. Vreven, K. N. Kudin, J. C. Burant, J. M. Millam, S. S. Iyengar, J. Tomasi, V. Barone, B. Mennucci, M. Cossi, G. Scalmani, N. Rega, G. A. Petersson, H. Nakatsuji, M. Hada, M. Ehara, K. Toyota, R. Fukuda, J. Hasegawa, M. Ishida, T. Nakajima, Y. Honda, O. Kitao, H. Nakai, M. Klene, X. Li, J. E. Knox, H. P. Hratchian, J. B. Cross, C. Adamo, J. Jaramillo, R. Gomperts, R. E. Stratmann, O. Yazyev, A. J. Austin, R. Cammi, C. Pomelli, J. W. Ochterski, P. Y. Ayala, K. Morokuma, G. A. Voth, P. Salvador, J. J. Dannenberg, V. G. Zakrzewski, S. Dapprich, A. D. Daniels, M. C. Strain, O. Farkas, D. K. Malick, A. D. Rabuck, K. Raghavachari, J. B. Foresman, J. V. Ortiz, Q. Cui, A. G. Baboul, S. Clifford, J. Cioslowski, B. B. Stefanov, G. Liu, A. Liashenko, P. Piskorz, I. Komaromi, R. L. Martin, D. J. Fox, T. Keith, M. A. Al-Laham, C. Y. Peng, A. Nanayakkara, M. Challacombe, P. M. W. Gill, B. Johnson, W. Chen, M. W. Wong, C. Gonzalez, J. A. Pople, *Gaussian 03*, Revision C.02, Gaussian, Inc., Wallingford CT, **2004**.

[20] a) M. Bühl, H. Kabrede, *J. Chem. Theory Comput.* **2006**, *2*, 1282–1290; b) M. P. Waller, M. Bühl, *J. Comput. Chem.* **2007**, *28*, 1531–1537; c) M. P. Waller, H. Braun, N. Hojdis, M. Bühl, *J. Chem. Theory Comput.* **2007**, *3*, 2234–2242; d) M. Bühl, C. Reimann, D. A. Pantazis, T. Bredow, F. Neese, *J. Chem. Theory Comput.* **2008**, *4*, 1449–1459.

[21] A. D. Becke, *J. Chem. Phys.* **1993**, *98*, 5648–5652.

[22] C. Lee, W. Yang, R. G. Parr, *Phys. Rev. B* **1988**, *37*, 785–789.

[23] a) K. G. Spears, *J. Phys. Chem. A* **1997**, *101*, 6273–6279; b) C. P. Aznar, Y. Deligiannakis, E. J. Tolis, T. Kabanos, M. Brynda, R. D. Britt, *J. Phys. Chem. A* **2004**, *108*, 4310–4321; c) I. Correia, J. Costa Pessoa, M. T. Duarte, R. T. Henriques, M. F. M. Piedade, L. F. Veiros, T. Jakusch, A. Dornyei, T. Kiss, M. M. C. A. Castro, C. F. G. C. Geraldes, F. Avecilla, *Chem. Eur. J.* **2004**, *10*, 2301–2317; d) K. Zborowski, R. Grybos, L. M. Proniewicz, *Inorg. Chem. Commun.* **2005**, *8*, 76–78; e) K. J. Ooms, S. E. Bolte, J. J. Smee, B. Baruah, D. C. Crans, T. Polenova, *Inorg. Chem.* **2007**, *46*, 9285–9293; f) L. L. G. Justino, M. L. Ramos, F. Nogueira, A. J. F. N. Sobral, C. F. G. C. Geraldes, M. Kaupp, H. D. Burrows, C. Fiolhais, V. M. S. Gil, *Inorg. Chem.* **2008**, *47*, 7317–7326.

[24] G. Micera, E. Garribba, *Int. J. Quantum Chem.* DOI: 10.1002/qua.23237.

[25] a) G. Micera, E. Garribba, *Dalton Trans.* **2009**, 1914–1918; b) G. Micera, E. Garribba, *J. Comput. Chem.* **2011**, *32*, 2822–2835.

[26] E. Lodyga-Chruscinska, D. Sanna, E. Garribba, G. Micera, *Dalton Trans.* **2008**, 4903–4916.

[27] A. W. Addison, T. N. Rao, J. Reedijk, J. van Rijn, G. C. Verschoor, *J. Chem. Soc., Dalton Trans.* **1984**, 1349–1356.

[28] a) *Calculation of NMR and EPR Parameters. Theory and Applications* (Eds.: M. Kaupp, M. Bühl, V. G. Malkin), Wiley-VCH, Weinheim, Germany, **2004**; b) C. Remenyi, R. Reviakine, A. V. Arbuznikov, J. Vaara, M. Kaupp, *J. Phys. Chem. A* **2004**, *108*, 5026–5033, and references therein.

[29] a) M. L. Munzarová, M. Kaupp, *J. Phys. Chem. B* **2001**, *105*, 12644–12652, and references cited therein; b) A. C. Saladino, S. C. Larsen, *J. Phys. Chem. A* **2003**, *107*, 1872–1878; c) F. Neese, *J. Chem. Phys.* **2003**, *118*, 3939–3948; d) A. C. Saladino, S. C. Larsen, *Catal. Today* **2005**, *105*, 122–133, and references cited therein.

[30] K. H. Thompson, B. D. Liboiron, Y. Sun, K. D. D. Bellman, I. A. Setyawati, B. O. Patrick, V. Karunaratme, G. Rawji, J. Wheeler, K. Sutton, S. Bhanot, C. Cassidy, J. H. McNeill, V. G. Yuen, C. Orvig, *J. Biol. Inorg. Chem.* **2003**, *8*, 66–74.

[31] a) Y. Sun, B. R. James, S. J. Rettig, C. Orvig, *Inorg. Chem.* **1996**, *35*, 1667–1673; b) Y. Sun, M. Melchior, D. A. Summers, R. C. Thompson, S. J. Rettig, C. Orvig, *Inorg. Chem.* **1998**, *37*, 3119–3121; c) B. Song, N. Aebischer, C. Orvig, *Inorg. Chem.* **2002**, *41*, 1357–1364; d) K. H. Thompson, J. Chiles, V. G. Yuen, J. Tse, J. H. McNeill, C. Orvig, *J. Inorg. Biochem.* **2004**, *98*, 683–690; e) A.-K. Bordbar, A. L. Creagh, F. Mohammadi, C. A. Haynes, C. Orvig, *J. Inorg. Biochem.* **2009**, *103*, 643–647.

[32] a) N. D. Chasteen, in: *Biological Magnetic Resonance* (Eds.: L. J. Berliner, J. Reuben), Plenum Press, New York, **1981**, vol. 3, pp. 53–119; b) T. S. Smith II, R. LoBrutto, V. L. Pecoraro, *Coord. Chem. Rev.* **2002**, *228*, 1–18.

[33] B. J. Hamstra, A. P. L. Houseman, G. J. Colpas, J. W. Kampf, R. LoBrutto, W. D. Frasch, V. L. Pecoraro, *Inorg. Chem.* **1997**, *36*, 4866–4874.

[34] S. Gorelsky, G. Micera, E. Garribba, *Chem. Eur. J.* **2010**, *16*, 8167–8180.

[35] F. Belaj, A. Basch, U. Muster, *Acta Crystallogr., Sect. C* **2000**, *56*, 921–922.

[36] C. J. Ballhausen, H. B. Gray, *Inorg. Chem.* **1962**, *1*, 111–122.

[37] a) G. Micera, E. Garribba, *Eur. J. Inorg. Chem.* **2010**, 4697–4710; b) E. Lodyga-Chruscinska, G. Micera, E. Garribba, *Inorg. Chem.* **2011**, *50*, 883–899; c) G. Micera, E. Garribba, *Eur. J. Inorg. Chem.* **2011**, 3768–3780.

[38] S. A. Dikanov, B. D. Liboiron, K. H. Thompson, E. Vera, V. G. Yuen, J. H. McNeill, C. Orvig, *J. Am. Chem. Soc.* **1999**, *121*, 11004–11005.
[39] M. Rangel, A. Leite, M. J. Amorim, E. Garribba, G. Micera, E. Lodyga-Chruscinska, *Inorg. Chem.* **2006**, *45*, 8086–8097.
[40] a) C. Gerard, R. Hugel, *J. Chem. Res.* **1978**, 404–405; b) T. Hedlund, L. O. Ohman, *Acta Chem. Scand.* **1988**, *A42*, 702–709; c) *IUPAC Stability Constants Database*, IUPAC-Academic Software, Otley, **1993**.
[41] a) J.-E. Berg, A.-M. Pilotti, A.-C. Söderholm, B. Karlsson, *Acta Crystallogr., Sect. B* **1978**, *34*, 3071–3072; b) M. C. Barret, M. F. Mahon, K. C. Molloy, J. W. Steed, P. Wright, *Inorg. Chem.* **2001**, *40*, 4384–4388.
[42] A. Jezierski, J. B. Raynor, *J. Chem. Soc., Dalton Trans.* **1981**, 1–7.
[43] B. S. Parajón-Costa, E. J. Baran, J. Romero, R. Sáez-Puche, G. Arrambide, D. Gambino, *J. Coord. Chem.* **2011**, *64*, 57–70.
[44] a) P. L. Paulson, *Chem. Rev.* **1955**, *55*, 9–136; b) W. v. E. Doering, L. Knox, *J. Am. Chem. Soc.* **1951**, *73*, 828–838; c) D. Dryssen, *Acta Chem. Scand.* **1954**, *8*, 1394–1397.
[45] a) M. Rangel, A. Tamura, C. Fukushima, H. Sakurai, *J. Biol. Inorg. Chem.* **2001**, *6*, 128–132; b) P. Buglyó, E. Kiss, T. Kiss, D. Sanna, E. Garribba, G. Micera, *J. Chem. Soc., Dalton Trans.* **2002**, 2275–2282.
[46] K. Zborowski, R. Grybos, L. M. Proniewicz, *J. Phys. Org. Chem.* **2005**, *18*, 250–254.
[47] T. M. Krygowski, M. K. Cyrański, *Chem. Rev.* **2001**, *101*, 1385–1419.
[48] H. Masui, *Coord. Chem. Rev.* **2001**, *219–221*, 957–992.
[49] K. Zborowski, M. Solà, J. Poater, L. M. Proniewicz, *J. Phys. Org. Chem.* **2011**, *24*, 499–506.
[50] I. Nagypál, I. Fábián, *Inorg. Chim. Acta* **1982**, *61*, 109–113.
[51] G. Gran, *Acta Chem. Scand.* **1950**, *4*, 559–577.
[52] H. Irving, M. G. Miles, L. D. Pettit, *Anal. Chim. Acta* **1967**, *38*, 475–488.
[53] L. Zékány, I. Nagypál, in: *Computation Methods for the Determination of Formation Constants* (Ed.: D. J. Leggett), Plenum Press, New York, **1985**, pp. 291–353.
[54] R. P. Henry, P. C. H. Mitchell, J. E. Prue, *J. Chem. Soc., Dalton Trans.* **1973**, 1156–1159.
[55] C. W. Davies, *J. Chem. Soc.* **1938**, 2093–2098.
[56] a) A. Komura, M. Hayashi, H. Imanaga, *Bull. Chem. Soc. Jpn.* **1977**, *50*, 2927–2931; b) L. F. Vilas Boas, J. Costa Pessoa, in: *Comprehensive Coordination Chemistry* (Eds.: G. Wilkinson, R. D. Gillard, J. A. McCleverty), Pergamon Press, Oxford, **1987**, vol. 3, pp. 453–583.
[57] *WINEPR SimFonia*, version 1.25, Bruker Analytische Messtechnik GmbH, Karlsruhe, Germany, **1996**.
[58] R. G. Parr, W. Yang, *Density-Functional Theory of Atoms and Molecules*, Oxford University Press, Oxford, **1989**.
[59] a) S. Miertus, E. Scrocco, J. Tomasi, *Chem. Phys.* **1981**, *55*, 117–129; b) S. Miertus, J. Tomasi, *Chem. Phys.* **1982**, *65*, 239–245; c) M. Cossi, V. Barone, R. Cammi, J. Tomasi, *Chem. Phys. Lett.* **1996**, *255*, 327–335.
[60] a) S. I. Gorelsky, *AOMix: Program for Molecular Orbital Analysis*, University of Ottawa, Ottawa, **2011**, http://www.sgchem.net; b) S. I. Gorelsky, A. B. P. Lever, *J. Organomet. Chem.* **2001**, *635*, 187–196.

Received: November 8, 2011
Published Online: February 3, 2012

DOI: 10.1002/ejic.201101385

Bidentate and Tetradentate β-Aminovinyl Trifluoromethylated Ketones and Their Copper(II) Complexes: Synthesis, Characterization and Redox Chemistry

Nicolas Chopin,[a] Maurice Médebielle,*[a] and Guillaume Pilet*[b]

Keywords: Electrochemistry / UV/Vis spectroscopy / Copper / Fluorine

New polyfunctional bidentate and tetradentate trifluoromethylated enaminone ligands that bear redox-active and photosensitive moieties were synthesized in moderate to good yields and their coordination chemistry with copper(II) was examined. The crystal structures revealed the formation of mononuclear Cu^{II} complexes with all ligands, where the metal ion is located in almost perfect to distorted square planar environments. The deviation from an ideal square plane influences the redox potentials of the metal centre within the complex as demonstrated by cyclic voltammetry. For all the complexes, a stable Cu^{I} species was evidenced by a quasireversible reduction step at potentials from –0.48 to –1.08 V (potential standards E^0), but the most stable Cu^{I} species originated from the Cu^{II} complex with the tetradentate ligand. UV/Vis absorption spectra revealed no major differences between the ligands and their Cu^{II} complexes.

Introduction

Trifluoromethylated β-aminovinyl ketones have been frequently used as building blocks to prepare various trifluoromethylated aromatic and heterocycle molecules.[1] The ability of enaminones to coordinate to a variety of transition metals has led to the preparation of a number of metallomesogens with interesting liquid crystal properties[2–5] and highly active catalysts for olefin polymerization, which include fluorinated enaminones.[6–8] β-Aminovinyl ketones with a fluoroalkyl moiety are interesting organic precursors that can be decorated in a number of useful synthetic sequences to produce diverse molecular entities with specific applications.[1,9–21] Their potentially broad coordination chemistry[21–29] combined with appropriate organic functionalities make them attractive for the design of a new generation of original materials with potential in catalysis, molecular magnetism and therapeutic applications. A series of fluorinated enaminones that bear two independent coordination centres have been obtained, and the crystal structure of a Cu^{II} complex has been reported.[21] The crystal structure of a Mn^{II} complex with a trifluoromethylated enaminone derivative of 3-imidazoline nitroxide has also been published, and the presence of weak ferromagnetic interactions between the metal centres has been evidenced.[22] In addition, the crystal structures of Cu^{II}, Ni^{II} and Pd^{II} bischelates with a trifluoromethylated enamino ketone derivative of 2-imidazoline nitroxide are also known.[23] In parallel, the redox chemistry of fluorinated enaminones and their metal complexes has been studied,[24] which showed that the reduction of the ligands in *N*,*N*-dimethylformamide (DMF) was irreversible and gave unstable radical anions as reduction products, and the corresponding Cu^{II} and Ni^{II} chelates were characterized in most cases by a quasireversible one-electron transfer. Most of the enaminones presented in that study did not feature possible multiple coordination sites, and no extension with potential applications in materials science, catalysis or as potential new metallodrugs has appeared in the literature.

We have recently launched a research program dedicated to the development of efficient and mild synthetic approaches for the synthesis of polyfunctional enaminones that bear a fluoroalkyl moiety with the aim to deliver useful enaminone building blocks, which offer the potential to generate molecular diversity (Figure 1).

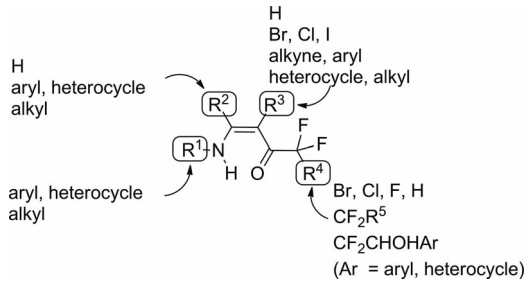

Figure 1. Fluoroalkylated enaminone.

[a] Université de Lyon and Université Claude Bernard Lyon 1, Institut de Chimie et Biochimie Moléculaires et Supramoléculaires (ICBMS), UMR CNRS-UCBL-INSA Lyon 5246, Equipe "Synthèse de Molécules d'Intérêt Thérapeutique (SMITH)", Bât. Curien, 43 boulevard du 11 novembre 1918, 69622 Villeurbanne cedex, France
E-mail: maurice.medebielle@univ-lyon1.fr
[b] Université de Lyon and Université Claude Bernard Lyon 1, Laboratoire des multiMatériaux et Interfaces, UMR CNRS-UCBL, 5615, Bât. Chevreul, 43 boulevard du 11 novembre 1918, 69622 Villeurbanne cedex, France
E-mail: guillaume.pilet@univ-lyon1.fr
Supporting information for this article is available on the WWW under http://dx.doi.org/10.1002/ejic.201101385.

These organic substrates can be structurally modified at different sites (R^1, R^2, R^3 and R^4), by variation of the amine (R^1), the substitution on the C=C bond (R^2 and R^3) and at the fluoroalkyl moiety (R^4).[14–20] In principle, organic functionalities with specific properties can be attached at the four positions of the enaminone from readily available starting materials using different synthetic strategies. The fluorine atoms are significant as they may induce specific interactions in the solid state such as F···H, F···F, F···O=C, F···N and F···S contacts; these properties have been used with success in materials science and crystal engineering,[30–31] in medicinal chemistry in order to design more active drug candidates and have been exemplified by cocrystallized structures of potent therapeutic agents with target enzymes.[32–34] Fluorine is also a useful probe in ^{19}F NMR spectroscopy with potential implications in biology.[35] In addition, the electron-withdrawing effect of fluorine should alter the redox properties of the ligands and metal complexes and could help cocrystallization due to the enhanced volatility of the latter.[27]

In continuation of our recent studies on the design of new polyfunctional enaminone-based ligands and their metal complexes, which can be used as new materials and are potential therapeutic agents, we wish to present the syntheses of a series of bidentate (NO) and tetradentate (N_2O_2) enaminone-based ligands (Figures 2 and 3). In the study presented herein, the explorative coordination chemistry of these original ligands with Cu^{II} will be presented as well as their structures, which are tentatively correlated to their redox chemistry in solution. Bidentate enaminones with a fluoroalkyl moiety are known to some extent, whereas tetradentate ligands and their metal complexes are less studied.[36,37] The structural variations of the reported fluoroalkylated enaminone ligands were not broad (R^1 and R^2 in Figure 1), few crystal structures and no electrochemical data have been reported. Significant attention has focused on the influence of tetrahedral distortion in four-coordinate copper complexes on their redox potentials in order to understand and mimic functions of different families of copper proteins.[38–40]

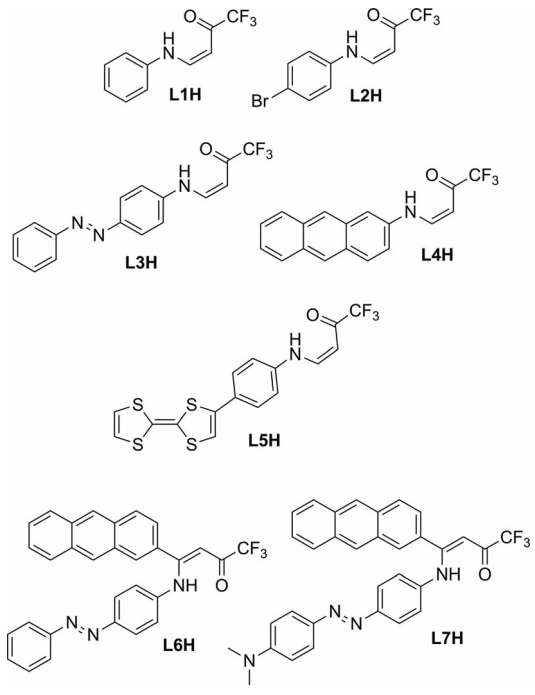

Figure 2. Bidentate ligands **L1H**–**L7H**.

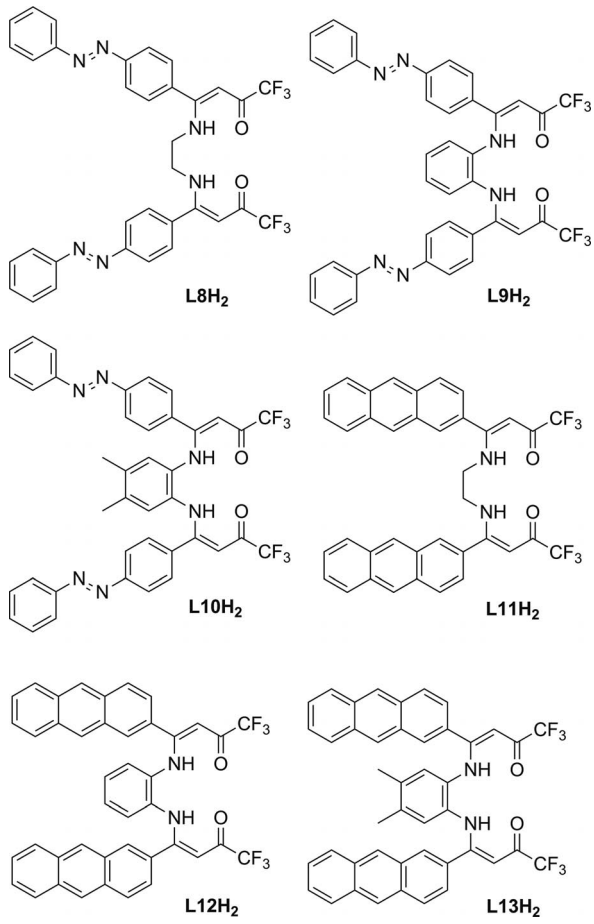

Figure 3. Tetradentate ligands **$L8H_2$**–**$L13H_2$**.

In this work, as our long-term goal is to study the interaction of a defined entity with a specific property with the redox metal centre, R^1 or R^2 were first modified with photosensitive (and redox active) entities (azobenzene, anthracene) and a redox-active unit (tetrathiafulvalene).

Results and Discussion

Ligand Syntheses

The structures of the trifluoromethylated β-aminovinyl ketones (enaminones) are presented in Figures 2 and 3. **L1H**–**L7H** are bidentate, and **$L8H_2$**–**$L13H_2$** were designed to be tetradentate. **L1H**–**L4H** were prepared in good to excellent yields (72–98%) in two straightforward steps: trifluoroacetylation of commercially available ethyl vinyl ether [trifluoroacetic anhydride (TFAA)/pyridine in anhydrous dichloromethane], followed by an O–N exchange reaction

of the crude (*E*)-4-ethoxy-1,1,1-trifluorobut-3-en-2-one (**1**) [41] with the appropriate amines (commercially available) in anhydrous acetonitrile (Scheme 1).

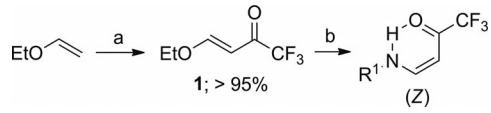

Scheme 1. Synthesis of **L1H**–**L4H**. Reagents and conditions: a) TFAA (1.0 equiv.), pyridine (1.0 equiv.), dichloromethane, room temp.; 18 h; b) amine R^1–NH_2 (1.0 equiv.), acetonitrile, room temp.; 5 h. **L1H** > 95%, **L2H** > 95%, **L3H** 94%, **L4H** 72%.

L1H and **L2H** were prepared in quantitative yields according to known procedures.[42,43] **L5H**, which bears a tetrathiafulvalene (TTF) moiety, was prepared in 25% yield from a Stille reaction between the stannylated-TTF **2**[44] and **L2H** (Scheme 2). This procedure was found to be more practical (no chromatographic purification) than the coupling reaction of the crude **1** with the precursor amine due to solubility problems and tedious purification of the intermediates.

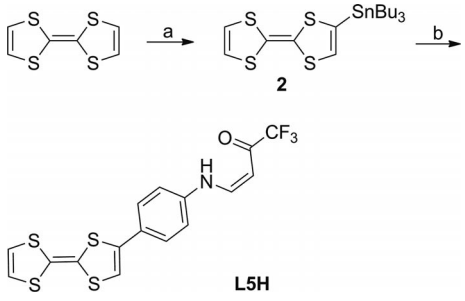

Scheme 2. Synthesis of **L5H**. Reagents and conditions: a) TTF (1.0 equiv.), *n*BuLi (1.0 equiv.), Bu_3SnCl (1.0 equiv.), tetrahydrofuran (THF), –78 °C to room temp.; 1 h; **2** > 95%; b) **L2H** (1.0 equiv.), $Pd(PPh_3)_4$ (5 mol-%), toluene, reflux, 48 h. **L5H** 25%.

L6H–**L7H** and **L8H$_2$**–**L13H$_2$** were prepared in moderate unoptimized yields in three straithforward steps: acetalization of suitable ketones **3** and **4**, trifluoroacetylation of dimethyl acetals **5** and **6** using a combination of TFAA (2 equiv.) and pyridine (4 equiv.) in anhydrous dichloromethane and an O–N exchange reaction of the resulting methoxyvinyl trifluoromethyl ketones **7** and **8** with the corresponding amines and diamines in anhydrous acetonitrile (Scheme 3). The ketone that bears the azobenzene unit **3** is mentioned in the literature[45] without full spectroscopic data; it was prepared in 71% isolated yield from *p*-aminoacetophenone and nitrosobenzene (both commercially available) in acetic acid at 90 °C overnight. Ketone **4** was commercially available.

All the ligands were obtained as *Z* isomers, as determined by ^{1}H NMR spectroscopy, which showed a deshielded peak of the amino proton at > 10.0 ppm due to hydrogen bonding between NH and C=O. The ligands were isolated as solids and were generally purified by silica gel chromatography.

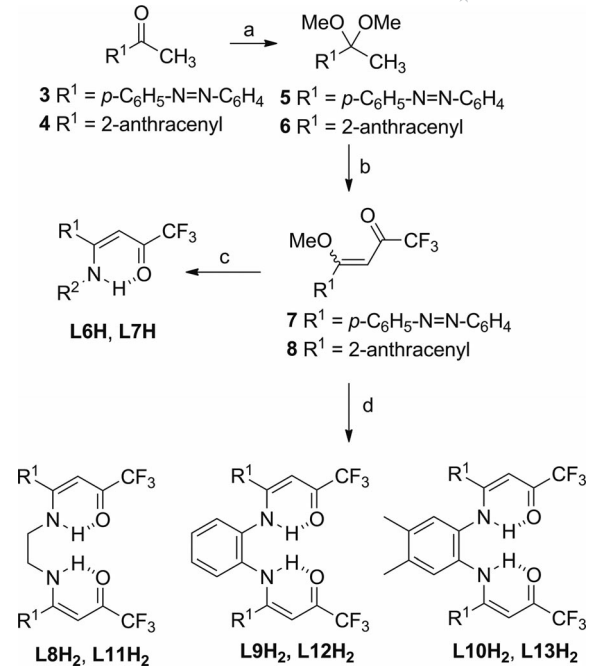

Scheme 3. Synthesis of **L6H**–**L13H$_2$**. Reagents and conditions: a) $(EtO)_3CH$ (1.5 equiv.), *p*-$CH_3C_6H_4SO_3H$ (0.7 mol-%), MeOH, 60 °C, 24 h; **5** > 95%, **6** > 95%; b) TFAA (2.0 equiv.), pyridine (4.0 equiv.), dichloromethane, 45 °C; 8–72 h; **7** 84%, **8** 60%; c) R^2–NH_2 (1.0 equiv.), **8** (1.0 equiv.), acetonitrile, room temp.; 5 h; **L6H** 68%, **L7H** 60%; d) diamine (0.5 equiv.), **7** or **8** (1.0 equiv.), acetonitrile, room temp.; 4 h; **L8H$_2$** 54%, **L9H$_2$** 50%, **L10H$_2$** 60%, **L11H$_2$** 42%, **L12H$_2$** 48%, **L13H$_2$** 63%.

Syntheses of Cu^{II} Complexes

The corresponding Cu^{II} complexes were generally prepared in good yields (> 70%) through dropwise addition of a methanolic solution of $CuCl_2 \cdot 2H_2O$ (0.75 equiv. for bidentate ligands and 1.50 equiv. for the tetradentate ligands) to a dichloromethane solution of the ligand that contained Et_3N (4 equiv.). The resulting green or brown solution was stirred for two hours at room temperature and concentrated to give a precipitate, which was washed with cold methanol or purified by filtration through silica gel (elution with dichloromethane) to give the desired complexes as green or brown powders. Slow evaporation of a dichloromethane/methanol (1:1) solution {with a small amount of toluene for [Cu(**L4**)$_2$]} gave single crystals suitable for single-crystal XRD. The copper complexes of **L1H**, **L3H**, **L6H** and **L12H$_2$** were obtained by following this procedure systematically.

Crystal Structure Description

The formulas obtained from the single-crystal XRD characterization of the complexes are [Cu(**L1**)$_2$] (**A**), [Cu(**L3**)$_2$] (**B**), [Cu(**L6**)$_2$] (**C**) and [Cu(**L12**)]·0.5(MeOH)·0.5(AcOEt) (**D**). Details of structural refinement can be found in Table 2. The crystal structures of **L4H**, **L10H$_2$** and [Cu(**L8**)$_2$] (**E**) can be found in the Supporting Information.

All of the neutral Cu^{II}-based complexes are mononuclear and the metal ion is located in a more or less distorted square planar N_2O_2 environment (Figure 4).

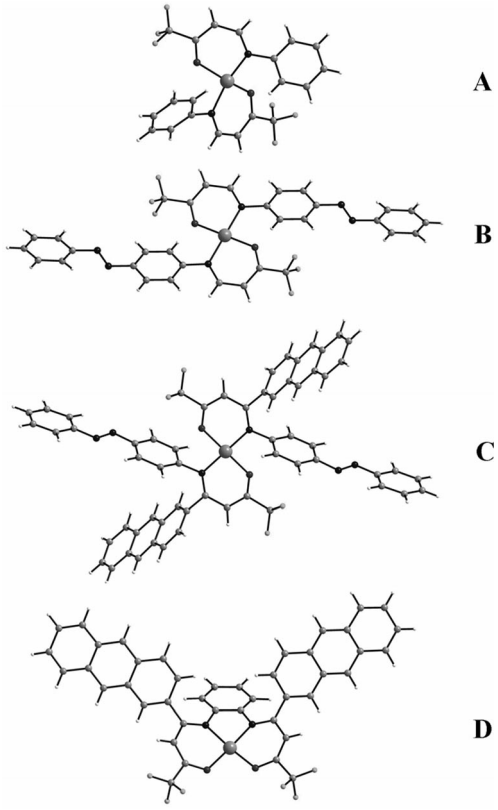

Figure 4. Structures of **A**, **B**, **C** and **D**.

A, **B** and **C** are built from two monodeprotonated bidentate ligands (**L1**$^-$, **L3**$^-$ and **L6**$^-$, respectively), whereas **D** is constructed from one doubly deprotonated tetradentate ligand (**L12**$^{2-}$). The metal ion is then coordinated to the enaminone pincer part. Cu–O,N bond lengths within the four complexes are similar: 1.910(3) and 1.941(3) Å for **A**, 1.897(3) and 2.008(4) Å for **B**, 1.897(4) and 2.018(4) Å for **C** and from 1.897(6) to 1.958(6) Å for **D**, which are in good agreement with literature values.[27,28]

A study of the N,O–Cu–N,O bond angles illustrates the distortion of the Cu^{II} square planar environment. In **B** and **C**, these angles are close to the theoretical values of 90 and 180° [88.6(1)–91.4(1)° and 180° for **B** and 88.9(2)–91.1(2)° and 180° for **C**], whereas in **A** and **D**, the deviation from the expected values is greater [94.6(1)–95.4(1)° and 140.4(2)–150.1(2)° for **A** and 83.5(1)–95.1(1)° and 175.4–177.9° for **D**].

A second way to evaluate the distortion from an ideal square planar environment is to measure the angle, the ω parameter, between the planes formed by the enaminone moiety of two ligands (**A**, **B** and **C**) with the central metal atom or of one ligand (**D**) with the Cu^{II} ion (Figure 5). Another parameter, β, which is used to evaluate the distortion of the local geometry of the metal centre, is defined as a half of the value of the mean *trans* ligand–metal–ligand angle, which is 90° for square planar geometry (D_{4h}) and 54.7° for tetrahedral geometry (T_d). A new parameter, τ_4,[46] has been introduced in order to index four-coordinate complexes, which corresponds to the sum of angles α and β, the two largest angles in the four-coordinate species, subtracted from 360° and divided by 141°. The value of τ_4 ranges from 0.00 to 1.00 for perfect square planar and perfect tetrahedral geometries, respectively. All these parameters for **A**, **B**, **C** and **D** are summarized in Table 1.[39]

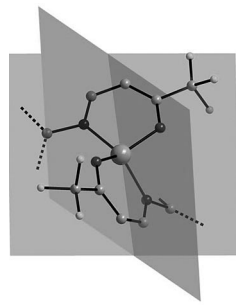

Figure 5. Illustration of planes between which the deviation from an ideal square plane can be evaluated (ω parameter).

Table 1. Correlation between Cu^{II}/Cu^{I} redox potentials and parameters that evaluate the deviation from an ideal square planar metal environment for **A**, **B**, **C** and **D**.

Complex	Substitution	Coordination mode	E^0 [a] [V]/β [°]/ω [°]/τ_4
A	phenyl	bidentate	–0.57/72.6/47.9/0.49
B	azobenzene	bidentate	–0.48/90/6.7/0.0
C	azobenzene anthracene anthracene	bidentate	–0.69/90/0.0/0.0
D	–	tetradentate	–1.08/88.3/14.5/0.05

[a] Potential standard $E^0 = (E_{pc} + E_{pa})/2$.

In conclusion, the Cu^{II} environment within **B** and **C** is almost perfectly square planar, whereas the environment deviates from ideal for **D** and **A**. The potential standards of the first Cu^{II}/Cu^{I} step should be affected by (i) the degree of tetrahedral distortion in four-coordinate complexes, (ii) the presence of different kinds of substituents on the ligand (steric and geometric effects, see below) and (iii) the nature of the solvent (coordinating vs. noncoordinating). Our X-ray data (Table 2) combined with our preliminary electrochemical data recorded in a coordinating solvent (DMF) seem to indicate that the closer the environment is to tetrahedral as in **A** (which is the preferred environment for a Cu^{I} ion), the more easily the metal will be reduced (compared with **C** and **D**). In addition, the fact that the Cu^{II}/Cu^{I} step in the tetradentate complex was found to be fully reversible may be due to some stabilization from the solvent and delocalization. Lastly, in the structures of **A**, **B**, **C** and **D**, each mononuclear complex is isolated from its neighbor, and the structural cohesion is maintained by F···H bonds, which form a dense network.

Table 2. Structural refinement for **A**, **B**, **C** and **D**.

	A	**B**	**C**	**D**
Formula	$C_{20}H_{14}CuF_6N_2O_2$	$C_{32}H_{22}CuF_6N_6O_2$	$C_{60}H_{38}CuF_6N_6O_2$	$C_{44.5}H_{30}CuF_6N_2O_{3.5}$
FW (g mol^{-1})	491.88	700.09	1052.53	826.26
Crystal system	monoclinic	triclinic	monoclinic	monoclinic
Space group	*C*2/*c*	$P\bar{1}$	*C*2/*c*	$P2_1/c$
a [Å]	22.776(7)	6.989(1)	33.676(3)	22.895(3)
b [Å]	8.497(1)	8.500(1)	5.9851(4)	22.866(2)
c [Å]	12.287(4)	13.420(2)	31.178(3)	14.306(2)
α [°]	90	80.09(1)	90	90
β [°]	119.67(4)	76.34(1)	120.19(1)	100.06(1)
γ [°]	90	81.45(1)	90	90
V [Å^3]	2066.0(13)	758.3(2)	5432(1)	7374(1)
Z	4	1	4	8
T [K]	293	293	293	100
D [g cm^{-3}]	1.581	1.533	1.285	1.495
μ [mm^{-1}]	0.439	0.798	0.469	0.673
Independent reflections	2332	3557	5343	17487
R_{int}	0.041	0.057	0.060	0.100
R (F^2)	0.0540	0.0584	0.0830	0.0783
R_w (F^2)	0.1123	0.1067	0.1729	0.1697
S	0.96	0.93	0.89	1.00
Number of reflections	2327	3556	5340	17487
Number of parameters	142	215	340	1028
$\Delta\rho_{max}$ [e$^-$ Å^{-3}]	0.65	0.88	1.45	2.11
$\Delta\rho_{min}$ [e$^-$ Å^{-3}]	–0.55	–1.36	–1.12	–2.18
Absorption correction	analytical	analytical	analytical	analytical

Electrochemistry of the Ligands

As a preliminary exploration, the redox behaviour of **L1H**, **L3H**, **L6H** and **L12H$_2$** was examined in anhydrous DMF that contained nBu$_4$NPF$_6$ as the supporting electrolyte. The data are collected in Table 3, and typical cyclic voltammograms of **L1H** and **L3H** are presented in Figures 6 and 7, respectively (see Supporting Information for the cyclic voltammograms of **L6H** and **L12H$_2$**). All ligands were oxidized irreversibly before the limit of solvent oxidation (ca. + 1.65 V) at potentials between +1.11 and +1.25 V (peak potential at 0.2 V s^{-1}) with **L3H** and **L12H$_2$** the easiest to be oxidized. The irreversible nature of these steps corresponds to the formation of an unstable radical cation of the enaminone moiety[47] and the anthracenyl moiety for **L6H** and **L12H$_2$**.[48] All the ligands exhibited a first one-electron irreversible reduction step at –2.02, –1.56, –1.46 and –1.58 V (peak potentials at 0.2 V s^{-1}) for **L1H**, **L3H**, **L6H** and **L12H$_2$**, respectively, which correspond to the formation of unstable radical anions, with **L6H** the easiest to be reduced; the irreversible nature of these steps indicates that a chemical reaction follows the initial electron transfer and gives rise to the formation of a new product and not the dianion.[49] For **L1H**, a second reversible reduction step was observed at –2.44 V (peak potential at 0.2 V s^{-1}; potential standard E^0 = –2.38 V, peak separation close to 0.12 V), which may be attributed to the reduction of the product that was formed after the initial electron transfer.[49] The other ligands gave additional reduction steps due to the redox-active azobenzene and anthracenyl moieties. For example, for the azobenzene-derived ligand **L3H**, three reduction steps were observed at –1.78, –1.91 and –2.56 V (peak potentials at 0.2 V s^{-1}). The reduction step at –1.78 V may be attributed to the reduction of the product that resulted from the initial uptake of one electron, whereas the reduction step at –1.91 V is attributed to the one-electron reversible reduction of the –N=N– of the azobenzene moiety or from the product that resulted from the initial electron transfer (potential standard E^0 = –1.84 V). The last reduction step at –2.56 V corresponds to the quasireversible formation of the azobenzene dianion[50,51] (potential standard E^0 = –2.43 V). Both ligands

Table 3. Electrochemical data for the reduction of **L1H**, **L3H**, **L6H** and **L12H**.

	E_{pc}[a] [V]	E_{pa}[b] [V]	E^0[c] [V]
L1H	–2.02 (E_{pc1})	–2.32 (E_{pa2})	–2.38 (E^0_2)
	–2.44 (E_{pc2})	+0.13 (E_{pa3})	
		+1.24 (E_{pa4})	
L3H	–1.56 (E_{pc1})	–1.78 (E_{pa3})	–1.84 (E^0_3)
	–1.78 (E_{pc2})	–2.30 (E_{pa4})	–2.43 (E^0_4)
	–1.91 (E_{pc3})	–0.24 (E_{pa5})	
	–2.56 (E_{pc4})	+1.11 (E_{pa6})	
L6H	–1.46 (E_{pc1})	–1.77 (E_{pa3})	–1.85 (E^0_3)
	–1.75 (E_{pc2})	+0.23 (E_{pa6})	
	–1.94 (E_{pc3})	+1.25 (E_{pa7})	
	–2.50 (E_{pc4})		
	–2.90 (E_{pc5})		
L12H	–1.58 (E_{pc1})	–1.05 (E_{pa6})	
	–1.82 (E_{pc2})	–0.70 (E_{pa7})	
	–2.49 (E_{pc3})	–0.17 (E_{pa8})	
	–2.94 (E_{pc4})	+0.25 (E_{pa9})	
	–3.20 (E_{pc5})	+1.12 (E_{pa10})	

[a] Cathodic peak potential in DMF at 293 K with a glassy carbon electrode and 0.1 M nBu$_4$NPF$_6$ as the supporting electrolyte; all potentials are vs. Ag/Ag$^+$ in acetonitrile, scan rate = 0.2 V s^{-1}. [b] Anodic peak potential. [c] Potential standard $E^0 = (E_{pc} + E_{pa})/2$.

also gave rise to irreversible oxidation steps at +0.13 V (**L1H**) and ca. –0.24 V (**L3H**), which were only observed after scanning the potential in the reductive direction and correspond to the oxidation of the products formed after the initial one-electron transfer.[49]

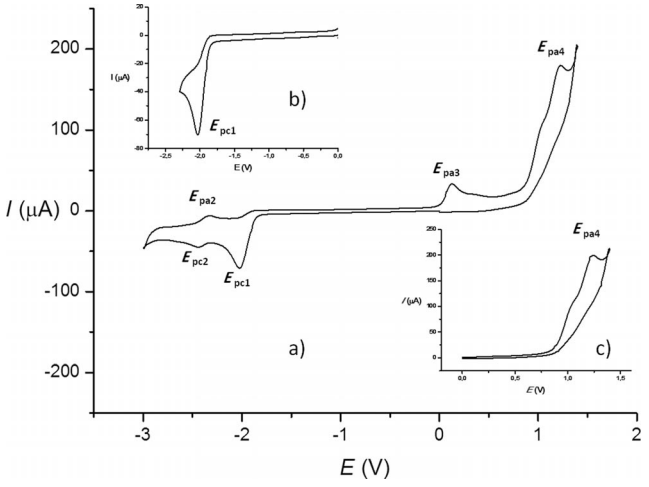

Figure 6. Cyclic voltammetry of **L1H** in anhydrous DMF + 0.1 M nBu_4NPF_6, glassy carbon electrode, scan rate = 0.2 V s^{-1}, T = 293 K. (a) scanning potential from 0.0 to –3.0 V, –3.0 to +1.4 V and +1.4 to 0.0 V; (b) Inset: scanning potential from 0.0 to –2.3 V and –2.3 to 0.0 V; (c) Inset: scanning potential from 0.0 to +1.4 V and +1.4 to 0.0 V.

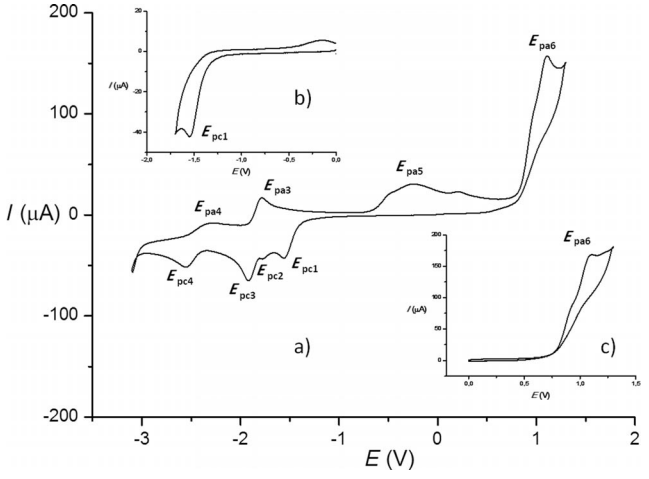

Figure 7. Cyclic voltammetry of **L3H** in anhydrous DMF + 0.1 M nBu_4NPF_6, glassy carbon electrode, scan rate = 0.2 V s^{-1}, T = 293 K. (a) scanning potential from 0.0 to –3.0 V, –3.0 to +1.3 V and +1.3 to 0.0 V; (b) Inset: scanning potential from 0.0 to –1.7 V and –1.7 to 0.0 V; (c) Inset: scanning potential from 0.0 to +1.3 V and +1.3 to 0.0 V.

Electrochemistry of the Cu^{II} Complexes

For comparison and in order to study the influence of the metal ion coordination to the ligand, the redox chemistry of the Cu^{II} complexes of **L1H**, **L3H**, **L6H** and **L12H$_2$** was also examined in anhydrous DMF that contained nBu_4NPF_6 as the supporting electrolyte. The data are collected in Table 4, and typical cyclic voltammograms of [Cu(**L1**)$_2$] and [Cu(**L3**)$_2$] are presented in Figures 8 and 9, respectively {see Supporting Information for the cyclic voltammograms of [Cu(**L6**)$_2$] and [Cu(**L12**)]}. All the com-

Table 4. Electrochemical data for the reduction of [Cu(**L1**)$_2$], [Cu(**L3**)$_2$], [Cu(**L6**)$_2$] and [Cu(**L12**)].

	E_{pc}[a] [V]	E_{pa}[b] [V]	E^0[c] [V]
[Cu(**L1**)$_2$]	–0.85 (E_{pc1})	–0.29 (E_{pa1})	–0.57 (E^0_1)
	–2.02 (E_{pc2})	+0.18 (E_{pa4})	+0.26 (E^0_5)[d]
	–2.63 (E_{pc3})	+1.08 (E_{pa5})	–0.52 (E^0_6)[d]
	–0.55 (E_{pc5})[d]	–0.24 (E_{pa6})[d]	
	–0.80 (E_{pc6})[d]		
[Cu(**L3**)$_2$]	–0.64 (E_{pc1})	–0.32 (E_{pa1})	–0.48 (E^0_1)
	–1.72 (E_{pc2})	–1.78 (E_{pa3})	–1.85 (E^0_3)
	–1.93 (E_{pc3})	–2.31 (E_{pa4})	–2.42 (E^0_4)
	–2.53 (E_{pc4})	+1.17 (E_{pa5})	+0.28 (E^0_5)[d]
	–0.60 (E_{pc5})[d]		–0.50 (E^0_6)[d]
	–0.75 (E_{pc6})[d]		
[Cu(**L6**)$_2$]	–0.96 (E_{pc1})	–0.43 (E_{pa1})	–0.69 (E^0_1)
	–1.79 (E_{pc2})	–1.82 (E_{pa3})	–1.89 (E^0_3)
	–1.96 (E_{pc3})	+0.18 (E_{pa7})	+0.31(E^0_8)[d]
	–2.31 (E_{pc4})	+1.17 (E_{pa8})	–0.43 (E^0_9)[d]
	–2.49 (E_{pc5})	–0.17 (E_{pa9})[d]	
	–2.93 (E_{pc6})		
	–0.55 (E_{pc8})[d]		
	–0.70 (E_{pc9})[d]		
[Cu(**L12**)]	–1.17 (E_{pc1})	–0.99 (E_{pa1})	–1.08 (E^0_1)
	–2.17 (E_{pc2})	–0.63 (E_{pa6})	+0.26(E^0_9)[d]
	–2.53 (E_{pc3})	–0.09 (E_{pa7})	–1.13 (E^0_{10})[d]
	–2.99 (E_{pc4})	+0.29 (E_{pa8})	
	–3.21 (E_{pc5})	+1.12 (E_{pa9})	
	–0.60 (E_{pc9})[d]	–0.27 (E_{pa10})[d]	
	–0.86 (E_{pc10})[d]		

[a] Cathodic peak potential in DMF at 293 K with a glassy carbon electrode and 0.1 M nBu_4NPF_6 as the supporting electrolyte; all potentials are vs. Ag/Ag^+ in acetonitrile, scan rate: 0.2 V s^{-1}. [b] Anodic peak potential. [c] Potential standard $E^0 = (E_{pc} + E_{pa})/2$. [d] Appears only after scanning from 0.0 to +1.4 V and scanning back to –1.0 V.

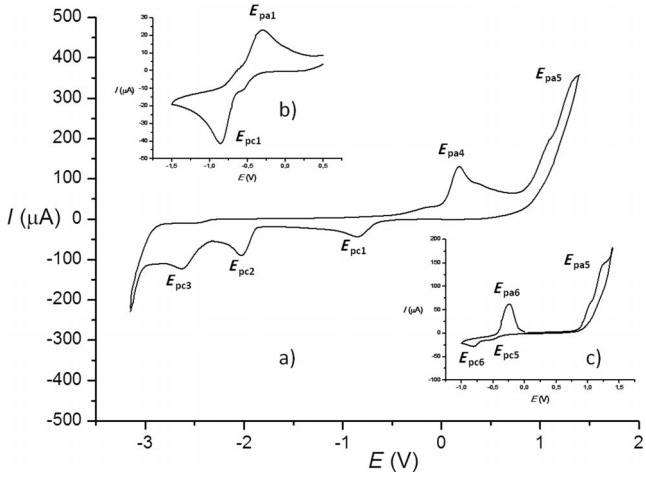

Figure 8. Cyclic voltammetry of [Cu(**L1**)$_2$] in anhydrous DMF + 0.1 M nBu_4NPF_6, glassy carbon electrode, scan rate = 0.2 V s^{-1}, T = 293 K. (a) scanning potential from 0.0 to –3.2 V, –3.2 to +1.4 V and +1.4 to 0.0 V; (b) Inset: scanning potential from 0.0 to –1.5 V and –1.5 to 0.0 V; (c) Inset: scanning potential from 0.0 to +1.4 V, +1.4 to –1.0 V and –1.0 to 0.0 V.

plexes gave rise to a one-electron quasireversible reduction step, which corresponds to a Cu^{II}/Cu^{I} process, at –0.57 V (potential standard E^0) for [Cu(**L1**)$_2$], –0.48 V (potential standard E^0) for [Cu(**L3**)$_2$], –0.69 V (potential standard E^0) for [Cu(**L6**)$_2$] and –1.08 V (potential standard E^0) for [Cu(**L12**)]. Additional reduction steps were generally observed at more negative reduction potentials, which correspond to the reduction of the ligand. The Cu^{I} species was the most stable for [Cu(**L12**)] with the tetradentate ligand as evidenced by the smallest peak separation ($\Delta E_p = E_{pc1} - E_{pa1} = 0.18$ V) and the smallest i_{pc1}/i_{pa1} ratio (i_{pc1} = cathodic current at E_{pc1}, i_{pa1} = anodic current at E_{pa1}). The complexes gave rise to an irreversible oxidation step generally located at potentials (peak potentials at 0.2 V s^{-1}) roughly equal to the oxidation step observed in the corresponding ligands (Table 3). On scanning back to the negative potentials, this oxidation led to the appearance of two additional reduction steps (between 0.0 and –1.0 V) with a typical redissolution peak for Cu^0 (close to –0.2 V). As such a redissolution peak was not observed with the ligands when scanned only in the reductive direction, it is possible that the oxidation of the Cu^{II} complexes gave rise to Cu^{III} species that are further reduced in two stepwise reduction steps, which correspond to the Cu^{III}/Cu^{II} and Cu^{II}/Cu^0 transitions.

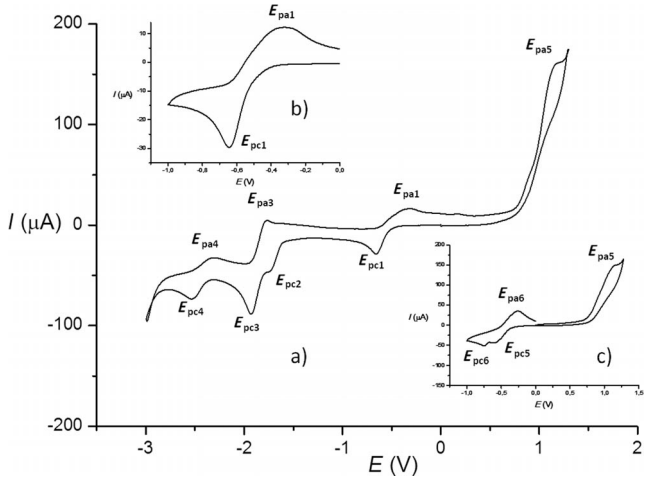

Figure 9. Cyclic voltammetry of [Cu(**L3**)$_2$] in anhydrous DMF + 0.1 M nBu$_4$NPF$_6$, glassy carbon electrode, scan rate = 0.2 V s^{-1}, T = 293 K. (a) scanning potential from 0.0 to –3.0 V, –3.0 to +1.3 V and +1.3 to 0.0 V; (b) Inset: scanning potential from 0.0 to –1.0 V and –1.0 to 0.0 V; (c) Inset: scanning potential from 0.0 to +1.3 V, +1.3 to –1.0 V and –1.0 to 0.0 V.

Spectroscopic Properties

UV/Vis absorption spectra indicate similar profiles between the different ligands and their corresponding copper complexes (Table 5). For **L1H**, an intense band is observed at 355 nm, and one at 356 nm is observed for [Cu(**L1**)$_2$]. This absorption is typical of the different π–π* transitions of the phenyl ring and the enaminone moiety. For **L3H** and [Cu(**L3**)$_2$] (Figure 10), absorption maxima at 381 and 376 nm were measured, respectively. These bands are associated with the π–π* transition of the azobenzene moiety. Usually this type of transition is accompanied by isomerization of the –N=N– unit and the conversion from *E* to *Z* configuration. For **L6H** and [Cu(**L6**)$_2$], a superposition of the characteristic profile of the fine structure of anthracene between 230 and 360 nm is observed with an absorption maximum at 251 nm in both cases and with the π–π* transition of the azobenzene at 386 and 382 nm, respectively. Finally, the different π–π* transitions of the anthracene moiety for **L12H** and [Cu(**L12**)] are also present with a lower band intensity for [Cu(**L12**)], probably due to a difference in geometry between the free ligand and the complex. Regarding the spectra of the complexes, the forbidden *d–d* transitions are too weak compared to the photosensitive moieties to be clearly observed at this concentration.

Table 5. UV/Vis absorptions of the ligands and complexes.

	λ [nm]	ε [a] [L mol^{-1} cm^{-1}]
L1H	355 (λ_{max})	19175
[Cu(**L1**)$_2$]	356 (λ_{max})	24656
L3H	381 (λ_{max})	26020
	≈ 300	
	≈ 245	
[Cu(**L3**)$_2$]	376 (λ_{max})	41959
	≈ 296	
L6H	386	
	354	
	334	
	251 (λ_{max})	67154
[Cu(**L6**)$_2$]	382	
	354	
	334	
	251 (λ_{max})	121510
L12H$_2$	≈ 353	
	331	
	245 (λ_{max})	179521
[Cu(**L12**)]	≈ 353	
	336	
	257 (λ_{max})	116680

[a] The molar extinction coefficient ε is calculated for λ_{max}.

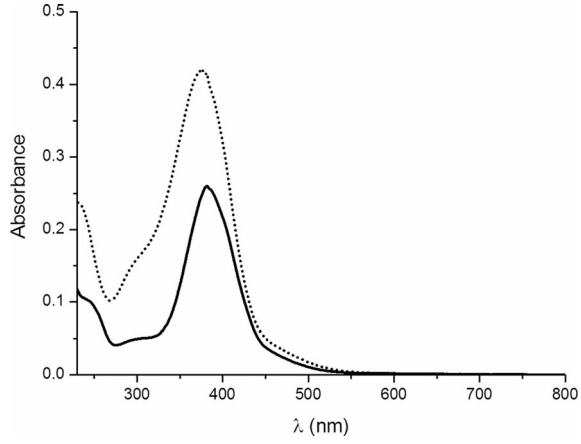

Figure 10. UV/Vis spectra of **L3H** (black line) and [Cu(**L3**)$_2$] (dashed line) in dichloromethane.

In summary, the UV/Vis absorption measurements show that the properties of the different ligands are retained in the corresponding copper complexes.

Conclusions

The synthesis, structural, UV/Vis and electrochemical characterization of a series of original multidentate ligands and their Cu^{II} complexes were achieved. The redox chemistry of the enaminone electroactive ligands was investigated as well as the electrochemical behaviour of the corresponding Cu^{II} complexes. All the complexes exhibited a quasireversible or reversible redox process in DMF, which corresponds to the formation of a stable Cu^{I} species with a low reduction potential, the most stable of which had a tetradentate ligand. The UV/Vis spectra show that the properties of the different ligands are retained in the corresponding copper complexes, which means that metal coordination does not have a dramatic impact.

Work is underway to extend current chemical methodologies to more elaborate ligands that bear new specific entities as well as to study the possible coordination chemistry with metals other than copper. The identification of the reduction and oxidation products and a proposed detailed mechanism for the redox chemistry of the ligands and complexes in solvents with different coordinating abilities will be performed in due course. The application of the copper complexes in catalysis and as potent metallodrugs are our future goals.

Experimental Section

General: Commercially available reagents were used as supplied, unless stated otherwise, and stored according to the manufacturer's recommendations. (*E*)-4-Ethoxy-1,1,1-trifluorobut-3-en-2-one (**1**),[41] **L1H**[42] and **L2H**[43] were prepared according to the literature. ^{1}H, ^{19}F and ^{13}C NMR spectra were recorded with a Bruker Avance 300 spectrometer (in $CDCl_3$) at 300, 282 and 75 MHz respectively. Chemical shifts are given in ppm relative to the residual solvent peak (δ_H = 7.26 ppm for $CHCl_3$, δ_C = 77.0 ppm for $CDCl_3$) or $CFCl_3$ (^{19}F). The following abbreviations are used: singlet (s), doublet (d), triplet (t), quartet (q), multiplet (m) and broad (br.). TLC was performed on Merck silica Gel 60 F_{254} plates with detection by UV light. Column chromatography was performed on Macherey–Nagel Silica gel 60 M (0.04–0.063 mm). Solvents for chromatography and work up are: dichloromethane (DCM), ethyl acetate (AcOEt), methanol (MeOH) and petroleum ether (PE). Mass spectra were recorded using a FINIGAN MAT 95 (EI and ESI) instrument, and UV/Vis spectra were recorded with a Lambda 35 spectrophotometer. Melting points were determined in capillary tubes with a Büchi apparatus. Electrochemical measurements were performed using an EG & G-Princeton Applied Research 263A all-in-one potentiostat, using a standard three-electrode setup with a glassy carbon electrode (working electrode), platinum wire auxiliary electrode and a nonaqueous Ag/Ag^+ system in acetonitrile as the reference electrode. DMF solutions of the compounds with 0.1 M supporting electrolyte nBu$_4$NPF$_6$ were measured with the voltage scan rate of 0.2 V s^{-1}. Under these experimental conditions the ferrocene/ferricinium couple, used as internal reference for potential measurements, was located at $E_{1/2}$ = +0.05 V in DMF.

General Procedure for the Synthesis of L1H–L4H: To a solution of **1** (1.5 g, 8.92 mmol) in acetonitrile (20 mL) was added a solution of the amine (8.92 mmol) in acetonitrile (10 mL). The mixture was stirred at room temperature under argon for 5 h. The resulting precipitate was washed with cold acetonitrile, filtered and the filtrate concentrated and purified by silica gel chromatography (PE/AcOEt = 8:2 for **L1H**, **L3H**, PE/DCM = 1:1 for **L2H** and DCM for **L4H**).

(*Z*)-1,1,1-Trifluoro-4-[4-{(*E*)-phenyldiazenyl}phenylamino]but-3-en-2-one (L3H): Yield 94%; yellow solid; m.p. 187 °C. ^{1}H NMR (300 MHz, $CDCl_3$): δ = 11.86 (br. d, J = 12.3 Hz, 1 H), 7.99 (d, J = 8.7 Hz, 2 H), 7.91 (dd, J = 8.4, 1.8 Hz, 2 H), 7.71 (dd, J = 12.9, 7.5 Hz, 1 H), 7.51 (m, 3 H), 7.26 (d, J = 9.0 Hz, 2 H), 5.73 (d, J = 7.5 Hz, 1 H) ppm. ^{19}F NMR (282 MHz, $CDCl_3$): δ = –77.6 (s) ppm. HRMS (ESI): calcd. for $C_{16}H_{11}F_3N_3O$ $[M - H]^-$ 318.08597; found 318.0861. $C_{16}H_{12}F_3N_3O$ (319.28): calcd. C 60.19, H 3.79, N 13.16; found C 60.42, H 3.64, N 13.18.

(*Z*)-4-(Anthracen-2-ylamino)-1,1,1-trifluorobut-3-en-2-one (L4H): Yield 72%; green-yellow solid; m.p. > 220 °C. ^{1}H NMR (300 MHz, $CDCl_3$): δ = 12.06 (br. d, J = 12.3 Hz, 1 H), 8.41–8.36 (m, 2 H), 8.11–7.99 (m, 3 H), 7.90–7.84 (m, 2 H), 7.68 (s, 1 H), 7.50–7.48 (m, 2 H), 5.74 (d, J = 7.2 Hz, 1 H) ppm. ^{19}F NMR (282 MHz, $CDCl_3$): δ = –77.5 (s) ppm. HRMS (ESI): calcd. for $C_{18}H_{13}F_3NO$ $[M + H]^+$ 316.09438; found 316.0941. $C_{18}H_{12}F_3NO$ (315.29): calcd. C 68.57, H 3.84, N 4.44; found C 68.61, H 4.01, N 4.66.

(3*Z*)-4-[(4-{2-(1,3-Dithiol-2-ylidene)-1,3-dithiol-4-yl}phenyl)amino]-1,1,1-trifluorobut-3-en-2-one (L5H): To a solution of tetrathiafulvalene (400 mg, 1.96 mmol) in anhydrous THF (15 mL) was added dropwise nBuLi (1.6 M in hexane, 1.22 mL, 1.96 mmol) at –78 °C over 20 min. The mixture was stirred at this temperature for 30 min. Bu_3SnCl (1.96 mmol) was added dropwise and the mixture was slowly warmed and stirred at room temperature for 1 h. The solution was poured into a phosphate buffer solution pH 7 (7 mL), the organic layer separated, extracted with AcOEt (2 × 10 mL) and washed (2 × 10 mL) with a brine. The combined organic layers were dried with sodium sulfate, filtered and the solvent was removed under reduced pressure. To a solution of this crude oil in anhydrous toluene (8 mL) was added **L2H** (578 mg, 1.96 mmol) and Pd(PPh_3)$_4$ (113 mg, 0.1 mmol). The mixture was heated to reflux under argon for 48 h. After cooling to room temperature, the black solution was evaporated to dryness, and the crude product was washed several times with acetonitrile and dichloromethane to give **L5H**. Yield 25%; red solid; m.p. 215 °C. ^{1}H NMR (300 MHz, $CDCl_3$): δ = 11.81 (br. d, J = 14.4 Hz, 1 H), 7.68–7.61 (m, 1 H), 7.43 (d, J = 8.4 Hz, 2 H), 7.12 (d, J = 8.4 Hz, 2 H), 6.50 (s, 1 H), 6.34 (s, 2 H), 5.69 (d, J = 7.2 Hz, 1 H) ppm. ^{19}F NMR (282 MHz, $CDCl_3$): δ = –77.5 (s) ppm. HRMS (ESI): calcd. for $C_{16}H_9F_3NOS_4$ $[M - H]^-$ 415.95245; found 415.9508. $C_{16}H_{10}F_3NOS_4$ (417.51): calcd. C 46.03, H 2.41, N 3.35; found C 46.23, H 2.49, N 3.16.

(*E*)-1-[4-(Phenyldiazenyl)phenyl]ethanone (3): Nitrosobenzene (161 mg, 1.5 mmol) was dissolved in glacial acetic acid (6 mL). To this stirred solution was added *p*-aminoacetophenone (135 mg, 1 mmol) and the mixture was stirred at 90 °C overnight. The solution was cooled to room temperature and poured into water (7 mL), and the aqueous layer was extracted with dichloromethane (5 × 10 mL). The combined organic layers were dried with sodium sulfate and filtered, and the solvents were removed under reduced pressure. Silica gel chromatography of the crude product (DCM) yielded **3**. Yield 71%; orange solid; m.p. 115 °C. ^{1}H NMR (300 MHz, $CDCl_3$): δ = 8.11 (d, J = 8.7 Hz, 2 H), 7.98 (d, J = 8.7 Hz, 2 H), 7.95 (m, 2 H), 7.53 (m, 3 H), 2.67 (s, 3 H) ppm. ^{13}C NMR (75 MHz, $CDCl_3$): δ = 197.2, 154.8, 152.4, 138.2, 131.6, 129.2, 129.1, 123.1, 122.8, 26.7 ppm. HRMS (EI): calcd. for $C_{14}H_{12}N_2O$ $[M]^{+\cdot}$ 224.09496; found 224.09491. $C_{14}H_{12}N_2O$ (224.26): calcd. C 74.98, H 5.39, N 12.49; found C 74.86, H 5.10, N 12.54.

General Procedure for Acetalization: Trimethylorthoformate (1.5 mmol) and *p*-toluenesulfonic acid (0.007 mmol) were dissolved in anhydrous methanol (9 mL) and the resulting solution was added to a round-bottomed flask that contained the ketone (1 mmol). The mixture was heated to 60 °C for 24 h under argon. Sodium carbonate was added for neutralization, and the mixture was filtered. The solvent was removed from the filtrate under reduced pressure, and the crude product was pure enough for the next step.

(*E*)-1-[4-(1,1-Dimethoxyethyl)phenyl]-2-phenyldiazene (5): Yield 99%; orange oil; ^{1}H NMR (300 MHz, $CDCl_3$): δ = 7.93 (m, 4 H), 7.68 (d, J = 8.4 Hz, 2 H), 7.50 (m, 3 H), 3.24 (s, 6 H), 1.60 (s, 3 H) ppm. ^{13}C NMR (75 MHz, $CDCl_3$): δ = 152.5, 151.9, 145.7, 130.8, 128.9, 127.0, 122.7, 122.5, 101.3, 48.8, 25.8 ppm. $C_{16}H_{18}N_2O_2$ (270.33): calcd. C 71.09, H 6.71, N 10.36; found C 70.88, H 6.65, N 10.23.

2-(1,1-Dimethoxyethyl)anthracene (6): Yield 99%; yellow solid; m.p. 80 °C. ^{1}H NMR (300 MHz, $CDCl_3$): δ = 8.52 (s, 1 H), 8.42 (s, 1 H), 8.36 (s, 1 H), 8.07–8.01 (m, 3 H), 7.69 (dd, J = 9.0, 1.5 Hz, 1 H), 7.52 (m, 2 H), 3.41 (s, 6 H), 1.80 (s, 3 H) ppm. ^{13}C NMR (75 MHz, $CDCl_3$): δ = 139.4, 131.7, 131.2, 131.0, 128.1, 128.0, 127.9, 126.7, 125.7, 125.5, 125.1, 123.9, 101.6, 48.9, 25.5 ppm. $C_{18}H_{18}O_2$ (266.33): calcd. C 81.17, H 6.81; found C 81.36, H 7.02.

General Procedure for the Trifluoroacetylation of Ketone Dimethyl Acetals: To a solution of ketone dimethyl acetal (1 mmol) and pyridine (4 mmol) in anhydrous dichloromethane (2 mL) at 0 °C was added dropwise TFAA (2 mmol). The mixture was slowly warmed to room temperature and heated to reflux for 72 h for **7** and 24 h for **8**. The mixture was washed with an aqueous solution of 0.1 M HCl (10 mL), a 10% aqueous solution of Na_2CO_3 (5 mL) and water (2 × 10 mL). The combined organic layers were dried with sodium sulfate, filtered and the solvent was removed under reduced pressure. The crude oil was purified by silica gel chromatography (PE/DCM = 1:1).

(*Z*)-1,1,1-Trifluoro-4-methoxy-4-[4-{(*E*)-phenyldiazenyl}phenyl]but-3-en-2-one (7): Yield 84%; orange-red solid; m.p. 61 °C. ^{1}H NMR (300 MHz, $CDCl_3$): δ = 7.98–7.95 (m, 4 H), 7.65 (d, J = 8.4 Hz, 2 H), 7.52–7.50 (m, 3 H), 5.89 (s, 1 H), 3.95 (s, 3 H) ppm. ^{13}C NMR (75 MHz, $CDCl_3$): δ = 177.1 (q, J = 35.1 Hz), 177.0, 153.7, 152.4, 135.6, 131.4, 129.9, 129.1, 123.2, 123.0, 116.7 (q, J = 290.0 Hz), 92.2, 57.4 ppm. ^{19}F NMR (282 MHz, $CDCl_3$): δ = –78.6 (s) ppm. HRMS (ESI): calcd. for $C_{17}H_{13}F_3N_2NaO_2$ $[M + Na]^+$ 357.0827; found 357.0822. $C_{17}H_{13}F_3N_2O_2$ (334.29): calcd. C 61.08, H 3.92, N 8.38; found C 61.42, H 4.20, N 8.36.

(*Z*)-4-(Anthracen-2-yl)-1,1,1-trifluoro-4-methoxybut-3-en-2-one (8): Yield 60%; yellow solid; m.p. 149 °C. ^{1}H NMR (300 MHz, $CDCl_3$): δ = 8.45 (s, 1 H), 8.37 (s, 1 H), 8.27 (s, 1 H), 7.98–7.96 (m, 3 H), 7.54–7.46 (m, 3 H), 5.97 (s, 1 H), 3.97 (s, 3 H) ppm. ^{13}C NMR (75 MHz, $CDCl_3$): δ = 177.9, 177.3 (q, J = 34.0 Hz), 132.7, 131.9, 131.8, 130.5, 130.3, 130.2, 128.2, 128.1, 128.0, 127.7, 126.2, 126.1, 125.6, 124.6, 116.9 (q, J = 290.0 Hz), 92.0, 57.3 ppm. ^{19}F NMR (282 MHz, $CDCl_3$): δ = –78.4 (s) ppm. HRMS (ESI): calcd. for $C_{19}H_{14}F_3O_2$ $[M + H]^+$ 331.0940; found 331.0951. $C_{19}H_{13}F_3O_2$ (330.30): calcd. C 69.09, H 3.97; found C 68.87, H 4.03.

General Procedure for the Synthesis of L6H and L7H: To a solution of **8** (300 mg, 0.91 mmol) in acetonitrile (4 mL) was added a solution of the primary amine (0.91 mmol) in acetonitrile (4 mL). The mixture was stirred at room temperature for 5 h. The solvent was removed under reduced pressure and the crude product was purified by silica gel chromatography (PE/DCM = 1:1).

(*Z*)-4-(Anthracen-2-yl)-1,1,1-trifluoro-4-[4-{(*E*)-phenyldiazenyl}-phenylamino]but-3-en-2-one (L6H): Yield 68%; orange solid; m.p. 158 °C. ^{1}H NMR (300 MHz, $CDCl_3$): δ = 12.68 (br. s, 1 H), 8.47 (s, 1 H), 8.40 (s, 1 H), 8.23 (s, 1 H), 8.05–8.01 (m, 2 H), 7.93–7.86 (m, 3 H), 7.74 (d, J = 8.4 Hz, 2 H), 7.57–7.48 (m, 5 H), 7.24 (d, J = 8.7 Hz, 1 H), 7.02 (d, J = 8.7 Hz, 2 H), 6.01 (s, 1 H) ppm. ^{13}C NMR (75 MHz, $CDCl_3$): δ = 178.3, 165.4, 152.4, 149.7, 140.3, 132.8, 132.1, 131.3, 131.1, 130.7, 130.4, 129.5, 129.0, 128.2, 128.1, 127.8, 126.5, 126.4, 126.2, 123.8, 123.7, 123.6, 122.8, 117.0 (q, J = 286.8 Hz), 93.9 ppm. ^{19}F NMR (282 MHz, $CDCl_3$): δ = –77.9 (s) ppm. HRMS (ESI): calcd. for $C_{30}H_{21}F_3N_3O$ $[M + H]^+$ 496.16312; found 496.1624. $C_{30}H_{20}F_3N_3O$ (495.49): calcd. C 72.72, H 4.07, N 8.48; found C 72.83, H 4.23, N 8.12.

(*Z*)-4-(Anthracen-2-yl)-4-[4-({*E*}-{4-(dimethylamino)phenyl}diazenyl)phenylamino]-1,1,1-trifluorobut-3-en-2-one (L7H): Yield 60%; red solid; m.p. > 220 °C. ^{1}H NMR (300 MHz, $CDCl_3$): δ = 12.69 (br. s, 1 H), 8.45 (s, 1 H), 8.38 (s, 1 H), 8.21 (s, 1 H), 8.02–8.00 (m, 2 H), 7.87 (d, J = 8.7 Hz, 1 H), 7.80 (d, J = 9.3 Hz, 2 H), 7.64 (d, J = 8.4 Hz, 2 H), 7.54–7.50 (m, 2 H), 7.22 (d, J = 8.7 Hz, 1 H), 6.98 (d, J = 8.7 Hz, 2 H), 6.70 (d, J = 9.0 Hz, 2 H), 5.95 (s, 1 H), 3.05 (s, 6 H) ppm. ^{13}C NMR (75 MHz, $CDCl_3$): δ = 177.7 (q, J = 33.2 Hz), 165.6, 152.5, 150.6, 143.5, 138.6, 132.8, 132.1, 131.3, 130.9, 130.5, 129.5, 128.9, 128.1, 127.8, 126.5, 126.4, 126.1, 125.0, 124.0, 123.8, 123.0, 122.9, 117.0 (q, J = 286.8 Hz), 111.4, 93.4, 40.2 ppm. ^{19}F NMR (282 MHz, $CDCl_3$): δ = –76.9 (s) ppm. HRMS (ESI): calcd. for $C_{32}H_{26}F_3N_4O$ $[M + H]^+$ 539.20532; found 539.2053. $C_{32}H_{25}F_3N_4O$ (538.56): calcd. C 71.36, H 4.68, N 10.40; found C 71.34, H 4.93, N 10.37.

General Procedure for the Synthesis of $L8H_2$–$L13H_2$: To a solution of **7** or **8** (0.66 mmol) in acetonitrile (3 mL) was added dropwise a solution of the diamine (0.33 mmol) in acetonitrile (3 mL) over 3 h. The mixture was then stirred at room temperature for 1 h. The precipitate formed was washed with cold acetonitrile, the filtrate evaporated to dryness, and the crude product was purified by silica gel chromatography (DCM for $\mathbf{L8H_2}$ and $\mathbf{L11H_2}$, PE/DCM = 1:1 for $\mathbf{L9H_2}$, $\mathbf{L10H_2}$, $\mathbf{L12H_2}$ and $\mathbf{L13H_2}$).

(3*Z*,3′*Z*)-4,4′-[Ethane-1,2-diylbis(azanediyl)]bis[1,1,1-trifluoro-4-(4-{(*E*) phenyldiazenyl}phenyl)but-3-en-2-one] ($L8H_2$): Yield 54%; orange solid; m.p. > 220 °C. ^{1}H NMR (300 MHz, $CDCl_3$): δ = 12.95 (br. s, 2 H), 7.97–7.93 (m, 8 H), 7.57–7.53 (m, 6 H), 7.35 (d, J = 8.4 Hz, 4 H), 5.50 (s, 2 H), 3.51 (t, J = 3.0 Hz, 4 H) ppm. ^{13}C NMR (75 MHz, $CDCl_3$): δ = 177.4 (q, J = 32.9 Hz), 169.9, 153.6, 152.4, 134.9, 131.8, 129.2, 128.4, 123.4, 123.2, 91.3, 45.1 ppm. ^{19}F NMR (282 MHz, $CDCl_3$): δ = –77.1 (s) ppm. HRMS (ESI): calcd. for $C_{34}H_{27}F_6N_6O_2$ $[M + H]^+$ 665.20942; found 665.2104. $C_{34}H_{26}F_6N_6O_2$ (664.60): calcd. C 61.45, H 3.94, N 12.65; found C 61.23, H 3.93, N 12.41.

(3*Z*,3′*Z*)-4,4′-[1,2-Phenylenebis(azanediyl)]bis[1,1,1-trifluoro-4-(4-{(*E*)-phenyldiazenyl}phenyl)but-3-en-2-one] ($L9H_2$): Yield 50%; yellow solid; m.p. 210 °C. ^{1}H NMR (300 MHz, $CDCl_3$): δ = 12.16 (br. s, 2 H), 7.78–7.74 (m, 4 H), 7.69 (d, J = 8.4 Hz, 4 H), 7.39–7.37 (m, 6 H), 7.15 (d, J = 8.4 Hz, 4 H), 6.87–6.84 (m, 2 H), 6.71–6.68 (m, 2 H), 5.78 (s, 2 H) ppm. ^{13}C NMR (75 MHz, $CDCl_3$): δ = 178.7 (q, J = 31.2 Hz), 165.5, 153.7, 152.4, 135.3, 132.3, 131.7, 129.1, 128.9, 126.9, 126.5, 123.1, 123.0, 117.1 (q, J = 286.9 Hz), 93.9 ppm. ^{19}F NMR (282 MHz, $CDCl_3$): δ = –77.1 (s) ppm. HRMS (ESI): calcd. for $C_{38}H_{27}F_6N_6O_2$ $[M + H]^+$ 713.20942; found 713.2083. $C_{38}H_{26}F_6N_6O_2$ (712.64): calcd. C 64.04, H 3.68, N 11.79; found C 63.72, H 3.44, N 11.58.

(3*Z*,3′*Z*)-4,4′-(4,5-Dimethyl-1,2-phenylene)bis(azanediyl)bis[1,1,1-tri-fluoro-4-(4-{(*E*)-phenyldiazenyl}phenyl)but-3-en-2-one] ($L10H_2$): Yield 60%; yellow solid; m.p. > 220 °C. ^{1}H NMR (300 MHz, $CDCl_3$): δ = 12.09 (br. s, 2 H), 7.88–7.86 (m, 4 H), 7.78 (d, J = 8.4 Hz, 4 H), 7.50–7.49 (m, 6 H), 7.23 (d, J = 8.4 Hz, 4 H), 6.62

(s, 2 H), 5.82 (s, 2 H), 2.02 (s, 6 H) ppm. ^{13}C NMR (75 MHz, $CDCl_3$): δ = 178.5 (q, J = 33.6 Hz), 165.7, 153.5, 152.4, 136.3, 135.5, 131.7, 129.8, 129.1, 128.8, 127.5, 123.1, 117.2 (q, J = 286.7 Hz), 93.1, 19.3 ppm. ^{19}F NMR (282 MHz, $CDCl_3$): δ = –77.1 (s) ppm. HRMS (ESI): calcd. for $C_{40}H_{30}F_6N_6NaO_2$ $[M + Na]^+$ 763.22266; found 763.2199. $C_{40}H_{30}F_6N_6O_2$ (740.70): calcd. C 64.86, H 4.08, N 11.35; found C 65.06, H 4.02, N 11.54.

(3*Z*,3′*Z*)-4,4′-[Ethane-1,2-diylbis(azanediyl)]bis[4-(anthracen-2-yl)-1,1,1-trifluorobut-3-en-2-one] ($L11H_2$): Yield 42%; yellow solid; m.p. > 220 °C. ^{1}H NMR (300 MHz, $CDCl_3$): δ = 11.07 (br. s, 2 H), 8.39 (s, 2 H), 8.16 (s, 2 H), 8.04 (d, J = 7.5 Hz, 2 H), 7.93–7.88 (m, 4 H), 7.65 (s, 2 H), 7.55 (m, 4 H), 7.15 (d, J = 8.4 Hz, 2 H), 5.56 (s, 2 H), 3.55 (t, J = 1.8 Hz, 4 H) ppm. ^{19}F NMR (282 MHz, $CDCl_3$): δ = –77.0 (s) ppm. HRMS (ESI): calcd. for $C_{38}H_{27}F_6N_2O_2$ $[M + H]^+$ 657.19712; found 657.1947. $C_{38}H_{26}F_6N_2O_2$ (656.62): calcd. C 69.51, H 3.99, N 4.27; found C 69.48, H 4.25, N 4.12.

(3*Z*,3′*Z*)-4,4′-[1,2-Phenylenebis(azanediyl)]bis[4-(anthracen-2-yl)-1,1,1-trifluorobut-3-en-2-one] ($L12H_2$): Yield 48%; yellow solid; m.p. > 220 °C. ^{1}H NMR (300 MHz, $CDCl_3$): δ = 12.40 (br. s, 2 H), 8.28 (s, 2 H), 7.92 (d, J = 8.4 Hz, 2 H), 7.86 (s, 2 H), 7.77 (d, J = 8.7 Hz, 2 H), 7.67 (d, J = 7.5 Hz, 2 H), 7.60 (s, 2 H), 7.51–7.43 (m, 4 H), 7.06 (d, J = 8.7 Hz, 2 H), 6.84–6.83 (m, 4 H), 5.96 (s, 2 H) ppm. ^{13}C NMR (75 MHz, $CDCl_3$): δ = 170.8 (m), 166.4, 132.8, 132.6, 132.1, 131.3, 130.2, 130.1, 129.2, 129.1, 128.2, 128.1, 127.7, 126.6, 126.5, 126.4, 126.3, 126.1, 123.4, 117.3 (q, J = 287.2 Hz), 93.9 ppm. ^{19}F NMR (282 MHz, $CDCl_3$): δ = –77.1 (s) ppm. HRMS (ESI): calcd. for $C_{42}H_{27}F_6N_2O_2$ $[M + H]^+$ 705.19712; found 705.1972. $C_{42}H_{26}F_6N_2O_2$ (704.66): calcd. C 71.59, H 3.72, N 3.98; found C 71.65, H 3.47, N 4.14.

(3*Z*,3′*Z*)-4,4′-(4,5-Dimethyl-1,2-phenylene)bis(azanediyl)bis[4-(anthracen-2-yl)-1,1,1-trifluorobut-3-en-2-one] ($L13H_2$): Yield 63%; yellow solid; m.p. > 220 °C. ^{1}H NMR (300 MHz, $CDCl_3$): δ = 12.27 (br. s, 2 H), 8.27 (s, 2 H), 7.90 (s, 4 H), 7.73 (s, 4 H), 7.61 (s, 2 H), 7.47 (s, 4 H), 7.03 (d, J = 8.7 Hz, 2 H), 6.60 (s, 2 H), 5.91 (s, 2 H), 1.90 (s, 6 H) ppm. ^{13}C NMR (75 MHz, $CDCl_3$): δ = 178.0 (m), 166.6, 135.9, 132.7, 132.0, 131.2, 130.4, 130.1, 129.9, 129.0, 128.9, 128.2, 128.1, 127.8, 127.2, 126.4, 126.3, 126.0, 123.3, 117.3 (q, J = 282.3 Hz), 93.3, 19.2 ppm. ^{19}F NMR (282 MHz, $CDCl_3$): δ = –76.9 (s) ppm. HRMS (ESI): calcd. for $C_{44}H_{31}F_6N_2O_2$ $[M + H]^+$ 733.22842; found 733.2272. $C_{44}H_{30}F_6N_2O_2$ (732.71): calcd. C 72.13, H 4.13, N 3.82; found C 72.40, H 4.09, N 3.99.

General Procedure for the Synthesis of the Complexes: To a solution of the ligand (0.2 mmol) in DCM (3 mL) was added Et_3N (0.11 mL, 0.8 mmol) followed by a MeOH solution (3 mL) of $CuCl_2{\cdot}2H_2O$ (25.6 mg, 0.15 mmol for **L2H**, **L3H**, **L6H** and **L7H** and 51.1 mg, 0.30 mmol for $L8H_2$, $L9H_2$, $L10H_2$, $L11H_2$, $L12H_2$ and $L13H_2$). The resulting mixture was stirred at room temperature for 2 h. Evaporation of the solvent under reduced pressure left a precipitate, which was collected by filtration and washed with cold MeOH to give the complex as a green or brown powder. For $L8H_2$ and $L9H_2$, evaporation of the MeOH followed by filtration through a short column of silica gel (DCM) was needed to give complexes in high purity. Single crystals suitable for X-ray characterization were obtained by slow evaporation of a DCM/MeOH (1:1) solution.

Single-Crystal XRD: Single-crystal XRD measurements were recorded on structures of the four original complexes. Data sets were collected with an Oxford diffractometer equipped with a CCD camera and related software.[52] An absorption correction (analytical)[52] was applied to all data. The structures were solved by direct methods using the SIR97 program[53] combined with Fourier difference synthesis and refined against F^2 and using the CRYSTALS program.[54] In Table 1, $R(F^2)$ and $R_w(F^2)$ are indicated for $I > 2\sigma(I)$. In each structure, all atomic displacements for non-hydrogen atoms were refined anisotropically. Hydrogen atoms on carbon atoms were located theoretically and the others (on oxygen atoms of noncoordinated solvent molecules) by Fourier difference, all were refined using a riding method.

CCDC-850706 (for **A**), -850707 (for **B**), -850708 (for **C**) and -850709 (for **D**) contain the supplementary crystallographic data this paper. These data can be obtained free of charge from The Cambridge Crystallographic Data Centre via www.ccdc.cam.ac.uk/data_request/cif.

Supporting Information (see footnote on the first page of this article): crystal structures of **L4H**, **L10H2** and [Cu(**L8**)$_2$] (**E**), cyclic voltammograms of **L6H**, $L12H_2$, [Cu(**L6**)$_2$] and [Cu(**L12**)].

Acknowledgments

We would like to thank the Centre National de la Recherche Scientifique (CNRS), Université Claude Bernard Lyon 1 and the Région Rhône-Alpes (CIBLE project "ENAMBRIMOLE") for financial support. N. C. is grateful to the Région Rhône-Alpes for a PhD fellowship. G. P. thanks the Centre de Diffraction Henri Longchambon for access to the single-crystal X-ray diffraction diffractometers. We would like to thank A. T. Bui and C. Morcel for help with some of the syntheses.

[1] S. V. Druzhinin, E. S. Balenkova, V. G. Nenajdenko, *Tetrahedron* **2007**, *63*, 7753–7808.
[2] U. M. Kauhanka, M. M. Kauhanka, *Liq. Cryst.* **2006**, *33*, 213–218.
[3] C. P. Roll, A. G. Martin, H. Görls, G. Leibeling, D. Guillon, B. Donnio, W. Weigand, *J. Mater. Chem.* **2004**, *14*, 1722–1730.
[4] U. Pietrasik, J. Szydlowska, A. Krowczynski, *Chem. Mater.* **2004**, *16*, 1485–1492.
[5] A. Krowczynski, J. Szydlowska, D. Pociecha, J. Przedmojski, E. Gorecka, *Liq. Cryst.* **1998**, *25*, 117–121.
[6] L. Zhang, M. Brookhar, P. S. White, *Organometallics* **2006**, *25*, 1868–1874.
[7] H.-Y. Wang, J. Zhang, X. Meng, G.-X. Jin, *J. Organomet. Chem.* **2006**, *691*, 1275–1281.
[8] X.-F. Li, K. Dai, W.-P. Ye, L. Pan, Y.-S. Li, *Organometallics* **2004**, *23*, 1223–1230.
[9] U. Beckmann, E. Eichberger, M. Lindner, M. Bongartz, P. C. Kunz, *Eur. J. Org. Chem.* **2008**, 4139–4147.
[10] K. Vlasov, N. Kalinovich, E. Lork, G.-V. Röschenthaler, *J. Fluorine Chem.* **2010**, *131*, 996–999.
[11] J. Przyborowski, E. Lork, G.-V. Röschenthaler, *J. Fluorine Chem.* **2000**, *104*, 207–213.
[12] J. A. Barten, A. A. Kadyrov, G.-V. Röschenthaler, *J. Fluorine Chem.* **2002**, *113*, 101–103.
[13] J. A. Barten, A. A. Kadyrov, E. Lork, G.-V. Röschenthaler, *J. Fluorine Chem.* **2002**, *116*, 87–92.
[14] M. Médebielle, S. Hohn, E. Okada, H. Myoken, D. Shibata, *Tetrahedron Lett.* **2005**, *46*, 7817–7821.
[15] M. Médebielle, O. Onomura, R. Keirouz, E. Okada, H. Yano, T. Terauchi, *Synthesis* **2002**, 2601–2608.
[16] F. Fenain, M. Médebielle, M. Rocher, O. Onomura, E. Okada, D. Shibata, *J. Fluorine Chem.* **2007**, *128*, 1286–1299.
[17] E. Okada, T. Kinomura, Y. Higashiyama, H. Takeuchi, M. Hojo, *Heterocycles* **1997**, *46*, 129–132.
[18] M. Hojo, R. Masuda, E. Okada, *Synthesis* **1986**, 1013–1014.
[19] M. Hojo, R. Masuda, E. Okada, H. Yamamoto, K. Morimoto, K. Okada, *Synthesis* **1990**, 195–198.
[20] N. Ota, T. Tomoda, N. Terai, Y. Kamitori, D. Shibata, M. Médebielle, E. Okada, *Heterocycles* **2008**, *76*, 1205–1217.

[21] N. S. Boltachova, O. V. Fedorova, I. G. Ovchinnikova, O. N. Kazheva, A. N. Chekhlov, O. A. Dyachenko, G. L. Rusinov, V. I. Filyakova, V. N. Charushin, *J. Fluorine Chem.* **2007**, *128*, 762–768.
[22] E. Yu. Fursova, V. I. Ovcharenko, G. V. Romanenko, V. N. Ikorskii, Yu. G. Shvedenkov, I. P. Asanov, L. N. Mazalov, *J. Struct. Chem.* **2001**, *42*, 251–260.
[23] G. V. Romanenko, I. V. Korobkov, V. I. Ovcharenko, *J. Struct. Chem.* **2000**, *41*, 1035–1040.
[24] H. C. Budnikov, O. Yu. Kargina, *J. Electroanal. Chem.* **1984**, *169*, 195–205.
[25] V. A. Reznikov, I. Yu. Bagryanskaya, Yu. V. Gatilov, *Russ. Chem. Bull.* **2000**, *49*, 899–905.
[26] G. I. Roshchupkina, T. V. Rybalova, Y. V. Gatilov, V. A. Reznikov, *Eur. J. Org. Chem.* **2003**, 3599–3602.
[27] G. Pilet, J.-B. Tommasino, F. Fenain, R. Matrak, M. Médebielle, *Dalton Trans.* **2008**, 5621–5626.
[28] G. Pilet, M. Médebielle, J.-B. Tommasino, G. Chastanet, B. Le Guennic, C. Train, *Eur. J. Inorg. Chem.* **2009**, 4718–4726.
[29] N. Chopin, S. Decamps, A. Gouger, M. Médebielle, S. Picot, A.-L. Bienvenu, G. Pilet, *J. Fluorine Chem.* **2011**, *132*, 850–857.
[30] D. Chopra, T. N. Guru Row, *CrystEngComm* **2011**, *13*, 2175–2186.
[31] T. Ono, Y. Hayakawa, Fluorine-Based Crystal Engineering, in: *Fluorine-Containing Synthons*, ACS Symposium Series, **2005**, vol. 911, pp. 498–513.
[32] K. D. Kreutter, T. Lu, L. Lee, E. C. Giardino, S. Patel, H. Huang, G. Xu, M. Fitzgerald, B. J. Haertlein, V. Mohan, C. Crysler, S. Eisennagel, M. Dasgupta, M. McMillan, J. C. Spurlino, N. D. Huebert, B. E. Maryanoff, B. E. Tomczuk, B. P. Damiano, M. R. Player, *Bioorg. Med. Chem. Lett.* **2008**, *18*, 2865–2870.
[33] L. Lee, K. D. Kreutter, W. Pan, C. Crysler, J. Spurlino, M. R. Player, B. Tomczuk, T. Lu, *Bioorg. Med. Chem. Lett.* **2007**, *17*, 6266–6269.
[34] E. Schweizer, A. Hoffmann-Röder, K. Schärer, J. A. Olsen, C. Fäh, P. Seiler, U. Obst-Sander, B. Wagner, M. Kansy, F. Diederich, *ChemMedChem* **2006**, *1*, 611–621.
[35] K. Tanabe, H. Harada, M. Narazaki, K. Tanaka, K. Inafuku, H. Komatsu, T. Ito, H. Yamada, Y. Chujo, T. Matsuda, M. Hiraoka, S.-I. Nishimoto, *J. Am. Chem. Soc.* **2009**, *131*, 15982–15983, and references cited therein.
[36] D. L. Chizhov, E. F. Khmara, P. A. Slepukhin, V. I. Filyakova, V. N. Charushin, *J. Struct. Chem.* **2010**, *51*, 288–295.
[37] D. L. Chizhov, M. G. Pervova, M. A. Samorukova, E. F. Khmara, V. I. Filyakova, V. I. Saloutin, V. N. Charushin, *J. Fluorine Chem.* **2011**, *132*, 394–401.
[38] G. S. Patterson, R. H. Holm, *Bioinorg. Chem.* **1975**, *4*, 257–275.
[39] A. W. Addison, *Spectroscopic and Redox Trends from Model Copper Complexes*, in: *Copper Coordination Chemistry: Biochemical and Inorganic Perspectives* (Eds.: K. D. Karlin, J. Zubieta), Adenine Press, New York, **1983**.
[40] A. W. Addison, *Inorg. Chim. Acta* **1989**, *162*, 217–220.
[41] M. Hojo, R. Masuda, Y. Kokuryo, H. Shioda, S. Matsuo, *Chem. Lett.* **1976**, 499–502.
[42] M. Hojo, R. Masuda, E. Okada, *Synthesis* **1986**, 1013–1014.
[43] H. Keller, M. Schlosser, *Tetrahedron* **1996**, *52*, 4637–4644.
[44] E. Miyasaki, Y. Morita, Y. Yakiyama, S. Maki, Y. Umemoto, M. Ohmoto, K. Nakasuji, *Chem. Lett.* **2007**, *36*, 1102–1103.
[45] J. H. Collins, H. H. Jaffe, *J. Am. Chem. Soc.* **1962**, *84*, 4708–4712.
[46] L. Yang, D. G. Powell, R. P. Houser, *Dalton Trans.* **2007**, 955–964.
[47] For electrochemical oxidation studies of nonfluorinated enaminones, see: W. Eleinberg, H. J. Schäfer, *Tetrahedron Lett.* **1984**, *25*, 5023–5026, and references cited therein.
[48] O. Hammerich, V. D. Parker, *J. Am. Chem. Soc.* **1974**, *96*, 4289–4296.
[49] We already know from our ongoing synthetic work that electrochemical reduction of several trifluoromethylated enaminones give rise to trifluoromethylated amino-derived cyclopentanes, which result from a dimerization–intramolecular aldol process, and the formation of the corresponding amines; C. Agostini, A. Bianco, M. Médebielle, J.-B. Tommasino, unpublished results.
[50] J. L. Sadler, A. J. Bard, *J. Am. Chem. Soc.* **1968**, *90*, 1979–1989.
[51] R. Lines, B. Svensmark Jensen, V. D. Parker, *Acta Chem. Scand. Sect. B* **1978**, *32*, 510–514.
[52] *CrysAlisPro*, Oxford Diffraction Ltd., version 1.171.33.46 (release 27–08–2009 CrysAlis171.NET); empirical absorption correction using spherical harmonics, implemented in SCALE3 ABSPACK scaling algorithm.
[53] G. Cascarano, A. Altomare, C. Giacovazzo, A. Guagliardi, A. G. G. Moliterni, D. Siliqi, M. C. Burla, G. Polidori, M. Camalli, *Acta Crystallogr., Sect. A: Found. Crystallogr.* **1996**, *52*, C-79.
[54] D. J. Watkin, C. K. Prout, J. R. Carruthers, P. W. Betteridge, in: *CRISTAL Issue 11*, Chemical Crystallography Laboratory, Oxford, UK, **1999**.

Received: December 13, 2011
Published Online: January 27, 2012

DOI: 10.1002/ejic.201100942

New Structural Features in Tetranuclear Iron Carbonyl Thiocarbonyls: Exotriangular Iron Atoms and Six-Electron-Donating Thiocarbonyl Groups Bridging Four Iron Atoms

Zhong Zhang,*[a,b] Qian-shu Li,[b,c] R. Bruce King,*[b,d] and Henry F. Schaefer III[d]

Keywords: Iron / Metal thiocarbonyls / Carbonyl ligands / Cluster compounds / Density functional calculations

DFT led to the discovery of two new structural motifs in tetranuclear iron carbonyl thiocarbonyls, $Fe_4(CS)_4(CO)_n$ (n = 12, 11, 10, 9), which are not found in their homoleptic analogues, $Fe_4(CO)_{n+4}$. Thus the lowest energy $Fe_4(CS)_4(CO)_{12}$ structures have a central Fe_3 triangle with an exotriangular iron atom joined to the Fe_3 triangle through a four-electron donor CS bridge. This contrasts with the structure of $Os_4(CO)_{16}$ and the predicted structure of $Fe_4(CO)_{16}$, which consist of an M_4 rhombus and two-electron donor carbonyl groups. An even more remarkable new structural motif for the $Fe_4(CS)_4(CO)_n$ derivatives is the irregular Fe_4 "rhombus" (actually a trapezium) bridged by a six-electron donor η^2-μ_4-CS group. This type of structure is found in the lowest energy structures of both $Fe_4(CS)_4(CO)_{10}$ and $Fe_4(CS)_4(CO)_9$ and makes $Fe_4(CS)_4(CO)_{10}$ viable enough to be a promising synthetic objective. On the contrary, $Fe_4(CS)_4(CO)_{11}$ is found to be thermochemically unfavorable both with respect to CO dissociation and disproportionation into $Fe_4(CS)_4(CO)_{12}$ and $Fe_4(CS)_4(CO)_{10}$.

1. Introduction

The three simple homoleptic iron carbonyls, $Fe(CO)_5$, $Fe_2(CO)_9$, and $Fe_3(CO)_{12}$, have been known since about 1930. Their structures were elucidated by X-ray diffraction (Figure 1) and they are now well-established, commercially available reagents for synthetic organoiron chemistry and other applications. However, despite the existence of these three stable homoleptic iron carbonyls, no stable neutral homoleptic tetranuclear carbonyls of iron, i.e. $Fe_4(CO)_n$, are known, even though the heavier congener of iron, osmium, forms the three homoleptic tetranuclear carbonyls $Os_4(CO)_n$ (n = 16, 15, 14). These tetranuclear osmium carbonyls provide examples of three different structural arrangements of the central Os_4 unit (Figure 2). $Os_4(CO)_{16}$ has a rhombus structure with four equivalent Os–Os single bonds,[1,2] $Os_4(CO)_{15}$ has a butterfly structure with five Os–Os single bonds,[3] and $Os_4(CO)_{14}$ has a tetrahedral structure with six Os–Os single bonds.[4] Both $Os_4(CO)_{15}$ and $Os_4(CO)_{14}$ appear to be very stable. However, $Os_4(CO)_{16}$, although sufficiently stable for low-temperature structural determination by X-ray diffraction, decomposes at room temperature to give mainly $Os_3(CO)_{12}$.

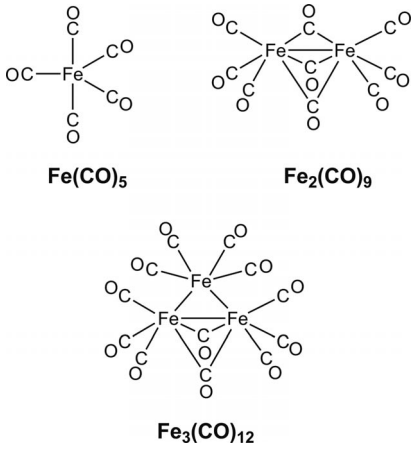

Figure 1. The three stable homoleptic iron carbonyls.

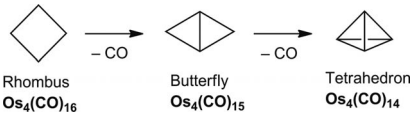

Figure 2. The three types of Os_4 frameworks in stable $Os_4(CO)_n$ derivatives.

A number of metal thiocarbonyl derivatives have been synthesized in which one or more carbonyl groups of a well-known homoleptic metal carbonyl have been replaced by a

[a] College of Science, Northwest A&F University, Yangling, Shanxi 712100, P. R. China
[b] Center for Computational Quantum Chemistry, South China Normal University, Guangzhou 510631, P. R. China
[c] Institute of Chemical Physics, Beijing Institute of Technology, Beijing 100081, P. R. China
[d] Department of Chemistry and Center for Computational Chemistry, University of Georgia, Athens, Georgia 30602, USA

Supporting information for this article is available on the WWW under http://dx.doi.org/10.1002/ejic.201100942.

thiocarbonyl group.[5,6] These include $M(CS)(CO)_5$ (M = Cr, Mo, W),[7] which is isoelectronic with $M(CO)_6$, and $Fe(CS)(CO)_4$,[8] which is isoelectronic with $Fe(CO)_5$. However, polynuclear metal derivatives that contain only CO and CS ligands have not yet been synthesized. Theoretical investigations of the thiocarbonyl analogues of the three stable homoleptic iron carbonyls and their unsaturated derivatives predict significant effects upon the substitution of a thiocarbonyl group for a carbonyl group, particularly in polynuclear derivatives.[9,10] Thus for $Fe_2(CS)_2(CO)_7$ and $Fe_3(CS)_3(CO)_9$, which are related to $Fe_2(CO)_9$ and $Fe_3(CO)_{12}$ but with bridging thiocarbonyl groups, are energetically preferred over analogous structures with bridging carbonyl groups. More dramatically, in unsaturated $Fe_2(CS)_2(CO)_n$ (n = 6, 5, 4, 3) and $Fe_3(CS)_3(CO)_n$ (n = 8, 7, 6), structures with four- and six-electron donor bridging thiocarbonyl groups that form metal–sulfur as well as metal–carbon bonds (Figure 3) are energetically preferred over those with metal–metal multiple bonds.

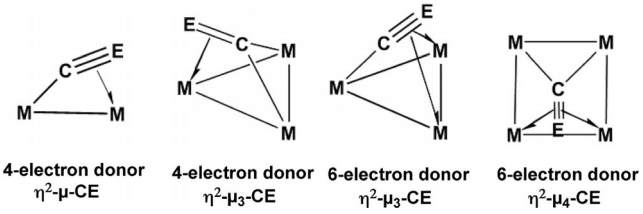

Figure 3. Four- and six-electron donor CE groups (E = O, S) bridging two to four metal atoms.

These differences between closely related homoleptic iron carbonyl derivatives $Fe_m(CO)_{n+m}$ and $Fe_m(CS)_m(CO)_n$ (m = 2 and 3) suggest the existence of viable tetranuclear $Fe_4(CS)_4(CO)_n$ derivatives, even though the corresponding homoleptic neutral $Fe_4(CO)_{n+4}$ derivatives are unknown as stable compounds. We have used density functional methods to investigate the series of tetranuclear iron carbonyl thiocarbonyls $Fe_4(CS)_4(CO)_n$ (n = 12, 11, 10, 9). The preferred structures of these tetranuclear iron carbonyl thiocarbonyls were found to be very different to those predicted for the analogous homoleptic $Fe_4(CO)_{n+4}$ in a previous study that used similar theoretical methods.[11] The following new features were observed in the low energy $Fe_4(CS)_4(CO)_n$ (n = 12, 11, 10, 9) structures reported in this paper:

(1) An exotriangular $Fe(CS)(CO)_3$ group bonded to a central Fe_3 triangle in low-energy $Fe_4(CS)_4(CO)_{12}$ structures.

(2) A six-electron donor η^2-μ_4-CS group that bridges all four iron atoms (Figure 3) in low-energy $Fe_4(CS)_4(CO)_n$ structures (n = 10, 9).

These theoretical observations suggest that photochemical or thermal decarbonylation of known $Fe(CS)(CO)_4$ under suitable conditions might lead to structures very different to $Fe_2(CO)_9$ and $Fe_3(CO)_{12}$ (Figure 1), which were obtained many years ago from $Fe(CO)_5$.

2. Theoretical Methods

Electron correlation effects were considered using DFT methods, which have evolved as a practical and effective computational tool especially for organometallic compounds.[12–27] Two DFT methods were used in this study. The first functional was the popular B3LYP method, which is the hybrid Hartree–Fock/DFT method that uses a combination of the three-parameter Becke exchange functional (B3) with the Lee–Yang–Parr (LYP) generalized gradient correlation functional.[28,29] The other DFT method used was BP86, which combines Becke's 1988 exchange functional (B) with Perdew's 1986 gradient corrected correlation functional (P86).[30,31] It has been noted elsewhere that the BP86 method may be somewhat more reliable than B3LYP for the type of organometallic systems considered here,[32,33,34] particularly for vibrational frequencies.

Basis sets were chosen to provide continuity with existing research on organometallic compounds. Fortunately, DFT methods are less basis-set-sensitive than higher-level methods such as coupled cluster theory. In this work all computations were performed using double-ζ plus polarization (DZP) basis sets. The DZP basis sets used for carbon, oxygen, and sulfur add one set of pure spherical harmonic d functions with orbital exponents $\alpha_d(C) = 0.75$, $\alpha_d(O) = 0.85$, and $\alpha_d(S) = 0.70$ to the standard Huzinaga–Dunning contracted DZ sets.[35,36,37] The loosely contracted DZP basis set for iron is the Wachters primitive set[38] augmented by two sets of p functions and one set of d functions, contracted according to Hood, Pitzer, and Schaefer,[39] and designated (14s11p6d/10s8p3d). For $Fe_4(CS)_4(CO)_{12}$, $Fe_4(CS)_4(CO)_{11}$, $Fe_4(CS)_4(CO)_{10}$, and $Fe_4(CS)_4(CO)_9$ there are 708, 678, 648, and 618 contracted Gaussian functions, respectively.

The geometries of all structures were fully optimized using the B3LYP/DZP and BP86/DZP methods. Vibrational frequencies were determined by analytically evaluating the second derivatives of the energy with respect to the nuclear coordinates. The corresponding infrared intensities were also evaluated analytically. All of the computations were carried out with the Gaussian 03 program,[40] exercising the fine grid option (75 radial shells, 302 angular points) to evaluate integrals numerically,[41] whereas the tight (10^{-8} Hartree) designation is the default for the self-consistent field convergence.

In the search for minima with all standard DFT methods, low magnitude imaginary vibrational frequencies are suspect because of significant limitations in the numerical integration procedures used in the DFT computations. Thus all imaginary vibrational frequencies with a magnitude less than $50i\ cm^{-1}$ were considered questionable and given less weight in the analysis.[42,43] Therefore, we do not always follow such low imaginary vibrational frequencies.

The optimized structures are depicted in Figures 4, 5, 6, and 7. Each $Fe_4(CS)_4(CO)_a$ structure is designated as **a**–**b** where **a** is the number of CO groups and **b** orders the structures according to their relative energies. Thus the lowest

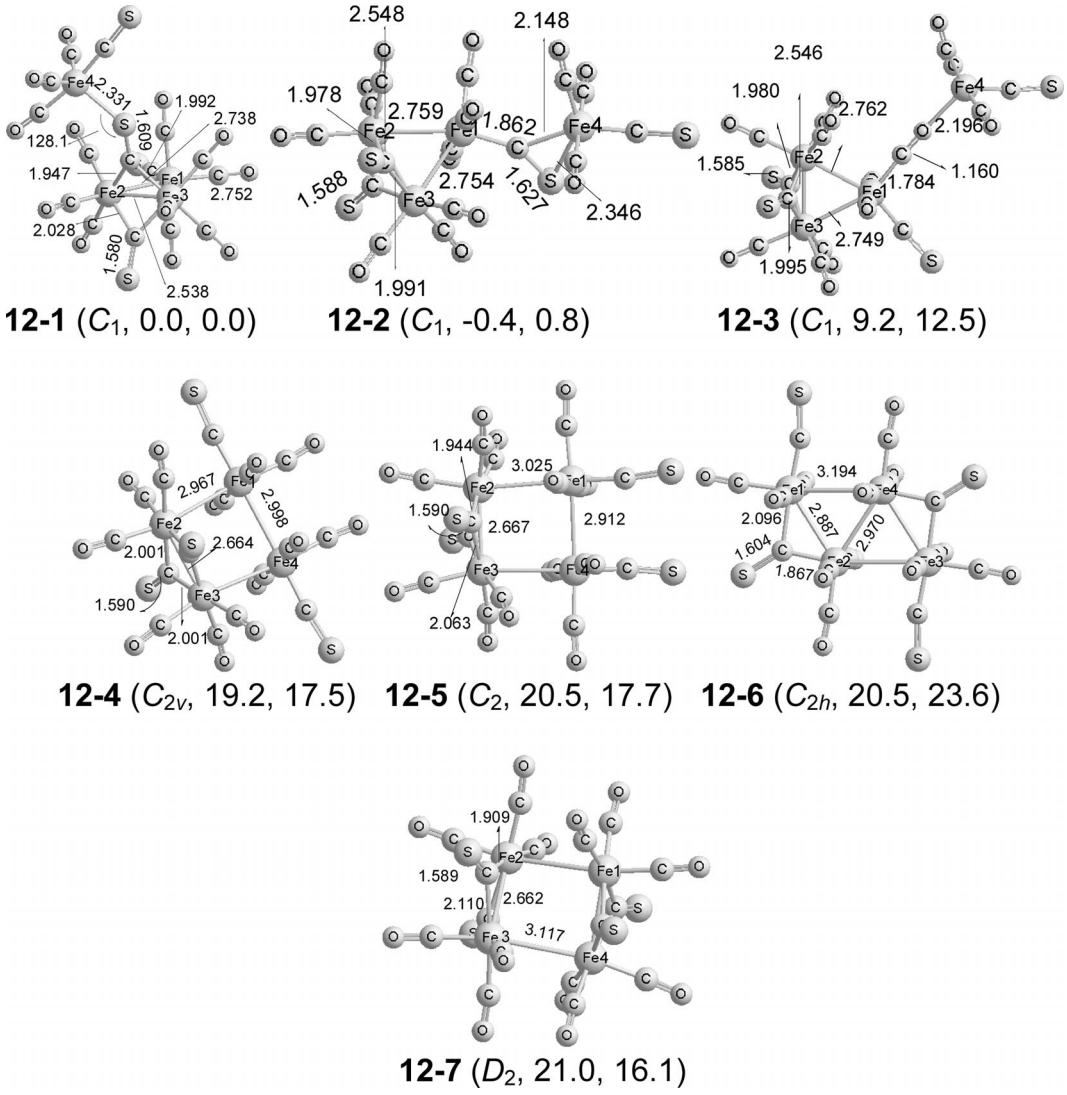

Figure 4. Optimized $Fe_4(CS)_4(CO)_{12}$ structures. In Figures 4–7 the distances are predicted by the B3LYP. The relative energies (ΔE, in kcal/mol) in parenthesis are predicted by the B3LYP and BP86 methods, respectively.

energy singlet structure of $Fe_4(CS)_4(CO)_{12}$ is designated **12**–**1**. Energies are reported as 5.9(2.9) kcal/mol corresponding to the results from the B3LYP(BP86) methods.

3. Results and Discussion

3.1 $Fe_4(CS)_4(CO)_{12}$

A total of seven structures were found for $Fe_4(CS)_4(CO)_{12}$, which includes three structures that have a four-electron donor CE (E = O, S) group that connects a central $Fe_3(CS)_3(CO)_9$ unit to an exotriangular $Fe(CS)(CO)_3$ unit, three structures with a central Fe_4 rhombus, and a single butterfly structure (Figure 4 and Table S1 in the Supporting Information). All of these $Fe_4(CS)_4(CO)_{12}$ structures were found to be genuine minima with all real vibrational frequencies except for **12**–**6**, which has a tiny imaginary frequency of 3(13)*i* cm^{-1}.

The lowest energy $Fe_4(CS)_4(CO)_{12}$ structure, **12**–**1** (Figure 4 and Table S1), was formed from the global minimum[10] of $Fe_3(CS)_3(CO)_9$ by the attachment of a $Fe(CS)(CO)_3$ fragment through the sulfur atom of a bridging CS group. Such a construction converts this bridging CS group from a two-electron donor to a pair of iron atoms to a four-electron donor to three iron atoms. The unique Fe2–Fe3 distance bridged by two CS groups is 2.538 Å, which is only ca. 0.01 Å shorter than that predicted for $Fe_3(CS)_3(CO)_9$. The unbridged Fe1–Fe2 and Fe1–Fe3 distances in **12**–**1** are predicted to be ca. 0.2 Å longer at 2.738 and 2.752 Å, respectively, and are comparable to the corresponding unbridged Fe–Fe bonds in $Fe_3(CS)_3(CO)_9$. In addition, the C=S distance in the end-on four-electron donor bridging CS group in **12**–**1** is found to be 1.609 Å, which is 0.013 Å longer than the C–S distance in the two-electron donor bridging CS groups (1.586 Å). The Fe4–S distance to the four-electron donor bridging CS group is relatively short at 2.331 Å, which indicates a direct Fe–S bond. The four-electron donor CS group in **12**–**1** exhibits a very low ν(CS) frequency of 1091 cm^{-1} (Table S5).

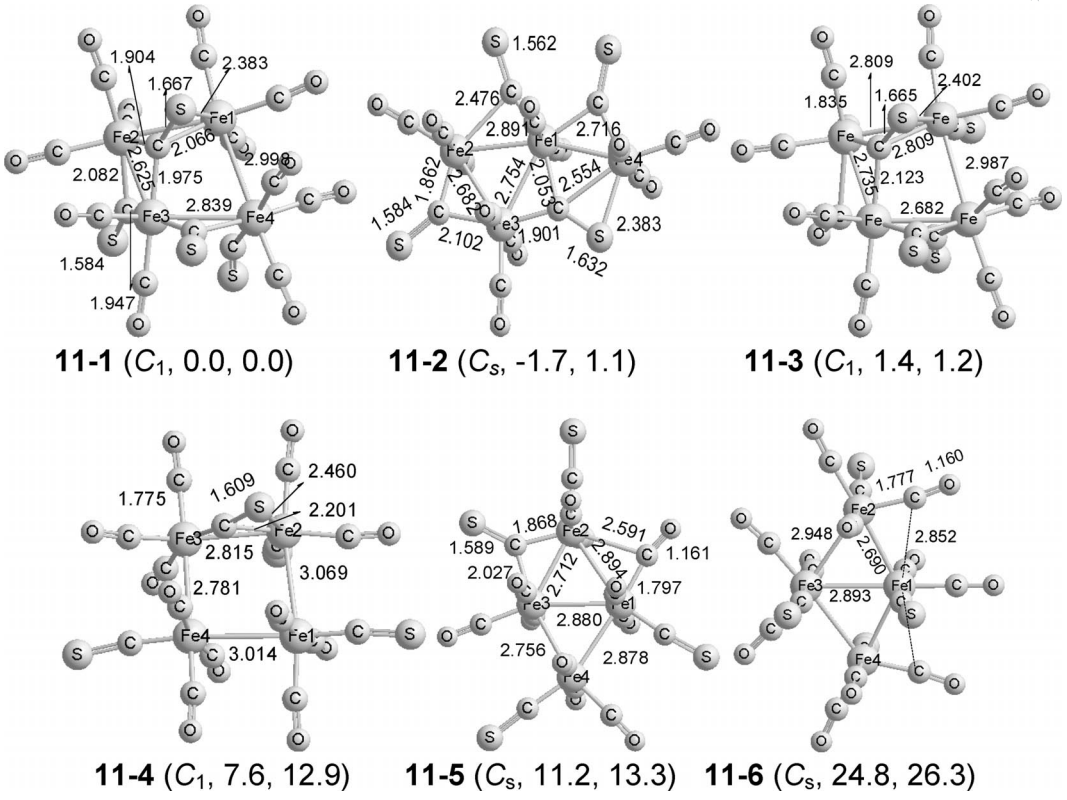

Figure 5. Optimized $Fe_4(CS)_4(CO)_{11}$ structures.

The next $Fe_4(CS)_4(CO)_{12}$ structure **12**–**2** has essentially the same energy as **12**–**1**, and lies 0.4 kcal/mol below **12**–**1** (B3LYP) or 0.8 kcal/mol above **12**–**1** (BP86, Figure 4 and Table S1). These two energetically close $Fe_4(CS)_4(CO)_{12}$ structures suggest a potentially fluxional system. Structure **12**–**2** can also be generated from the $Fe_3(CS)_3(CO)_9$ global minimum by the addition of an $Fe(CS)(CO)_3$ fragment to the terminal thiocarbonyl group. The predicted Fe4–S and Fe4–C(S) distances in **12**–**2** are 2.346 and 2.148 Å, respectively, which implies the donation of a pair of π electrons from this CS group to the unsaturated $Fe(CS)(CO)_3$ fragment. The Fe–Fe distances in the Fe_3 triangle of **12**–**2** are comparable to those previously obtained[10] for the lowest energy structure of $Fe_3(CS)_3(CO)_9$.

The $Fe_4(CS)_4(CO)_{12}$ structure **12**–**3** has a linear four-electron donor bridging CO group that connects the $Fe_3(CS)_3(CO)_9$ and $Fe(CS)(CO)_3$ fragments (Figure 4 and Table S1). The short Fe–O distance in **12**–**3** of 2.196 Å indicates a direct bond between the oxygen atom of this bridging CO group and Fe4. Structure **12**–**3** is predicted to lie 9.2(12.5) kcal/mol above **12**–**1**. This suggests that the Fe–O bond to the four-electron donor bridging CO group is weaker than the Fe–S bond to the four-electron donor bridging CS group in **12**–**1**.

These three lowest energy $Fe_4(CS)_4(CO)_{12}$ structures all have a single four-electron donor CE (E = O, S) group and three Fe–Fe single bonds in their Fe_3 triangles that lead to the favored 18-electron configuration for each iron atom. In addition, the two $Fe_4(CS)_4(CO)_{12}$ structures **12**–**4** and **12**–**5** with a central Fe_4 rhombus and two symmetric bridging CS groups are found at the relatively high energies of at least 19(17) kcal/mol above **12**–**1** (Figure 4 and Table S1). These two structures can be generated by the replacement of the bridging CO group in the binuclear $Fe_2(\mu\text{-}CS)_2(\mu\text{-}CO)(CO)_6$ structure[9] with an unbridged $Fe_2(CS)_2(CO)_6$ fragment. The doubly bridged Fe2–Fe3 bond lengths in these two structures are predicted to be ca. 2.66 Å, which is ca. 0.13 Å longer than the doubly bridged Fe2–Fe3 distances in **12**–**1** or **12**–**2**. The unbridged Fe–Fe distances are predicted to be greater than 2.91 Å. The remaining $Fe_4(CS)_4(CO)_{12}$ structure with a central Fe_4 rhombus, **12**–**7**, with four bridging CS groups lies at the relatively high energy of 21.0(16.1) kcal/mol above **12**–**1**. Structure **12**–**7** can be generated by replacing the bridging CO group in $Fe_2(\mu\text{-}CS)_2(\mu\text{-}CO)(CO)_6$ with a doubly bridged $Fe_2(\mu\text{-}CS)_2(CO)_6$ fragment. The Fe_4 rhombus in **12**–**7** is nonplanar because of steric repulsion that particularly involves the seven-coordinate iron atoms Fe1, Fe2, Fe3, and Fe4. In all three of the $Fe_4(CS)_4(CO)_{12}$ structures **12**–**4**, **12**–**5**, and **12**–**7** having a central Fe_4 rhombus, all two-electron donor CE (E = O, S) groups, and four Fe–Fe single bonds, all four iron atoms have the favored 18-electron configuration.

The only butterfly $Fe_4(CS)_4(CO)_{12}$ structure found in this work, **12**–**6**, lies at the relatively high energy of 20.5(23.6) kcal/mol above **12**–**1** and has two bridging CS groups (Figure 4 and Table S1). The CS bridged Fe–Fe distances and unbridged Fe–Fe distances in **12**–**6** are found to be relatively long at 2.887 and 3.194 Å, respectively. The diagonal

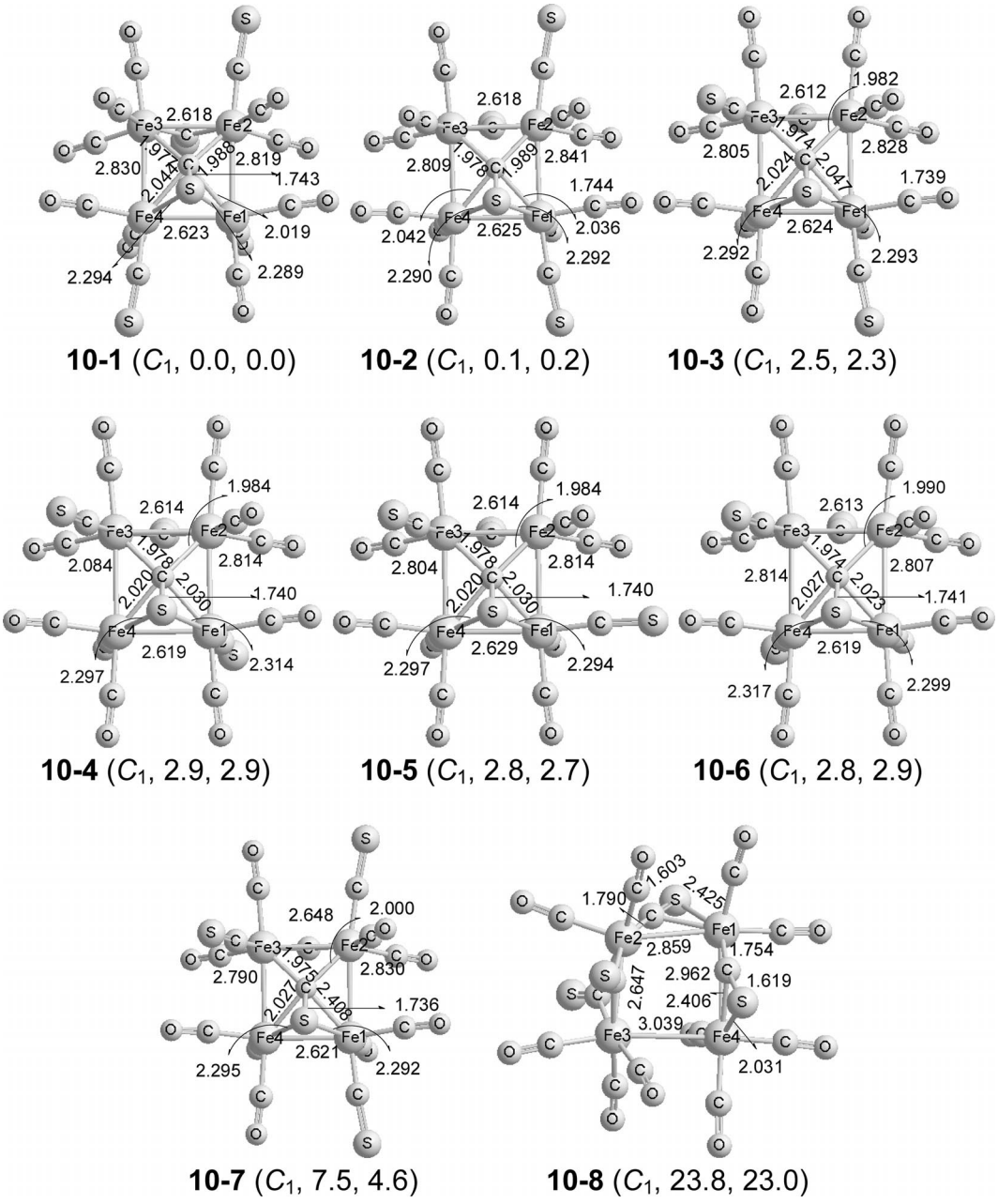

Figure 6. Optimized $Fe_4(CS)_4(CO)_{10}$ structures.

Fe2–Fe4 distance of 2.970 Å, which corresponds to the "body" of the Fe_4 butterfly, indicates a direct Fe–Fe interaction. A butterfly $Fe_4(CS)_4(CO)_{12}$ structure with five formal Fe–Fe single bonds and sixteen two-electron donor CE (E = O, S) groups would have an unfavorable 20-electron configuration for one of the iron atoms and a favorable 18-electron configuration for the remaining three iron atoms. This may explain the relatively long Fe1–Fe4 distance in **12**–**6** compared with the other $Fe_4(CS)_4(CO)_{12}$ structures.

Unbridged rhombus $Fe_4(CS)_4(CO)_{12}$ structures were also investigated, analogous to the experimental structure of $Os_4(CO)_{16}$.[1,2] However, such structures were found to lie more than 25 kcal/mol above **12**–**1** and thus are not discussed further.

3.2 $Fe_4(CS)_4(CO)_{11}$

Six $Fe_4(CS)_4(CO)_{11}$ structures were found within 25 kcal/mol in energy (Figure 5 and Table S2). All six structures were predicted to be genuine minima without any imaginary frequencies except **11**–**5** and **11**–**6**, which have small imaginary frequencies of 20*i* (BP86) and 32*i* cm^{-1} (B3LYP).

The lowest energy $Fe_4(CS)_4(CO)_{11}$ structure **11**–**1** can be formulated as $Fe_4(\eta^2\text{-}\mu_3\text{-}CS)(\mu\text{-}CS)_3(CO)_{11}$ (Figure 5 and Table S2). This structure can be generated from the doubly CS-bridged rhombus $Fe_4(CS)_4(CO)_{12}$ structure **12**–**4** (Figure 4) by loss of a terminal CO group from Fe1 with concurrent bending of a CS group to bridge across three of the four iron atoms in the Fe_4 rhombus. The Fe1–S and Fe1–

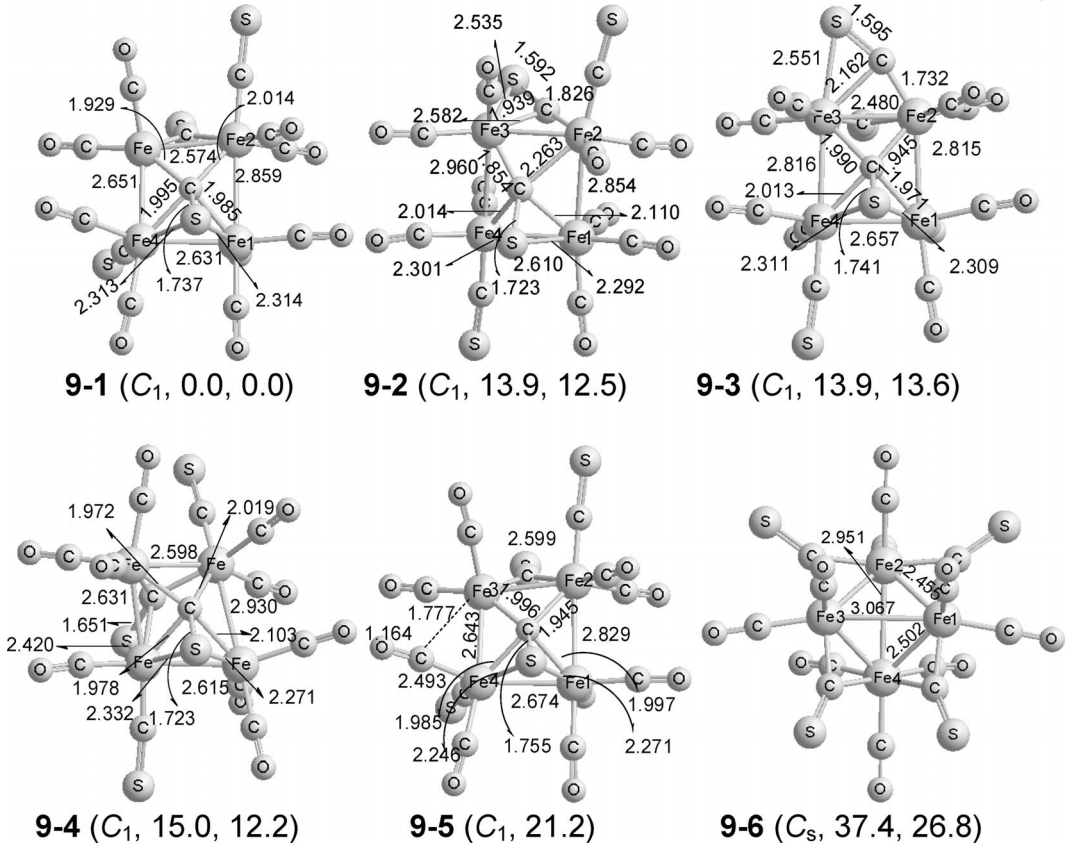

Figure 7. Optimized $Fe_4(CS)_4(CO)_9$ structures.

C(S) distances to the CS bridge are predicted to be 2.383 and 2.066 Å, respectively. The short Fe–S distance indicates that this bridging CS group is a four-electron donor η^2-μ_3-CS group. The C–S distance of 1.667 Å in this four-electron donor CS group, which bridges three iron atoms, is even longer than the corresponding C–S distances in the four-electron donor CS groups that bridge only two iron atoms in **12**–**1** and **12**–**2**. This is consistent with the very low ν(CS) frequency at 997 cm^{-1} for this η^2-μ_3-CS group in **11**–**1** (Table S6).

The $Fe_4(CS)_4(CO)_{11}$ structure **11**–**3**, which lies only 1.4(1.2) kcal/mol above **11**–**1**, is also formulated as $Fe_4(\eta^2$-μ_3-CS)(μ-CS)$_3$(μ-CO)(CS)$(CO)_{10}$ (Figure 5 and Table S2). Structure **11**–**3** can be generated from **11**–**1** by interchanging the bridging CS group in **11**–**1** with a terminal CO group. Structure **11**–**2**, at only –1.7 kcal/mol below **11**–**1** (B3LYP) or 1.1 kcal/mol above **11**–**1** (BP86), is similarly formulated as $Fe_4(\eta^2$-μ_3-CS)(μ-CS)$_3(CO)_{11}$. However, in **11**–**2** three of the four iron atoms form an Fe_3 triangle with the fourth iron atom being exotriangular. The close energy spacing of the three lowest energy $Fe_4(CS)_4(CO)_{11}$ structures suggests a fluxional molecule.

The remaining rhombus $Fe_4(CS)_4(CO)_{11}$ structure, $Fe_4(\eta^2$-μ-CS)$(CS)_3(CO)_{11}$ **11**–**4**, contains a single four-electron donor CS group, which is indicated by the short Fe2–S distance of 2.460 Å. Structure **11**–**4** is predicted to lie 7.6(12.9) kcal/mol in energy above **11**–**1**. All four iron atoms in each of the $Fe_4(CS)_4(CO)_{11}$ structures that contain a single four-electron donor η^2-μ-CS group, **11**–**1** to **11**–**4**, have the favored 18-electron configuration because the "extra" two electrons from the four-electron donor CS group compensate for the loss of one carbonyl group from $Fe_4(CS)_4(CO)_{12}$.

The central Os_4 unit in the $Os_4(CO)_{15}$ structure found experimentally[3] has a butterfly configuration (Figure 2) with five Os–Os bonds. Two similar Fe_4 butterfly structures, **11**–**5** and **11**–**6**, were found for isovalent $Fe_4(CS)_4(CO)_{11}$ (Figure 5 and Table S2). Structure **11**–**5**, which lies 11.2(13.3) kcal/mol in energy above **11**–**1**, was found to have both a bridging CS group and a semibridging CO group. Structure **11**–**6**, which lies at the relatively high energy of 24.8(26.3) kcal/mol above **11**–**1**, was found to have two equivalent semibridging CO groups with short Fe–C distances of 1.777 Å and long Fe–C distances of 2.852 Å. The ca. 10 kcal/mol higher energy of **11**–**6** relative to **11**–**5** is another demonstration that bridging CS groups are more favorable than bridging CO groups.

3.3 $Fe_4(CS)_4(CO)_{10}$

The tetranuclear osmium carbonyl $Os_4(CO)_{14}$ has been shown by X-ray crystallography to have a central Os_4 tetrahedron with six Os–Os single bonds along the tetrahedron edges.[4] For the isovalent $Fe_4(CS)_4(CO)_{10}$, starting structures with central Fe_4 rhombuses, butterflies, and tetrahedra

were all considered. However, the butterfly and tetrahedral structures were predicted to lie at least 30 kcal/mol above the lowest energy rhombus structure, so only the rhombus structures were considered in detail. Strictly speaking, however, the low symmetry of the ligand distributions in these $Fe_4(CS)_4(CO)_{10}$ structures makes the central Fe_4 quadrilaterals not true rhombuses with equal Fe–Fe edges but irregular quadrilaterals (trapezia), with four significantly unequal Fe–Fe edges. However, the term "rhombus" has been used previously to describe related structures so, for convenience, it will be used here. A total of eight rhombus $Fe_4(CS)_4(CO)_{10}$ structures were found (Figure 6 and Table S3) and all eight are genuine minima with no imaginary vibrational frequencies.

The global minimum of $Fe_4(CS)_4(CO)_{10}$, **10**–**1**, has two different types of bridging CS groups, namely, an unusual six-electron donor η^2-μ_4-CS group that bridges all four iron atoms in the Fe_4 rhombus and a more usual two-electron donor μ-CS group that bridges one of the Fe–Fe edges (Figure 6 and Table S3). The carbon atom of the η^2-μ_4-CS group of **10**–**1** is situated almost exactly in the center of the Fe rhombus but slightly above the Fe_4 plane. The four Fe–C(S) distances are predicted to be 2.019 Å for Fe1–C, 1.988 Å for Fe2–C, 1.977 Å for Fe3–C, and 2.044 Å for Fe4–C, which are all bonding distances. The sulfur atom of the η^2-μ_4-CS group in **10**–**1** is nearly symmetrically situated across the Fe1–Fe4 edge of the Fe_4 rhombus. The Fe1–S and Fe4–S distances are 2.289 and 2.294 Å, respectively, which are consistent with direct Fe–S bonds. The C–S distance in the η^2-μ_4-CS group is unusually long at 1.743 Å, which indicates a relatively low effective C–S bond order consistent with the very low predicted ν(CS) frequency of 882 cm^{-1}. The Fe1–C–S–Fe4 dihedral angle in **10**–**1** is predicted to be close to the ideal 90° at 84.2°, compatible with the donation of electron pairs from each of the two perpendicular doubly-occupied π orbitals in the C≡S triple bond. Thus the η^2-μ_4-CS group in **10**–**1** is a six-electron donor, which leads to the favored 18-electron configuration for each of the four iron atoms. A similar six-electron donor η^2-μ_4-CS group is known experimentally in $Fe_5(CO)_{13}(S)_2(CS)$.[44] In **10**–**1**, our predicted bond lengths for the η^2-μ_4-CS group to the Fe_4 rhombus are similar to the corresponding experimental bond lengths in $Fe_5(CO)_{13}(S)_2(CS)$. Similarly the low ν(CS) frequency of 882 cm^{-1} in **10**–**1** is close to the experimental 921 cm^{-1} ν(CS) frequency of the η^2-μ_4-CS group in $Fe_5(CO)_{13}(S)_2(CS)$.[44]

The next five $Fe_4(CS)_4(CO)_{10}$ structures (**10**–**2** to **10**–**6**) are similar to **10**–**1** as they contain both a six-electron donor η^2-μ_4-CS group that bridges the central Fe_4 rhombus and a two-electron donor μ-CS group that bridges one of the Fe–Fe edges of the rhombus (Figure 6 and Table S3). These five $Fe_4(CS)_4(CO)_{10}$ structures differ from **10**–**1** only in the locations of the two terminal CS groups relative to the central $Fe_4(\eta^2$-μ_4-CS)(μ-CS) system. This minor structural difference led to very closely spaced relative energies in the narrow range of 0.1(0.2)–2.9(2.9) kcal/mol above **10**–**1**. Thus $Fe_4(CS)_4(CO)_{10}$ was predicted to be a highly fluxional system.

The $Fe_4(CS)_4(CO)_{10}$ structure **10**–**7** also has a six-electron donor η^2-μ_4-CS group that bridges an Fe_4 rhombus (Figure 6 and Table S3). However, the two-electron donor edge-bridging group in **10**–**7** is a μ-CO group rather than the μ-CS group found in the structures **10**–**1** to **10**–**6**. This structural change led to a somewhat higher energy. Thus structure **10**–**7** was predicted to lie 7.5(4.6) kcal/mol above **10**–**1**.

The lowest energy $Fe_4(CS)_4(CO)_{10}$ structure found without a six-electron donor bridging η^2-μ_4-CS group is **10**–**8**, which has two four-electron donor η^2-μ-CS groups and two two-electron donor bridging μ-CS groups. This is a relatively high energy $Fe_4(CS)_4(CO)_{10}$ structure, lying 23.8(23.0) kcal/mol above **10**–**1**. Thus the six-electron donor η^2-μ_4-CS group is an important structural feature in all of the low energy $Fe_4(CS)_4(CO)_{10}$ structures, which probably include all such structures of chemical significance.

The molecular orbitals of **10**–**1** with a six-electron donor η^2-μ_4-CS group (Figure S40) suggest that there are three different interactions between the CS group and the central Fe_4 fragment, namely, σ-bonding, π-bonding, and π*-antibonding interactions. The σ- and π-bonding interactions directly transfer electrons from the σ and π orbitals of the CS ligand into molecular orbitals of the Fe_4 fragment. The π*-antibonding interaction transfers electrons from orbitals of the Fe_4 fragment to π*-antibonding orbitals of the CS group. The natural bond orbital index of the six-electron donor CS group is predicted to be 0.950, which is smaller than that of the two-electron donor CS group (1.443) and the terminal CS ligand (1.579). Comparison of CS and CO valence orbitals (Figure S41) indicates that the π and π* orbitals of CS are concentrated more on the sulfur atom than the corresponding π and π* orbitals of CO are concentrated on the oxygen atom. This is consistent with the greater tendency of the CS ligand to bond through the sulfur atom than the CO ligand to bond through the oxygen atom.

3.4 $Fe_4(CS)_4(CO)_9$

Structures for $Fe_4(CS)_4(CO)_9$ with rhombus, butterfly, and tetrahedral Fe_4 frameworks (Figure 2) were investigated. Five rhombus structures and one tetrahedral structure were found within 30 kcal/mol of the global minimum (Figure 7 and Table S4). The five rhombus $Fe_4(CS)_4(CO)_9$ structures were all found to be genuine minima with all real vibrational frequencies except for **9**–**6**, which has a small imaginary vibrational frequency of 44(18)*i* cm^{-1}. The $Fe_4(CS)_4(CO)_9$ global minimum, **9**–**1**, has a six-electron donor η^2-μ_4-CS group and a two-electron donor μ-CS group. Structure **9**–**1** is derived from the $Fe_4(CS)_4(CO)_{10}$ global minimum (**10**–**1** in Figure 6) by loss of a terminal CO group from Fe3 with relatively little change to the central $Fe_4(\eta^2$-μ_4-CS)(μ-CS) unit. Structure **9**–**1** lies more than 12 kcal/mol below any of the other $Fe_4(CS)_4(CO)_9$ structures found and thus must be considered to be a particularly favorable structure.

The higher energy $Fe_4(CS)_4(CO)_9$ structure most closely related to the global minimum **9**–**1** is **9**–**5**, which was obtained only by the B3LYP method. Structure **9**–**5** has the same central $Fe_4(\eta^2\text{-}\mu_4\text{-CS})(\mu\text{-CS})$ core but a different arrangement of the terminal CS ligands (Figure 7 and Table S4). However, **9**–**5** was a relatively high energy $Fe_4(CS)_4(CO)_9$ structure, which lies 21.2 kcal/mol above **9**–**1**. Attempted optimization of **9**–**5** using the BP86 method led to **9**–**1**.

The second lowest energy $Fe_4(CS)_4(CO)_9$ structure (**9**–**2**), lying 13.9(12.5) kcal/mol above **9**–**1**, was predicted to have a six-electron donor $\eta^2\text{-}\mu_4$-CS group and a four-electron donor $\eta^2\text{-}\mu$-CS group (Figure 7 and Table S4). Structure **9**–**2** can be derived from **10**–**1** by the loss of a terminal CO group from Fe3 with concurrent bending of the two-electron donor bridging μ-CS group into a four-electron donor $\eta^2\text{-}\mu$-CS group. The $Fe_4(CS)_4(CO)_9$ structure **9**–**3**, which lies 13.9(13.6) kcal/mol above **9**–**1**, is closely related to **9**–**2** but has an additional edge-bridging μ-CS group. Thus **9**–**3** has examples of all four types of CS groups, namely, one six-electron donor bridging $\eta^2\text{-}\mu_4$-CS group, one four-electron donor edge-bridging $\eta^2\text{-}\mu$-CS group, one two-electron donor edge-bridging μ-CS group, and one terminal CS group. The $Fe_4(CS)_4(CO)_9$ structure **9**–**4**, which lies 15.0(12.2) kcal/mol above **9**–**1**, has a six-electron donor bridging $\eta^2\text{-}\mu_4$-CS group and a four-electron donor bridging $\eta^2\text{-}\mu_3$-CS group. In this sense **9**–**4** is related to **9**–**2** but has a different relative position of the two bridging CS groups.

The lowest energy $Fe_4(CS)_4(CO)_9$ structure with a tetrahedral Fe_4 unit is **9**–**6**, but this is a high energy structure that lies at 37.4(26.8 kcal/mol) above the **9**–**1** global minimum. Structure **9**–**6** also has a small imaginary vibrational frequency of 44(18)*i* cm^{-1}. In **9**–**6** all four CS groups are two-electron donor edge-bridging μ-CS groups.

3.5 Thermochemistry

The dissociation energies reported here were obtained from the differences between the total energies of the dissociation products and that of the original complex. Table 1 summarizes the energies for different dissociation pathways for the global minima of $Fe_4(CS)_4(CO)_n$ (n = 12, 11, 10). These data were obtained by using total energies calculated by the same methods for the dissociation fragments $Fe_3(CS)_3(CO)_n$ (n = 9, 8, 7),[10] $Fe_2(CS)_2(CO)_n$ (n = 7, 6, 5),[9] $Fe(CS)(CO)_n$ (n = 4, 3, 2),[9] and CO. Some comparison with dissociation energies for the corresponding $Fe_4(CO)_{n+4}$ derivatives is also presented in Table 1. The experimental carbonyl dissociation energies for $Ni(CO)_4$, $Fe(CO)_5$, and $Cr(CO)_6$ are 27, 41, and 37 kcal/mol, respectively.[45]

The data in Table 1 suggest major differences between the chemistry of $Fe_4(CS)_4(CO)_n$ and the corresponding $Fe_4(CO)_{n+4}$ derivatives. Thus $Fe_4(CS)_4(CO)_{12}$ is predicted to be viable as its dissociation into $Fe_3(CS)_3(CO)_9$ and $Fe(CS)(CO)_3$ is predicted to be endothermic requiring 13.4(18.6) kcal/mol and its carbonyl dissociation to $Fe_4(CS)_4(CO)_{11}$ is appreciable at ca. 25 kcal/mol. This contrasts with the carbonyl analogue $Fe_4(CO)_{16}$ for which the dissociation into $Fe_3(CO)_{12}$ and $Fe(CO)_4$ was predicted to be nearly thermoneutral with a small predicted energy change of +1.5(5.8) kcal/mol.[11]

The thermochemical data in Tables 1 and 2 also suggest that $Fe_4(CS)_4(CO)_{10}$ is a viable compound with a CO dissociation energy of 17.7(22.0) kcal/mol and an energy of 19.6(24.9) kcal/mol for dissociation into two binuclear $Fe_2(CS)_2(CO)_5$ fragments. In addition, the disproportionation of $Fe_4(CS)_4(CO)_{10}$ into $Fe_4(CS)_4(CO)_{11}$ and $Fe_4(CS)_4(CO)_9$ is strongly endothermic requiring 30.1(25.0) kcal/mol. This contrasts with $Fe_4(CS)_4(CO)_{11}$, which is predicted

Table 1. Dissociation energies (ΔE, kcal/mol) for the lowest energy structures of $Fe_4(CS)_4(CO)_n$ (n = 12, 11, 10).

	B3LYP	BP86
$Fe_4(CS)_4(CO)_{12}$ (**12**–**1**) → $Fe_4(CS)_4(CO)_{11}$ (**11**–**1**) + CO	25.6	25.1
$Fe_4(CS)_4(CO)_{12}$ (**12**–**1**) → $Fe_3(CS)_3(CO)_9$ + $Fe(CS)(CO)_3$	13.4	18.6
$Fe_4(CO)_{16}$ → $Fe_3(CO)_{12}$ + $Fe(CO)_4$	1.5	5.8
$Fe_4(CS)_4(CO)_{11}$ (**11**–**1**) → $Fe_4(CS)_4(CO)_{10}$ (**10**–**1**) + CO	–12.4	–3.0
$Fe_4(CS)_4(CO)_{11}$ (**11**–**1**) → $Fe_3(CS)_3(CO)_7$ + $Fe(CS)(CO)_4$	–30.1	–19.7
$Fe_4(CO)_{15}$ → $Fe(CO)_5$ + $Fe_3(CO)_{10}$	3.3	6.2
$Fe_4(CS)_4(CO)_{11}$ (**11**–**1**) → $Fe_2(CS)_2(CO)_6$ + $Fe_2(CS)_2(CO)_5$	–10.1	0.6
$Fe_4(CO)_{15}$ → $Fe_2(CO)_8$ + $Fe_2(CO)_7$	15.0	17.4
$Fe_4(CS)_4(CO)_{10}$ (**10**–**1**) → $Fe_4(CS)_4(CO)_9$ (**9**–**1**) + CO	17.7	22.0
$Fe_4(CS)_4(CO)_{10}$ (**10**–**1**) → $2Fe_2(CS)_2(CO)_5$	19.6	24.9
$Fe_4(CO)_{14}$ → 2 $Fe_2(CO)_7$	29.6	51.2

Table 2. Energies (ΔE, kcal/mol) for disproportionation of $Fe_4(CS)_4(CO)_n$ (n = 11, 10) into $Fe_4(CS)_4(CO)_{n+1}$ and $Fe_4(CS)_4(CO)_{n-1}$ considering the lowest energy structures and including the energies with zero-point corrections (ΔE_{ZPC}).

	B3LYP		BP86	
	ΔE	ΔE_{ZPC}	ΔE	ΔE_{ZPC}
$2Fe_4(CS)_4(CO)_{11}$ (**11**–**1**) → $Fe_4(CS)_4(CO)_{12}$ (**12**–**1**) + $Fe_4(CS)_4(CO)_{10}$ (**10**–**1**)	–38.0	–38.3	–28.0	–28.3
$2Fe_4(CS)_4(CO)_{10}$ (**10**–**1**) → $Fe_4(CS)_4(CO)_{11}$ (**11**–**1**) + $Fe_4(CS)_4(CO)_9$ (**9**–**1**)	30.1	29.3	25.0	24.2

to be unstable with respect to several criteria. Thus the CO dissociation of $Fe_4(CS)_4(CO)_{11}$ is actually an exothermic process and liberates 12.4(3.0) kcal/mol. Furthermore, the dissociation of $Fe_4(CS)_4(CO)_{11}$ into $Fe_3(CS)_3(CO)_7$ and $Fe(CS)(CO)_4$ is strongly exothermic and liberates 31.0(19.7) kcal/mol. Finally, the disproportionation of $Fe_4(CS)_4(CO)_{11}$ into $Fe_4(CS)_4(CO)_{12}$ and $Fe_4(CS)_4(CO)_{10}$ is also an exothermic process and liberates 38.0(28.0) kcal/mol. The predicted viability of $Fe_4(CS)_4(CO)_{10}$ and instability of $Fe_4(CS)_4(CO)_{11}$ appears to be a consequence of the stability of the central $Fe_4(\eta^2\text{-}\mu_4\text{-CS})(\mu\text{-CS})$ unit found in the low energy structures of $Fe_4(CS)_4(CO)_{10}$. These thermochemical predictions suggest that $Fe_4(CS)_4(CO)_{10}$ might be synthesized by the oligomerization of unsaturated intermediates that arise from the decarbonylation of the known[8] $Fe(CS)(CO)_4$ by photochemical or thermal methods or by oxidation of one of the CO groups with trimethylamine *N*-oxide.

4. Conclusions

Two new structural motifs are found in the tetranuclear iron carbonyl thiocarbonyls $Fe_4(CS)_4(CO)_n$ (n = 12, 11, 10, 9). Such structures are not found in their homoleptic analogues $M_4(CO)_{n+4}$ (M = Fe or Os). Thus the lowest energy $Fe_4(CS)_4(CO)_{12}$ structures have a central Fe_3 triangle with an exotriangular iron atom joined to the Fe_3 triangle through a four-electron donor "end-on" CS bridge. This contrasts with the structure of the known[1,2] $Os_4(CO)_{16}$ and the predicted[11] $Fe_4(CO)_{16}$ structure, which both consist of a central M_4 rhombus with all two-electron donor carbonyl groups.

An even more important new structural motif for the $Fe_4(CS)_4(CO)_n$ derivatives is the irregular Fe_4 "rhombus" (actually a trapezium) bridged by a six-electron donor $\eta^2\text{-}\mu_4$-CS group (Figure 3). This structural unit is found in the lowest energy structures of both $Fe_4(CS)_4(CO)_{10}$ and $Fe_4(CS)_4(CO)_9$. This very energetically favorable structural feature not only makes $Fe_4(CS)_4(CO)_{10}$ viable enough to be a promising synthetic objective but also $Fe_4(CS)_4(CO)_{11}$ thermodynamically unfavorable both with respect to CO dissociation and disproportionation into $Fe_4(CS)_4(CO)_{12}$ and $Fe_4(CS)_4(CO)_{10}$.

Supporting Information (see footnote on the first page of this article): The total energies (E, in Hartree), relative energies (ΔE, in kcal/mol), and numbers of imaginary frequencies (N_{img}) for the optimized $Fe_4(CS)_4(CO)_n$ (n = 12, 11, 10, 9) structures; theoretical harmonic vibrational frequencies for $Fe_4(CS)_4(CO)_{12}$ (seven structures), $Fe_4(CS)_4(CO)_{11}$ (six structures), $Fe_4(CS)_4(CO)_{10}$ (eight structures), and $Fe_4(CS)_4(CO)_9$ (six structures) using the BP86 method; theoretical Cartesian coordinates for $Fe_4(CS)_4(CO)_{12}$ (seven structures), $Fe_4(CS)_4(CO)_{11}$ (six structures), $Fe_4(CS)_4(CO)_{10}$ (eight structures), and $Fe_4(CS)_4(CO)_9$ (six structures) using the B3LYP method; optimized $Fe_4(CS)_4(CO)_n$ (n = 12, 11, 10, 9) structures with both B3LYP and BP86 methods; occupied orbitals of **10**–**1** that involve the six-electron donor CS group; comparison of the valence orbitals of CS and CO; complete reference for Gaussian03 (ref.[40]).

Acknowledgments

We are indebted to the Research Fund for the Doctoral Program of Higher Education (20104407110007), the National Natural Science Foundation of China (NSFC) (20973066), and the U. S. National Science Foundation (NSF) (grant numbers CHE-1054256 and CHE-1057466) for financial support.

[1] V. J. Johnston, F. W. B. Einstein, R. K. Pomeroy, *J. Am. Chem. Soc.* **1987**, *109*, 8111–8812.
[2] F. W. B. Einstein, V. J. Johnston, R. K. Pomeroy, *Organometallics* **1990**, *9*, 2754–2762.
[3] V. J. Johnston, F. W. B. Einstein, R. K. Pomeroy, *J. Am. Chem. Soc.* **1987**, *109*, 7220–7222.
[4] V. J. Johnston, F. W. B. Einstein, R. K. Pomeroy, *Organometallics* **1988**, *7*, 1869–1871.
[5] P. V. Broadhurst, *Polyhedron* **1985**, *4*, 1801–1846.
[6] W. Petz, *Coord. Chem. Rev.* **2008**, *252*, 1689–1733.
[7] B. D. Dombek, R. J. Angelici, *J. Am. Chem. Soc.* **1978**, *95*, 7516–7518.
[8] W. Petz, *J. Organomet. Chem.* **1978**, *146*, C23–C25.
[9] Z. Zhang, Q.-S. Li, Y. Xie, R. B. King, H. F. Schaefer, *Inorg. Chem.* **2009**, *48*, 1974–1988.
[10] Z. Zhang, Q.-S. Li, Y. Xie, R. B. King, H. F. Schaefer, *Inorg. Chem.* **2009**, *48*, 6167–6177.
[11] T. Shi, Q.-S. Li, Y. Xie, R. B. King, H. F. Schaefer, *New J. Chem.* **2010**, *34*, 208–214.
[12] A. W. Ehlers, G. Frenking, *J. Am. Chem. Soc.* **1994**, *116*, 1514–1520.
[13] B. Delley, M. Wrinn, H. P. Lüthi, *J. Chem. Phys.* **1994**, *100*, 5785–5790.
[14] J. Li, G. Schreckenbach, T. Ziegler, *J. Am. Chem. Soc.* **1995**, *117*, 486–494.
[15] V. Jonas, W. Thiel, *J. Chem. Phys.* **1995**, *102*, 8474–8484.
[16] T. A. Barckholtz, B. E. Bursten, *J. Am. Chem. Soc.* **1998**, *120*, 1926–1927.
[17] E. D. Jemmis, K. T. Giju, *J. Am. Chem. Soc.* **1998**, *120*, 6952–5964.
[18] S. Niu, M. B. Hall, *Chem. Rev.* **2000**, *100*, 353–406.
[19] F. A. Cotton, N. E. Gruhn, J. Gu, P. Huang, D. L. Lichtenberger, C. A. Murillo, L. O. Van Dorn, C. C. Wilkinson, *Science* **2002**, *298*, 1971–1973.
[20] P. Macchi, A. Sironi, *Coord. Chem. Rev.* **2003**, *238*, 383–412.
[21] P. E. M. Siegbahn, *J. Am. Chem. Soc.* **2005**, *127*, 17303–17314.
[22] T. Ziegler, J. Autschbach, *Chem. Rev.* **2005**, *105*, 2695–2722.
[23] A. J. Mota, A. Dedieu, C. Bour, J. Suffert, *J. Am. Chem. Soc.* **2005**, *127*, 7171–7182.
[24] M. Bühl, H. Kabrede, *J. Chem. Theory Comput.* **2006**, *2*, 1282–1290.
[25] M. Brynda, L. Gagliardi, P. O. Widmark, P. P. Power, B. O. Roos, *Angew. Chem.* **2006**, *118*, 3888; *Angew. Chem. Int. Ed.* **2006**, *45*, 3804–3807.
[26] Y. Zhao, D. G. Truhlar, *J. Chem. Phys.* **2006**, *124*, 224105–224110.
[27] N. S. Strickland, J. N. Harvey, *J. Phys. Chem. B* **2007**, *111*, 841–852.
[28] A. D. Becke, *J. Chem. Phys.* **1993**, *98*, 5648–5652.
[29] C. Lee, W. Yang, R. G. Parr, *Phys. Rev. B* **1988**, *37*, 785–789.
[30] A. D. Becke, *Phys. Rev. A* **1988**, *38*, 3098–3100.
[31] J. P. Perdew, *Phys. Rev. B* **1986**, *33*, 8822–8824.
[32] See especially F. Furche, J. P. Perdew, *J. Chem. Phys.* **2006**, *124*, 044103–044110.
[33] H. Wang, Y. Xie, R. B. King, H. F. Schaefer, *J. Am. Chem. Soc.* **2005**, *127*, 11646–11651.
[34] H. Wang, Y. Xie, R. B. King, H. F. Schaefer, *J. Am. Chem. Soc.* **2006**, *128*, 11376–11384.
[35] T. H. Dunning, *J. Chem. Phys.* **1970**, *53*, 2823–2833.

[36] T. H. Dunning, P. J. Hay, *Methods of Electronic Structure Theory* (Ed.: H. F. Schaefer), Plenum, New York, **1977**, pp. 1–27.
[37] S. Huzinaga, *J. Chem. Phys.* **1965**, *42*, 1293–1032.
[38] A. J. H. Wachters, *J. Chem. Phys.* **1970**, *52*, 1033–1036.
[39] D. M. Hood, R. M. Pitzer, H. F. Schaefer, *J. Chem. Phys.* **1979**, *71*, 705–712.
[40] M. J. Frisch et al. (see Supporting Information for full details), *Gaussian 03*, rev. C 02, Gaussian, Inc., Wallingford CT, **2004**
[41] B. N. Papas, H. F. Schaefer, *J. Mol. Struct.* **2006**, *768*, 175–181.
[42] H. Jacobsen, T. Ziegler, *J. Am. Chem. Soc.* **1996**, *118*, 4631–4635.
[43] J. M. L. Martin, C. W. Bauschlicher, A. Ricca, *J. Comp. Physiol.* **2001**, *133*, 189–201.
[44] P. V. Broadhurst, B. F. G. Johnson, J. Lewis, P. R. Raithby, *J. Am. Chem. Soc.* **1981**, *103*, 3198–3200.
[45] L. S. Sunderlin, D. Wang, R. R. Squires, *J. Am. Chem. Soc.* **1993**, *115*, 12060–12070.

Received: September 6, 2011
Published Online: January 17, 2012

DOI: 10.1002/ejic.201101191

Ferrocenyl Maleimides – Synthesis, (Spectro-)Electrochemistry, and Solvatochromism

Alexander Hildebrandt,[a] Steve W. Lehrich,[a] Dieter Schaarschmidt,[a] Romy Jaeschke,[b] Katja Schreiter,[b] Stefan Spange,[b] and Heinrich Lang*[a]

Keywords: Iron / Sandwich complexes / Maleimide / Electrochemistry / Solvatochromism

Ferrocenylmaleimides have been synthesized from 2,5-dibromo-*N*-methyl-1*H*-pyrrole. Bromine shift and oxidation of the pyrrole core with subsequent ferrocenylation using the Negishi C–C cross-coupling protocol led to the formation of 3-ferrocenyl-*N*-methylmaleimide (**3**), 3-bromo-4-ferrocenyl-*N*-methylmaleimide (**4**), and 3,4-diferrocenyl-*N*-methylmaleimide (**5**). The structural properties of **4** and **5** were investigated by single-crystal X-ray diffraction. Cyclic and square-wave voltammetry, in situ UV/Vis/NIR and IR spectroelectrochemistry (**5**) highlight the electrochemical properties of these compounds. Compounds **3** and **4** exhibit one reversible ferrocenyl-based redox event, whereas **5** shows two separate electrochemically reversible one-electron transfer processes with remarkably high $\Delta E^{\circ\prime}$ values and reduction potentials of $E_1^{\circ\prime}$ = 50 and $E_2^{\circ\prime}$ = 380 mV ($\Delta E^{\circ\prime}$ = 330 mV), respectively, with $[NBu_4][B(C_6F_5)_4]$ as the supporting electrolyte. The NIR measurements confirm the electronic communication between the iron centers (Fe^{II}/Fe^{III}) as intervalence charge transfer absorptions were observed in $\mathbf{5}^{+}$. Compound **5** was classified as a weakly coupled class II system, according to Robin and Day. UV/Vis investigations of the solvatochromic behavior of **3**–**5** revealed the complex solvation of these push–pull systems, which reflects that three important solvent properties (hydrogen bond formation ability, polarizability, and solvation of the carbonyl group and the C=C bond) affect $\tilde{\nu}_{max}$.

Introduction

Ferrocenyl-substituted polyenes have attracted increasing attention because they can be regarded as model compounds for the investigation of electron transfer through the polyene "wire" motif.[1] Moreover, these π-conjugated organometallics offer the possibility to form mixed-valent multiferrocenyl compounds, which may be suitable for the design of new electroactive materials.[2] The toolbox of spectroelectrochemical methods enables the investigation of these properties and especially demonstrates how structural changes may influence the optical characteristics of such molecules.[3] To date, the electron-transfer characteristics of many diferrocenylethylenes that bear electron-donating functionalities have been studied,[1] whereas only a few examples exist that have electron-withdrawing groups attached to the C=C bond. In this respect, we present the synthesis and electrochemical properties of 3-ferrocenyl-*N*-methylmaleimide (**3**), 3-bromo-4-ferrocenyl-*N*-methylmaleimide (**4**), and 3,4-diferrocenyl-*N*-methylmaleimide (**5**). The maleimide functionality acts as the electron-withdrawing group and a rigid element to stabilize the *Z* conformation of the ferrocenyl unit. Independently, Nemykin et al.[4] have reported the synthesis of a similar molecule using a different synthetic strategy. They reacted dimethyl (*Z*)-2,3-bis(ferrocenyl)-2-butenedioate with $NaNH_2$ in liquid ammonia to form a ferrocenyl-substituted maleimide. We report an alternative, straightforward route to ferrocenylmaleimides, which offers an excellent tolerance towards functional substituents.

[a] Technische Universität Chemnitz, Fakultät für Naturwissenschaften, Institut für Chemie, Lehrstuhl für Anorganische Chemie,
Straße der Nationen 62, 09111 Chemnitz, Germany
Fax: +49-371-531-21219
E-mail: heinrich.lang@chemie.tu-chemnitz.de
[b] Technische Universität Chemnitz, Fakultät für Naturwissenschaften, Institut für Chemie, Lehrstuhl für Polymerchemie,
Straße der Nationen 62, 09111 Chemnitz, Germany

Results and Discussion

Synthesis and Characterization

The reaction of 2,5-dibromo-*N*-methyl-1*H*-pyrrole (**1**) with nitric acid in acetic acid led to the formation of 3-bromo-*N*-methylmaleimide (**2a**) and 3,4-dibromo-*N*-methylmaleimide (**2b**) (Scheme 1). The mechanism of this bromine shift and subsequent oxidation of the pyrrolic ring has been described.[5] Negishi ferrocenylation of **2a** and **2b** with ferrocenylzinc chloride, accessible by monolithiation of ferrocene[6] followed by treatment with zinc chloride in the presence of catalytic amounts of tetrakis(triphenylphosphane)palladium(0), led to the formation of **3**–**5** (Scheme 1).

Compounds **3**–**5** are stable towards air and moisture in the solid state and solution. They have been identified by elemental analysis and IR, UV/Vis, and NMR (^{1}H,

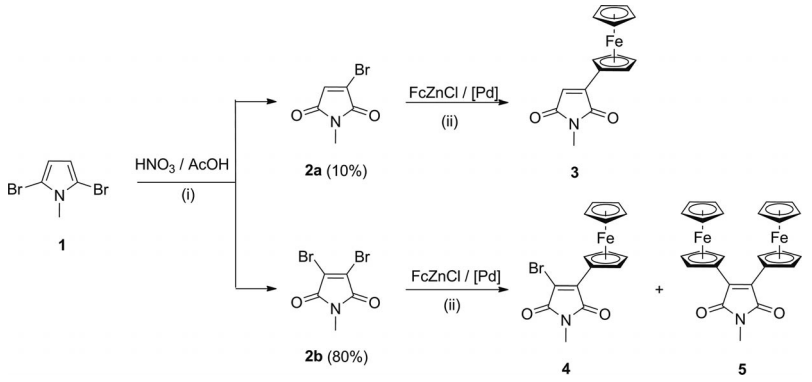

Scheme 1. Synthesis of **3**–**5**. (i) 25 °C, 2 h; (ii) tetrahydrofuran, 60 °C, 48 h, [Pd] = $Pd(PPh_3)_4$.

$^{13}C\{^1H\}$) spectroscopy. HRMS and single-crystal X-ray structure analysis (**4** and **5**) were also carried out. The electrochemical behavior of all of the compounds [cyclic voltammetry (CV), square-wave voltammetry (SWV)] was studied. The spectroelectrochemical characteristics (in situ UV/Vis/NIR and IR spectroscopy) of **5** were determined.

In the ^1H NMR spectra of **3**–**5**, one singlet for the ferrocenyl C_5H_5 units and two pseudotriplets with J_{HH} = 1.8 Hz (C_5H_4), which is typical for AA′XX′ spin systems, were found. The nitrogen-bonded methyl group was observed at 3.06 ppm (**3**) or 3.11 ppm (**4** and **5**). Maleimide **3** additionally exhibits a characteristic singlet at 6.37 ppm for the proton at the C=C bond. The carbonyl carbon atoms were found in the $^{13}C\{^1H\}$ NMR spectra at characteristic chemical shifts. Asymmetric **3** and **4** exhibit two signals for the carbonyl functionality at 170.3/171.5 ppm (**3**) and 166.5/168.6 ppm (**4**), whereas symmetric **5** shows a single resonance at 170.6 ppm. Despite the asymmetry in **3** and **4**, only one carbonyl stretching vibration was found in the IR spectra of all of the compounds at 1701 (**3**), 1706 (**4**), and 1701 cm^{-1} (**5**).

Single crystals of **4** and **5** suitable for X-ray diffraction analysis were obtained by the diffusion of hexane into a chloroform solution of **4** or **5** at ambient temperature. The molecular structures of **4** and **5** in the solid state are shown in Figures 1 and 2, respectively. Important bond lengths, bond angles, and torsion angels are summarized in the figure captions. The crystal and structure refinement data can be found in the Experimental Section.

Compound **4** crystallizes in the monoclinic space group $P2_1/c$. The ferrocenyl substituent is rotated by 9.8(1)° out of the plane of the maleimide core. The cyclopentadienyl ligands at the iron center exhibit an eclipsed conformation [–6.2(2)°]. The ^cC_4N arrangement is planar [root mean square (r.m.s.) deviation: 0.0166 Å, highest deviation from planarity observed for N1: –0.0237(16) Å].

Compound **5** crystallizes in the monoclinic space group $P2_1/c$ as dark violet needles. The ferrocenyl groups are oriented on different sites of the maleimide core and are rotated by 32.9(2) (Fe1) and 27.2(2)° (Fe2) out of the plane of the C_4N arrangement, which is a significantly larger distortion than that observed for **4**. This twist of the ferrocenyl units is most probably caused by the steric strain of these

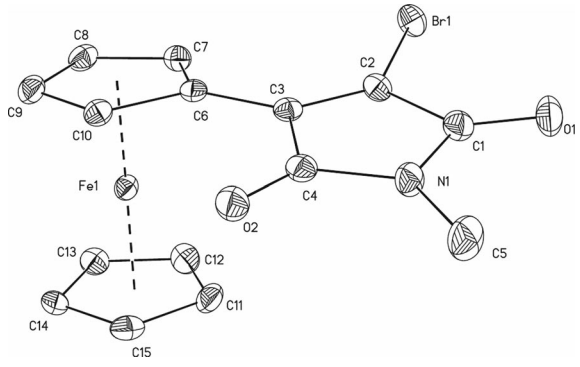

Figure 1. ORTEP diagram (50% probability level) of **4**. Selected bond lengths [Å] and angles [°]: D1–Fe1 1.6511(3), D2–Fe1 1.6412(3), N1–C1 1.388(3), N1–C4 1.383(3), N1–C5 1.451(3), C1–C2 1.486(3), C1–O1 1.212(3), C4–O2 1.209(3), C4–C3 1.516(3), C2–C3 1.337(3), C2–Br1 1.865(2), C3–C6 1.448(3), C5–N1–C1 125.0(2), N1–C4–O2 124.3(2), C3–C2–Br1 130.9(2), (D1 denotes the centroid of C_5H_5 at Fe1; D2 denotes the centroid of C_5H_4 at Fe1).

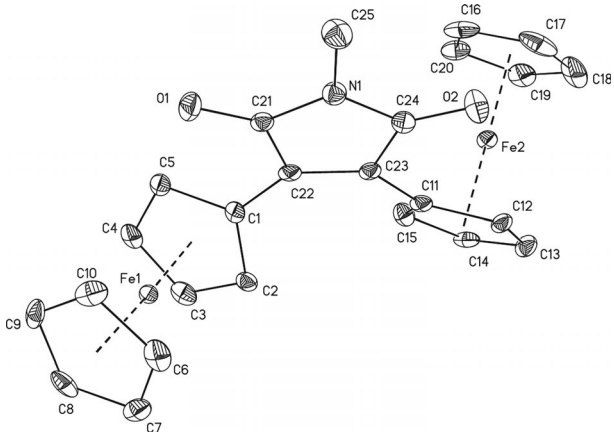

Figure 2. ORTEP diagram (50% probability level) of **5**. Selected bond lengths [Å] and angles [°]: D1–Fe1 1.6614(4), D2–Fe1 1.6506(4), D3–Fe2 1.6458(5), D4–Fe2 1.6412(5), N1–C21 1.379(4), N1–C24 1.381(4), N1–C25 1.452(4), C21–C22 1.508(4), C21–O1 1.217(4), C24–O2 1.212(4), C24–C23 1.510(4), C22–C23 1.353(4), C22–C1 1.454(4), C23–C11 1.456(4), C21–N1–C24 110.8(3), C22–C21–O1 128.8(3), C23–C24–O2 128.7(3), (D1 denotes the centroid of C_5H_5 at Fe1; D2 denotes the centroid of C_5H_4 at Fe1; D3 denotes the centroid of C_5H_5 at Fe2; D4 denotes the centroid of C_5H_4 at Fe2).

bulky units. The cyclopentadienyl ligands at the iron centers show an almost staggered conformation [–27.9(3)°] for Fe1 and an almost eclipsed conformation [–9.5(3)°] for Fe2. As expected, the $^{\alpha}C_4N$ core is planar (r.m.s. deviation: 0.0101 Å, highest deviation from planarity observed for C22: –0.0142(18) Å]. The bond distances and angles are comparable to those found in other ferrocenyl-substituted heterocycles.[3]

Electrochemistry and Spectroelectrochemistry

The redox characteristics of **3**–**5** were studied by CV, SWV (Table 1, Figure 3), UV/Vis/NIR spectroscopy (see Figures 4 and 5), and in situ spectroelectro-IR measurements (Figure 6). As the supporting electrolyte, 0.1 mol L^{-1} dichloromethane solutions of $[NBu_4][B(C_6F_5)_4]$ were used.[7] The CV studies were carried out at a scan rate of 100 mV s^{-1} and are summarized in Table 1. All potentials are referenced to the FcH/FcH^+ redox couple ($E^{\circ\prime}$ = 0.0 mV).[8]

Table 1. CV data (potentials vs. FcH/FcH^+), scan rate 100 mV s^{-1} at a glassy-carbon electrode of 0.5 mmol L^{-1} solutions of **3**–**5** in dry dichloromethane with 0.1 mol L^{-1} of $[NBu_4][B(C_6F_5)_4]$ as the supporting electrolyte at 25 °C.[a]

	$E^{\circ\prime}$ [mV]	ΔE_p [mV]	$\Delta E^{\circ\prime}$ [mV]
3	225	72	–
4	250	72	–
5	50	72	330
	380	73	330

[a] $E^{\circ\prime}$ = reduction potential of the ferrocenyl based redox events; ΔE_p = difference between cathodic and anodic peak potentials; $\Delta E^{\circ\prime}$ = difference between the first and second redox potential.

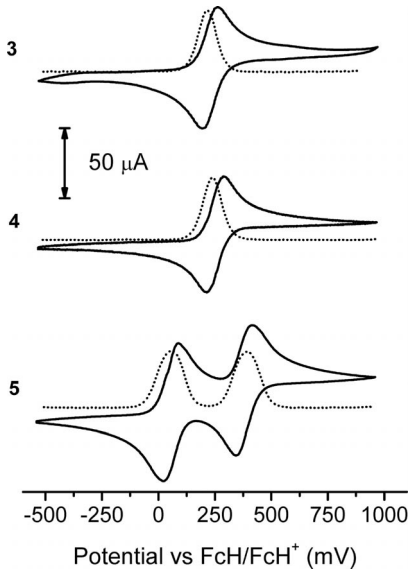

Figure 3. CVs (solid line) and SWVs (dotted line) of **3** (top), **4** (middle), and **5** (bottom); scan rate: 100 mV, dichloromethane, analyte concentration: 1.0 mmol L^{-1}, 25 °C, supporting electrolyte: $[NBu_4][B(C_6F_5)_4]$ (0.1 mol L^{-1}).

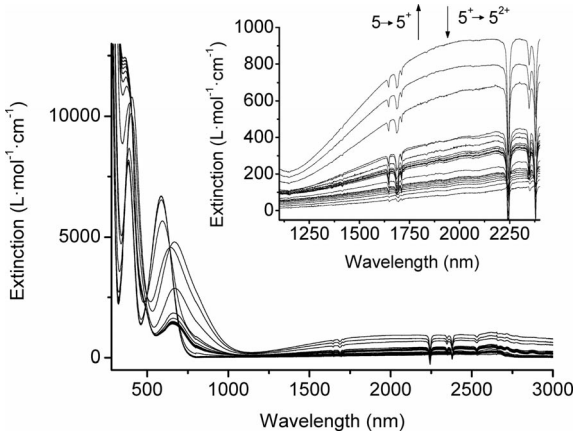

Figure 4. UV/Vis/NIR spectra of **5** at rising potentials (–200 to 1000 mV vs. Ag/AgCl) at 25 °C, in dichloromethane, supporting electrolyte 0.1 mol L^{-1} $[NBu_4][B(C_6F_5)_4]$. Arrows indicate an increase or decrease of absorptions.

Compounds **3** and **4** showed a reversible ferrocenyl-based redox process with ΔE_p values of 72 mV. The bromine atom in **4**, as an electron-withdrawing group, causes a shift of the ferrocenyl redox potential from 225 (**3**) to 250 mV (**4**). Due to the decreased electron density at the iron atom, it is more difficult to oxidize the ferrocenyl moiety. The two ferrocenyl groups in **5** could be oxidized separately. The first oxidation occurs at 50 mV (ΔE_p = 72 mV), which is significantly easier to oxidize than that of **3** and **4**. The redox event of the second ferrocenyl termini was observed at $E^{\circ\prime}$ = 380 mV (ΔE_p = 73 mV). Hence, a redox splitting of $\Delta E^{\circ\prime}$ = 330 mV was achieved for the ferrocenyl related processes in **5**, which indicates considerable interactions between the ferrocenyl moieties (Table 1 and Figure 3). Due to the short distance between the ferrocenyl units, the $\Delta E^{\circ\prime}$ values are influenced to some extent by electrostatic interactions between the individual ferrocenyl termini.

The spectroelectrochemical studies were conducted by the stepwise increase of the potential from –200 to 1000 mV vs. Ag/AgCl in an optically transparent thin-layer electrochemical (OTTLE) cell, which contained dichloromethane solutions of **5** (1.0 mmol L^{-1}) and $[NBu_4][B(C_6F_5)_4]$ (0.1 mol L^{-1}) as the supporting electrolyte. The potential increase was performed using varying step heights of 25, 50, and 100 mV. This procedure allowed the in situ generation of $\mathbf{5}^+$ and $\mathbf{5}^{2+}$.

Homovalent **5** does not show any absorption between 1000 and 3000 nm. However, upon increasing the potential, mixed-valent $\mathbf{5}^+$ was formed and a broad, weak absorption was detected in the NIR region. In the UV/Vis part of the spectrum, a narrow absorption band at 585 nm was shifted to 670 nm during the first oxidation process. The band at ca. 2000 nm indicates electron transfer between the two ferrocenyl termini, which are characteristic of intervalence charge transfer (IVCT) excitations.[9,10] Determination of the physical parameters [wavenumber (ν_{max}), extinction coefficient (ε_{max}), full-width-at-half-maximum (FWHM) ($\Delta\nu_{1/2}$)] was achieved by deconvolution of the NIR data

using three Gaussian-shaped overlapping absorptions (Figure 5). The sum of these spectral components closely matches the measured spectra. Two of the three Gaussians seem to contribute to the transition and one was used for background correction. The small and narrow (ε_{max} = 310 L mol^{-1} cm^{-1}, $\Delta\nu_{1/2}$ = 750 cm^{-1}) absorption at 3650 cm^{-1} was assigned to a ligand-to-metal charge transfer (LMCT) excitation, whereas the more intense band showed characteristics of an IVCT absorption (ε_{max} = 750 L mol^{-1} cm^{-1}, $\Delta\nu_{1/2}$ = 3350 cm^{-1}, ν_{max} = 4900 cm^{-1}). According to Hush, the FWHM was calculated using Equation (1).[10,11] The classification criteria of Brunschwig, Creutz, and Sutin[12] derived from the theoretical and experimental $\Delta\nu_{1/2}$ values [Equation (2)] confirms **5** as a weakly coupled class II system (Γ = 0.004).

$$(\Delta\nu_{1/2})_{theo} = (2310\nu_{max})^{1/2} \quad (1)$$

$$\Gamma = 1 - [(\Delta\nu_{1/2})/(\Delta\nu_{1/2})_{theo}] \quad (2)$$

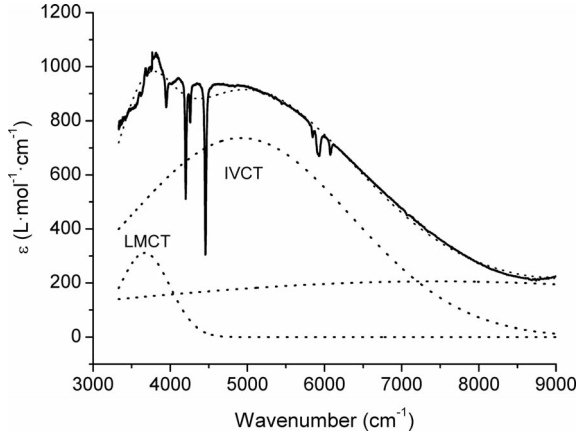

Figure 5. Deconvolution of the NIR absorptions of **5**$^{+}$ using three Gaussian-shaped bands determined by spectroelectrochemistry in an OTTLE cell.

Figure 6 shows the results of in situ spectroelectro-IR measurements. The ν_{CO} band of the carbonyl functionalities in **5** shifted from 1701 cm^{-1} in its neutral form to 1716 cm^{-1} in **5**$^{2+}$. Monocationic **5**$^{+}$ shows two bands at 1706 and 1716 cm^{-1}. The appearance of these two absorptions indicates asymmetry within **5**$^{+}$ as expected for the valence-trapped mixed-valent species. Nevertheless, the fact that the first band is slightly shifted from 1701 to 1706 cm^{-1} accounts for some charge delocalization within the system as the oxidation affects both carbonyl functionalities at the same time.

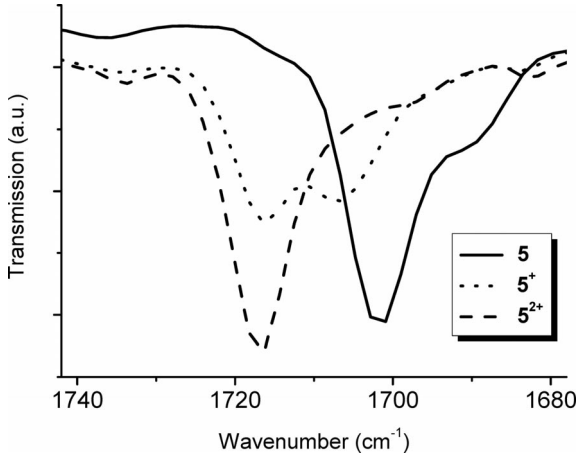

Figure 6. IR spectra of **5** (carbonyl stretching vibration) at rising potentials (–200 to 1000 mV vs. Ag/AgCl); 25 °C, in dichloromethane, supporting electrolyte 0.1 mol L^{-1} [NBu$_4$][B(C$_6$F$_5$)$_4$].

Solvatochromism

UV/Vis spectra of **3**–**5** were measured in 39 common solvents of different polarity and hydrogen bonding ability (Table 2 and Figure 7). The concentration of **3**–**5** was ca. 10^{-5} mol L^{-1}. $\tilde{\nu}_{max}$ shows no dependence on the concentration of **3**–**5**, which is an indication that it is not affected by the aggregation behavior of the compounds.

Table 2. UV/Vis absorption maxima [cm^{-1}] of **3**–**5** in 39 solvents.

Solvent	10^{-3} $\tilde{\nu}_{max}$		
	3	**4**	**5**
N,*N*-Dimethylformamide	18.08	18.08	17.27
Dimethyl sulfoxide	18.05	17.98	16.97
Tetramethylurea	18.12	18.08	[a]
Tetrahydrofuran	18.25	18.28	17.33
Diethyl ether	18.42	18.38	17.45
1,1,1,3,3,3-Hexafluoro-2-propanol	16.23	16.28	15.69
Acetone	18.18	18.21	17.42
1-Propanol	17.83	17.79	16.95
2-Propanol	17.76	17.79	17.09
Ethanol	17.86	17.86	17.06
Methanol	17.83	17.83	17.09
Pyridine	17.92	17.92	17.09
Dichloromethane	17.83	17.83	17.06
Ethyl acetate	18.32	18.32	17.45
Toluene	18.18	18.18	17.15
p-Xylene	18.25	18.28	17.24
2,2,2-Trifluoroethanol	16.95	16.92	16.21
1-Butanol	17.83	17.79	17.12
Tetrachloromethane	18.18	18.21	17.12
Acetonitrile	18.15	18.12	17.33
Anisole	17.99	17.99	17.09
Benzene	18.12	18.08	17.12
4-Butyrolactone	18.02	17.99	17.21
Ethane-1,2-diol	[a]	17.67	[a]
1,2-Dichloroethane	17.95	17.92	17.12
Nitromethane	17.95	17.95	16.61
Triethylamine	18.48	18.48	17.48
Formamide	[a]	17.48	[a]
1,1,2,2-Tetrachloroethane	17.57	17.57	16.78
Chloroform	17.64	17.67	16.89
1-Decanol	17.95	17.92	17.12
1,4-Dioxane	18.32	18.32	17.33
1,2-Dimethoxyethane	18.21	18.28	17.30
N,*N*-Dimethylacetamide	18.05	18.02	17.24
Hexamethylphosphoramide	18.08	17.99	17.24
Benzonitrile	17.92	17.92	17.12
Water	[a]	[a]	[a]
Cyclohexane	18.55	18.52	17.48
Hexane	18.69	18.66	17.51
$\Delta\tilde{\nu}$ [cm^{-1}]	2460	2380	1820

[a] Analyte is insoluble.

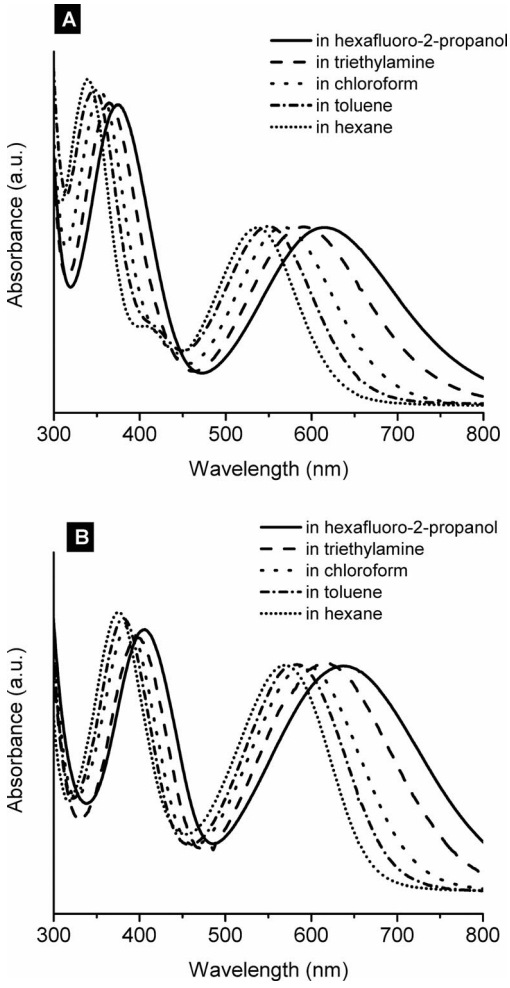

Figure 7. UV/Vis absorption spectra of **4** (A, top) and **5** (B, bottom) measured in five solvents.

Maleimides **3**–**5** show the largest bathochromic shift λ_{max} in 1,1,1,3,3,3-hexafluoro-2-propanol with λ_{max} = 616 (**3**), 614 (**4**), and 637 nm (**5**). The shortest λ_{max} was measured in hexane [λ_{max} = 535 (**3**), 536 (**4**), 571 nm (**5**)]. Thus, **3**–**5** show positive solvatochromism with a solvatochromic range ($\Delta\tilde{\nu}_{max}$ = $\tilde{\nu}_{max,largest\ hypsochromic\ shift}$ − $\tilde{\nu}_{max,largest\ bathochromic\ shift}$) of $\Delta\tilde{\nu}_{max}$ = 2460 (**3**), 2380 (**4**), and 1820 cm^{-1} (**5**), which is a mediocre solvatochromic range. The weakly accepting maleimide substituent causes the ferrocenyl substituents to be push substituents, which is sufficient to induce solvatochromic properties. Compound **5** shows a smaller solvatochromic shift, which can be explained by the cross-conjugation of the whole electron system due to the two ferrocenyl substituents disturbing each other, whereas the effect of the bromine substituent on solvatochromism is of less importance.

To show the effect of the different solvent properties on $\tilde{\nu}_{max}$, the Kamlet–Taft correlation analyses was used.[13] The Kamlet–Taft equation [Equation (3)], in its simple form, is:

$$\tilde{\nu}_{max} = (\tilde{\nu}_{max})_0 + a\alpha + b\beta + s\pi^* \quad (3)$$

where $\tilde{\nu}_{max}$ is the result of a solvent-dependent process, $(\tilde{\nu}_{max})_0$ is a reference system, for example, the gas phase or a nonpolar solvent, α describes the hydrogen bond donating ability (HBD), β describes the hydrogen bond basicity, and π^* the dipolarity/polarizability of the solvent; a, b, and s are the solvent-independent correlation coefficients, which reflect predictions of the influence of the respective parameters on the result of the chemical process.

The results of the square correlation analysis using the data from Table 2 and the Kamlet–Taft solvent parameters from the literature[13] are shown in Table 3.

Table 3. Solvent-independent correlation coefficients a, b, and s of Kamlet–Taft parameters α, β, and π^*, respectively, solute property of reference system $(\tilde{\nu}_{max})_0$, correlation coefficient (R), significance (F), standard deviation (SD), and number of solvents (n) calculated for the solvatochromism of **3**–**5**.

	3	**4**	**5**
$(\tilde{\nu}_{max})_0$	18.517 (±0.067)	18.497 (±0.067)	17.434 (±0.067)
a	–0.748 (±0.050)	–0.707 (±0.049)	–0.574 (±0.050)
b	0.359 (±0.075)	0.327 (±0.077)	0.452 (±0.076)
s	–0.788 (±0.094)	–0.746 (±0.092)	–0.591 (±0.094)
n	36	38	35
R	0.950	0.945	0.927
F	< 0.0001	< 0.0001	< 0.0001
SD	0.140	0.144	0.140

The solvatochromic properties of **3**–**5** are very similar. There is no significant difference in their solvatochromic properties with respect to a, b, and s of Equation (3). With the increase of the dipolarity/polarizability of the solvent, a bathochromic shift occurs, which is documented by the negative sign of s. A similar effect influences the HBD ability of the solvent: due to the solvation of the carbonyl oxygen atom by HBD solvents the push–pull character is enhanced. This effect is of the same order of magnitude as the influence of the dipolarity/polarizability.

The positive sign of b is surprising due to the absence of classical HBD groups in **3**–**5**. In addition to the HBA ability of the solvent, the electron pair donating ability (EPD) also has to be taken into account. In this way interactions with Lewis acidic centers in **3**–**5** can occur, which have a disturbing effect on the π-electron system and result in a positive value of b. However, a complex solvation of **3**–**5** occurs, which reflects that three important solvent properties (hydrogen bond formation ability, polarizability, and solvation of the carbonyl group and the C=C bond) affect $\tilde{\nu}_{max}$.

Conclusions

3-Ferrocenyl-*N*-methylmaleimide (**3**), 3-bromo-4-ferrocenyl-*N*-methylmaleimide (**4**), and 3,4-diferrocenyl-*N*-methylmaleimide (**5**) have been prepared by a straightforward synthetic methodology, which includes a bromine shift, the oxidation of dibromo-*N*-methylpyrrole, and Negishi C–C cross-coupling. The molecular structures of **4** and **5** in the

solid state have been determined by single crystal X-ray structure analysis. Electrochemical (CV and SWV) and spectroelectrochemical (in situ UV/Vis/NIR and IR) measurements highlight the redox and electron-transfer properties of these new organometallics. Compounds **3** and **4** show one reversible redox process for the ferrocenyl moiety, which is slightly shifted from 225 (**3**) to 250 mV (**4**) caused by the electron-withdrawing character of the bromine substituent. Diferrocenylmaleimide **5** exhibits two well-resolved ferrocenyl-based redox events at $E^{\circ}_1{}' = 50$ and $E^{\circ}_2{}' = 380$ mV ($\Delta E^{\circ\prime} = 330$ mV). The relatively high $\Delta E^{\circ\prime}$ value indicates some electronic communication between the ferrocenyl termini. This assumption was verified by the observation of an IVCT absorption in the UV/Vis/NIR spectroscopic measurements. Band-shape analysis of the IVCT excitation allows the classification of **5** as a weakly coupled class II system according to Robin and Day[14] using the criteria of Brunschwig, Creutz, and Sutin.[12] In situ IR spectroscopic studies also indicated some electron delocalization. UV/Vis spectroscopic investigations of the solvatochromic behavior of **3**–**5** revealed the complex solvation of these push–pull systems, which reflects that three important solvent properties (hydrogen bond formation ability, polarizability, and solvation of the carbonyl group and the C=C bond) affect $\tilde{\nu}_{max}$.

Experimental Section

General Conditions: All reactions were carried out under an atmosphere of nitrogen using standard Schlenk techniques. Tetrahydrofuran (THF), toluene, hexane, and pentane were purified by distillation from sodium/benzophenone ketyl; dichloromethane was purified by distillation from calcium hydride.

Instrumentation: IR spectra were recorded with a FT-Nicolet IR 200 instrument. ^{1}H NMR spectra were recorded with a Bruker Avance III 500 spectrometer operating at 500.303 MHz in the Fourier transform mode, and $^{13}C\{^1H\}$ NMR spectra were recorded at 125.800 MHz. Chemical shifts are reported in ppm downfield from tetramethylsilane with the solvent as a reference signal (^{1}H NMR: $\delta(CHCl_3) = 7.26$ ppm; $^{13}C\{^1H\}$ NMR: $\delta(CDCl_3) = 77.00$ ppm). UV/Vis spectra between 210 and 1010 nm were recorded with a Carl Zeiss MCS 400 spectrometer utilizing CLD 300 (210–600 nm) and CLX 11 lamps (300–1010 nm). The melting points of analytically pure samples (sealed in nitrogen-purged capillaries) were determined with a Gallenkamp MFB 595 010 M melting point apparatus. Microanalyses were performed with a Thermo FLASHEA 1112 Series instrument. Spectroelectrochemical measurements were carried out in an OTTLE cell similar to that described previously[15] in dichloromethane solutions that contained 0.1 mol L^{-1} of $[NBu_4][B(C_6F_5)_4]$ as the supporting electrolyte with a Varian Cary spectrometer. HRMS were recorded with a micrOTOF QII Bruker Daltonite workstation.

X-ray Diffraction: Data were collected with an Oxford Gemini S diffractometer at 110 K using Mo-K_α ($\lambda = 0.71073$ Å) radiation. The structures were solved by direct methods and refined by full-matrix least square procedures on F^2.[17] All non-hydrogen atoms were refined anisotropically and a riding model was employed in the refinement of the hydrogen atom positions.

Electrochemistry: Measurements of 1.0 mmol L^{-1} solutions of **3**–**5** in dry, air-free dichloromethane that contained 0.1 mol L^{-1} of $[NBu_4][B(C_6F_5)_4]$ as the supporting electrolyte were conducted under a blanket of purified argon at 25 °C utilizing a Radiometer Voltalap PGZ 100 electrochemical workstation interfaced with a personal computer. A three-electrode cell, which utilized a Pt auxiliary electrode, a glassy carbon working electrode (surface area 0.031 cm^2), and an Ag/Ag$^+$ (0.01 mol L^{-1} $[AgNO_3]$) reference electrode mounted on a Luggin capillary, was used. The working electrode was pretreated by polishing on a Buehler microcloth first with 1 micron and then $^1/_4$ micron diamond paste. The reference electrode was constructed from a silver wire inserted into a solution of 0.01 mol L^{-1} $[AgNO_3]$ and 0.1 mol L^{-1} of $[NBu_4][B(C_6F_5)_4]$ in acetonitrile in a Luggin capillary with a Vycor tip. This Luggin capillary was inserted into a second Luggin capillary with a Vycor tip filled with a 0.1 mol L^{-1} $[NBu_4][B(C_6F_5)_4]$ solution in dichloromethane. Successive experiments under the same experimental conditions showed that all formal reduction and oxidation potentials were reproducible within 5 mV. Experimental potentials were referenced against an Ag/Ag$^+$ reference electrode but results are presented referenced against ferrocene as an internal standard as required by IUPAC.[8] To achieve this, as the ferrocene couple interferes with the ferrocenyl signals of **3**–**5**, each experiment was first performed in the absence of any internal standard and then repeated in the presence of 1 mmol L^{-1} of ferrocene. The data were then manipulated in a Microsoft Excel worksheet to set the formal reduction potentials of the FcH/FcH$^+$ couple to 0.0 V. Under these conditions, the FcH/FcH$^+$ couple was at 220 mV vs. Ag/Ag$^+$, ΔE_p = 61 mV.[16]

Reagents: 2,5-Dibromo-1-methyl-1*H*-pyrrole,[18] $[NBu_4][B(C_6F_5)_4]$,[19] 3-bromo-*N*-methylmaleimide,[5] and 3,4-dibromomaleimide[5] were prepared according to published procedures. All other chemicals were purchased from commercial suppliers and were used as received.

Synthesis of Ferrocenylmaleimides 3–5: To ferrocene (380 mg, 2.0 mmol) and KO*t*Bu (22 mg, 0.2 mmol) in THF (20 mL) was added *tert*-butyllithium (2.0 mL, 3.2 mmol, 1.6 M) in pentane dropwise at –30 °C. After 1 h of stirring at this temperature, dry $[ZnCl_2{\cdot}2thf]$ (1.25 g, 4.8 mmol) was added in a single portion. The solution was kept for 1 h at –30 °C and an additional hour at 25 °C before **2a** (308 mg, 1.64 mmol) or **2b** (220 mg, 0.82 mmol) and $[Pd(PPh_3)_4]$ (12 mg, 0.01 mmol, 0.5 mol-% based on ferrocene) of were added in a single portion, and the reaction solution was stirred for 48 h at 60 °C. After evaporation of all volatiles, the precipitate was dissolved in dichloromethane (200 mL) and washed with water (3 × 100 mL). The organic phase was dried with $MgSO_4$ and the solvent was removed in vacuo. The remaining solid was purified by column chromatography on silica gel using hexane/toluene (2:1, v/v) as eluent to separate unreacted ferrocene and minor byproducts before the eluent was changed to dichloromethane/hexane (3:1, v/v). The reaction of **2a** gave **3** (368 mg, 1.24 mmol, 76% based on **2a**) after removing all volatiles as a dark purple solid. The use of **2b** as reactant led to two fractions by column chromatography. Fraction one afforded **4** (86 mg, 0.23 mmol, 28% based on **2b**) as a dark purple solid, and the second fraction gave dark blue **5** (211 mg, 0.44 mmol, 54% based on **2b**) as solid material.

3-Ferrocenyl-*N*-methylmaleimide (3): $C_{15}H_{13}FeNO_2$ (295.11): calcd. C 61.05, H 4.44, N 4.75; found C 61.28, H 4.49, N 4.34. M.p. 243 °C. IR (KBr): $\tilde{\nu}$ = 3086 m, 2918 w, 1701 s, 1606 s, 1436 s, 1384 s, 1257 m, 1105 m, 1027 s, 818 m cm^{-1}. ^{1}H NMR ($CDCl_3$): δ = 3.06 (s, 3 H, CH_3), 4.17 (s, 5 H, C_5H_5), 4.60 (pt, J_{HH} = 1.8 Hz, 2 H,

C_5H_4), 4.96 (pt, J_{HH} = 1.8 Hz, 2 H, C_5H_4), 6.37 (s, 1 H, HC_4N) ppm. $^{13}C\{^1H\}$ NMR ($CDCl_3$): δ = 23.86 (CH_3), 69.39 (C_5H_4), 70.61 (C_5H_5), 71.69 (^iC–C_5H_4), 72.33 (C_5H_4), 118.15 (CH–C_4N), 148.71 (^iC–C_4N), 170.30 (CO–C_4N), 171.48 (CO–C_4N) ppm. HFMS (ESI-TOF): calcd. for $C_{15}H_{13}FeNO_2$ $[M]^+$ 295.0296; found 295.0280.

3-Bromo-4-ferrocenyl-*N*-methylmaleimide (4): $C_{15}H_{12}BrFeNO_2$ (374.01): calcd. C 48.17, H 3.23, N 3.75; found C 48.36, H 3.23, N 3.52. M.p. 212 °C. IR (KBr): $\tilde{\nu}$ = 3087 m, 2924 w, 1706 s, 1606 s, 1432 s, 1379 s, 1283 m, 1136 m, 822 m cm^{-1}. ^1H NMR ($CDCl_3$): δ = 3.11 (s, 3 H, CH_3), 4.20 (s, 5 H, C_5H_5), 4.66 (pt, J_{HH} = 1.8 Hz, 2 H, C_5H_4), 5.38 (pt, J_{HH} = 1.8 Hz, 2 H, C_5H_4) ppm. $^{13}C\{^1H\}$ NMR ($CDCl_3$): δ = 24.79 (CH_3), 70.35 (C_5H_4), 70.58 (C_5H_5), 71.00 (^iC–C_5H_4), 72.45 (C_5H_4), 113.82 (CBr–C_4N), 143.58 (^iC–C_4N), 166.48 (CO–C_4N), 168.55 (CO–C_4N) ppm. HRMS (ESI-TOF): calcd. for $C_{15}H_{12}{}^{79}BrFeNO_2$ $[M]^+$ 372.9401; found 372.9383; calcd for $C_{15}H_{12}{}^{81}BrFeNO_2$ $[M]^+$ 374.9380; found 374.9358.

3,4-Diferrocenyl-*N*-methylmaleimide (5): $C_{25}H_{21}Fe_2NO_2$ (479.13): calcd. C 62.67, H 4.42, N 2.92; found C 62.45, H 4.36, N 2.84. M.p. 245 °C. IR (KBr): $\tilde{\nu}$ = 3089 m, 2931 w, 1701 s, 1688 w, 1606 s, 1481 s, 1439 s, 1381 s, 1107 m, 1029 s, 815 m, 492 s cm^{-1}. ^1H NMR ($CDCl_3$): δ = 3.11 (s, 3 H, CH_3), 4.11 (s, 10 H, C_5H_5), 4.47 (pt, J_{HH} = 1.8 Hz, 4 H, C_5H_4), 4.83 (pt, J_{HH} = 1.8 Hz, 4 H, C_5H_4) ppm. $^{13}C\{^1H\}$ NMR ($CDCl_3$): δ = 24.05 (CH_3), 70.36 (C_5H_4), 70.52 (C_5H_5), 70.59 (C_5H_4), 74.10 (^iC–C_5H_4), 134.36 (^iC–C_4N), 170.57 (CO–C_4N) ppm. HRMS (ESI-TOF): calcd. for $C_{25}H_{21}Fe_2NO_2$ $[M]^+$ 479.0271; found 479.0266.

Crystal Data for 4: $C_{15}H_{12}BrFeNO_2$, M = 374.01 gmol^{-1}, crystal dimensions 0.35 × 0.25 × 0.20 mm, T = 110 K, monoclinic, $P2_1/c$, a = 10.2409(2), b = 14.3279(3), c = 9.3032(2) Å, β = 106.059(2)°, V = 1311.80(5) Å^3, Z = 4, $\rho_{calcd.}$ = 1.894 gcm^{-3}, μ = 4.194 mm^{-1}, θ range = 2.98–26.00°, reflections collected: 5552, independent: 2572 (R_{int} = 0.0229), R_1 = 0.0263, wR_2 = 0.0585 [$I > 2\sigma(I)$].

Crystal Data for 5: $C_{25}H_{21}Fe_2NO_2$, M = 479.13 gmol^{-1}, crystal dimensions 0.38 × 0.10 × 0.05 mm, T = 110 K, monoclinic, $P2_1/c$, a = 10.29310(10), b = 23.4710(2), c = 32.2056(3) Å, β = 93.7060(10)°, V = 7764.26(12) Å^3, Z = 16, $\rho_{calcd.}$ = 1.640 gcm^{-3}, μ = 12.167 mm^{-1}, θ range = 3.33–62.50°, reflections collected: 27542, independent: 12108 (R_{int} = 0.0441), R_1 = 0.0416, wR_2 = 0.1049 [$I > 2\sigma(I)$].

CCDC-849489 (for **4**) and -849490 (for **5**) contain the supplementary crystallographic data for this paper. These data can be obtained free of charge from The Cambridge Crystallographic Data Centre via http://www.ccdc.cam.ac.uk/data_request/cif.

Acknowledgments

We are grateful to the Deutsche Forschungsgemeinschaft (DFG) and the Fonds der Chemischen Industrie for generous financial support. We gratefully acknowledge Sascha Dietrich and Colin Georgi for many fruitful discussions.

[1] See, for example: a) Y. J. Chen, D.-S. Pan, C.-F. Chiu, J.-X. Su, S. J. Lin, K. S. Kwan, *Inorg. Chem.* **2000**, *39*, 953–958; b) C. Patoux, C. Coudret, J.-P. Launay, C. Joachim, A. Gourdon, *Inorg. Chem.* **1997**, *36*, 5037–5049; c) A.-C. Ribou, J.-P. Launay, M. L. Sachtleben, H. Li, C. W. Spangler, *Inorg. Chem.* **1996**, *35*, 3735–3740; d) T. Y. Dong, T. J. Ke, S. M. Peng, S. K. Yeh, *Inorg. Chem.* **1989**, *28*, 2103–2106; e) A. J. Fry, P. S. Jain, R. L. Krieger, *J. Organomet. Chem.* **1981**, *214*, 381–390; f) F. Oton, I. Ratera, A. Espinosa, A. Tarraga, J. Veciana, P. Molina, *Inorg. Chem.* **2010**, *49*, 3183–3191; g) M. Kurosawa, T. Nankawa, T. Matsuda, K. Kubo, M. Kurihara, H. Nishihara, *Inorg. Chem.* **1999**, *38*, 5113–5123.

[2] a) S. C. Jones, S. Barlow, D. O'Hare, *Chem. Eur. J.* **2005**, *11*, 4473–4481; b) S. Barlow, D. O'Hare, *Chem. Rev.* **1997**, *97*, 637–669; c) I. M. Bruce, *Coord. Chem. Rev.* **1997**, *166*, 91–119; d) M. Ratner, J. Jortner, *Molecular Electronics*, Blackwell Science, Malden, **1997**; e) M. J. Tour, *Acc. Chem. Res.* **2000**, *33*, 791–804; f) P. C. Collier, W. E. Wong, M. Belohradsky, M. F. Raymo, F. J. Stoddart, J. P. Kuekes, S. R. Williams, R. J. Heath, *Science* **1999**, *285*, 391–394; g) R. L. Carroll, C. B. Gorman, *Angew. Chem.* **2002**, *114*, 4556; *Angew. Chem. Int. Ed.* **2002**, *41*, 4378–4400; N. Robertson, C. A. McGowan, *Chem. Soc. Rev.* **2003**, *32*, 96–103.

[3] a) A. Hildebrandt, D. Schaarschmidt, H. Lang, *Organometallics* **2011**, *30*, 556–563; b) A. Hildebrandt, D. Schaarschmidt, R. Claus, H. Lang, *Inorg. Chem.*, DOI: 10.1021/ic200916z; c) A. Hildebrandt, D. Schaarschmidt, H. Lang *Dalton Trans.*, DOI: 10.1039/c1dt10997a; d) C. Lapinte, *J. Organomet. Chem.* **2008**, *693*, 793–801; e) K. Kaleta, A. Hildebrandt, F. Strehler, P. Arndt, H. Jiao, A. Spannenberg, H. Lang, U. Rosenthal, *Angew. Chem.* **2011**, *123*, 11444–11448, *Angew. Chem. Int. Ed.* **2011**, *50*, 11248–11252; f) A. Hildebrandt, U. Pfaff, H. Lang, *Rev. Inorg. Chem.* **2011**, *31*, 111–141.

[4] V. P. Solntsev, S. V. Dudkin, J. R. Sabin, V. N. Nemykin, *Organometallics* **2011**, *30*, 3037–3046.

[5] D. Choi, S. Huang, M. Huang, T. S. Barnard, R. D. Adams, J. M. Seminario, J. M. Tour, *J. Org. Chem.* **1998**, *63*, 2646–2655.

[6] R. Sanders, U. T. Mueller-Westerhoff, *J. Organomet. Chem.* **1996**, *512*, 219–224.

[7] For information concerning the use of $[NBu_4][B(C_6F_5)_4]$ as a supporting electrolyte, see: a) R. J. LeSuer, C. Buttolph, W. E. Geiger, *Anal. Chem.* **2004**, *76*, 6395–6401; b) F. Barriére, W. E. Geiger, *J. Am. Chem. Soc.* **2006**, *128*, 3980–3989; c) H. J. Gericke, N. I. Barnard, E. Erasmus, J. C. Swarts, M. J. Cook, M. A. S. Aquino, *Inorg. Chim. Acta* **2010**, *363*, 2222–2232; d) E. Fourie, J. C. Swarts, D. Lorcy, N. Bellec, *Inorg. Chem.* **2010**, *49*, 952–959; e) J. C. Swarts, A. Nafady, J. H. Roudebush, S. Trupia, W. E. Geiger, *Inorg. Chem.* **2009**, *48*, 2156–2165; f) D. Chong, J. Slote, W. E. Geiger, *J. Electroanal. Chem.* **2009**, *630*, 28–34; g) V. N. Nemykin, G. T. Rohde, C. D. Barrett, R. G. Hadt, J. R. Sabin, G. Reina, P. Galloni, B. Floris, *Inorg. Chem.* **2010**, *49*, 7497–7509; h) V. N. Nemykin, G. T. Rohde, C. D. Barrett, R. Hadt, G. C. Bizzarri, P. Galloni, B. Floris, I. Nowik, R. H. Herber, A. G. Marrani, R. Zanoni, N. M. Loim, *J. Am. Chem. Soc.* **2009**, *131*, 14969–14978.

[8] G. Gritzner, J. Kuta, *Pure Appl. Chem.* **1984**, *56*, 461–466.

[9] a) M. Lohan, F. Justaud, T. Roisnel, P. Ecorchard, H. Lang, C. Lapinte, *Organometallics* **2010**, *29*, 4804–4817; b) C.-J. Yao, L.-Z. Sui, H.-Y. Xie, W.-J. Xiao, Y.-W. Zhong, J. Yao, *Inorg. Chem.* **2010**, *49*, 8347–8350; c) S. Ghumaan, B. Sarkar, S. Maji, V. G. Puranik, J. Fiedler, F. A. Urbanos, R. Jimenez-Aparicio, W. Kaim, G. K. Lahiri, *Chem. Eur. J.* **2008**, *14*, 10816–10828; d) M. Lohan, P. Ecorchard, T. Rüffer, F. Justaud, C. Lapinte, H. Lang, *Organometallics* **2009**, *28*, 1878–1890.

[10] D. M. D'Alessandro, F. R. Keene, *Chem. Soc. Rev.* **2006**, *35*, 424–440.

[11] N. S. Hush, *Prog. Inorg. Chem.* **1967**, *8*, 391–444.

[12] B. S. Brunschwig, C. Creutz, N. Sutin, *Chem. Soc. Rev.* **2002**, *31*, 168–184.

[13] a) M. J. Kamlet, J. L. M. Abboud, R. W. Taft, *J. Am. Chem. Soc.* **1977**, *99*, 6027–6038; b) M. J. Kamlet, J. L. M. Abboud, M. H. Abraham, R. W. Taft, *J. Org. Chem.* **1983**, *48*, 2877–2887; c) C. Reichardt, *Solvents and Solvent Effects in Organic Chemistry* (3rd ed.), Wiley-VCH, Weinheim, Germany, **2003**; d) C. Reichardt, *Chem. Rev.* **1994**, *94*, 2319–2358; e) R. W. Taft, M. J. Kamlet, *J. Am. Chem. Soc.* **1976**, *98*, 2886–2894; f) M. J. Kamlet, R. W. Taft, *J. Am. Chem. Soc.* **1976**, *98*, 377–383; g)

T. Yokoyama, M. J. Kamlet, R. W. Taft, *J. Am. Chem. Soc.* **1976**, *98*, 3233–3237; h) M. J. Kamlet, T. N. Hall, J. Boykin, R. W. Taft, *J. Org. Chem.* **1979**, *44*, 2599–2604; i) M. J. Kamlet, J. L. M. Abboud, R. W. Taft, *J. Am. Chem. Soc.* **1977**, *99*, 6027–6038.
[14] M. B. Robin, P. Day, *Adv. Inorg. Chem. Radiochem.* **1967**, *10*, 247–423.
[15] M. Krejčik, M. Daněk, F. J. Hartl, *Electroanal. Chem.* **1991**, *317*, 179–184.
[16] J. Ruiz, M.-C. Daniel, D. Astruc, *Can. J. Chem.* **2006**, *84*, 288–299.
[17] a) G. M. Sheldrick, *Acta Crystallogr., Sect. A* **1990**, *46*, 467–473; b) G. M. Sheldrick, *SHELXL-97*, *Program for Crytsal Structure Refinement*, **1997**, University of Göttingen, Germany.
[18] H. M. Gilow, D. E. Burton, *J. Org. Chem.* **1981**, *46*, 2221–2225.
[19] a) D. Alberti, K.-R. Pörschke, *Organometallics* **2004**, *23*, 1459–1460; b) W. E. Geiger, F. Barrière, *J. Am. Chem. Soc.* **2006**, *128*, 3980–3989.

Received: October 27, 2011
Published Online: January 31, 2012

DOI: 10.1002/ejic.201101197

Expected and Unconventional Ag^+ Binding Modes in Heteronuclear Pt,Ag Coordination Polymers Derived from *trans*-$[Pt(methylamine)_2(pyrazole)_2]^{2+}$

Pilar Brandi-Blanco,[a][‡] Pablo J. Sanz Miguel,*[a,b] and Bernhard Lippert*[a]

Keywords: Heterometallic complexes / Coordination polymers / Platinum / Silver / Ag–C interactions

The combination of $AgNO_3$ and *trans*-$[Pt(ma)_2(Hpz)_2]^{2+}$ (**1**; ma = methylamine; Hpz = neutral pyrazole) in water yields mixed Pt,Ag coordination polymers of different stoichiometries, depending on the ratio between Ag and Pt, as well as the pH. The products that were isolated and X-ray structurally characterized display both conventional (Ag^+ coordination to pyrazole-N) and unconventional Ag^+ binding modes (η^1 and η^2 binding to C atoms of the pyrazole/pyrazolate ligands; Pt → Ag dative bonds). Specifically, in *trans*-$[Pt(ma)_2(Hpz)_2]Ag_2(NO_3)_4$ (**2**) and in *trans*-$[Pt(ma)_2(pz)_2]_2Ag_3(NO_3)_3$ (**4**), silver ions bind to C4 positions of Hpz (**2**) and pz^- (**4**) ligands in η^1 fashions, with Ag–C distances of 2.574(4) and 2.643(16) Å, respectively. In **4** there is additional cross-linking by a second Ag^+ of N2 sites of adjacent pz^- rings, further reinforced by weak dative bonds from Pt to Ag. Ag–N coordination to both a neutral Hpz and an anionic pz^- ligand is observed in *trans*-$[Pt(ma)_2(pz)_2]Ag_2(Hpz)_2(NO_3)_2$ (**5**), with individual trinuclear $PtAg_2$ entities associated through weak η^2 contacts that involve the C3 and C4 positions of the neutral Hpz ligands. As in **4**, intramolecular Pt–Ag distances of 3.1374(6) Å suggest weak dative bond interactions between Pt and Ag. The acidities of the two Hpz ligands in **1** are distinctly different (pK_a values of 7.25 and 9.08 in H_2O), thereby suggesting a stabilization of the monodeprotonated species *trans*-$[Pt(ma)(Hpz)(pz)]^+$ (**1c**) in solution, probably through intermolecular hydrogen-bond formation between Hpz and pz^- ligands.

Introduction

The combination of silver and platinum in discrete heteronuclear complexes or coordination polymers is not only an appealing one from a philological point of view (silver, in Spanish: *plata*; platinum, in Spanish: *platino*, hence "little silver"), but rather (and foremost) from a chemical one. In general, the Pt–ligand entities in these compounds represent, relatively speaking, the "inert" building blocks, whereas the more "labile" Ag^+ ions function as the "glue" between the former. With model nucleobases[1] as well as related N-heterocyclic ligands[2] or even aliphatic amides,[3] we and others have frequently demonstrated this principle. Both discrete entities (e.g., stacks of three or four metal ions,[1a,1b] squares,[1k] rings[1f]) and polymeric ones (e.g., helices[1j,1m]) have been obtained upon addition of Ag^+ ions to Pt–ligand complexes. The role of Ag^+ in connecting the Pt units typically involves coordination to an available donor site at the ligand not yet occupied by Pt, sometimes complemented by Pt → Ag dative bond formation.[11] Occasionally, dative bonds from Pt^{II} to Ag^+ are exclusively responsible for formation of mixed Pt,Ag compounds.[4]

Here we report mixed Pt,Ag coordination polymers derived from bis(pyrazole) and bis(pyrazolate) (Hpz = pyrazole; pz^- = pyrazolate)[5] complexes of *trans*-(ma)Pt^{II} (ma = methylamine). Examples of complexes with pyrazole/pyrazolate or their substituted derivatives with either Pt^{II}[6,7] or Ag^+[8] are numerous, and mixed-metal complexes that contain both ions[7e,8] are likewise known. Mixed Pt^{II},Pd^{II} complexes with unsubstituted pyrazolato ligands have recently caught our attention because of the ease by which amido-bridged complexes are formed in aqueous solution[9] and stereogenic N centers can be generated.[9a] Interest in multinuclear pyrazolato complexes stems, among others, from their astonishing cyclic architectures, which make them excellent building blocks for metal–organic frameworks,[10] and their properties such as mixed valency[7i] or chemoluminescence.[11] Our initial goal, which eventually was not reached, was the preparation of flat, cationic mixed-metal metallacycles of general composition *trans*-$\{[Pt(ma)_2(pz)Ag]^{2+}\}_n$ (with n = 3 or 4) for potential use as DNA quadruplex binders.[12] Instead, only coordination polymers were obtained, which, however, revealed in several cases unconventional binding modes of the Ag^+ ions. Given the known versatility of metal-coordination patterns of pyrazole and pyrazolate ligands,[6] this finding was not entirely surprising.

[a] Fakultät Chemie, Technische Universität Dortmund, 44221 Dortmund, Germany
Fax: +49-231-755-3797
E-mail: bernhard.lippert@tu-dortmund.de
[b] Departamento de Química Inorgánica, Instituto de Síntesis Química y Catálisis Homogénea (ISQCH), Universidad de Zaragoza – CSIC, 50009 Zaragoza, Spain
E-mail: pablo.sanz@unizar.es
[‡] Present address: Departamento de Química Inorgánica, Universidad de Granada, 18071 Granada, Spain

Supporting information for this article is available on the WWW under http://dx.doi.org/10.1002/ejic.201101197.

Results and Discussion

Pt Starting Compound

trans-[Pt(ma)$_2$(Hpz)$_2$] was conveniently prepared by treating *trans*-[Pt(ma)$_2$(H$_2$O)$_2$](NO$_3$)$_2$ with an excess amount of Hpz in water and subsequently crystallizing the product. The compound was isolated in two modifications, **1a** and **1b**, which display differences in cation geometries and crystal packing. Selected structural features of the two cations are compiled in Table 1. A view of one of the two cations is given in Figure 1. Both cations are centrosymmetric and hence have the two pyrazole ligands in a head-to-tail arrangement. The major difference between cations **1a** and **1b** refers to different dihedral angles between the PtN$_4$ plane and the pyrazole planes, 77.9(1) and 87.1(2)°, respectively. Although both packing motifs are similar, this different inclination affects the hydrogen-bonding pattern of both complexes, thus leading to slightly different distances between NH protons and the nitrate counteranions: N1H···O11, 2.807(5) (**1a**) and 2.791(8) Å (**1b**); N11H$_2$···O11, 3.091(5) (**1a**) and 3.060(7) Å (**1b**); and N11H$_2$···O13, 3.152(5) (**1a**) and 3.063(8) Å (**1b**).

Table 1. Selected angles [°] and bond lengths [Å] for **1a** and **1b**.

	1a	1b	2	4[a]	5[b]
Pt–N2	1.995(3)	1.987(6)	1.996(3)	1.992(11) 2.007(11)	2.002(4)
Pt–N11	2.048(3)	2.060(6)	2.043(4)	2.032(13) 2.071(13)	2.038(5)
N1–N2	1.335(4)	1.370(7)	1.356(5)	1.344(16) 1.361(16)	1.344(7) 1.345(7)
N1–C5	1.326(5)	1.314(9)	1.338(6)	1.337(19) 1.303(19)	1.338(7) 1.338(7)
C4–C5	1.343(6)	1.348(10)	1.381(6)	1.38(2) 1.41(2)	1.371(9) 1.375(9)
C3–C4	1.366(6)	1.386(10)	1.404(6)	1.40(2) 1.40(2)	1.358(8) 1.394(9)
N2–C3	1.321(5)	1.300(9)	1.332(6)	1.349(18) 1.330(18)	1.328(7) 1.333(7)
PtN$_4$/pz	77.9(1)	87.1(2)	87.5(2)	87.6(5) 80.2(5)	82.8(2) 50.6(2)
C3–C4–C5	106.9(4)	105.3(7)	105.3(4)	103.7(14) 103.1(13)	104.7(5) 105.1(5)
Pt1–Ag1	–	–	–	3.1732(12) 3.2205(12)	3.1374(6)
Ag–C4	–	–	2.575(4)	2.643(16)	–
Ag–N	–	–	–	2.111(12) 2.119(12)	2.110(5) 2.084(5)

[a] Contains two non-symmetrically related pyrazole rings coordinated to platinum. [b] The second pyrazole ring (down) is only coordinated to silver.

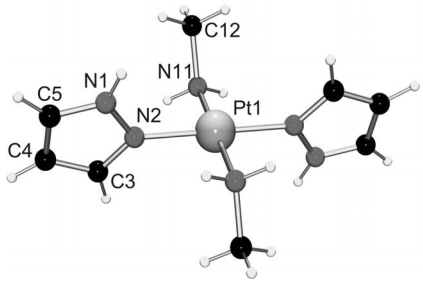

Figure 1. View of the centrosymmetric cation *trans*-[Pt(ma)$_2$(Hpz)$_2$]$^{2+}$ (**1a**) with atom-numbering scheme.

The ^{1}H NMR spectrum of **1a**/**1b** in D$_2$O (see the Supporting Information) displays two doublets (H3, H5) at low field, a doublet-of-doublets (H4) at intermediate field, and the methyl resonance of the ma ligands at high field. If isotopic exchange of the NH$_2$ protons against ^{2}D is completed, the CH$_3$ resonance represents a sharp singlet with ^{195}Pt satellites of ^3J = 41 Hz. All resonances are pD-dependent (Figure 2 for H3 and H5), and a plot of δ [ppm] versus pD reveals two separate deprotonation steps of the first and the second Hpz ligand (Figure 3, shown for H4). pK_a values

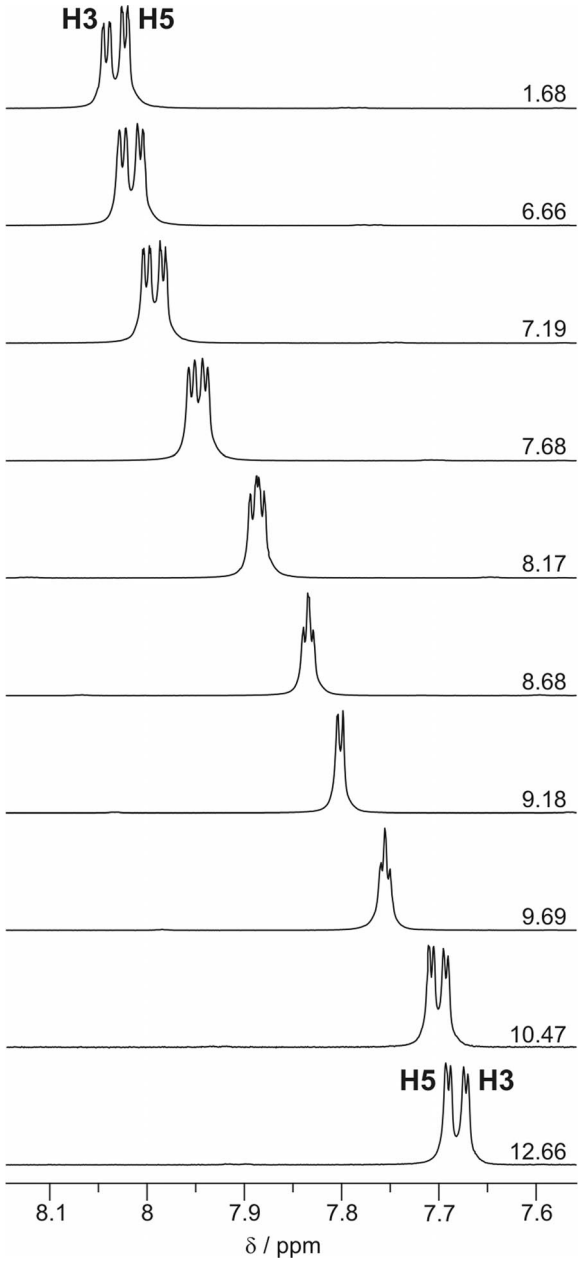

Figure 2. Low-field ^{1}H NMR spectrum sections of **1** in D$_2$O (pD from 1.68 to 12.66).

derived are $pK_{a1} = 7.81 \pm 0.02$ (D_2O), which corresponds to 7.25 ± 0.02 in H_2O, and $pK_{a2} = 9.67 \pm 0.02$ (D_2O), which corresponds to 9.08 ± 0.02 in H_2O:

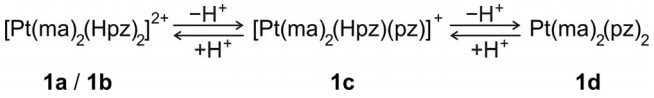

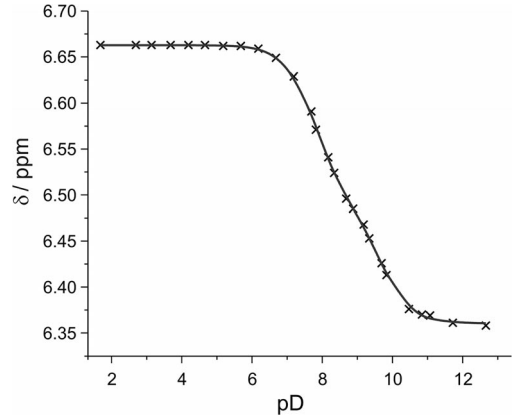

Figure 3. pD dependence of H4 resonances of **1a/1b**, showing two different deprotonation steps.

These pK_a values are similar to those of approximately 14.2 for deprotonation of the free ligand, and values of 6–7 for a series of cationic $[M(NH_3)_5(Hpz)]^{3+}$ complexes with trivalent metal ions,[13,14] and values of around 11 for anionic $[M(CN)_5(Hpz)]^{2-}$ compounds.[13] Compound **1** thus behaves normally, namely, by showing a slightly weaker acidification than the complexes with metals in +III oxidation states. Still, the acidification is quite substantial and reflects the close proximity of Pt and the proton at N2. Interestingly, the two deprotonation steps of **1** do not overlap strongly as is the case in numerous other bis(ligand) complexes of *cis*- or *trans*-a_2Pt^{II} (a = NH_3 or amine).[15] This observation strongly suggests that the hemideprotonated complex **1c** is stabilized prior to the second deprotonation step that leads to **1d**. Based on the solid-state structures of Pt^{II} complexes that simultaneously contain Hpz and pz ligands, which reveal either intra- or intermolecular hydrogen-bond formation between Hpz and pz ligands (hence pz···Hpz) depending on the mutual arrangement,[7c,7e] we propose that an intermolecular stabilization as sketched in Figure 4 is operative with **1c**.

It is analogous to the situation found in dinuclear $[\{Pt(pz)_2(Hpz)_2\}_2]$, which is formed in aqueous solution,[7c] and reminiscent of intermolecular hydrogen bonding between free pyrazole molecules.[16] Twofold deprotonation of **1** leads to the neutral complex *trans*-$[Pt(ma)_2(pz)_2]$ (**1d**), which is poorly soluble in water. Although isolated in microcrystalline form, an X-ray crystal structure determination of **1d** was not achieved, but elemental analysis data, the ^1H NMR spectrum, and the IR spectrum (absence of nitrate modes) are consistent with its composition.

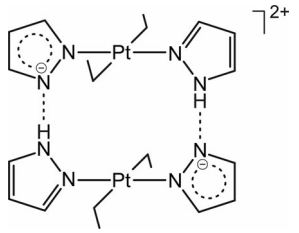

Figure 4. Proposed intermolecular stabilization of hemideprotonated **1a**(**1b**) in **1c** as origin for two distinctly different pK_a values of the two pyrazole ligands of **1a**(**1b**).

Ag^+Adducts of 1a/1b and of 1d

If the reaction between *trans*-$[Pt(ma)_2(H_2O)_2]^{2+}$ and Hpz is carried out in the presence of $AgNO_3$, different Ag^+ adducts of **1a/1b** and **1d** can be isolated, depending on pH, concentration and prevailing Ag/Pt ratio. Figure 5 lists four mixed Ag,Pt complexes **2**–**5**, three of which have been fractionally crystallized from a single reaction mixture that consisted of the Pt aqua complex, a moderate excess amount of Hpz, and a larger excess amount of $AgNO_3$. The very same compounds have also been obtained upon cocrystallizing **1a/1b** and **1d**, respectively, with $AgNO_3$ under more specific conditions (see below). It is possible and even likely that additional Ag^+ derivatives are realized under different conditions, and that the choice of the counteranion likewise can affect the outcome.

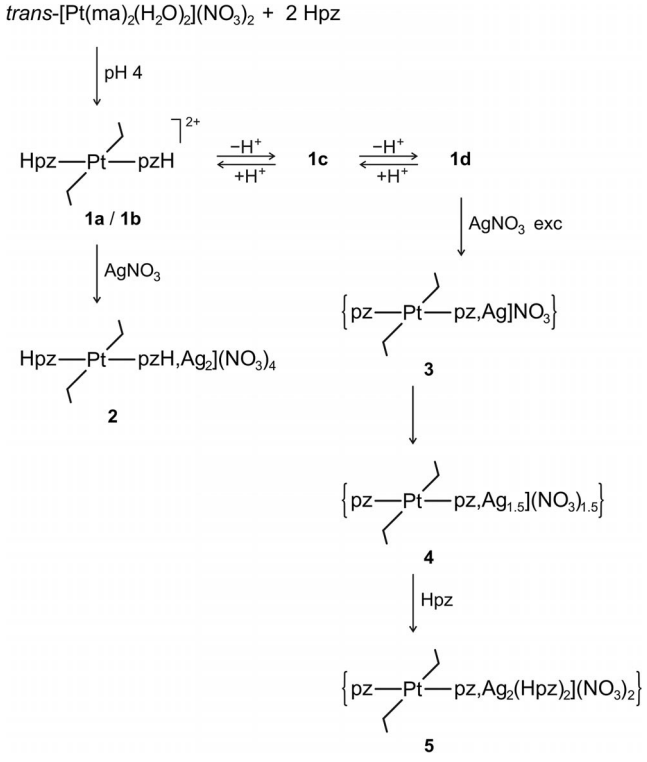

Figure 5. Formation scheme of complexes **1**–**5**.

The first complex to crystallize from the reaction mixture mentioned above, and alternatively obtained upon crystallizing **1a/1b** from water (pH 3) with a moderate excess

amount of $AgNO_3$, was *trans*-$[Pt(ma)_2(Hpz)_2]Ag_2(NO_3)_4 \cdot H_2O$ (**2**). Figure 6 provides a schematic view of the compound and a section of the extended crystal structure, and Table 1 contains selected structural data. As can be seen, the Ag^+ ions have not displaced the protons at the N1 positions of the Hpz ligands, but rather are η^1-bonded to the C4 atoms of the neutral pyrazole ligands, with Ag^+ ions virtually above the C4 positions [noteworthy distances are Ag1–C4 2.575(4) Å; Ag1–pz plane, 2.507(5) Å; Ag1–C3, 3.094(4) Å; Ag1–C5, 3.078(5) Å]. This situation is reminiscent of the first step of an electrophilic substitution at an aromatic system, and in fact it is the π-electron-rich C4 position in pyrazole that allows reactions with electrophiles.

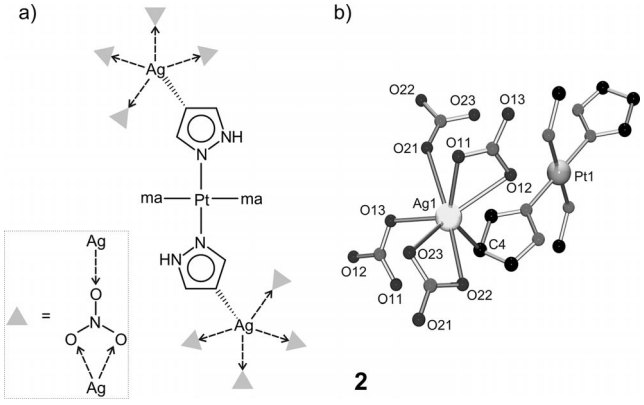

Figure 6. (a) Schematic representation of the intricated polymeric structure of **2**. (b) Detail of the coordination sphere of Ag^+ in this polymer.

Concerning the influence of the silver ion on the pyrazole geometry, there are two interesting aspects: (i) the pyrazole ring remains aromatic and planar; and (ii) both C–C bond lengths that involve C4 are slightly longer than in the absence of silver (Table 1; e.g., **1a/1b**). The coordination sphere of Ag^+ is completed by four bridging nitrate anions (Figure 6) in square-pyramidal geometry [Ag1–O11, 2.518(3) Å; Ag1–O12, 2.616(3) Å; Ag1–O13′, 2.467(3) Å; Ag1–O21′, 2.855(3) Å; Ag1–O22, 2.560(3) Å; Ag1–O23, 2.565(4) Å]. Each nitrate bridges an additional symmetry-related Ag1, thereby resulting in the assembly of a three-dimensional coordination polymer, with $\{trans\text{-}[Pt(ma)_2(Hpz)_2]\}_2Ag_6(NO_3)_4$ as basic units and the silver atoms occupying the nodes of the net (Figure 7). Some hydrogen-bonding interactions are observed within this coordination polymer: N11H···O23′, 2.837(6) Å; N11H···O12, 2.975(5) Å; N11H···O12′, 3.024(5) Å; N1H···O13′, 2.806(5) Å; N1H···O21′, 3.055(5) Å.

A system that involves the unconventional Ag^+ binding mode shown in **2** was described by Forniés et al.,[17] in which each silver η^1-coordinates two different 3,5-dimethylpyrazolate ligands and two bridging perchlorates, instead of a single pyrazole and four nitrates, as described here.

Cocrystallization of the neutral complex *trans*-$[Pt(ma)_2(pz)_2]$ (**1d**) with $AgNO_3$ at slightly higher pH (around 4) yielded a poorly soluble white solid which, according to elemental analysis, is of composition $[Pt(ma)_2(pz)_2] \cdot AgNO_3$ (**3**). Compound **3** was even obtained at pH 2, albeit in lower yield than at pH 4. We propose that this complex is a coordination polymer with pz ligands bridging *trans*-$(ma)_2Pt^{II}$ units and Ag^+ ions.

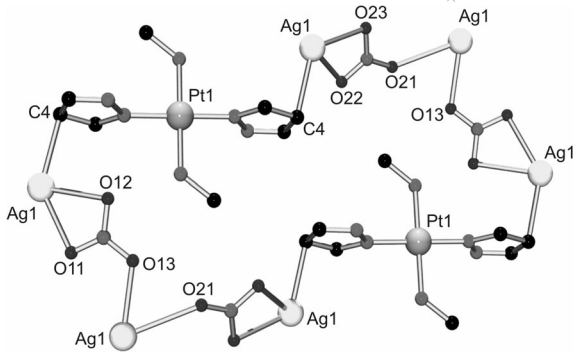

Figure 7. Units $\{trans\text{-}[Pt(ma)_2(Hpz)_2]\}_2Ag_6(NO_3)_4$ as motif of the 3D coordination polymer assembled in **2**.

It was found that poorly soluble **3** partly redissolved when treated with $AgNO_3$ in water. Colorless needles were isolated from the soluble supernatant upon slow evaporation in low yield, which proved to be *trans*-$[Pt(ma)_2(pz)_2]_2Ag_3(NO_3)_3$ (**4**), according to X-ray crystallography and elemental analysis. Compound **4** was also isolated as second component from the reaction mixture mentioned above. Figure 8 gives a schematic representation of polymeric **4** and a detailed view of a section of the structure. Salient features are included in Table 1. Compound **4** contains indeed the polymeric strand anticipated to occur in complex **3**, with pyrazolate ligands bridging the two different metal ions. Pt–Ag distances within the coordination polymer strand are 3.2205(12) Å (Pt1–Ag1) and 3.1732(12) Å (Pt1–Ag1′). The individual polymer strands are cross-linked by additional Ag^+ ions, which again interconnect the C4 sites. Ag–C4 distances are slightly longer than in **2** [2.643(16) Å], but unlike in **2**, the ligand pz is deprotonated.

A view of the one-dimensional polymeric structure of *trans*-$[Pt(ma)_2(pz)_2]_2Ag_3(NO_3)_3$ (**4**) and its schematic representation are depicted in Figure 8. This structure incorporates two different Ag^+ units, with their respective nitrate counteranions, to the initial *trans*-$[Pt(ma)_2(pz)_2]$ (**1d**) complex. The first silver atom (Ag1) connects consecutive head-to-tail-oriented **1d** through their available N1 sites at the pyrazolate rings [Ag1–N1a, 2.111(12) Å; Ag1–N1b′, 2.119(12) Å]. The Ag–Pt proximity allows the construction of heterometallic Pt···Ag···Pt···Ag rows, which are roughly linear, with identical intermetallic angles of 167.39(5)°. Pyrazole rings are almost coplanarly disposed and form dihedral angles with the platinum coordination plane of 87.6(5) and 80.2(5)°, for $pz_{(a)}$ and $pz_{(b)}$, respectively. This, and the fact that the square-planar coordination of the platinum atom is maintained almost unaltered, forces the Ag^+ ion to display a significantly distorted square-planar geometry, with angles that deviate 30° from a right angle: N1a–Ag1–Pt1, 61.9(3)°; N1b′–Ag1–Pt1′, 62.1(3)°; N1a–Ag1–Pt1′, 120.2(3)°, N1b′–Ag1–Pt1 115.5(3)°; N1a–Ag1–N1b′,

177.3(4)°. Its interaction sphere is completed by two apical oxygen atoms from close nitrate counteranions: Ag1–O22, 2.72(3) Å; Ag1–O13′, 2.977(12) Å.

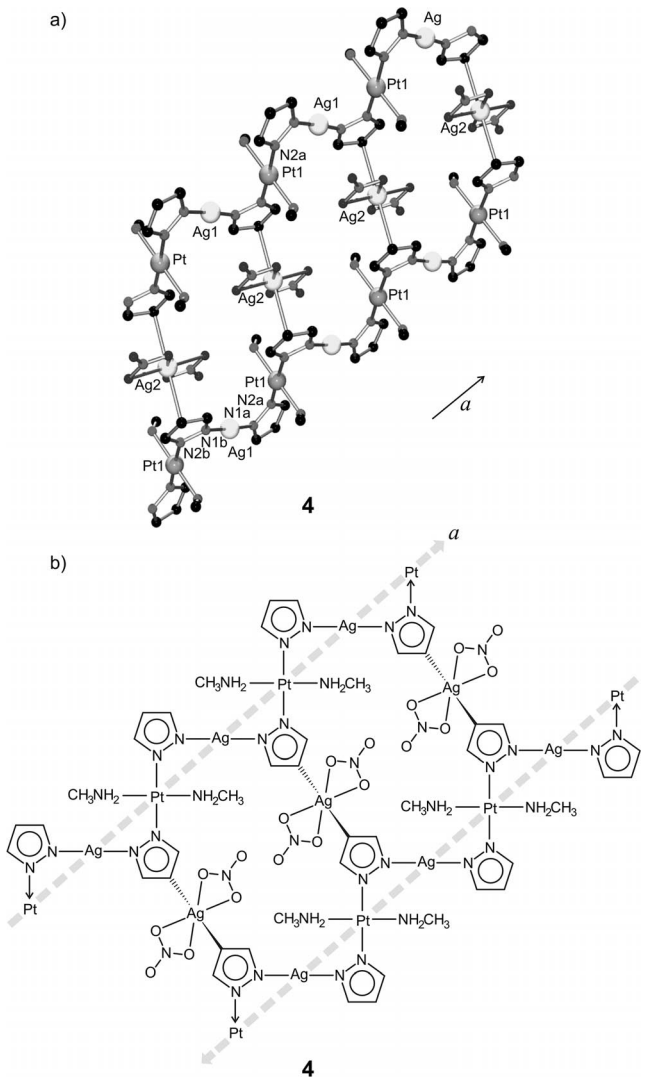

Figure 8. (a) View of the polymeric structure of *trans*-$[Pt(ma)_2(pz)_2]_2Ag_3(NO_3)_3$ (**4**). (b) Schematic representation of the structure growth along the *a* axis, emphasizing the $Pt^{II}\cdots Ag^+$ interactions.

The second Ag^+ unit (Ag2) in **4** displays a similar Ag–C coordination fashion as in **2**, although two different pyrazole rings are joined from their C4 sites: Ag2–C4b is slightly longer in this case [2.643(16) Å], and perpendicularity to the pyrazole rings is also observed. Ag2 exhibits a rare coordination geometry for Ag^+: a distorted octahedral coordination with both C4b *trans* to each other in the apical positions, and two chelating nitrates as equatorial ligands, also *trans*-positioned (Figure 9). Distances and angles within this geometry are as follows: Ag2–C4b, 2.643(16) Å; Ag2–O11, 2.393(11) Å; Ag2–O12, 2.680(12) Å; angles O–Ag–C are 88.4(4) and 91.6(4)°; whereas 180° is observed for *trans* O–Ag–O and C–Ag–C. Angles O11–Ag2–O12, which involve the same chelating nitrate, are 50.1(3)°, and between both *trans*-positioned chelates, the O11–Ag2–O12′ angles are 129.9(3)°. Despite this wide equatorial angle value, no further argentophilic contacts or interactions are observed for Ag2. From the supramolecular point of view, only $pz_{(b)}$ rings of the *trans*-$[Pt(ma)_2(pz)_2]$ units show these silver contacts, whereas no silver ions are placed in the proximity of $pz_{(a)}$. Thus, Ag2 joins two antiparallel Pt···Ag···Pt···Ag chains in a *trans* fashion and assembles a ladder-type 1D coordination polymer (Figure 8). The crystal packing is completed by additional parallel polymers, which extend along the *a* axis. We postulate that despite of the high standard deviation of the data (poor quality of the data), the geometry of $pz_{(b)}$ in **4** is affected by Ag^+, with a similar tendency of elongation of the C–C distances that involve C4, the atom to which Ag2 is anchored (Table 1).

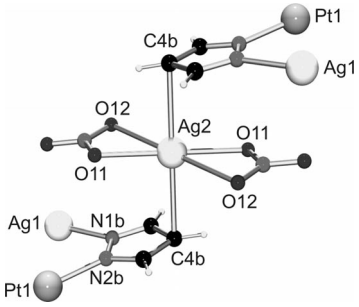

Figure 9. Environment of Ag2 in *trans*-$[Pt(ma)_2(pz)_2]_2Ag_3(NO_3)_3$ (**4**).

Finally, a complex of composition *trans*-$[Pt(ma)_2(pz)_2]$-$Ag_2(Hpz)_2(NO_3)_2$ (**5**) was isolated and structurally characterized. Compound **5** incorporates two Ag^+ units (Ag1) bonded through the available N1 sites of both $pz_{(A)}$. Each Ag1 binds an additional $Hpz_{(B)}$ ligand [N1a–Ag1–N2b, 170.8(2)°], in a *Z*-like geometrical disposition. Both Pt–Ag distances [3.1374(6) Å] are slightly shorter than in **4** and form discrete Ag···Pt···Ag interactions. As in **2** and **4**, the *trans*-$[Pt(ma)_2(pz)_2]$ unit has the usual square-planar coordination, head-to-tail arrangement and coplanarity of the pz^- ligands. Besides, both pyrazole ligands *trans* attached to silver ($pz_{(a)}$ and $Hpz_{(b)}$) are twisted 77.5(3)° to each other. A view of the resulting trimetallic unit is depicted in Figure 10. In **5**, trinuclear *trans*-$[Pt(ma)_2Ag_2(pz)_2(Hpz)_2]^{2+}$ cations associate through weak contacts between the Ag^+ cations and the C4=C5 bonds of the neutral Hpz ligands, with longer distances [Ag1–C4b, 3.183(7) Å, Ag1–C5b, 3.076(7) Å] than in previously reported examples of η^2-arene complexes of Ag^+.[18] This includes the case of polymeric $Ag(Hpz)(NO_3)$, in which a combination of Ag–N coordination and η^2 binding to C=C is realized.[19] Both cations have their $Hpz_{(b)}$ disposed in an antiparallel orientation, thereby building a stabilized interaction square (Figure 10, b) in which the $Hpz_{(b)}$ ligands partially overlap their N1b–N2b bonds, thereby showing very short distances between the rings [N2b–N2b′, 3.204(10) Å; N2b–$Hpz'_{(b)}$-plane, 3.171(7) Å], probably due to the combination of interactions. The coordination sphere of silver is also relatively empty, completed with a bonded nitrate anion [Ag1–

O12′, 3.159(5) Å], which interacts weakly with another silver atom: O13–Ag1, 3.541(6) Å. Concerning the pyrazole geometry, there is a clear trend towards an elongation of the C=C bond to which Ag^+ is bonded.

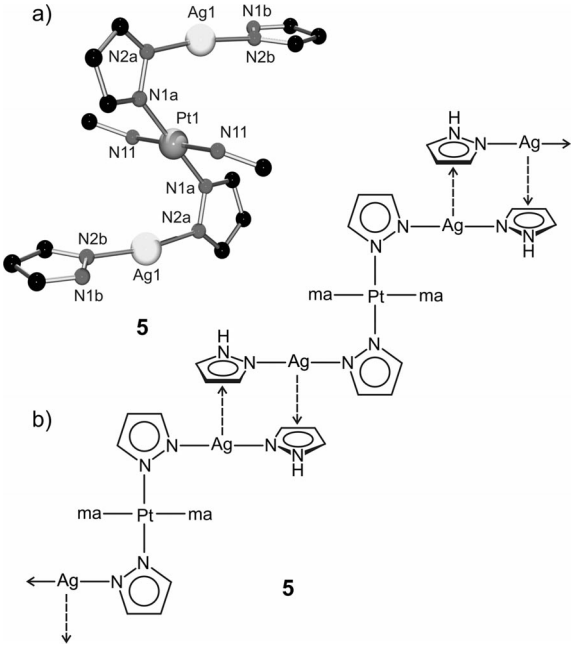

Figure 10. (a) View of the *trans*-$[Pt(ma)_2Ag_2(pz)_2(Hpz)_2]^{2+}$ cation **5**. (b) Polymeric association observed in **5**.

Conclusion

The X-ray crystal structure analyses of three heteronuclear Pt,Ag coordination polymers **2**, **4**, **5** isolated from aqueous solutions reveal a multitude of Ag^+ binding patterns to the platinated pyrazole ligands in *trans*-$[Pt(ma)_2(Hpz)_2]^{2+}$. Contrary to our expectations that the still-available ring-N atom of the pyrazole ligand would be the preferred binding site of Ag^+, it was found that Ag^+ does not readily displace the proton bonded to this position, despite its appreciable acidification by the adjacent Pt^{II}. Rather, the silver ion displays a remarkable affinity for the carbon atoms of the pyrazole ring by forming η^1 and η^2 complexes. Even if the second N is coordinated to a silver ion and the ligand hence deprotonated, there is still this tendency of Ag^+ to interact with ring carbon atoms. For arene ligands, this behavior is not too surprising and well documented,[18,20] but for N-heterocyclic ligands and in the presence of the highly coordinating solvent water it certainly is.

Experimental Section

General: K_2PtCl_4, $AgNO_3$, methylamine (ma), and pyrazole (Hpz) were of commercial origin. *trans*-$[Pt(ma)_2Cl_2]$ was prepared as reported.[21] ^1H NMR spectra were recorded in D_2O with Bruker AC 300 and Bruker DRX 400 instruments, and with TSP used as internal reference. pD values were determined by use of a glass electrode and a pH meter, and the addition of 0.4 units to the pH meter reading. pK_a values were determined by means of pD-dependent ^1H NMR spectroscopy and evaluated as described elsewhere.[22] The pK_a values for D_2O were subsequently converted to H_2O by applying the relationship pK_a (H_2O) = [$pK_a(D_2O)$ – 0.45]/1.015.[23] IR spectra were recorded as KBr pellets with a Bruker Fourier IFS 28 spectrometer. Elemental analyses for C, H, N were carried out with a Leco CHNS-932 instrument.

***trans*-$[Pt(ma)_2(Hpz)_2](NO_3)_2$ (1a):** A suspension of *trans*-$[Pt(ma)_2Cl_2]$ (930 mg, 2.83 mmol) and $AgNO_3$ (962 mg, 5.66 mmol) in water (50 mL) was stirred in a stoppered flask for 12 h at 40 °C with daylight excluded. The resultant AgCl precipitate was then filtered off and pyrazole (578 mg, 8.49 mmol) was added to the filtrate. The pH of the solution was adjusted to 7 by the addition of NaOH, and the mixture stirred for 24 h at 50 °C. Subsequently, the clear solution was concentrated to a volume of 5 mL by rotary evaporation (40 °C) and the solution allowed to stand at room temperature. A first crop of colorless microcrystals (776 mg) was harvested after 4 d. It was recrystallized from a mixture of water/methanol (2:1, 6 mL) with crystals suitable for X-ray analysis recovered after a week. The yield of **1a** was 659 mg (45%). $C_8H_{18}N_8O_6Pt$ (517.39): calcd. C 18.57, H 3.51, N 21.66; found C 18.6, H 3.5, N 22.2. A second modification of this compound, **1b**, was obtained in low yield from the aqueous solution after filtration of the first crop of **1a** after two more days at room temperature. ^1H NMR spectra of **1a** and **1b** were identical. ^1H NMR (D_2O, pD 3.5): δ = 8.04 (d, J = 2.8 Hz), 8.02 (d, J = 2.4 Hz), 6.66 (dd, J = 2.4 Hz, 2.8 Hz), 2.04 (s, ^{195}Pt satellites of J = 41 Hz) ppm.

***trans*-$[Pt(ma)_2(pz)_2]$ (1d):** Complex **1d** was prepared analogously to **1a**, except that the concentrated solution was treated with an excess amount of aqueous NH_3 (3 N), which immediately led to a white precipitate. Filtration, washing with water, and drying in air gave **1d** in 38% yield. $C_8H_{16}N_6Pt$ (391.35): calcd. C 24.55, H 4.13, N 21.48; found C 24.5, H 4.2, N 21.4. ^1H NMR (D_2O, pD 8.3): δ = 7.88 (d), 2.87 (d), 6.53 (dd), 2.04 (s, ^{195}Pt satellites) ppm.

***trans*-$[Pt(ma)_2(Hpz)_2]Ag_2(NO_3)_4$ (2):** Compound **1d** (782 mg, 2 mmol) was suspended in water (10 mL), the compound brought into solution by adding HNO_3 initially (pH 1.3) and then KOH to reach pH 3, and $AgNO_3$ (601 mg, 3.54 mmol) was added. After brief heating to 50 °C, the solution was evaporated to near dryness, whereupon colorless crystals of **2** formed. They were collected by filtration (1.06 g, 62%). $C_8H_{18}Ag_2N_{10}O_{12}Pt$ (857.12): calcd. C 11.21, H 2.12, N 16.34; found C 11.2, H 2.0, N 16.2.

***trans*-$[Pt(ma)_2(pz)_2]AgNO_3$ (3):** Compound **1d** (782 mg, 2 mmol) was suspended in water (10 mL) and warmed to solubilize **1d** somewhat. $AgNO_3$ (601 mg, 3.54 mmol) was added to result in the formation of a white precipitate and a drop in pH to around 4. The mixture was heated to 60 °C, then the precipitate was filtered off, washed with a small amount of water, and dried in air (146 mg; 13%). $C_8H_{16}AgN_7O_3Pt$ (561.27): calcd. C 17.11, H 2.88, N 17.47; found C 17.1, H 2.8, N 17.4. From the filtrate, after concentration to a volume of 3 mL, crystals of **2** were isolated after one day (757 mg, 43%). They were identified by X-ray crystallography.

***trans*-$[Pt(ma)_2(pz)_2]_2Ag_3(NO_3)_3$ (4):** Compound **3** (52 mg, 0.09 mmol) and $AgNO_3$ (94 mg, 0.55 mmol) were suspended in water (50 mL) and heated for 1 h to 50 °C. After removal of undissolved **3** (22.7 mg) by centrifugation, the resulting solution was brought by rotary evaporation to a volume of around 3 mL and then placed in a refrigerator at 3 °C. After three days, colorless needles of **4** were recovered in low yield (11.6 mg), which were characterized by X-ray analysis.

***trans*-$[Pt(ma)_2(pz)_2]Ag_2(Hpz)_2(NO_3)_2$ (5):** Complex **2** (639 mg, 0.72 mmol) and Hpz (102 mg, 1.5 mmol) were mixed in water

(7 mL) and the pH was raised from 2.7 to 6.1 by means of KOH (1 N). The sample was heated to 60 °C for 10 min, then the undissolved material was removed by centrifugation, and the resulting solution was brought to near dryness. Colorless crystals of **5** were isolated in low yield (14 mg). The compound was characterized by X-ray crystallography.

Fractional Crystallization of 3, 4, 5: In another experiment, **1** was prepared in situ in the presence of a slight excess amount of Hpz (10% based on stoichiometric amount) and a large excess amount of $AgNO_3$ (100%). After filtration of AgCl, the mixture (pH adjusted to 7 by means of NaOH) was concentrated by rotary evaporation and allowed to evaporate slowly in air. Crystals of **2** formed initially, followed later by those of **4**. Eventually also a grayish powder was recovered, which upon recrystallization from water gave crystals of **5**.

X-ray Crystal Structure Determination: Crystal structures **1a**, **1b**, **2**, **4**, and **5** were determined with a Xcalibur S diffractometer (graphite monochromated Mo-K_α radiation, 0.71073 Å). Data reduction was done with the CrysAlisPro software.[24] The structures were solved by direct methods and full-matrix least-squares refined on F^2 using SHELXL-97 and WinGX software.[25] All non-hydrogen atoms were refined anisotropically, whereas hydrogen atoms were positioned geometrically and refined with isotropic displacement parameters according to the riding model. Isor constraints were used for four atoms in complex **4**. Calculations were performed with SHELXL-97 software.[25b] Refinement parameters are as follows:

***trans*-[Pt(ma)$_2$(Hpz)$_2$](NO$_3$)$_2$ (1a):** [$C_8H_{18}N_8O_6Pt$], monoclinic, $P2_1/c$, a = 7.6675(6) Å, b = 11.8021(7) Å, c = 9.8712(8) Å, β = 112.117(9)°, Z = 2, M_r = 517.39 g mol^{-1}, V = 827.54(11) Å^3, $D_{calcd.}$ = 2.076 g cm^{-3}, μ = 8.520 mm^{-1}, 5054 reflections collected, 1920 unique (R_{int} = 0.0273), $R1$ (F_o) = 0.0218 [$I > 2\sigma(I)$], $wR2$ (F_o^2) = 0.0374 (all data), GOF = 1.006.

***trans*-[Pt(ma)$_2$(Hpz)$_2$](NO$_3$)$_2$ (1b):** [$C_8H_{18}N_8O_6Pt$], monoclinic, $P2_1/c$, a = 7.4227(8) Å, b = 11.5439(9) Å, c = 10.3661(15) Å, β = 113.875(10)°, Z = 2, M_r = 517.39 g mol^{-1}, V = 812.23(16) Å^3, $D_{calcd.}$ = 2.116 g cm^{-3}, μ = 8.681 mm^{-1}, 5678 reflections collected, 1893 unique (R_{int} = 0.0674), $R1$ (F_o) = 0.0357 [$I > 2\sigma(I)$], $wR2$ (F_o^2) = 0.0621 (all data), GOF = 1.055.

***trans*-[Pt(ma)$_2$(Hpz)$_2$]Ag$_2$(NO$_3$)$_4$ (2):** [$C_8H_{18}Ag_2N_{10}O_{12}Pt$], monoclinic, $P2_1/c$, a = 6.7730(5) Å, b = 15.1893(11) Å, c = 11.0704(10) Å, β = 117.506(6)°, Z = 2, M_r = 857.15 g mol^{-1}, V = 1010.15(14) Å^3, $D_{calcd.}$ = 2.818 g cm^{-3}, μ = 8.911 mm^{-1}, 5094 reflections collected, 2308 unique (R_{int} = 0.0255), $R1$ (F_o) = 0.0261 [$I > 2\sigma(I)$], $wR2$ (F_o^2) = 0.0579 (all data), GOF = 0.992.

***trans*-[Pt(ma)$_2$(pz)$_2$]$_2$Ag$_3$·(NO$_3$)$_3$ (4):** [$C_{16}H_{32}Ag_3N_{15}O_9Pt_2$], triclinic, $P\bar{1}$, a = 6.3551(5) Å, b = 8.3149(6) Å, c = 15.6125(12) Å, α = 80.384(6)°, β = 87.873(6)°, γ = 76.608(6)°, Z = 1, M_r = 1292.36 g mol^{-1}, V = 791.28(10) Å^3, $D_{calcd.}$ = 2.712 g cm^{-3}, μ = 10.700 mm^{-1}, 8630 reflections collected, 3646 unique (R_{int} = 0.0554), $R1$ (F_o) = 0.0669 [$I > 2\sigma(I)$], $wR2$ (F_o^2) = 0.1828 (all data), GOF = 1.073.

***trans*-[Pt(ma)$_2$(pz)$_2$]Ag$_2$(Hpz)$_2$(NO$_3$)$_2$ (5):** [$C_{14}H_{24}Ag_2N_{12}O_6Pt$], monoclinic, $C2/c$, a = 20.636(3) Å, b = 8.1699(8) Å, c = 14.6983(17) Å, β = 98.844(11)°, Z = 4, M_r = 867.28 g mol^{-1}, V = 2448.6(5) Å^3, $D_{calcd.}$ = 2.353 g cm^{-3}, μ = 7.339 mm^{-1}, 7742 reflections collected, 2830 unique (R_{int} = 0.0520), $R1$ (F_o) = 0.0339 [$I > 2\sigma(I)$], $wR2$ (F_o^2) = 0.0581 (all data), GOF = 1.026.

CCDC-850292 (for **1a**), -850293 (for **1b**), -850294 (for **2**), -850295 (for **4**), -850296 (for **5**) contain the supplementary crystallographic data for this paper. These data can be obtained free of charge from The Cambridge Crystallographic Data Centre via www.ccdc.cam.ac.uk/data_request/cif.

Supporting Information (see footnote on the first page of this article): ^{1}H NMR spectrum of **1** and additional information.

Acknowledgments

This work was supported by the Deutsche Forschungsgemeinschaft (DFG) and a postdoctoral fellowship from the Foundation Ramón Areces for P. B.-B. P. J. S. M. thanks the Spanish Ministry of Science and Innovation (MICINN) for funding through the "Ramón y Cajal" program.

[1] a) B. Lippert, D. Neugebauer, *Inorg. Chim. Acta* **1980**, *46*, 171–179; b) B. Lippert, D. Neugebauer, *Inorg. Chim. Acta* **1982**, *21*, 451–452; c) H. Schöllhorn, U. Thewalt, B. Lippert, *J. Chem. Soc., Chem. Commun.* **1984**, 769–770; d) U. Thewalt, D. Neugebauer, B. Lippert, *Inorg. Chem.* **1984**, *23*, 1713–1718; e) H. Schollhorn, U. Thewalt, B. Lippert, *Inorg. Chim. Acta* **1987**, *135*, 155–159; f) B. Lippert, H. Schollhorn, U. Thewalt, *Inorg. Chem.* **1987**, *26*, 1736–1741; g) I. Dieter, B. Lippert, H. Schollhorn, U. Thewalt, *Z. Naturforsch. B* **1990**, *45*, 731–740; h) D. Holthenrich, M. Krumm, E. Zangrando, F. Pichierri, L. Randaccio, B. Lippert, *J. Chem. Soc., Dalton Trans.* **1995**, 3275–3279; i) F. Zamora, H. Witkowski, E. Freisinger, J. Muller, B. Thormann, A. Albinati, B. Lippert, *J. Chem. Soc., Dalton Trans.* **1999**, 175–182; j) I. B. Rother, E. Freisinger, A. Erxleben, B. Lippert, *Inorg. Chim. Acta* **2000**, *300–302*, 339–352; k) I. B. Rother, M. Willermann, B. Lippert, *Supramol. Chem.* **2002**, *14*, 189–197; l) G. Kampf, P. J. Sanz Miguel, M. Morell Cerdà, M. Willermann, A. Schneider, B. Lippert, *Chem. Eur. J.* **2008**, *14*, 6882–6891; m) L. Yin, P. J. Sanz Miguel, W.-Z. Shen, B. Lippert, *Chem. Eur. J.* **2009**, *15*, 10723–10726; n) A. Khutia, P. J. Sanz Miguel, B. Lippert, *Chem. Eur. J.* **2011**, *17*, 4205–4216.

[2] a) R.-D. Schnebeck, E. Freisinger, F. Glahé, B. Lippert, *J. Am. Chem. Soc.* **2000**, *122*, 1381–1390; b) J. A. R. Navarro, E. Freisinger, B. Lippert, *Inorg. Chem.* **2000**, *39*, 1059–1065; c) M. Willermann, C. Mulcahy, R. K. O. Sigel, M. Morell Cerdà, E. Freisinger, P. J. Sanz Miguel, M. Roitzsch, B. Lippert, *Inorg. Chem.* **2006**, *45*, 2093–2099; d) M.-E. Moret, P. Chen, *J. Am. Chem. Soc.* **2009**, *131*, 5675–5690; e) S. Jamali, Z. Mazloomi, S. M. Nabavizadeh, D. Milic, R. Kia, M. Rashidi, *Inorg. Chem.* **2010**, *49*, 2721–2726; f) J. Forniés, V. Sicilia, J. M. Casas, A. Martín, J. López, C. Larraz, P. Borja, C. Ovejero, *Dalton Trans.* **2011**, *40*, 2898–2912.

[3] A. Erxleben, B. Lippert, *J. Chem. Soc., Dalton Trans.* **1996**, 2329–2333.

[4] See, for example: a) F. D. Rochon, R. Melanson, *Acta Crystallogr., Sect. C: Cryst. Struct. Commun.* **1988**, *44*, 474–477; b) W.-Z. Shen, R.-D. Schnebeck, E. Freisinger, B. Lippert, *Dalton Trans.* **2008**, 4044–4049; c) T. Yamaguchi, F. Yamazaki, T. Ito, *J. Am. Chem. Soc.* **2001**, *123*, 743–744; d) J. M. Casas, L. R. Falvello, J. Forniés, A. Martín, *Inorg. Chem.* **1996**, *35*, 7867–7872; e) R. Usón, J. Forniés, M. Tomás, J. M. Casas, F. A. Cotton, L. R. Falvello, *Inorg. Chem.* **1987**, *26*, 3482–3486; f) R. Usón, J. Forniés, *Inorg. Chim. Acta* **1992**, *198–200*, 165–177.

[5] The term "pyrazolide" for deprotonated pyrazole is also used.

[6] For reviews, see: a) C. Pettinari, N. Masciocchi, L. Pandolfo, D. Pucci, *Chem. Eur. J.* **2010**, *16*, 1106–1123; b) M. A. Halcrow, *Dalton Trans.* **2009**, 2059–2073; c) R. Mukherjee, *Coord. Chem. Rev.* **2000**, *203*, 151–218; d) L. A. Oro, M. A. Ciriano, C. Tejel, *Pure Appl. Chem.* **1998**, *70*, 779–788; e) G. La Monica, G. A. Ardizzoia, *Prog. Inorg. Chem.* **1997**, *46*, 151–238; f) S. Trofimenko, *Prog. Inorg. Chem.* **1986**, *34*, 115–210.

[7] See, for example: a) C. G. van Kralingen, J. K. Ridder, J. Reedijk, *Inorg. Chim. Acta* **1979**, *36*, 69–77; b) W. Burger, J. Strähle,

Z. Anorg. Allg. Chem. **1985**, *529*, 111–117; c) W. Burger, J. Strähle, *Z. Anorg. Allg. Chem.* **1986**, *539*, 27–32; d) A. B. Goel, S. Goel, D. Vanderveer, *Inorg. Chim. Acta* **1984**, *82*, L9–L10; e) G. Lopez, J. Ruiz, C. Vicente, J. M. Marti, G. Garcia, P. A. Chaloner, P. B. Hitchcock, R. M. Harrison, *Organometallics* **1992**, *11*, 4090–4096; f) K. Umakoshi, Y. Yamauchi, K. Nakamiya, T. Kojima, M. Yamasaki, H. Kawano, M. Onishi, *Inorg. Chem.* **2003**, *42*, 3907–3916; g) S. Teletchéa, S. Komeda, J.-M. Teuben, M.-A. Elizondo-Riojas, J. Reedijk, J. Kozelka, *Chem. Eur. J.* **2006**, *12*, 3741–3753; h) A. V. Khripun, S. I. Selivanov, V. Y. Kuikushkin, M. Haukka, *Inorg. Chim. Acta* **2006**, *359*, 320–326; i) K. Umakoshi, T. Kojima, Y. H. Kim, M. Onishi, Y. Nakao, S. Sakaki, *Chem. Eur. J.* **2006**, *12*, 6521–6527.

[8] See, for example: a) V. García-Pacios, M. Arroyo, N. Antón, D. Miguel, F. Villafañe, *Dalton Trans.* **2009**, 2135–2141; b) G. Yang, R. G. Raptis, *Inorg. Chim. Acta* **2007**, *360*, 2503–2506; c) M. A. Omary, M. A. Rawashdeh-Omary, M. W. A. Gonser, O. Elbjeirami, T. Grimes, T. R. Cundari, H. V. K. Diyabalanage, C. S. P. Gamage, H. V. R. Dias, *Inorg. Chem.* **2005**, *44*, 8200–8210; d) H. H. Murray, R. G. Raptis, J. P. Fackler, Jr., *Inorg. Chem.* **1988**, *27*, 26–33.

[9] a) P. Brandi-Blanco, P. J. Sanz Miguel, B. Lippert, *Dalton Trans.* **2011**, *40*, 10316–10318; b) A. Schneider, E. Freisinger, B. Beck, B. Lippert, *J. Chem. Soc., Dalton Trans.* **2000**, 837–838.

[10] V. Colombo, S. Galli, H. J. Choi, G. D. Han, A. Maserpo, G. Palmisano, N. Masciocchi, J. R. Long, *Chem. Sci.* **2011**, *2*, 1311–1319, and references cited therein.

[11] K. Umakoshi, K. Saito, Y. Arikawa, M. Onishi, S. Ishizaka, N. Kitamura, Y. Nakao, S. Sakaki, *Chem. Eur. J.* **2009**, *15*, 4238–4242.

[12] For details of this concept, see: a) J. E. Reed, A. A. Arnal, S. Neidle, R. Vilar, *J. Am. Chem. Soc.* **2006**, *128*, 5992–5993; b) K. Suntharalingam, D. Gupta, P. J. Sanz Miguel, B. Lippert, R. Vilar, *Chem. Eur. J.* **2010**, *16*, 3613–3616.

[13] C. R. Johnson, W. W. Henderson, R. E. Shepherd, *Inorg. Chem.* **1984**, *23*,2754–2763.

[14] a) J. R. Winter, D. Caruso, R. E. Shepherd, *Inorg. Chem.* **1988**, *27*, 1086–1089; b) M. G. Elliott, R. E. Shepherd, *Transition Met. Chem.* **1989**, *14*, 251–257.

[15] See, for example: a) P. Brandi-Blanco, P. J. Sanz Miguel, B. Müller, E. Gil-Bardají, M. Willermann, B. Lippert, *Inorg. Chem.* **2009**, *48*, 5208–5215; b) R. Griesser, G. Kampf, L. E. Kapinos, S. Komeda, B. Lippert, J. Reedijk, H. Sigel, *Inorg. Chem.* **2003**, *42*, 32–41.

[16] R. G. Raptis, R. J. Staples, C. King, J. P. Fackler Jr., *Acta Crystallogr., Sect. C: Cryst. Struct. Commun.* **1993**, *49*, 1716–1719, and references cited therein.

[17] a) L. R. Falvello, J. Fornies, A. Martin, R. Navarro, V. Sicilia, P. Villarroya, *Chem. Commun.* **1998**, 2429–2430; b) J. Fornies, A. Martin, V. Sicilia, L. F. Martin, *Chem. Eur. J.* **2003**, *9*, 3427–3435.

[18] See, for example: a) D. Salazar-Mendoza, S. A. Baudron, M. W. Hosseini, *Chem. Commun.* **2007**, 2252–2254; b) M. Munakata, L. P. Wu, G. L. Ning, *Coord. Chem. Rev.* **2000**, *198*, 171–203, and references cited therein; c) A. N. Klobystov, A. J. Blake, N. R. Champness, D. A. Lemenovskii, A. G. Majouga, N. V. Zyk, M. Schröder, *Coord. Chem. Rev.* **2001**, *222*, 155–192, and references cited therein.

[19] G. Meyer, M. Sehabi, I. Pantenburg, in: *Design and Construction of Coordination Polymers* (Eds.: L. Chen, M.-C. Hong), Wiley, Hoboken, NJ, USA, **2009**, pp. 1–23.

[20] Selected examples of η^1 complexes of Ag^+ with arene ligands: a) K. Shelly, D. C. Finster, Y. J. Lee, W. R. Scheidt, C. A. Reed, *J. Am. Chem. Soc.* **1985**, *107*, 5955–5959; b) J. E. Gano, G. Subramaniam, R. Birnbaum, *J. Org. Chem.* **1990**, *55*, 4760–4763.

[21] J. Arpalahti, B. Lippert, H. Schöllhorn, U. Thewalt, *Inorg. Chim. Acta* **1988**, *153*, 45–49.

[22] R. K. O. Sigel, S. M. Thompson, E. Freisinger, F. Glahé, B. Lippert, *Chem. Eur. J.* **2001**, *7*, 1968–1980.

[23] R. B. Martin, *Science* **1963**, *139*, 1198–1203.

[24] *CrysAlisPro*, Oxford Diffraction Poland, **2009**.

[25] a) G. M. Sheldrick, *SHELXS97 and SHELXL97*, University of Göttingen, Germany, **1997**; b) L. J. Farrugia, *WinGX*, University of Glasgow, UK, **1998**.

Received: October 27, 2011
Published Online: January 30, 2012

DOI: 10.1002/ejic.201101202

Di-, Tetra-, Penta- and Polynuclear Zinc Complexes Supported by a Flexible Tetradentate Schiff Base Ligand

David J. D. Wilson,[a] Christine M. Beavers,[b] and Anne F. Richards*[a]

Keywords: Zinc / Halides / Multinuclear complexes / Schiff bases

When treated with Et_2Zn, the tetradentate Schiff base *N*,*N*′-ethylenebis(4-iminopentan-2-one) (H_2**L**) led to the formation of dimers, [$\mathbf{L}_2Zn_2$], a tetranuclear complex, [$\mathbf{L}_4Zn_4$] (**1**) and a polymeric material [**L**Zn(Et)]$_n$ (**2**), thus highlighting the coordinative versatility of the ligand. Halogenation of **1** with SO_2Cl_2 or Br_2 afforded in moderate yield the dinuclear zinc complexes [**L**Zn(thf)·$ZnCl_2$] (**3**) and [**L**Zn(thf)·$ZnBr_2$] (**4**). [**L**Zn·ZnI(μ-OEt)]$_2$ (**5**) was isolated from the reaction of an in situ generated mixture of **1** and **2** with iodine. This product likely results from adventitious oxygen in the reaction mixture. This was seemingly confirmed by the diffusion of air into a solution of **2** in toluene, thereby resulting in a pentanuclear zinc complex, [(**L**Zn·ZnEt)$_2${Zn(μ-OEt)$_4$}] (**6**). Complex **6** features a central $Zn(OEt)_4$ unit, in which the ethoxide groups bridge two dinuclear fragments. The identities of complexes **1**–**6** were conclusively identified by X-ray crystallography, thereby revealing similar structural features that were confirmed by spectroscopic data and, for **1**–**5**, supported by DFT calculations.

Introduction

Schiff base ligands continue to play an important role in coordination chemistry.[1] Of particular interest are Schiff base complexes of zinc, as these have found numerous applications, for example, as fluorescent emitters and as active layers in organic light-emitting diodes (OLEDs).[2] More recently, zinc cages and polymers have found roles as porous structures with well-defined interfaces for storage of different gases (e.g., CH_4, CO_2).[3] Zinc(II) systems are very applicable for this purpose due to the large number of available precursors for their preparation, and the d^{10} electron configuration of Zn^{2+} being free of crystal field influences, which allows flexibility when forming metallo species.[4] Diethylzinc is a particularly useful precursor, as it is highly reactive and will coordinate to ligands through removal of the acidic protons, thus generating ethane gas. In recent years, we have investigated the reactions of diethylzinc with the ketiminate ligands DippN(H)[C(Me)]$_2$C(Me)=O (Dipp = 2,6-diisopropylphenyl) and ($C_2H_4NEt_2$)N(H)C(Me)-CHC(Me)=O,[5] the latter of which afforded a tetranuclear species with an accessible internal cavity. We were interested in exploiting this chemistry further by investigating whether larger cages could be generated for use as gas-storage or ion-sequestering materials. For this purpose, the tetradentate Schiff base *N*,*N*′-ethylenebis(4-iminopentan-2-one), H_2**L**, was selected for reaction with Et_2Zn. Multitopic ligands with N,N,O (carbonyl)-type donor sets have only infrequently been employed in the metal-ion-directed assembly of coordination architectures. However, such ligands have been demonstrated to form helicate complexes, in particular with lanthanide metal ions.[6]

Previous work by Kotova and co-workers found that the stoichiometric reaction of Et_2Zn with H_2**L** yielded a dinuclear helical species, [$\mathbf{L}_2Zn_2$].[7] Herein we report how changing the reaction stoichiometry can increase the nuclearity of the resultant complexes to afford a tetranuclear complex, [$\mathbf{L}_4Zn_4$] (**1**), and a 1D polymer, [**L**Zn(Et)]$_n$ (**2**). The reactivity of **1** and **2** with SO_2Cl_2, Br_2 and I_2 was investigated. The aim of these reactions was to generate zinc centres with a reactive Zn–X bond that could be used as well-defined molecular building blocks for the synthesis of larger cages and clusters. From these reactions, a series of di-, tetra- and pentanuclear zinc complexes with related structural features were isolated.

Results and Discussion

The 1:1 stoichiometric reaction of diethylzinc with H_2**L** [**L** = *N*,*N*′-ethylenebis(4-iminopentan-2-one)] afforded the previously reported neutral bimetallic helical structure [$\mathbf{L}_2Zn_2$].[7] To determine whether increasing the ratio of $ZnEt_2$ to H_2**L** would lead to two zinc molecules per ligand being incorporated into the final product, thereby increasing the nuclearity of the resultant complex, the 1:2.1 reaction of Et_2Zn with H_2**L** was carried out (Scheme 1).

Tetranuclear **1** (Figure 1) was isolated in good yield as pale yellow crystals from toluene and appears to have been

[a] Department of Chemistry, La Trobe Institute of Molecular Sciences, La Trobe University,
Melbourne 3086, Australia
[b] Advanced Light Source, Berkeley Laboratory,
1 Cyclotron Road, MS6R2100,
Berkeley, CA 94720, USA
Supporting information for this article is available on the WWW under http://dx.doi.org/10.1002/ejic.201101202.

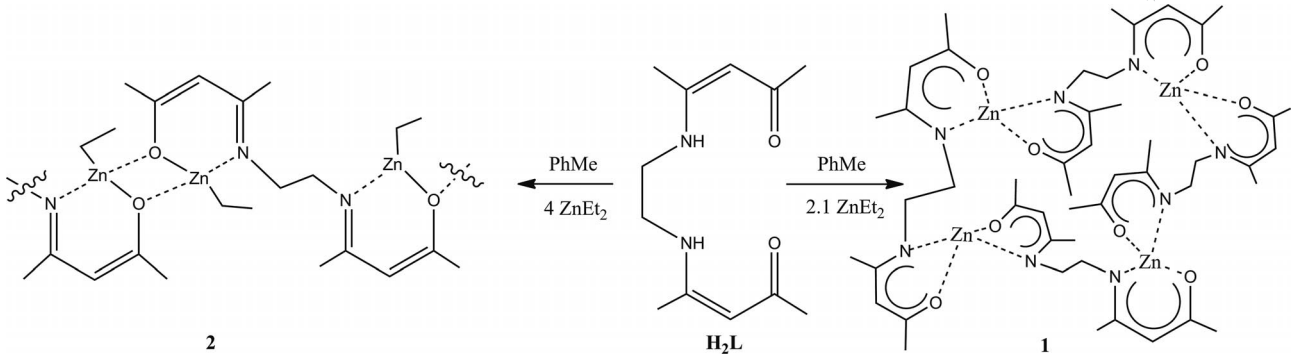

Scheme 1. The reaction of H_2**L** with $ZnEt_2$ under various stoichiometries.

formed from 1:1 stoichiometry. The isolation of a tetranuclear product instead of the dimer is likely due to an equilibrium between the two products, although it is not known if the presence of an excess amount of Et_2Zn in the reaction mixture favours the formation of **1**. A solid-state analysis found that the four zinc centres are complexed to four deprotonated ligands. The coordination sites around each zinc centre are occupied by two oxygen atoms and two nitrogen atoms, each from different ligands. This favoured tetrahedral geometry is possible because of the flexible nature of the chelating ligands, whereas complexes that incorporate Schiff base ligands with aromatic bridges are found to be more rigid and favour mononuclear pentacordinate structures.[8] The zinc centres are linked by bridging ethylenediamine groups with Zn–Zn distances in the range 5.7144(6) Å (Zn3–Zn4) to 5.9130(6) Å (Zn1–Zn4). These values can be compared to a Zn–Zn separation of approximately 7.7 Å in the tridentate ketiminato zinc complex $[\{(C_2H_5)_2N(H)C(Me)CHC(Me)=O\}Zn]_4$.[5] In other related tetranuclear Schiff base zinc complexes, a variety of different cavity sizes and shapes are observed that are derived from the different configurations of Schiff base ligands, with Zn–Zn distances ranging from 3.2 to 11.11 Å.[9] Dimeric [$\mathbf{L}_2Zn_2$] has a much shorter Zn–Zn distance of approximately 3.7 Å with the NO chelates arranged in *cis* geometry relative to the NCCN bond.[7] The degree of association between the zinc atoms is believed to be dependent on ligand size and decreases with increasing bulk.[5] The tetradentate ligand **L** is able to hold the zinc atoms in closer proximity, therefore decreasing the Zn–Zn separation.

The skewed arrangement of the molecules in the solid state means that the molecule is not symmetrical and is arranged to minimize steric repulsions with two lattice toluene molecules that affect the crystal-packing arrangements. The solid-state structure of **1** highlights the flexibility of the ligand around the NCCN linker. In its uncomplexed form, the ligand adopts a *syn*-periplanar conformation around the ethylenediamine linker with N–C–C–N torsion angles of 64–66°,[10] whereas in **1** the N1–C6–C7–N2 torsion angles are in the range of 176–179° for the four ligands. The Zn–O and Zn–N bond lengths in **1** compare well with [$\mathbf{L}_2Zn_2$] and other related species.[7,11] The C–C bond lengths within the ligand backbone [Figure 2, b and c (as

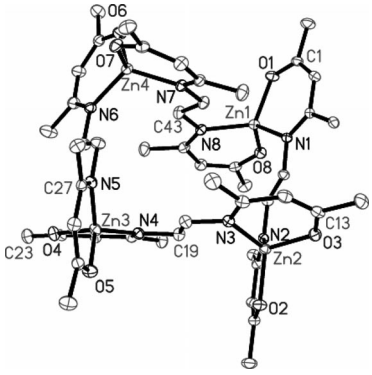

Figure 1. Crystal structure of **1**. Thermal ellipsoids are drawn at 30% probability level and hydrogen atoms are omitted for clarity. Selected bond lengths [Å] and angles [°]: Zn1–O8 1.939(3), Zn1–N8 1.996(3), Zn4–O6 1.936(3), Zn4–N6 1.984(3); N8–Zn1–O8 97.85(12), N6–Zn4–N7 118.14(12).

representative bond lengths for the whole complex)] show distinct variations from 1.320(5) to 1.432(5) Å, but there is less distinction in the C–O and C–N bond lengths, which are all of similar values within the tetrameric complex and range from 1.281(5) (O6–C32) to 1.293(5) Å (O1–C1) and 1.306(5) (N5–C27) to 1.321(5) Å (N3–C15). Given the keto–enol tautomerism that is characteristic of Schiff base ligands, the bond lengths are indicative of electron delocalization over the ligand backbone (Figure 2, a–d). Pertinent bond lengths and angles for **1** (and all crystal structures in this paper) are listed in Table 1.

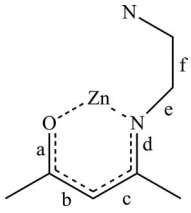

Figure 2. Labelling of ligand–Zn ring bond lengths.

The proton NMR spectrum of **1** exhibited characteristic ligand peaks with a small amount of decomposition of free ligand. This data suggests that in deuterated benzene, a more symmetrical structure is in place, or that the tetranu-

Table 1. Comparison of bond lengths [Å] and angles [°] in complexes **1**–**6**. Bonds labelled (a–d) are identified in Figure 2. For complex **1**, the bond lengths of O1, N1, N1–Zn1–N8 and N1–Zn1–O1 are used as representative distances for the molecule.

	1	**2**	**3**	**4**	**5**	**6**
Zn1–O1	1.939(3)	2.1392(17)	2.009(4)	2.001(3)	2.043(4)	2.050(4)
Zn1–N1	2.002(3)	2.0131(19)[a]	1.997(5)	2.006(3)	2.028(5)	2.022(5)
a	1.293(5)	1.318(3)	1.304(7)	1.325(5)	1.313(7)	1.335(8)
b	1.380(6)	1.365(3)	1.359(9)	1.367(6)	1.367(9)	1.357(10)
c	1.401(5)	1.434(3)	1.469(9)	1.437(7)	1.436(9)	1.417(10)
d	1.316(4)	1.307(3)	1.290(7)	1.294(6)	1.289(9)	1.281(8)
Zn–X		–	2.1964(18)[b] 2.2007(17)	2.3399(7)[b] 2.3476(7)	2.5455(11)	–
O–Zn–O					77.52(16)	99.65(16)
N–Zn–N	119.69(12)	–	85.6(2)	84.62(15)	82.8(2)	82.6(2)
N–Zn1–O	97.12(12)	92.51(7)	91.69(18)	92.66(13)	89.3(2)	89.3(2)

[a] N1–Zn1A. [b] Zn2.

clear molecule dissociates into monomeric units. The mass spectral analysis on **1** exhibited a molecular isotope pattern consistent with the presence of zinc atoms but no molecular ion peak was seen. The infrared spectra of the zinc Schiff base complexes display the typical ν(CO) and ν(CN) vibrations in the regions 1490–1600 cm^{-1}, whereas the IR spectra of the free ligands displays ν(N–H) vibrations in the region 3000–3250 cm^{-1}. No emission spectra from solution luminescent measurements were observed at room temperature. Complex **1** is thermally stable but was found to decompose into a red oil at 151–156 °C.

In view of the unexpected isolation of a tetranuclear product through an increase in the stoichiometry of the zinc reactant present, we wondered whether higher-nuclearity complexes could be achieved through a further increase in the ratio of diethylzinc to H_2**L**. To this end, the 1:4 reaction of H_2**L** with $ZnEt_2$ was carried out. Colourless crystals of **2** were isolated from toluene in high yield and a single-crystal X-ray diffraction study was performed. Complex **2** was found to be a 1D polymeric material as depicted in Figure 3, in which the ethylenediamine linker is found to link the zinc centres. Every zinc atom is coordinated to an ethyl group, retained from the diethylzinc, a nitrogen atom and two oxygen atoms from different ligands. The angles around each zinc centre range from 83.19(7) to 103.66(7)° and so represent a highly distorted tetrahedral geometry. Polymer **2** is of interest, as alkylzinc complexes are of importance in catalysis, organic synthesis and materials.[12] Polymeric **2** is readily soluble in hydrocarbon solvents and is quite thermally stable, with decomposition observed at temperatures greater than 200 °C.

Examination of the ^1H and ^{13}C NMR spectra to determine whether the polymeric form of **2** is retained in solution revealed a complex mixture of products with signals that could be assigned to at least two different products, probably due to the possible Schlenk equilibrium. To ascertain the identity of the products in solution, the NMR spectroscopy tube was left uncapped in the glovebox overnight. The following day, large colourless crystals were extracted from the NMR spectroscopy tube. These crystals were found to be the zinc dimer [L_2Zn_2].[7] Therefore it is apparent that in solution **2** does not retain the polymeric structure and at least one of the products found is [L_2Zn_2]. At present, it is not known how this is product is formed, though it could arise from a redistribution reaction. A survey of the Cambridge crystallographic database[13] revealed 18 related complexes in which zinc is N/O coordinated from reactions with diethylzinc in which zinc retains an ethyl group. Of these complexes, only two were found to be polymeric,[14] with the most closely related being salicylaldiminato Zn complexes and anilido–aldimine Zn complexes in which the ligated zinc centres are separated by aliphatic methylene spacer groups of between 3 and 6 carbon atoms to allow for differing separation of the two metal centres.[14a] Complex **2** is of importance and interest as N′,O-chelated zinc complexes have proved effective for metal-catalyzed lactide polymerization with activity and selectivity dependent on the nature of the X group; they are particularly active when X is an alkyl group.[15]

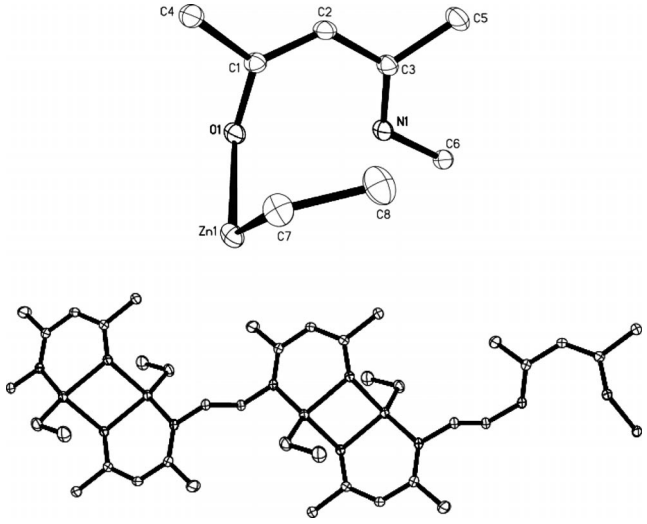

Figure 3. Crystal structure of **2**. The asymmetric unit (left) and polymeric form of **2** (right). Thermal ellipsoids are shown at 30% probability level. Selected bond lengths [Å] and angles [°]: Zn1–C7 1.970(2); Zn1–O1–Zn1a 96.81(7).

Given the ease with which complexes **1** and **2** could be isolated, we were interested in further exploring the chemistry of these molecules with the goal of utilizing it as a build-

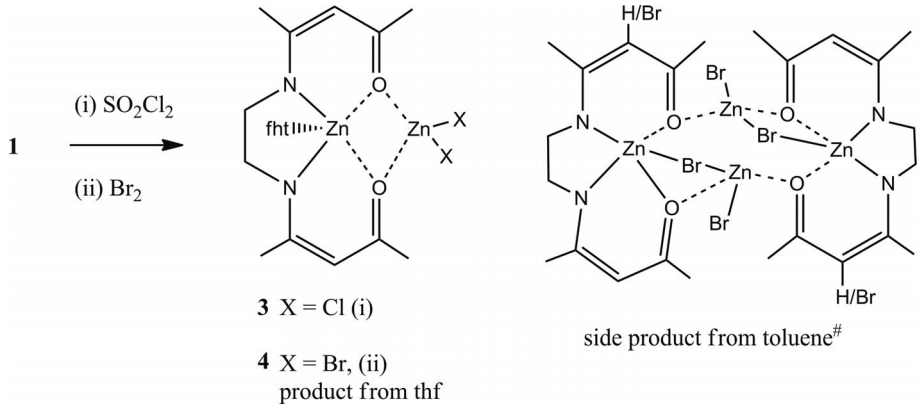

Scheme 2. Synthesis of complexes **3** and **4** (# details in the Supporting Information).

ing block for the synthesis of larger cages or supramolecular structures. To this end, complex **1** was treated with SO_2Cl_2 or Br_2 with the aim of halogenating the zinc centres, which would then allow for zinc functionalization (Scheme 2).

From the structures of complexes **3** and **4** (Figure 4), it can be seen that the addition of sulfuryl chloride or bromine to solutions of **1** in thf results in the binuclear zinc complexes [**L**Zn(thf)·ZnX_2] [X = Cl (**3**), Br (**4**)]. Complexes **3** and **4** are isostructural; their crystal structures differ only by the presence of a lattice thf molecule in the chloride derivative **3**.

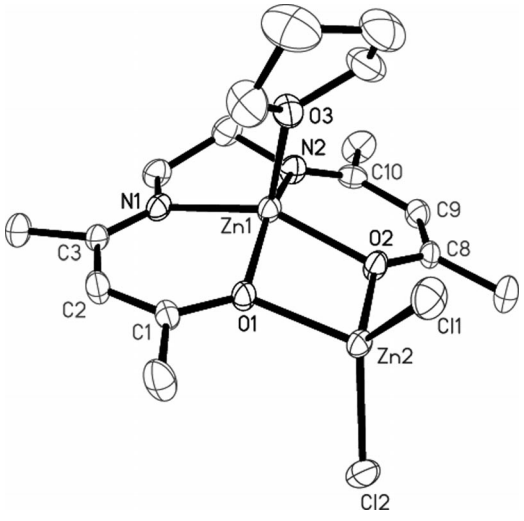

Figure 4. Crystal structure of complex **3** [**L**Zn(thf)·$ZnCl_2$] (also representative of complex **4**). Thermal ellipsoids are drawn at the 30% probability level. Hydrogen atoms and a disordered lattice thf molecule are omitted for clarity. Selected bond lengths [Å] and angles [°]: Zn2–Cl1 2.1964(18), Zn2–Cl2 2.2007(17), O1–Zn2 2.007(4), O2–Zn2 2.023(4); N1–Zn1–O3 108.22(19), O1–Zn2–O2 80.02(15), Cl1–Zn2–Cl2 121.74(7). Complex **4**: Zn2–Br1 2.3399(7), Zn2–Br2 2.3476(7), O1–Zn2 2.013(3), O2–Zn2 2.013(4); N1–Zn1–O3 106.81(16), O1–Zn2–O2 79.00(11), Br1–Zn2–Br2 119.90(2).

The two zinc atoms have two different coordination environments. The central Zn atom, labelled Zn1, is five-coordinate and chelated by two nitrogen and two oxygen atoms in square-pyramidal geometry. The N/O donor atoms chelate Zn1 in the basal plane, whereas a thf molecule in the axial position causes the zinc atom to deviate from the NO–NO plane. The second zinc atom, labelled Zn2, is four-coordinate and ligated to two oxygen atoms through dative interactions with angles that range from 79.00(11) to 121.98(2)°. The Zn–Zn separations are similar, 3.0720(9) Å in **3** and 3.1088(6) Å in **4**, the latter slightly longer to accommodate the presence of the larger bromide atoms. The increase in coordination number by the incorporation of a solvent molecule into the coordination sphere is because of the inability of the Schiff base to provide a tetrahedral environment for the zinc centres.[8] More recently it has been demonstrated that zinc favours five-coordination in salen-type complexes.[16] The Zn–O and Zn–N bond lengths are within the normal range, 2.028(5)–2.076(6) Å,[11] as are the Zn–X distances, which correspond well with literature values of 2.3–2.4 Å.[17] Coordination by an additional ZnX_2 fragment to the carbonyl oxygen atoms causes a narrowing of the O–Zn–O angle with respect to the value of about 109° generally found in M(acen) units.[18] The secondary zinc atom, Zn2, associated with each ligand has two halide atoms attached, which suggests a dative interaction with the carbonyl oxygen atom, although similarly to **1**, there is likely to be some delocalization over the ligand system. These dative bonds are longer than the Zn–O bonds for Zn1 in the NO chelate but are similar to other reported values.[19]

Related to complexes **3** and **4** are the complexes [H_2**L**·$ZnCl_2$] and [**L**Fe·$ZnCl_2$], reported by Velezheva et al.[20] and Floriani et al.,[21] respectively. [H_2**L**·$ZnCl_2$] was prepared from the direct reaction of H_2**L** with anhydrous $ZnCl_2$ in dichloromethane and is a mononuclear zinc complex in which the zinc(II) chloride is coordinated to the ligand through two oxygen atoms in a similar fashion to Zn2 in **3** and **4**. Velezheva and co-workers were studying the Nenitzescu indole synthesis and found that the mononuclear complex failed to react with *p*-benzoquinone, but when deprotonated with triethylamine, increased activity and decreased reaction times were observed. The deprotonated enaminone–$ZnCl_2$ was proposed to be an intermediate in the Nenitzescu reaction with diketodienamines, which suggests possible catalytic applications for complexes **3** and **4**.

[LFe·$ZnCl_2$], from the reaction of the transition-metal Schiff base complex [**L**Fe] with $ZnCl_2$, is a further related complex and isostructural to complex **4**.[21] Given that binuclear complexes could be formed by direct reaction of the ligand with the metal halide, H_2**L** was treated at reflux with $ZnCl_2$ (2 equiv.) in thf in the presence of a base. Crystals of H_2**L** and $[ZnCl_2·(thf)_2]_n$ were isolated, but no zinc complex was isolated. In a further attempt to obtain dinuclear products, H_2**L** was deprotonated at –78 °C with BuLi and then treated with $ZnCl_2$ (2 equiv.). Numerous attempts to obtain crystalline materials were unsuccessful and NMR spectroscopy was inconclusive about the nature of the product.

Attempts to form the iodide analogue of complexes **3** and **4** led to **5** (Figure 5), presumably due to the presence of **2** in the in situ preparation of **1** and adventitious oxygen or moisture. Nevertheless, **5** can be reproducibly prepared but in lower yield than complexes **3** and **4**.

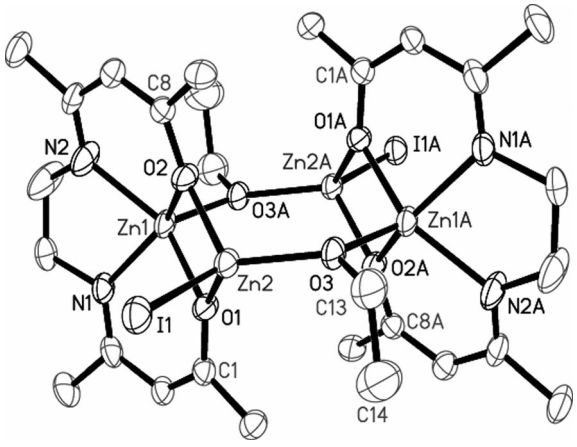

Figure 5. Crystal structure of **5**. Thermal ellipsoids are drawn at 30% probability and hydrogen atoms are omitted for clarity. Selected bond lengths [Å] and angles [°]: Zn2–I1 2.5455(11), Zn2–O1 2.004(4), Zn2–O2 1.985(4), Zn2–O3 1.914(4); Zn2–O3–Zn1A 128.8(2), I1–Zn2–O1 113.69(14).

The dimeric structure of **5** is generated through a bridged ethoxide group. The ethoxide group is likely a result of the elimination of ethane and subsequent oxygen insertion into the reactive Zn–Et bond, as has previously been observed.[22] The Zn–Zn (Zn1–Zn2a) separation of 3.5057(13) Å is quite short and is attributed to the smaller, more electronegative bridging ethoxide. Zinc iodide complexes are less common than their lighter halogen congeners, and zinc iodide complexes with a reactive alkoxide group are limited to just a handful.[23] Williams and coworkers carried out an extensive study on dinuclear zinc complexes by utilizing *p*-cresol as a bridging ligand between the zinc centres.[23a] In this study, [**L**Zn_2(μ-OEt)I_2] [**L** = 2,6-bis(R)-*p*-cresol, R = $CH_2NMe(CH_2)_2NMe_2$], was structurally characterized with similar metric parameters to those found in **5** and was found to be an active initiator for the ring-opening polymerization of lactide.[23a]

The incorporation of adventitious oxygen in complex **5**, which results in a zinc ethoxide group, prompted us to investigate the stability of polymer **2**. Evidence for the insertion of oxygen into the reactive Zn–Et bond was obtained by the diffusion of air into a solution of **2** in toluene. Large, colourless crystals of a pentanuclear zinc cage, [(**L**Zn·$ZnEt)_2${$Zn(μ-OEt)_4$}], complex **6**, were isolated in 24% yield. The solid-state analysis of **6** (Figure 6) shows that the polymeric form of **2** has been disrupted by insertion of oxygen into the Zn–Et bonds, thereby resulting in a central $Zn(OEt)_4$ fragment that links two Zn_2**L** units. Interestingly, the ethyl groups on Zn2 and Zn4 remain intact with no further reactivity observed even when the reaction time is increased. Further reactions with O_2 in an attempt to generate larger alkoxide cages is ongoing work because of their rich structural and bonding applications and their related applications.[24]

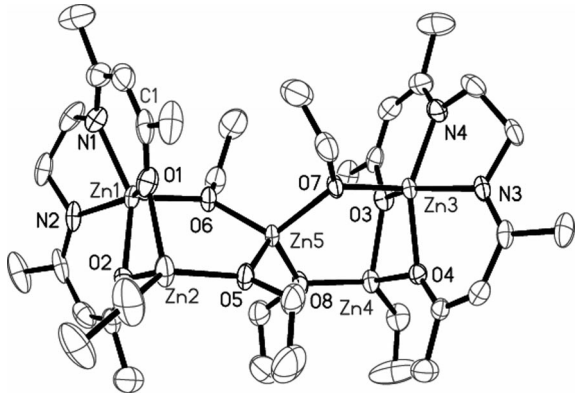

Figure 6. Crystal structure of **6**, [(**L**Zn·$ZnEt)_2${$Zn(μ-OEt)_4$}]. Thermal ellipsoids are drawn at 30% probability level and hydrogen atoms are omitted for clarity. Selected bond lengths [Å] and angles [°]: Zn1–O6 1.946(3), Zn2–O5 1.951(4), Zn2–O2 2.057(4), Zn3–O4 2.045(4), Zn3–O3 2.045(4), Zn4–O8 1.941(4), Zn4–O4 2.074(4), Zn5–O6 1.948(3), Zn5–O5 1.964(4); N2–Zn1–O2 88.7(2), O5–Zn2–O2 95.41(17), N3–Zn3–O4 88.80(17), O7–Zn3–O3 99.88(16), O8–Zn4–O4 95.50(16), O6–Zn5–O7 117.33(17), O6–Zn5–O5 108.61(14).

A comparison of the bond lengths and angles between complexes **5** and **6** shows them to be remarkably similar (Table 1). This similarity arises because complexes **5** and **6** are structurally related.

Theoretical Calculations

Theoretical methods have been applied to understand the probable driving force that contributes to the difference in the reaction products. Geometries predicted by DFT methods (gas-phase) are in good agreement with the solid-phase experimental data. Results are given as Supporting Information (Tables S1–S6).

Semiempirical AM1, PM3 and PM6 calculations on tetrameric **1** all predict the gas-phase structure to have C_2 point-group symmetry, whereas B3LYP-DFT with 3-21G and LanL2MB basis sets suggest that **1** has C_1 symmetry. The crystal structure is of C_1 symmetry and is perturbed in the solid state by the packing arrangements of the lattice toluene molecules. Whereas these explicit toluene molecules were not included in the calculations for reasons of compu-

tational efficiency, it still appears that the B3LYP-DFT results more closely represent the symmetry of the crystal structure. The AM1 and PM3 methods yielded consistent Zn–O bond lengths, although in both cases they are 0.1–0.2 Å greater than that of the crystal structure. The Zn–Zn separations are in close agreement with that of the experiments. The PM6 method yielded Zn–O and Zn–N distances within 0.06 Å of experimental values; however, the Zn–Zn separation differs by over 0.5 Å. The PM6 method additionally yields a N–C–C–N torsional angle that varies significantly from planarity, in contrast to the AM1 and PM3 methods. The semiempirical methods do predict some geometry parameters in agreement with the experiments; however, it is clear that none of these semiempirical methods produce geometries of **1** that are in complete agreement with the experimental data. This is emphasized by the semiempirical methods that give preference to a C_2 symmetry structure. The B3LYP-optimized geometry, with the 3-21G basis set on nonmetal atoms and the LanL2MB basis set and associated effective core potential (ECP) on zinc, yields Zn–O, Zn–N and Zn–Zn distances that are consistently larger than that from the experiments, although the deviation is relatively small. Higher levels of theory would be expected to yield more accurate and reliable structures; however, such calculations are not yet routinely feasible.

Calculated structures for complexes **3** and **4** [**L**Zn(thf)·ZnX_2] are in good agreement with the experimental data. Calculations were performed for the two complexes both with and without the explicit thf molecule, for which the effect of the thf molecule is significant. When thf is excluded, then the optimized structure has a quasiplanar geometry around the Zn1 atom. However, the presence of the thf molecule (coordinated to Zn1) causes the Zn–ligand complex to adopt an "envelope-type" arrangement as seen in the solid-state crystal structures (see Figure 4). The coordinated thf molecule even influences the linking N–C–C–N torsional angle and causes it to increase by about 2°. There are some discrepancies between the calculated and observed angles around Zn2, the ZnX_2 moiety. Experimentally, the X–Zn–X, angles are 121.8° for **3** and 119.9° for **4**, whereas the calculated values are 130–131°. The disagreement is even worse if the coordinated thf molecule is not included. Computational data for complex **5** shows good agreement with the experimental data but similarly to **1**, the Zn–O and Zn–N distances are approximately 0.1–0.2 Å longer than observed in the solid state. The small deviations between the experimental and theoretical values are likely due to crystal-packing effects and the close contacts that are predicted for the halogen-containing complexes.

Conclusion

In this paper we have demonstrated the versatile nature of the tetradentate Schiff base ligand H_2**L**, which has been used to prepare a series of high-yielding zinc complexes of varying dimensionalities. Moreover, the described methods are a facile and convenient method for the synthesis of binuclear zinc halide complexes that have numerous end-use applications. Theoretical results are in good agreement with the experimental structures. Further work will examine the catalytic abilities of these complexes. In this respect, an initial preliminary study has shown **2** to ring-open γ-butyrolactone. The chemical reactivity of the zinc halide complexes as building blocks for higher-dimensional zinc cages and clusters.

Experimental Section

General: All manipulations were performed under anaerobic conditions using standard Schlenk techniques. Hexane and toluene were dried with an MBraun-SPS solvent purification system. Tetrahydrofuran was dried and distilled from potassium. The ligand H_2**L** was prepared according to published procedures.[25] All other reagents were purchased from Aldrich and used as received. Crystal data were collected with an Oxford Gemini diffractometer and molybdenum or copper radiation (λ = 0.7107, 1.54178 Å, respectively) at –100 °C. Crystals were mounted on glass fibres by using paratone oil. Structures were solved by direct methods and refined by means of full-matrix least-squares.[26a] Crystal data for **1**–**6** can be found in Table 2. Hydrogen atoms were placed in idealized positions. In complex **3**, there is a highly disordered lattice thf molecule. An initial orientation was determined from the difference map and restrained using bond-length similarity restraints. The thermal parameters were fixed to be equal, and the occupancy was refined. An occupancy of approximately 0.25 was determined, so the molecule was fixed at 0.25. From the residual electron density left on the site, the total occupancy of the site was assumed to be 0.5 of a thf molecule. A second orientation was determined and made similar to the first by using bond-length similarity restraints. The occupancy was set to 0.25 for this second orientation, and this approximation gave decent thermal parameters, which confirmed its validity. Disordered components with less than 0.5 occupancy do not usually refine well anisotropically, and these thf orientations did not, so they were left isotropic for the remainder of the refinement. The residual density on the thf site was mopped up by anisotropic refinement, but the ellipsoids were highly unfavourable and lent no further chemical information to the structure. This structure shows some hallmarks of unresolved twinning, with $F_{obsd.} > F_{calcd.}$, which could be responsible for the higher R values; however, no suitable twin law has been determined. The refinement statistics were greatly improved by using SQUEEZE[26d] and the data for the solvent-removed structure has CCDC reference number 855918. The ^{1}H and ^{13}C NMR spectra were recorded with a Bruker Avance 500 operating at 500.1 and 125.7 MHz, respectively. IR analysis was conducted as Nujol Mulls with NaCl plates with a MIDAC M4000 Fourier transform infrared (FTIR) instrument. Samples for high-resolution mass spectrometry analysis were prepared in a dry box (under N_2). The samples and matrix were dissolved in anhydrous and degassed thf. The sample and matrix were spotted on the sample plate at varied concentrations. The sample plate was maintained under anaerobic conditions and rapidly inserted into the Ultraflex III TOF/TOF mass spectrometer (Bruker Daltonics, Germany) or prepared as a thf solution in the dry box and injected into a Bruker Esquire 6000. Samples were run under positive and negative ionization modes by using α-cyano-4-hydroxycinnamic acid as the matrix. Elemental analysis was recorded at Campbell Microanalytical laboratory, Otago, or at London Metropolitan University. Melting points were determined in capillaries under a nitrogen atmosphere and are uncorrected.

Table 2. Crystal data for compounds **1**–**6**.

	[L_4Zn_4]·2PhMe	[LZn(Et)]$_n$	[LZn(thf)·$ZnCl_2$]·0.5thf	[LZn(thf)·$ZnBr_2$]	[LZn·ZnI(μ-OEt)]$_2$	[(LZn·ZnEt)$_2$-{Zn(μ-OEt)$_4$}]
Chemical formula	$C_{62}H_{88}N_8O_8Zn_4$	$C_8H_{14}NOZn$	$C_{72}H_{120}N_8Cl_8O_{14}Zn_8$	$C_{16}H_{26}Br_2N_2O_3Zn_2$	$C_{28}H_{46}I_2N_4O_6Zn_4$	$C_{36}H_{66}N_4O_8Zn_5$
M_r	1334.88	205.57	2128.32	584.95	1049.97	1009.78
Crystal system	monoclinic	triclinic	monoclinic	triclinic	monoclinic	triclinic
Space group	$P2_1/n$	$P\bar{1}$	$P2_1/n$	$P\bar{1}$	$P2_1/c$	$P\bar{1}$
T [K]	173(2)	173(2)	173(2)	173(2)	173(2)	173(2)
a [Å]	11.0229(2)	7.0314(12)	14.3550(6)	8.0526(2)	10.7581(6)	11.3946(3)
b [Å]	23.0954(4)	8.3361(10)	10.4927(4)	9.8619(3)	15.2307(7)	14.7028(4)
c [Å]	25.2462(4)	9.3193(7)	17.2563(7)	14.1047(4)	11.1079(8)	15.4427(4)
α [°]	90	69.984(9)	90	107.937(2)	90	67.897(2)
β [°]	98.469(2)	70.659(11)	101.494(4)	90.501(2)	101.923(6)	73.303(2)
γ [°]	90	67.696(13)	90	98.665(2)	90	86.350(2)
V [Å^3]	6357.05(19)	461.95(10)	2547.06(18)	1051.69(5)	1780.80(18)	2292.77(11)
Z	4	2	1	2	2	2
Reflections collected	55876	8238	19061	5296	6849	25232
Indep. reflections	12823	2084	6260	5296	3495	10215
Data/restraints/param.	12823/59/745	2084/0/103	6260/42/270	5296/0/226	3495/0/204	10215/0/492
R_{int}	0.0329	0.0391	0.0327	0.0264	0.0358	0.0286
$D_{calcd.}$ [Mgm^{-3}]	1.395	1.478	1.388	1.847	1.958	1.460
F(000)	2800	214	1096	580	1032	1044
R indices (all data)	$R1$ = 0.0663, $wR2$ = 0.1339	$R1$ = 0.0394, $wR2$ = 0.0730	$R1$ = 0.0923, $wR2$ = 0.2636	$R1$ = 0.0564, $wR2$ = 0.1209	$R1$ = 0.0661, $wR2$ = 0.1263	$R1$ = 0.0869, $wR2$ = 0.1589
Final R indices [$I > 2\sigma(I)$]	$R1$ = 0.0488, $wR2$ = 0.1222	$R1$ = 0.0321, $wR2$ = 0.0700	$R1$ = 0.0756, $wR2$ = 0.2556	$R1$ = 0.0448 $wR2$ = 0.1138	$R1$ = 0.0453, $wR2$ = 0.1121	$R1$ = 0.0611, $wR2$ = 0.1398
Largest diff. peak/hole [e Å^{-3}]	1.595/–0.640	0.556/–0.302	1.163/–0.760	3.280/–0.579	0.607/–0.746	4.080/–2.400 (0.9 Å from Zn2)

CCDC-840517 (for **1**), -840518 (for **2**), -840519 (for **3**), -840520 (for **4**), -840522 (for **5**) and -840840 (for **6**) contain the supplementary crystallographic data for this paper. These data can be obtained free of charge from The Cambridge Crystallographic Data Centre via www.ccdc.cam.ac.uk/data_request/cif.

Synthesis of [L_4Zn_4] (1): H_2**L** (0.3 g, 1.3 mmol) was dissolved in toluene and cooled to –78 °C. $ZnEt_2$ (1.82 mL, 2.73 mmol of a 1.5 M solution in hexanes) was added dropwise. The resultant pale yellow solution was warmed to room temperature and stirred for around 6 h. The toluene solution was concentrated and stored at room temperature overnight to afford pale yellow crystals of **1**; yield 0.34 g, (77%); m.p. 151–156 °C (turned red). ^{1}H NMR (500 MHz, C_6D_6): δ = 4.81, (s, CH), 3.26 (br. quartet of doublets, –NCH_2), 1.98, 1.36 (s, –CH_3), 194.0 (*C*O), 161.2 (*C*N), 95.2 (CH), 42.3 (NC), 28.1, 17.3 (CH_3) ppm. IR (Nujol mull): $\tilde{\nu}$ = 1579, 1504 (CO, CN) cm^{-1}. Elemental analysis calcd. C 50.10, H 6.31, N 9.73; found C 50.81, H 5.78, N 9.92.

Synthesis of [LZn(Et)]$_n$ (2): $ZnEt_2$ in heptanes (3.6 mL, 1.5 M, 5.4 mmol, 1:4 ratio) was added to a stirred solution of H_2**L** in toluene (0.3 g, 1.34 mmol) at –78 °C. The solution was slowly warmed to ambient temperature and stirred for around 16 h. The reaction mixture was concentrated, filtered and slow-cooled for crystallization. Successive concentrations under vacuum reduced the volume to around 5 mL. Colourless crystals of **2** could be isolated after overnight storage at –30 °C; yield 0.20 g, (74%); m.p. from 87 to 200 °C the clear crystals gradually turned yellow-brown, and at 220 °C they decomposed and turned black. ^{1}H NMR (500 MHz, C_6D_6): the NMR spectra was quite complicated, which is attributed to the likely existence of monomer and dimer formation: δ = 4.54, 4.52, 4.47, 4.46 (overlapping singlets, CH), 2.0–2.5 (overlapping signals, O*C*$H_2$$CH_3$), 1.65, 1.62 (s), 1.18–1.41 (br. m, CH_3) ppm. ^{13}C NMR: δ = 183.1, 180.9, 173.0, 172.7, 169.4, 97.5, 96.3, 49.2, 46.7, 26.2, 21.3, 20.0, 19.8 ppm. IR (Nujol mull): $\tilde{\nu}$ = 1577, 1459 cm^{-1} (CO, CN). Elemental analysis calcd. C 46.74, H 6.86, N 6.81; found 46.27, H 5.59, N 6.31.

Synthesis of [LZn(thf)·$ZnCl_2$] (3): Compound **1** (0.5 g, 0.43 mmol) was dissolved in toluene/thf (80:20, 40 mL) and cooled to –78 °C. SO_2Cl_2 (0.14 mL, 1.7 mmol) was added dropwise at –78 °C. The pale yellow reaction mixture was removed from the cold bath, allowed to reach room temperature and stirred for 7 h. The reaction mixture was concentrated and the toluene solution was filtered into a clean Schlenk flask. Storage of the solution at –30 °C for 48 h afforded colourless crystals of **3**; yield 0.15 g (65%); m.p. 111–115 °C (decomp.). ^{1}H NMR (500 MHz, $CDCl_3$): δ = 11.28 (br. s, NH/OH) (due to a small amount of decomposition to free ligand), 5.09 (CH), 3.6 and 1.78 (m, thf), 2.22 (br. s, CH_2), 1.96 (s, CH_3) ppm. (The second CH_3 peak was not observed as it was obscured by a multiplet from thf). ^{13}C NMR: CO, CN not observed. Variable-temperature (VT) NMR to 0 °C and altering the relaxation delay were not successful. δ = 97.7 (CH), 67.9 (thf), 43.2 (NCCN), 28.4 (thf), 25.6, 19.1 (CH_3) ppm. IR (Nujol mull): $\tilde{\nu}$ = 1597, 1543 (CO, CN) cm^{-1}. Satisfactory elemental analysis could not be obtained. The crystal structure of **3** has a disordered thf molecule at 0.5 occupancy. Attempts were made to obtain acceptable elemental analysis on pure crystals and on material that had been dried under vacuum but were unsuccessful.

Synthesis of [LZn(thf)·$ZnBr_2$] (4): H_2**L** (0.6 g, 2.6 mmol) was dissolved in toluene/thf (80:20, 40 mL) and cooled to –78 °C. $ZnEt_2$ (5.4 mL, 1.5 M) was added dropwise. The resultant pale yellow solution was warmed to room temperature and stirred for around 6 h. The solution was recooled to –78 °C and Br_2 (0.12 mL, 2.6 mmol) was added slowly dropwise. An immediate colour change to a bright orange solution was observed. The orange colour faded as the solution warmed to room temperature and returned to the initial yellow solution. The reaction mixture was concentrated, which caused the formation of a precipitate. The toluene solution was filtered into a clean Schlenk flask. Storage of the toluene solution overnight at –30 °C afforded colourless crystals of **4**. The remaining precipitate was dissolved in thf and also filtered and placed in the freezer overnight. A low-yielding dimeric product, [LZn(-μBr)-

ZnBr]$_2$ (**7**), was isolated. Details of the crystal structure of this complex can be found in the Supporting Information. Yield of **4**: 0.49 g (31%); m.p. 180–187 °C (turned orange). ^{1}H NMR (500 MHz, $CDCl_3$): δ = 5.09, 4.79 (CH), 3.68 and 1.79 (m, thf), 2.24 (br. t, ^1J = 16 Hz, CH_2), 1.88, 2.00 (s, CH_3) ppm. ^{13}C NMR: δ = 167.3 (CO), CN not observed, 97.1 (CH), 67.1 (thf), 46.8, 42.3 (NCCN), 30.2 (thf), 28.7, 24.5, 20.6, 18.3 (CH_3) ppm. IR (Nujol mull): $\tilde{\nu}$ = 1608, 1541 (CO, CN) cm^{-1}. LRMS calcd. for [**L**ZnBr_2(K)] 486; found 487. Elemental analysis calcd. C 32.85, H 4.48, N 4.79; found C 32.41, H 4.32, N 4.39.

Synthesis of [LZn·ZnI(μ-OEt)]$_2$ (5): H_2**L** (0.3 g, 1.3 mmol) was dissolved in toluene, cooled to –78 °C, and $ZnEt_2$ (2.7 mL) was added dropwise (4.0 mmol of a 1.5 M solution). The resultant pale yellow solution was warmed to room temperature and stirred for around 2 h. The solution was recooled to –78 °C and freshly sublimed I_2 (0.16 g, 1.3 mmol) was added by a solid addition funnel. The solution became dark purple and faded to colourless over a few hours. The solution was concentrated, filtered and stored at –30 °C for 3 d, after which time colourless crystals of **5** were isolated; yield 0.29 g (42%); m.p. 192–193 °C, turned purple/brown, melted 201–202 °C to a purple solution. The product had limited solubility in deuterated benzene or toluene. The compound was soluble in deuterated chloroform; however, a white precipitate was observed, and only weak signals attributed to the ethoxide group were observed. ^{1}H NMR (500 MHz, $CDCl_3$): δ = 4.73 (s, 2 H, C–*H* backbone), 3.61, 3.33 (d, ^1J = 13.6 Hz, NCH_2CH_2N), 1.84, 1.83 (overlapping singlets, CH_3, 6 H each) ppm. ^{13}C NMR (500 MHz, $CDCl_3$): δ = 180.6 (*C*O), 173.5 (*C*N), 96.9 (C-H), 49.5 (N*C*H_2*C*H_2N), 26.4, 21.9 (*C*H_3) ppm. IR (Nujol mull): $\tilde{\nu}$ = 1574, 1511 cm^1. LRMS calcd. (negative mode) 796; found 796 [M – 2I]$^-$; calcd (positive mode) 541; found 541 [1/2M + O]$^+$. The elemental analysis for carbon was not within the acceptable limit due to rapid sample decomposition.

Synthesis of [(LZn·ZnEt)$_2${Zn(μ-OEt)$_4$}] (6): Polymer **2** was prepared as described above and the unit-cell parameters of the crystalline material checked. Compound **2** was redissolved in toluene and left in the Schlenk flask with the tap open to air for slow diffusion into the solution. After 48 h large yellow crystals of **6** were isolated; yield 0.23 g (24%); m.p. 165–167 °C started to turn brown, decomposed at 201–204 °C. ^{1}H NMR (500 MHz, C_6D_6): δ = 4.7 (s, CH), 3.59, 2.88, (d, ^1J = 15.6 Hz, NCH_2CH_2N), 2.0 (t, OCH_2CH_3), 1.92, 1.62 (CH_3), 1.42 [br. q, OCH_2CH_3] ppm. ^{13}C NMR: δ = 182.0 (*C*O), 173.9 (*C*N), 97.3 (*C*H), 50.2 (N*CC*N), not observed (O*C*H_2CH_3), 27.2, 22.3, 21.1 (CH_3) ppm. IR (Nujol mull): $\tilde{\nu}$ = 1578, 1508 cm^{-1}. Elemental analysis calcd. C 42.82, H 6.59, N 5.40; found C 42.67, H 6.46, N 5.55.

Theoretical Methods: Unless otherwise noted, calculations were carried out within the Gaussian 09 suite of programs.[27] Geometries were optimized in the absence of solvent. Semiempirical AM1, PM3 and PM6 methods were utilized in the geometry optimization of complex **1**. All density functional theory (DFT) calculations employed the B3LYP functional.[28] Unless otherwise noted, the 6-31G(d) basis set[29] was used for all H, C, N, O and Cl atoms. The LANL2DZ basis set and effective-core potential (ECP) were employed for Zn, Br and I.[30] For complex **1**, the 3-21G basis set[31] and LANL2MB basis and ECP[32] were used. An SCF convergence criteria of 10^{-8} a.u. was employed throughout. Geometry optimizations with Grimme's third-generation dispersion correction (D3)[33] in conjunction with the B3LYP functional (D3-B3LYP) were carried out within GAMESS-US.[34]

Supporting Information (see footnote on the first page of this article): Computational data with calculated bond lengths and angles.

Acknowledgments

A. F. R. acknowledges the Australian Research Council for the award of a Future Fellowship (FT100100003). D. J. D. W. acknowledges support from the National Computational Infrastructure National Facility (NCI-NF), Victorian Partnership for Advanced Computing (VPAC), Victorian Life Science Computing Initiative (VLSCI) and the high-performance computing facility of La Trobe University.

[1] a) D. J. Darensbourg, *Chem. Rev.* **2007**, *107*, 2388; b) M. L. Mejía, J. H. Rivers, S. F. Swingle, Z. Lu, X. Yang, M. Findlater, G. Reeske, B. J. Holliday, *Main Group Chem.* **2010**, *9*, 167.
[2] a) M. E. Germain, M. J. Knapp, *J. Am. Chem. Soc.* **2008**, *130*, 5422; b) P. Wang, Z. Hong, Z. Xie, S. Tong, O. Wong, C.-S. Lee, N. Wong, L. Hung, S. Lee, *Chem. Commun.* **2003**, 1664; c) G. Yu, S. Yin, Y. Liu, Z. Shuai, D. Zhu, *J. Am. Chem. Soc.* **2003**, *125*, 14816; d) J. Zhang, S. Gao, C.-M. Che, *Eur. J. Inorg. Chem.* **2004**, 956.
[3] a) A. K. Cheetham, C. N. R. Rao, R. K. Feller, *Chem. Commun.* **2006**, 4780; b) M. Eddaoudi, J. Kim, N. Rosi, D. Vodak, J. Wachter, M. O'Keeffe, O. M. Yaghi, *Science* **2002**, *295*, 469; c) B. Wang, A. P. Côté, H. Fukukawa, M. O'Keefe, O. M. Yaghi, *Nature* **2008**, *453*, 207; d) O. M. Yaghi, M. O'Keeffe, N. W. Ockwig, H. K. Chae, M. Eddaoudi, J. Kim, *Nature* **2003**, *423*, 705.
[4] A. L. Johnson, N. Hollingsworth, G. Kociok-Köhn, K. C. Molloy, *Inorg. Chem.* **2008**, *47*, 12040.
[5] L. A. Lesikar, A. F. Gushwa, A. F. Richards, *J. Organomet. Chem.* **2008**, *693*, 3245.
[6] a) V. Patroniak, P. N. W. Baxter, J.-M. Lehn, M. Kubicki, M. Nissinen, K. Rissanen, *Eur. J. Inorg. Chem.* **2003**, 4001; b) C. Piguet, G. Bernardinelli, G. Hopfgartner, *Chem. Rev.* **1997**, *97*, 2005; c) B.-X. Zhu, Q.-L. Zhang, Y.-Q. Zhang, T. Zhu, J. K. Clegg, L. F. Lindoy, G. Wei, *Inorg. Chem.* **2008**, *47*, 10053.
[7] O. Kotova, S. Semenov, S. Eliseeva, S. Troyanov, K. Lyssenko, N. Kuzmina, *Eur. J. Inorg. Chem.* **2009**, 3467.
[8] a) G. E. Batley, D. P. Graddon, *Aust. J. Chem.* **1967**, *20*, 877; b) G. E. Batley, D. P. Graddon, *Aust. J. Chem.* **1967**, *20*, 885.
[9] a) Z. He, C. He, Z.-M. Wang, E.-Q. Gao, Y. Liu, C.-H. Yan, *Dalton Trans.* **2004**, 502; b) M. Fondo, A. M. García-Diebe, N. Ocampo, J. Sanmartin, M. R. Bermejo, *Dalton Trans.* **2004**, 2135; c) S. Range, D. F.-J. Piesik, S. Harder, *Eur. J. Inorg. Chem.* **2008**, *22*, 3442.
[10] N. Bresciani-Pahor, M. Calligaris, G. Nordin, L. Randaccio, *Acta Crystallogr., Sect. B: Struct. Sci.* **1979**, *35*, 2776.
[11] a) A. P. Dove, V. C. Gibson, E. L. Marshall, A. J. P. White, D. J. Williams, *Dalton Trans.* **2004**, 570; b) F. H. Van der Steen, J. Boersma, A. L. Spek, G. Van Koten, *Organometallics* **1991**, *10*, 2467; c) J. Vela, L. Zhu, C. J. Flaschenriem, W. W. Brennessel, R. J. Lachicotte, P. L. Holland, *Organometallics* **2007**, *26*, 3416.
[12] a) N. Meyer, K. Lohnwitz, A. Zulys, P. W. Roesky, M. Dochnahl, S. Blechert, *Organometallics* **2006**, *25*, 3730; b) G. Parkin, *Chem. Rev.* **2004**, *104*, 699.
[13] Cambridge Crystallographic Database, version 1.13.
[14] a) D. J. Doyle, V. C. Gibson, A. J. P. White, *Dalton Trans.* **2007**, 358; b) E. Wissing, R. W. A. Havenith, J. Boersma, W. J. J. Smeets, A. L. Spek, G. van Koten, *J. Org. Chem.* **1993**, *58*, 4228.
[15] Y. Huang, W.-C. Hung, M.-Y. Liao, T.-E. Tsai, Y.-L. Peng, C.-C. Lin, *J. Polym. Sci., Part 1, Polym. Chem.* **2009**, *47*, 2318.
[16] a) M. E. Germain, T. R. Vargo, P. G. Khalifah, M. J. Knapp, *Inorg. Chem.* **2007**, *46*, 4422; b) J. Reglinski, S. Morris, D. E. Stevenson, *Polyhedron* **2002**, *21*, 2175.
[17] a) L. E. Breyfogle, C. K. Williams, J. V. G. Young, M. A. Hillmyer, W. B. Tolman, *Dalton Trans.* **2006**, 928; b) R. S. Forgan, J. E. Davidson, S. G. Galbraith, D. K. Henderson, S. Parsons, P. A. Tasker, F. J. White, *Chem. Commun.* **2008**, 4049; c)

R. A. Gossage, P. N. Yadav, T. D. MacInnis, J. W. Quail, A. Decken, *Can. J. Chem.* **2009**, *87*, 368.
[18] M. D. Hobday, T. D. Smith, *Coord. Chem. Rev.* **1973**, *9*, 311.
[19] a) S. C. Goel, M. Y. Chiang, W. E. Buhro, *J. Am. Chem. Soc.* **1991**, *113*, 7069; b) L.-C. Yu, L. Lai, R. Xia, S.-L. Liu, *J. Coord. Chem.* **2009**, *62*, 1313.
[20] V. S. Velezheva, A. I. Sokolov, A. G. Kornienko, K. A. Lyssenko, Y. V. Nelyubina, I. A. Godovikov, A. S. Peregudov, A. F. Mironov, *Tetrahedron Lett.* **2008**, *49*, 7106.
[21] E. Solari, F. Corazza, C. Floriani, A. Chiesi-Villa, C. Guastini, *J. Chem. Soc., Dalton Trans.* **1990**, 1345.
[22] a) J. Lewiński, M. Dranka, W. Bury, W. Śliwiński, I. Justyniak, J. Lipkowski, *J. Am. Chem. Soc.* **2007**, *129*, 3096; b) J. Lewiński, W. Śliwiński, M. Dranka, I. Justyniak, J. Lipkowski, *Angew. Chem.* **2006**, *118*, 4944; *Angew. Chem. Int. Ed.* **2006**, *45*, 4826; c) J. Lewiński, W. Marciniak, J. Lipkowski, I. Justyniak, *J. Am. Chem. Soc.* **2003**, *125*, 12698.
[23] a) P. D. Knight, A. J. P. White, C. K. Williams, *Inorg. Chem.* **2008**, *47*, 11711; b) S. J. Wezenberg, E. C. Escudero-Adan, J. Benet-Bucholz, A. W. Kleij, *Chem. Eur. J.* **2009**, *15*, 5695.
[24] a) E. Grunova, T. Roisnel, J.-F. Carpentier, *Dalton Trans.* **2009**, 9010; b) C. K. Williams, L. E. Breyfogle, S. K. Choi, W. Nam, V. G. Young Jnr, M. A. Hillmyer, W. B. Tolman, *J. Am. Chem. Soc.* **2003**, *125*, 11350; c) R. M. Haak, A. Decortes, E. C. Escudero-Adán, M. Martínez Belmonte, E. Martin, J. Benet-Buchholz, A. W. Kleij, *Inorg. Chem.* **2011**, *50*, 7934.
[25] X. Pang, H. Du, X. Chen, X. Wang, X. Jing, *Chem. Eur. J.* **2008**, *14*, 3126.
[26] a) O. V. Dolomanov, L. J. Bourhis, R. J. Gidea, J. A. K. Howard, H. Peschmann, *J. Appl. Crystallogr.* **2009**, *42*, 339; b) G. M. Sheldrick, *SHELXS-97*, Program for the solution of crystal structures, University of Göttingen, Germany, **1997**; c) G. M. Sheldrick, *SHELXL-97*, Program for the refinement of crystal structures, University of Göttingen, Germany, **1997**; d) A. L. Spek, **2005**, *PLATON*, A Multipurpose Crystallographic Tool, Utrecht University, Utrecht, The Netherlands.
[27] M. J. Frisch, G. W. Trucks, H. B. Schlegel, G. E. Scuseria, M. A. Robb, J. R. Cheeseman, G. Scalmani, V. Barone, B. Mennucci, G. A. Petersson, H. Nakatsuji, M. Caricato, X. Li, H. P. Hratchian, A. F. Izmaylov, J. Bloino, G. Zheng, J. L. Sonnenberg, M. Hada, M. Ehara, K. Toyota, R. Fukuda, J. Hasegawa, M. Ishida, T. Nakajima, Y. Honda, O. Kitao, H. Nakai, T. Vreven, J. J. A. Montgomery, J. E. Peralta, F. Ogliaro, M. Bearpark, J. J. Heyd, E. Brothers, K. N. Kudin, V. N. Staroverov, R. Kobayashi, J. Normand, K. Raghavachari, A. Rendell, J. C. Burant, S. S. Iyengar, J. Tomasi, M. Cossi, N. Rega, J. M. Millam, M. Klene, J. E. Knox, J. B. Cross, V. Bakken, C. Adamo, J. Jaramillo, R. Gomperts, R. E. Stratmann, O. Yazyev, A. J. Austin, R. Cammi, C. Pomelli, J. W. Ochterski, R. L. Martin, K. Morokuma, V. G. Zakrzewski, G. A. Voth, P. Salvador, J. J. Dannenberg, S. Dapprich, A. D. Daniels, Ö. Farkas, J. B. Foresman, J. V. Ortiz, J. Cioslowski, D. J. Fox, *Gaussian 09*, revision A.1, Gaussian, Inc., Wallingford CT, **2009**.
[28] a) A. D. Becke, *Phys. Rev. A* **1988**, *38*, 3098; b) A. D. Becke, *J. Chem. Phys.* **1993**, *98*, 5648; c) C. Lee, W. Yang, R. G. Parr, *Phys. Rev. B: Condens. Matter* **1988**, *37*, 785.
[29] a) T. Clark, J. Chandrasekhar, G. W. Spitznagel, P. v. R. Schleyer, *J. Comput. Chem.* **1983**, *4*, 294; b) W. J. Hehre, R. Ditchfield, J. A. Pople, *J. Chem. Phys.* **1972**, *56*, 2257.
[30] a) T. H. Dunning Jr, P. J. Hay, in: *Methods of Electronic Structure Theory* (Ed.: H. F. Schaefer III), Plenum Press, **1977**, vol. 2; b) P. J. Hay, W. R. Wadt, *J. Chem. Phys.* **1985**, *82*, 270.
[31] a) J. S. Binkley, J. A. Pople, W. J. Hehre, *J. Am. Chem. Soc.* **1980**, *102*, 939; b) M. S. Gordon, J. S. Binkley, J. A. Pople, W. J. Pietro, W. J. Hehre, *J. Am. Chem. Soc.* **1982**, *104*, 2797.
[32] a) J. B. Collins, P. v. R. Schleyer, J. S. Binkley, J. A. Pople, *J. Chem. Phys.* **1976**, *64*, 5142; b) T. H. Dunning Jr, P. J. Hay, in: *Modern Theoretical Chemistry* (Ed.: H. F. Schaefer III), Plenum, New York, **1976**, *vol. 3*, p. 1; c) W. J. Hehre, R. F. Stewart, J. A. Pople, *J. Chem. Phys.* **1969**, *51*, 2657.
[33] S. Grimme, J. Antony, S. Ehrlich, H. Krieg, *J. Chem. Phys.* **2010**, *132*, 154104.
[34] a) M. W. Schmidt, K. K. Baldridge, J. A. Boatz, S. T. Elbert, M. S. Gordon, J. H. Jensen, S. Koseki, N. Matsunaga, K. A. Nguyen, S. J. Su, T. L. Windus, M. Dupuis, J. A. Montgomery, *GAMESS-US*, 1 Oct **2010** (R3), Iowa State University, Ames, USA, **2010**; b) M. S. Gordon, M. W. Schmidt, in: *Theory and Applications of Computational Chemistry: The First Forty Years* (Eds.: C. E. Dykstra, G. Frenking, K. S. Kim, G. E. Scuseria), Elsevier, Amsterdam, **2005**, p. 1167; c) M. W. Schmidt, K. K. Baldridge, J. A. Boatz, S. T. Elbert, M. S. Gordon, J. H. Jensen, S. Koseki, N. Matsunaga, K. A. Nguyen, S. Su, T. L. Windus, M. Dupuis, J. A. Montgomery, *J. Comput. Chem.* **1993**, *14*, 1347.

Received: October 29, 2011
Published Online: January 24, 2012

DOI: 10.1002/ejic.201101263

Molecular Structure of a Hydridoniobocene Complex $[Nb(\eta^5\text{-}C_5H_4SiMe_3)_2(H)_3]$ and Its Use as Catalyst for the Ring-Opening Polymerization of Cyclic Esters

Carlos Alonso-Moreno,[a] Antonio Antiñolo,*[b] Joaquín C. García-Martínez,[a] Santiago García-Yuste,[b] Isabel López-Solera,[b] Antonio Otero,*[b] Juan C. Pérez-Flores,[b] and Maria T. Tercero-Morales[b]

Keywords: Metallocenes / Ring-opening polymerization / Hydride ligands / Niobium / Lactones

The second polyhydridoniobocene complex that was characterized by X-ray diffraction is reported. On the basis of H–H distances and H–Nb–H angles, $[Nb(\eta^5\text{-}C_5H_4SiMe_3)_2(H)_3]$ (**1**) is classified as a "compressed hydride". Compound **1** acts as an efficient single-component initiator for the ring-opening polymerization of ε-caprolactone and δ-valerolactone. ε-Caprolactone and δ-valerolactone are both polymerized within a few hours to yield high-to-medium-molecular-weight polymers with medium to broad polydispersities. Polymer end-group analysis showed that the polymerization proceeds through a coordination–insertion mechanism based on the cleavage of the ring between the oxygen atom and the acyl carbon atom.

Introduction

Transition metal hydride derivatives are thought to be involved in a wide variety of organic transformations.[1] In this interesting research field, some of us reported the synthesis of various trihydride derivatives of Nb and Ta. Amongst these, $[Nb(\eta^5\text{-}C_5H_4SiMe_3)_2(H)_3]$ (**1**) shows anomalous spectroscopic properties, such as large temperature-dependent H–H coupling constants in its ^1H NMR spectra.[2] It is now well-accepted that the unusual NMR proton spin couplings between labile hydride protons in transition metal trihydride complexes are due to quantum mechanical hydrogen exchange.[3] Additionally, **1** has shown a broad range of interesting reactivity patterns, namely: (1) easy thermal H_2 elimination as a synthetic method for the preparation of 18-electron Nb^{III} $[Nb(\eta^5\text{-}C_5H_4SiMe_3)_2(H)L]$ (L = π-acid ligand) species;[4] (2) σ-bond activation of a considerable number of chemical species (e.g. H–Ge, H–N, H–Si, H–Sn, etc.);[5] (3) insertion reactions of alkynes into the Nb–H bond;[6] (4) formation of acid–base adducts with Lewis acidic coinage (group 11) metal cations[7] or borane species;[8] (5) synthesis and kinetic studies of hydride olefin derivatives.[6] This broad reactivity makes it possible to consider **1** in a prominent place in group 5 transition metal polyhydride derivatives. Over 80 references evidence its impact in the scientific literature, describing its reactivity and special spectroscopic properties.[9]

Despite the rich reactivity of **1**, to the best of our knowledge, styrene polymerization is the only catalytic process that has been reported.[10] In the last two decades of the twentieth century, we have witnessed a paradigm shift from biostable biomaterials to biodegradable biomaterials for medical and related applications.[11] In fact, this current trend has promoted spectacular advances in new polyester materials, with the development of therapeutic devices such as scaffolds for tissue engineering and drug delivery vehicles.[12] Ring-opening polymerization (ROP) is the most appropriate synthetic strategy to produce polyesters.[13] It has been demonstrated that a broad range of organometallic derivatives of the main group metals Al, Ca, Mg, and Sn, as well as transition and rare-earth metals such as Nd, Y, Yb, Sm, La, Fe, Zn, Zr, and Ti, can promote the ROP of cyclic esters.[14] However, the need for biodegradable polymeric materials with novel microstructures and/or properties still requires the synthesis of novel catalysts.

Herein, we describe our latest advances aimed at understanding the structural characterization of **1** by means of X-ray diffraction studies and its reactivity as a single-component initiator for the ROP of lactones under well-controlled conditions.

[a] Departamento de Química Inorgánica, Orgánica y Bioquímica, Facultad de Farmacia, Universidad de Castilla-La Mancha, Campus Universitario de Albacete, 02071 Albacete, Spain
[b] Departamento de Química Inorgánica, Orgánica y Bioquímica, Facultad de Ciencias Químicas, Universidad de Castilla-La Mancha, Campus Universitario de Ciudad Real, 13071 Ciudad Real, Spain
Fax: +34-926-29-53-18
E-mail: Antonio.Otero@uclm.es

Results and Discussion

X-ray Molecular Structure of Complex 1

Attempts to obtain molecular structure proofs in polyhydride complexes are difficult. In fact, a limited number of group 5 polyhydride molecular structures have been reported by X-ray or neutron diffraction techniques.[9] Providentially, single crystals of **1** suitable for study by X-ray diffraction appeared in a saturated solution of **1** in deoxygenated EtOH at 249 K after 2 h. Selected bond lengths and angles are collected in Table 1. The molecular structure is depicted in Figure 1 and consists of a monomeric arrangement in the solid state. To the best of our knowledge, since Koetzle published the crystal structures of $[M(\eta^5\text{-}C_5H_5)_2(H)_3]$ (M = Nb, Ta) in 1977,[15] no other X-ray structures of polyhydridoniobocene complexes have been reported.

Table 1. Selected interatomic bond lengths and angles for **1**.

Bond lengths (Å)[a]		Angles (°)[a]	
Nb1–H1	1.66(3)	H1–Nb1–H2	57(1)
Nb1–H2	1.72(3)	H2–Nb1–H3	62(1)
Nb1–H3	1.69(3)	H1–Nb1–H3	119(1)
H1–H2	1.60(4)	Cent1–Nb1–Cent2	141.9(1)
H2–H3	1.76(4)		
H1–H3	2.87(4)		
Nb1-Cent1	2.061		
Nb1-Cent2	2.060		
Avg. Nb1–C(11–15)	2.386(2)		
Avg. Nb1–C(21–25)	2.387(2)		

[a] Cent1 and Cent2 are the centroids of C11-C15 and C21-C25, respectively.

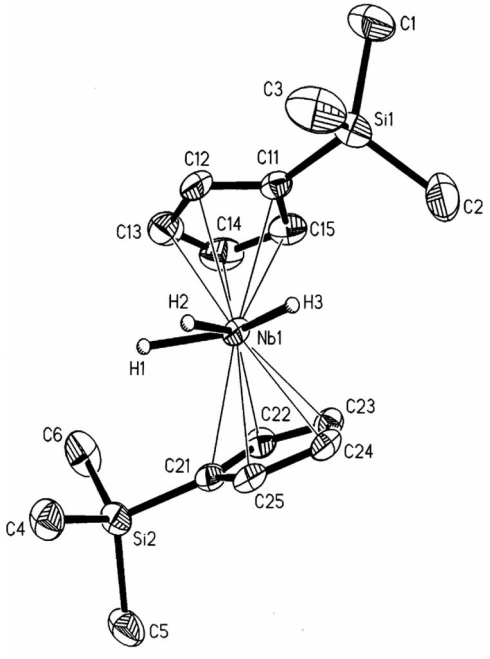

Figure 1. ORTEP view of the molecular structure of **1** with 30% probability ellipsoids. Some hydrogen atoms have been omitted for clarity.

Figure 1 shows the structure of a typical bent niobocene system with three hydride hydrogen atoms bonded to the niobium atom. Both cyclopentadienyl rings are η^5-bonded to the niobium atom in η^5 fashion with a Cent1–Nb1–Cent2 angle of 141.9°. The centroid–niobium distances [2.061(1) and 2.060 (l) Å for centroid 1 and 2, respectively] and the average Nb–C [2.386(2) and 2.387(2) for centroid 1 and 2, respectively] and C–C [1.411(4) and 1.418(3) Å for Cp1 and Cp2, respectively] bond lengths are close to the corresponding values found in $[M(\eta^5\text{-}C_5H_5)_2(H)_3]$ (M = Nb, Ta).[15] The two cyclopentadienyl rings are eclipsed with the two $SiMe_3$ groups in *trans* positions [Si1–Cent1–Cent2–Si2 angle of 150.3°], probably to minimize their mutual repulsion. The average Nb–H distance (1.69 Å) agrees very well with those found in $[Nb(\eta^5\text{-}C_5H_5)_2(H)_3]$[15] and $[Nb(\eta^5\text{-}C_5H_4SiMe_3)_2(\eta^2\text{-}H_2BC_8H_{14})]$.[8] The central H atom is situated in a bisecting position. The differences between the Nb–H bond lengths are not considered to be significant.

The most interesting feature of the structure of **1** is the coordination mode of the hydride ligands.[16] Two marked differences were observed in the parameters of their molecular structure. Firstly, the H1–H2 distance is shorter than the H2–H3 distance. The H1–H2 value of 1.60(4) Å might indicate a "compressed hydride" nature for **1**.[17] The second difference concerns the value of the H1–Nb1–H3 angle, which is 8° lower in **1** than in $[Nb(\eta^5\text{-}C_5H_5)_2(H)_3]$.[15] These two facts seem intuitively to be related, and this led us to envisage a facile H_2 elimination in complex **1** by thermolytic treatment.[2,4] These findings are also consistent with the observed fluxionality of the hydride ligand at high temperature, a process responsible for their special spectroscopic properties.[2,3]

ROP Studies

Following our studies on the preparation of biodegradable polymeric materials by catalytic ROP,[18] we decided to explore the reactivity of **1** in ROP due to the vacant coordination position generated by the easy thermal elimination of H_2. Therefore, **1** was tested for activity in the ROP of lactones in toluene at 60 °C. Complex **1** acts as an efficient single-component initiator for the polymerization of ε-caprolactone (ε-CL) to give high-molecular-weight polymers without a cocatalyst; the results are collected in Table 2. A variety of polymerization conditions were explored (entries 1–7 in Table 2). Complex **1** does not initiate polymerization of ε-CL after 48 h at room temperature (entry 1) but gives almost complete conversion of 500 equiv. of ε-CL in 2 h at 60 °C (entry 2). The polymerization is well-controlled and yields high-molecular-weight polymers with a medium to broad polydispersity (M_w = 53000, M_w/M_n = 1.60). The well-controlled polymerization process is evidenced by a narrow M_w/M_n range and a linear relationship between the experimental M_n and the percentage of conversion (Figure 2). Not unexpectedly, raising the temperature to 130 °C resulted in complete conversion of the monomer within 1 h and a high molecular weight distribution (M_w/M_n = 2.07, entry 4).

Table 2. Polymerization of lactones catalyzed by [Nb(η5-C5H4SiMe3)2(H)3].[a]

Entry	T (°C)	M[f]	Time (h)	Conv. (%)[g]	$M_{n(theor)}$ (Da)	$M_{n(exp)}$ (Da)[h]	M_w/M_n
1	Room temp.	ε-CL	48	Traces	n.d.[i]	n.d.	n.d.
2	60	ε-CL	2	89	50700	53000	1.60
3[b]	60	ε-CL	48	Traces	n.d.	n.d.	n.d.
4	130	ε-CL	1	92	52400	65800	2.07
5[c]	60	ε-CL	1.5	52	59280	72000	1.62
6[d]	60	ε-CL	9	65	33350	39900	1.34
7[e]	60	ε-CL	1	50	28500	20500	1.72
8	60	δ-VL	4	62	31000	30800	1.20
9	130	β-BL	48	Traces	n.d.	n.d.	n.d.
10	130	*rac*-Lac	48	Traces	n.d.	n.d.	n.d.

[a] Polymerization conditions: 90 μmol of initiator, 20 mL of toluene as solvent, $[\varepsilon\text{-CL}]_0/[\text{initiator}]_0 = 500$. [b] 70 μmol of initiator. [c] $[\varepsilon\text{-CL}]_0/[\text{initiator}]_0 = 1000$. [d] 20 mL of THF as solvent. [e] Solvent-free. [f] Monomer. [g] Percentage conversion of the monomer [(weight of polymer recovered/weight of monomer) × 100]. [h] Determined by GPC relative to polystyrene standards in THF. Experimental M_n was calculated considering Mark–Houwink's corrections[19] for M_n [$M_{n(obsd)} = 0.56 \times M_{n(GPC)}$]. [i] Not determined.

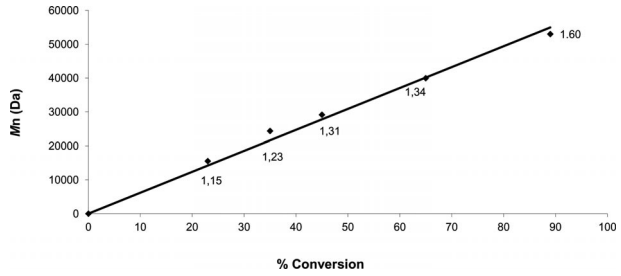

Figure 2. M_n vs. ε-CL conversion, M_w/M_n values are indicated (linear fit, $R^2 = 0.984$).

In these tests, the polymer molecular weights were limited by a monomer/initiator ratio of 500:1. Increasing this ratio twofold gave polymers with significantly higher molecular weights and broader molecular weight distributions (entry 5). Two possibilities can account for the relatively broad polydispersities observed with this complex: (1) initiation is delayed with respect to propagation and (2) backbiting/transesterification reactions take place as side reactions, resulting in the formation of macrocycles with a wide range of molecular weights. The M_n values measured by gel permeation chromatography (GPC) were substantially higher than those predicted on the basis of conversion and the assumption that each niobium center is catalytically active. This deviation is consistent with poor rates of initiation (monomer insertion into the Nb–H bond) relative to propagation (insertion into the Nb–O bond of the growing chains), which is a well-established feature of metal alkyl initiators.[18a,20]

As expected, when the polymerization was carried out in tetrahydrofuran (THF) the activity decreased, and after 9 h only 65% of the monomer was converted (entry 6). This reduced activity can be explained by a competition reaction between the coordinating solvent and the monomer moiety for the metal center. Polycaprolactones (PCLs) can be synthesized both in solution and by bulk polymerization.[21] However, the solution polymerization suffers from certain disadvantages such as being susceptible to the impurity level. The bulk polymerization is thus often preferred for the large-scale production of polyesters.[22] For the bulk polymerization procedure the monomer ε-CL and the initiator were heated at 60 °C. Complex **1** initiates very rapid polymerization of ε-CL in bulk conditions and gives 50% conversion of 500 equiv. of ε-CL in 1 h (entry 7). Under bulk conditions, this complex affords lower-molecular-weight polymers with a higher molecular weight distribution than that of the product in solution. This may be caused by a high level of side reactions, such as interchain or intrachain transesterification, resulting in a chain-transfer reaction.

In order to gain more insight into the reactivity of **1** in ROP, we investigated its use for the polymerization of other monomers of cyclic esters, such as β-butyrolactone (β-BL), δ-valerolactone (δ-VL), and *rac*-lactide (*rac*-Lac). As can be seen in Table 2, **1** is capable of successfully initiating the homopolymerization of δ-valerolactone with similar results observed for ε-caprolactone, albeit with less productivity (entry 8). Unfortunately, for β-butyrolactone and *rac*-lactide, polymerization was unsuccessful: only traces of the polymers were observed in the reactions (entries 9–10).

The polymerizations of ε-CL and δ-VL were monitored over time by manual sampling followed by ^{1}H NMR analysis to determine the degree of monomer conversion. The polymerization kinetics was studied with $[CL]_0/[Nb] = 500$ and $[Nb] = 4.5 \times 10^{-3}$ M at 60 °C in toluene. The semilogarithmic plot of $\ln([M]_0/[M]_t)$ against reaction time is shown in Figure 3, where $[M]_0$ is the initial lactone monomer concentration and $[M]_t$ the lactone concentration at a given reaction time t. In all cases, the linearity of the plot shows that the propagation was first-order with respect to lactone monomer when polymerized at 60 °C in toluene. The linearity of the plot also illustrates that termination reactions did not occur during polymerization. The apparent rate constant (k_{app}) for ε-CL was roughly one order higher than the k_{app} for δ-VL.

The mechanism of ROP depends on the type of initiator. There are three major reaction mechanisms: carbocationic, anionic, and coordination–insertion. However, high-molecular-weight polyesters have only been obtained by using anionic or coordination–insertion ROP.[23] In order to improve our understanding of the initiation mechanism that **1** follows in the ROP process, we have to consider the 18-electron nature of the derivative. This precatalyst must go forward to the true initiator intermediate, which is able to

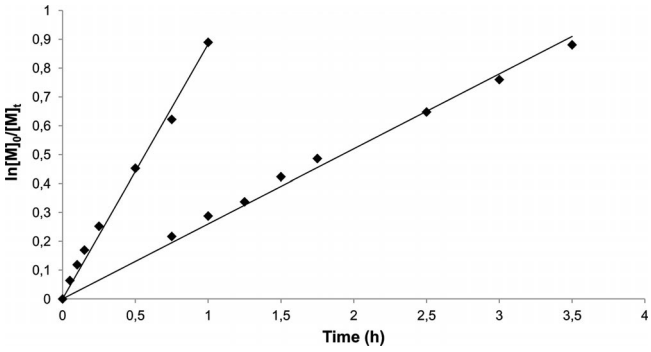

Figure 3. (a) Semilogarithmic plot of ε-CL against time k_{app} = 2.45×10^{-4} s^{-1} (linear fit, R^2 = 0.9918). (b) Semilogarithmic plot of δ-VL vs. time k_{app} = 7.22×10^{-5} s^{-1} (linear fit, R^2 = 0.9924).

coordinate a monomer molecule. We propose an unsaturated 16-electron monohydride intermediate as the initiator, which is easily generated from trihydride **1** by thermal elimination of H_2, which provides an open coordination site (Scheme 1). This intermediate has previously been proposed to be present in different processes.[4,6] Subsequently, a lactone monomer would coordinate to the metal center through the acyl oxygen atom. At this point, two pathways were envisaged for the opening of the lactone ring: cleavage of the bond between the oxygen atom and the alkyl carbon atom (C–O), to form carboxylate active centers, or cleavage of the bond between the oxygen atom and the acyl carbon atom [C(O)–O], resulting in the formation of alkoxide active centers. Mountford et al.[24] explored the ROP mechanism of ε-CL by employing [Eu(η^5-$C_5H_4SiMe_3)_2$H] as the initiator in a DFT study. This work revealed that cleavage of the bond between the oxygen and the acyl carbon atom [C(O)–O] is the most favorable pathway. In a similar way, we could propose an insertion of the coordinated lactone into the Nb–H bond, followed by the generation of a metal alkoxide–aldehyde propagating species. However, an alternative pathway involving direct insertion of the lactone into the Nb–H bond without prior coordination cannot be ruled out.[25] Afterward, a successive nucleophilic substitution at the acyl C=O bond would result in polymer growth. A PCL sample was characterized by matrix-assisted laser desorption time-of-flight mass spectrometry (MALDI-TOF MS) (Figure 4) to ascertain the nature of the initiating group. The MALDI-TOF MS spectrum allowed us to establish beyond doubt the nature of the termini and confirmed that the ROP of ε-CL catalyzed by **1** proceeded by a coordination–insertion mechanism.

The MALDI-TOF MS spectrum was obtained by using *trans*-2-[3-(4-*tert*-butylphenyl)-2-methyl-2-propenylidene]-malononitrile (DCTB) and NaI as matrix and cationization agent, respectively. A typical MALDI-TOF MS spectrum of PCL prepared with this catalyst shows a monotonic distribution of peaks (Figure 4) corresponding to a unique, well-defined polymer structure. The mass spectrum shows a cluster of homologous peaks separated by a molecular mass corresponding to the repeating unit of the analyzed polymer. This peak separation is 114.1 Da andcorresponds

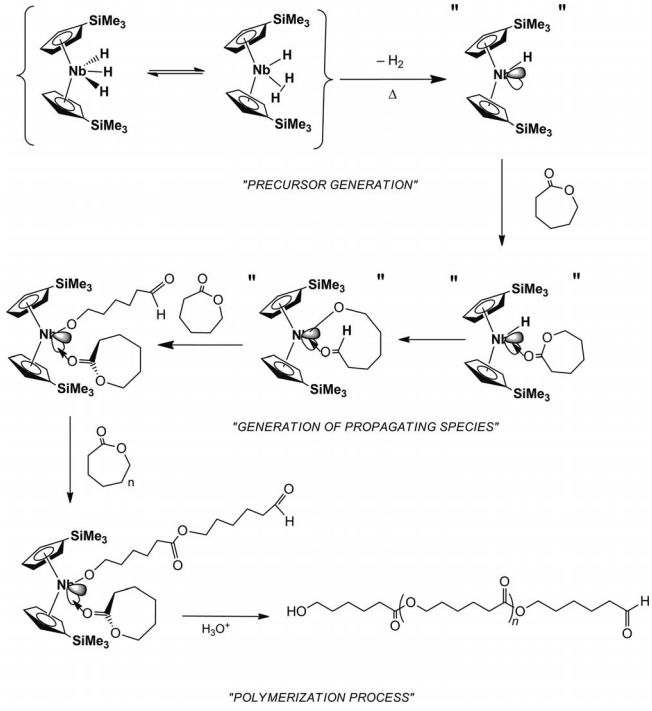

Scheme 1. Reaction path proposed for the ROP of ε-CL by **1**.

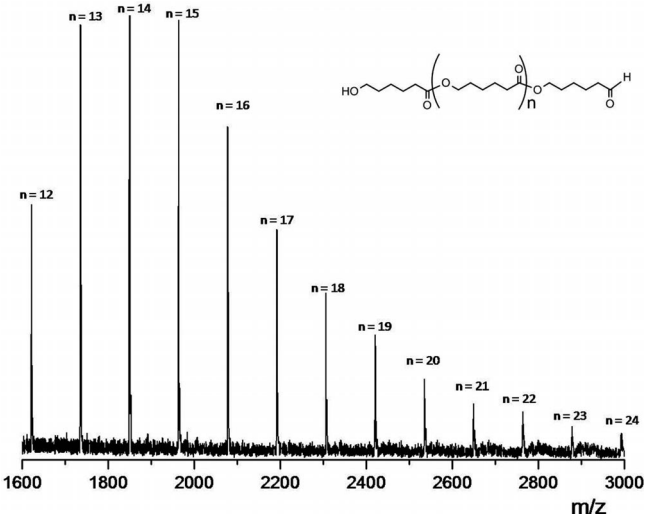

Figure 4. MALDI-TOF mass spectrum of a low-molecular-weight PCL having a number average molecular weight M_n of 2000 g mol^{-1}, prepared with ε-CL/[Nb(η^5-$C_5H_4SiMe_3)_2(H)_3$] in relative amounts of 20:1 (90% conversion).

to just one ε-CL unit ($C_6H_{10}O_2$), and the series can be assigned to the linear polymer H[O($CH_2)_5$CO]$_m$H associated with Na^+. The match between experimental and simulated isotopic patterns of the peaks confirms the expected well-defined structure. As an example, the peak at 1848.85 Da ([M + Na]$^+$) corresponds to a polymer with ε-CL as the repeating unit bearing formyl and hydroxy groups with m = 16. The absence of other peaks rules out the formation of other polymers such as carboxyl end-group polymers or those from intramolecular transesterification reactions (back-biting reactions).

Conclusions

The second example of an X-ray molecular structure of a polyhydridoniobocene complex, namely [Nb(η5-$C_5H_4SiMe_3)_2(H)_3$], has been described. On the basis of the values found for the H–H distances, a "compressed hydride" nature for this complex may be postulated. Additionally, this complex has been employed as a precursor to an initiator for the ROP of ε-CL and δ-VL. End-group analysis by MALDI-TOF MS suggests that the polymerization proceeds through a coordination–insertion mechanism based on cleavage of the ring between the oxygen atom and the acyl carbon atom. Further studies are underway aimed at thoroughly examining the effects that changes in both metal center and the substituents of the ligand framework have on the polymerization behavior of complexes. The synthesis of new polyester architectures is also under investigation.

Experimental Section

General Procedures: All reactions were performed by using standard Schlenk techniques under an atmosphere of dry nitrogen. Solvents were distilled from appropriate drying agents and degassed before use. [Nb(η5-$C_5H_4SiMe_3)_2(H)_3$] was prepared according to a literature procedure.[2] Lactones were dried by stirring over fresh CaH_2 for 48 h, then distilled under reduced pressure, and stored over activated 4 Å molecular sieves.

General Procedure for Polymerization: Polymerizations of lactones were carried out on a Schlenk line in a flame-dried round-bottomed flask equipped with a magnetic stirrer. In a typical procedure, the initiator was dissolved in the appropriate amount of solvent and temperature equilibration was ensured. The solution was stirred for 15 min at the appropriate temperature. Lactone was injected, and polymerization times were measured from that point. Polymerizations were terminated by addition of acetic acid (5 vol.-%) in methanol. Polymers were precipitated in methanol, filtered, washed with methanol, and dried in vacuo to constant weight.

Polymerization Kinetics: Lactone polymerization kinetic experiments were carried out at 60 °C by using stock solutions of the reagents. Specifically, at appropriate time intervals, aliquots were removed with a syringe and quickly quenched in 1 mL vials containing undried $CDCl_3$ (0.6 mL). The quenched aliquots were analyzed by ^1H NMR spectroscopy. For ε-CL polymerization, the $[CL]_0/[CL]_t$ ratio was determined by integration of the peaks for ε-CL (4.2 ppm for the OCH_2 signal) and PCL (4.0 ppm for OCH_2 signal) according to the equation $[CL]_0/[CL]_t$ $(A_{4.2} + A_{4.0})/A_{4.2}$. For δ-VL polymerization, the $[VL]_0/[VL]_t$ ratio was determined by integration of the peaks for δ-VL (4.4 ppm for the OCH_2 signal) and PCL (4.1 ppm for OCH_2 signal) according to the equation $[VL]_0/[VL]_t$ $(A_{4.4}+ A_{4.1})/A_{4.4}$. Apparent rate constants were extracted from the slopes of the best-fit lines to the plots of $\ln([M]_0/[M]_t)$ against time.

Polymer Characterization: GPC measurements were performed with a Polymer Laboratories PL-GPC-220 instrument equipped with a TSK-GEL G3000H column and an ELSD-LTII light-scattering detector. The GPC column was eluted with THF at 45 °C at 1 mL min^{-1} and was calibrated with eight monodisperse polystyrene standards in the range 580–483000 Da. The MALDI-TOF spectra were acquired with a Bruker Autoflex II TOF/TOF spectrometer using DCTB as matrix and NaI as the cationization agent. Samples cocrystallized with the matrix in a ratio of 100:1:1 (matrix/sample/NaI) on the probe were ionized in the positive reflector mode. External calibration was performed by using Peptide Calibration Standard II (covered mass range: 700–3200 Da) and Protein Calibration Standard I (covered mass range: 5000–17500 Da).

X-ray Crystallographic Structure Determination

Single crystals suitable for crystallographic analysis were obtained from a saturated solution of **1** in deoxygenated EtOH solvent at 298 K. The crystals were mounted on a glass fiber and transferred to a Nonius-Mach3 four-circle diffractometer, equipped with graphite-monochromated Mo-K_α (0.71073 Å) radiation, and analyzed by using the $\omega/2\theta$ scan-technique at 153 K. Unit-cell parameters were determined from automatic centering of 25 reflections ($12° < \theta < 21°$) and refined by least-squares methods. During the data collection, three standard reflections were measured every two hours as orientation and intensity control, significant intensity decay was not observed. No absorption correction was made. Crystallographic details are summarized in Table 3.

Table 3. Crystal data and refinement details for **1**.

Empirical formula	$C_{16}H_{29}NbSi_2$
Formula weight	370.48
Temperature (K)	153(2)
Wavelength (Å)	0.71073
Crystal system, space group	Monoclinic, $P2_1/c$
a (Å)	12.050(1)
b (Å)	13.185(1)
c (Å)	13.041(1)
α (°)	90
β (°)	113.60(1)
γ (°)	90
Volume (Å^3)	1898.7(3)
Z	4
Calculated density (Mg m^{-3})	1.296
Absorption coefficient (mm^{-1})	0.748
F(000)	776
Crystal size (mm)	$0.35 \times 0.28 \times 0.23$
Theta range for data collection (°)	2.30 to 28.02
Limiting indices	$-15 \le h \le 14$
	$0 \le k \le 17$
	$0 \le l \le 17$
Reflections collected/unique	4785/4589 [R(int) = 0.0130]
Completeness to θ = 28.02 (%)	99.6
Refinement method	Full-matrix least-squares on F^2
Data/restraints/parameters	4589/0/199
Goodness-of-fit on F^2	1.059
Final R indices [$I > 2\sigma(I)$]	$R1$ = 0.0276, $wR2$ = 0.0712
R indices (all data)	$R1$ = 0.0406, $wR2$ = 0.0760
Largest diff. peak and hole (e Å^{-3})	0.450 and –0.593

The structure was solved by direct methods, by using the SHELXS computer program,[26] and refined by full-matrix least-squares methods with the SHELX93 computer program.[27] All H atoms were computed and refined with an overall isotropic temperature factor using a riding model, except H1, H2, and H3, which were located in the difference electron density map and then refined.

CCDC-853313 contains the supplementary crystallographic data for this paper. These data can be obtained free of charge from The Cambridge Crystallographic Data Centre via www.ccdc.cam.ac.uk/data_request/cif.

Acknowledgments

We gratefully acknowledge financial support from the Ministerio de Ciencia e Innovación (MICINN), Spain (MCINN CTQ2009–09214/BQU and Consolider-Ingenio 2010 ORFEO CSD2007–00006), and the Junta de Comunidades de Castilla-La Mancha, Spain (PCI08–0032). Thanks are due to the Consejo Superior de Investigaciones Científicas (CSIC),, for the award of a license for the use of the Cambridge Crystallographic Database (CCD).

[1] M. Peruzzini, R. Poli, *Recent Advances in Hydride Chemistry*, Elsevier, Amsterdam, **2001**, p. 4.

[2] A. Antiñolo, B. Chaudret, G. Commenges, M. Fajardo, F. Jalón, R. H. Morris, A. Otero, C. T. Schweitzer, *J. Chem. Soc., Chem. Commun.* **1988**, 1210–1212.

[3] S. Camanyes, F. Maseras, M. Moreno, A. Lledós, J. M. Lluch, J. Bertrán, *J. Am. Chem. Soc.* **1996**, *118*, 4617–4621.

[4] A. Antiñolo, F. Carrillo-Hermosilla, M. Fajardo, J. Fernandez-Baeza, S. García-Yuste, A. Otero, S. Camanyes, F. Maseras, M. Moreno, A. Lledós, J. M. Lluch, *J. Am. Chem. Soc.* **1997**, *119*, 6107–6114.

[5] A. Antiñolo, F. Carrillo-Hermosilla, M. Fajardo, J. Fernandez-Baeza, S. García-Yuste, A. Otero, *Coord. Chem. Rev.* **1999**, *193–195*, 43–72.

[6] A. Antiñolo, F. Carrillo, S. García-Yuste, A. Otero, *Organometallics* **1994**, *13*, 2761–2766.

[7] A. Antiñolo, F. Carrillo-Hermosilla, B. Chaudret, M. Fajardo, J. Fernandez-Baeza, M. Lanfranchi, H. H. Limbach, M. Maurer, A. Otero, M. A. Pellinghelli, *Inorg. Chem.* **1996**, *35*, 7873–7881.

[8] A. Antiñolo, F. Carrillo-Hermosilla, J. Fernandez-Baeza, S. García-Yuste, A. Otero, A. M. Rodriguez, J. Sánchez-Prada, E. Villaseñor, M. Moreno, J. M. Lluch, A. Lledós, *Organometallics* **2000**, *19*, 3654–3663.

[9] A. Antiñolo, A. Otero, A. Lara-Sanchez, *Comprehensive Organometallic Chemistry III*, Elsevier, Oxford, UK, **2007**, vol. 5, p. 61.

[10] T. Keii, Y. Doi, *Shiyokubai Jpn.* **1979**, *21*, 32.

[11] a) S. W. Shalaby, K. J. L. Burg, *Absorbable and Biodegradable Polymers (Advances in Polymeric Materials)*, CRC Press, Boca Raton, **2003**; b) A. J. Domb, D. M. Wiseman, *Handbook of Biodegradable Polymers*, CRC Press, Boca Raton, **1998**.

[12] L. S. Nair, C. T. Laurencin, *Prog. Polym. Sci.* **2007**, *32*, 762–798.

[13] a) C. Jérôme, P. Lecomte, *Adv. Drug Delivery Rev.* **2008**, *60*, 1056–1076; b) C. L. Wanamaker, M. J. Bluemle, L. M. Pitet, L. E. O'Leary, W. B. Tolman, M. A. Hillmyer, *Biomacromolecules* **2009**, *10*, 2904–2911; c) D. Bourissou, S. Moebs-Sanchez, B. Martin-Vaca, *C. R. Chim.* **2007**, *10*, 775–794; d) S. F. Williams, D. P. Martin, *Biopolymers* (Eds.: A. Steinbüchel, Y. Doi), Wiley-VCH, Weinheim, **2002**, vol. 4, pp. 91–127.

[14] See selected reviews: a) M. K. Kiesewetter, E. J. Shin, J. L. Hedrick, R. M. Waymouth, *Macromolecules* **2010**, *43*, 2093–2107; b) C. M. Thomas, *Chem. Soc. Rev.* **2010**, *39*, 165–173; c) P. Dubois, O. Coulembier, J.-M. Raquez, *Handbook of Ring-Opening Polymerization*, Wiley-VCH, Weinheim, **2009**; d) A. P. Dove, *Chem. Commun.* **2008**, 6446–6470; e) J. Wu, T.-L. Yu, C.-T. Chen, C.-C. Lin, *Coord. Chem. Rev.* **2006**, *250*, 602–626; f) O. Dechy-Cabaret, B. Martin-Vaca, D. Bourissou, *Chem. Rev.* **2004**, *104*, 6147–6176; g) C. A. Wheaton, P. G. Hayes, B. J. Ireland, *Dalton Trans.* **2009**, 4832–4846.

[15] R. D. Wilson, T. F. Koetzle, D. W. Hart, A. Kwick, D. L. Tipton, R. Bau, *J. Am. Chem. Soc.* **1977**, *99*, 1775–1781.

[16] S. Camanyes, F. Maseras, M. Moreno, A. Lledós, J. M. Lluch, J. Bertrán, *Chem. Eur. J.* **1999**, *5*, 1166–1171.

[17] G. J. Kubas, *Chem. Rev.* **2007**, *107*, 4152–4205.

[18] Some representative examples: a) A. Otero, A. Lara-Sanchez, J. Fernandez-Baeza, C. Alonso-Moreno, M. I. Marquez-Segovia, J. A. Castro-Osma, L. F. Sanchez-Barba Merlo, A. M. Rodriguez, J. C. García-Martínez, *Organometallics* **2011**, *30*, 1507–1522; b) A. Otero, J. Fernandez-Baeza, A. Lara-Sanchez, C. Alonso-Moreno, M. I. Marquez-Segovia, L. F. Sanchez-Barba Merlo, A. M. Rodriguez, *Angew. Chem.* **2009**, *121*, 2210–2213; *Angew. Chem. Int. Ed.* **2009**, *48*, 2176–2179; c) L. F Sanchez-Barba Merlo, A. Garces Osado, J. Fernandez-Baeza, A. Otero, C. Alonso-Moreno, A. Lara-Sanchez, A. M. Rodriguez, *Organometallics* **2011**, *30*, 2775–2789.

[19] I. Barakat, P. Dubois, R. Jérôme, P. Teyssié, *J. Polym. Sci., Part A: Polym. Sci.* **1993**, *31*, 505–514.

[20] a) B. Chamberlain, M. Cheng, D. Moore, T. Ovitt, E. Lobkovsky, G. W. Coates, *J. Am. Chem. Soc.* **2001**, *123*, 3229–3238; b) C. Alonso-Moreno, A. Garces Osado, L. F. Sanchez-Barba Merlo, J. Fernandez-Baeza, A. Otero, A. Lara-Sanchez, A. Antiñolo, L. Broomfield, I. Lopez-Solera, *Organometallics* **2008**, *27*, 1310–1321.

[21] a) T. R. Jensen, C. P. Schaller, M. A. Hillmyer, W. B. Tolman, *J. Organomet. Chem.* **2005**, *690*, 5881–5891; b) M. H. Chisholm, J. C. Huffman, K. Phomphrai, *J. Chem. Soc., Dalton Trans.* **2001**, 222–224; c) M. Cheng, A. B. Attygalle, E. B. Lobkovsky, G. W. Coates, *J. Am. Chem. Soc.* **1999**, *121*, 11583–11584.

[22] D. Garlotta, *J. Polym. Environ.* **2001**, *9*, 63–84.

[23] A.-C. Albertsson, I. K. Varma, *Biomacromolecules* **2003**, *4*, 1466–1486.

[24] N. Barros, P. Mountford, S. M. Guillaume, L. Maron, *Chem. Eur. J.* **2008**, *14*, 5507–5518.

[25] N. K. Szymczak, D. R. Tyler, *Coord. Chem. Rev.* **2008**, *252*, 212–230.

[26] G. M. Sheldrick, *Acta Crystallogr., Sect. A* **1990**, *46*, 467–473.

[27] G. M. Sheldrick, *SHELX93: Program for Determination of Crystal Structure*, University of Göttingen, Germany, **1994**.

Received: November 11, 2011
Published Online: February 3, 2012

